

Electrochemical Passivation of Ni-Cr and Ni-Cr-Mo Alloys: The Fate of Alloying Elements and
Implications of Oxide Dopants and Defects Towards Passivation and Breakdown

A Dissertation

Presented to
the Faculty of the School of Engineering and Applied Science
University of Virginia

In Partial Fulfillment of the
Requirements for the Degree of

Doctor of Philosophy (Materials Science and Engineering)

by

Katie Lutton Cwalina

August 2019

Executive Summary

Ni-Cr-based alloys are regarded amongst the most corrosion resistant variety used in commercial and industrial applications. This benefit is due to the interaction of Mo alloyed in synergy with Cr and other minor elements (i.e. W). The role of Mo in stabilization and repassivation is understood, but its role in oxide formation and growth and dopant behavior is controversial. The exact atomistic mechanism by which electrochemical localized corrosion initiation is hindered or even prevented has, however, not been thoroughly studied. The first step towards achieving this understanding can be attained by a more comprehensive investigation of the role(s) of Mo and W in passive film formation and growth. Understanding the exact fate of alloying elements is also a challenge in multi-component alloys. The influence of Mo on growth rate and electronic doping of semiconducting passive films has similarly been limited in previous literature. The overall objectives of this thesis are to (1) establish an in operando electrochemical framework for investigating the kinetics of atomic scale aqueous passivation for multi-element alloys, (2) apply this framework in tandem with in-depth surface characterization in order to investigate the electrochemical passivation behavior of selected Ni-Cr and Ni-Cr-Mo alloys in acidic and alkaline sulfate and (3) chloride environments with more complex kinetic processes, (4) uncover the specific role of Mo dopants during Ni-Cr alloy passivation by promoting film growth and encouraging repassivation, and (5) demonstrate the influence of solute capture during fast electrochemical reactions on the electrochemical stability and electronic properties of passive films.

First, single frequency electrochemical impedance spectroscopy (SF-EIS) was applied for novel measurements of film growth during potentiostatic and galvanostatic polarization through analysis of an oxide as an electrical constant phase element. The unique application of online inductively coupled plasma-mass spectrometry (ICP-MS) for evaluation of element-specific contributions to dissolution and oxidation was also presented. From both of these techniques, the oxidation current density was extractable and more in-depth analysis yields the role of individual elements towards passivation or dissolution reaction kinetics. The material parameters required for broad and precise application of these techniques were additionally obtained for the alloys in additional sulfate and chloride-containing environments. The combination of methods enabled *in*

operando tracking of the total current densities for (i) oxidation, (ii) cation ejection by multiple paths, and (iii) oxide film growth during non-steady state passivation.

The electrochemical passivation behavior of selected Ni-Cr and Ni-Cr-Mo alloys were studied in acidic and alkaline sulfate media through application of the previously established techniques and the addition of surface science methods. Specifically, the influence of Cr and Mo alloying on passivity and the inhibition of localized film dissolution were probed using the *in operando* electrochemical techniques described above. Complementary *in situ* and *ex situ* analysis of chemical and atomic structure were conducted using polarized neutron reflectometry (PNR), atomic force microscopy (AFM), X-ray photoelectron spectroscopy (XPS), ellipsometry, and 3D atom probe tomography (3DAPT) to investigate the oxide composition, thickness, and morphology in detail, along with additional application of Mott-Schottky analysis to EIS data (MS-EIS) for indication of the variation of electronic properties during potentiostatic growth processes. The specific roles of pH and Mo on passivation kinetics are presented and the results provide an increased understanding of both thermodynamics and electronic factors on electrochemical measurements without the complication of chloride-assisted localized corrosion. The environment pH was found to have an impact on the relative chemical stability of Ni-Cr passive films but not noticeably for Ni-Cr-Mo ones. In addition, Mo was observed to act as an electronic dopant, increasing growth kinetics and modifying the concentration of point defects in oxides.

The initial understanding of Ni-Cr-Mo alloy passivation obtained for sulfate environments was extended to those containing chloride. There, localized corrosion was significantly increased via pitting, crevice corrosion, and general film dissolution assisted by chloride anion incorporation at the film/solution interface. In these environments, the influence of Mo was especially visible as it bolstered the resistance of films to such corrosion events and, upon their initiation, facilitated repassivation. The specific roles of pH and Mo during passivation and breakdown kinetics are highlighted, providing an insight into the fate of the elements which comprise the alloys, and their effects on passivation behavior. It was observed that early oxidation of both Ni and Cr-species occurred in the presence of acidic electrolyte. Preferential dissolution of Ni^{2+} at later times enabled gradual Cr^{3+} enrichment within the surface film. However, greater relative stability of NiO and $\text{Ni}(\text{OH})_2$ was observed in the alkaline condition. Upon alloying with Mo, Cr^{3+} became increasingly

enriched in the surface film during anodic polarization. Oxides were interpreted to consist of non-stoichiometric solid solutions formed via solute capture.

The specific role of Mo towards increasing an alloy and oxide's resistance to passive film breakdown initiation of localized corrosion and promoting repassivation at a constant potential in acidic, chloride-containing environments was studied in depth. The influence of increasing Mo concentrations on the chemical, physical, and electronic properties of the passive films grown were identified through additional application of similar techniques: DC electrochemistry including metastable pitting analysis, SF-EIS, XPS, and MS-EIS. The results provide an increased understanding of the influence Mo cations, when acting as substitutional dopants within a passive film, can have during several stages of passivity: nucleation, growth, breakdown, and repassivation. The 9 wt% Mo alloy yielded the optimal corrosion resistance and excessive doping can occur for higher Mo base alloy concentrations. This phenomena results in poor repassivation due to a decline in the surface enrichment of available, solute-captured $\text{Mo}^{4,6+}$ cations.

These findings concerning the role of alloying elements toward passivation processes were extended to examine specifically galvanostatic, or "rate-controlled", passive film growth and the implications of passivation kinetics and solute capture on the electrochemical stability, electronic properties, structure, and early breakdown initiation of passive films. This investigation into the implications of "fast" versus "slow" passive film growth utilized systematic investigation by galvanostatic SF-EIS and subsequent metastable pitting analysis, MS-EIS, XPS, and AFM. The effect of solute capture on modifying the composition and distribution of metal cations within the passive films, along with the beneficial effect of Mo capture in Ni-Cr-Mo compared to Cr in Ni-Cr are presented. It was found that the higher valency of Mo dopants enabled greater film resistivity to breakdown and enabled faster repassivation following any metastable events by inhibiting the diffusion of detrimental metal cation vacancies. Growth at slower rates produced films with segregation of Ni^{2+} and $\text{Mo}^{4,6+}$ to the film/electrolyte interface, leaving Cr^{3+} enriched at the metal/film interface.

This thesis contributed to the scientific understanding of the passivation mechanisms for Ni-based alloys in acidic and alkaline chloride-containing environments, and the additional influence of Mo as a minor alloying element on growth rate and ultimately the corrosion initiation process through its influence specifically on electrochemical stability, structure, and electronic

properties of electrochemically grown oxide films. This progress shed light on the precise alloying element attributes which enable passivity and their function in a solute capture-type, or conversely a phase-separated, oxide.

Acknowledgements

I would like to thank my advisor, Dr. John Scully, for first teaching me about corrosion and offering me a place as an undergraduate researcher back in 2013. I will be forever grateful for the countless opportunities he has provided. I am also especially grateful to my mentor and friend, Dr. Rebecca Schaller, for convincing me that I should stay at UVa for my PhD. She showed me what it meant to be an excellent scientist in and out of the lab. I would also like to thank and acknowledge the members of my thesis committee: Dr. Petra Reinke, Dr. James Fitz-Gerald, Dr. Patrick Hopkins, and Dr. Elizabeth Opila for their assistance with my research.

I am indebted to my many MURI collaborators at Northwestern University and the University of Wisconsin Madison for synthesizing materials used in this study, modeling various aspects of oxidation and passivation, and performing complicated and detailed microscopy for me. I would especially like to recognize the help Dr. Reinke and her students, Dr. Gopal Ramalingam, Cameron Volders, and William Blades, have given me regarding electronic properties of semiconducting films, XPS experiments, and data analysis. In addition, I would like to thank Dr. Nick Birbilis and Dr. Noemie Ott who assisted with the ICP-MS results presented in this thesis.

I appreciate the help and support of the students and faculty in the Center for Electrochemical Science and Engineering over the past few years. In particular, I would like to thank Kate Quiambao Tomko, Dr. Veronica Rafla, Lauren Singer, Ryan Katona, Lindsey Blohm, Dr. Michael Hutchison, Dr. Leslie Bland, and Dr. Raymond Santucci for their friendship and advice. I also would like to thank my non-MSE friends for their love and support over the years: Chelsea and Daniel Marlowe, Sharon Davis, Abbi Dobbertin, Gloria Duan, and Shelby Smith among many others. You all have made my otherwise boring life so incredibly fun and interesting.

Most of all, I would like to thank my family. My parents for not only always encouraging and supporting me, but for being such excellent role models. I also want to thank my adoptive family via my husband, for always being proud and reassuring. And to Tim, my biggest fan and would-have-been editor of this thesis— I couldn't have done any of this without you. I wish you were here to enjoy this next chapter. Thank you for supporting me through the many highs and lows during my eight years at UVa and for giving me the best dog children. This thesis is dedicated to you, Moose, and Chief.

Bibliography

The publications that resulted/will result from this dissertation and other relevant work are listed below:

1. K. Lutton, K. Gusieva, N. Ott, N. Birbilis, and J. R. Scully. (2017). Understanding multi-element alloy passivation in acidic solutions using operando methods. *Electrochemistry Communications*, 80(7), 44-47.
2. J. R. Scully, K. Lutton. (2018). Polarization Behavior of Active Passive Metals and Alloys, *Elsevier Encyclopedia of Interfacial Chemistry: Surface Science and Electrochemistry*, 6, 271-283.
3. K. Lutton, J. R. Scully. (2018). Kinetics of Oxide Growth of Passive Films on Transition Metals, *Elsevier Encyclopedia of Interfacial Chemistry: Surface Science and Electrochemistry*, 6, 284-209.
4. X. Yu, A. Gulec, Q. Sherman, K. Lutton Cwalina, J. R. Scully, J. H. Perepezko, P. W. Voorhees, L. D. Marks. (2018). Nonequilibrium solute capture in passivating oxide films, *Physics Review Letters*, 121(14), 145701.
5. K. Gusieva, K. Lutton Cwalina, W. H. Blades, G. Ramalingam, J. H. Perepezko, P. Reinke, J. R. Scully. (2018). Repassivation behavior of individual grain facets on dilute Ni-Cr and Ni-Cr-Mo alloys in acidified chloride solution, *Journal of Physics Chemistry C*, 122(34), 19499-19513.
6. K. Lutton Cwalina, A. Y. Gerard, C. R. Demarest, J. R. Scully. Revisiting the Effects of Molybdenum and Tungsten Alloying on Corrosion Behavior of Nickel-Chromium Alloys in Aqueous Corrosion. *Current Opinion in Solid State and Materials Science*. (2019).
7. X. Yu, A. Gulec, K. Lutton Cwalina, J. R. Scully, L. D. Marks. New insights on the role of chloride during the onset of local corrosion: TEM, APT, surface energy, and morphological instabilities. (2019). *CORROSION*. \
8. K. Lutton Cwalina, N. Ott, N. Birbilis, J. R. Scully. In Operando Analysis of Passive Film Growth on Ni-Cr and Ni-Cr-Mo Alloys in Chloride Solutions. (2019). *Journal of the Electrochemical Society*. 166(11), C3241-C3253.
9. L.F. Huang, H. M. Ha, K. Lutton Cwalina, J. R. Scully, J. M. Rondinelli, Understanding Electrochemical Stabilities of Ni-based nanofilms from a comparative theory-experiment approach. *To be submitted to ACS Nano*.
10. K. Lutton Cwalina, W. H. Blades, P. Reinke, J. R. Scully. The Influence of Chloride During Nanoscale Electrochemical Passivation Processes. *In Progress*.

Table of Contents

Executive Summary	i
Acknowledgements.....	v
Bibliography	vi
Table of Contents	vii
List of Figures	xvi
List of Tables	xl
1 Introduction	1
1.1 Motivation and Overview of Problem.....	1
1.2 General Corrosion Improvements via Minor Alloying Additions	2
1.3 Overview of Passivation by Alloying with Cr and Mo.....	3
1.4 Effect of Alloying on Polarization Behavior.....	5
1.5 Potential Step Passivation	6
1.6 Passive Film Growth Mechanism	8
1.7 Influence of Studying Passivation <i>In Operando</i> versus <i>Ex Situ</i> at Steady State Condition	9
1.8 Critical Unresolved Issues.....	9
1.8.1 In Operando Methods.....	9
1.8.2 Atomic Scale Understanding of Corrosion Processes Linked with Meso-Scale Behavior	10
1.8.3 Role of Mo and its Influence on Passive Film Chemistry and Properties: ...	10
1.8.4 Influence of Growth Rate on Corrosion and Passive Film Properties:	11
1.9 Research Objectives	11
1.10 Thesis Organization.....	12
1.11 References	14

1.12	Tables.....	20
1.13	Figures	22
2.	<i>In Operando</i> Measurement of Oxide Film Thickening: Application of Single Frequency Electrochemical Impedance Spectroscopy and Atomic Emission Spectroelectrochemistry.....	25
2.1	Abstract	25
2.2	Introduction	25
2.2.1	Impedance Theory.....	25
2.2.2	Single Frequency Electrochemical Impedance Spectroscopy (SF-EIS) Technique	28
2.2.3	Atomic Emission Spectroelectrochemical (AESEC) Theory.....	29
2.2.4	Application and Analysis of Online AESEC	31
2.3	Objective	32
2.4	Application of the SF-EIS Framework	33
2.4.1	Determination of $\alpha(t)$	33
2.4.1.1	Evolution of the Bode plot	34
2.4.2	Evolution of $Q(t)$ and $\alpha(t)$	35
2.4.3	Determination of $\rho\delta$	36
2.4.4	Application of Potentiostatic Single Frequency Electrochemical Impedance Spectroscopy (pSF-EIS).....	38
2.4.5	Application of Galvanostatic Single Frequency Electrochemical Impedance Spectroscopy (gSF-EIS).....	39
2.5	Discussion	40
2.6	Conclusions	43
2.7	References	43

2.8	Tables	48
2.9	Figures	49
3.	Potential-Controlled Passivation and Surface Characterization of Ni, Ni-Cr, and Ni-Cr-Mo – Part I. Sulfate Environments	68
3.1	Abstract	68
3.2	Collaborations	68
3.3	Introduction	69
3.3.1.1	Passivation in Sulfate Environments	69
3.3.1.2	Fundamental Roles of Alloying Additions in Ni-based Alloys	70
3.4	Objective	71
3.5	Experimental Methods	71
3.5.1.1	Materials	72
3.5.1.2	Fundamental Electrochemical Characterization	72
3.5.1.3	SF-EIS	73
3.5.1.4	ICP-MS	73
3.5.1.5	Mott-Schottky Impedance Analysis	74
3.5.1.6	X-ray Photoelectron Spectroscopy Analysis	76
3.5.1.7	Neutron Reflectometry	77
3.5.1.8	Atomic Force Microscopy	78
3.5.1.9	Three-Dimensional Atom Probe Tomography (3DAPT)	78
3.6	Results	79
3.6.1	Fundamental Electrochemistry of Ni-Alloys in Aqueous Sulfate Environments 79	
3.6.2	In Operando Passivation	80
3.6.2.1	AESEC in 0.1 M Na ₂ SO ₄	80

3.6.2.2	SF-EIS Application in Varying Environments	81
3.6.3	<i>In Situ</i> Characterization.....	82
3.6.3.1	Mott-Schottky Analysis.....	82
3.6.3.2	Neutron Reflectometry.....	83
3.6.3.3	<i>Ex situ</i> Characterization	84
3.6.3.4	Atomic Force Microscopy.....	84
3.6.3.5	XPS Analysis.....	86
3.6.3.6	3D Atom Probe Tomography.....	87
3.6.4	Film Breakdown Following Passivation.....	88
3.7	Discussion	88
3.7.1	Chemical Identity of the Passive Films.....	88
3.7.2	Electronic Properties of the Passive Films.....	90
3.8	Conclusions	91
3.9	References	91
3.10	Tables.....	96
3.11	Figures	97
4.	Potential-Controlled Passivation and Surface Characterization of Ni, Ni-Cr, and Ni-Cr-Mo – Part II. Chloride Environments	127
4.1	Abstract	127
4.2	Collaborations	127
4.3	Introduction	128
4.3.1	Influence of Chloride Chemisorption.....	128
4.3.2	Film Surface Roughness and Local Dissolution	129
4.3.3	Preferential Dissolution and Passive Film Composition.....	129

4.4	Objective	130
4.5	Experimental Methods	130
4.5.1	Materials.....	131
4.5.2	Fundamental Electrochemical Characterization.....	131
4.5.3	SF-EIS	132
4.5.4	ICP-MS.....	132
4.5.5	Mott-Schottky Analysis.....	133
4.5.6	X-ray Photoelectron Spectroscopy.....	133
4.5.7	Neutron Reflectometry.....	134
4.5.8	Atomic Force Microscopy.....	135
4.5.9	Three-Dimensional Atom Probe Tomography (3DAPT).....	136
4.6	Results	136
4.6.1	Fundamental Electrochemistry of Ni-Alloys in Aqueous Chloride Environments	136
4.6.2	<i>In Operando</i> Characterization.....	137
4.6.2.1	0.1 M NaCl pH 4.....	137
4.6.2.2	0.1 M NaCl pH 10.....	139
4.6.3	<i>In Situ</i> Characterization.....	141
4.6.3.1	Mott-Schottky Analysis.....	141
4.6.3.2	Neutron Reflectometry.....	142
4.6.4	<i>Ex situ</i> Characterization	144
4.6.4.1	Atomic Force Microscopy.....	144
4.6.4.2	X-ray Photoelectron Spectroscopy.....	146
4.6.4.3	3D Atom Probe Tomography.....	147

4.7	Discussion	149
4.7.1	Influence of Chloride and pH.....	149
4.7.2	Chemical Identity of Passive Films.....	151
4.7.3	Electronic Properties of Passive Films.....	152
4.8	Conclusions	153
4.9	References	153
4.10	Tables.....	160
4.11	Figures	161
5.	Understanding the Benefit(s) of Mo in a Ni-Cr Alloy: Linking Passivity to Localized Film Initiation and Breakdown in Acidic Environments.....	193
5.1	Abstract	193
5.2	Introduction	193
5.2.1	Phase-Separated Oxides, E-pH, and Speciation Diagrams	194
5.2.2	Observed Passive Films and Fate of Minor Alloying Elements	195
5.2.1	Mechanism for Localized Breakdown	198
5.2.2	Defect Chemistry with Minor Alloying Elements	199
5.2.3	Stabilization and Repassivation of Local Corrosion Sites	200
5.3	Objective	201
5.4	Approach	202
5.5	Experimental Methods	202
5.5.1	Materials.....	202
5.5.2	Fundamental Electrochemical Characterization.....	203
5.5.3	SF-EIS	203
5.5.4	Mott-Schottky Technique.....	204

5.5.5	Angle-Resolved X-ray Photoelectron Spectroscopy.....	204
5.5.6	Metastable Pit Event Analysis.....	205
5.6	Results.....	206
5.6.1	Fundamental Electrochemistry of Ni-Cr-Mo Alloys in Aqueous Chloride Environments	206
5.6.2	<i>In Operando</i> Characterization.....	206
5.6.3	Mott-Schottky Analysis.....	207
5.6.4	Angle-Resolved X-Ray Photoelectron Spectroscopy	208
5.6.5	Metastable Pitting Event Analysis	210
5.7	Discussion.....	211
5.7.1	Chemical Identity of Passive Films.....	211
5.7.2	Electronic Behavior of Passive Films	212
5.7.3	Influence of Mo.....	213
5.8	Conclusions.....	215
5.9	References.....	215
5.10	Tables.....	222
5.11	Figures.....	223
6.	Influence of Solute Capture Versus Phase Separation Produced by Fast and Slow Film Growth on Passivity, Electrochemical Stability, and Local Breakdown Events.....	252
6.1	Abstract.....	252
6.2	Collaborations	252
6.3	Introduction.....	252
6.3.1	Liquid to Solid Transformations and Solute Trapping.....	252
6.3.2	Solid to Solid Transformations and Non-Equilibrium Solute Capture	254
6.3.3	Implications of Non-Equilibrium Solute Capture for Material Properties..	256

6.4	Objective	258
6.5	Approach	258
6.6	Experimental Methods	259
6.6.1	Materials.....	259
6.6.2	gSF-EIS	260
6.6.3	Mott-Schottky Impedance Analysis	260
6.6.4	Atomic Force Microscopy Surface Imaging	260
6.6.5	Angle-Resolved X-ray Photoelectron Spectroscopy.....	261
6.6.6	Metastable Pitting Event Analysis	261
6.7	Results	262
6.7.1	Initial Assessment of Fast Versus Slow Passivation and Film Breakdown	262
6.7.2	<i>In Operando</i> Galvanostatic Passivation	263
6.7.3	Mott-Schottky Analysis of Passive Film Electronic Properties	264
6.7.4	Surface Topography Following Fast and Slow Passivation.....	265
6.7.5	Angle Resolved X-ray Photoelectron Spectroscopy	266
6.7.6	Metastable Pitting Event Analysis	268
6.8	Discussion	269
6.8.1	Role of Solute Capture on Film Chemical Composition.....	269
6.8.2	Effect of Cr Versus Mo Capture	271
6.8.3	Role of Solute Capture on Overall Electrochemical Performance.....	272
6.9	Conclusions	273
6.10	References	273
6.11	Tables.....	278
6.12	Figures	279

7.	Thesis Conclusions and Suggested Future Work.....	310
7.1	Conclusions	310
7.2	Future Work	313

List of Figures

- Figure 1.1. CALPHAD-calculated E-pH diagram for Inconel 600 (Ni-15.5 Cr-8 Fe, wt%) in 1 kg H₂O at 25°C and 1 atm. The red dashed lines are reversible potentials for hydrogen and oxygen evolutions, and the yellow dashed lines are the metal/aqueous ion equilibrium lines for pure constituent elements. The red region indicates where oxidized aqueous species are stable, green where Cr₂O₃ is stable, blue where Fe-Ni, Fe-Cr spinels are stable with some overlap with the green, and orange where oxides are stable^{95,96} 22
- Figure 1.2. Passive current density as a function of Fe-Cr alloy composition (wt%)⁹⁷.... 23
- Figure 1.3. Upward polarization curve of various Ni-based alloys, with their compositions given in wt%, in deaerated 0.1 M NaCl pH 4⁴⁷ 23
- Figure 1.4. Dependence of the anodic current density, *i*, at +200 mV_{OCP}, on the Mo content for Ni-22 Cr-x Mo, wt%, model alloys. Tests were performed in deaerated 1 M HCl solution at 22, 50, and 85°C with the calculated mass-transport-limited current density range, *ilim*, shown for comparison.⁴⁹ 24
- Figure 1.5. Localized corrosion breakdown potentials for various commercial Ni-Cr-Mo-W alloys as a function of temperature measured using galvanostatic polarization for up to 40 hr in 1 M NaCl solution where the shaded region corresponds to alloys with both high Cr and high Mo+W content³¹ 24
- Figure 2.1. General estimation of the relative inefficiencies (15.8% overall) of potentiostatic passivation for 72 ks at +0.2 V_{SCE} on Ni-22 Cr-6 Mo, wt%, in a relatively benign environment, 0.1 M Na₂SO₄ acidified to pH 4 using H₂SO₄. The black curve corresponds to the thickness computed by integrating under the total *iEC* and assuming 100% whereas for the red curve, EIS was applied during passivation to more accurately determine *lox*..... 49
- Figure 2.2. Graphical representation of complex impedance plane where quadrant IV corresponds to perfect resistors, capacitors, and constant phase elements and thus is most commonly used in electrochemistry 49
- Figure 2.3. Simulated impedance spectra for an RC parallel circuit via a) Nyquist plot and b) Bode plot for a perfect capacitor ($QCPE = 10 - 6 s\alpha \Omega - 1$ and $\alpha = 1.0$) and a constant phase element (CPE) ($QCPE = 10 - 6 s\alpha \Omega - 1$ and $\alpha = 0.75$) produced using Zview..... 50

Figure 2.4. Appearance of an impedance spectra as a result of nested time constants for two RC circuits in series with each other (shown in the inset) where each capacitive loop is indicated with the red curves	50
Figure 2.5. Functional block diagram of an ICP-AES system ¹⁷	51
Figure 2.6. Residence time distribution from an electrochemical flow cell following a 10 mA pulse applied to pure Cu in 1.2 M HCl and the Cu emission intensity was measured in response. Three measures were superimposed to show the reproducibility. The lag time, t_0 , is defined as the time between the initial pulse and the first point at which the signal rises above the background ($I\lambda_0$) A blowup of the onset near t_0 is shown in the inset. The residence time distribution, τ , is defined as the time between t_0 and the peak maximum. ¹⁷	52
Figure 2.7. Numerical model of the substance distribution (C) in mole m^{-3} from the electrode area following a 10^{-7} mole mass pulse for $3\text{ cm}^3\text{ min}^{-1}$ flow rate into the feed capillary after 3, 10, and 30 s (t_1 , t_2 , and t_3 respectively) ²⁸	53
Figure 2.8. Simulated residence time distribution τ (circles) and β (squares) parameters as a function of fe . The filled points show experimental measurements while the empty points give the simulated parameters ²⁸	54
Figure 2.9. Schematic of the relative dissolution and oxidation reactions occurring for a Ni-Cr-Mo alloy with the corresponding current densities indicated ⁶²	54
Figure 2.10. Schematic of the vertical three-electrode electrochemical cell used for various <i>in operando</i> and <i>in situ</i> characterization techniques, where a Pt mesh was used as the counter electrode and the reference was either a SCE or MMSE electrode for NaCl and Na ₂ SO ₄ electrolytes, respectively	55
Figure 2.11. Full spectrum EIS measured sequentially on Ni-22 Cr, wt%, in 0.1 M Na ₂ SO ₄ + H ₂ SO ₄ pH 4 over approximately 10 ks. Each scan iteration lasted on average 35 s and the first ten, along with the last, are shown and indicate the increase in the film impedance during the passivation process	55
Figure 2.12. Full spectrum EIS measured sequentially on Ni-22 Cr, wt%, in 0.1 M NaCl + HCl pH 4 over approximately 10 ks. Each scan iteration lasted on average 35 s and the first ten, along with the last, are shown and indicate the increase in the film impedance during the passivation process until film dissolution initiated after the 7 th scan (i.e. approximately 250 s). 56	56

Figure 2.13. Circuit model used to fit the CPE parameters Q and α and their evolution with time. 56

Figure 2.14. a) Q and b) α CPE parameters used in Equation 2.6 to calculate lox and measured as a function of time for various Ni-based alloys (wt%) passivated in 0.1 M Na₂SO₄ + H₂SO₄ pH 4 by fitting the sequential, full EIS spectra to a simple CPE in parallel with a resistor (Figure 2.13) 57

Figure 2.15. a) Q and b) α CPE parameters used in Equation 2.6 to calculate lox and measured as a function of time for various Ni-based alloys (wt%) passivated in 0.1 M NaCl + HCl pH 4 by fitting the sequential, full EIS spectra to a simple CPE in parallel with a resistor (Figure 2.13) 57

Figure 2.16. Schematic of potential-controlled passivation and resulting variations in current (I), oxide thickness (x), and imaginary impedance ($-Z''$) with time. 58

Figure 2.17. Equivalent circuit model used to fit EIS spectra and obtain α , given as a2 for the CPE Yo1, for application of Equation 2.6 using Gamry Echem Analyst..... 58

Figure 2.18. Comparison of the total $-Z''$ spectra of Ni-22% Cr-6% Mo, wt, after 10 ks of potentiostatic polarization at +0.2 V_{SCE} in 0.1 M NaCl pH 4 versus a ZView simulation using a simplified circuit fit containing only a constant phase element and a resistor with the same measured $QCPE$, α , and Rox from fitting the total spectra (Figure 2.17), as indicated in the inset model where the red outline indicates the oxide portion, demonstrating that using $-Z''$ at 1 Hz correlates to the oxide properties 59

Figure 2.19. Full spectrum EIS obtained following 10 ks of passivation at +0.2 V_{SCE} on various Ni-Cr-Mo alloys in 0.1 M Na₂SO₄ solution, where the chosen frequency for SF-EIS (1 Hz) is shown and suggests that Z_{phz} is near its maximum and between the two nested time constants corresponding to the oxide for all alloys..... 60

Figure 2.20. Film growth curves obtained on various Ni-based alloys during passivation at +0.2 V_{SCE} for up to 10 ks in 0.1 M Na₂SO₄ solution using $\alpha = 0.95$ in order to directly compare $-Z''$ and lox for all alloys using the same axes 61

Figure 2.21. Oxidation current density, iox , computed by applying Equation 2.7 to data in Figure 2.20 smoothed with a polynomial fit and compared to the iEC measured for each alloy to obtain η during the potentiostatic passivation at +0.2 V_{SCE} 61

Figure 2.22. Schematic of the expected evolution of potential and oxide thickness as a function of time during galvanostatic control conditions 62

Figure 2.23. *In situ* impedance measurements using fits of full EIS spectra (Figure 2.17 and Equation 2.2) to obtain lox during ordinary DC galvanostatic polarization of Ni-22 Cr-6 Mo at 30 $\mu\text{A}/\text{cm}^2$ in 0.1 M Na_2SO_4 acidified to pH 4 using H_2SO_4 63

Figure 2.24. Schematic of the variations in the imaginary impedance, $-Z''$, and lox as a function of $iapp$. Thinning via transpassive dissolution occurs at the same potentials as suggested in Figure 2.22, but vastly different times due to the direct proportionality between $iapp$ and $dloxdt$ 64

Figure 2.25. Potential changes during current-controlled passivation of Ni-22 Cr-6 Mo, wt%, at varying rates dictated by $iapp$ in 0.1 M Na_2SO_4 (pH 5.5). 64

Figure 2.26. Imaginary impedance, $-Z''$, variations measured during the current-controlled passivation shown in Figure 2.25 as a function of a) time and b) potential at 1 Hz and using $iAC = 5 \text{ nA}/\text{cm}^2$. The corresponding lox computed using Equation 2.6 is provided on the right y-axis. 65

Figure 2.27. Analysis of iox and the corresponding η for each applied galvanostatic passivation rate (Figure 2.26) according to Equation 2.11 and Equation 2.12. The curves are provided as a function of a,c) passivation time and b,d) potential to demonstrate their influence on the competition between oxidation and dissolution kinetics. 66

Figure 2.28. Electrochemical impedance spectra Bode plot of the impedance magnitude and phase following galvanostatic passivation at varying rates until a potential of +0.2 V_{SCE} was reached for Ni-22 Cr-6 Mo in deaerated 0.1 M Na_2SO_4 67

Figure 2.29. Comparison between $lox(t)$ on Ni-22 Cr-6 Mo (wt%) during 10 ks of potentiostatic SF-EIS passivation at +0.2 V_{SCE} in 0.1 M Na_2SO_4 pH 4 calculated using the fixed, steady-state α measured using a full EIS spectrum fit and $\alpha(t)$ given in Figure 2.14b 67

Figure 3.1. E-pH diagrams computed using OLI⁷⁶ for a generic Ni-Cr-Mo alloy exposed to 0.1 M Na_2SO_4 . The gray regions suggest regions of base metal immunity, whereas green and yellow indicate passivity and corrosion, respectively, for specific Ni, Cr, and Mo films. 97

Figure 3.2. EBSD diffraction patterns for the microstructures of the recrystallized a) Ni-22 Cr and b) Ni-22 Cr-6 Mo (wt%) alloys used in this dissertation 98

Figure 3.3. Schematic of the transition from cathodic bias (charge accumulation) to n-type (charge depletion) and p-type (inversion) behavior with increasing anodic bias during a Mott-Schottky potential sweep ⁷⁷ . Holes and electrons are indicated by green and yellow circles, respectively.	98
Figure 3.4. Schematic of the expected Mott-Schottky behavior in the accumulation, depletion, and inversion conditions ⁷⁷	99
Figure 3.5. Schematic of the angle-resolved XPS set-up and effect of sample tilting on the probe depth.....	99
Figure 3.6. Schematic of the <i>in situ</i> neutron reflectometry (NR) experiment at the D3 beamline in the NRL reactor.....	100
Figure 3.7. Schematic of the potential steps used during <i>in situ</i> neutron reflectometry experiments	100
Figure 3.8. Sample profile subtraction for passivated Ni-22 Cr-6 Mo, wt%, where SLD profiles for the unoxidized metal and the H ₂ O were subtracted from the experimental data in order to isolate the profile for the passive film. The same analysis method applied for all alloys and environments.....	101
Figure 3.9. a) DC current and b) AC impedance variations during upward potentiodynamic polarization of Ni-22 Cr and Ni-22 Cr-6 Mo, wt%, in deaerated 0.1 M Na ₂ SO ₄ at pH 4 and 10 with the potential used in this study (+0.2 V _{SCE}) indicated	102
Figure 3.10. Measured increase in $-Z''$ at 1 Hz during passivation of various Ni-alloys at +0.2 V _{SCE} in deaerated 0.1 M Na ₂ SO ₄ pH 4 for 72 ks with a subsequent full EIS spectrum obtained and fitted in order to compare <i>lox</i> for each method at the end of passivation time	103
Figure 3.11. Influence of electrolyte pH on the measured film thickness, η , computed using Equation 2.6 for Ni-22 Cr, wt%, in 0.1 M Na ₂ SO ₄	103
Figure 3.12. Influence of electrolyte pH on the measured <i>itot</i> and <i>iox</i> computed using the pSF-EIS results in Figure 3.11 and Equation 2.11, and the current efficiency, η , computed using Equation 2.12 for Ni-22 Cr, wt%, in 0.1 M Na ₂ SO ₄	104
Figure 3.13. Influence of electrolyte pH on the measured film thickness, <i>lox</i> , computed using Equation 2.6 for Ni-22 Cr-6 Mo, wt%, in 0.1 M Na ₂ SO ₄	105

Figure 3.14. Influence of electrolyte pH on the measured $itot$ and iox computed using the pSF-EIS results in Figure 3.13 and Equation 2.11, and the current efficiency, η , computed using Equation 2.12 for Ni-22 Cr-6% Mo, wt%, in 0.1 M Na ₂ SO ₄	105
Figure 3.15. Calculated ICP-MS current densities for cation emission versus total element specific current densities for congruent dissolution from Ni-22% Cr, wt%, held at +0.2 V _{SCE} in 0.1 M Na ₂ SO ₄ pH 5.5.....	106
Figure 3.16. Calculated ICP-MS current densities for cation emission versus total element specific current densities for congruent dissolution from Ni-22% Cr-6% Mo, wt%, held at +0.2 V _{SCE} in 0.1 M Na ₂ SO ₄ pH 5.5.....	106
Figure 3.17. Measured ICP-MS and SF-EIS total repassivation iEC , total dissolution current density, $idiss$, and oxide current density, iox for passivation at +0.2 V _{SCE} for Ni-22% Cr-6% Mo, wt%, in 0.1 M Na ₂ SO ₄ pH 5.5	107
Figure 3.18. Relative accumulation of metal cations in the passive films during growth until localized corrosion initiation at +0.2 V _{SCE} according to ICP-MS (lines) and XPS (symbols) measurements on Ni-22 Cr and Ni-22 Cr-6 Mo, wt%, in 0.1 M Na ₂ SO ₄ (pH 5.5) (ICP-MS) and 0.1 M Na ₂ SO ₄ pH 4 (XPS).....	107
Figure 3.19. Relative accumulation of metal cations in the passive films during growth until localized corrosion initiation at +0.2 V _{SCE} according to XPS measurements on Ni-22 Cr and Ni-22 Cr-6 Mo, wt%, in 0.1 M Na ₂ SO ₄ pH 10.....	108
Figure 3.20. Evolution of Mott-Schottky spectra with passivation time for a) Ni-22 Cr and b) Ni-22 Cr-6 Mo, wt%, passivated at +0.2 V _{SCE} for times up to 10,000 s in 0.1 M Na ₂ SO ₄ pH 4 where the potential sweeps were performed at 1,000 Hz	108
Figure 3.21. Evolution of Mott-Schottky spectra with passivation time for a) Ni-22 Cr and b) Ni-22 Cr-6 Mo, wt%, passivated at +0.2 V _{SCE} for times up to 10,000 s in 0.1 M Na ₂ SO ₄ pH 10 where the potential sweeps were performed at 1,000 Hz	109
Figure 3.22. Concentration of semiconductor n-type (N _D) and p-type (N _A) point defects during passivation, computed using Equation 3.3 and the data shown in Figure 3.20 and Figure 3.21 for Ni-22 Cr and Ni-22 Cr-6 Mo, wt%, passivated at +0.2 V _{SCE} for times up to 10,000 s in 0.1 M Na ₂ SO ₄ pH 4 and pH 10.....	109

Figure 3.23. Measured semiconductor flat band potentials for a) n-type and b) p-type behavior, computed using Equation 3.3 as indicated in Figure 3.4 for Ni-22 Cr and Ni-22 Cr-6 Mo, wt%, passivated at +0.2 V_{SCE} for times up to 10,000 s in 0.1 M Na₂SO₄ pH 4 and pH 10 (Figure 3.20 and Figure 3.21) 110

Figure 3.24. Measured reflectivity curves for a) Ni-20 Cr and b) Ni-20 Cr-10 Mo, wt%, oxidized in 0.1 M Na₂SO₄ pH 4 at various potential steps (Figure 3.7) from OCP, to -0.8 V_{SCE}, and up to +0.2 V_{SCE} in 200 mV steps every 6 hours where the NR measurements started 1 hr after the applied potential was switched to the set value and each measurement took approximately 90 min to complete..... 111

Figure 3.25. Full SLD profiles for a) Ni-20 Cr and b) Ni-20 Cr-10 Mo, wt%, oxidized in 0.1 M Na₂SO₄ pH 4 at various potential steps from OCP, to -0.8 V_{SCE}, and up to +0.2 V_{SCE} in 200 mV steps every 6 hours where the NR measurements started 1 hr after the applied potential was switched to the set value and each measurement took approximately 90 min to complete. SLD values for the expected species are given for different film compounds and the spectra, at low depths, corresponds to the electrolyte layer and at high depths, the alloy layer. 112

Figure 3.26. Simulated SLD profiles for a) a non-stoichiometric oxide, Ni_{1-x}Cr_xO, containing varying % Cr³⁺ and b) a bilayer oxide comprised of Cr₂O₃ and NiO with varying thicknesses of each conformal layer. An interfacial roughness of 5 Å was used to replicate the experimental parameter..... 113

Figure 3.27. Analysis of the NR profiles given in Figure 3.25 where a sample profile for the base metal exposed to water on a SiO₂ substrate was simulated and subtracted from the overall reflectometry curve in order to obtain that of just the passive film for a) Ni-20 Cr and b) Ni-20 Cr-10 Mo, wt%, in 0.1 M Na₂SO₄ pH 4 where the peak SLD correlates to the Cr³⁺ cation fraction and the approximate *lox* is indicated by the peak width 114

Figure 3.28. a) Metal cation fraction and b) passive film thickness computed from the peak SLD in Figure 3.27 for Ni-20 Cr and Ni-20 Cr-10 Mo, wt%, in 0.1 M Na₂SO₄ pH 4 oxidized at varying potentials..... 114

Figure 3.29. Topography images taken with AFM after 10, 100, 1,000, and 10,000 s of passivation of Ni-22 Cr, wt%, in 0.1 M Na₂SO₄ pH 4 with 500 nm² image insets. The insets are

representative of the area used to measure oxide height (Figure 3.30) and RMS surface roughness. All scale bars are 500 nm and the color bars in units of nm. 115

Figure 3.30. Line scans of the surface topography after exposure to 0.1 M Na₂SO₄ pH 4 where the red lines represent the bright protrusion of the electrochemically grown oxide, while the black lines represent the roughness of a fresh surface that has only been air-oxidized for the same amount of time. 115

Figure 3.31. Average root mean square (RMS) surface roughness computed for Ni-22 Cr, wt%, passivated at +0.2 V_{SCE} for various times in deaerated 0.1 M Na₂SO₄ pH 4. The RMS was calculated at various areas across the electrochemically oxidized surface to obtain the average RMS value and error bars. 116

Figure 3.32. Topography image taken with AFM after 10,000 s of passivation of Ni-22 Cr-6 Mo, wt%, in 0.1 M Na₂SO₄ pH 4 (RMS = 2.64 nm). The color bars in units of nm. 116

Figure 3.33. Focused, deconvoluted XPS spectra for a) Ni 2p^{3/2}, b) Cr 3p^{3/2}, c) Mo 3d, and d) O 1s bands collected on Ni-22 Cr-6 Mo, wt%, passivated at +0.2 V_{SCE} for 10,000 s in 0.1 M Na₂SO₄ pH 4 where the solid black and magenta lines indicate the Shirley background and overall fit to the spectra, respectively 117

Figure 3.34. a) Ni 2p^{3/2}, b) Cr 2p^{3/2}, and c) O 1s peaks normalized to the metal peaks for Ni-22 Cr, wt%, passivated at +0.2 V_{SCE} for various times up to 10 ks in 0.1 M Na₂SO₄ pH 4. 118

Figure 3.35. a) Ni 2p^{3/2}, b) Cr 2p^{3/2}, c) Mo 3d, and d) O 1s peaks normalized to the metal peaks for Ni-22 Cr-6 Mo, wt%, passivated at +0.2 V_{SCE} for various times up to 10 ks in 0.1 M Na₂SO₄ pH 4 119

Figure 3.36. a) Ni 2p^{3/2}, b) Cr 2p^{3/2}, and c) O 1s peaks normalized to the metal peaks for Ni-22 Cr, wt%, passivated at +0.2 V_{SCE} for various times up to 10 ks in 0.1 M Na₂SO₄ pH 10 120

Figure 3.37. a) Ni 2p^{3/2}, b) Cr 2p^{3/2}, c) Mo 3d, and d) O 1s peaks normalized to the metal peaks for Ni-22 Cr-6 Mo, wt%, passivated at +0.2 V_{SCE} for various times up to 10 ks in 0.1 M Na₂SO₄ pH 10 121

Figure 3.38. a,b) Ni 2p^{3/2} and c,d) Cr 2p^{3/2} angle-resolved XPS spectras which were normalized to the metal peaks for Ni-22 Cr, wt%, passivated at +0.2 V_{SCE} for various times up to 10 ks in 0.1 M Na₂SO₄ a,c) pH 4 and b,d) pH 10. The ratio of the oxide areas for each angle measurement is included for reference. 122

Figure 3.39. a) Ni 2p^{3/2}, b) Cr 2p^{3/2}, and c) Mo 3d angle-resolved XPS spectras which were normalized to the metal peaks for Ni-22 Cr-6 Mo, wt%, passivated at +0.2 V_{SCE} for various times up to 10 ks in 0.1 M Na₂SO₄ pH 4. The ratio of the oxide areas for each angle measurement is included for reference. 123

Figure 3.40. a) Ni 2p^{3/2}, b) Cr 2p^{3/2}, and c) Mo 3d angle-resolved XPS spectras which were normalized to the metal peaks for Ni-22 Cr-6 Mo, wt%, passivated at +0.2 V_{SCE} for various times up to 10 ks in 0.1 M Na₂SO₄ pH 10. The ratio of the oxide areas for each angle measurement is included for reference. 124

Figure 3.41. Film cation fraction according to angle-resolved XPS measurements at 90° and 45° on Ni-22 Cr and Ni-22 Cr-6 Mo, wt%, surfaces following 10 ks of potentiostatic passivation at +0.2 V_{SCE} in 0.1 M Na₂SO₄ at pH 4 and 10 125

Figure 3.42. APT result for Ni-22 Cr, wt%, with a 12 at% O isosurface corrected for detection efficiencies where the included 1D composition profile through the center of the tip shows the relative Cr-enrichment following a 10 ks exposure to 0.1 M Na₂SO₄ pH 4 + 1 mM K₂S₂O₈ (E_{OCP} = +0.2 V_{SCE})..... 125

Figure 3.43. APT result for Ni-22 Cr-6 Mo, wt%, with a 12 at% O isosurface corrected for detection efficiencies where the provided 1D composition profile through the center of the tip to show the enrichment of each species following a 10 ks exposure to 0.1 M Na₂SO₄ pH 4 + 1 mM K₂S₂O₈ (E_{OCP} = +0.2 V_{SCE})..... 126

Figure 3.44. Influence of 10 ks surface pretreatment in deaerated 0.1 M Na₂SO₄ pH 4 on the chemical stability and surface roughness of an electrochemically grown passive film that was sequentially exposed to deaerated 1.0 M NaCl pH 4 for 10 ks..... 126

Figure 4.1. Surface energy of NiO (111) following chemisorption of chloride anions in 0.1 and 0.001 M NaCl at varying pH's predicted using DFT⁴. The reference energy for the oxide in a chloride-free environment is given by the dashed line. 161

Figure 4.2. Comparison between metal-rich oxide and chloride DFT-predicted formation energies for different metals¹⁹ 161

Figure 4.3. Cohesive energy as a proxy descriptor for metal dissolution resistance, plotted against the oxide formation as a proxy for ease of passivation, based on various thermodynamic modeling approaches^{19,106,107} 162

Figure 4.4. Relationship between the wave vector wavelength of a surface perturbation, k , and the apparent surface roughness²⁰ where notably, small fluctuations at the metal/film interface significantly influence the observed oxide morphology 162

Figure 4.5. Local dissolution current, j_{diss} , and oxidation rate, σ , modeled for morphological instabilities of varying wavelengths corresponding to k . The resulting model of the perturbed potential across the peaks and troughs of the film/electrolyte interface is given, where the red line are equipotentials, meant to give an indication of the direction of the perturbed electric field, and at the troughs of the interface, the potential drop through the Helmholtz layer is increased. 163

Figure 4.6. Effect of increased chloride absorption on the surface energy and resulting oxidation and dissolution rates²⁰ 163

Figure 4.7. E-pH diagrams computed using OLI¹⁰⁸ for a generic Ni-Cr-Mo alloy exposed to 0.1 M NaCl. The gray regions suggest regions of base metal immunity, whereas green and yellow indicate passivity and corrosion, respectively, for specific Ni, Cr, and Mo films. 164

Figure 4.8. a) DC current and b) AC impedance variations during upward potentiodynamic polarization of Ni-22 Cr and Ni-22 Cr-6 Mo, wt%, in deaerated 0.1 M NaCl at pH 4 and 10 with the potential used in this study (+0.2 V_{SCE}) indicated 165

Figure 4.9. a) Calculated ICP-MS current densities for cation emission or dissolution versus the total element-specific current densities assuming congruent dissolution and b) ICP-MS and SF-EIS overall (iEC), total dissolution ($iICP$), and oxidation (iox) current densities along with calculated film growth (lox) during passivation of Ni-22 Cr, wt%, at +0.2 V_{SCE} in 0.1 M NaCl pH 4. Instantaneous DC currents had their time convoluted in order to put them on the same scale as ICP-MS measurements. 166

Figure 4.10. a) Calculated ICP-MS current densities for cation emission or dissolution versus the total element-specific current densities assuming congruent dissolution and b) ICP-MS and SF-EIS overall (iEC), total dissolution ($iICP$), and oxidation (iox) current densities along with calculated film growth (lox) during passivation of Ni-22 Cr-6 Mo, wt%, at +0.2 V_{SCE} in 0.1 M NaCl pH 4. Instantaneous DC currents had their time convoluted in order to put them on the same scale as ICP-MS measurements. 167

Figure 4.11. Relative accumulation of metal cations in the passive films during growth until localized corrosion initiation at +0.2 V_{SCE} according to ICP-MS (lines) and XPS (symbols, results obtained from Figure 4.32 and Figure 4.33) measurements on Ni-22 Cr and Ni-22 Cr-6 Mo, wt%, in 0.1 M NaCl pH 4 168

Figure 4.12. a) Calculated ICP-MS current densities for cation emission or dissolution versus the total element-specific current densities assuming congruent dissolution and b) ICP-MS and SF-EIS overall (*iEC*), total dissolution (*iICP*), and oxidation (*iox*) current densities along with calculated film growth (*lox*) during passivation of Ni-22 Cr, wt% at +0.2 V_{SCE} in 0.1 M NaCl pH 10. Instantaneous DC currents had their time convoluted in order to put them on the same scale as ICP-MS measurements. 169

Figure 4.13. a) Calculated ICP-MS current densities for cation emission or dissolution versus the total element-specific current densities assuming congruent dissolution and b) ICP-MS and SF-EIS overall (*iEC*), total dissolution (*iICP*), and oxidation (*iox*) current densities along with calculated film growth (*lox*) during passivation of Ni-22 Cr-6 Mo, wt% at +0.2 V_{SCE} in 0.1 M NaCl pH 10. Instantaneous DC currents had their time convoluted in order to put them on the same scale as ICP-MS measurements. 170

Figure 4.14. Relative accumulation of metal cations in the passive films during growth until localized corrosion initiation at +0.2 V_{SCE} according to ICP-MS (lines) and XPS (symbols) measurements on Ni-22 Cr and Ni-22 Cr-6 Mo, wt%, in 0.1 M NaCl pH 10 171

Figure 4.15. Evolution of Mott-Schottky spectra with passivation time for a) Ni-22 Cr and b) Ni-22 Cr-6 Mo, wt%, passivated at +0.2 V_{SCE} in 0.1 M NaCl pH 4 where the potential sweeps were performed at 1,000 Hz..... 171

Figure 4.16. Evolution of Mott-Schottky spectra with passivation time for a) Ni-22 Cr and b) Ni-22 Cr-6 Mo, wt%, passivated at +0.2 V_{SCE} in 0.1 M NaCl pH 10 where the potential sweeps were performed at 1,000 Hz..... 172

Figure 4.17. Concentration of n-type (N_D) and p-type (N_A) point defects during passivation, computed using Equation 3.3 and the data shown in Figure 4.15 and Figure 4.16 for Ni-22 Cr and Ni-22 Cr-6 Mo, wt%, passivated at +0.2 V_{SCE} for times up to 10,000 s in 0.1 M NaCl pH 4 and pH 10..... 173

Figure 4.18. Measured semiconductor flat band potentials, E_{FB} , for a) n-type and b) p-type behavior, computed using Equation 3.3 as indicated in Figure 3.3 for Ni-22 Cr and Ni-22 Cr-6 Mo, wt%, passivated at +0.2 V_{SCE} for times up to 10,000 s in 0.1 M NaCl pH 4 and pH 10 (Figure 4.15 and Figure 4.16) 173

Figure 4.19. Measured reflectivity curves for Ni-20 Cr and Ni-20 Cr-10 Mo, wt%, oxidized in 0.1 M NaCl pH 4 at various potential steps (Figure 3.5) from OCP, to -0.8 V_{SCE} , and up to +0.2 V_{SCE} in 200 mV steps every 6 hours where the NR measurements started 1 hr after the applied potential was switched to the set value and each measurement took approximately 90 min to complete 174

Figure 4.20. Measured reflectivity curves for Ni-20 Cr and Ni-20 Cr-10 Mo, wt%, oxidized in 0.1 M NaCl pH 10 at various potential steps (Figure 3.5) from OCP, to -0.8 V_{SCE} , and up to +0.2 V_{SCE} in 200 mV steps every 6 hours where the NR measurements started 1 hr after the applied potential was switched to the set value and each measurement took approximately 90 min to complete 175

Figure 4.21. Full SLD profiles for a) Ni-20% Cr and b) Ni-20% Cr-10% Mo, wt%, oxidized in 0.1 M NaCl pH 4 at various potential steps from OCP, to -0.8 V_{SCE} , and up to +0.2 V_{SCE} in 200 mV steps every 6 hours where the NR measurements started 1 hr after the applied potential was switched to the set value and each measurement took approximately 90 min to complete. SLD values for the expected species are given for different film compounds and the spectra, at low depths, corresponds to the electrolyte layer and at high depths, the alloy layer 176

Figure 4.22. Full SLD profiles for a) Ni-20% Cr and b) Ni-20% Cr-10% Mo, wt%, oxidized in 0.1 M NaCl pH 10 at various potential steps from OCP, to -0.8 V_{SCE} , and up to +0.2 V_{SCE} in 200 mV steps every 6 hours where the NR measurements started 1 hr after the applied potential was switched to the set value and each measurement took approximately 90 min to complete. SLD values for the expected species are given for different film compounds and the spectra, at low depths, corresponds to the electrolyte layer and at high depths, the alloy layer 176

Figure 4.23. Analysis of the NR profiles given in Figure 4.21 where a sample profile for the base metal exposed to water on a SiO_2 substrate was simulated and subtracted from the overall reflectometry curve in order to obtain that of just the passive film for a) Ni-20 Cr and b) Ni-20 Cr-

10 Mo, wt%, in 0.1 M NaCl pH 4 where the peak SLD correlates to the Ni²⁺ cation fraction and the approximate *lox* is indicated by the peak width 177

Figure 4.24. Analysis of the NR profiles given in Figure 4.22 where a sample profile for the base metal exposed to water on a SiO₂ substrate was simulated and subtracted from the overall reflectometry curve in order to obtain that of just the passive film for a) Ni-20 Cr and b) Ni-20 Cr-10 Mo, wt%, in 0.1 M NaCl pH 4 where the peak SLD correlates to the Ni²⁺ cation fraction and the approximate *lox* is indicated by the peak width 178

Figure 4.25. a) Metal cation fraction and b) passive film thickness computed from the peak SLD in Figure 4.23 for Ni-20 Cr and Ni-20 Cr-10 Mo, wt%, in 0.1 M NaCl pH 4 oxidized at varying potentials 178

Figure 4.26. a) Metal cation fraction and b) passive film thickness computed from the peak SLD in Figure 4.24 for Ni-20 Cr and Ni-20 Cr-10 Mo, wt%, in 0.1 M NaCl pH 10 oxidized at varying potentials 179

Figure 4.27. Topography images taken with AFM after 10, 100, 1,000, and 10,000 s of passivation of Ni-22 Cr, wt%, in 0.1 M NaCl pH 4 with 500 nm² image insets. The insets are representative of the area used to measure oxide height (Figure 4.28) and RMS surface roughness (Figure 4.29). All scale bars are 500 nm and the color bars in units of nm 179

Figure 4.28. Line scans of the surface topography after exposure to 0.1 M NaCl pH 4 where the red lines represent the bright protrusion of the electrochemically grown oxide, while the black lines represent the roughness of a fresh surface that has only been air-oxidized for the same amount of time 180

Figure 4.29. Average root mean square (RMS) surface roughness computed for Ni-22 Cr, wt%, passivated at +0.2 V_{SCE} for various times in deaerated 0.1 M NaCl pH 4. The RMS was calculated at various areas across the electrochemically oxidized surface to obtain the average RMS value and error bars. 181

Figure 4.30. Comparison of surface topography images taken with AFM after exposure of a) Ni-22 Cr-6 Mo (RMS = 1.36 nm) and b) Ni-22 Cr (RMS = 1.14 nm), wt%, to 0.1 M NaCl pH 4 for 1,000 s. The color bar is given in in units of nm 181

Figure 4.31. Focused, deconvoluted XPS spectra for a) Ni 2p^{3/2}, b) Cr 3p^{3/2}, c) Mo 3d, and d) O 1s bands collected on Ni-22 Cr-6 Mo, wt%, passivated at +0.2 V_{SCE} for 10,000 s in 0.1 M

NaCl pH 4 where the solid black and magenta lines indicate the Shirley background and overall fit to the spectra, respectively 182

Figure 4.32. XPS spectra using an Al- α source ($h\nu = 1,486.68$ eV) for a) Ni $2p^{3/2}$, b) Cr $2p^{3/2}$, and c) O 1s obtained at 12 kV with a 20 eV pass energy for Ni-22 wt% Cr, Shirley background-subtracted, normalized to the corresponding metallic peaks, and offset for clarity following passivation at $+0.2 V_{SCE}$ for up to 10 ks in deaerated 0.1 M NaCl pH 4 184

Figure 4.33. XPS spectra using an Al- α source ($h\nu = 1,486.68$ eV) for a) Ni $2p^{3/2}$, b) Cr $2p^{3/2}$, c) Mo 3d, and d) O 1s obtained at 12 kV with a 20 eV pass energy for Ni-22 Cr-6 Mo, wt%, Shirley background-subtracted, normalized to the corresponding metallic peaks, and offset for clarity following passivation at $+0.2 V_{SCE}$ for up to 10 ks in deaerated 0.1 M NaCl pH 4 185

Figure 4.34. XPS spectra using an Al- α source ($h\nu = 1,486.68$ eV) for a) Ni $2p^{3/2}$, b) Cr $2p^{3/2}$, and c) O 1s obtained at 15 kV with a 50 eV pass energy for Ni-22 wt% Cr, Shirley background-subtracted, normalized to the corresponding metallic peaks, and offset for clarity following passivation at $+0.2 V_{SCE}$ for up to 10 ks in deaerated 0.1 M NaCl pH 10 186

Figure 4.35. XPS spectra using an Al- α source ($h\nu = 1,486.68$ eV) for a) Ni $2p^{3/2}$, b) Cr $2p^{3/2}$, c) Mo 3d, and d) O 1s obtained at 15 kV with a 50 eV pass energy for Ni-22 Cr-6 Mo, wt%, Shirley background-subtracted, normalized to the corresponding metallic peaks, and offset for clarity following passivation at $+0.2 V_{SCE}$ for up to 10 ks in deaerated 0.1 M NaCl pH 10 187

Figure 4.36. a,b) Ni $2p^{3/2}$ and c,d) Cr $2p^{3/2}$ angle-resolved XPS spectras which were normalized to the metal peaks for Ni-22 Cr, wt%, passivated at $+0.2 V_{SCE}$ for 10 ks in 0.1 M NaCl a,c) pH 4 and b,d) pH 10. The ratio of the oxide areas for each angle measurement is included for reference..... 188

Figure 4.37. a) Ni $2p^{3/2}$, b) Cr $2p^{3/2}$, and c) Mo 3d angle-resolved XPS spectras which were normalized to the metal peaks for Ni-22 Cr-6 Mo, wt%, passivated at $+0.2 V_{SCE}$ for 10 ks in 0.1 M NaCl pH 4. The ratio of the oxide areas for each angle measurement is included for reference. 189

Figure 4.38. a) Ni $2p^{3/2}$, b) Cr $2p^{3/2}$, and c) Mo 3d angle-resolved XPS spectras which were normalized to the metal peaks for Ni-22 Cr-6 Mo, wt%, passivated at $+0.2 V_{SCE}$ for 10 ks in 0.1 M NaCl pH 10. The ratio of the oxide areas for each angle measurement is included for reference. 190

Figure 4.39. Film cation fraction according to angle-resolved XPS measurements at 90° and 45° on Ni-22 Cr and Ni-22 Cr-6 Mo, wt%, surfaces following 10 ks of potentiostatic passivation at +0.2 V _{SCE} in 0.1 M NaCl at pH 4 and 10.....	191
Figure 4.40. APT result for Ni-22 Cr, wt%, with a 10 at% O isosurface corrected for detection efficiencies where the included 1D composition profile through the center of the tip shows the relative Cr-enrichment following a 10 ks exposure to 0.1 M NaCl pH 4 + 1 mM H ₂ O ₂ (E _{OCP} = +0.2 V _{SCE}).....	191
Figure 4.41. Overall APT result for a Ni-22 Cr-6 Mo, wt%, tip oxidized for 10 ks in 0.1 M NaCl pH 4 + 1mM H ₂ O ₂ (E _{OCP} = +0.2 V _{SCE}) with a 5 at% O isosurface.....	192
Figure 4.42. a) Detailed chemical data for the oxide on Ni-22 Cr-6 Mo, wt%, for the APT results in Figure 4.41 including a b) 2D compositional line scan and c) a focus on the slight enrichment of Mo throughout the oxide thickness	192
Figure 5.1. Influence of Mo alloying additions on the passivity of Ni-Cr-Mo alloys during upward potentiodynamic polarization in deaerated 1 M HCl ⁶⁶	223
Figure 5.2. Current measured during potentiostatic passivation at +200 mV _{SCE} for various Ni-based alloys (wt%) in 0.1 M NaCl pH 4 where the initial decay indicates film growth, whereas the low concentration alloys exhibited abrupt current increases at longer times, indicative of localized pitting or crevice corrosion.....	223
Figure 5.3. Pourbaix diagrams computed using OLI ¹¹¹ for a generic Ni-Cr-Mo alloy exposed to 1.0 M NaCl. The gray regions suggest regions of base metal immunity, whereas green and yellow indicate passivity and corrosion, respectively, for specific, stoichiometric Ni, Cr, and Mo oxide films.....	224
Figure 5.4. Film composition of various commercial Ni-alloys measured using XPS following passivation at +305 mV _{SCE} for 3 d in aqueous 1.0 M NaCl pH 0 solution heated to 75°C ²⁷ . The analysis considered only stoichiometric, phase-separated oxides and hydroxides.	225
Figure 5.5. a) In situ TEM images of initial layer-by-layer growth of NiO on Ni-Cr-Mo surfaces at 700°C where the NiO island has {100} surfaces and the blue arrows show the layer-by-layer growth direction. For comparison, b) presents in situ TEM images showing Kirkendall voids (dotted circles) formed near the oxide-metal interface of the Ni-Cr alloy ⁴⁰	225

Figure 5.6. Comparison of the FCC-site oxygen absorption energy at 0.25 ML for the cases of the (111) alloy surfaces directly cut from the bulk and Mo-doped alloy surfaces with the relevant doped cases shown on the right⁴⁹ 226

Figure 5.7. Processes leading to the breakdown of passive films according to the Point Defect Model⁴ 226

Figure 5.8. Schematic of the production of a metal cation vacancy following chloride adsorption and the subsequent formation of an immobile complex upon interaction with a Mo dopant..... 227

Figure 5.9. Cross-sectional SEM images of the specimens after 500 h oxidation at 800°C in air: (a) Fe-22 Cr-0.5 Mn and (b) Fe-22 Cr-0.5 Mn-0.1 Mo, wt%⁴⁵ 227

Figure 5.10. EBSD images of the Ni-Cr-xMo alloys used in this chapter: a) Ni-22 Cr-3 Mo, b) Ni-22 Cr-5 Mo, c) Ni-22 Cr-9 Mo, and d) Ni-22 Cr-12 Mo, wt%. The average grain sizes for the alloys were computed to be, respectively, 7,830 μm^2 ; 5,063 μm^2 ; 4,490 μm^2 ; and 6,770 μm^2 . For reference, the stereographic triangle is inset..... 228

Figure 5.11. Example of a single metastable event showing the entire event above the background passive current, where the lifetime of the pit and its peak current are indicated⁶⁹. The peak integrated charge is determined above the baseline between the start and finish times for the event..... 229

Figure 5.12. Schematic of the metastable pit sizes that are able to be measured using the given data acquisition rate (20 Hz) and potentiostat sensitivity (approximately 1 nA) based on their elapsed time and peak currents 230

Figure 5.13. a) DC current and b) AC impedance variations during upward potentiodynamic polarization of Ni-22 Cr-x Mo, wt%, where x = 3, 6, 9, and 12 wt% in deaerated 1.0 M NaCl at pH 4 with the passivation potential used in this study (+0.2 V_{SCE}) indicated..... 231

Figure 5.14. a) Increases in $-Z''$ and the corresponding lox (Equation 2.16) and b) corresponding total electrochemical (iEC , solid line) and oxidation (iox , dashed line) (Equation 2.11) current densities along with the resulting current efficiencies (η , scatter) (Equation 2.12) for comparison during potentiostatic SF-EIS of Ni-22 Cr-x Mo, wt%, where x = 3, 6, 9, and 12 wt% in deaerated 1.0 M NaCl at pH 4 232

Figure 5.15. Evolution of Mott-Schottky spectra with passivation time for Ni-22 Cr-x Mo, wt%, alloys where x = a) 3 b) 6, c) 9, and d) 12 wt% Mo passivated at +0.2 V _{SCE} in 1.0 M NaCl pH 4 where the potential sweeps were performed at 1,000 Hz	233
Figure 5.16. Concentration of n-type (N _D) and p-type (N _A) point defects according to Mott-Schottky analysis of Figure 5.15 (Section 3.5.5)	233
Figure 5.17. a) p-type and b) n-type semiconductor flat band potentials according to Mott-Schottky analysis of Figure 5.15 (Section 3.5.5)	234
Figure 5.18. Schematic of the effect of n-type and p-type dopants on the band gap structure in a semiconductor	235
Figure 5.19. XPS spectra obtained at 90° using an Al-k α source (hv = 1,486.68 eV) for a) Ni 2p ^{3/2} , b) Cr 2p ^{3/2} , c) Mo 3d, and d) O 1s obtained at 15 kV with a 50 eV pass energy for Ni-22 Cr-3 Mo, wt%, Shirley background-subtracted, normalized to the corresponding metallic peaks, and offset for clarity following passivation at +0.2 V _{SCE} for up to 10 ks in deaerated 1.0 M NaCl pH 4.....	236
Figure 5.20. XPS spectra obtained at 90° using an Al-k α source (hv = 1,486.68 eV) for a) Ni 2p ^{3/2} , b) Cr 2p ^{3/2} , c) Mo 3d, and d) O 1s obtained at 15 kV with a 50 eV pass energy for Ni-22 Cr-6 Mo, wt%, Shirley background-subtracted, normalized to the corresponding metallic peaks, and offset for clarity following passivation at +0.2 V _{SCE} for up to 10 ks in deaerated 1.0 M NaCl pH 4.....	237
Figure 5.21. XPS spectra obtained at 90° using an Al-k α source (hv = 1,486.68 eV) for a) Ni 2p ^{3/2} , b) Cr 2p ^{3/2} , c) Mo 3d, and d) O 1s obtained at 15 kV with a 50 eV pass energy for Ni-22 Cr-9 Mo, wt%, Shirley background-subtracted, normalized to the corresponding metallic peaks, and offset for clarity following passivation at +0.2 V _{SCE} for up to 10 ks in deaerated 1.0 M NaCl pH 4.....	238
Figure 5.22. XPS spectra obtained at 90° using an Al-k α source (hv = 1,486.68 eV) for a) Ni 2p ^{3/2} , b) Cr 2p ^{3/2} , c) Mo 3d, and d) O 1s obtained at 15 kV with a 50 eV pass energy for Ni-22 Cr-12 Mo, wt%, Shirley background-subtracted, normalized to the corresponding metallic peaks, and offset for clarity following passivation at +0.2 V _{SCE} for up to 10 ks in deaerated 1.0 M NaCl pH 4.....	239

Figure 5.23. Relative accumulation of metal cations in the passive films during growth until localized corrosion initiation at +0.2 V _{SCE} according to XPS measurements on Ni-22 Cr-x Mo where x = a) 3, 6 and b) 9, 12, wt%, in 1.0 M NaCl pH 4	240
Figure 5.24. a) Ni 2p ^{3/2} , b) Cr 2p ^{3/2} , and c) Mo 3d angle-resolved XPS spectras obtained at 45° which were normalized to the metal peaks for Ni-22 Cr-3 Mo, wt%, passivated at +0.2 V _{SCE} for 10 ks in 1.0 M NaCl pH 4. The ratio of the oxide areas for each angle measurement is included for reference.	241
Figure 5.25. a) Ni 2p ^{3/2} , b) Cr 2p ^{3/2} , and c) Mo 3d angle-resolved XPS spectras obtained at 45° which were normalized to the metal peaks for Ni-22 Cr-6 Mo, wt%, passivated at +0.2 V _{SCE} for 10 ks in 1.0 M NaCl pH 4. The ratio of the oxide areas for each angle measurement is included for reference.	242
Figure 5.26. a) Ni 2p ^{3/2} , b) Cr 2p ^{3/2} , and c) Mo 3d angle-resolved XPS spectras obtained at 45° which were normalized to the metal peaks for Ni-22 Cr-9 Mo, wt%, passivated at +0.2 V _{SCE} for 10 ks in 1.0 M NaCl pH 4. The ratio of the oxide areas for each angle measurement is included for reference.	243
Figure 5.27. a) Ni 2p ^{3/2} , b) Cr 2p ^{3/2} , and c) Mo 3d angle-resolved XPS spectras obtained at 45° which were normalized to the metal peaks for Ni-22 Cr-12 Mo, wt%, passivated at +0.2 V _{SCE} for 10 ks in 1.0 M NaCl pH 4. The ratio of the oxide areas for each angle measurement is included for reference.	244
Figure 5.28. Film cation fraction according to angle-resolved XPS measurements at 90° and 45° on Ni-22 Cr-x Mo where x = 3, 6, 9, 12, wt%, surfaces following 10 ks of potentiostatic passivation at +0.2 V _{SCE} in 1.0 M NaCl pH 4.....	245
Figure 5.29. Metastable activity for the film on Ni-22 Cr-3 Mo, wt%, during passivation at +0.2 V _{SCE} for 10 ks in deaerated 1.0 M NaCl pH 4. Runs 1-3 remained passive following the observed localized breakdown events, whereas some crevice corrosion occurred during run 4 until repassivation around 4 ks occurred.....	246
Figure 5.30. Metastable activity for the film on Ni-22 Cr-12 Mo, wt%, during passivation at +0.2 V _{SCE} for 10 ks in deaerated 1.0 M NaCl pH 4.....	247
Figure 5.31. Comparison of the passivity of Ni-22 Cr-x Mo where x = 3, 6, 9, 12, wt%, at +0.2 V _{SCE} for 10 ks in deaerated 1.0 M NaCl pH 4.....	247

Figure 5.32. Focused Figure 5.31 over 1,000 to 1,200 s following the initial, often rapid film breakdown where characteristic individual metastable pitting events for each alloy can be observed 248

Figure 5.33. Comparison between the cumulative a) number, b) rate, and c) charge of metastable pitting events and the corresponding damaged area fraction relative to the total exposed one (0.1 cm²) following passivation of Ni-22 Cr-x Mo where x = 3, 6, 9, 12, wt%, at +0.2 V_{SCE} for 10 ks in 1.0 M NaCl pH 4 (Figure 5.31)..... 249

Figure 5.34. Cumulative probability plots of metastable peak a) current heights and b) integrated charge of events following passivation of Ni-22 Cr-x Mo where x = 3, 6, 9, 12, wt%, at +0.2 V_{SCE} for 10 ks in 1.0 M NaCl pH 4 (Figure 5.31 and Figure 5.33)..... 250

Figure 5.35. Average final cumulative number of metastable pitting events and charge during a +0.2 V_{SCE} hold for 10 ks on Ni-22 Cr-x Mo, wt%, where x = 3, 6, 9, and 12 wt% Mo, in deaerated, 1.0 M NaCl pH 4. 250

Figure 5.36. Schematic of the passive film composition evolutions with increasing concentrations of Mo within the bulk alloy. Both the fraction of solute captured Cr³⁺ and Moⁿ⁺ increase with [Mo], but some clustering of local Mo-oxides can occur at higher concentrations and produce local precipitates, indicated by the dark regions within the film. 251

Figure 6.1. Schematic of the influence of the temperature gradient, G, and growth rate, R, on the resulting microstructure following L-S transformation of a metal⁶⁸..... 279

Figure 6.2. Plot of the free energy for the different possible crystallographic phases in J/mol as a function of Cr composition assuming that the valences are always Ni²⁺ and Cr³⁺ with the oxygen content adjusted to achieve valence neutrality as appropriate. Points are from DFT calculations and lines are from a thermodynamic database, both computed using an atmosphere of 700°C and log(pO₂) = -1.56.¹⁸ 279

Figure 6.3. Sample phase diagram of Cr₂O₃-NiO computed using fundamental thermodynamics and CALPHAD software⁶⁹ 280

Figure 6.4. Relationship between the measurable electrochemical rate, i, and the effective velocity, *v_{eff}*, of various electrochemical phenomena of various length scales from thin film dissolution at steady-state, *i_{corr}*, to the accelerated dissolution found during the propagation of

corrosion pits. Based on an estimated vD of $10 - 6 \text{ nms}$, NSC is predicted to occur for the majority of electrochemical processes due to the rapidly moving oxide interfaces.¹⁸ 280

Figure 6.5. Plot of the kinetic conditions for solute capture during oxidation using kinetics based upon literature diffusion constants and reaction rates as a function of exposure temperature and pO_2 in atmospheres where $lox = 5 \text{ nm}$ and $a = 1 \text{ nm}$ is assumed..... 281

Figure 6.6. Simulation of the oxidation and diffusion velocity ratios for a) various applied electric field strengths at room temperature and b) various solution temperatures at a constant field strength assuming $a = 1 \text{ nm}$ where $\log v_{eff} v d > 0$ indicates NSC as $\beta > 1$ 281

Figure 6.7. TEM diffraction patterns of Ni-20% Cr, wt%, oxidized in dry air for 1 min at 600°C (left) and subsequent annealing steps in either vacuum at 650°C for 2 hr (center) or in air for 650°C for 2 hr³¹ 282

Figure 6.8. Chemical data for the oxide on Ni-22% Cr-6% Mo, wt%, chemically oxidized in $0.1 \text{ M Na}_2\text{SO}_4 \text{ pH } 4 + \text{K}_2\text{S}_2\text{O}_8$ ($V_{OCP} = +0.2 \text{ V}_{SCE}$) for 10 ks. A) High-angle annular dark field (left) and bright field (right) images with b) EELS line scan composition profile. C) 3DAPT tomography with a 12 at.% O isosurface and b) a compositional line scan corrected for the oxygen detection efficiency.¹⁸ The 3DAPT results (c,d) were previously shown in Figure 3.30. 282

Figure 6.9. TEM diffraction patterns of the metal/oxide interface of Ni-22%Cr-6% Mo, wt%, initially oxidized at 800°C for 24 hr in air with two fresh TEM samples prepared a year apart¹⁸ 283

Figure 6.10. Schematic illustration of Al-doping effects on the equilibrium defect chemistry cuprite (Cu_2O) electronic properties for a) intrinsic defects compared to b) Al-doped³⁵ 283

Figure 6.11. Approximate point defect carrier densities computed using Mott-Schottky analysis of the capacitive impedance behavior versus potential for cuprous (Cu_2O) passive films on Cu and Cu-Al alloys formed via NSC at open circuit in artificial perspiration solution³⁵ 284

Figure 6.12. Electrochemical breakdown in $0.1 \text{ M NaCl pH } 4$ of oxide scales formed in air on Ni-22 Cr, wt%, following exposure at room temperature air for 2 yr and heating at 100 and 200°C following polishing to 1200 grit using SiC papers. The oxidation times were selected to produce a similar oxide thickness ($\sim 5 \text{ nm}$)⁷⁰. While the areas were not the exact same, they were

similar enough so that the absolute current, I , for each sample can be compared relative to each other. 284

Figure 6.13. Comparison between the cumulative a) number, b) rate, and c) charge of metastable pitting events in deaerated 0.1 M NaCl pH 4 following air, 100 °C (6 hr), and 200 °C (1 min) oxidation of Ni-22 Cr, wt%, (Figure 6.12) 285

Figure 6.14. SF-EIS measurements of film thickening and thinning during galvanostatic passivation of Ni-22 Cr-6 Mo, wt%, at varying applied rates in 0.1 M NaCl pH 4. The results for the a) entire potential range and b) passive region only are indicated..... 286

Figure 6.15. Analysis of the a) oxidation current density, i_{ox} , and b) efficiency, η , for galvanostatic passivation within the passive region for Ni-22Cr-6 Mo, wt%, at varying rates in 0.1 M NaCl pH 4..... 287

Figure 6.16. Galvanostatic SF-EIS measurements at 1 Hz during the passivation at slow ($0.5 \mu\text{A}/\text{cm}^2$) and fast ($50 \mu\text{A}/\text{cm}^2$) rates of Ni-22 Cr and Ni-22Cr-6 Mo, wt%, in 0.1 M NaCl pH 4, shown for the passive region only 288

Figure 6.17. Analysis of the a) oxidation current density, i_{ox} , and b) efficiency, η , for galvanostatic passivation at slow ($0.5 \mu\text{A}/\text{cm}^2$) and fast ($50 \mu\text{A}/\text{cm}^2$) rates within the passive region of Ni-22 Cr and Ni-22 Cr-6 Mo, wt%, in 0.1 M NaCl pH 4..... 289

Figure 6.18. Mott-Schottky impedance sweeps at 1,000 Hz of Ni-22 Cr and Ni-22 Cr-6 Mo, wt%, following fast and slow galvanostatic passivation (Figure 6.16) in 0.1 M NaCl pH 4 290

Figure 6.19. Mott-Schottky impedance sweeps at 1,000 Hz of Ni-22 Cr Mo, wt%, following passivation at varying galvanostatic rates (Figure 6.14) up to +0.2 V_{SCE} in 0.1 M NaCl pH 4..... 290

Figure 6.20. Mott-Schottky analysis of the electronic character of passive films on Ni-22 Cr, wt%, formed at varying applied galvanostatic rates in 0.1 M NaCl H 4 (Figure 6.21) 291

Figure 6.21. Mott-Schottky impedance sweeps at 1,000 Hz of Ni-22 Cr-6 Mo, wt%, following passivation at varying galvanostatic rates (Figure 6.14) up to +0.2 V_{SCE} in 0.1 M NaCl pH 4..... 291

Figure 6.22. Mott-Schottky analysis of the electronic properties of passive films on Ni-22 Cr-6 Mo, wt%, formed at varying applied galvanostatic rates in 0.1 M NaCl H 4 (Figure 6.21)	292
Figure 6.23. Measured AFM topography images for Ni-22 Cr, wt%, immediately following a) fast ($i_{app} = 50 \mu\text{A}/\text{cm}^2$) and b) slow passivation ($i_{app} = 0.5 \mu\text{A}/\text{cm}^2$) in 0.1 M NaCl pH 4	293
Figure 6.24. Measured AFM topography images for Ni-22 Cr-6 Mo, wt%, immediately following a) fast ($i_{app} = 50 \mu\text{A}/\text{cm}^2$) and b) slow passivation ($i_{app} = 0.5 \mu\text{A}/\text{cm}^2$) in 0.1 M NaCl pH 4	294
Figure 6.25. a) Ni $2p^{3/2}$, b) Cr $2p^{3/2}$, and c) O 1s peaks obtained at 90° and normalized to the metal peaks for Ni-22 Cr, wt%, passivated at 0.5, 5, and $50 \mu\text{A}/\text{cm}^2$ until $+0.2 V_{SCE}$ was reached in 0.1 M NaCl pH 4	295
Figure 6.26. a) Ni $2p^{3/2}$, b) Cr $2p^{3/2}$, c) Mo 3d, and d) O 1s peaks obtained at 90° and normalized to the metal peaks for Ni-22 Cr-6 Mo, wt%, passivated at 0.5, 5, and $50 \mu\text{A}/\text{cm}^2$ until $+0.2 V_{SCE}$ was reached in 0.1 M NaCl pH 4	296
Figure 6.27. a) Ni $2p^{3/2}$ and b) Cr $2p^{3/2}$ peaks normalized to the metal peaks for Ni-22 Cr-6 Mo, wt%, passivated at 0.5, 5, and $50 \mu\text{A}/\text{cm}^2$ until $+0.2 V_{SCE}$ was reached in 0.1 M NaCl pH 4 measured at 45° . The ratio of the oxide areas for these measurements to those at 90° (Figure 6.25) are included for reference.	297
Figure 6.28. a) Ni $2p^{3/2}$, b) Cr $2p^{3/2}$, and c) Mo 3d peaks normalized to the metal peaks for Ni-22 Cr-6 Mo, wt%, passivated at 0.5, 5, and $50 \mu\text{A}/\text{cm}^2$ until $+0.2 V_{SCE}$ was reached in 0.1 M NaCl pH 4 measured at 45° . The ratio of the oxide areas for these measurements to those at 90° (Figure 6.26) are included for reference.	298
Figure 6.29. Film cation fraction according to angle-resolved XPS measurements at 90° and 45° on a) Ni-22 Cr and b) Ni-22 Cr-6 Mo, wt%, surfaces following galvanostatic passivation at 0.5, 5, and $50 \mu\text{A}/\text{cm}^2$ until $+0.2 V_{SCE}$ was reached in 0.1 M NaCl pH 4	299
Figure 6.30. Comparison of the passivity of Ni-22 Cr-6 Mo, wt%, ribbons at $+0.2 V_{SCE}$ for 10 ks immediately following slow oxidation at $0.5 \mu\text{A}/\text{cm}^2$ and fast oxidation at $50 \mu\text{A}/\text{cm}^2$ in deaerated 0.1 M NaCl pH 4	300

Figure 6.31. Comparison of the passivity of Ni-22Cr and Ni-22 Cr-6 Mo, wt%, ribbons at +0.2 V_{SCE} for 10 ks immediately following air oxidation for 1 yr, slow oxidation at 0.5 μA/cm², and fast oxidation at 50 μA/cm² in deaerated 0.1 M NaCl pH 4. Included are the results previously given in Figure 6.30. 300

Figure 6.32. Comparison between the cumulative a) number, b) rate, and c) charge of metastable pitting events and the corresponding damaged area fraction relative to the total exposed one (0.1 cm²) following air, slow (0.5 μA/cm²), and fast (50 μA/cm²) passivation of Ni-22 Cr and Ni-22 Cr-6 Mo, wt%, in 0.1 M NaCl pH 4 (Figure 6.31)..... 301

Figure 6.33. Metastable pitting events occurring for the passive films grown galvanostatically at various applied rates, *iDC*, up to +0.2 V_{SCE} on Ni-22 Cr, wt%, in 0.1 M NaCl pH 4..... 302

Figure 6.34. Focused metastable breakdown as given in Figure 6.33, for the passive films grown galvanostatically at various applied rates, *iDC*, up to +0.2 V_{SCE} on Ni-22 Cr, wt%, in 0.1 M NaCl pH 4 303

Figure 6.35. Comparison between the cumulative a) number, b) rate, and c) charge of metastable pitting events and the corresponding damaged area fraction relative to the total exposed one (0.1 cm²) following galvanostatic passivation at varying rates, given by *iDC*, of Ni-22 Cr, wt%, in 0.1 M NaCl pH 4 (Figure 6.33) 304

Figure 6.36. Cumulative probability plots of metastable peak a) current heights and b) integrated charge of events following galvanostatic passivation at varying rates, given by *iDC*, for Ni-22 Cr, wt%, in 0.1 M NaCl pH 4 (Figure 6.33 and Figure 6.35)..... 305

Figure 6.37. Metastable pitting events occurring for the passive films grown galvanostatically at various applied rates, *iDC*, up to +0.2 V_{SCE} on Ni-22 Cr-6 Mo, wt%, in 0.1 M NaCl pH 4 305

Figure 6.38. Focused metastable breakdown from 0.5 to 1.5 ks, as given in Figure 6.37, for the passive films grown galvanostatically at various applied rates, *iDC*, up to +0.2 V_{SCE} on Ni-22 Cr-6 Mo, wt%, in 0.1 M NaCl pH 4 306

Figure 6.39. Comparison between the cumulative a) number, b) rate, and c) charge of metastable pitting events and the corresponding damaged area fraction relative to the total exposed

one (0.1 cm^2) following galvanostatic passivation at varying rates, given by i_{DC} , of Ni-22 Cr-6 Mo, wt%, in 0.1 M NaCl pH 4 (Figure 6.37)..... 307

Figure 6.40. Cumulative probability plots of metastable peak a) current heights and b) integrated charge of events following galvanostatic passivation at varying rates, given by i_{DC} , for Ni-22 Cr-6 Mo, wt%, in 0.1 M NaCl pH 4 (Figure 6.37 and Figure 6.39)..... 308

Figure 6.41. Average final cumulative number of metastable pitting events and charge during a $+0.2 \text{ V}_{SCE}$ hold for 10 ks on Ni-22 Cr and Ni-22 Cr-6 Mo, wt%, following passivation at varying galvanostatic rates, i_{DC} , in 0.1 M NaCl pH 4 309

List of Tables

Table 1.1. Summary of the proposed roles of Mo as a minor alloying element present in literature	20
Table 1.2. Common commercial, low-temperature Ni-based alloys present in literature that are applicable for this review. Included are PREN values computed using Equation 1.1.....	21
Table 2.1. Constants used to compute lox from XPS spectra fitting results	48
Table 2.2. Computation of $\rho\delta$ using impedance and XPS spectra analysis following 10 ks passivation at +0.2 V_{SCE} for various alloys and environment combinations. The units for $\rho\delta$ and Z'' are $\Omega\text{-cm}$ and $\Omega\text{-cm}^2$, respectively. For reference, $\rho\delta\alpha - 1$ is also included to demonstrate the influence of this parameter on lox in Equation 2.6.	48
Table 3.1. Spectral fitting parameters used to fit XPS data and obtain film composition analysis based on previous literature ⁴⁰ where only three most prominent peaks were used	96
Table 4.1. Averaged oxidation efficiency (%) (Equation 2.12) computed for the results shown in Figure 4.9 - Figure 4.13) for Ni-22 Cr and Ni-22 Cr-6 Mo, wt%, passivated at +0.2 V_{SCE} in 0.1 M NaCl for 10,000 s with the pH adjusted to either 4 or 10	160
Table 5.1. Averaged oxidation efficiency (%) (Equation 2.12) computed for the results shown in Figure 5.14 for for Ni-22 Cr-x Mo where x = 3, 6, 9, 12, wt%, passivated at +0.2 V_{SCE} in 1.0 M NaCl pH 4 for 10,000 s	222
Table 6.1. Selected applied current densities and the corresponding passivation rate and β for the typically estimated $vD = 10 - 6$ nm/s obtained using Faraday's law and assuming 100% current efficiency	278
Table 6.2. Air oxidation conditions used in Figure 6.12 to achieve films approximately 5 nm in thickness with the estimated oxide growth velocity, vi , and corresponding β included to demonstrate the propensity for NSC.....	278
Table 6.3. Comparison of the semiconductor electronic behavior for Ni-22 Cr and Ni-22 Cr-6Mo, wt%, measured following galvanostatic grown at slow ($0.5 \mu\text{A}/\text{cm}^2$) and fast ($50 \mu\text{A}/\text{cm}^2$) applied currents.....	278
Table 6.4. Computed RMS from AFM topography images of passivated Ni-22 Cr and Ni-22 Cr-6 Mo, wt%, surface, as indicated in Figure 6.23 for various passivation rates	278

List of Symbols

a	Interatomic lattice spacing
A	Sample area
C	Capacitance
C_M	Concentration of element M
D	Atomic diffusivity
E_{app}	Applied potential
E_{fb}	Flat band potential
E_{pp}	Critical passivation potential
f	Applied frequency
f_e	Electrolyte flow rate
F	Faraday's constant
g	SF-EIS interpolation function
i	Current density
$i_{cong\ diss}^M$	Estimated congruent dissolution current for element M
i_{diss}	Total measured dissolution current density
i_{diss}^M	Dissolution current density for element M
i_{EC}	Total electrochemical current density
i_{ox}	Total oxidation current density
i_{ox}^M	Oxidation current density for element M
i_{pass}	Passive current density
I_m	Integrated metal photoelectron peak intensity
I_o	Integrated oxide photoelectron peak intensity
I_λ	Measured emission intensity of element M
I_λ^o	Background emission intensity
k	Proportionality constant
l_{ox}	Passive film thickness
M_M	Molar mass of element M
M_{ox}	Molar mass of oxide film
n	Molecular cation valency
N_a	Density of electron acceptors
N_A	Avogadro's number
N_d	Density of electron donors
N_m	Metal atom volume density in the metal phase
N_M	Atomic surface area density of element M
N_o	Metal atom volume density in the oxide phase
q	Electron elementary charge

q_{ox}	Total integrated oxidation charge
q_{ox}^M	Integrated oxidation charge of element M
Q_{CPE}	Constant phase element parameter
Q_{beam}	Reflectivity scattering vector
R	Resistance
t	Time
v_{diff}	Long-rate diffusive speed of solute
v_{diss}	Effective velocity of the dissolution front e.g. dissolution rate
v_{echem}	Net measured electrochemical reaction rate
v_{eff}	Total effective oxidation rate during electrochemical passivation
v_{int}	Overall solidification rate
V	Potential
z	Cation Valency
Z_C	Impedance of a capacitor
Z_{CPE}	Impedance of a constant phase element
Z_{imag}	Imaginary impedance component
Z_L	Impedance of an inductor
Z_{real}	Real impedance component
Z_R	Impedance of a resistor
Z''	Alternative way to express Z_{imag}
α	Constant phase element exponent
β	High field growth constant
B	Predictor of the likelihood for NSC to occur
ΔG_f^0	Standard Gibb's energy of fusion
ϵ	Dielectric constant
ϵ_0	Vacuum permittivity of free space
θ	Beam incident angle
θ_z	Phasor angle in the impedance plane
λ	Neutron beam wavelength
λ_m	Photoelectron inelastic mean free path in the metal
λ_o	Photoelectron inelastic mean free path in the oxide
μ_{solute}	Solute chemical potential
ρ_{ox}	Oxide density
ρ_δ	Boundary interfacial resistivity
τ	Time constant for a capacitor to discharge
ω	Angular frequency

1 Introduction

1.1 Motivation and Overview of Problem

Nickel and nickel-based alloys are the structural materials of choice in a variety of aggressive corrosive and high temperature environments. They are superior to stainless steels in terms of corrosion resistance and high temperature stability in certain environments which historically create vulnerabilities for stainless steels. These include strong, concentrated reducing acids and chloride-containing environments, and certain molten salts. There are various classes for nickel alloys, including many single phase, solid solution alloys such as Ni-Cu, Ni-Mo, Ni-Cr, Ni-Cr-Mo, Ni-Cr-Fe, and Ni-Cr¹. Ni-Cr and Ni-Cr-Mo solid solution alloys are particularly corrosion resistant in a number of natural and industrial environments². Ni-Cr alloys alloyed with increasing concentrations of Cr produce stable passive films that persist in harsh aqueous conditions³. A significant amount of literature has been developed for various applications, e.g. marine⁴, nuclear waste repositories⁵, and in environments of importance to the chemical process industry, such as concentrated HCl containing Fe³⁺ impurities⁶. These studies largely focus on dependencies associated with effects of alloying and structure in these select applications and environments.

Prior understandings of passivity generally fall into one of two broad categories: (i) improvements for alloys with a critical concentration of Cr plus minor amounts of Mo, combined with a homogeneous microstructure free of phases (which deplete beneficial alloying elements and interfere with passivity) and (ii) local corrosion (mainly crevice), stabilization, and repassivation at active corrosion sites. Most studies within the former category focus on compositional, electronic, and physical attributes of the oxide such as the passive film thickness and descriptions of passivating layers. For instance, Mo is thought to exist as Mo(IV) in inner layers while Mo(VI) is present in an outer, cation-selective layer on Fe-Cr-Mo alloys^{7,8}. Similar layering has been proposed for Ni-Cr-Mo alloys^{9,10}. In contrast, most studies concerning that latter alloy focus on critical temperature, critical potentials, crevice geometry, and dissolution rate parameters which indicate thresholds for crevice attack versus repassivation. These phenomena are associated with geometric crevice at the micrometer scale¹¹ and often consider how Mo affects these processes. This distinction is important because prior passivity studies have focused on benefits conferred within a nanometer oxide film while localized breakdown occurs by phenomena at active corrosion sites.

A gap in understanding exists because descriptions of oxide characteristics fall short of directly linking atomic scale details of how alloying elements such as Mo affect passivity and inhibit localized corrosion and film breakdown events within actual pits or crevices. Extensive research efforts have been expended in order to design commercial Ni-based alloys in order to resist corrosion¹². The process is often Edisonian, relying on trial-and-error or incremental advances in corrosion beyond CALPHAD¹³ and E-pH Pourbaix diagram¹⁴ predictions of the optimum concentrations of alloying elements necessary for a set of desired properties and design restrictions. The type of simplistic predictions of alloy stability in a given environment is provided in Figure 1.1 for a multi-element high entropy alloy based on the composition of commercial Ni-Cr-Mo alloys. Notably, only thermodynamics is accounted for in Pourbaix-type models whereas corrosion phenomena like localized corrosion – and somewhat passivity – are controlled by kinetic factors. Therefore, the passivity of oxides is complicated, especially when minor alloying elements come into play, and predicting any long-term stability necessitates a more advanced understanding of the passive film than what is given in Figure 1.1.

1.2 General Corrosion Improvements via Minor Alloying Additions

Stainless steel alloys are a well-understood material system with respect to the influence of minor alloying elements on corrosion initiation, and film repassivation^{15,16}. However, the precise effects of minor alloying elements in the passive stage are closely tied to those in the Ni-alloy system and are similarly unclear. From the framework of stainless steel corrosion and empirical data, the pitting resistance equivalent number (PREN) was developed to predict the susceptibility of an alloy as a function of its minor element concentration in aqueous chloride environments. For example, a PREN of 32 is widely considered the minimum for an alloy to exhibit pitting resistance in seawater environments but this minimum varies for different metallurgies¹⁷. The PREN (Equation 1.1) is based on empirical data concerning minor element alloying and is successful in many applications and for generic Fe- and Ni-based alloys:

$$\text{PREN} = [\text{Cr}] + 3.3 [\text{Mo}] + 0.5 [\text{W}] \quad \text{Equation 1.1}$$

When applied to carbon-supersaturated 316L austenitic stainless steel, an alloy which classically agrees with PREN predictions, the addition of low concentrations of B, Si, W, or even Y has been shown to instigate a dramatic increase in the alloy's corrosion resistance despite all

having the same PREN¹⁸. The dependence of corrosion predictions on empirical observations, rather than a specific atomistic understanding, has generated inaccurate results in other relevant applications. There are further shortcomings such as lack of predictability for alloy microstructure, the influence of defects, and the influence of environment.

The beneficial impact of minor alloying elements on corrosion properties has been somewhat advanced in literature by employing the increased understandings of select systems¹⁹. In general, Ni is alloyed with Cr and Mo and small concentrations of W and Fe in order to maximize corrosion properties². The best-known Ni-based alloy, Hastelloy C-22 (Ni-22 Cr-13 Mo-3 Fe-3 W, wt%), exhibits exceptional resistance to both oxidizing and non-oxidizing chemicals and provides protection from pitting, crevice attack, and stress corrosion cracking in even high temperature and concentrated chloride environments^{5,10,20-23}. This optimal alloy composition was, however, reached by adding these previously established beneficial elements using trial-and-error methods within the framework of the PREN. As a result, there are numerous ongoing studies to appropriately characterize the passive film on C-22 and model its long-term stability for nuclear applications²⁴⁻³².

1.3 Overview of Passivation by Alloying with Cr and Mo

Similar to stainless steels, additions of Cr will decrease the corrosion rate of Ni-Cr alloys in reducing acid, neutral, and chloride solutions³³. The corrosion rate drops significantly, however, when a critical concentration is reached (>12 wt% Cr for Fe, >8-11 wt% Cr for Ni) and a uniform, Cr-rich, passive film layer (often assumed to be Cr₂O₃ or Cr(OH)₃) forms across the oxide surface^{9,34-36}. This is shown schematically for Fe-Cr alloys in Figure 1.2. Likewise, alloying of Mo and W encourage a similar decrease in the measured uniform passive corrosion rate in both Fe-Cr and Ni-Cr-based alloys³⁷. The classic example of the influence of small concentrations of Mo on corrosion behavior is SS304 (Fe-19Cr-9.25Ni-0.08C, wt%) when compared to SS316 (Fe-17Cr-12Ni-2.5Mo-0.08C, wt%). The latter is significantly less susceptible to various forms of localized corrosion and stress corrosion cracking³⁸.

The quantitative effects of alloying Fe with Cr, Ni, Mo, and W on passivation kinetics have been studied in literature. Both the passivation rate and protectiveness of the film were found to generally increase with the concentration of minor elements³⁷. A synergistic affect has been

previously observed for both Ni-based and stainless steel alloys, where Mo and W, when alloyed in tandem, increase the localized corrosion resistance of Cr-rich passive films by improving passivity, increasing the induction time for pit formation and the pitting potential, and decreasing the passive current density^{4,10,19,39,40}. Similarly, the influences of these alloying additions on high temperature oxidation were found to be similar, where Cr cation transport controls scale growth⁴¹. Mo is theorized to impact growth by increasing the passivation rate by an unknown mechanism⁴².

The influence of Mo on the atomic-scale physical, chemical, and electronic processes relevant for passive film growth has been proposed^{7,19,42-46} but several controversial models have been proposed. These previous conjectures are indicated in Table 1.1. Notably, the Solute Vacancy Interaction Model (SVIM) – an extension of Macdonald’s Point Defect Model (PDM) for the passive state – suggests addition of alloying elements such as Mo have a direct influence on the transport of point defects necessary for film growth¹⁹. The SVIM indicates that Mo can become incorporated in oxide films as a charged substitutional defect which can electrostatically interact with cation vacancies present and reduce their mobility^{19,47}.

In passive films on Ni-based alloys, Ni typically exists as a +2 charged metal cation (Ni^{2+}), Cr as Cr^{3+} , Mo as $\text{Mo}^{4,5,6+}$, and W as $\text{W}^{4,6+}$ ⁹. In situations where solute capture occurs during film growth, cations of varying oxidation states can become trapped into a single phase onto certain oxide sites. For the situation where Mo^{+6} is substituted onto a Ni^{2+} or Cr^{3+} lattice site, the net positive electrostatic charge results in the aforementioned attraction of negatively charged defects, such as metal cation vacancies formed at the film/solution interface by halide anion adsorption. The resulting complex is neutrally charged and will not contribute towards growth of the cation vacancy condensates which the PDM proposes is a precursor for pit formation⁴⁸. This suggested influence of alloying additions such as Mo on point defect transport across passive films corresponds well with previous work concerning the inhibition of the earliest stages of crevice corrosion on commercial Ni-based superalloys where the effect was largely brought about by low concentrations of Mo⁴⁹⁻⁵².

The influence of minor alloying elements on the chemical identity of passive films grown slowly on Ni-Cr-based alloys by high temperature oxidation^{41,53-55} or using applied or open circuit electrochemical potentials^{9,10,56,57} has been well-addressed. It has been found that, in general, Cr and Mo preferentially segregate to the metal/film and film/electrolyte interfaces, respectively⁵⁸.

Ni-enrichment in passive films on various Ni-Cr-Mo alloys similarly occurs at the inner interface, resulting in the common observation of a distinct “layered” structure of distinct phase-separated oxides with a thin MoO_x outer layer, followed by thick CrO_x and then NiO_x closest to the metal⁹. This analysis might be flawed as it is based on binding energies similar to Mo^{4,5,6+}, Cr³⁺ and Ni²⁺ as seen in MoO_x, CrO_x, and NiO_x but chemical characterization findings do not indicate structural information.

1.4 Effect of Alloying on Polarization Behavior

The significant influence of minor alloying elements on passivity are often illustrated using E-log (i) polarization plots which report the relationship between the current density and applied potential⁵⁹. The basic details of these diagrams and the implications for passivity are discussed elsewhere^{33,59,60}. For passive materials, there is a potential at which the metal-electrolyte interface begins to undergo an active to passive transition, E_{pp} , often occurring at a “nose” or peak in the current density. Following this potential, the measured current density decreases by several orders of magnitude before reaching a pseudo-constant value which corresponds to the corrosion rate of the alloy in the passive state, i_{pass} . Upon adding certain alloying elements such as Mo and increasing their concentrations, E_{pp} is typically shifted to more negative potentials and i_{pass} decreases significantly. This is evident in Figure 1.3 where i_{pass} decreases as more Cr, Mo, and W are added to the alloys. Notably, Ni-11 wt% Cr, the least concentrated alloy, has the highest i_{pass} . Further increases of Cr or Mo and W additions are proposed to suppress i_{pass} and facilitate passivity by the (i) formation of continuous, stoichiometric oxide layers such as Cr₂O₃, (ii) doping with Moⁿ⁺ in M^{m+} lattice (where n > m) and the possible inhibition of cation vacancy motion, and/or (iii) promotion of Cr³⁺ enrichment in the film by Mo and/or W alloying as will be discussed in greater detail below.

At increasing potentials, the passive films tend to breakdown due to either localized corrosion (e.g. crevice or pitting) or Cr³⁺/Cr⁶⁺ transpassive dissolution^{61–64} ($2Cr^{3+} + 7H_2O = Cr_2O_7^{2-} + 14H^+ + 6e^-$, $E(pH\ 4) \approx +780\ mV_{SHE} = +540\ mV_{SCE}$)¹⁴. O₂ evolution is also possible at high electrode potentials. Alloying with W further decreases the passive film dissolution rate at high potentials where Cr transpassivity is offset by Mo and W oxide formation⁹. The most evidence of this effect is seen for the Ni-Fe-Cr-Ru-Mo-W high entropy alloy (HEA) in

Figure 1.3. Along with decreasing i_{pass} , increasing the Mo+W concentration in an alloy will result in an increased breakdown potential for local corrosion. This effect becomes significant in more corrosive (i.e. acidic, chloride-rich, or high temperature) solutions. Figure 1.4 demonstrates that even in an 85°C solution where most alloys would undergo fast, localized corrosion attack at +200 mV_{OCP}, increasing [Mo] results in a lower corrosion rate.

1.5 Potential Step Passivation

For alloys under a constant and anodic applied potential above E_{pp} , but below where transpassive or localized corrosion would occur, the thickness of a passive film increases⁶⁵. The kinetics of this phenomenon have been the subject of several passivation models⁶⁶⁻⁷³. At long passivation times in aqueous environments, a limiting thickness is typically reached where the oxidation rate at the metal/oxide interface becomes equivalent to that of oxide dissolution, whether oxidative or chemical, at the oxide/electrolyte interface⁷⁴. Both the chemical dissolution and chloride-induced breakdown of passive films can be quantified through application of various rate equations^{48,75,76}. Additionally, the initiation and propagation of pitting on the surface of oxides has been the subject of modeling efforts^{11,48,77-79}. For the case of Ni-based alloys, it has been seen that increasing the applied potential results in a pseudo-linear increase in film thickness up until chemical dissolution causes linear thinning^{9,22}. Similarly, increasing the alloying ratio of Cr:Mo results in thicker films at a given potential⁹. It was also found that W additions in C-276 and C-22 (Table 1.2) further increased the film thickness compared to C-2000, which possesses a similar Cr and Mo content⁹.

Several recent studies have investigated the influence of crystallographic orientation on the competition between passivation and chemical dissolution for Ni-based alloys^{21,80}. Through the application of single frequency electrochemical impedance spectroscopy and atomic force microscopy, a greater propensity for conformal film formation was seen on low index grain orientations close to (1 0 1) for a Ni-11 wt% Cr alloy, The test was conducted in an acidic NaCl solution during potential controlled passivation. In the case of Ni-11 wt% Cr-6 wt% Mo, repassivation was observed at all orientations under potential control⁸⁰. For a more corrosion resistant alloy, C-22, it has been shown however that greater dissolution occurs for (1 1 0) grains during etching in 3 M HCl likely without an oxide, with (1 1 1) exhibiting the least damage²¹.

However, upon etching the surfaces in 1 M HCl where an oxide was likely present, the (1 1 0) oriented grains were observed to have a lower corrosion rate due to stability of a favorable oxide and the decreased likelihood of chloride-assisted film breakdown²¹.

Pitting and crevice corrosion, especially stabilization and propagation, can be inhibited by alloying with Mo and W because of lower active dissolution rates and the greater propensity for repassivation^{33,49,81,82}. The exact mechanism by which this occurs is not fully understood, but there are multiple theories that will be discussed below. In general, however, the induction time for pitting or crevice corrosion events will increase with the combination of higher Cr+Mo+W alloying content. The crevice corrosion initiation behavior trends for several Ni-based commercial alloys are given in Figure 1.5. Upon comparing this behavior to the compositions and approximate PREN values provided in Table 1.2, it is evident that the optimal alloying combination is high Cr alloying ($[\text{Cr}] \geq 21$ wt%) with added Mo and W in tandem ($[\text{Mo}+\text{W}] > 16$) for the alloys 686, C-2000, and 59. This results in the highest computed PREN value of 76, with the exemption of the high strength C-22 alloy which is not included in Figure 1.5. However, there were slight differences in the breakdown behavior of the alloys that Equation 1.1 was not able to predict. Alloy 686 was marginally better than C-2000, but both were much more corrosion resistant than 59. Additionally, C-22 had similar compositions of Cr, Mo, and W and yet exhibited poor breakdown performance at 85°C. This further supports the previous notion that interpolating passivation behavior from the bulk metallic composition is an inadequate technique and instead, an understanding of the fate of minor alloying elements in the passive film and their roles at enabling film growth and resisting breakdown is instead necessary.⁴⁷

While in general the empirical corrosion properties of Ni-alloys, especially common commercial ones like C-22, are well-established^{12,29,83-85}, a full understanding of the exact atomic mechanism by which specific alloying elements function has not yet been achieved¹⁵. The results are mainly empirical with some mechanistic insights from work on waste repository engineered container work on specific commercial alloys^{9,10,22,32,57,85}. Disagreements in literature even exist for the growth mechanism, location, and function of minor alloying elements, along with the structure of passive films formed in electrochemical environments. This disparity is valid specifically with regards to the role of Mo atoms on promoting passivation and repassivation reactions through an unknown, synergistic interaction with the major alloying addition, Cr, whose

single influence is thoroughly understood^{4,7,9,19,43}. Because of the uncertainty, the effects of other dopants as alloying elements cannot be predicted.

1.6 Passive Film Growth Mechanism

The bulk of literature concerning the constant-potential passivation of Ni-based super alloys, such as C-22, has been accomplished in moderately concentrated NaCl solutions and reports layered, phase-separated oxides according to XPS and ToF-SIMS measurements where a Cr₂O₃ or Cr(OH)₃-rich film is present at the inner interface and an outer NiO or Ni(OH)₂ film^{29,46,56}. Segregation of Mo⁺⁶ and/or Mo⁺⁵ cations to the oxide/electrolyte interface has also been reported as a separate MoO_x phase. More recent work utilizing 3DAPT has observed similar distribution of elements throughout the film; however, non-stoichiometric oxide compounds were instead detected⁸⁶. As for the mechanism of film growth, *in situ* transmission electron microscopy (TEM) was applied to the early stages of Ni-Cr alloys at 700 °C^{53,54}. In these studies, the initial stage oxidation of Ni-10 at% Cr was revealed to proceed by an adatom mechanism involving surface diffusion of the Ni and O atoms and the nucleation of sub-surface Cr₂O₃⁵³. There was some nucleation of NiCr₂O₄ islands, but it was observed that secondary NiO “whisker” phases grew out of the oxide plane and resulted in uneven layering of the different oxides. For the case of Ni-20 at% Cr, the subsurface Cr₂O₃ nuclei are able to coalesce and large NiCr₂O₄ islands emerged from the NiO layer⁵⁴. These results are, however, only indicative of film growth in hot, dry conditions. There will be a significant influence of dissolution during nucleation and growth in electrochemical environments and thus the mechanism will likely adjust⁷⁴. This effect of dissolution has not yet been measured *in situ* for electrochemical passivation conditions.

The mentioned discrepancies with respect to film properties and the role of individual minor alloying elements result in broad and often incorrect assumptions of film composition and chemical reaction efficiency during electrochemical passivation processes⁷⁴. Most models of oxide growth in aqueous or gaseous environments are limited to single elements. As such, previously applied methods for characterizing passive film growth and stability in electrochemical environments are unreliable and do not reliably indicate the roles of individual minor alloying elements.

1.7 Influence of Studying Passivation *In Operando* versus *Ex Situ* at Steady State Condition

Very little attention has been given to the implications of growth rate and the “state” of the solute on the physical, chemical, and electronic properties of these films. The majority of literature studies on film properties during and following passivation concern the potentiostatic condition which rarely occurs in engineering applications. Slowly grown films have demonstrated the ability to anneal out point defects and produce more crystalline structures⁹. Instead, growth can occur faster than this idealized case due the presence of oxidizers in aqueous environments which cause continual breakdown and repair processes and may produce defective films not expected by thermodynamic considerations. In such a case, the growth interface velocity moves much faster than diffusion and the resulting film can possess considerably different properties than those formed slowly, a phenomena called “solute capture”⁸⁶. Following this process, metal cation substitutional defects functioning as electronic dopants in passive films and modify many corrosion and electronic properties⁸⁶. The extent of this effect is not yet understood.

The electrochemical techniques used to growth passive films and measure their properties *ex situ* are, as such, unrepresentative of in-service conditions. In addition, typical *ex situ* characterization methods (i.e. XPS, TEM, ToF-SIMS) likely introduce chemical changes in passive film structure and identity. Even classic *in situ* methods such as EIS are only applicable at steady state where film growth is assumed negligible. These drawbacks present challenges with accurately characterizing the role of minor alloying elements and electrochemical growth conditions on relevant passive film properties. The following critical unresolved issues have been identified that are central to this thesis.

1.8 Critical Unresolved Issues

1.8.1 In Operando Methods

Predominantly, techniques capable of studying electrochemically grown passive films are applied *in situ* or *ex situ* following the completion of the electrochemical processes up to a desired degree of oxidation. Novel application of existing techniques is necessary for completing such measurements *in operando*, or while they are occurring instead of after steady-state has been achieved (e.g. *in situ*) or the samples are removed from the relevant environment (e.g. *ex situ*). The

results will produce a more accurate picture of the exact mechanism by which passive film nucleation, growth, and the establishment of a quasi-steady state occur on Ni-based alloys in various environments, along with the individual influence of minor alloying elements. *Operando* techniques additionally provide much greater time resolution and as such the early stages of passivation can be captured.

1.8.2 Atomic Scale Understanding of Corrosion Processes Linked with Meso-Scale Behavior

Existing and commonly-applied techniques used to characterize passive films often do so on a meso- to micro- or nano-meter scales in depth, but not laterally. Often, these methods can only characterize one aspect of the film, i.e. its chemical, electronic, or physical properties. In order to completely understand the exact atomic scale mechanism for the chemical and electrochemical reactions occurring at the metal/film and film/solution interfaces, along with those occurring across the film itself, combinations of advanced and nontraditional techniques for the field of corrosion must be implemented, i.e. 3DAPT and AFM. Only then can the aforementioned and complex mechanisms for passivation and the role of individual alloying elements be surmised.

1.8.3 Role of Mo and its Influence on Passive Film Chemistry and Properties:

The role of Mo with regards to its location and influence on electrochemical behavior has been debated for decades. These confusions and Mo's specific relationship with Cr in passivity is, in part, due to the challenge of characterizing small concentrations of Mo. In commercial Ni-Cr-Mo-based alloys, [Mo] typically ranges from 3 to 16 wt%, with the most corrosion resistant alloys possessing a concentration in-between. The development of new, *in operando*, and atomic-scale techniques provide greater resolution and means of tracking Mo. Application of these tools provides the opportunity to better understand how certain minor alloying elements facilitate and improve passivity, repassivation, and resistance to breakdown. More generically, the effect of M^{p+} dopants in N^{q+} oxides where $p > q$ needs to be more thoroughly explored and the presence of $Mo^{4,6+}$ dopants in Cr^{3+} or Ni^{2+} rich oxides formed on Ni-Cr-Mo provides an excellent alloying system to pursue this aspect of passivity.

1.8.4 Influence of Growth Rate on Corrosion and Passive Film Properties:

Predominantly passive films are studied following slow, potential-controlled growth. This method makes possible the annealing of point defects present in films during growth and the transformation from pseudo-amorphous structures into compact, crystalline, and phase-separated oxides^{9,10,32}. As such, the growth rate of passive films has significant implications for both the corrosion behavior and electronic properties of passive films. In cases where the metal/film interface moves sufficiently quickly such that atoms are not able to suitably diffuse to form phase-separated oxides, metal cations can become “solute captured” in films as species not predicted through thermodynamic or kinetic considerations which exhibit significantly different behavior from those achieved by slow growth. The impact of minor alloying elements such as Mo on the corrosion properties of solute captured films is similarly not understood as the films can become increasingly doped, resulting in further modification of oxide properties. Most previous studies of passive oxides theorized phase-separated layers existed, including distinct MoO₃ and/or MoO₂ phases⁴⁷.

1.9 Research Objectives

The exact relationships between alloy composition and corrosion performance are well-established for the case of the Fe-Cr system. For Ni-Cr, however, fundamental research is still lacking and the preponderance of literature focuses on the global properties and corrosion performance of commercial alloys. Very few studies have investigated the atomic-scale processes which govern corrosion behavior as a function of alloy and environment concentrations using model alloys. This presents a dearth of prior knowledge on the exact mechanism by which the minor alloying elements in specifically the Ni-Cr-Mo system enable passivation, repassivation, and their influence on the structure, composition, and relevant electronic properties of passive films. The crevice repassivation stage was investigated because of the ease of conducting experiments and characterization. This dissertation aims to couple the meso- and nano-scale properties of passive films and explain the effect and fate of Mo dopants on passive film properties and localized corrosion resistance in both acidic and alkaline sulfate and chloride environments following both fast, solute-captured and slow, phase-separated oxide growth. In addition, a better understanding is reached for the influence of growth rate and solute capture on the physical,

chemical, and electrochemical properties of passive films. A knowledge of these relationships enhances the understanding of alloying elements in passive films and enable intelligent materials design and predictions of long-term film stability in harsh environments.

1.10 Thesis Organization

This thesis is organized by the needs, gaps, and opportunities pertaining to the passivation of Ni, Ni-Cr, and Ni-Cr-Mo alloys in aqueous sulfate and chloride-containing environments.

Chapter 2 introduces an electrochemical framework that will be used in the following chapters to quantify and characterize passivation processes. Specifically, a novel and complimentary application of single frequency electrochemical impedance spectroscopy (SF-EIS) and an atomic emission spectroelectrochemical technique, inductively coupled plasma mass spectroscopy (ICP-MS), were used in tandem to assess film growth during potentiostatic and galvanostatic passivation. The use of ICP-MS further advances the understanding of the role individual minor alloying elements can play regarding film growth by directly measuring any preferential dissolution, and thus preferential enrichment in passive films. These two techniques were thoroughly quantified and the former was demonstrated for a non-pH adjusted sulphate solution (0.1 M Na₂SO₄) chosen to provide an initial, simplified system for testing the applicability.

Chapter 3 develops an in-depth understanding of the atomic-scale passivation of Ni-Cr, and Ni-Cr-Mo alloys in acidified (pH 4) and alkaline (pH 10) sulphate environments (0.1 M Na₂SO₄). The framework established in Chapter 2, along with *in situ* polarized neutron reflectometry (PNR) and *ex situ* atomic force microscopy (AFM), X-ray photoelectron spectroscopy (XPS), and 3D atom probe tomography (3DAPT), were applied to characterize the influence of Cr and Mo alloying on passivity and their enrichment as a function of time. The specific chemical and electrochemical reaction kinetics were analyzed and divulged the direct roles of kinetics and thermodynamics during film growth processes. A simplified influence of the role of pH on passive film stability was additionally obtained. The comprehensive understanding presented in this chapter directly facilitates the analysis performed in Chapter 4, where the additional and significant complexity of chloride anion attack and localized corrosion are introduced.

Chapter 4 advances upon the comprehensive understanding presented in Chapter 3 by introducing the additional and significant influence of chloride anion attack and localized corrosion during passivation processes of Ni-Cr and Ni-Cr-Mo alloys. Even before the initiation of pitting or crevice corrosion, chloride-facilitated dissolution at the film/solution interface results in greatly different chemical, structural, and electronic properties of passive films. Like Chapter 3, the influence of pH on such properties of potentiostatically growth films was addressed, along with the effect of the aqueous chloride concentration (0.1 M NaCl) in the context of Ni-Cr versus Ni-Cr-Mo passivation. The role of Mo on facilitating passivation processes was studied and discussed in detail.

Chapter 5 specifically investigates the atomistic influence Mo additions have regarding passive film properties of Ni-Cr-based alloys. Notably, its impact on the morphological (i.e. surface roughness), chemical (i.e. Mo cations within the film, preferential segregation, film thickness), and electronic properties (i.e. defect density and flat band potential) were characterized and compared to various measurable electrochemical parameters such as pitting potential and metastable pit initiation. Alloys with increasing concentrations of Mo and a constant fraction of Cr in the bulk alloy were investigated. The coupled understanding of structural, chemical, and electronic properties helped to elucidate how Mo additions encourage film growth, repassivation, and resistance to localized corrosion initiation.

Chapter 6 introduces the concept of solute capture and how it pertains to passivation reactions. This phenomenon was quantified by applying the electrochemical framework from Chapter 2 but using a constant applied current density to fix the growth rate of passive films. The preferential enrichment, segregation, and dissolution were quantified using ICP-MS, XPS, and 3DAPT. In addition, the electrochemical corrosion resistance of the film growth at various rates was studied using metastable pitting analysis to examine what factored were important. Through measurements of the film electronic properties, solute captured films are shown to be inherently more defective and prone to localized film breakdown.

Chapter 7 presents the conclusions and key results relevant to understanding the passivation of Ni-based alloys and the significant functions of minor alloying elements as electronic dopants and electrochemical stabilizers. The remaining questions and a discussion of proposed future work are also detailed.

1.11 References

1. Davis, J. R. *ASM Specialty Handbook: Nickel, Cobalt, and Their Alloys. Uses of Nickel* (2000). doi:10.1361/ncta2000p013
2. Rebak, R. B. *Corrosion and Environmental Degradation. Corrosion and Environmental Degradation Vol. II* (2000).
3. Rebak, R. B. Corrosion of Non-Ferrous Alloys. I. Nickel-, Cobalt-, Copper-, Zirconium- and Titanium-Based Alloys. in *Materials Science and Technology* 71–111 (Wiley-VCH Verlag GmbH & Co. KGaA, 2013). doi:10.1002/9783527603978
4. Lillard, R. S., Jurinski, M. P. & Scully, J. R. Crevice Corrosion of Alloy-625 in Chlorinated ASTM Artificial Ocean Water. *Corrosion* **50**, 251–265 (1994).
5. Carranza, R. M. & Rodríguez, M. A. Crevice corrosion of nickel-based alloys considered as engineering barriers of geological repositories. *npj Mater. Degrad.* **1**, 1–9 (2017).
6. Mishra, A., Shoesmith, D. & Manning, P. Materials Selection for Use in Concentrated Hydrochloric Acid. *CORROSION* **73**, 68–76 (2017).
7. Clayton, C. R. & Lu, Y. C. A Bipolar Model of the Passivity of Stainless Steel: The Role of Mo Addition. *J. Electrochem. Soc.* **133**, 2465–2473 (1986).
8. Marcus, P. *Corrosion Mechanisms in Theory and Practice, Third Edition - Google Books.* (CRC Press, 2012).
9. Lloyd, A. C., Noël, J. J., McIntyre, S. & Shoesmith, D. W. Cr, Mo and W alloying additions in Ni and their effect on passivity. *Electrochim. Acta* **49**, 3015–3027 (2004).
10. Lloyd, A. C., Noël, J. J., McIntyre, N. S. & Shoesmith, D. W. The open-circuit ennoblement of alloy C-22 and other Ni-Cr-Mo alloys. *JOM* **57**, 31–35 (2005).
11. Frankel, G. S., Li, T. & Scully, J. R. Localized Corrosion: Passive Film Breakdown vs Pit Growth Stability. *J. Electrochem. Soc.* **164**, C180–C181 (2017).
12. Rebak, R. B. & Crook, P. Influence of the Environment on the General Corrosion Rate of Alloy 22. in *American Society of Mechanical Engineers Pressure Vessels and Piping Division Conference* 1–8 (2004). doi:10.1115/PVP2004-2793
13. Spencer, P. J. A brief history of CALPHAD. *Calphad Comput. Coupling Phase Diagrams Thermochem.* **32**, 1–8 (2008).
14. Pourbaix, M. *Atlas of electrochemical equilibria in aqueous solutions.* (National Association of Corrosion Engineers, 1974).
15. Scully, J. R. Corrosion chemistry closing comments: opportunities in corrosion science facilitated by operando experimental characterization combined with multi- scale computational modelling. *Faraday Discuss. Faraday Discuss* **180**, 577–593 (2015).
16. Olsson, C.-O. . & Landolt, D. Passive films on stainless steels—chemistry, structure and growth. *Electrochim. Acta* **48**, 1093–1104 (2003).
17. Kovach, C. W. & Redmond, J. D. Correlation Between the Critical Crevice Temperature ‘Pre-Number’, and Long-Term Crevice Corrosion Data for Stainless Steels. in *NACE Annual Conference and Corrosion Show* (National Association of Corrosion Engineers, 1993).
18. Heuer, A. H. *et al.* Enhanced corrosion resistance of interstitially hardened stainless steel: Implications of a critical passive layer thickness for breakdown. *Acta Mater.* **60**, 716–725 (2012).
19. Urquidi, M. & Macdonald, D. D. Solute-vacancy interaction model and the effect of minor

- alloying elements on the initiation of pitting corrosion. *J. Electrochem. Soc.* **132**, 555–558 (1985).
20. Macdonald, D. D., Sun, A., Priyantha, N. & Jayaweera, P. An electrochemical impedance study of Alloy-22 in NaCl brine at elevated temperature: II. Reaction mechanism analysis. *J. Electroanal. Chem.* **572**, 421–431 (2004).
 21. Gray, J. J., El Dasher, B. S. & Orme, C. A. Competitive effects of metal dissolution and passivation modulated by surface structure: An AFM and EBSD study of the corrosion of alloy 22. *Surf. Sci.* **600**, 2488–2494 (2006).
 22. Jakupi, P., Zagidulin, D., Noël, J. J. & Shoesmith, D. W. The impedance properties of the oxide film on the Ni-Cr-Mo Alloy-22 in neutral concentrated sodium chloride solution. *Electrochim. Acta* **56**, 6251–6259 (2011).
 23. Priyantha, N., Jayaweera, P., Macdonald, D. D. & Sun, A. An electrochemical impedance study of alloy 22 in NaCl brine at elevated temperature. I. Corrosion behavior. *J. Electroanal. Chem.* **572**, 409–419 (2004).
 24. Rodríguez, M. A., Carranza, R. M. & Rebak, R. B. Influence of halide ions and alloy microstructure on the passive and localized corrosion behavior of alloy 22. *Metall. Mater. Trans. A* **36A**, 1179–1185 (2005).
 25. Dunn, D. S., Pan, Y.-M., Yang, L. & Cragolino, G. A. Localized Corrosion Susceptibility of Alloy 22 in Chloride Solutions: Part 2—Effect of Fabrication Processes. *CORROSION* **62**, 3–12 (2006).
 26. Quiambao, K. F. *et al.* Passivation of a corrosion resistant high entropy alloy in non-oxidizing sulfate solutions. *Acta Mater.* **164**, 362–376 (2019).
 27. Kobe, B. *et al.* Application of quantitative X-ray photoelectron spectroscopy (XPS) imaging: investigation of Ni-Cr-Mo alloys exposed to crevice corrosion solution. *Surf. Interface Anal.* **49**, 1345–1350 (2017).
 28. Ebrahimi, N., Biesinger, M. C., Shoesmith, D. W. & Noël, J. J. The influence of chromium and molybdenum on the repassivation of nickel-chromium-molybdenum alloys in saline solutions. *Surf. Interface Anal.* **49**, 1359–1363 (2017).
 29. Zagidulin, D., Zhang, X., Zhou, J., Noël, J. J. & Shoesmith, D. W. Characterization of surface composition on Alloy 22 in neutral chloride solutions. *Surf. Interface Anal.* **45**, 1014–1019 (2013).
 30. Henderson, J. D., Li, X., Shoesmith, D. W., Noël, J. J. & Ogle, K. Molybdenum surface enrichment and release during transpassive dissolution of Ni-based alloys. *Corros. Sci.* **147**, 32–40 (2019).
 31. Mishra, A. K. & Shoesmith, D. W. Effect of Alloying Elements on Crevice Corrosion Inhibition of Nickel-Chromium-Molybdenum-Tungsten Alloys Under Aggressive Conditions: An Electrochemical Study. *Corrosion* **70**, 721–730 (2014).
 32. Mishra, A. K., Ramamurthy, S., Biesinger, M. & Shoesmith, D. W. The activation/depasivation of nickel-chromium-molybdenum alloys in bicarbonate solution: Part I. *Electrochim. Acta* **100**, 118–124 (2013).
 33. McCafferty, E. *Introduction to corrosion science*. Springer (Springer, 2010). doi:10.1007/978-1-4419-0455-3
 34. McCafferty, E. Relationship Between Graph Theory and Percolation Approaches in the Passivity of Fe–Cr Binary Alloys. *J. Electrochem. Soc.* **155**, C501–C505 (2008).
 35. McCafferty, E. Graph theory and the passivity of binary alloys. *Corros. Sci.* **42**, 1993–2011

- (2000).
36. McCafferty, E. Oxide networks, graph theory, and the passivity of binary alloys. *Corros. Sci.* **44**, 1393–1409 (2002).
 37. Cho, E.-A., Kim, C.-K., Kim, J.-S. & Kwon, H.-S. Quantitative analysis of repassivation kinetics of ferritic stainless steels based on the high field ion conduction model. *Electrochim. Acta* **45**, 1933–1942 (2000).
 38. Scott, P. Review of irradiation assisted stress corrosion cracking. *J. Nucl. Mater.* **211**, 101–122 (1994).
 39. Ebrahimi, N. The Influence of Alloying Elements on The Crevice Corrosion Behaviour of Ni-Cr-Mo Alloys. (The University of Western Ontario, 2015).
 40. Marshall, P. I. & Burstein, G. T. Effects of alloyed molybdenum on the kinetics of repassivation on austenitic stainless steels. *Corros. Sci.* **24**, 463–478 (1984).
 41. Takei, A. & Nii, K. The Growth Process of Oxide Layers in the Initial Stage of Oxidation of 80Ni-20Cr Alloy. *Trans. Japan Inst. Met.* **17**, 211–219 (1976).
 42. Yun, D. W., Seo, H. S., Jun, J. H., Lee, J. M. & Kim, K. Y. Molybdenum effect on oxidation resistance and electric conduction of ferritic stainless steel for SOFC interconnect. *Int. J. Hydrogen Energy* **37**, 10328–10336 (2012).
 43. Sugimoto, K. & Sawada, Y. Role of Alloyed Molybdenum in Austenitic Stainless Steels in the Inhibition of Pitting in Neutral Halide Solutions. *Corrosion* **32**, 347–352 (1976).
 44. Bojinov, M. *et al.* Influence of molybdenum on the conduction mechanism in passive films on iron-chromium alloys in sulphuric acid solution. *Electrochim. Acta* **46**, 1339–1358 (2001).
 45. Maurice, V. *et al.* Effects of molybdenum on the composition and nanoscale morphology of passivated austenitic stainless steel surfaces. *Faraday Discuss* **180**, 151–170 (2015).
 46. Hayes, J. R., Gray, J. J., Szmodis, A. W. & Orme, C. A. Influence of chromium and molybdenum on the corrosion of nickel-based alloys. *Corrosion* **62**, 491–500 (2006).
 47. Lutton Cwalina, K., Demarest, C. R., Gerard, A. Y. & Scully, J. R. Revisiting the effects of molybdenum and tungsten alloying on corrosion behavior of nickel-chromium alloys in aqueous corrosion. *Curr. Opin. Solid State Mater. Sci.* (2019).
 48. Lin, L. F., Chao, C. Y. & Macdonald, D. D. A point defect model for anodic passive films II. Chemical breakdown and pit initiation. *J. Electrochem. Soc.* **128**, 1194–1198 (1981).
 49. Bocher, F., Huang, R. & Scully, J. R. Prediction of critical crevice potentials for Ni-Cr-Mo alloys in simulated crevice solutions as a function of molybdenum content. *Corrosion* **66**, 1–15 (2010).
 50. Kehler, B. A., Ilevbare, G. O. & Scully, J. R. Comparison of the crevice corrosion resistance of alloys 625 and C22. *Passiv. Localized Corros. an Int. Symp. Honor Profr. Norio Sato* **99**, 644–654 (1999).
 51. Kehler, B. a, Ilevbare, G. O. & Scully, J. R. Crevice Corrosion Stabilization and Repassivation Behavior of Alloys 625 and 22. *Corrosion* **57**, 1042–1065 (2001).
 52. Kehler, B. A. & Scully, J. R. Role of metastable pitting in crevices on crevice corrosion stabilization in Alloys 625 and 22. *Corrosion* **61**, 665–684 (2005).
 53. Luo, L. *et al.* In-situ transmission electron microscopy study of surface oxidation for Ni-10Cr and Ni-20Cr alloys. *Scr. Mater.* **114**, 129–132 (2016).
 54. Luo, L. *et al.* In situ atomic scale visualization of surface kinetics driven dynamics of oxide growth on a Ni–Cr surface. *Chem. Commun.* **52**, 3300–3303 (2016).

55. Luo, H., Gao, S., Dong, C. & Li, X. Characterization of electrochemical and passive behaviour of Alloy 59 in acid solution. *Electrochim. Acta* **135**, 412–419 (2014).
56. Zhang, X., Zagidulin, D. & Shoesmith, D. W. Characterization of film properties on the NiCrMo Alloy C-2000. *Electrochim. Acta* **89**, 814–822 (2013).
57. Lloyd, A. C., Shoesmith, D. W., McIntyre, N. S. & Noël, J. J. Effects of Temperature and Potential on the Passive Corrosion Properties of Alloys C22 and C276. *J. Electrochem. Soc.* **150**, B120–B130 (2003).
58. Marcus, P. On some fundamental factors in the effect of alloying elements on passivation of alloys. *Corros. Sci.* **36**, 2155–2158 (1994).
59. Scully, J. R. & Lutton, K. Polarization Behavior of Active Passive Metals and Alloys. *Encyclopedia of Interfacial Chemistry: Surface Science and Electrochemistry* (2018).
60. Kaesche, H. *Corrosion of Metals: Physiochemical Principles and Current Problems*. (Springer-Verlag, 2003). doi:10.1007/978-3-642-96038-3
61. Betova, I. *et al.* Mechanism of transpassive dissolution of nickel-based alloys studied by impedance spectroscopy and rotating ring-disc voltammetry. *Electrochim. Acta* **47**, 2093–2107 (2002).
62. Bojinov, M. *et al.* Transpassive dissolution of Ni-Cr alloys in sulphate solutions - Comparison between a model alloy and two industrial alloys. *Electrochim. Acta* **47**, 1697–1712 (2002).
63. Bojinov, M. *et al.* Mechanism of transpassive dissolution of Ni-Cr alloys in sulphate solutions. *Electrochim. Acta* **45**, 2791–2802 (2000).
64. Betova, I., Bojinov, M. & Tzvetkoff, T. Oxidative dissolution and anion-assisted solubilisation in the transpassive state of nickel-chromium alloys. *Electrochim. Acta* **49**, 2295–2306 (2004).
65. Lutton, K. & Scully, J. R. Kinetics of Oxide Growth of Passive Films on Transition Metals. *Encyclopedia of Interfacial Chemistry: Surface Science and Electrochemistry* **6**, 284–290 (2018).
66. Verwey, E. J. Electrolytic Conduction of a Solid Insulator at High Fields: The Formation of the Anodic Oxide Film on Aluminium. *Physica* **2**, 1059–1063 (1935).
67. Cabrera, N. & Mott, N. F. Theory of the oxidation of metals. *Reports Prog. Phys.* **12**, 163–184 (1949).
68. Fehlner, F. P. & Mott, N. F. Low-temperature oxidation. *Oxid. Met.* **2**, 59–99 (1970).
69. Chao, C. Y., Lin, L. F. & Macdonald, D. D. A point defect model for anodic passive films I. Film growth kinetics. *J. Electrochem. Soc.* **128**, 1187–1194 (1981).
70. Momeni, M. & Wren, J. C. A Mechanistic Model for Oxide Growth and Dissolution during Corrosion of Cr-Containing Alloys. *Faraday Discuss.* **180**, 1–23 (2015).
71. Leistner, K. *et al.* Oxide Film Growth Kinetics on Metals and Alloys: II. Numerical Simulation of Transient Behavior. *J. Electrochem. Soc.* **160**, C197–C205 (2013).
72. Beverskog, B. *et al.* A mixed-conduction model for oxide films on Fe, Cr and Fe-Cr alloys in high-temperature aqueous electrolytes - I. Comparison of the electrochemical behaviour at room temperature and at 200 °C. *Corros. Sci.* **44**, 1901–1921 (2002).
73. Beverskog, B. *et al.* A mixed-conduction model for oxide films on Fe, Cr and Fe-Cr alloys in high-temperature aqueous electrolytes - II. Adaptation and justification of the model. *Corros. Sci.* **44**, 1923–1940 (2002).
74. Lutton, K., Gusieva, K., Ott, N., Birbilis, N. & Scully, J. R. Understanding multi-element

- alloy passivation in acidic solutions using operando methods. *Electrochem. commun.* **80**, 44–47 (2017).
75. Seyeux, A., Maurice, V. & Marcus, P. Oxide Film Growth Kinetics on Metals and Alloys: I. Physical Model. *J. Electrochem. Soc.* **160**, C189–C196 (2013).
 76. Momeni, M., Behazin, M. & Wren, J. C. Mass and Charge Balance (MCB) Model Simulations of Current, Oxide Growth and Dissolution during Corrosion of Co-Cr Alloy Stellite-6. *J. Electrochem. Soc.* **163**, C94–C105 (2016).
 77. Li, T., Scully, J. R. & Frankel, G. S. Localized Corrosion: Passive Film Breakdown vs Pit Growth Stability: Part II. A Model for Critical Pitting Temperature. *J. Electrochem. Soc.* **165**, C484–C491 (2018).
 78. Srinivasan, J., Liu, C. & Kelly, R. G. Geometric Evolution of Flux from a Corroding One-Dimensional Pit and Its Implications on the Evaluation of Kinetic Parameters for Pit Stability. *J. Electrochem. Soc.* **163**, C694–C703 (2016).
 79. Srinivasan, J. & Kelly, R. G. One-Dimensional Pit Experiments and Modeling to Determine Critical Factors for Pit Stability and Repassivation. *J. Electrochem. Soc.* **163**, C759–C767 (2016).
 80. Gusieva, K. *et al.* Repassivation Behavior of Individual Grain Facets on Dilute Ni–Cr and Ni–Cr–Mo Alloys in Acidified Chloride Solution. *J. Phys. Chem. C* **122**, 19499–19513 (2018).
 81. Jones, D. A. *Principles and prevention of corrosion.* (Prentice Hall, 1996).
 82. Marcus, P., Maurice, V. & Strehblow, H. H. Localized corrosion (pitting): A model of passivity breakdown including the role of the oxide layer nanostructure. *Corros. Sci.* **50**, 2698–2704 (2008).
 83. Gray, J. J., Hayes, J. R., Gdowski, G. E., Viani, B. E. & Orme, C. A. Influence of Solution pH, Anion Concentration, and Temperature on the Corrosion Properties of Alloy 22. *J. Electrochem. Soc.* **153**, B61–B67 (2006).
 84. Rebak, R. B. & Payer, J. H. Passive corrosion behavior of alloy 22. in *11th International High Level Radioactive Waste Management Conference* 1–7 (2006).
 85. Jakupi, P., Noël, J. J. & Shoesmith, D. W. The evolution of crevice corrosion damage on the Ni-Cr-Mo-W alloy-22 determined by confocal laser scanning microscopy. *Corros. Sci.* **54**, 260–269 (2012).
 86. Yu, X. X. *et al.* Nonequilibrium Solute Capture in Passivating Oxide Films. *Phys. Rev. Lett.* **121**, 145701 (2018).
 87. Yu, X. *et al.* In-situ observations of early stage oxidation of Ni-Cr and Ni-Cr-Mo alloys. *Corrosion* **74**, 939–946 (2018).
 88. Olefjord, I. The passive state of stainless steels. *Mater. Sci. Eng.* **42**, 161–171 (1980).
 89. Sugimoto, K. & Sawada, Y. The role of molybdenum additions to austenitic stainless steels in the inhibition of pitting in acid chloride solutions. *Corros. Sci.* **17**, 425–445 (1977).
 90. Yang, W., Ni, R. C., Hua, H. Z. & Pourbaix, A. The behavior of chromium and molybdenum in the propagation process of localized corrosion of steels. *Corros. Sci.* **24**, 691–707 (1984).
 91. Samin, A. J. & Taylor, C. D. First-principles investigation of surface properties and adsorption of oxygen on Ni-22Cr and the role of molybdenum. *Corros. Sci.* **134**, 103–111 (2018).
 92. Wegrelius, L. Passivation of Stainless Steels in Hydrochloric Acid. *J. Electrochem. Soc.* **146**, 1397 (1999).

93. Hornus, E. C., Giordano, C. M., Rodríguez, M. a., Carranza, R. M. & Rebak, R. B. Effect of Temperature on Crevice Corrosion Susceptibility of Nickel Alloys for Nuclear Repositories. *Corrosion* **162**, 1–13 (2013).
94. Sosa, S., Rodriguez, M. A. & Carranza, R. M. Determining the Effect of the Main Alloying Elements on Localized Corrosion in Nickel Alloys using Artificial Neural Networks. *Procedia Mater. Sci.* **8**, 21–28 (2015).
95. Taylor, C. D., Lu, P., Saal, J., Frankel, G. S. & Scully, J. R. Integrated computational materials engineering of corrosion resistant alloys. *npj Mater. Degrad.* **2**, 1–10 (2018).
96. Lu, P., Engelhardt, G. R., Kursten, B. & Macdonald, D. D. The Kinetics of Nucleation of Metastable Pits on Metal Surfaces : The Point Defect Model and Its Optimization on Data Obtained on Stainless Steel , Carbon Steel , Iron , Aluminum and Alloy-22. *J. Electrochem. Soc.* **163**, C156–C163 (2016).
97. King, P. F. & Uhlig, H. H. Passivity in the Iron-Chromium Binary Alloys. *J. Phys. Chem.* **63**, 2026–2032 (1959).

1.12 Tables

Table 1.1. Summary of the proposed roles of Mo as a minor alloying element present in literature

Theory	Proposed Role of Mo	Implication for Passivity	Evidence
Solute Vacancy Interaction Model (SVIM)	Highly charged Mo^{4+} and Mo^{6+} cations are substitutional defects in Cr^{3+} films, resulting in a net positive charge which form complexes with negative cation vacancy clusters	Reduced flux of cations from film/solution interface	<ul style="list-style-type: none"> • Reduced i_{pass} and increased V_{crit} and t_{ind} for film breakdown¹⁹ • Reduction in voids observed within films^{42,87}
Molybdate inhibits chemical dissolution	Mo-films preferentially dissolves as soluble MoO_4^{2-} compounds which stabilize Cr_2O_3	<ul style="list-style-type: none"> • Classic anodic inhibitor for localized film breakdown by resisting incorporation of Cl^- anions • Enables repassivation following pit initiation • Increases metal-metal bond strength and thus lowers anodic dissolution 	<ul style="list-style-type: none"> • Increased dissolution current density of 316L⁴⁰ • Fast repassivation kinetics following scratch^{28,40} • Surface depletion of Mo in passive films^{40,88} <ul style="list-style-type: none"> • Formation of nanostructured molybdate species at the outer part of the passive film⁴⁵
Protective MoOx films	MoO_2 and MoO_3 is stable at low pH and high Cl-concentrations and form to protect Cr_2O_3	Enrichment of Mo cations at the film/solution interface protect Cr_2O_3 from breakdown	<ul style="list-style-type: none"> • Increase in total l_{ox} with $[\text{Mo}]$⁸⁹ • Outer enrichment of $\text{Mo}^{4,5,6+}$ oxides detected using ToF-SIMS⁴⁵ and XPS^{45,90}
Promoter of Cr_2O_3	The presence of Mo allows preferential oxidation of Cr^{3+} into Cr_2O_3	Greater enrichment of passive Cr_2O_3 films	<ul style="list-style-type: none"> • Decrease in O adsorption energy for Cr with an adjacent Mo⁹¹ • MoO_4^{2-} enrichment at outer layer deprotonates OH^- and supplies O^{2-} for Cr^{3+} oxidation⁹² • More Cr_2O_3 film growth with added Mo^{9,10,57,74}

Table 1.2. Common commercial, low-temperature Ni-based alloys present in literature that are applicable for this review. Included are PREN values computed using Equation 1.1.

Minor Alloying (Mo and W) of Ni-Based Commercial Alloys^{5,12,93,94}			
Alloy	UNS	Chemical Composition (wt.%)	PREN
825	N08825	43Ni-21Cr-30Fe-3Mo-2.2Cu-1Ti	31
C-276	N10276	59Ni-16Cr-16Mo-4W-5Fe	71
625	N06625	62Ni-21Cr-9Mo-3.7Nb	51
C-22	N06200	59Ni-22Cr-13Mo-3W-3Fe	66
C-2000	N06059	59Ni-23Cr-16Mo-1.6Cu	76
59	N06059	59Ni-23Cr-16Mo-1Fe	76
686	N06686	46Ni-21Cr-16Mo-4W-5Fe	76
C-22HS	N07022	59Ni-21Cr-17Mo	77
HYBRID-BC1	N10362	62Ni-22Mo-15Cr-2Fe-0.3Al	72
600	N06600	72.87Ni-16.49Cr-9.46Fe- [CMnSiSCuNbTaTiAlCoP]<0.4	16

1.13 Figures

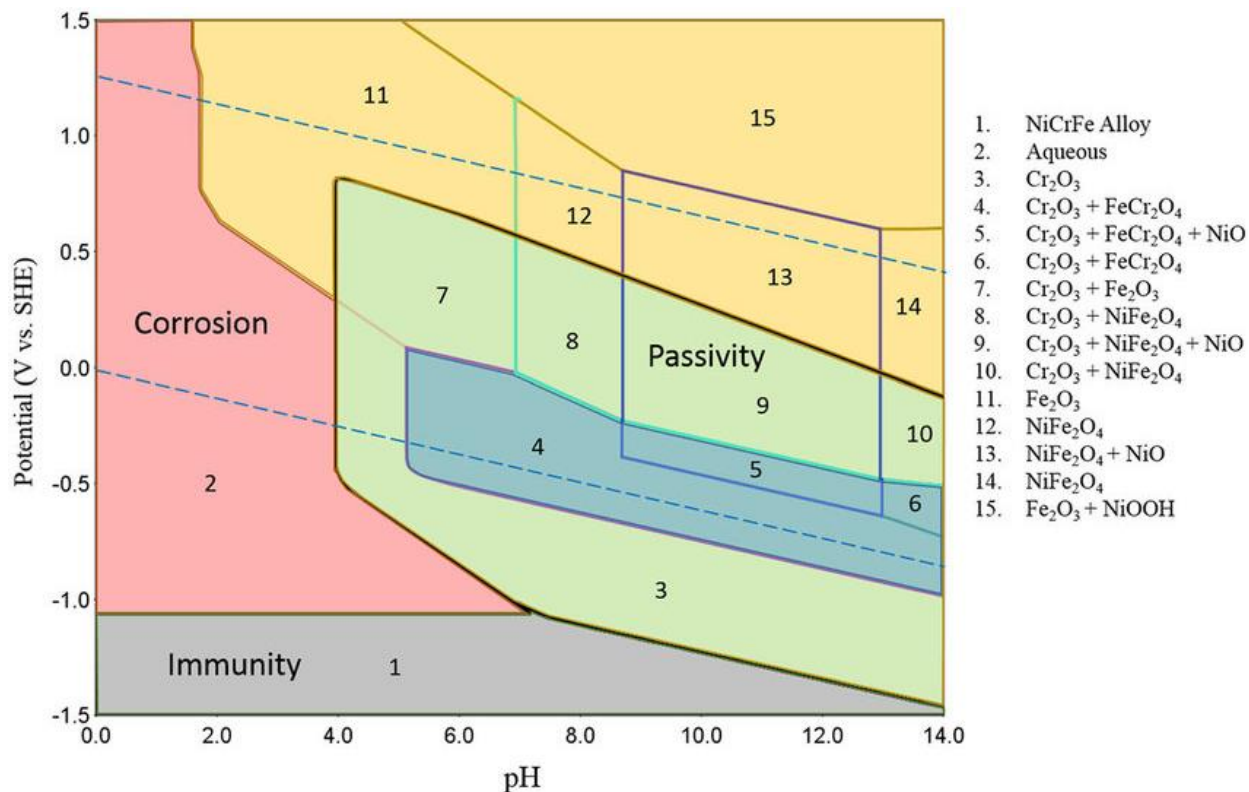


Figure 1.1. CALPHAD-calculated E-pH diagram for Inconel 600 (Ni-15.5 Cr-8 Fe, wt%) in 1 kg H₂O at 25°C and 1 atm. The red dashed lines are reversible potentials for hydrogen and oxygen evolutions, and the yellow dashed lines are the metal/aqueous ion equilibrium lines for pure constituent elements. The red region indicates where oxidized aqueous species are stable, green where Cr₂O₃ is stable, blue where Fe-Ni, Fe-Cr spinels are stable with some overlap with the green, and orange where oxides are stable^{95,96}

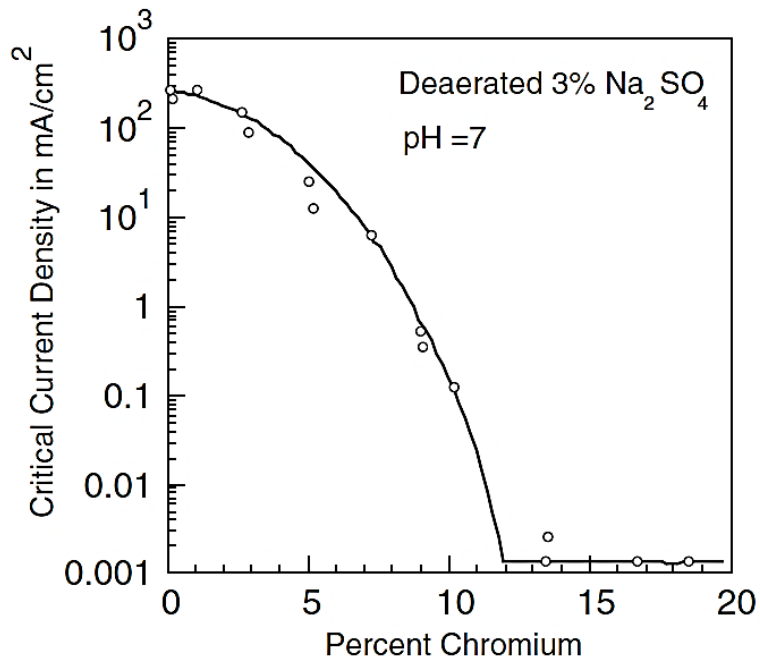


Figure 1.2. Passive current density as a function of Fe-Cr alloy composition (wt%)⁹⁷

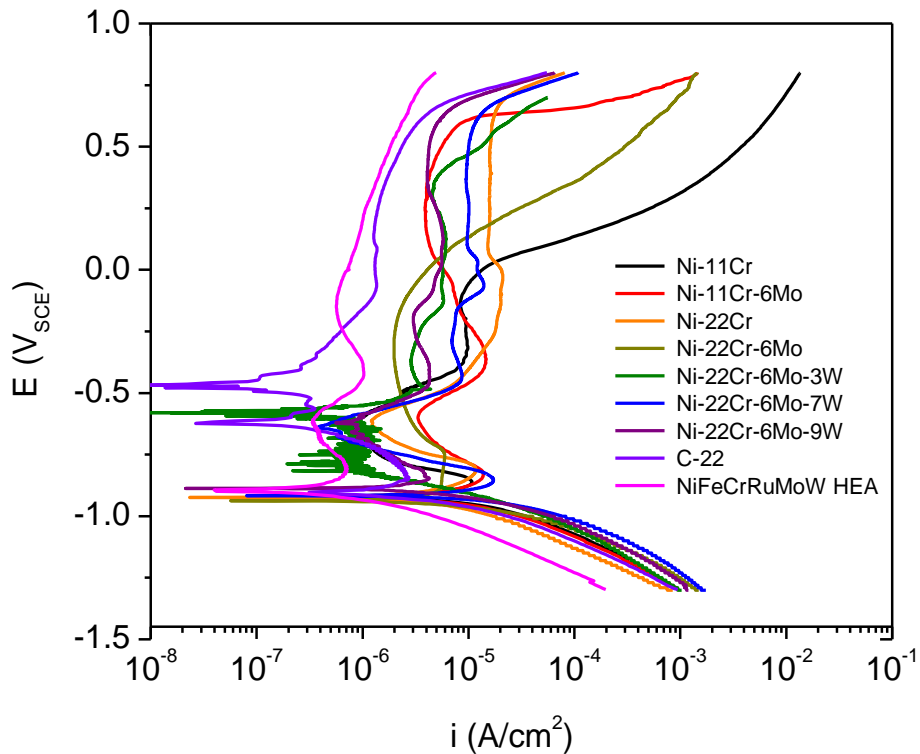


Figure 1.3. Upward polarization curve of various Ni-based alloys, with their compositions given in wt%, in deaerated 0.1 M NaCl pH 4⁴⁷

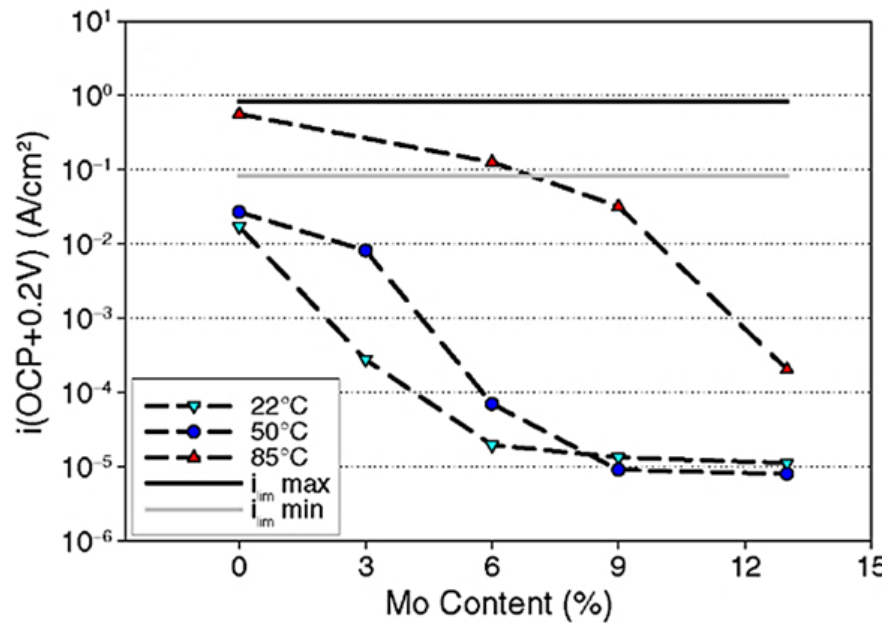


Figure 1.4. Dependence of the anodic current density, i , at $+200\text{ mV}_{OCP}$, on the Mo content for Ni-22Cr-xMo, wt%, model alloys. Tests were performed in deaerated 1 M HCl solution at 22, 50, and 85°C with the calculated mass-transport-limited current density range, i_{lim} , shown for comparison.⁴⁹

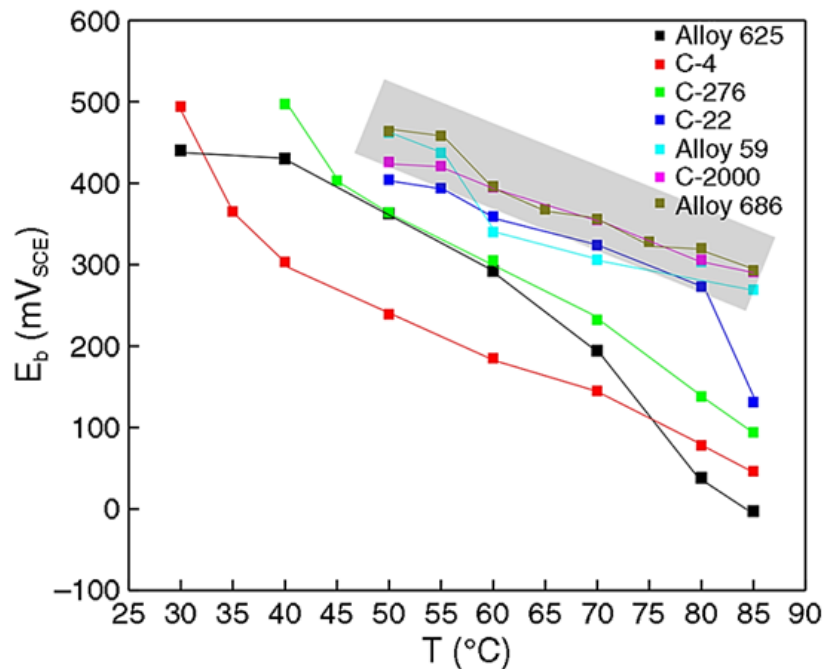


Figure 1.5. Localized corrosion breakdown potentials for various commercial Ni-Cr-Mo-W alloys as a function of temperature measured using galvanostatic polarization for up to 40 hr in 1 M NaCl solution where the shaded region corresponds to alloys with both high Cr and high Mo+W content³¹

2. *In Operando* Measurement of Oxide Film Thickening: Application of Single Frequency Electrochemical Impedance Spectroscopy and Atomic Emission Spectroelectrochemistry

A manuscript based on this chapter has been published:

K. Lutton, K. Gusieva, N. Ott, N. Birbilis, and J. R. Scully. (2017). Understanding multi-element alloy passivation in acidic solutions using operando methods. *Electrochemistry Communications*, 80(7), 44-47.

2.1 Abstract

The kinetics of passivation and dissolution of many corrosion resistant engineering alloys remain incompletely characterized. Clarification of such kinetics and the unique role of alloying elements were investigated upon select Ni-based alloys in an acidic chloride-free sulfate environment using simultaneous electrochemistry and single frequency-electrochemical impedance spectroscopy (SF-EIS). The unique application of online inductively coupled plasma-mass spectrometry (ICP-MS) for evaluation of element-specific contributions to dissolution and oxidation was also presented. The material parameters required for broad and precise application of these techniques were additionally obtained for the alloys in additional sulfate and chloride-containing environments. The combination of methods enabled *in operando* tracking of the total current densities for (i) oxidation, (ii) cation ejection by multiple paths, and (iii) oxide film growth during non-steady state passivation. An improved and physically accurate interpretation of passivation processes is presented and demonstrated to be reliable. Further application of the presented methods will be used throughout the thesis.

2.2 Introduction

2.2.1 Impedance Theory

The investigation of aqueous passivation of metals and alloys under varying experimental conditions for the purposes of assessing passive film thickness and composition is nominally carried out by AC or DC electrochemical techniques¹⁻⁴, ellipsometry⁵⁻⁷, neutron reflectometry⁸, X-ray photoelectron spectroscopy (XPS)^{3,9-11}, and surface-enhanced Raman spectroscopy¹². There is difficulty detecting molecular compounds *in situ* and *ex situ* as well as to track *in operando* film thickness¹². For instance, in order to apply typical techniques such as Faraday's law to passivation data for assessing oxide film kinetics, the oxidation state and current density associated with each

element contributing to growth versus cation ejection into the electrolyte and film dissolution must be extracted from the total current density¹³⁻¹⁵. Such nuances are particularly relevant to understanding the passivation (and repassivation) of multi-element corrosion resistant alloys.

In works to date, repassivation studies of passivating metals are predominantly limited to analysis of single elements in unbuffered or buffered borate electrolytes of alkaline pH, where single cation-containing passive hydroxylated oxides were assumed to be thermodynamically stable, and direct cation ejection or film thinning by chemical dissolution was assumed to be negligible^{5,13,14,16}. Therefore, the total measured current density and charge were presumed to be due to oxide growth^{14,15}. There, however, exists a knowledge gap in the literature regarding *in operando* growth, especially for alloys with multiple cation generation in acidic environments where direct cation ejection, film thinning, and/or chemical dissolution of the oxide film can all occur simultaneously¹⁷.

The assumption that the measured electrochemical current contributes only toward film growth containing a single cation may be unjustified. Similarly, the roles of individual elements in an alloy are often simplified during passivation studies, leading to generalizations such as Cr³⁺ oxides (or hydroxides) are assumed to form while Ni²⁺ and Fe³⁺ dissolve such as from Ni-Cr-Fe¹⁸. Early in the repassivation process, dissolution occurs due to uneven coverage of oxide nanoparticles as they nucleate before coalescing into a continuous layer^{19,20}. Even at extended times when an oxide has fully thickened, film growth compensated by continuous cation ejection and/or dissolution can lead to a quasi-steady state or limiting thickness²¹. These dissolution sources thwart attempts to understand passivation of multi-component alloys in acidic solutions where assuming 100% efficiency in the oxide formation current is invalid. The significant influence of dissolution on passivation in even a chloride-free environment, most notably after a limiting thickness has been reached, is demonstrated in Figure 2.1.

Electrochemical impedance spectroscopy (EIS) is often applied to measure bulk corrosion properties as it is an easy, simple, and automated technique which can characterize both the bulk and interfacial properties of many material types at even steady state conditions. In addition, EIS is non-destructive and capable of making measurements in low conductivity electrolytes. Analysis of passive film thickness is of particular interest to this proposal, but other possible parameters

include polarization resistance, corrosion current density, double layer capacitance, diffusivity, electrode morphology, and the structure of various interfaces amongst others²².

Impedance spectroscopy relies on complex variables to analyze a material-electrode system within the frequency domain. For the purposes of corrosion experiments, a metal/film/electrolyte system is modeled as a circuit containing any number of resistors, inductors, capacitors, constant phase elements, and Warburg diffusion elements. For instance, an ideally polarized metal electrode surface in contact with a Helmholtz double layer in solution can be modeled as a capacitor and resistor in series, the former corresponding to the double layer and the latter for the solution resistance^{22,23}.

However, perfect capacitors and resistors are often not observed for electrochemically growth passive films. Instead, impedance spectroscopy is often represented with phasor quantities where i and V are in-phase, out-of-phase, or anywhere in-between. A constant phase element is often used to quantify impedance when the phasor angle, θ_Z , is between 0 and -90° where the real component indicates resistive behavior while the imaginary indicates capacitive. The complex plane and corresponding unit vectors for a resistor (Z_R), capacitor (Z_C), inductor (which are not relevant for Ni-based alloy passivity and thus outside the scope of this proposal) (Z_L), and an arbitrary constant phase element (Z_{CPE}) phasor at an angle, θ_Z , between Z_R and Z_C are shown in Figure 2.2.

Constant phase elements are used in impedance spectroscopy due to the appearance of a time-constant or frequency distribution resulting from variations in the electrode reactivity. Time constants appear in impedance spectra as capacitive loops or perfect semicircles in a Nyquist plot of quadrant IV in the complex impedance plane (Z_{real} vs $-Z_{imag}$) but for a constant phase element, this loop will be slightly distorted as demonstrated in Figure 2.3. For a perfect capacitor, the time constant, τ , is related to the time needed to decrease the current to approximately 37% of its initial value and can be given for a simple RC circuit as²²:

$$\tau = RC \quad \text{Equation 2.1}$$

The angular frequency, ω , at which the maximum $-Z_{imag}$ in the capacitive loop found in Nyquist plots indicates τ as they are inversely related. Additionally, a capacitive loop can be shifted to the right depending on its corresponding R value, resulting in some overlap of the overall spectra.

Typically, time constants are embedded within one another and difficult to distinguish without the use of spectra fitting. This results in a broad curve within the Bode or Nyquist-type impedance plots. In general, lower frequencies tend to correlate to the impedance of the metal substrate or metal/film interfaces in passive materials, followed by moderate frequencies which correspond to the film itself, leaving higher frequencies for the film/solution interfaces and the solution resistance²². Fitting of this overlapping behavior can be obtained using an electrical circuit model fit where this and the complication of overlapping time constants for a complicated oxide layer is shown in Figure 2.4.

2.2.2 Single Frequency Electrochemical Impedance Spectroscopy (SF-EIS) Technique

As previously indicated in Figure 2.2, the imaginary impedance component of a constant phase element indicates capacitive behavior. The local capacitance, C , of a passive film is directly correlated to its surface area, A , film thickness, l_{ox} , and the film and vacuum dielectric constants, ε and ε_o , respectively:

$$C = \frac{\varepsilon\varepsilon_o A}{l_{ox}} \quad \text{Equation 2.2}$$

A constant phase element (CPE), however, exhibits both capacitive and resistive responses to potential and current fluctuations²³. During fitting impedance spectra to electrical circuits, two parameters are computed: α and Q_{CPE} . For a perfect capacitor, $\alpha = 1$, whereas for resistors, $\alpha = 0$. Hence, α is directly correlated to the CPE phasor rotation angle. Q_{CPE} similarly is related to the magnitude of Z_{CPE} ²³. A constant phase element possesses a similar relationship to l_{ox} , given as²⁴:

$$Q_{CPE} = \frac{(\varepsilon\varepsilon_o)^\alpha A}{g l_{ox} \rho_\delta^{1-\alpha}} \quad \text{Equation 2.3}$$

where ρ_δ corresponds to the film boundary resistivity, A the sample area, and g is a function of α and corresponds to²⁴:

$$g = 1 + 2.88(1 - \alpha)^{2.375} \quad \text{Equation 2.4}$$

The relationship between a CPE and the imaginary impedance, henceforth referred to as Z'' , has previously been established as²⁵:

$$Q_{CPE} = \sin\left(\frac{\alpha\pi}{2}\right) \frac{-1}{Z''(2\pi f)^\alpha} \quad \text{Equation 2.5}$$

In the complex impedance plane, $Z'' < 0$ for capacitive behavior, resulting in a positive Q . From equating Equation 2.3 and Equation 2.5, then, Z'' can be directly correlated to the film thickness by²⁶:

$$l_{ox}(t) = \frac{-Z''(t)(2\pi f \varepsilon \varepsilon_0)^\alpha A}{\rho_\delta^{1-\alpha} \sin\left(\frac{\alpha\pi}{2}\right) [1 + 2.88(1 - \alpha)^{2.375}]} \quad \text{Equation 2.6}$$

Equation 2.6 gives the essential expression for application of SF-EIS to analysis of passive film growth. From measurements of Z'' at a specified frequency, f , over a specific amount of time, l_{ox} variations can be measured across the exposed sample area. The CPE constant, α , is found by fitting an EIS spectrum acquired across a range of high to low frequencies to a circuit model. In addition, the frequency chosen to measure Z'' must correspond to the characteristic one for the passive film time constant. These parameters are highly sensitive to the specifics of electrochemical systems, enabling broad application of SF-EIS for measurements of passive film growth, but must be correctly characterized in order to ensure accurate calculations. Less significantly, ρ_δ must also be quantified for each alloy and solution environment combination but $l_{ox}(t)$ is only marginally dependent on this parameter, as $l_{ox}(t) \propto \rho_\delta^{\alpha-1}$ and α is very close to 1 for a capacitive CPE.

2.2.3 Atomic Emission Spectroelectrochemical (AESEC) Theory

The unique application of AESEC towards measuring partial anodic dissolution rates *in operando* was first performed on 304 stainless steel during linear scan voltammetry, the traditional method for analyzing the overall corrosion behavior of a material at a given potential¹⁷. However, this more antiquated technique requires the decoupling of anodic and cathodic half cells and it is only realistically applicable for pure metals, as even binary alloys typically exhibit preferential dissolution of one element²⁷. As such, online AESEC methods have been developed. The most common of these include inductively coupled plasma optical emission spectrometry (ICP-OES) and inductively coupled plasma mass spectrometry (ICP-MS). ICP emission spectrometry is advantageous as it is sensitive to most elements in solution, has a linear dynamic range around five to six orders of magnitude, and can typically detect up to 16 elements at any given time and trace quantities of elements can be detected at parts per billion concentration levels. In addition, the oxidative mass gains measured using ICP-OES were confirmed using gravimetric measurements²⁷.

Each technique utilizes a flow electrochemical cell connected to a nebulizer and chromator, shown schematically in Figure 2.5, where the elemental concentration transients are measured downstream throughout the experiment time at relatively short intervals.

The major limitation of the technique is the temporal resolution and hydrodynamic range due to the fast, low volume flow from the cell and the limits presented by the aspiration-nebulization system present within the spectrometer¹⁷. This has been thoroughly characterized and modeled^{17,28} by, first experimentally later computationally, using high current galvanostatic or potentiostatic pulse to quickly dissolve a metal or alloy, followed by measuring the shape and width of the temporal concentration profile. An example of this process is given in Figure 2.6 where the respective experimental setup has a resolution of $\tau \approx 15$ s. Another characteristic parameter of the residence time distribution, β , can be determined from the full width-half max of the Gaussian peak. This setup characterization provides measurements of the residence time distribution as a functional of various experimental parameters (i.e. flow cell volume and flow rate). The Gaussian velocity distribution profile during the laminar flow produced by the flow cells causes this observed spread of data evident in Figure 2.7, and as such it must be computed. The time resolution, given by τ , can be improved by increasing the flow rate, but doing this excessively can result in heterogeneous electrolyte flow across the surface²⁸. This relationship, along with the effect of flow rate on β is given in Figure 2.8. Once the solution hits the nebulizer, the solution is aspirated and processed through a spectrometer to produce the emission spectra. By comparing these spectra to those produced by aqueous standards of known concentrations, the exact concentration of each element within the flow can be determined as a function of time²⁹.

As mentioned previously, there are two common types of flow cell AESEC applied in literature and each has its own advantages: ICP-MS and ICP-OES. ICP-MS is often used for applications with more dilute constituents as it can often detect to the previously mentioned limit of 1 part per billion. The mass-sensitivity of the spectrometer can also distinguish between unique isotopes. While the incredibly high resolution is only possible for a few elements using ICP-AES, it typically has faster acquisition than its counterpart and the resulting spectra have less matrix effects due to the aspiration of molecular compounds. Additionally, the systems themselves are less expensive²⁹. For this thesis, all AESEC work presented was obtained using an online ICP-MS located at Monash University in Melbourne, Australia through a collaboration with the Materials

Science and Engineering Department. MS was selected over OES for its optimal concentration resolution, as the dilute Mo concentrations and minimal Cr dissolution commonly observed for Ni-based alloys would be otherwise difficult to detect. The AESEC experiments and the results are included in Chapters 3-6.

2.2.4 Application and Analysis of Online AESEC

The application of AESEC for analysis of individual element dissolution and oxidation kinetics is as computationally complex as previously discussed for SF-EIS. The concentration of a specific element can be directly calculated from the emission spectra:

$$C_M(t) = k[I_\lambda(t) - I_\lambda^o] \quad \text{Equation 2.7}$$

where k is a proportionally constant obtained by measuring the emission intensity of several standardized solutions of known and varying concentrations, I_λ is the emission intensity at any given time and wavelength which corresponds to the desired element, M , and I_λ^o is the background intensity. Both of these are shown schematically in Figure 2.6. From this concentration profile, the dissolution current density measured by the ICP-MS setup can be directly obtained:

$$i_{diss}^M(t) = \frac{zFf_e C_M(t)}{M_M} \quad \text{Equation 2.8}$$

where z is the metal cation valency, F is Faraday's constant, f_e is the electrolyte flow rate, and M_M is the molar mass of element M . The total dissolution current density is then the sum for all elements in an alloy:

$$i_{diss}(t) = \sum i_{diss}^M(t) \quad \text{Equation 2.9}$$

The novel application of this technique comes from the computation of the individual oxidation contribution for a given element: $i_{ox}^M(t)$. Equation 2.8 and Equation 2.9 give only the current flux corresponding to dissolution. The total electrochemical current commonly measured using a potentiostat, i_{EC} , includes i_{diss} and the current density corresponding to oxidation, i_{ox} :

$$i_{EC}(t) = i_{ox}(t) + i_{diss}(t) \quad \text{Equation 2.10}$$

Analysis of the oxidation current is possible through the derivation of $i_{ox}(t)$ through Faraday's law:

$$i_{ox}(t) = \frac{n\rho_{ox}F}{M_{ox}} \frac{dl_{ox}}{dt} \quad \text{Equation 2.11}$$

where n is the cation valency for the molecules present in the passive film, ρ_{ox} is the average film density, and M_{ox} is the average molar mass, all approximated from *ex situ* film composition measurements. From either the SF-EIS or ICP-MS methods, the oxidation efficiency of the current can be computed:

$$\eta = \frac{i_{ox}}{i_{EC}} \quad \text{Equation 2.12}$$

However, Equation 2.11 only gives the global rate of film thickening, not the coveted contribution of individual elements towards passivation. In order to obtain selective $i_{ox}^M(t)$, the average, total electrochemical current was assumed to be approximately that caused by congruent dissolution based on the alloy composition:

$$i_{cong\ diss}^M(t) = (at\% M)i_{EC}(t) \quad \text{Equation 2.13}$$

This approximation will be shown in later chapters to be valid for the passive film, especially at short times due to the solute capture of the bulk metal into non-equilibrium oxides. Based on Equation 2.13, the rate of metal cation accumulation in the passive film, $i_{ox}^M(t)$, can be obtained:

$$i_{ox}^M(t) = i_{cong\ diss}^M(t) - i_{diss}^M(t) \quad \text{Equation 2.14}$$

The surface accumulation of metal cations (atom/cm²) is directly related to this oxidation flux by the expression:

$$N_M = \frac{N_A}{zF} q_{ox}^M = \frac{N_A}{zF} \int_0^t i_{ox}^M(t) dt \quad \text{Equation 2.15}$$

where N_A is Avogadro's number and q_{ox}^M is the integrated oxidation charge for element M. The concentration (at%), then, of a given cation is given by:

$$C_M(t) = \frac{N_M(t)}{\sum N_M(t)} \quad \text{Equation 2.16}$$

A general schematic of the relative oxidation and dissolution for individual alloying elements is given in Figure 2.9.

2.3 Objective

The primary objective of this chapter is to develop an electrochemical framework for analyzing operando film growth during potentiostatic and galvanostatic passivation experiments.

Single frequency electrochemical impedance spectroscopy (SF-EIS) is used to measure variations in the imaginary impedance of a passive film during growth by superimposing an AC signal onto a constant applied DC potential or current density. The SF-EIS technique enables accurate measurement of the film thickness changes with time and the relevant oxidation current density independent from the total electrochemical one typically measured using electrochemistry. This chapter aids in analyzing the growth rate independently from dissolution and cation-ejection reactions and enables accurate analysis of growth kinetics by disregarding the currents corresponding to film thinning or localized corrosion events.

2.4 Application of the SF-EIS Framework

2.4.1 Determination of $\alpha(t)$

The metallic samples used for this study were polycrystalline Ni-based alloys prepared by induction arc-melting, followed by casting, cooling, sectioning, and annealing to produce fine-grained microstructures. The compositions (wt%) for the investigated alloys are as follows: Ni, Ni-11 Cr, Ni-11 Cr-6 Mo, Ni-22 Cr, and Ni-22 Cr-6 Mo. Before electrochemical testing, these samples were sequentially ground to 1200 grit using SiC paper and rinsed in deionized water before being inserted into the conventional three-electrode electrochemical cell used for experiments, shown schematically in Figure 2.10. This setup included a Pt mesh counter electrode and either a saturated calomel (SCE) or mercury-mercurous sulfate (MMSE) ($V_{MMSE} = -210 \text{ mV}_{SCE}$) electrode for the aqueous NaCl and Na₂SO₄-containing environments, respectively. Crevice corrosion was mitigated by using a new Teflon O-ring before each experiment, allowing the impedance measurements to correspond only to the film and not any localized corrosion processes.

The solutions were prepared using reagent-grade NaCl and Na₂SO₄ and acidified to pH 4 using HCl or H₂SO₄, respectively. The chemistries are given as: 0.1 M Na₂SO₄ and 0.1 M NaCl. These chemicals were dissolved in ultra-high purity deionized water dispensed from a Milli-Q (resistivity of 18.2 M Ω -cm) and during experimentation, the solutions were deaerated using high-purity N₂ gas.

An initial cathodic reduction step at $-1.3 \text{ V}_{\text{SCE}}$ ¹ for 10 min was used before all electrochemical experiments in order to minimize the existence of air-formed oxides on the alloy surface. During this step, gaseous H_2 was evolved on the surface due to the high cathodic applied potential and collected at the surface due to the presence of the O-ring. The bubbles were periodically removed during the reduction step via an added pipette filled with same solution as the cell body. This enabled the metal electrode to remain in contact with the electrolyte. Following this, rapid EIS scans were obtained at frequencies from 1,000 to 1 Hz at an applied DC potential of $+0.2 \text{ V}_{\text{SCE}}$ with a superimposed AC amplitude of $+20 \text{ mV}_{\text{rms}}$. This enabled one spectrum to be obtained approximately every 32 s. In addition, the use of a passivating potential results in the nucleation, convergence, and thickening of the film layer to be captured by the evolution of the EIS spectrums. The impedance measurements were performed sequentially until 300 spectra were recorded. It is worth noting that this results in passivation for just under 10,000 s.

From these numerous spectra, fitting to a simplistic circuit containing a CPE in parallel with a resistor, R_p , in series with another resistor, R_s , where the former corresponds to the polarization resistance of the passive film and the latter the solution ohmic resistance. This circuit is indicated below in Figure 2.13. For the sake of simplicity, such analysis was only performed and plotted for certain scan numbers. Fitting was performed using Gamry Echem Analyst software.

2.4.1.1 Evolution of the Bode plot

For comparison, Bode-type plots of the first 10 spectrums obtained on the most and least corrosion-prone alloys, Ni and Ni-22 Cr-6 Mo, during passivation in the Na_2SO_4 and NaCl environments are given in Figure 2.11 and Figure 2.12. The last spectra are additionally provided to demonstrate the steady-state condition that is merely approached during the first several hundred seconds. The results demonstrate a clear influence of solution chemistry. In only 0.1 M NaCl at pH 4, Ni is unable to uniformly passivate at all times. The slight increase in Z_{phz} up until scan 5 indicates some increasingly capacitive behavior, but it declines after this short time interval.

The effect of alloying additions can be similarly seen by comparing the sets of spectra. In Na_2SO_4 , both the film thickness, as indicated by an increase in Z_{mod} , and the capacitive behavior,

¹ This potential was chosen based on Pourbaix predictions for the stability of Cr and Ni metal phases versus their oxides in pH 4 and 10 environments⁵⁶

due to the slight increase in Z_{phz} , were greater for the more alloyed material. This trend was consistent with the spectrums measured for Ni-11 Cr, Ni-11 Cr-6 Mo, and Ni-22 Cr where the film improved in a similar manner as the % Cr and % Mo increased. Evident in the chloride solutions, the addition of Mo greatly enabled the film to remain passive at the low scans and the final one. Only Ni-22 Cr-6 Mo exhibited a continued increase in Z_{mod} and a decrease in Z_{phz} during the entire passivation time as a result of its strong alloying.

2.4.2 Evolution of $Q(t)$ and $\alpha(t)$

The calculated CPE parameters, $Q(t)$ and $\alpha(t)$, were calculated by fitting the full spectra (e.g. Figure 2.11 and Figure 2.12) to the simple circuit model shown in Figure 2.13. The results are given in Figure 2.14 and Figure 2.15 for the acidified Na_2SO_4 and NaCl environments, respectively. In the former solution, there was a general decrease in $Q(t)$ as the concentration of alloying elements increased. This indicates a thicker film, as Q and l_{ox} are inversely proportional in Equation 2.3. The drop between Ni and Ni-11 wt% Cr was most notable, demonstrating the strong effect of Cr as a passivation promoter as 11 wt% is past the predicted concentration where a continuous Cr-oxide/hydroxide layer can form³⁰⁻³³. From the results, it can also be surmised that at early times, the passive films nucleate and grow until they converge and form a conformal layer at approximately 70 – 100 s. This nucleation and growth processes is apparently faster for the more alloyed materials due to the lower initial Q value measured.

In the chloride environment, a similar trend in Q versus $[\text{Cr} + \text{Mo}]$ was observed. The influence of the minor alloying elements was much greater, as there is a discernable difference between Ni, the Ni-11 Cr-based, and the Ni-22 Cr-based alloys. This is due to the greater passivity of the high $[\text{Cr} + \text{Mo}]$ alloys in the corrosive chloride environment. The films, in general, exhibited a thicker film than in the sulfate environment, evident by the decrease in Q when comparing Figure 2.14a and Figure 2.15a. After a few hundred seconds of passivation, there is a clear leveling off in Q due to the limiting thickness being reached for the passive films. At this point, the chloride-assisted dissolution becomes equivalent to that of passivation and there are no discernable gains in l_{ox} . This is very different from what can be observed in Figure 2.14a, where Q continues to decrease even at long times as the limiting l_{ox} is not reached for the less harsh environment.

The trends in $\alpha(t)$ are similar to those previously explained, where a clear increase is observed for the more alloyed materials (Figure 2.14b and Figure 2.15b). This is most notable at early times, where Ni and Ni-11 Cr had very low measured values of α that rapidly increased after 70-100 s. This was the same observed time to presumably nucleate and grow sufficiently such that a conformal film can be achieved. The binary and ternary alloys all showed increasing values of α with a later plateau after a few hundred seconds. The difference between them was very slight, with Ni-22 Cr exhibiting the greatest α at almost all times. Ni, however, decreased after 300 s. This can be attributed to film dissolution in even the chloride-free environment. Due to the acidic nature and the lack of Cr-rich species in the film, the film becomes more resistive after reaching the limiting thickness observed in Figure 2.14a. Finally, the more alloyed materials had the greatest measured α initially due to favorable nucleation, especially when Mo was synergistically alloyed in tandem with Cr³⁴.

As for the NaCl environment, there was once again a strong observed effect of alloying content. The higher [Cr + Mo] materials had a higher initial α but very quickly became overtaken and the order flips, with Ni being the highest after approximately 300 s. This suggests the greater capacitive behavior of the Ni-rich films compared to the more resistive Cr and Mo-rich ones. The α for NaCl is higher than that in Na₂SO₄ for all times, presumably due to greater Cr-enrichment versus Ni. This phenomenon has been observed in previous literature on Alloy 22, where increasing [Cl⁻] results in a corresponding increase in the film's fraction of Cr³⁺ cations^{1,10,35}.

2.4.3 Determination of ρ_δ

In the original formulation of the Power-Law CPE fit^{24,36}, the boundary resistivity constant, ρ_δ , was provided with no justification of its physical significance. Instead it is used to better equate the thickness computed using a CPE fit for a given oxide to its true thickness. The closest literature constant is given as 450 Ω -cm for the film on stainless steel³⁷. As such, this parameter needs to be evaluated to more accurately analyze SF-EIS results. From Equation 2.6, ρ_δ can be obtained as:

$$\rho_\delta = \left[-\frac{(2\pi\epsilon\epsilon_0 f)^\alpha Z''}{g(\alpha)l_{ox} \sin\left(\alpha\frac{\pi}{2}\right)} \right]^{\frac{1}{1-\alpha}} \quad \text{Equation 2.17}$$

Most evident from Equation 2.18 is the exponential dependence of ρ_δ on all the experimental constants. Since the assumption $\alpha = 0.95$ for most of this thesis, $\frac{1}{1-\alpha} = 20$. Small variations in l_{ox} and Z'' will result in significant changes in ρ_δ .

Independent computation of l_{ox} is necessary to determine ρ_δ . This is most commonly done using through fits of XPS spectra³⁸:

$$l_{ox} = \lambda_o \sin \theta \ln \left[\frac{N_m \lambda_m I_o}{N_o \lambda_o I_m} + 1 \right] \quad \text{Equation 2.18}$$

where λ_o , λ_m = the inelastic mean free path of the appropriate photoelectrons in the oxide and metal, respectively; θ = the electron take-off angle with respect to the sample surface; N_o , N_m = the volume free density of metal atoms in the oxide and metal, respectively; I_o , I_m = the total integrated peak area intensities of the oxide and metal photoelectron peaks, respectively. The relevant constants are included below in Table 2.1. This expression assumes a single uniform over-layer so that the signal attenuation is appropriately characterized by the ratio in peak areas^{38,39}.

For many of the alloys in this thesis, dilute minor additions (e.g. Cr and Mo) can experience depletion within the metal at the metal/oxide interface. This will result in their observed I_M being lower than it would be for the bulk as the probing depth of an XPS is approximately 5 nm. Because of this, the area of the Ni-metal peak was often used as a reference to correct for the depletion of other elements. To obtain the true, undepleted peak intensity, I'_M , the metal composition of the minor element (in at%) and the atomic sensitivity factor, A_M , of it and Ni were used⁴⁰:

$$I'_M = \frac{I_{Ni} A_M}{A_{Ni}} \left(\frac{\text{at}\% M}{\text{at}\% Ni} \right) \quad \text{Equation 2.19}$$

Combined application of Equation 2.17 - Equation 2.19 result in measured values of ρ_δ . The values calculated for the passive films formed on Ni-22 Cr and Ni-22 Cr-6 Mo, wt%, following potentiostatic holds at +0.2 V_{SCE} for 10 ks in several environments are given in Table 2.2. The XPS results will be presented later, but the measured final film thicknesses, l_{ox} , from the SF-EIS results and the XPS spectra analysis are included for reference.

2.4.4 Application of Potentiostatic Single Frequency Electrochemical Impedance Spectroscopy (pSF-EIS)

Gamry Instruments possesses a potentiostatic SF-EIS (pSF-EIS) experiment in their commercial framework. In it, an applied DC potential (E_{app}), AC voltage (typically 10 or 20 mV_{rms}), frequency, and total acquisition time are required. The output data includes the time of measurement, Z' , Z'' , the impedance phasor's modulus (Z_{mod}) and phase angle (Z_{phz}), and the total electrochemical current density (i_{EC}), as shown schematically in Figure 2.16. Initially, the frequency of the AC signal was established for the electrochemical cell opening used ($A = 0.1 \text{ cm}^2$) through modeling of the impedance for only the oxide layer (Figure 2.18) and inspection of a full EIS spectrum (Figure 2.19). The maximum in Z_{phz} was interpreted as the frequency best corresponding to the time constant for capacitive passive film behavior at steady state (assumed to be seen after 72 ks). The frequency approximated as 1 Hz from this method. While 10 Hz may also seem like a suitable choice, it often corresponds to a buried interfacial time constant and thus is not as reliable for extensive application. For changes in areas, a corresponding change in the SF-EIS frequency will occur (i.e. 100 Hz for $A = 0.1 \text{ mm}^2$ wire samples).

A typical three-electrode flat cell was used for the SF-EIS experiments with a Pt mesh counter electrode and a mercury-mercurous sulfate reference electrode. The still solution was identically deaerated and air-formed oxides were cathodically reduced at -1.3 V_{SCE} for 10 min^{3,41}. A Gamry Reference 600 potentiostat and the SF-EIS script was applied at $+0.2 \text{ V}_{SCE}$ with 1 Hz frequency and a 20 mV AC amplitude. Following SF-EIS, an EIS spectrum was acquired from 100 kHz to 1 mHz for correlation of imaginary impedance, $Z''(t)$, to an oxide thickness, $l_{ox}(t)$, using an equivalent circuit model for Ni-alloys³ (Equation 2.6).

An example of pSF-EIS data produced using Gamry's script is given in Figure 2.20. It is evident that film growth observations typical nucleation and growth processes over the first few hundred seconds before hitting a limiting thickness. Because of small fluctuations in the measured Z_{imag} due to application of an AC signal, the pSF-EIS data will need to be smoothed before calculating a derivative. The i_{ox} curves computed from the data in Figure 2.20 are shown in Figure 2.21.

2.4.5 Application of Galvanostatic Single Frequency Electrochemical Impedance Spectroscopy (gSF-EIS)

Similar to pSF-EIS, galvanostatic SF-EIS (gSF-EIS) is possible using a Gamry Framework script which sets constant, applied DC and AC currents and measures variations in the real and imaginary impedance components with time. The major distinction between potentiostatic and galvanostatic film growth is that the final thickness is fixed and the current changes in response to the film thickness increase for the former method whereas its growth rate is controlled by the latter and the measured potential changes are in response to film thickening^{15,42,43}. Equation 2.11 will be similarly applied to gSF-EIS data in order to measure passive film growth under galvanostatic conditions. An example of the influence of applied current density on film growth is shown in Figure 2.22.

Because of the potential for rapid passivation rates at high applied current densities, *in operando* gSF-EIS is necessary to measure film thickening. Measurement of impedance spectra during galvanostatic polarization is possible, as shown in Figure 2.23. Data acquisition is, however, time-consuming and the results are very scattered. As such, overall trends can only be predicted. Application of gSF-EIS can remediate this issue and produce curves more representative of the *in operando* passivation process under galvanostatic-control (Figure 2.24) via the same correlation of the imaginary impedance to an oxide thickness previously established for the potentiostatic case (Equation 2.6). As with pSF-EIS, a constant frequency (1 Hz) and AC fluctuations ($i_{AC} = 0.05 \mu\text{A}/\text{cm}^2$) were applied.

As previously done for pSF-EIS method, gSF-EIS was applied to the same materials to characterize passivation in a 0.1 M Na_2SO_4 environment. A periodic current was imposed during current-controlled passivation up to +0.2 V_{SCE} (Figure 2.25) in order to measure the impedance, as shown in Figure 2.26. The same analysis of l_{ox} , i_{ox} , and η was applied as demonstrated in Figure 2.20 and Figure 2.21. Notably, the i_{EC} in Equation 2.12 is interpreted to be i_{app} in this case as it is the overall reaction rate of oxidation and dissolution for the system.

The results demonstrate that thicker films are achieved at lower rates. This is likely caused by an increase in dissolution during fast passivation at a high i_{app} and the challenging kinetics necessary for nucleation and growth of oxide films. In Figure 2.26b, it is evident that all alloys

nucleated and grew passive films around $-500 \text{ mV}_{\text{SCE}}$. This is often interpreted as the critical passivation potential, E_{pp} . Similar to potential-controlled passivation (Figure 2.20), a pseudo-limiting thickness was reached for each i_{app} . Upon analysis of i_{ox} (Figure 2.27ab), i_{ox} also goes towards 0 at long times (or high potentials). However, fluctuations in $-Z''$ as shown in Figure 2.26 resulted in negative values for i_{ox} when thinning is predicted. Within the passive region from -500 to $+200 \text{ mV}_{\text{SCE}}$, however, it remains positive for the most part (Figure 2.27b). Based on the computed i_{ox} and the corresponding i_{app} , η also appears to be initially higher for lower i_{app} (Figure 2.27cd). At long times however, $\eta \rightarrow 0$.

Following the thoroughly analyzed gSF-EIS passivation, a full EIS spectrum was obtained in order to compare the films *in situ* (Figure 2.28). There are slight increases evident in the modulus and phase of the passive film portion of the impedance spectra around 1 Hz, the frequency used for gSF-EIS, for slow i_{app} data. This indicates a thicker and more capacitive film as a result of the slow growth. The differences are, however, slight. There is no shift in the oxide time constant due to a distinctly different film being formed at fast or slow rates or the emergence of a second time constant altogether. Additionally, no broadening of the phase modulus is evident as this would suggest a defective film being formed at high rates. As such, films that can be thought to behave similarly electrochemically with slight differences in l_{ox} were achieved using current-controlled passivation and characterized through application of gSF-EIS.

2.5 Discussion

The influence of chloride-assisted film dissolution is significant when passive films are considered to exhibit constant phase element-like behavior. While the physical interpretation of CPE behavior has been contested in previous literature, the results presented herein demonstrated that the presence of chloride anions produced films with greater capacitive behavior and thicknesses, evident by the increase in $\alpha(t)$ and decrease in $Q(t)$. Increasing surface roughness has also been shown to result in a greater α exponent⁴⁴⁻⁴⁶. This notion supports the observation that the alloys have higher measured α values in the chloride environment, which has been recently shown to induce greater RMS as found using AFM following passivation⁴⁷. One recent publication correlated α to the anomalous diffusion power, n , where it was shown that when $\alpha = n = 1$, diffusion occurs as it does for a perfect capacitor⁴⁸. In the case of semiconductors like the expected

passive film on Ni-Cr-Mo alloys, charge transfer results in slowed subdiffusional processes and thus $n < 1$. The increased α and decreased Q directly support faster diffusion and therefore film thickening in the NaCl environment when compared to the Na₂SO₄ one.

During the early stages of passivation in either environment, the Mo-containing alloys exhibited higher measured α values than their Ni-Cr counterparts. In the context of subdiffusion, this supports the thought in literature that Mo acts in synergy with Cr to promote nucleation and growth of passive films³⁴. The same logic applies to the sulfate environment at all times, where Ni had a much lower α (i.e. slower n) than the alloys containing Cr and Cr + Mo. However, at longer times in the chloride-containing solution, α decreases with alloying content. As such, Mo is perhaps slowing the diffusion of point defects necessary for passivation. Literature supports this notion, where Mo-containing alloys have been found to form a thinner passive film^{1,35,49,50}. Additionally, Mo, when incorporated in passive films as a substitutional defect on a Cr³⁺ or Ni²⁺ site (i.e. Mo_{Cr}³⁺ or Mo_{Ni}⁴⁺ for a Mo⁶⁺ defect), has been proposed to slow the migration of cation vacancies by forming immobile complexes^{34,51}. This idea further supports the decreasing α in chloride-containing solutions, as local film dissolution generates such point defects^{52,53}. In aqueous Na₂SO₄, such an effect would be minimal due to the low amount of film dissolution induced by the acidic environment.

The exponential dependence of l_{ox} on α (Equation 2.6) is greatly impacted by these factors. During previous application of the SF-EIS method in literature^{26,39,54}, the α used in Eq. 3 was assumed to be constant and the value used was measured using a full EIS spectrum following the conclusion of passivation. Typically, this would yield values of ~0.95 after 10 ks for the various Ni-based alloys that have been investigated. However, Figure 2.14b and Figure 2.15b demonstrate that this is an inaccurate assumption for approximately the first 100 s when nucleation and growth are still occurring rather than film thickening. As such, there is greater experimental error in the early stage of passivation. In fact, if the $\alpha(t)$ curves are applied to SF-EIS data, it results in enormous and unrealistic values of l_{ox} at early times as indicated in Figure 2.29. When a continuous film is reached, α is approximately constant during the region of film thickening.

It can be argued that using this limiting value of α measured following passivation is not entirely accurate for describing the behavior of the system as a whole during early film growth, but it is indeed valid when measuring only the passive film itself. Multi-frequency EIS spectra

provide a global measure of the system and cannot distinguish the passive film independently from the double layer, interfaces, or the metal electrode. As a result, the measurements of α are impacted by these artifacts. Especially during the measurements of a non-continuously covered film layer, the incredibly resistive and exposed metal surface would decrease the overall α despite the adjacent, high α oxide nuclei. The $\alpha(t)$ thus does not apply to specifically the oxide layer and rather fits better for the system as a whole. The low, initial values should then not be used to calculate $l_{ox}(t)$ and the steady-state value can be used as a more accurate representation of the passive film itself and not the other components of the system.

As for the boundary film resistivity parameter, ρ_δ , its measured values for various Ni-Cr(-Mo) alloys exposed to the environments of interest in this dissertation were highly dependent on the film thicknesses according to XPS analysis as they varied more than those measured using pSF-EIS. This is likely caused by the only valid application for Strohmeier's electron spectroscopy for chemical analysis (ESCA) method (Equation 2.18) is for distinct layers of the NiO, Ni(OH)₂, Cr₂O₃, Cr(OH)₃, MoO₂, and MoO₃ layers^{38,55}. Any non-heterogeneities in the film would result in the oxide thickness being overestimated and any resulting value of ρ_δ to vary greatly. The results in Table 2.2 suggest the same uncertainties. In general, it was observed that ρ_δ was higher in the sulfate environments and also for Ni-Cr in the alkaline NaCl one due the strong stability of NiO/Ni(OH)₂ at high pH values⁵⁶⁻⁶⁰.

These variations in ρ_δ will, however, not substantially impact any application of SF-EIS to potentiostatic or galvanostatic passivation. Notably, Ni-Cr exhibited the highest and lowest values in 0.1 M NaCl at pH 10 and pH 4, respectively. Since $l_{ox} \propto \rho_\delta^{\alpha-1}$ and α is commonly approximated to be 0.95 for long-term passivation, for the aforementioned values (1,456 at pH 10 and 151 at pH 4) will instead be reduced to 0.70 and 0.78. This suggests that any changes in ρ_δ will not strongly influence SF-EIS. In general, using the literature value, 450 $\Omega\text{-cm}^2$, for every alloy and environment combination as an average approximation is therefore valid. This is likely because it was established for stainless steels, which often possess films rich in Ni and Cr oxide species. With passivation time, ρ_δ should intuitively vary as the passive film composition does. But again, this would be insignificant due to the weak dependence of l_{ox} on ρ_δ . Testing the temporal variations proves challenging because of the need to perform in-depth XPS analysis at

each time step and as such, only the steady-state films have been considered^{24,36,55,61}. For the remainder of this dissertation, however, the values of ρ_δ from Table 2.2 will be used.

2.6 Conclusions

Aqueous oxide growth under potentiostatic conditions was investigated *in operando* using Single Frequency Electrochemical Impedance Spectroscopy (SF-EIS) in a chloride-free environment under both potential- and current-control. The oxidation current density, i_{ox} , was successfully monitored by SF-EIS. The measurement of *in operando* film thickness in real-time has revealed the significant impact of cation ejection during all stages of passivation in acid, especially at longer times, whilst highlighting the contribution of individual alloying elements on the reactions occurring. Processes governing oxide growth must be taken into consideration in order to construct accurate growth laws for thin film passivation. The temporal nature of α has a significant effect on application of SF-EIS as a result of variable film diffusional processes at different time scales. The variations in $\alpha(t)$ during electrochemical passivation are reported. In general, it was found that α increased with time as the passive films nucleated, grew, and converged into a conformal layer. These relatively small changes can result in large experimental errors at early times, as the common convention is to use the α measured after passivation and $l_{ox}(t)$ is exponentially dependent on α . However, it is unclear whether the early values are impacted by the exposed metal surface before the film converges and thickens, resulting in a validation of using the steady-state α . There was also a strong observed influence of solution chemistry and alloying content, where the presence of chlorides espouses diffusion and film growth. The charge transfer inherent to semiconducting films results in $\alpha < 1$ at all times, but each alloy exposed to each solution has relative increases or decreases in its diffusion behavior. The measured ρ_δ similarly varied with alloying content and exposure environment, but this influence on Equation 2.6 was minimal, as demonstrated in Table 2.2.

2.7 References

1. Lloyd, A. C., Noël, J. J., McIntyre, S. & Shoesmith, D. W. Cr, Mo and W alloying additions in Ni and their effect on passivity. *Electrochim. Acta* **49**, 3015–3027 (2004).
2. MacDonald, D. D. & Sun, A. An electrochemical impedance spectroscopic study of the passive state on Alloy-22. *Electrochim. Acta* **51**, 1767–1779 (2006).
3. Jakupi, P., Zagidulin, D., Noël, J. J. & Shoesmith, D. W. The impedance properties of the oxide film on the Ni-Cr-Mo Alloy-22 in neutral concentrated sodium chloride solution.

- Electrochim. Acta* **56**, 6251–6259 (2011).
4. Chao, C. Y., Lin, L. F. & Macdonald, D. D. A point defect model for anodic passive films III. Impedance response. *J. Electrochem. Soc.* **129**, 1874–1879 (1982).
 5. Sato, N. & Kudo, K. An ellipsometric study of anodic passivation of nickel in borate buffer solution. *Electrochim. Acta* **19**, 461–470 (1974).
 6. Seo, M., Saito, R. & Sato, N. Ellipsometry and Auger Analysis of Chromium Surfaces Passivated in Acidic and Neutral Aqueous Solutions. *J. Electrochem. Soc.* **127**, 1909–1912 (1980).
 7. Lukac, C., Lumsden, J. B., Smialowska, S. & Staehle, R. W. Effects of Temperature on the Kinetics of Passive Film Growth on Iron. *J. Electrochem. Soc.* **122**, 1571–1597 (1975).
 8. Tun, Z., Noel, J. J. & Shoesmith, D. W. Electrochemical Modification of the Passive Oxide Layer on a Ti Film Observed by In Situ Neutron Reflectometry. *J. Electrochem. Soc.* **146**, 988–994 (1999).
 9. Willenbruch, R. D., Clayton, C. R., Oversluizen, M., Kim, D. & Lu, Y. An XPS and electrochemical study of the influence of molybdenum and nitrogen on the passivity of austenitic stainless steel. *Corros. Sci.* **31**, 179–190 (1990).
 10. Zagidulin, D., Zhang, X., Zhou, J., Noël, J. J. & Shoesmith, D. W. Characterization of surface composition on Alloy 22 in neutral chloride solutions. *Surf. Interface Anal.* **45**, 1014–1019 (2013).
 11. De Vito, E. & Marcus, P. XPS study of passive films formed on molybdenum-implanted austenitic stainless steel. *Surf. Interface Anal.* **19**, 403–408 (1992).
 12. Oblonsky, L. J. & Devine, T. M. A surface enhanced Raman spectroscopic study of the passive films formed in borate buffer on iron, nickel, chromium and stainless steel. *Corros. Sci.* **37**, 17–41 (1995).
 13. Davenport, A. J. & Burstein, G. T. Concerning the Distribution of the Overpotential during Anodic Oxide Film Growth. *J. Electrochem. Soc.* **137**, 1496–1501 (1990).
 14. Davenport, A. J. & Lee, B. K. Passive Film Growth Kinetics for Iron and Stainless Steel. *Electrochemical Society Proceedings* **13**, 187–197 (2002).
 15. Burstein, G. T. & Davenport, A. J. The Current-Time Relationship during Anodic Oxide Film Growth under High Electric Field. *J. Electrochem. Soc.* **136**, 936–941 (1989).
 16. Sato, N. & Cohen, M. The Kinetics of Anodic Oxidation of Iron in Neutral Solution I. Steady Growth Region. *J. Electrochem. Soc.* **111**, 512–519 (1964).
 17. Ogle, K. & Weber, S. Anodic Dissolution of 304 Stainless Steel Using Atomic Emission Spectroelectrochemistry. *J. Electrochem. Soc.* **147**, 1770–1780 (2000).
 18. Marcus, P. & Grimal, J. M. The anodic dissolution and passivation of NiCrFe alloys studied by ESCA. *Corros. Sci.* **33**, 805–814 (1992).
 19. Maurice, V., Yang, W. P. & Marcus, P. X-Ray Photoelectron Spectroscopy and Scanning Tunneling Microscopy Study of Passive Films Formed on (100) Fe-18Cr-13Ni Single-Crystal Surfaces. *J. Electrochem. Soc.* **145**, 909 (1998).
 20. Machet, A. *et al.* XPS and STM study of the growth and structure of passive films in high temperature water on a nickel-base alloy. *Electrochim. Acta* **49**, 3957–3964 (2004).
 21. Cabrera, N. & Mott, N. F. Theory of the oxidation of metals. *Reports Prog. Phys.* **12**, 163–184 (1949).
 22. Orazem, M. E. & Tribollet, B. *Electrochemical Impedance Spectroscopy*. (John Wiley & Sons, Inc., 2008). doi:10.1002/9780470381588

23. Brug, G. J., van den Eeden, A. L. G., Sluyters-Rehbach, M. & Sluyters, J. H. The analysis of electrode impedances complicated by the presence of a constant phase element. *J. Electroanal. Chem.* **176**, 275–295 (1984).
24. Hirschorn, B. *et al.* Constant-Phase-Element Behavior Caused by Resistivity Distributions in Films: I. Theory. *J. Electrochem. Soc.* **157**, C452–C457 (2010).
25. Orazem, M. E., Pébère, N. & Tribollet, B. Enhanced Graphical Representation of Electrochemical Impedance Data. *J. Electrochem. Soc.* **153**, B129–B136 (2006).
26. Lutton, K., Gusieva, K., Ott, N., Birbilis, N. & Scully, J. R. Understanding multi-element alloy passivation in acidic solutions using operando methods. *Electrochem. commun.* **80**, 44–47 (2017).
27. Hamm, D., Ogle, K., Olsson, C. O., Weber, S. & Landolt, D. Passivation of Fe-Cr alloys studied with ICP-AES and EQCM. *Corros. Sci.* **44**, 1443–1456 (2002).
28. Shkirskiy, V., Maciel, P., Deconinck, J. & Ogle, K. On The Time Resolution of the Atomic Emission Spectroelectrochemistry Method. *J. Electrochem. Soc.* **163**, C37–C44 (2016).
29. Ogle, K. Atomic Emission Spectroelectrochemistry: A new look at the corrosion, dissolution, and passivation of complex materials. *Corros. Mater* **37**, 60–67 (2012).
30. McCafferty, E. Graph theory and the passivity of binary alloys. *Corros. Sci.* **42**, 1993–2011 (2000).
31. McCafferty, E. Relationship Between Graph Theory and Percolation Approaches in the Passivity of Fe–Cr Binary Alloys. *J. Electrochem. Soc.* **155**, C501–C505 (2008).
32. McCafferty, E. Oxide networks, graph theory, and the passivity of binary alloys. *Corros. Sci.* **44**, 1393–1409 (2002).
33. McCafferty, E. Oxide networks, graph theory, and the passivity of Ni-Cr-Mo ternary alloys. *Corros. Sci.* **50**, 3622–3628 (2008).
34. Lutton Cwalina, K., Demarest, C. R., Gerard, A. Y. & Scully, J. R. Revisiting the effects of molybdenum and tungsten alloying on corrosion behavior of nickel-chromium alloys in aqueous corrosion. *Curr. Opin. Solid State Mater. Sci.* (2019).
35. Lloyd, A. C., Noël, J. J., McIntyre, N. S. & Shoesmith, D. W. The open-circuit ennoblement of alloy C-22 and other Ni-Cr-Mo alloys. *JOM* **57**, 31–35 (2005).
36. Hirschorn, B. *et al.* Constant-Phase-Element Behavior Caused by Resistivity Distributions in Films: II. Applications. *J. Electrochem. Soc.* **157**, C458–C463 (2010).
37. Chen, Y.-M., Rudawski, N. G., Lambers, E. & Orazem, M. E. Application of Impedance Spectroscopy and Surface Analysis to Obtain Oxide Film Thickness. *J. Electrochem. Soc.* **164**, C563–C573 (2017).
38. Strohmeier, B. R. An ESCA method for determining the oxide thickness on aluminum alloys. *Surf. Interface Anal.* **15**, 51–56 (1990).
39. Quiambao, K. F. *et al.* Passivation of a corrosion resistant high entropy alloy in non-oxidizing sulfate solutions. *Acta Mater.* **164**, 362–376 (2019).
40. Moulder, J. F., Stickle, W. F., Sobol, P. E. & Bomben, K. D. *Handbook of x-ray photoelectron spectroscopy: A reference book of standard spectra for identification and interpretation of XPS data.* (Physical Electronics, 1992).
41. Sato, N. Anodic breakdown of passive films on metals. *J. Electrochem. Soc.* **129**, 255–260 (1982).
42. Kao, K. C. Theory of High-Field Electric Conduction and Breakdown in Dielectric Liquids. *IEEE Trans. Electr. Insul.* **EI-11**, 121–128 (1976).

43. O'Dwyer, J. J. Theory of high field conduction in a dielectric. *J. Appl. Phys.* **40**, 3887–3890 (1969).
44. De Levie, R. The influence of surface roughness of solid electrodes on electrochemical measurements. *Electrochim. Acta* **10**, 113–130 (1965).
45. Rammelt, U. & Reinhard, G. On the applicability of a constant phase element (CPE) to the estimation of roughness of solid metal electrodes. *Electrochim. Acta* **35**, 1045–1049 (1990).
46. Alexander, C. L., Tribollet, B. & Orazem, M. E. Contribution of Surface Distributions to Constant-Phase Element (CPE) Behavior: 1. Influence of Roughness. *Electrochim. Acta* **173**, 566–573 (2015).
47. Lutton Cwalina, K., Blades, W. H., Reinke, P. & Scully, J. R. Oxide Morphologies during Electrochemical Passivation in Sulfate and Chloride Environments PLACEHOLDER. (2019).
48. Rezaei Niya, S. M. & Hoorfar, M. On a possible physical origin of the constant phase element. *Electrochim. Acta* **188**, 98–102 (2016).
49. Ebrahimi, N., Biesinger, M. C., Shoesmith, D. W. & Noël, J. J. The influence of chromium and molybdenum on the repassivation of nickel-chromium-molybdenum alloys in saline solutions. *Surf. Interface Anal.* **49**, 1359–1363 (2017).
50. Ebrahimi, N. The Influence of Alloying Elements on The Crevice Corrosion Behaviour of Ni-Cr-Mo Alloys. (The University of Western Ontario, 2015).
51. Urquidi, M. & Macdonald, D. D. Solute-vacancy interaction model and the effect of minor alloying elements on the initiation of pitting corrosion. *J. Electrochem. Soc.* **132**, 555–558 (1985).
52. Lin, L. F., Chao, C. Y. & Macdonald, D. D. A point defect model for anodic passive films II. Chemical breakdown and pit initiation. *J. Electrochem. Soc.* **128**, 1194–1198 (1981).
53. Marcus, P., Maurice, V. & Strehblow, H. H. Localized corrosion (pitting): A model of passivity breakdown including the role of the oxide layer nanostructure. *Corros. Sci.* **50**, 2698–2704 (2008).
54. Gusieva, K. *et al.* Repassivation Behavior of Individual Grain Facets on Dilute Ni–Cr and Ni–Cr–Mo Alloys in Acidified Chloride Solution. *J. Phys. Chem. C* **122**, 19499–19513 (2018).
55. Benoit, M. *et al.* Comparison of different methods for measuring the passive film thickness on metals. *Electrochim. Acta* **201**, 340–347 (2016).
56. Pourbaix, M. *Atlas of electrochemical equilibria in aqueous solutions*. (National Association of Corrosion Engineers, 1974).
57. Huang, L.-F. & Rondinelli, J. Electrochemical Stabilities of Ni-Based Compounds from Bulk to Nanoscale Dimensions. *Bull. Am. Phys. Soc.* (2018).
58. Huang, L.-F., Hutchison, M. J., Santucci, R. J., Scully, J. R. & Rondinelli, J. M. Improved Electrochemical Phase Diagrams from Theory and Experiment: The Ni-Water System and Its Complex Compounds. *J. Phys. Chem. C* **121**, 9782–9789 (2017).
59. Huang, L.-F., Ha, H. M., Lutton Cwalina, K., Scully, J. R. & Rondinelli, J. M. Electrochemical Stabilities of Ni-Compound Nanofilms Revealed by A Comparative Theory-Experiment Approach. *Submitt. to J. Phys. Chem. C* (2019).
60. Liu, J. *et al.* Understanding Chemical Bonding in Alloys and the Representation in Atomistic Simulations. *J. Phys. Chem. C* **122**, 14996–15009 (2018).
61. Hirschorn, B. *et al.* Constant-Phase-Element Behavior Caused by Coupled Resistivity

- Distributions in Films. *J. Electrochem. Soc.* **157**, C424–C428 (2010).
62. Lutton Cwalina, K. *et al.* In Operando Analysis of Passive Film Growth on Ni-Cr and Ni-Cr-Mo Alloys in Chloride Solutions. *J. Electrochem. Soc.* **166**, C3241–C3253 (2019).

2.8 Tables

Table 2.1. Constants used to compute l_{ox} from XPS spectra fitting results

Element	Compound	A_M	λ_o, λ_m (Å)	N_o, N_m (mol/cm ³)
Ni	Ni	4.044	7.3	0.1518
	NiO		12.9	0.0893
	Ni(OH) ₂			0.0442
Cr	Cr	2.427	9.4	0.1383
	Cr ₂ O ₃		16.8	0.0687
	Cr(OH) ₃			0.0302
Mo	Mo	3.321	15	0.1071
	MoO ₂		21	0.0506
	MoO ₃			0.0326

Table 2.2. Computation of ρ_δ using impedance and XPS spectra analysis following 10 ks passivation at +0.2 V_{SCE} for various alloys and environment combinations. The units for ρ_δ and Z'' are Ω -cm and Ω -cm², respectively. For reference, $\rho_\delta^{\alpha-1}$ is also included to demonstrate the influence of this parameter on l_{ox} in Equation 2.6.

Method	Parameter	0.1 M Na ₂ SO ₄				0.1 M NaCl			
		pH 4		pH 10		pH 4		pH 10	
		Ni-Cr	Ni-Cr-Mo	Ni-Cr	Ni-Cr-Mo	Ni-Cr	Ni-Cr-Mo	Ni-Cr	Ni-Cr-Mo
XPS	$l_{ox}^{Ni(OH)_2}$	1.45	1.41	1.26	1.42	0.82	1.52	2.24	0.55
	$l_{ox}^{Cr(OH)_3}$	2.92	3.46	2.28	1.51	2.80	3.33	2.17	2.09
	l_{ox}^{total}	4.37	4.87	3.54	2.93	3.62	4.86	4.41	2.64
SF-EIS	$l_{ox}^{\rho_\delta=450}$	4.59	5.09	3.43	2.97	3.44	4.91	4.68	2.56
	ρ_δ	1,211	1,060	1,154	570	151	543	1,456	245
	$\rho_\delta^{\alpha-1}$	0.701	0.706	0.703	0.728	0.778	0.730	0.695	0.760

2.9 Figures

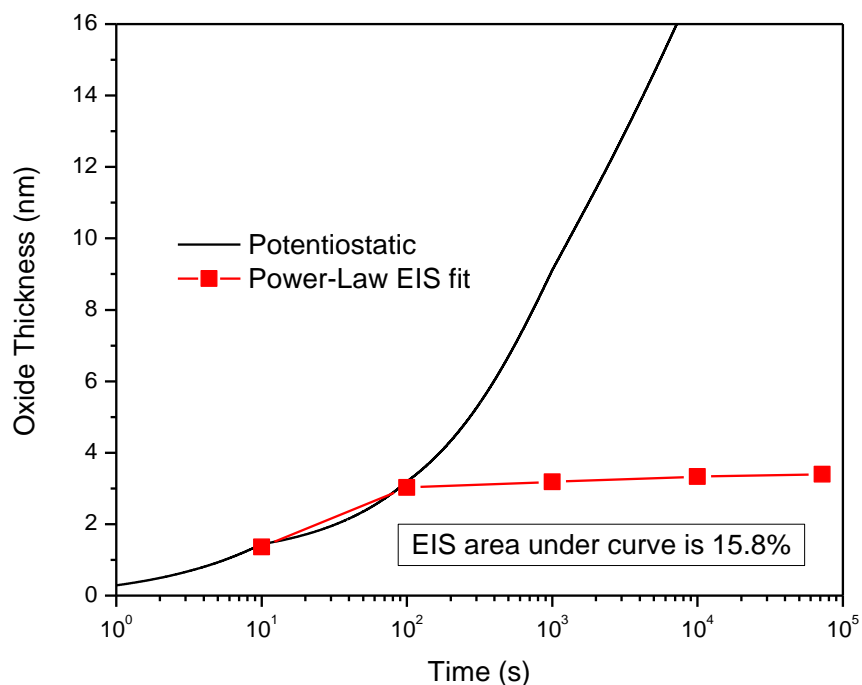


Figure 2.1. General estimation of the relative inefficiencies (15.8% overall) of potentiostatic passivation for 72 ks at $+0.2 V_{SCE}$ on Ni-22 Cr-6 Mo, wt%, in a relatively benign environment, 0.1 M Na_2SO_4 acidified to pH 4 using H_2SO_4 . The black curve corresponds to the thickness computed by integrating under the total i_{EC} and assuming 100% whereas for the red curve, EIS was applied during passivation to more accurately determine l_{ox} .

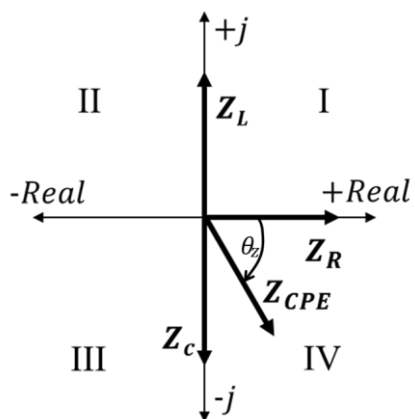


Figure 2.2. Graphical representation of complex impedance plane where quadrant IV corresponds to perfect resistors, capacitors, and constant phase elements and thus is most commonly used in electrochemistry

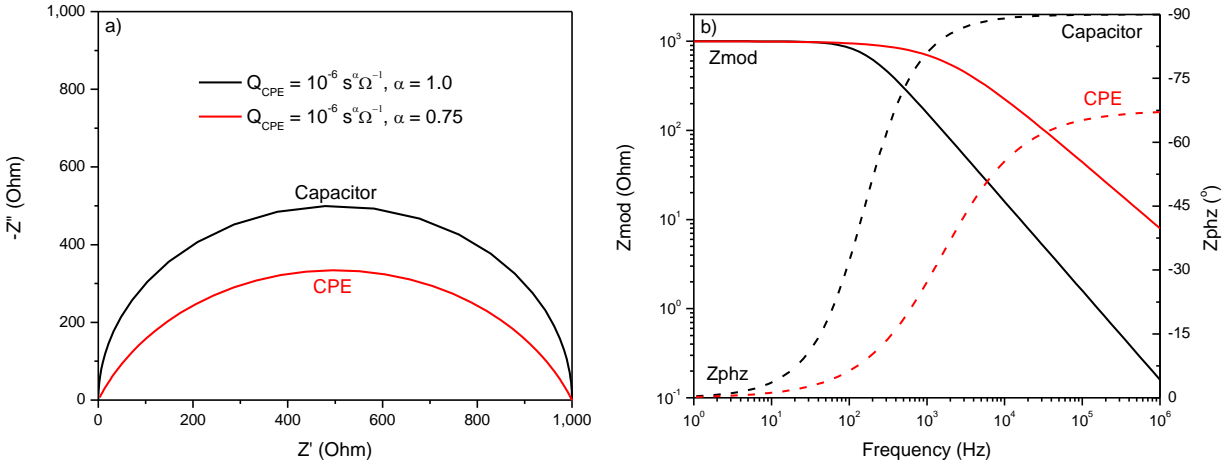


Figure 2.3. Simulated impedance spectra for an RC parallel circuit via a) Nyquist plot and b) Bode plot for a perfect capacitor ($Q_{CPE} = 10^{-6} s^\alpha \Omega^{-1}$ and $\alpha = 1.0$) and a constant phase element (CPE) ($Q_{CPE} = 10^{-6} s^\alpha \Omega^{-1}$ and $\alpha = 0.75$) produced using Zview

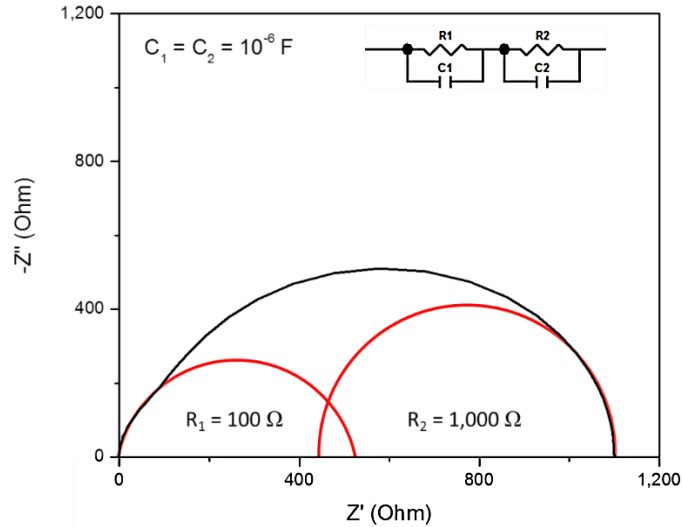


Figure 2.4. Appearance of an impedance spectra as a result of nested time constants for two RC circuits in series with each other (shown in the inset) where each capacitive loop is indicated with the red curves

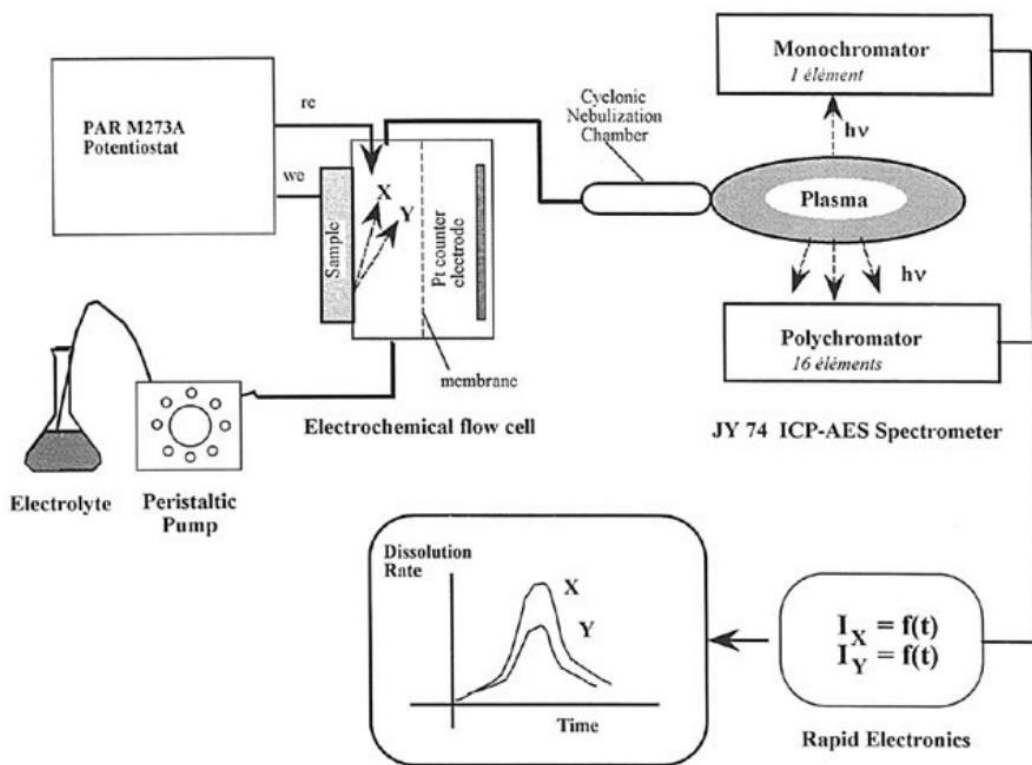


Figure 2.5. Functional block diagram of an ICP-AES system¹⁷

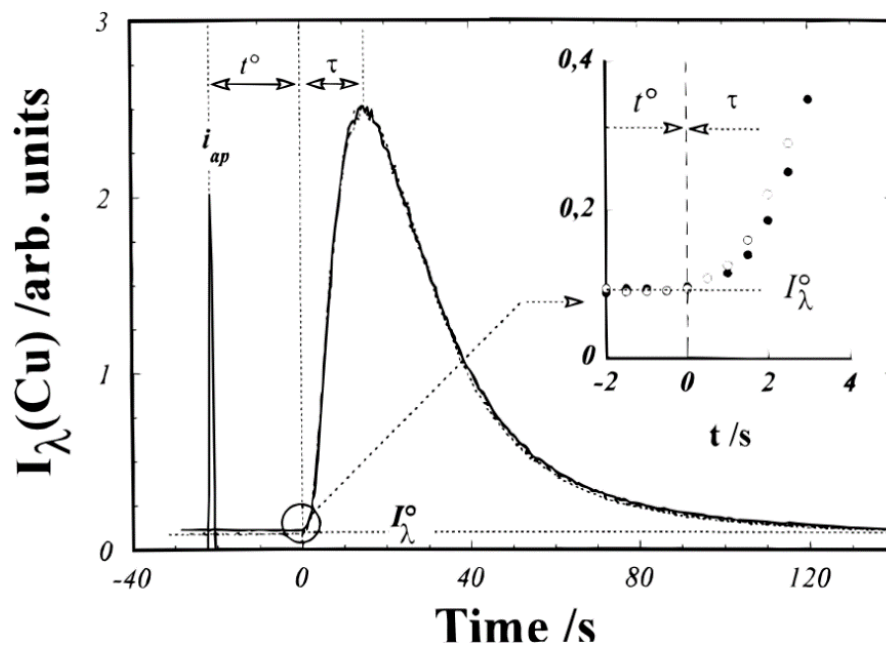


Figure 2.6. Residence time distribution from an electrochemical flow cell following a 10 mA pulse applied to pure Cu in 1.2 M HCl and the Cu emission intensity was measured in response. Three measures were superimposed to show the reproducibility. The lag time, t^0 , is defined as the time between the initial pulse and the first point at which the signal rises above the background (I_λ^0). A blowup of the onset near t^0 is shown in the inset. The residence time distribution, τ , is defined as the time between t^0 and the peak maximum.¹⁷

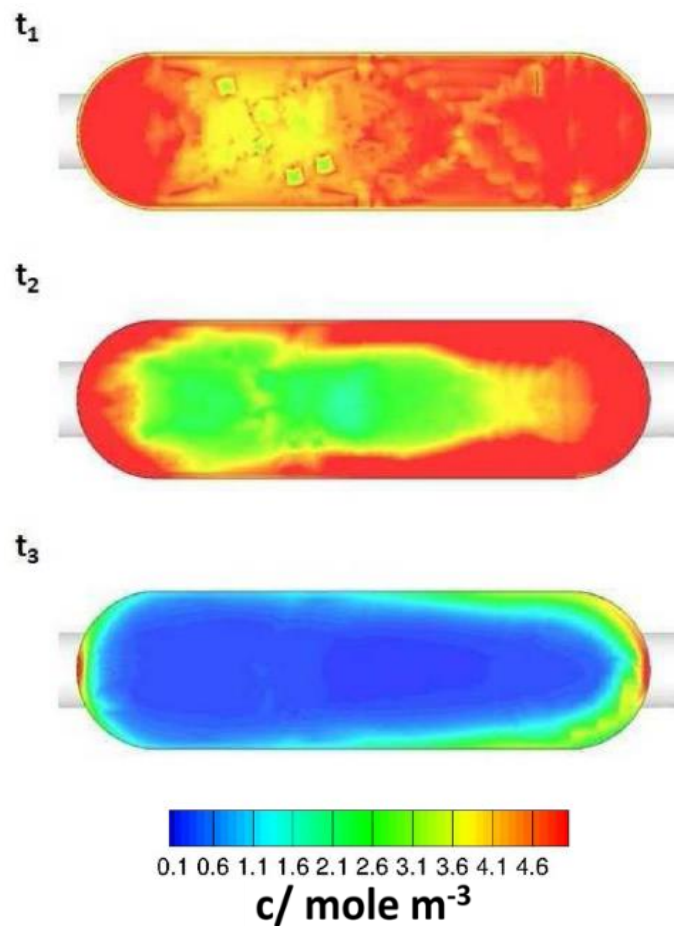


Figure 2.7. Numerical model of the substance distribution (C) in mole m^{-3} from the electrode area following a 10^{-7} mole mass pulse for $3 \text{ cm}^3 \text{ min}^{-1}$ flow rate into the feed capillary after 3, 10, and 30 s (t_1 , t_2 , and t_3 respectively)²⁸

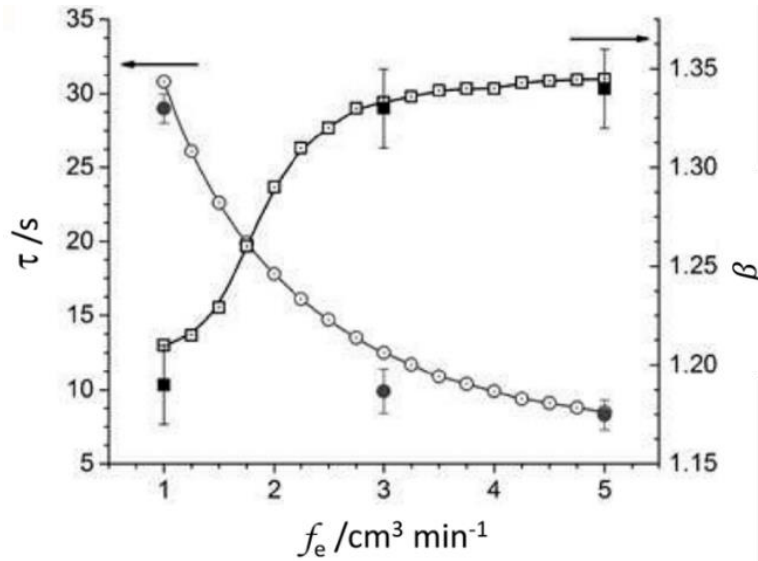


Figure 2.8. Simulated residence time distribution τ (circles) and β (squares) parameters as a function of f_e . The filled points show experimental measurements while the empty points give the simulated parameters²⁸

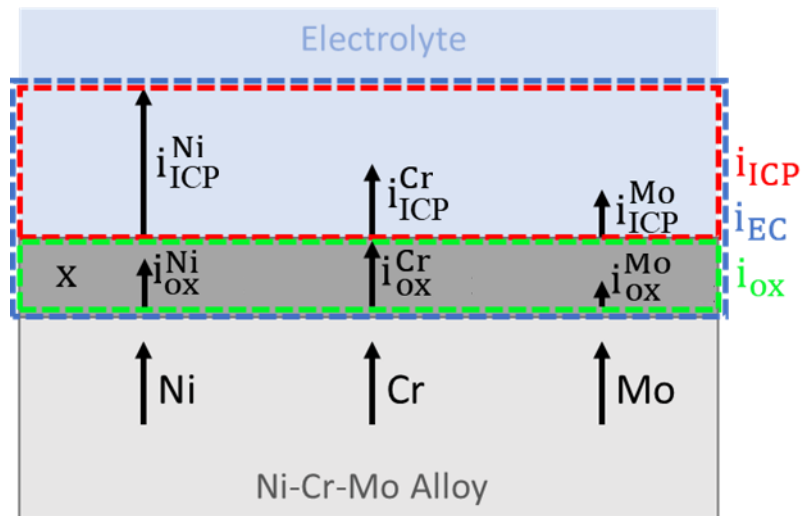


Figure 2.9. Schematic of the relative dissolution and oxidation reactions occurring for a Ni-Cr-Mo alloy with the corresponding current densities indicated⁶²

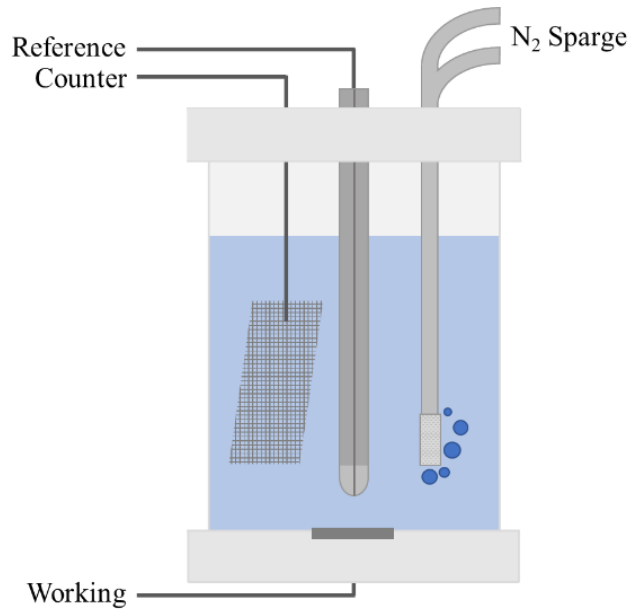


Figure 2.10. Schematic of the vertical three-electrode electrochemical cell used for various *in operando* and *in situ* characterization techniques, where a Pt mesh was used as the counter electrode and the reference was either a SCE or MMSE electrode for NaCl and Na₂SO₄ electrolytes, respectively.

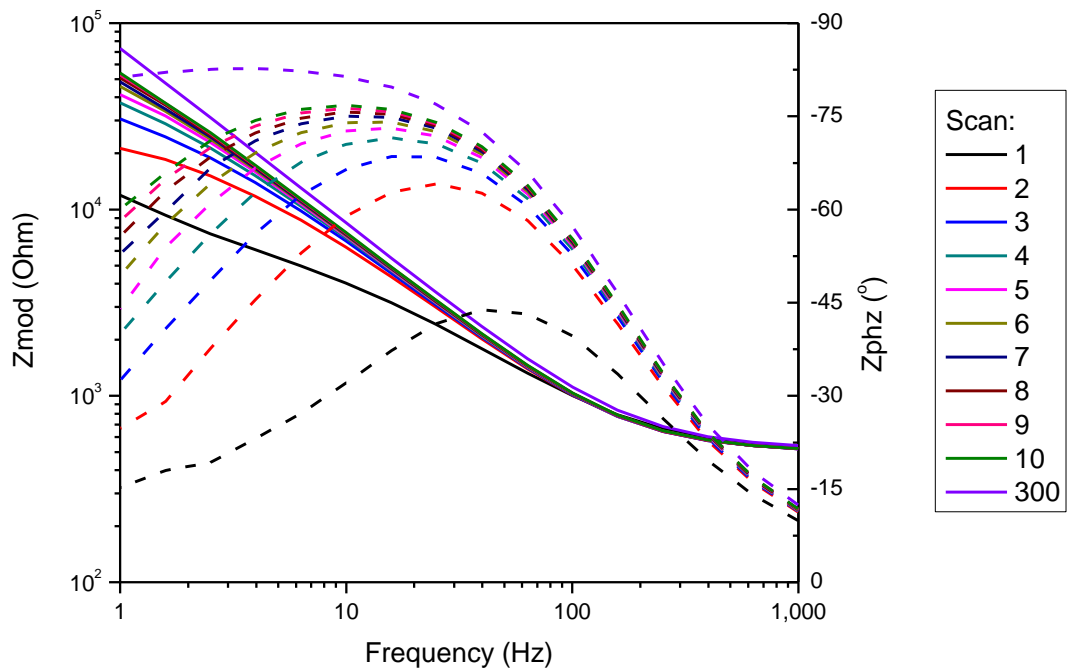


Figure 2.11. Full spectrum EIS measured sequentially on Ni-22 Cr, wt%, in 0.1 M Na₂SO₄ + H₂SO₄ pH 4 over approximately 10 ks. Each scan iteration lasted on average 35 s and the first ten, along with the last, are shown and indicate the increase in the film impedance during the passivation process.

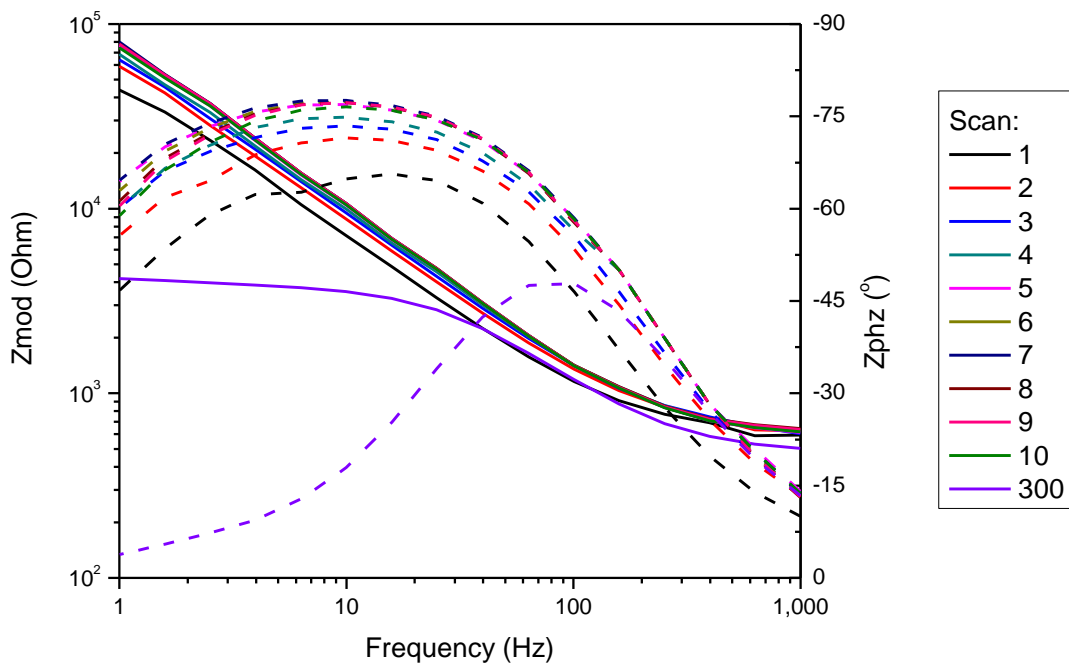


Figure 2.12. Full spectrum EIS measured sequentially on Ni-22 Cr, wt%, in 0.1 M NaCl + HCl pH 4 over approximately 10 ks. Each scan iteration lasted on average 35 s and the first ten, along with the last, are shown and indicate the increase in the film impedance during the passivation process until film dissolution initiated after the 7th scan (i.e. approximately 250 s).



Figure 2.13. Circuit model used to fit the CPE parameters Q and α and their evolution with time.

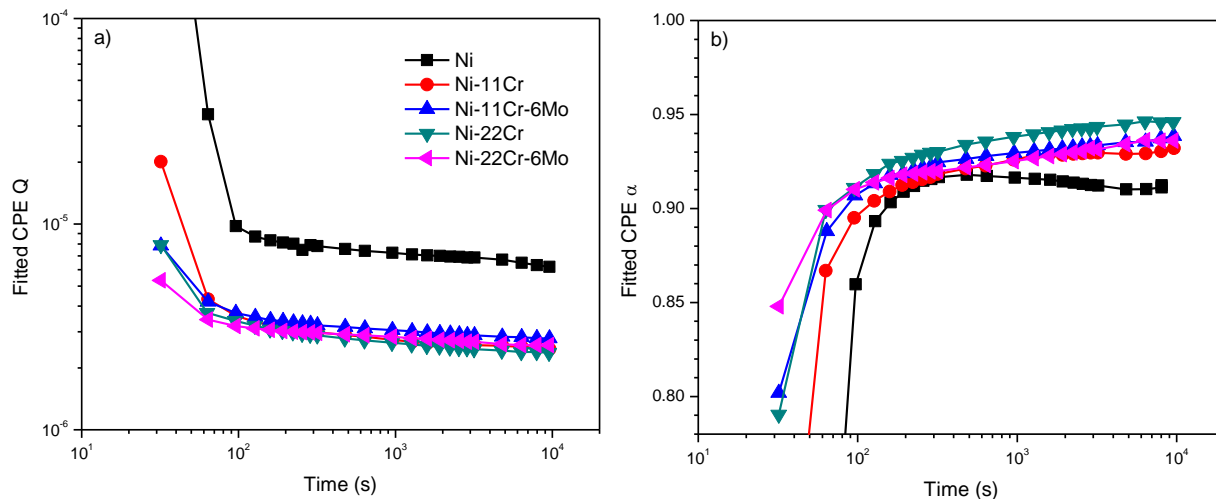


Figure 2.14. a) Q and b) α CPE parameters used in Equation 2.6 to calculate l_{ox} and measured as a function of time for various Ni-based alloys (wt%) passivated in 0.1 M $\text{Na}_2\text{SO}_4 + \text{H}_2\text{SO}_4$ pH 4 by fitting the sequential, full EIS spectra to a simple CPE in parallel with a resistor (Figure 2.13)

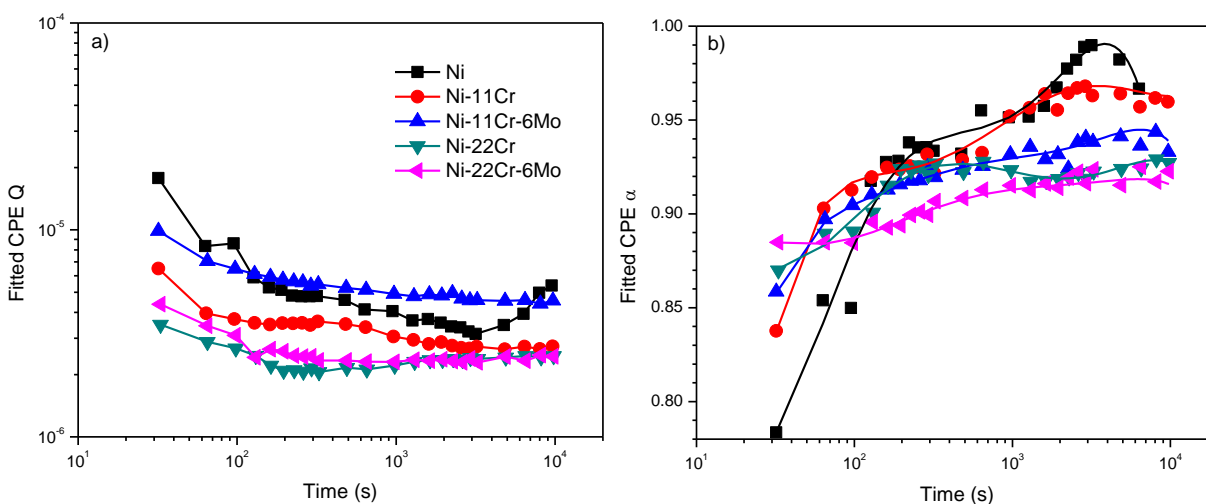


Figure 2.15. a) Q and b) α CPE parameters used in Equation 2.6 to calculate l_{ox} and measured as a function of time for various Ni-based alloys (wt%) passivated in 0.1 M $\text{NaCl} + \text{HCl}$ pH 4 by fitting the sequential, full EIS spectra to a simple CPE in parallel with a resistor (Figure 2.13)

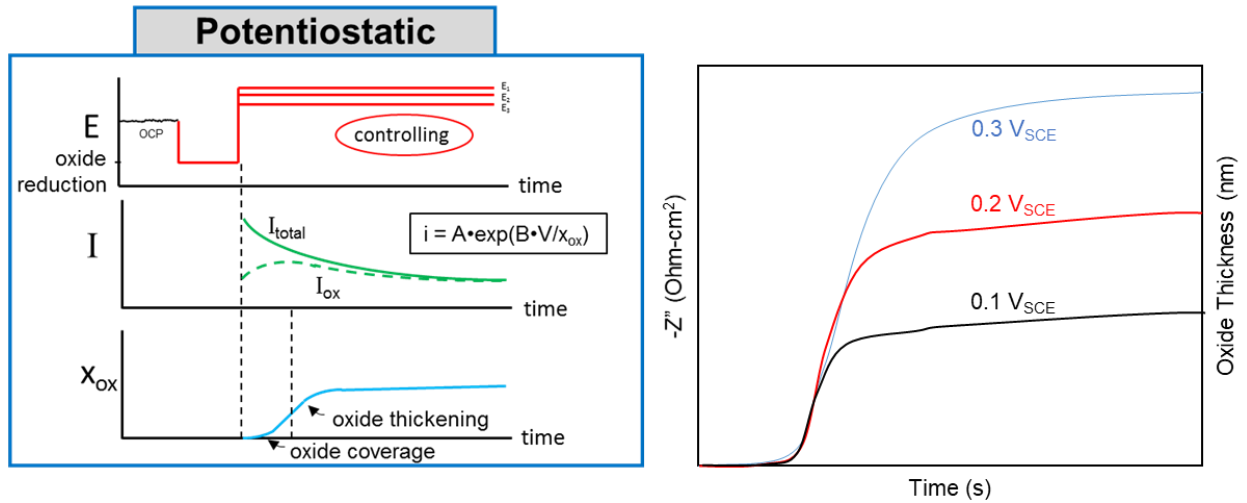


Figure 2.16. Schematic of potential-controlled passivation and resulting variations in current (I), oxide thickness (x), and imaginary impedance ($-Z''$) with time.

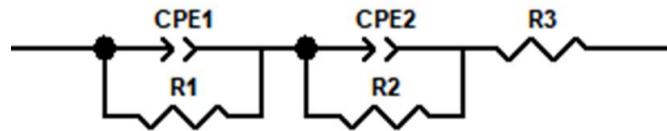


Figure 2.17. Equivalent circuit model used to fit EIS spectra and obtain α , given as a2 for the CPE Yo1, for application of Equation 2.6 using Gamry Echem Analyst

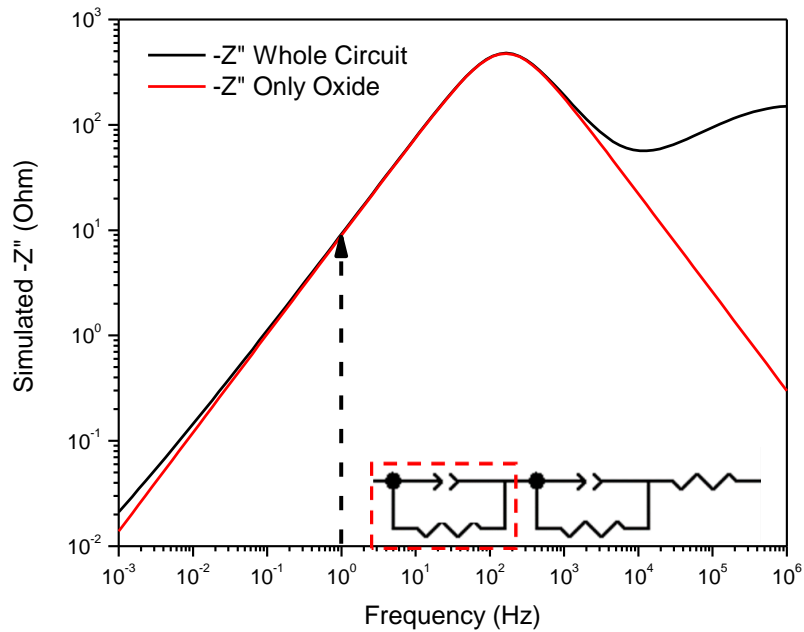


Figure 2.18. Comparison of the total $-Z''$ spectra of Ni-22% Cr-6% Mo, wt, after 10 ks of potentiostatic polarization at +0.2 V_{SCE} in 0.1 M NaCl pH 4 versus a ZView simulation using a simplified circuit fit containing only a constant phase element and a resistor with the same measured Q_{CPE} , α , and R_{ox} from fitting the total spectra (Figure 2.17), as indicated in the inset model where the red outline indicates the oxide portion, demonstrating that using $-Z''$ at 1 Hz correlates to the oxide properties

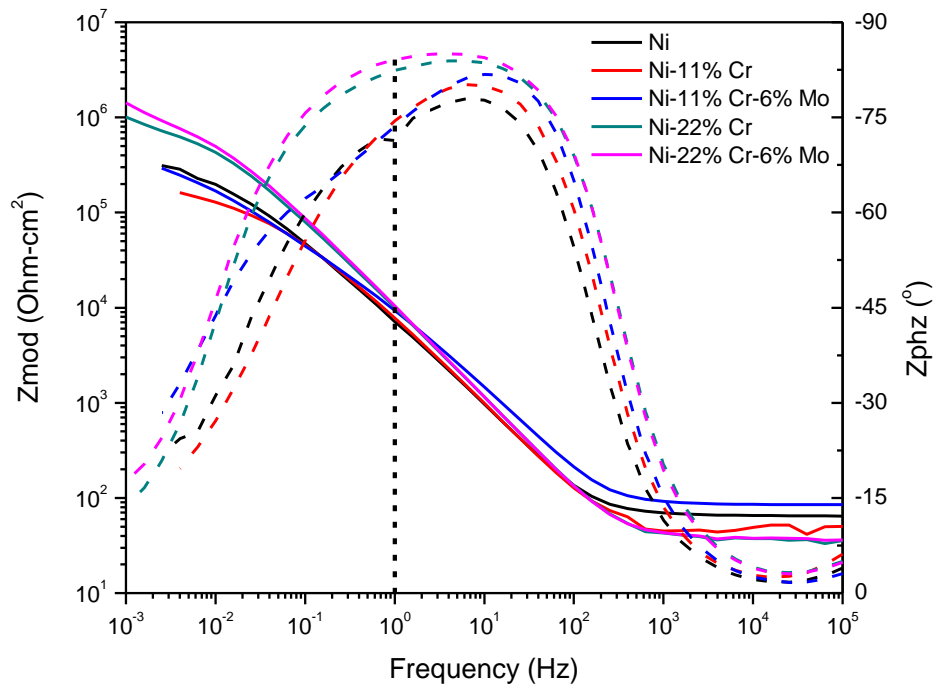


Figure 2.19. Full spectrum EIS obtained following 10 ks of passivation at +0.2 V_{SCE} on various Ni-Cr-Mo alloys in 0.1 M Na₂SO₄ solution, where the chosen frequency for SF-EIS (1 Hz) is shown and suggests that Z_{phz} is near its maximum and between the two nested time constants corresponding to the oxide for all alloys

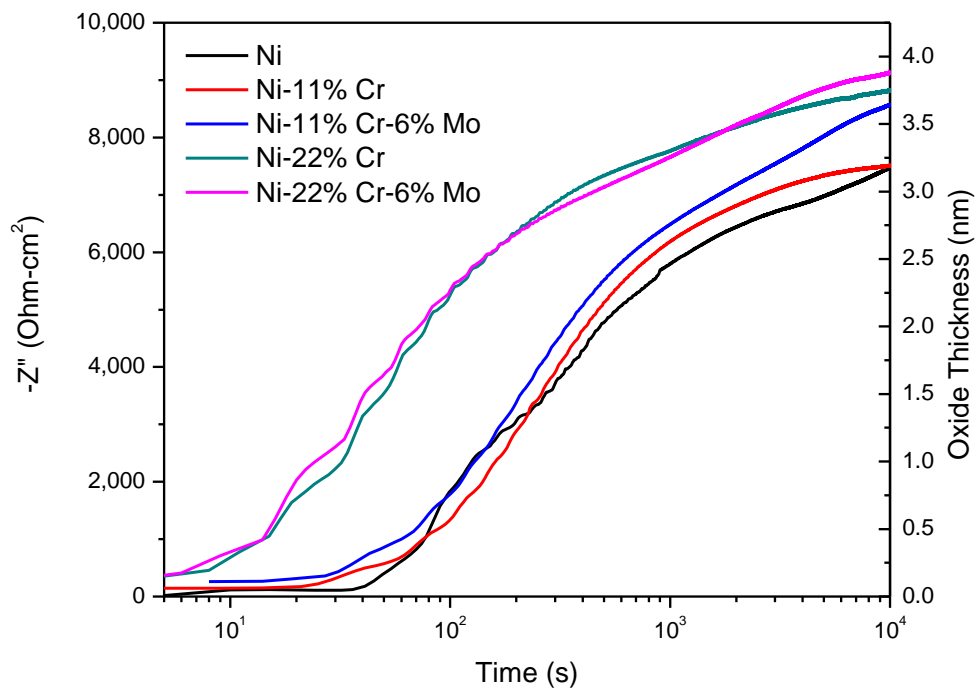


Figure 2.20. Film growth curves obtained on various Ni-based alloys during passivation at +0.2 V_{SCE} for up to 10 ks in 0.1 M Na₂SO₄ solution using $\alpha = 0.95$ in order to directly compare $-Z''$ and l_{ox} for all alloys using the same axes

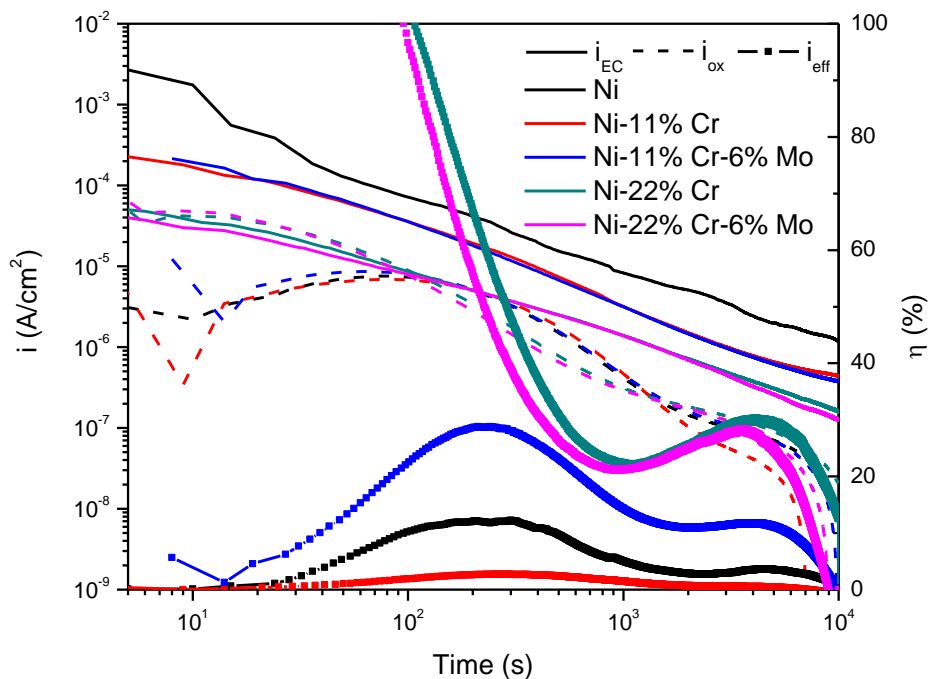


Figure 2.21. Oxidation current density, i_{ox} , computed by applying Equation 2.7 to data in Figure 2.20 smoothed with a polynomial fit and compared to the i_{EC} measured for each alloy to obtain η during the potentiostatic passivation at +0.2 V_{SCE}

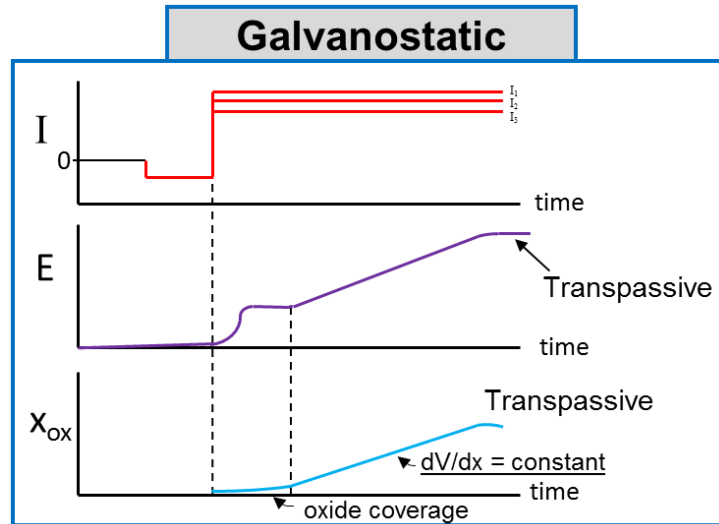


Figure 2.22. Schematic of the expected evolution of potential and oxide thickness as a function of time during galvanostatic control conditions

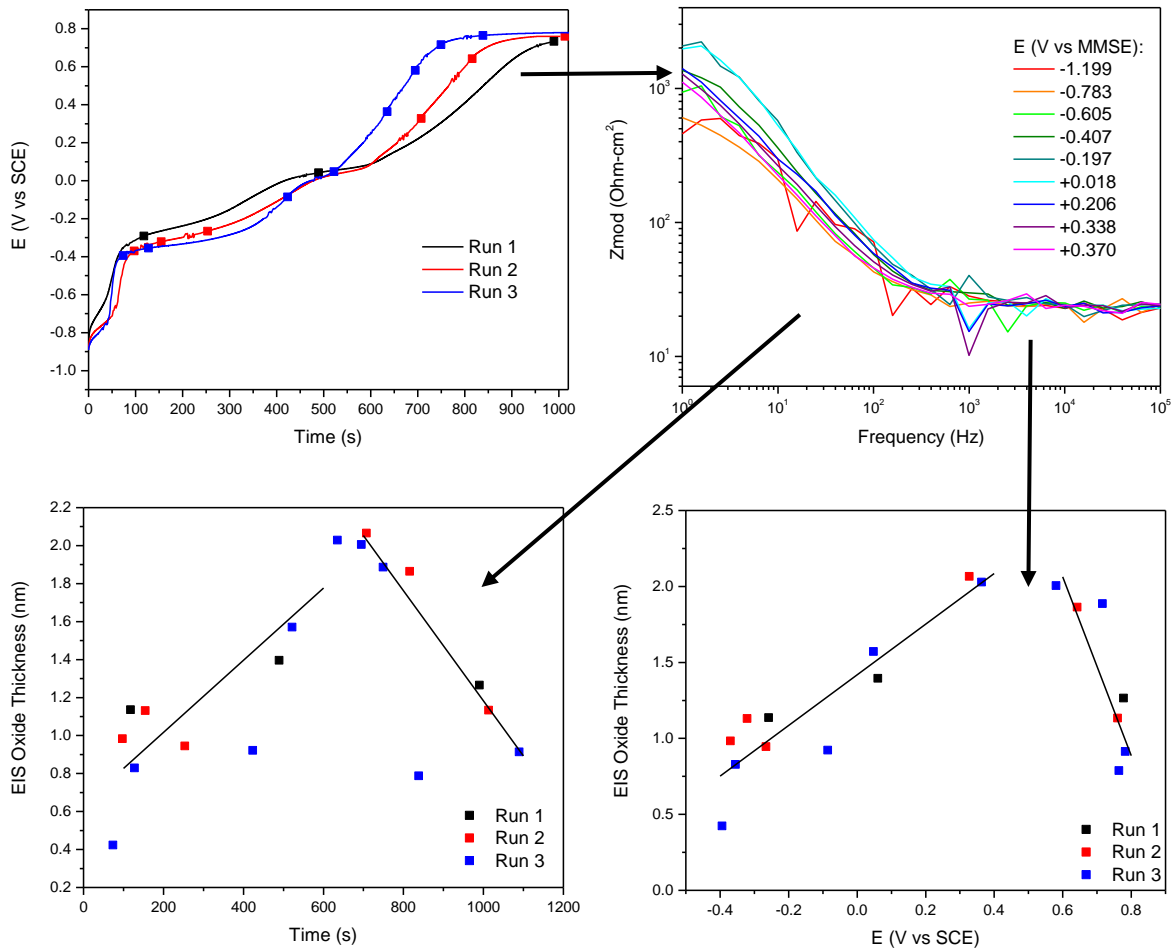


Figure 2.23. *In situ* impedance measurements using fits of full EIS spectra (Figure 2.17 and Equation 2.2) to obtain l_{ox} during ordinary DC galvanostatic polarization of Ni-22 Cr-6 Mo at 30 $\mu\text{A}/\text{cm}^2$ in 0.1 M Na_2SO_4 acidified to pH 4 using H_2SO_4

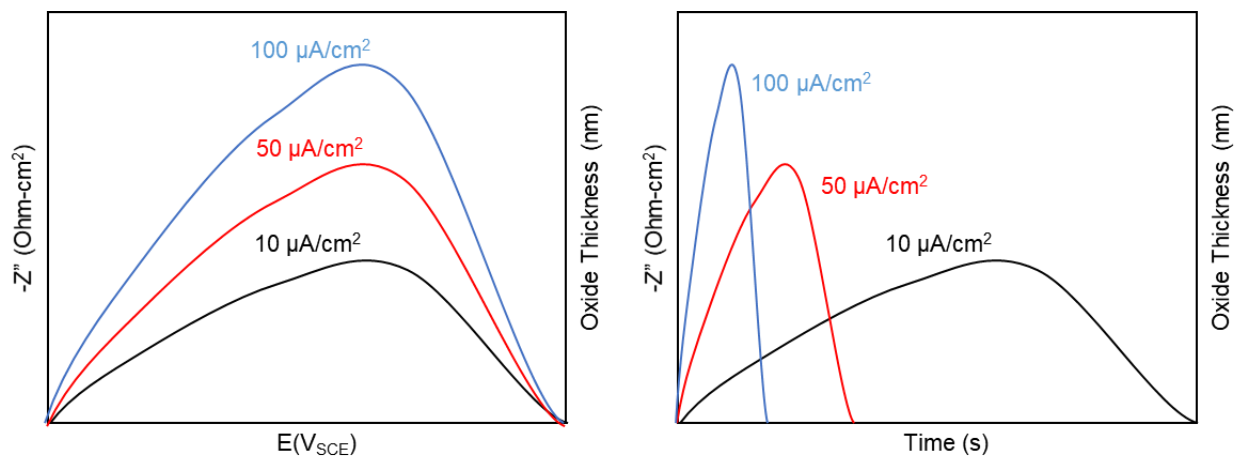


Figure 2.24. Schematic of the variations in the imaginary impedance, $-Z''$, and l_{ox} as a function of i_{app} . Thinning via transpassive dissolution occurs at the same potentials as suggested in Figure 2.22, but vastly different times due to the direct proportionality between i_{app} and $\frac{dl_{ox}}{dt}$.

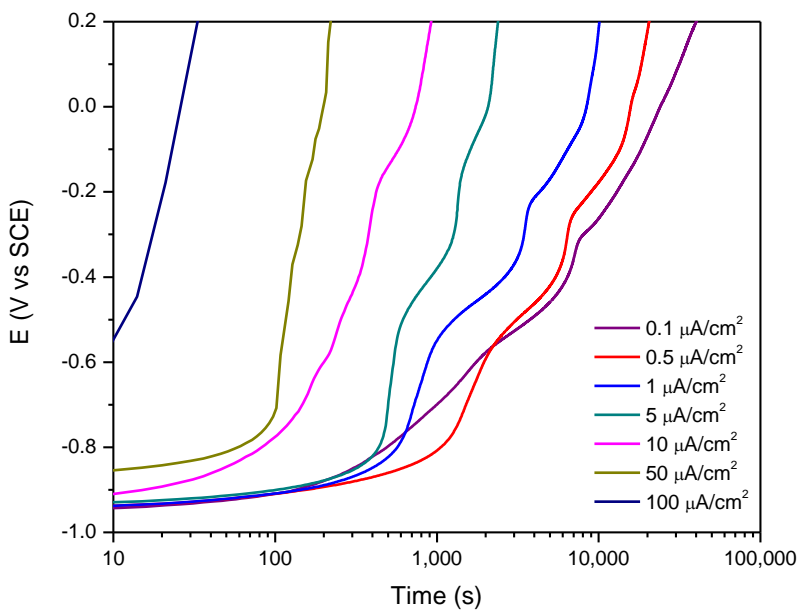


Figure 2.25. Potential changes during current-controlled passivation of Ni-22 Cr-6 Mo, wt%, at varying rates dictated by i_{app} in 0.1 M Na_2SO_4 (pH 5.5).

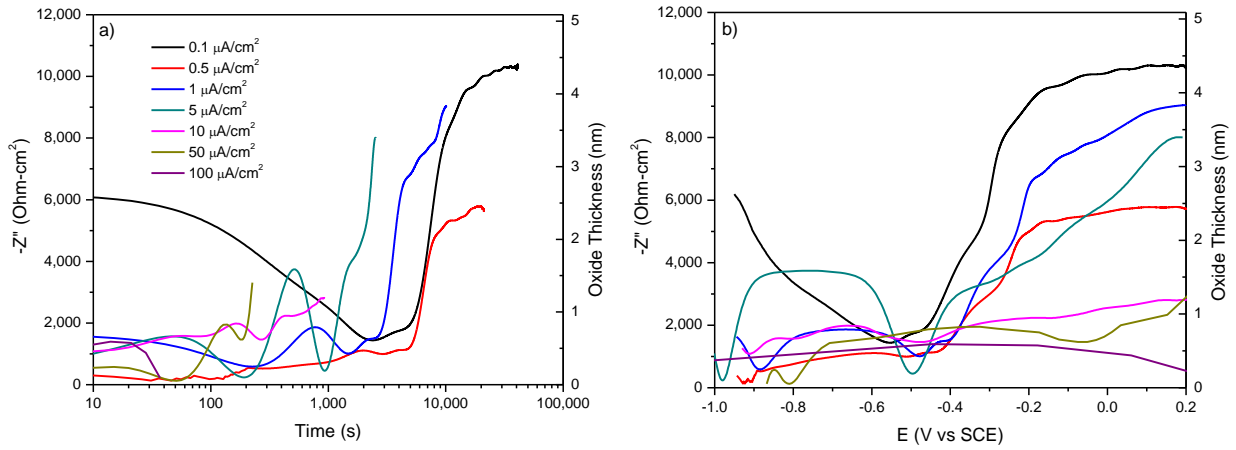


Figure 2.26. Imaginary impedance, $-Z''$, variations measured during the current-controlled passivation shown in Figure 2.25 as a function of a) time and b) potential at 1 Hz and using $i_{AC} = 5 \text{ nA}/\text{cm}^2$. The corresponding l_{ox} computed using Equation 2.6 is provided on the right y-axis.

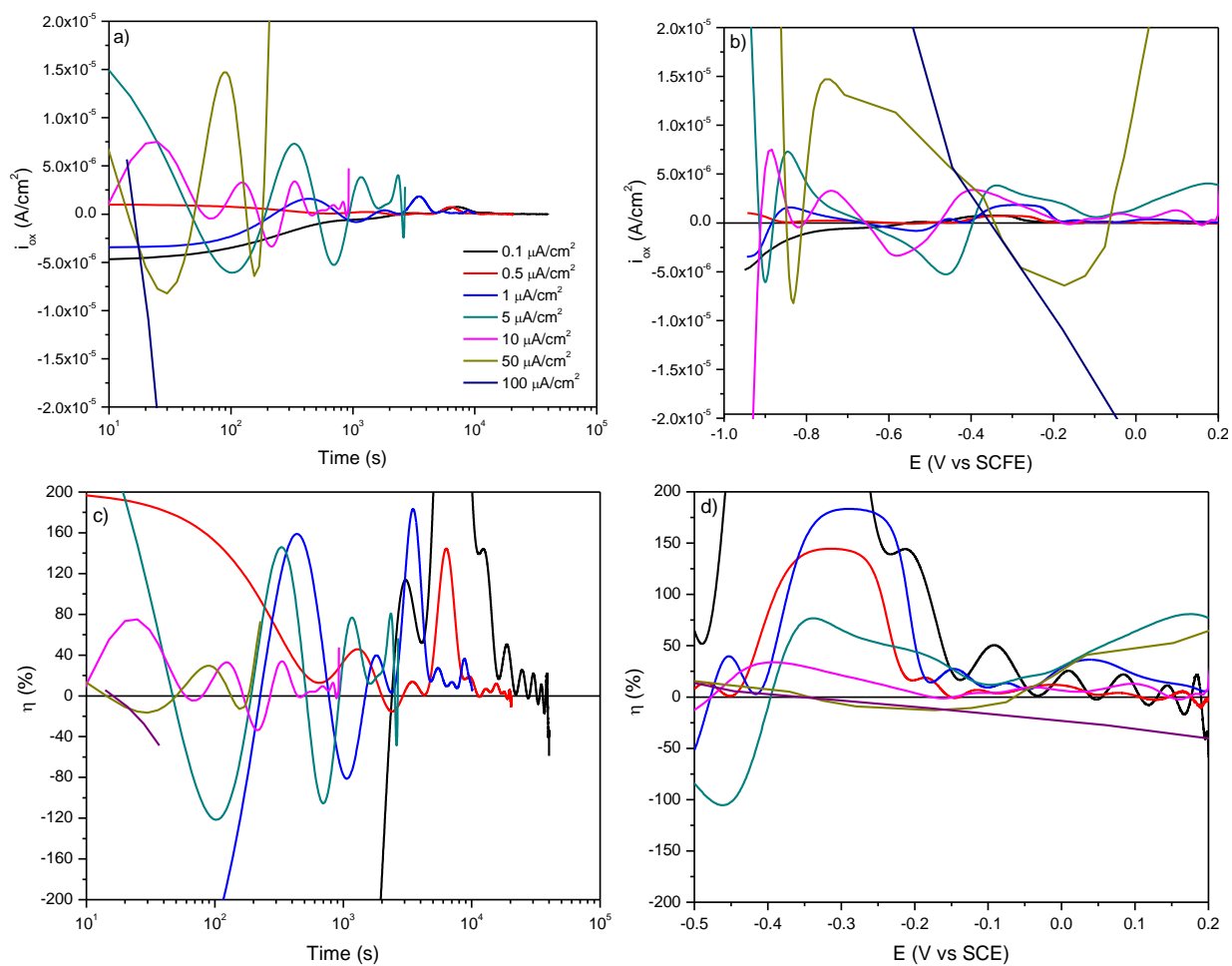


Figure 2.27. Analysis of i_{ox} and the corresponding η for each applied galvanostatic passivation rate (Figure 2.26) according to Equation 2.11 and Equation 2.12. The curves are provided as a function of a,c) passivation time and b,d) potential to demonstrate their influence on the competition between oxidation and dissolution kinetics.

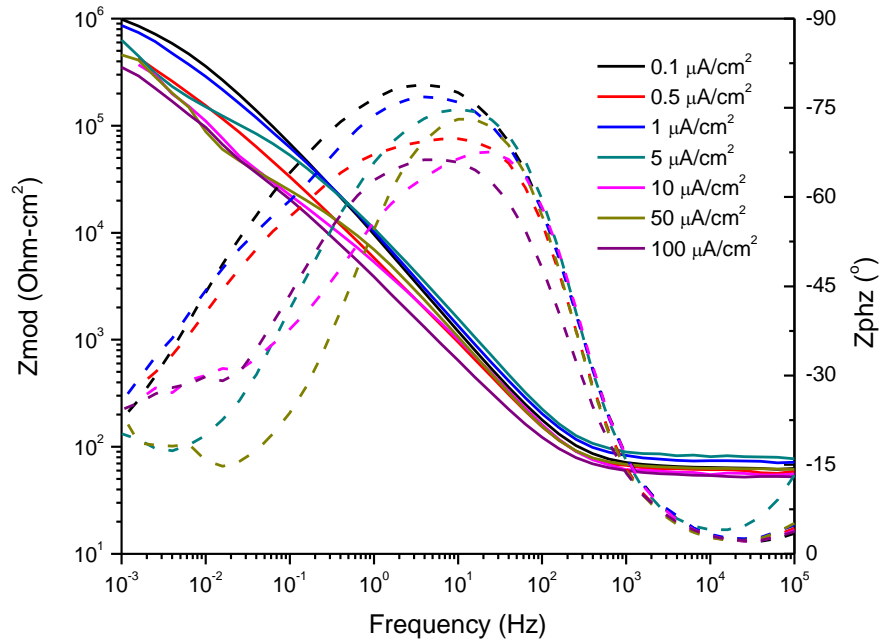


Figure 2.28. Electrochemical impedance spectra Bode plot of the impedance magnitude and phase following galvanostatic passivation at varying rates until a potential of +0.2 V_{SCE} was reached for Ni-22 Cr-6 Mo in deaerated 0.1 M Na₂SO₄

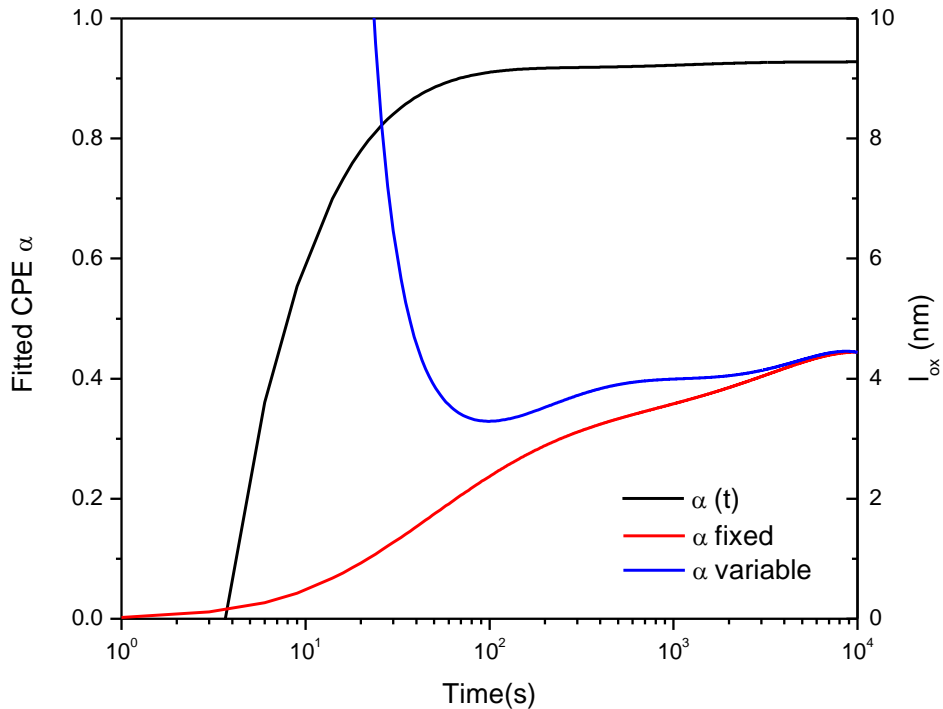


Figure 2.29. Comparison between $l_{ox}(t)$ on Ni-22 Cr-6 Mo (wt%) during 10 ks of potentiostatic SF-EIS passivation at +0.2 V_{SCE} in 0.1 M Na₂SO₄ pH 4 calculated using the fixed, steady-state α measured using a full EIS spectrum fit and $\alpha(t)$ given in Figure 2.14b

3. Potential-Controlled Passivation and Surface Characterization of Ni, Ni-Cr, and Ni-Cr-Mo – Part I. Sulfate Environments

A manuscript based on this chapter has been published:

K. Lutton, K. Gusieva, N. Ott, N. Birbilis, and J. R. Scully. (2017). Understanding multi-element alloy passivation in acidic solutions using operando methods. *Electrochemistry Communications*, 80(7), 44-47.

3.1 Abstract

The instantaneous kinetics of passivation during potential control by oxide formation, film thickening, passive film dissolution, and breakdown via localized corrosion were investigated for Ni-22 Cr and Ni-22 Cr-6 Mo, wt%. Experiments were conducted in specific acidic and alkaline sulfate environments using simultaneous electrochemistry, on-line inductively coupled plasma-mass spectrometry (ICP-MS), and single frequency-electrochemical impedance spectroscopy (SF-EIS) along with *in situ* neutron reflectometry (NR), and *ex situ* X-ray photoelectron spectroscopy (XPS), atomic force microscopy (AFM), and 3D atom probe tomography (3DAPT) following electrochemical testing. The specific roles of pH and Mo on passivation kinetics are presented and the results provide an increased understanding of both thermodynamic and kinetic factors governing passivation without the complication of chloride-assisted localized corrosion. Specifically, it was found that pH has an impact on the relative chemical stability of Ni-Cr passive films but not noticeably for Ni-Cr-Mo ones. In addition, oxidized Mo was observed to function as an electronic dopant within the passive film, increasing growth kinetics and modifying the concentration of electronic defects.

3.2 Collaborations

Several collaborations have occurred to perform the broad range of experimental techniques presented in this chapter. In order of appearance, these include: on-line ICP-MS experiments were performed by Dr. Noemie Ott at Monash University, NR experiments and initial analysis were done by Dr. Hung Ha at the Canadian Nuclear Laboratories, AFM measurements and RMS analysis by William Blades at the University of Virginia, and APT sample preparation, measurements, and imaging were performed by Dr. Xiao-Xiang Yu at Northwestern University.

3.3 Introduction

3.3.1.1 Passivation in Sulfate Environments

Aqueous sulfate solutions are often the environment of choice for electrochemical passivity studies as most films are stable at a wide range of potentials and do not undergo localized dissolution, such as occurs in chloride-containing solutions¹. For example, Fe-15 Cr and Fe-25 Cr, wt%, passivation has previously been studied in 0.4 M Na₂SO₄ + 0.1 M H₂SO₄ using AESEC². The results indicated that Fe had strong preferential dissolution independent on alloy composition, occupying 90% of the total mass dissolved. Upon stepping the potential from 0 mV_{SHE} to +800 mV_{SHE}, a sharp spike in Fe and a slight increase in Cr-dissolution was observed. The growth kinetics of the predominantly Cr passive film were measured using an electrochemical quartz crystal microbalance (EQCM). There was a linear decrease in the film mass during the 0 mV_{SHE} hold, followed by a sharp decrease which leveled back towards a linear trend after stepping to +800 mV_{SHE}. The EQCM mass loss agreed well with the Fe dissolution observed through integration of the ICP signal peaks.

The passivation of pure Ni metal³⁻¹² and Ni-based alloys^{5,11,13-17} in sulfate environments has been well-studied in previous literature. On Ni, the passive film is often described by a bilayer structure due to the appearance of inner, crystalline NiO and outer, porous, and hydrated Ni(OH)₂ layers. This configuration is observed for acidic sulfuric and perchloric, along with alkaline, solutions with limiting thicknesses measured on the order of a nanometer³.

MacDougall previously established that in 0.15 N Na₂SO₄ solution acidified to pH 2.8, NiO film formation occurs initially through oxygen chemisorption up until a monolayer of coverage and blocking of active Ni sites has been achieved, followed by lateral and somewhat defective film growth⁸. At steady state, additional anodization may result in healing and hydration of the Ni(OH)₂ layer into a crystalline NiO structure. The mechanism of dissolution differs as a function of passivation stage. For existing films, the authors found that dissolution often occurs within the pore structure, followed by penetration to the metal and undermining of the metal/oxide interfacial cohesion. In another study, MacDougall showed that steady-state, defective films on NiO are annealed through a balance of dissolution and re-growth of crystalline NiO in the place of Ni(OH)₂¹².

3.3.1.2 Fundamental Roles of Alloying Additions in Ni-based Alloys

Electrochemical passivation can be greatly improved with the addition of minor alloying elements. At lower Cr concentrations, the passive film formed will be predominantly NiO-based as there is not sufficient Cr present for formation of a continuous film^{16,18,19}. Previous work has additionally observed that the addition of a few at% of Cr to Ni alters the preferred oxidation mechanism from one dominated by outward cation diffusion to one where oxygen ingress is substantial²⁰. Past approximately 11 wt% Cr, Ni-Cr will preferentially form a continuous Cr-rich oxide/hydroxide film as those particular compounds are more thermodynamically stable than Ni-rich ones which are favored kinetically^{15,19}. In the case of high temperature oxidation, it was observed that NiO forms first, followed by subsurface Cr₂O₃ enrichment at the inner interface and eventually the emergence of large NiCr₂O₄ islands¹⁷. While in general the addition of Cr to Ni provides excellent resistance to localized corrosion and increases film stability in acidic, halide-free transpassive dissolution is possible for Cr-rich passive films in highly oxidizing environments. This can be remediated through alloying of other elements.

The most common minor alloying element used in the Ni-Cr system is Mo. Alloying of Mo to pure Ni metal provides a less significant effect on the passive film structure when compared to the effect of Cr. Ni alloyed with 13 wt% Mo and passivated in 1 N Na₂SO₄ acidified to pH 2.8 has previously been studied using scanning transmission electron microscopy and diffraction indicated only the presence of crystalline NiO particles with approximately 3 nm diameters¹¹. Mo was found to be, however, either finely dispersed in the anodic NiO film or present as an amorphous species that does not appear in diffraction. While Cr alone increases passivity, Mo additions have been shown to monotonically increase the passive current density and the film growth rate²¹. Another study proposed that a defective, amorphous (Mo⁴⁺, Mo⁶⁺)_xO_y layer is produced which increases the defect concentration in NiO, resulting in observed increases in the passive current density²².

Alloying with a combination of Cr and Mo, however, results in a highly synergistic relationship with regards to the passivity of Fe and Ni-based systems. While this effect is especially notable in chloride-environments, corrosion behavior is additionally reinforced in acidic sulfate ones. Alloy 59 (Ni-22.5 Cr-15.5 Mo-0.9 Fe, wt%) has been studied in sulfuric acid solutions through potentiodynamic electrochemistry, EIS, Mott-Schottky (MS), XPS, and Auger depth

profiling²³. The results indicate the substantial increase in passivity through alloying of high concentrations of Cr and Mo when compared to pure Ni and its binary alloys. Films grown in air exhibited (Cr,Ni)-oxide films whereas those in solution were hydrated (Cr,Ni)-hydroxides²³. Additionally, the air-oxidized films were thicker by approximately a nanometer due to the influence of sulfuric acid on the competition between film growth and dissolution. The structure of the passive film was not found to exhibit a bi- or multi-layered structure; instead, depth profiling revealed that the aforementioned oxide species were distributed throughout the film with no preferential segregation to the inner or outer interfaces²³.

3.4 Objective

The objective of this chapter is to couple ICP-MS with SF-EIS measurements of elemental contributions to film growth rate in both acidic and alkaline sulfate environments to provide *in operando* analysis of film growth. During film growth at a constant applied potential, independent XPS, MS, and 3D atom probe tomography (3DAPT) was be utilized for evaluation of film composition, thickness, electronic properties, and their variations with passivation time. In addition, the role of pH will be investigated through direct comparison of an acidic (pH 4) condition with an alkaline one (pH 10). The passive film surface was additionally studied using AFM local probe measurements of surface structures and roughness resulting from electrochemical processes. Finally, this chapter aids in revealing the fate of the elements during electrochemical passivity without the added influence of localized halide attack. The results helped to establish an understanding of the role of Mo during acidic and alkaline passive film growth and the specifics of its synergistic relationship when alloyed with Cr.

3.5 Experimental Methods

A variety of characterization techniques have been used for the evaluation of passive films grown electrochemically on the Ni-based alloys. In particular, ICP-MS and SF-EIS, whose application was previously discussed in Chapter 2, were be used in tandem for independent measurement of i_{ox} from the total and dissolution current densities, i_{EC} and i_{diss} . In addition, the fate of individual elements can be comprehended with the assistance of partial elemental dissolution current densities measured through ICP-MS. This alloying element-specific tracking aids analysis of overall film growth and composition as a function of time. The information

produced by the supplementary surface techniques will inform analysis of SF-EIS and ICP-MS trends, as the calculation of i_{ox} is dependent on certain film properties (e.g. z , M_{ox} , ρ_{ox}).

3.5.1.1 Materials

The samples used for this study were polycrystalline, solid solution Ni-alloys that model common Cr and Mo concentrations found in commercial Ni-superalloys with the following compositions: Ni-22% Cr and Ni-22% Cr-6% Mo, wt%. The E-pH diagrams for a generic Ni-Cr-Mo alloy in a dilute NaCl environment is given in Figure 3.1. The materials were arc-melted, cast, rolled, solutionized, recrystallized, and sectioned. The characteristic microstructures for each alloy were obtained using electron backscatter diffraction analysis (EBSD) and are provided in Figure 3.2. Prior to each experiment, the samples were wet-polished up to 1200 grit using SiC paper, ultrasonically cleaned in alcohol, and rinsed with deionized water (resistivity of 18.2 M Ω -cm) before being placed into the flat cell window. In the case of highly surface-sensitive techniques such as AFM or EBSD, subsequent polishing using polycrystalline diamond suspensions on felt microcloth pads down to 1 or 0.25 μ m and a final ion polishing step for 20 min.

The solution used was 0.1 M Na₂SO₄ acidified to pH 4 using 1 M H₂SO₄ and 0.1 M Na₂SO₄ pH 10 prepared using 1 M NaOH for pH adjustment. All prepared solutions used reagent grade chemicals dissolved in deionized water dispensed from a Milli-Q and were deaerated using ultra-high purity N₂ gas during electrochemical experimentation.

3.5.1.2 Fundamental Electrochemical Characterization

To initially test the electrochemical passivation behavior of the Ni-Cr and Ni-Cr-Mo alloys in the sulfate environments, cyclic polarization scans were performed. This was done by initially mechanically grinding the samples to 1200 grit using successively finer SiC papers. Then, the materials were rapidly placed into the window of a vertical three-electrode electrochemical cell (Figure 2.8) which was then filled with the appropriate solution. Upon insertion of a mercury-mercurous sulfate (MMSE, +0.41 V vs SCE) electrode, the solution was then deaerated with N₂ gas through a glass bubbler. Potential and current control was accomplished using a Reference 600 Gamry potentiostat.

An initial cathodic reduction step at -1.3 V_{SCE} for 10 min was used before all electrochemical experiments in order to minimize the existence of air-formed oxides on the alloy

surface. Then, the sample was potentiodynamically polarized from $-1.3 V_{SCE}$ up to $0.8 V_{SCE}$ and back to $-1.3 V_{SCE}$ in 1 mV steps/s . While this speed is higher than what is typical for passivity studies performed to ASTM standards²⁴ (0.1667 mV/s), a faster sweep was necessary to prevent the agglomeration of H_2 gas bubbles evolved at the metal electrode surface when the potential was sufficiently cathodic. Unlike during the reduction step, their removal was not possible using the pipette attachment as the electrolyte stirring greatly impacted the current measurements. By comparing the current response to the cyclic applied potential for the alloys in different pH environments, the relative improvements via the effects of minor alloying additions and solution chemistry can be inferred. However, these findings are not absolute and as such, the following characterization techniques have been additionally applied.

3.5.1.3 SF-EIS

The details of the sample preparation and experimental set-up for the SF-EIS experiments are the same as that discussed above. Following the reduction step, the Gamry SF-EIS script was applied at $+0.2 V_{SCE}$ with 1 Hz frequency and a 20 mV AC amplitude. This enabled the measurement of the impedance components Z' and Z'' of the oxide film during passivation (Chapter 2). The measurement time was chosen to be $10,000 \text{ s}$ as a pseudo steady-state in l_{ox} was achieved at this point. In order to apply Equation 2.6 to the SF-EIS results, a full frequency EIS spectrum was acquired from 100 kHz to 1 mHz to obtain α via a circuit model fit²⁵ (Figure 2.15) and correlate $Z''(t)$ to an oxide thickness, $l_{ox}(t)$. From these results, $i_{ox}(t)$ could also be calculated (Equation 2.11) for each alloy and electrolyte condition.

3.5.1.4 ICP-MS

In operando ICP-MS experiments² were carried out using an experimental setup that have been detailed previously, along with the relevant limits of detection: $2.70 \pm 0.30 \mu\text{g/L}$ for Cr^{50} , $0.27 \pm 0.12 \mu\text{g/L}$ for Ni^{58} and $0.074 \pm 0.013 \mu\text{g/L}$ for Mo^{98} ¹⁵. In terms of the dissolution current density limit of detections, this corresponds to approximately $7.0 \times 10^{-7} \text{ A/cm}^2$ for Cr^{3+} , $4.1 \times 10^{-8} \text{ A/cm}^2$ for Ni^{2+} , and $2.1 \times 10^{-8} \text{ A/cm}^2$ for Mo^{6+} (Equation 2.8). Only concentration data above the detection limits were considered. The electrochemical control was conducted using a Bio-Logic

² Due to experimental challenges with the AESEC setup at Monash, the ICP-MS experiments were limited to $0.1 \text{ M Na}_2\text{SO}_4$ (pH 5.5).

SP-150 potentiostat. An initial cathodic reduction step to minimize the contribution of an air-formed oxide was conducted by holding the working electrode at $-1.3 \text{ V}_{\text{SCE}}$ for 10 minutes^{25,26}. Following this, a potentiostatic step to $+0.2 \text{ V}_{\text{SCE}}$, was implemented to grow the oxide within the passive region for times up to 10,000 seconds. At this potential, the stable oxidation states are Ni^{2+} , Cr^{3+} , and Mo^{6+} ¹. The element-specific current density contributions for cation species, M^{n+} , released into solution and not retained in the oxide as determined by the ICP measurements, $i_{diss}^M(t)$, were computed and summed to obtain $i_{diss}(t)$, the total current density for dissolution and cation ejection reactions (Equations 2.7 to 2.9). The total ICP current was then subtracted from the total electrochemically measured DC current density, i_{tot} , associated with the total metal oxidation and dissolution in order to compute the total oxide formation current density, i_{ox} (Equation 2.10).

In order to evaluate the contribution of a specific element, M, towards passivation rather than direct cation ejection or film dissolution, the expected, element-specific dissolution current density based on congruent alloy dissolution³ where E_{app} is well above E_{pp} for each element was computed and the oxidation contribution was similarly obtained using i_{diss}^M (Equation 2.13 and 2.14). The film's overall atomic composition, C_M , can then be calculated from ICP-MS using Equation 2.16. It is recognized that this computed composition does not account for potential layering. A general schematic of the relative oxidation and dissolution for individual alloying elements is given in Figure 2.8.

3.5.1.5 Mott-Schottky Impedance Analysis

The measurement of electronic property variation was measured during film growth through application of *in situ* MS-EIS. This was accomplished by changing the voltage of the semiconductor artificially through application of a potentiostat, where the semiconductor Fermi levels separate and band-bending is induced. This triggers either charge depletion or accumulation in the semiconductor depending on if the potential is in the n-type or p-type regimes as indicated in Figure 3.3²⁷. These shifts in the electronic properties of the semiconductor correspond to the capacitive behavior, C , shown schematically in Figure 3.4. According to Poisson's equation in one

³ Congruent dissolution is a starting point and a reasonable assumption when there are large thermodynamic driving forces for dissolution of each alloying element, i.e. $i_{diss} \gg i_{ox}$.

dimension, the relationship between the charge density, ρ , and the potential, ϕ , across a semiconductor is given generally as:

$$\frac{\partial^2 \phi}{\partial x^2} = -\frac{\rho}{\varepsilon \varepsilon_0} \quad \text{Equation 3.1}$$

This can be solved to produce the Mott-Schottky equation:

$$\frac{1}{C^2} = \frac{2}{\varepsilon \varepsilon_0 q N_{D,A} A^2} \left(E - E_{FB} - \frac{k_B T}{q} \right) \quad \text{Equation 3.2}$$

where ε is the film dielectric constant, ε_0 is the vacuum permittivity, q is the electron charge, N_D is the density of n-type defects (e.g. electrons and oxygen vacancies), N_A is the density of p-type defects (e.g. metal cation vacancies and holes), A is the sample area, E is the applied potential, E_{FB} is the flat band potential, k_B is Boltzmann's constant, and T is the temperature. Based on this equation, the capacitance data can be linearized to measure E_{FB} as approximately the x-intercept when $E = 0$ (Figure 3.4) and N_D or N_A are proportional to the slope in the n- and p-type regimes, respectively:

$$N_{D,A} = \pm \frac{2}{\varepsilon \varepsilon_0 q A^2} \left(\frac{dC^{-2}}{dE} \right)^{-1} \quad \text{Equation 3.3}$$

The capacitance can be obtained by measurements of Z'' at a specific frequency, f :

$$-Z''(E) = \frac{1}{2\pi f C(E)} \quad \text{Equation 3.4}$$

where f is sufficiently high that the passive film and space charge layers will not vary during the potential sweep. A typical frequency used in this dissertation and previous literature is 1,000 Hz²⁷⁻³⁶.

For these experiments, fast MS impedance sweeps were performed at 1,000 Hz following film growth at +0.2 V_{SCE} from +0.3 V_{SCE} down to -0.6 V_{SCE} with 20 mV steps, resulting in sufficiently rapid data acquisition. This was accomplished *in situ* following any amount of experimental passivation, at various times from 0 to 10,000 s. As mentioned previously, this scan rate was selected in order to measure the impedance variations as a function of potential without the possibility of the space charge layer adjusting.

3.5.1.6 X-ray Photoelectron Spectroscopy Analysis

The variation of film composition and thicknesses will be additionally characterized using XPS spectra obtained periodically throughout potentiostatic passive film growth. This technique is well-established in literature for analysis of the identity, concentration, and thicknesses of individual compounds present in films³⁷, especially in the case of Ni-based alloys^{25,38,39}. All XPS spectra were obtained using a monochromatic Al- α photon source ($E = 1,486.7$ eV) with surface characterization following various durations of oxide growth. The angle between the sample and detector was adjusted to 30 and 90°, whereas that between detector and the X-ray source was fixed at 54.7° (Figure 3.5). Spectra were calibrated to the 4f^{7/2} binding energy of a metallic Au reference (B.E. = 84 eV) measured at the same time. Survey spectra were recorded on all samples using a pass energy of 200 eV, followed by high resolution spectra of the Ni 2p, Cr 3p, Mo 3d, and O 1s regions using a pass energy of 20 eV.

Commercial CasaXPS software was used to perform Shirley background corrections and spectra fitting based on the peaks and parameters for the expected oxide species (Table 3.1)⁴⁰⁻⁴². The concentrations of Ni²⁺, Cr³⁺, and Mo^{4,6+} cations in the passive films were computed by fitting the spectra to their observed metallic and oxide/hydroxide peaks, as established in previous literature^{38,39,42-45} and correcting these integrated peak areas to atomic sensitivity factors for Ni, Cr, and Mo (4.044, 2.427, and 3.321 for this detector and source configuration, respectively)⁴²:

$$x_{Ni^{2+}} = \frac{\frac{A_{NiO}^{tot} + A_{Ni(OH)_2}^{tot}}{S_{Ni}}}{\left[\frac{A_{NiO}^{tot} + A_{Ni(OH)_2}^{tot}}{S_{Ni}} + \frac{A_{Cr_2O_3}^{tot} + A_{Cr(OH)_3}^{tot}}{S_{Cr}} + \frac{A_{MoO_2}^{tot} + A_{MoO_3}^{tot}}{S_{Mo}} \right]} \quad \text{Equation 3.5}$$

$$x_{Cr^{3+}} = \frac{\frac{A_{Cr_2O_3}^{tot} + A_{Cr(OH)_3}^{tot}}{S_{Cr}}}{\left[\frac{A_{NiO}^{tot} + A_{Ni(OH)_2}^{tot}}{S_{Ni}} + \frac{A_{Cr_2O_3}^{tot} + A_{Cr(OH)_3}^{tot}}{S_{Cr}} + \frac{A_{MoO_2}^{tot} + A_{MoO_3}^{tot}}{S_{Mo}} \right]} \quad \text{Equation 3.6}$$

$$x_{Mo^{4,6+}} = \frac{\frac{A_{MoO_2}^{tot} + A_{MoO_3}^{tot}}{S_{Mo}}}{\left[\frac{A_{NiO}^{tot} + A_{Ni(OH)_2}^{tot}}{S_{Ni}} + \frac{A_{Cr_2O_3}^{tot} + A_{Cr(OH)_3}^{tot}}{S_{Cr}} + \frac{A_{MoO_2}^{tot} + A_{MoO_3}^{tot}}{S_{Mo}} \right]} \quad \text{Equation 3.7}$$

3.5.1.7 Neutron Reflectometry

NR results can be similarly analyzed to produce information regarding the molecular identity and layering of passive films. This is made possible using an *in situ* NR experimental setup at the D3 beamline at the National Research Universal (NRU) reactor (Chalk River, Ontario, Canada), shown schematically in Figure 3.6. This setup allowed NR measurements performed concurrently with electrochemical experiments. For the purpose of these experiments, thin films were prepared by an electron-beam evaporation system (Angstrom, Ontario, Canada) to produce approximate 25 nm thick Ni-Cr and Ni-Cr-Mo alloys on 100 mm diameter x 6 mm thick polished Si(111) wafers. XPS analysis following thin film preparation yielded bulk compositions of Ni-20 Cr and Ni-20 Cr-10 Mo (wt%).

The thin film samples prepared for NR were stored in a vacuum desiccator and, prior to experiments, were cleaned with methanol and dried in air. Figure 3 shows a schematic of the *in situ* NR experimental setup at the D3 beamline at the National Research Universal (NRU) reactor (Chalk River, Ontario, Canada). This setup allowed NR measurements to be performed concurrently with electrochemical experiments⁴. A conventional three-electrode electrochemical cell with a Pt thin foil counter electrode and a KCl saturated Ag/AgCl reference electrode ($V_{\text{Ag/AgCl}} = +47 \text{ mV}_{\text{SCE}}$) was used. A Solartron 1287A potentiostat and a Solartron 1255 frequency analyzer were used in electrochemical experiments. A cathodic potential of $-1.2 \text{ V}_{\text{SCE}}$ was applied for 5 min to reduce the air-formed oxide, followed by steps from $-0.8 \text{ V}_{\text{SCE}}$ up to $+0.2 \text{ V}_{\text{SCE}}$ in $0.2 \text{ V}_{\text{SCE}}$ steps every 6 hr, shown schematically in Figure 3.7. The thin film samples, Pt foil, and reference electrode were connected to the corresponding terminal of the potentiostat for potential control and electrochemical measurements and the neutron beam travelled to the metal/electrolyte interface through the Si wafer. The NR measurements started 1 hr after the applied potential was switched to the set value and each measurement took approximately 90 min to complete.

D3 uses a collimated neutron beam with a wavelength of 2.37 \AA . The neutron beam travelled through the Si wafer before it reached the metal/film interface at a small grazing angle. The intensity of the specular reflected beam was recorded at different grazing angles and the reflectivity curves were plotted as a function of the scattering vector, Q_{beam} , whose magnitude is

⁴ Because of the unfortunate shutdown of the D3 neutron beam line, *in situ* passivation measurements were only performed for 0.1 M Na_2SO_4 acidified to pH 4.

related to the incident beam angle, θ , and the neutron wavelength, λ , by the following expression^{46,47}:

$$Q_{beam} = \frac{4\pi}{\lambda} \sin \theta \quad \text{Equation 3.8}$$

The thickness, roughness, and scattering length density (SLD) profile of the layers in the thin film sample were obtained by fitting the reflectivity curves to a thin film model using a least square fit algorithm which includes a recursion algorithm developed by Parratt⁴⁶⁻⁴⁹.

For analysis of the passive film composition and thickness, the profiles for the unoxidized alloys deposited on SiO₂ and H₂O exposed to a vacuum environment were simulated using GenX software using the experimental interfacial roughness and SLD values (Figure 3.8)⁴⁹. The SLD for the simulated base metal and environment were then subtracted from the experimental profiles at the first deviation from the alloy SLD, as indicated in Figure 3.8, in order to extract the SLD versus depth data for only the passive films.

3.5.1.8 Atomic Force Microscopy

Following electrochemical passivation, the samples were removed from the cell, rinsed with deionized water, and sonicated in ethanol to remove any residual salt from the surface that would obstruct imaging. The surface morphology of each sample was captured using an AFM with NT-MDT Solver Pro. The AFM tip, ETALON HA/NC with a radius of curvature less than 10 nm, was kept in tapping mode during imaging. The surface roughness of the samples was ascertained from deviations in the root mean square (RMS) of local surface areas. The RMS data in this study was found using Gwyddion⁵⁰, an open source software package used for surface probe microscopy analysis. To obtain consistent and physically meaningful RMS values, each image was planarized by mean plane subtraction. The variations caused by the contact between the tip and sample along the horizontal scanning directions were also corrected by leveling the horizontal line directions with linear or quadratic polynomials depending on the magnitude of the deviations.

3.5.1.9 Three-Dimensional Atom Probe Tomography (3DAPT)

More in-depth sample preparation steps were required in order to produce tips appropriate for analysis in TEM or 3DAPT⁵¹. A standard electropolishing step was used to pre-thin alloy bars (0.5mm×0.5mm×2cm) in an electrolyte of 10 vol% perchloric acid in acetic acid using 12-20 V_{DC}.

Afterwards, 2 vol% perchloric acid in a butoxyethanol electrolyte and 12-15 V_{DC} were used to accomplish the final sample thinning. A CAMECA Local Electrode Atom Probe 4000XSi with an ultrafast detector capability was used for APT experiments. Picosecond pulses of a UV laser were utilized to evaporate individual atoms at a repetition rate of 250 kHz with a pulse energy of 20 pJ and an average detection rate of 0.005 ions/pulse. The specimen tip temperature was maintained at 25 K. Data analysis was performed on the 3D reconstructions of the specimen utilizing IVAS V3.6.1 software.

It is established that the oxide compositions measured using APT depend on the laser energy/pulse, with more accurate results achieved at lower energies. To calibrate the data, a tip of pure Ni was prepared, oxidized, and used as a calibrant. This sample indicates that the detection efficiency of O atoms was 0.67. All data herein has been corrected for this inefficiency.

3.6 Results

3.6.1 Fundamental Electrochemistry of Ni-Alloys in Aqueous Sulfate Environments

The E-log *i* passivation behavior of Ni-22 Cr and Ni-22 Cr-6 Mo, wt%, in the acidic and alkaline solutions of concern for most of this study was established initially (Figure 3.9a). The impedance was then measured at 1 Hz to assess the imaginary component of the film impedance and its corresponding capacitance across the same range of applied potentials during a potentiodynamic sweep from -1.3 V_{SCE} to +0.8 V_{SCE} at 1 mV/s (Figure 3.9b). The significant effect of minor alloying additions and pH can be inferred using cyclic voltammetry (Figure 3.9a). Both Ni-Cr and Ni-Cr-Mo exhibit strong passivity in the environments. Notably, even Ni-Cr remains stable at the highest potential, +0.8 V_{SCE}. Adding another 6 wt% Mo results in even greater passivity. In Figure 3.9, the approximately constant, passive corrosion rate decreases by half due to the synergistic effect of Mo and Cr when alloyed in tandem. In Figure 3.9b, $-Z''$ is increasing up until +0.5 V_{SCE} where transpassive dissolution of the film occurs for both alloys. At the potential of interest, however, there is thicker film and faster thickening rate evident for Ni-Cr-Mo.

Comparable passivity of Ni-Cr and Ni-Cr-Mo around +0.2 V_{SCE} is evident in the alkaline environment (Figure 3.9). At lower potentials, slight improvements in the corrosion rate and film thickness are observed for the Mo-containing alloy due to the effect of the minor solute on inhibiting dissolution. The films formed during cyclic polarization were, in general, thicker in the

pH 10 environment when compared to the behavior in the acid. Both alloys also exhibited similar film thickening and thinning rates in terms of nm/V, with film formation and dissolution initiating sooner due to, again, the effect of Mo and its low electrochemical stability in alkaline environments¹.

3.6.2 In Operando Passivation

3.6.2.1 AESEC in 0.1 M Na₂SO₄

The dissolution current densities, i_{diss}^M , for each element determined by ICP-MS for the binary Ni-Cr (Figure 3.15) and ternary Ni-Cr-Mo (Figure 3.16) alloys are shown by solid lines with a comparison to the partial electrochemical current densities for all elements ($i_{cong\ diss}^M$) obtained assuming congruent dissolution of the alloy. The differences between the i_{diss} versus time behavior for each element (i_{diss}^{Ni} , i_{diss}^{Cr} , i_{diss}^{Mo}) and i_{EC} indicate the element-specific individual contributions towards film growth and element dissolution into solution by either direct injection or film dissolution. The physical processes dominating each stage of passivation are annotated in Figure 3.15 and Figure 3.16.

The comparison of i_{diss} to i_{EC} indicates that there is a very high efficiency for oxide growth versus dissolution at early times, notably for Ni over the first 60 s and later Cr. A significant role of cation ejection during passivation in acidic sulfate solutions is indicated at all times. In the case of the binary alloy, Ni-22 wt% Cr, the ICP-MS data shown in Figure 3.15 indicates that there is first significant Ni formation, likely hydroxylated Ni²⁺ oxide or Ni(OH)₂, followed by an increase in the preferential dissolution of Ni while a passive, Cr-rich oxide film builds up continually over the first 1,000 s (i.e. $i_{ox} > 0$ for Cr). At longer times, however, the total anodic current density, i_{EC} , levels off which indicates that the oxide film has reached a limiting thickness. In this stage, i_{diss}^{Ni} is nearly zero while i_{diss}^{Cr} approaches the measured i_{EC} .

The ternary alloy, Ni-22% Cr-6% Mo, wt%, shown in Figure 3.16 has similar early kinetically favorable hydroxylated Ni(OH)₂ formation over the first 50 seconds followed by Ni dissolution during subsequent Cr-enrichment of the passive film. From 60 to 1,000 s there are equivalent rates of Ni and Mo dissolution which dominate i_{EC} , indicated by i_{diss}^{Ni} and i_{diss}^{Mo} compared to i_{EC} . A gradual decrease in the Ni ICP signal, i_{diss}^{Ni} , nearly matches i_{EC} whereas Cr, i_{diss}^{Cr} , and Mo, i_{diss}^{Mo} , remain constant and below i_{EC} at long times. At longer times, however, there

is ejection of all elements as a quasi-limiting thickness is attained. However, a Cr-rich oxide has formed over the first 700 s while Ni was dissolving equal to total Ni production after 50 s. The behavior of i_{diss}^{Mo} indicates that, after early Mo release during Cr-film enrichment, it likely becomes incorporated in the oxide at small concentrations. At longer times during the quasi-steady state stage, Mo^{6+} is ejected somewhat congruently with Cr^{3+} into solution.

Figure 3.17 shows a comparison of the total electrochemical DC and ICP-measured currents, i_{EC} and i_{diss} , plotted versus time for Ni-22% Cr-6% Mo, wt%. The difference between i_{EC} and i_{diss} indicates i_{ox} , the total oxide growth rate for the alloy. The measured i_{EC} and computed i_{ox} from the SF-EIS method are plotted for comparison. There is reasonable agreement between i_{EC} and i_{ox} obtained from either *operando* SF-EIS or ICP-MS. Additionally, l_{ox} calculated from both methods in Figure 3 are in good agreement with previous values obtained in literature for Ni-based alloys using EIS²⁵, XPS^{38,39}, and time-of-flight secondary ion mass spectrometry³⁸. Both the ICP-MS and SF-EIS results indicate a high current efficiency for oxide growth over the first 60 s evident by the small difference between i_{EC} and i_{ox} . The efficiency decreases with time and after 60 s, i_{EC} is nearly equivalent to i_{diss} and the oxide reaches a limiting thickness with continued film formation balanced by cation ejection. Continued oxidation and net gains in film formation no longer occur globally at times when the efficiency is low.

3.6.2.2 SF-EIS Application in Varying Environments

Potentiostatic passivation of Ni-22 Cr and Ni-22 Cr-6 Mo, wt%, at +0.2 V_{SCE} was investigated in acidic (pH 4) and alkaline (pH 10) 0.1 M Na_2SO_4 and monitored using SF-EIS and ICP-MS to investigate the varying thermodynamic and kinetic favorability of oxide species in these environments. The measured increases in l_{ox} in the acidic environment for Ni-Cr and Ni-Cr-Mo using the former technique at 1 Hz and +0.2 V_{SCE} are given in Figure 3.10. The measured $-Z''(t)$ and the corresponding $l_{ox}(t)$ appear to decrease with alloying content for all times. This includes at early time, where Ni-11 Cr had slightly improved initial oxidation over Ni-22 Cr and Ni-22 Cr-6 Mo.

Pourbaix-like thermodynamic predictions given in Figure 3.1 suggest that pH will have a significant effect on passivation^{1,52-55}. The passivation of Ni-22 Cr (Figure 3.11) and Ni-22 Cr-6 Mo (Figure 3.13), wt%, in 0.1 M Na_2SO_4 solution adjusted to various pH values were studied. The

film thicknesses on both Ni-Cr and Ni-Cr-Mo appear to generally increase with pH due to the increased chemical stability of oxides. This was confirmed through analysis of the oxidation rate, i_{ox} , and the efficiency, η , for the alloys, given in Figure 3.12 and Figure 3.14.

As predicted by the faster passivation with increasing pH values, η also improves for each alloy. There is also no discernable effect of Mo in the sulfate environments due to the minimal preferential Ni dissolution and Cr enrichment (Figure 3.15 and Figure 3.16). The use of specifically pH 4 and 10 for the in-depth studies herein are justified by the *in operando* passivation results using SF-EIS, as very different thermodynamics and kinetics can be inferred. Therefore, the general effect of pH can be understood by comparing these two environments.

3.6.3 *In Situ* Characterization

3.6.3.1 Mott-Schottky Analysis

During passivation in the 0.1 M Na₂SO₄ environments, Mott-Schottky analysis of fast impedance sweeps was applied at times during passivation to characterize the electronic properties of the film and their evolution with time. Noticeably in Figure 3.20, the films predominantly behave as n-type semiconductors within the passive potential region. However, at the passivation potential, +0.2 V_{SCE}, the films exhibit p-type behavior. This suggests that at lower potentials, the dominant electronic point defects are electrons and/or metal cation vacancies. However, it seems that during the previous *in operando* passivation experiments, it is likely ionic oxygen vacancies that control the oxidation process and the relevant kinetics. The flux of the latter was the point defect within a passive film that has been previously theorized to be the rate determining step for passivation⁵⁶⁻⁵⁸. Overall, a clear decrease in the capacitance (and therefore an increase in the oxide thickness) was observed during the passivation time. The shift from n-to-p-type behavior remained around +0.2 V_{SCE}, however. The impedance sweeps in the alkaline environment (Figure 3.21) exhibited very different behavior with primarily p-type semiconductance being observed at early times before the transition potential shifted to higher values and mostly n-type behavior was measured. Based on the observed magnitude differences in C^{-2} , it appears the films were thicker and more resistive in the alkaline environment.

Mott-Schottky analysis of these impedance spectra enabled computation of the n- and p-type point defect concentrations, N_D and N_A , respectively, (Figure 3.22) along with the respective

flat band potential (Figure 3.23). The concentrations do not appear to vary significantly, with a few exceptions. In the acidic environment, the concentration of n-type and p-type defects appear to initially decrease as the film forms. There is a significant drop in the concentration of defects in Ni-Cr in this environment. The alloys otherwise appear to have similar electronic properties based on Figure 3.22.

Analysis of the passive film flat band potentials provides additional insight into the different behavior of the alloys exposed to acidic and alkaline sulfate environments (Figure 3.23). Ni-Cr-Mo tended to have a higher n-type and p-type E_{FB} than Ni-Cr in each condition. At early times in 0.1 M Na_2SO_4 pH 10, however, Ni-Cr was measured to have a higher p-type EFB and thus higher corrosion resistance. This is likely caused by the fast dissolution of Mo as it is not thermodynamically stable in alkaline environments. After 1,000 s when a thick passive film is achieved, the dissolution of Mo is slowed and E_{FB} for Ni-Cr-Mo increases.

3.6.3.2 Neutron Reflectometry

The reflectivity curves for the two alloys in 0.1 M Na_2SO_4 pH 4 are given in Figure 3.24. These data sets were fit using an algorithm developed by Parratt⁴⁶⁻⁴⁹ to produce neutron SLD profiles versus depth (Figure 3.25). At low depths, the SLD corresponded to the electrolyte layer, followed by a steep, almost linear increase upon reaching the oxide layer. Finally, the SLD of the base metal alloys was reached at still greater depths. Annotated on Figure 3.25 as horizontal lines are the theoretical SLD of several stoichiometric oxides. Based on the figures, the profiles suggest films rich in Ni-oxide species. There is no clear layering within the passive film as a plateau within the pseudo-linear region would be evident, and instead there is a continuous increase between the theoretical value for $\text{Cr}(\text{OH})_3$ and either the SLD peak (for Ni-Cr) or the base metal (for Ni-Cr-Mo).

Simulated SLD profiles were produced using GenX software for a non-equilibrium film with varying Cr^{3+} content or a bilayer oxide composed of varying thickness NiO and Cr_2O_3 layers (Figure 3.26). Upon comparing Figure 3.25 to Figure 3.26, it is evident that the SLD profiles agree with non-stoichiometric, solid solution oxides, as shown in Figure 3.26a. It could be argued that the layered NiO and Cr_2O_3 appear to agree when there is a small l_{ox} for the latter species, but it is

apparent in the ICP-MS results (Figure 3.15 and Figure 3.16) that this would not accurately apply to the observed film composition.

Upon subtraction of the metal and electrolyte SLD (Figure 3.8), the oxide peaks do not demonstrate any layers (Figure 3.27). These results additionally allow for the estimation of l_{ox} and the Cr^{3+} cation fraction using the width and height of the profile, respectively (Table 3). Films with an SLD closer to the value of NiO ($8.7 \times 10^{-6} \text{ \AA}^{-2}$) will have a lower % Cr^{3+} compared to those near the value of Cr_2O_3 ($5.1 \times 10^{-6} \text{ \AA}^{-2}$), and the non-stoichiometric film possessing an SLD in-between the two. There is some Ni-enrichment apparent at the metal/film interface, as previous work has reported^{38,59,60}, but for Ni-Cr-Mo the outer SLD decreases with applied potential as Ni^{2+} undergoes selective dissolution in favor of Cr-enrichment (Figure 3.27b). Since the fraction of Mo cations in the film is insignificant compared to Ni^{2+} and Cr^{3+} (Figure 3.16), any substitutional $\text{Mo}^{4,6+}$ defects within the oxide would not result in the observed, substantial decrease in the SLD for passivated Ni-Cr-Mo. There is also a rough, outer interface of the passive films that is very highly hydrated. The thickness of this region is estimated to be approximately 1 nm, which is on the order of the experimental passive film surface roughness⁶¹.

Analysis of the Cr^{3+} metal cation fraction and the passive film thickness using the profile width and peak SLD values in Figure 3.27 in Figure 3.28. As suggested previously, Ni-Cr-Mo exhibited greater Cr-enrichment across all potentials than Ni-Cr (Figure 3.28a). The film thickness was also consistently greater on Ni-Cr-Mo at every potential, suggesting the effect of Mo on promoting Cr-oxidation. There is minimal variation in both the Cr^{3+} cation fraction and the film thickness with applied potential due to relatively slow dissolution kinetics in sulfate environments. The slight thinning of the film at higher potentials can be attributed to transpassive oxide dissolution. At higher potentials (e.g. +550 mV_{SCE})¹, fast transpassive dissolution of Cr^{3+} would result in more noticeable thinning⁶².

3.6.3.3 *Ex situ* Characterization

3.6.3.4 Atomic Force Microscopy

At various times throughout the passivation processes, AFM imaging provided additional details concerning the influence of solution chemistry on the development of the surface topography. Once the oxide was electrochemically grown, the alloy surfaces were measured

immediately after exposure to reduce the effect of ambient conditions on the surfaces. Several area sizes were measured using AFM (e.g. 5x5 and 2x2 μm^2), with smaller areas (e.g. 100x100 to 500x500 nm^2) used to provide representative topography measurements between polishing marks. Figure 3.29 shows a representative set of the AFM images captured after different passivation times for Ni-Cr in 0.1 M Na_2SO_4 pH 4. The inset images give an accurate representation of the areas used to perform the RMS surface roughness measurements. The coverage of the oxide particles increases with exposure time to the environment (Figure 3.29). This can also be represented using line scans across the inset images as given in Figure 3.30. Individual particles are evident after 10 s, and as the passivation time increases, these apparently grow and coalesce to form a continuous layer after 1,000 s. The surface after 10 ks appears to be the smoothest, with some particles evident due to nucleation of new oxide particles at the continuous film surface. The topographies of the air-oxidized surface are given separately from the electrochemically oxidized ones in Figure 3.30. The significant difference in each of these topographies measured using line scans demonstrates that the images and the relevant changes in surface morphology in Figure 3.29 are caused by electrochemically passivation and not any underlying roughness of the metal following polishing.

The RMS values for Ni-Cr following passivation in the aqueous environment are given in Figure 3.31. The average value consistently decreases with exposure time as the oxide particles grow laterally and coalesce into a conformal layer. After this occurs around 1,000 s, the film continuously smooths out any surface perturbations and the RMS values further decrease. The variability across the surface, indicated by the error bars in Figure 3.31, also decreases with time. This suggests that less morphological oxide features remain at longer passivation times and only smaller undulations indicative of the conformal passive film persist⁶³.

Ni-Cr-Mo, however, has a noticeably different surface topography after the same passivation conditions (Figure 3.32). Numerous perturbations exist at the surface, causing the measured RMS to be greater for Ni-Cr-Mo (2.64 nm) than even the initial measurement for Ni-Cr after 10 s of passivation (1.06 nm). This surface roughness can be attributed to the effect of Mo and provides evidence of it likely being enriched at the surface. Previously, Mo has been observed to repassivate at the film surface in low pH environments in the form of polymeric species containing Mo^{6+} ^{62,64}. While no localized breakdown is occurring in this sulfate environment,

dissolution of the passive film is still occurring and redeposition of Mo cations on the surface can still occur and produce the rough morphology evident in Figure 3.32.

3.6.3.5 XPS Analysis

An example of the XPS spectra deconvolution for Ni-Cr-Mo passivated for 10 ks in 0.1 M NaCl pH 4 is shown in Figure 3.33. The fitted peaks indicate each observed metallic, hydroxide, and oxide species. Based on the spectra peaks, the consistent hydroxide and oxide species included were Ni(OH)₂, NiO, Cr(OH)₃, Cr₂O₃, MoO₂, and MoO₃ with the utilized spectral fitting parameters given in Table 3.1. It should be noted that previous literature has additionally identified spinel compounds (e.g. NiCr₂O₄)^{16,17,65-67}, but they were found during peak fitting to constitute an insignificant fraction (~1%) of the total integrated area and as such was excluded from analysis. The integrated peak areas for the aforementioned passive film species are directly compared to each other, and the ICP-MS measurements of film metal cation composition for both alloys passivated at +0.2 V_{SCE} in 0.1 M Na₂SO₄ (pH 5.5) are given an approximate comparison to the acidic XPS results in Figure 3.18.

In the acidic environment, Ni-Cr-Mo exhibited greater enrichment of Cr-species, resulting in a higher cation fraction of Cr³⁺ according to the peak areas and Equation 3.6 (Figure 3.35 and Figure 3.37). This result agrees with the previous observation that Ni-rich films form first, followed by the slower growth of Cr-rich ones (Figure 3.15 and Figure 3.16 and Figure 3.34-Figure 3.37)^{51,67}. Additionally, the result supports the previous theory⁶⁸ that Mo alloying promotes the oxidation of Cr. Upon comparing passivation in an acidic environment (Figure 3.18) to that in an alkaline one (Figure 3.19), there is an apparent difference between the films. Notably, the fraction of Ni²⁺ as measured using XPS peak fitting and ICP-MS analysis remained steady for Ni-Cr, whereas there was minor enrichment of Cr³⁺ within the film on Ni-Cr-Mo throughout the passivation time. For all times, there was additionally a slightly greater fraction of Cr³⁺ within the film on Ni-Cr-Mo than on Ni-Cr after 10 ks (Figure 3.18). Finally, the calculated enrichment of Mo^{4,6+} cations was lower for pH 10 (Figure 3.19) than that observed at pH 4 (Figure 3.18), due to its likely selective dissolution in the alkaline environment as MoO₄²⁻.

In the alkaline environment, some NiO peaks were discernable at 10 s, but afterwards the measured spectra was essentially representative of only Ni metal and Ni(OH)₂ (Figure 3.36 and

Figure 3.37). The same applied for Cr, where Cr_2O_3 and $\text{Cr}(\text{OH})_3$ formed quickly and the former became quickly hydrated. There was clear oxide species present at all times in the acidic environment because of the influence of its favorable thermodynamics over the hydroxides, whereas both were stable at pH 10 and the oxides remain hydrated as $\text{Ni}(\text{OH})_2$ and $\text{Cr}(\text{OH})_3$. Less $\text{Mo}^{4,6+}$ was found within the passive film and, as explained previously, this can be attributed to its poor thermodynamic stability in high pH environments. The low oxide concentration and corresponding depletion of Mo at the surface of the base alloy caused a weak Mo 3d signal, requiring more cumulative scans to produce Figure 3.37.

3.6.3.6 3D Atom Probe Tomography

The atomic resolution of APT enables a more detailed representation of the physical and chemical properties of nanometer-thick passive films on Ni-Cr (Figure 3.42) and Ni-Cr-Mo (Figure 3.43). At first glance, there is no apparent layering of any Ni or Cr-oxides within the film layer formed on Ni-Cr following passivation in the sulfate environment. Rather, the atomic fraction of Ni- and Cr-oxides remains approximately constant, 45 and 20 at%, respectively, until increasing at the metal/film interface as the fraction of O decreases significantly in unoxidized area of the tip (Figure 3.42). There is additionally no noticeable segregation within the film despite the assertions in previous literature of this phenomena^{38,59,60}. Instead the oxide appears to be more akin to a solid solution of both $\text{NiO}/\text{Ni}(\text{OH})_2$ and $\text{Cr}_2\text{O}_3/\text{Cr}(\text{OH})_3$ based on the valence states detected by XPS (Figure 3.34). This observation is indicative of a solute-captured passive oxide forming, which will be explained in more detail in Chapter 6.

The APT results for Ni-Cr-Mo appear very similar to those included for Ni-Cr (Figure 3.43). No segregation of the passive film composition is apparent with the exception of Mo, which appears to have noticeably enriched at the oxide/solution interface (Figure 3.43). Similar behavior has been proposed in previous literature based on angle-resolved XPS and ToF-SIMS^{38,59,69-73}. However, the peak concentration was only 10 at%, approximately the same as Cr^{3+} and much less than O^{2-} and Ni^{2+} . The formation of a distinct Mo-oxide layer is therefore unlikely. Otherwise, a similar mixture of $\text{NiO}/\text{Ni}(\text{OH})_2$ and $\text{Cr}_2\text{O}_3/\text{Cr}(\text{OH})_3$ was evident within the passive film with an approximately constant concentration of Ni^{2+} and Cr^{3+} throughout the thickness. The total thicknesses for Ni-Cr (Figure 3.42) and Ni-Cr-Mo (Figure 3.43) appear similar, with the former

being slightly greater. This is however, speculative, because the interface between the metal and oxide is rather diffuse.

Overall the APT findings confirm several of the previous assertions made using *in operando*, *in situ*, and even the *ex situ* XPS results. The passive films are enriched in Ni²⁺ relative to Cr³⁺ and, for Ni-Cr-Mo, Mo^{4,6+}. There is no apparent cation segregation within the oxide layer and instead, the ratio between Ni²⁺ and Cr³⁺ remains approximately constant (Figure 3.42 and Figure 3.43). While there is enrichment of Mo^{4,6+} at the film/electrolyte interface (Figure 3.43), it is likely insufficient to form a distinct phase and rather the cations are operating as substitutional defects in the Ni-rich oxide.

3.6.4 Film Breakdown Following Passivation

To test the electrochemical stability of the passive film formed by oxidation in these sulfate environments, the surface of Ni-Cr generated following 10 ks at +0.2 V_{SCE} in 0.1 M Na₂SO₄ pH 4 was exposed to 1.0 M NaCl pH 4 at the same potential for a subsequent 10 ks. The variations in the current during these steps are given in Figure 3.44. Only some slight fluctuations in i_{EC} were observed, suggesting that no metastable pitting or crevice corrosion occurred. The film instead remained stable in the concentrated NaCl environment and did not undergo breakdown. The subsequently obtained AFM topography images, also included in Figure 3.44, suggest that no additional roughening of the film occurred as a result of chloride-assisted dissolution at the surface. Rather, the RMS did not vary: 0.180 ± 0.02 nm after 10 ks in NaCl compared to 0.183 ± 0.03 nm after 10 ks in Na₂SO₄. Had the pretreated film been physical or electronically defective, localized breakdown could have initiated upon the adsorption of chloride at any of these local sites.

3.7 Discussion

3.7.1 Chemical Identity of the Passive Films

The results allude to an early dominance by hydroxylated NiO or Ni(OH)₂ possibly containing Cr followed by steady formation of a Cr-rich passive film. Later from 1,000 s until the end of the experiment, the electrochemical oxidation rate becomes equivalent to the rate of cation ejection into solution. This is substantially different from literature observations which often assume a stable Cr₂O₃ film at all times as it is more thermodynamically stable than Ni-based hydroxides ($\Delta G_f^o_{Cr_2O_3} = -1,058 \frac{kJ}{mol}$, $\Delta G_f^o_{Ni(OH)_2} = -216 \frac{kJ}{mol}$, and $\Delta G_f^o_{NiCr_2O_4} = -1257 \frac{kJ}{mol}$).

Here we observe instead that Ni^{2+} oxides form early possibly due to faster growth kinetics^{25,74}. Moreover, NiO or dehydrated $\text{Ni}(\text{OH})_2$, has a strong cube-on-cube epitaxial relationship with FCC surfaces such as Ni-based alloys⁷⁵. This plays a significant role on growth of NiO islands on the surface as they will introduce a lower metal/film interfacial strain energy than NiCrO_3 or Cr_2O_3 which have a hexagonal corundum structure¹⁶. The early kinetic favorability leads to rapid growth of conformal NiO cubic crystals and their subsequent hydration into $\text{Ni}(\text{OH})_2$. The higher kinetic barriers for NiCrO_3 , Cr_2O_3 , and NiCr_2O_4 growth lead to the earlier Ni-oxide dominance. At longer times, however, the increased thermodynamic stability of Cr-rich oxides leads to their eventual enrichment in the film as Ni^{2+} becomes ejected. In fact, the oxide composition of Ni, O, Cr, and Mo is very consistent with the notion of 50% NiO or $\text{Ni}(\text{OH})_2$ and 50% NiCrO_3 and not phase separated $\text{NiO} + \text{Cr}_2\text{O}_3$. Finally, Mo is incorporated into the oxide in low concentrations, indicated by a low i_{diss}^{Mo} .

The results performed in the acidic (pH 4) and alkaline (pH 10) sulfate environments demonstrate very different characteristics of the passive film. Notably, less preferential Ni-dissolution and subsequent Cr-enrichment was observed in the alkaline environment due to the increased thermodynamic stability of these oxides (Figure 3.19). This is well supported by Pourbaix predictions¹, where NiO and $\text{Ni}(\text{OH})_2$ should not dissolve past pH 5 (Figure 3.1). This phenomenon resulted in very different electronic properties of the film, as was observed using Mott-Schottky characterization. The passive films formed in the acidic sulfate environment exhibited a distribution of cations that exemplifies the principle of nonequilibrium solute capture (Figure 3.41 - Figure 3.43), where a mixed oxide (e.g. $\text{Ni}_{1-x}\text{Cr}_x\text{O}_y$) was observed instead of the traditionally expected, phase-distinct, bilayer structure (e.g. $\text{NiO}/\text{Cr}_2\text{O}_3/\text{Ni-Cr(-Mo)}$) (Figure 3.26). For the film formed in the alkaline sulfate environment, however, angle-resolved XPS exhibited some outer enrichment of predominantly NiO (Figure 3.41). The difference was, albeit, slight but the stability of Ni^{2+} in the film resulted in some segregation to the film/solution interface. Interestingly, Mo was not observed to vary in composition throughout the film formed in either environment as a result of solute capture. Due to the low concentration within the alloy, no segregation was observed.

The competition between cation ejection or dissolution and oxidation reactions occurs at all times during electrochemical passivation. In more acidic or chloride-containing aqueous

environments, the thermodynamic stability of oxides and hydroxides may become an even less significant factor than kinetics, leading to unexpected *operando* passivation than cannot be predicted from thermodynamics considerations.

3.7.2 Electronic Properties of the Passive Films

The varying chemical identity of the passive films as a result of various experimental parameters (e.g. alloy, pH, time) resulted in varying electronic behavior. In general, films with greater Ni^{2+} content tended to exhibit lower $N_{D,A}$ (Figure 3.22) and E_{FB} (Figure 3.23). At +0.2 V_{SCE} in the pH 4 electrolyte, the passive films were controlled by n-type defects whereas p-type ones were governing in pH 10. This was a result of the dominant point defects for each alloy and environment combination. At +0.2 V_{SCE} , however, p-type defects always dominated. This suggests that for the *operando* passivation results shown, oxygen vacancies dictate the relevant oxidation kinetics⁵⁶. The flux of the latter was the point defect within a passive film has been previously theorized to be the rate determining step for passivation⁵⁶⁻⁵⁸. Greater range of p-type defect dominance was measured for Ni-Cr-Mo due the substitutional doping of Mo as a positively-charged defect.

The effect of Mo was minimal besides some slightly favorable enrichment of Cr^{3+} within the film. This resulted in slight increases in E_{FB} and decreases in $N_{D,A}$ with the exception of the alkaline environment where, despite the lower Ni^{2+} content overall, an initially higher concentration of n-type defects and lower p-type E_{FB} was measured. This suggests that the poor thermodynamic favorability of $\text{Mo}^{4,6+}$ at high pH environments results in the formation of some point defects, possibly cation vacancies produced by ejection of these cations into the solution. At longer times, the enrichment of Cr past approximately 100 s resulted in improvements in this electronic behavior, evident by the measured decreases in $N_{D,A}$ and increases in E_{FB} .

The combination of smoothing passive film structures (Figure 3.31) and improving electronic behavior discussed above resulted in more electrochemically stable passive films. Decreased film dissolution occurred at later times based on measurements of i_{EC} . Notably, upon introducing concentrated NaCl into the passive environment, film breakdown did not occur due to this favorable combination of physical, chemical, and electronic properties. Typically, which an exposure would result in significant film roughening and localized corrosion. This favorable film

behavior will be especially interesting when compared to the subsequent study of passivation in NaCl detailed in Chapter 4.

3.8 Conclusions

The passivation and dissolution of Ni-22 Cr and Ni-22-6 Mo (wt%), were investigated during *in operando* potentiostatic conditions using electrochemical ICP-MS and SF-EIS in both an acidic and alkaline Na₂SO₄ environment, coupled with *in situ* NR and *ex-situ* XPS conducted during and following film growth. The combination of the techniques utilized enabled determination of i_{ox} distinctly from i_{EC} with high temporal resolution. It was determined that Ni-rich films form early during the passivation process, indicating the substantial influence of kinetic factors. At longer times, Cr³⁺ enrichment was observed when thermodynamics began to dictate the film composition. Surface films produced during anodic polarization at +0.2 V_{SCE} were consistent with non-stoichiometric solid solution rocksalt and corundum oxide structures, likely containing solute captured Ni²⁺, Cr³⁺, and Mo^{4,6+} cations. No substantial layering was observed during oxide formation, with the films instead being Ni-rich at the film/electrolyte and Cr-rich at the metal/film interfaces. Oxides were first formed, with compositions governed by non-equilibrium solute capture. The electrochemical stability of Cr³⁺ cations also increased with alloying of Mo in the base metal, noted by the respective dissolution currents being measured below the detection limit for the Ni-Cr-Mo alloy in each environment. Surface films produced during anodic polarization in the alkaline environment were found to be enriched in Ni²⁺ cations because of the increased stability of NiO and Ni(OH)₂.

3.9 References

1. Pourbaix, M. *Atlas of electrochemical equilibria in aqueous solutions*. (National Association of Corrosion Engineers, 1974).
2. Hamm, D., Ogle, K., Olsson, C. O., Weber, S. & Landolt, D. Passivation of Fe-Cr alloys studied with ICP-AES and EQCM. *Corros. Sci.* **44**, 1443–1456 (2002).
3. Zuili, D., Maurice, V. & Marcus, P. Surface Structure of Nickel in Acid Solution Studied by In Situ Scanning Tunneling Microscopy. *J. Electrochem. Soc.* **147**, 1393–1400 (2000).
4. MacDougall, B. Breakdown of Oxide Films on Nickel. *J. Electrochem. Soc.* **124**, 1185 (1977).
5. Oblonsky, L. J. & Ryan, M. P. In situ XANES study on the active and transpassive dissolution of Ni and Ni-Cr alloys in 0.1 M H₂SO₄. *J. Electrochem. Soc.* **148**, B405–B411 (2001).
6. Sato, N. & Okamoto, G. A Mechanism of the Anodic Passivation Nickel in Acid Solution:

- Higher Valence Oxide Film Theory. *Trans. Japan Inst. Met.* **2**, 113–119 (1961).
7. Sato, N. & Okamoto, G. Anodic Passivation of Nickel in Sulfuric Acid Solutions. **110**, 605–614 (1963).
 8. Macdougall, B. & Cohen, M. Mechanism of the Anodic Oxidation of Nickel. *J. Electrochem. Soc.* **123**, 1783–1789 (1976).
 9. Scherer, J., Ocko, B. M. & Magnussen, O. M. Structure, dissolution, and passivation of Ni(111) electrodes in sulfuric acid solution: An in situ STM, X-ray scattering, and electrochemical study. *Electrochim. Acta* **48**, 1169–1191 (2003).
 10. Iida, M. & Ohtsuka, T. Ellipsometry of passive oxide films on nickel in acidic sulfate solution. *Corros. Sci.* **49**, 1408–1419 (2007).
 11. Moriya, M. & Ives, M. B. The Structure of Anodic Films Formed on Nickel and Nickel-13 w/o Molybdenum Alloy in pH 2.8 Sodium Sulfate Solution. *Corrosion* **40**, 62–72 (1984).
 12. MacDougall, B., Mitchell, D. F. & Graham, M. J. Changes in Oxide Films on Nickel during Long-Term Passivation. *J. Electrochem. Soc.* **132**, 2895 (1985).
 13. Inc., T. I. N. C. *The Corrosion Resistance of Nickel-Containing Alloys in Sulfuric Acid and Related Compounds.* (1983).
 14. Ter-Ovanessian, B., Mary, N. & Normand, B. Passivity Breakdown of Ni-Cr Alloys: From Anions Interactions to Stable Pits Growth. *J. Electrochem. Soc.* **163**, C410–C419 (2016).
 15. Lutton, K., Gusieva, K., Ott, N., Birbilis, N. & Scully, J. R. Understanding multi-element alloy passivation in acidic solutions using operando methods. *Electrochem. commun.* **80**, 44–47 (2017).
 16. Luo, L. *et al.* In situ atomic scale visualization of surface kinetics driven dynamics of oxide growth on a Ni–Cr surface. *Chem. Commun.* **52**, 3300–3303 (2016).
 17. Luo, L. *et al.* In-situ transmission electron microscopy study of surface oxidation for Ni-10Cr and Ni-20Cr alloys. *Scr. Mater.* **114**, 129–132 (2016).
 18. McCafferty, E. Oxide networks, graph theory, and the passivity of Ni-Cr-Mo ternary alloys. *Corros. Sci.* **50**, 3622–3628 (2008).
 19. McCafferty, E. Graph theory and the passivity of binary alloys. *Corros. Sci.* **42**, 1993–2011 (2000).
 20. Kim, C. & Hobbs, L. Identification of diffusing species and the dynamic nature of diffusion paths during oxidation of a dilute Ni-Cr alloy. *Oxid. Met.* **47**, 69–89 (1997).
 21. Frankenthal, R. P., Kruger, J., Tachibana, K. & Ives, M. B. Passivity of Metals. in *Proceedings of the Fourth International Symposium on Passivity* (eds. Frankenthal, R. P. & Kruger, J.) **85**, 878 (The Electrochemical Society, Inc., 1978).
 22. Mitrovic-Spepanovic, V. & Ives, M. B. The Nature of Anodic Films on Nickel and Single Phase Nickel-Molybdenum Alloys. *J. Electrochem. Soc.* **127**, 1903–1908 (1980).
 23. Luo, H., Gao, S., Dong, C. & Li, X. Characterization of electrochemical and passive behaviour of Alloy 59 in acid solution. *Electrochim. Acta* **135**, 412–419 (2014).
 24. Standard test method for conducting cyclic potentiodynamic polarization measurements to determine the corrosion susceptibility of small implant devices. *ASTM F2129-06* (2001).
 25. Jakupi, P., Zagidulin, D., Noël, J. J. & Shoesmith, D. W. The impedance properties of the oxide film on the Ni-Cr-Mo Alloy-22 in neutral concentrated sodium chloride solution. *Electrochim. Acta* **56**, 6251–6259 (2011).
 26. Sato, N. Anodic breakdown of passive films on metals. *J. Electrochem. Soc.* **129**, 255–260 (1982).

27. Gelderman, K., Lee, L. & Donne, S. W. Flat-Band Potential of a Semiconductor: Using the Mott–Schottky Equation. *J. Chem. Educ.* **84**, 685–688 (2007).
28. Ren, Y. & Zhou, G. Rediscovering Mott-Schottky Plots: A Knee-point in the Plot for Passive Films on Chromium. *J. Electrochem. Soc.* **164**, C182–C187 (2017).
29. Bonham, D. B. A Mathematical Model for the Influence of Deep-Level Electronic States on Photoelectrochemical Impedance Spectroscopy I. Theoretical Development. *J. Electrochem. Soc.* **139**, 118–126 (1992).
30. Metikoš-Huković, M., Katić, J., Grubač, Z. & Škugor Rončević, I. Electrochemistry of CoCrMo implant in Hank's solution and Mott-Schottky probe of alloy's passive films. *Corrosion* **73**, 1401–1412 (2017).
31. Marcelin, S., Ter-Ovanessian, B. & Normand, B. Electronic properties of passive films from the multi-frequency Mott-Schottky and power-law coupled approach. *Electrochem. commun.* **66**, 62–65 (2016).
32. Kim, J., Cho, E. & Kwon, H. Photo-electrochemical analysis of passive film formed on Cr in pH 8.5 buffer solution. *Electrochim. Acta* **47**, 415–421 (2001).
33. Raja, K. S., Namjoshi, S. A. & Misra, M. Improved corrosion resistance of Ni-22Cr-13Mo-4W Alloy by surface nanocrystallization. *Mater. Lett.* **59**, 570–574 (2005).
34. Ter-Ovanessian, B., Alemany-Dumont, C. & Normand, B. Electronic and transport properties of passive films grown on different Ni-Cr binary alloys in relation to the pitting susceptibility. *Electrochim. Acta* **133**, 373–381 (2014).
35. Cheng, Y. F. & Luo, J. L. Comparison of the pitting susceptibility and semiconducting properties of the passive films on carbon steel in chromate and bicarbonate solutions. *Appl. Surf. Sci.* **167**, 113–121 (2000).
36. Hakiki, N. B., Boudin, S., Rondot, B. & Da Cunha Belo, M. The electronic structure of passive films formed on stainless steels. *Corros. Sci.* **37**, 1809–1822 (1995).
37. Strohmeier, B. R. An ESCA method for determining the oxide thickness on aluminum alloys. *Surf. Interface Anal.* **15**, 51–56 (1990).
38. Lloyd, A. C., Noël, J. J., McIntyre, S. & Shoesmith, D. W. Cr, Mo and W alloying additions in Ni and their effect on passivity. *Electrochim. Acta* **49**, 3015–3027 (2004).
39. Lloyd, A. C., Noël, J. J., McIntyre, N. S. & Shoesmith, D. W. The open-circuit ennoblement of alloy C-22 and other Ni-Cr-Mo alloys. *JOM* **57**, 31–35 (2005).
40. Biesinger, M. C. *et al.* Resolving surface chemical states in XPS analysis of first row transition metals, oxides and hydroxides: Cr, Mn, Fe, Co and Ni. *Appl. Surf. Sci.* **257**, 2717–2730 (2011).
41. Werfel, F. & Minni, E. Photoemission study of the electronic structure of Mo and Mo oxides. *J. Phys. C Solid State Phys.* **16**, 6091–6100 (1983).
42. Moulder, J. F., Stickle, W. F., Sobol, P. E. & Bomben, K. D. Handbook of X-ray Photoelectron Spectroscopy. 261 (1992).
43. Biesinger, M. C., Payne, B. P., Lau, L. W. M., Gerson, A. & Smart, R. S. C. X-ray photoelectron spectroscopic chemical state Quantification of mixed nickel metal, oxide and hydroxide systems. *Surf. Interface Anal.* **41**, 324–332 (2009).
44. Biesinger, M. C. *et al.* Quantitative chemical state XPS analysis of first row transition metals, oxides and hydroxides. *J. Phys. Conf. Ser.* **100**, 012025 (2008).
45. Baltrusaitis, J. *et al.* Generalized molybdenum oxide surface chemical state XPS determination via informed amorphous sample model. *Appl. Surf. Sci.* **326**, 151–161 (2015).

46. Fritzsche, H. *et al.* Neutron Reflectometry. in *Neutron Scattering and Other Nuclear Techniques for Hydrogen in Materials* 115–158 (Springer, Cham, 2016). doi:10.1007/978-3-319-22792-4_5
47. Penfold, J. & Thomas, R. K. The application of the specular reflection of neutrons to the study of surfaces and interfaces. *J. Phys. Condens. Matter* **2**, 1369–1412 (1990).
48. Parratt, L. G. Surface studies of solids by total reflection of x-rays. *Phys. Rev.* **95**, 359–369 (1954).
49. Björck, M. & Andersson, G. GenX: An extensible X-ray reflectivity refinement program utilizing differential evolution. *J. Appl. Crystallogr.* **40**, 1174–1178 (2007).
50. Nečas, D. & Klapetek, P. Gwyddion: An open-source software for SPM data analysis. *Cent. Eur. J. Phys.* **10**, 181–188 (2012).
51. Yu, X. X. *et al.* Nonequilibrium Solute Capture in Passivating Oxide Films. *Phys. Rev. Lett.* **121**, 145701 (2018).
52. Huang, L.-F., Hutchison, M. J., Santucci, R. J., Scully, J. R. & Rondinelli, J. M. Improved Electrochemical Phase Diagrams from Theory and Experiment: The Ni-Water System and Its Complex Compounds. *J. Phys. Chem. C* **121**, 9782–9789 (2017).
53. Huang, L.-F. & Rondinelli, J. Electrochemical Stabilities of Ni-Based Compounds from Bulk to Nanoscale Dimensions. *Bull. Am. Phys. Soc.* (2018).
54. Liu, J. *et al.* Understanding Chemical Bonding in Alloys and the Representation in Atomistic Simulations. *J. Phys. Chem. C* **122**, 14996–15009 (2018).
55. Huang, L.-F., Ha, H. M., Lutton Cwalina, K., Scully, J. R. & Rondinelli, J. M. Electrochemical Stabilities of Ni-Compound Nanofilms Revealed by A Comparative Theory-Experiment Approach. *Submitt. to J. Phys. Chem. C* (2019).
56. Seyeux, A., Maurice, V. & Marcus, P. Oxide Film Growth Kinetics on Metals and Alloys: I. Physical Model. *J. Electrochem. Soc.* **160**, C189–C196 (2013).
57. Chao, C. Y., Lin, L. F. & Macdonald, D. D. A point defect model for anodic passive films I. Film growth kinetics. *J. Electrochem. Soc.* **128**, 1187–1194 (1981).
58. Bojinov, M. *et al.* Electrochemical study of the passive behavior of Ni-Cr alloys in a borate solution - a mixed-conduction model approach. *J. Electroanal. Chem.* **504**, 29–44 (2001).
59. Zhang, X. & Shoesmith, D. W. Influence of temperature on passive film properties on Ni-Cr-Mo Alloy C-2000. *Corros. Sci.* **76**, 424–431 (2013).
60. Zhang, X., Qin, Z., Zagidulin, D., Noël, J. J. & Shoesmith, D. W. Effect of Oxide Film Properties on the Kinetics of O₂ Reduction on Alloy C-22. *J. Electrochem. Soc.* **164**, 911–917 (2017).
61. Lutton Cwalina, K., Blades, W. H., Reinke, P. & Scully, J. R. Oxide Morphologies during Electrochemical Passivation in Sulfate and Chloride Environments PLACEHOLDER. (2019).
62. Henderson, J. D., Li, X., Shoesmith, D. W., Noël, J. J. & Ogle, K. Molybdenum surface enrichment and release during transpassive dissolution of Ni-based alloys. *Corros. Sci.* **147**, 32–40 (2019).
63. Ramanathan, R. & Voorhees, P. W. Morphological Stability of Steady-State Passive Oxide Films. *Electrochim. Acta* (2019).
64. Jakupi, P., Wang, F., Noël, J. J. & Shoesmith, D. W. Corrosion product analysis on crevice corroded Alloy-22 specimens. *Corros. Sci.* **53**, 1670–1679 (2011).
65. Baran, G. R. Oxide Compounds on Ni-Cr Alloys. *J. Dent. Res.* **63**, 1332–1334 (1984).

66. Unutulmazsoy, Y., Merkle, R., Mannhart, J. & Maier, J. Chemical diffusion coefficient of Ni in undoped and Cr-doped NiO. *Solid State Ionics* **309**, 110–117 (2017).
67. Yu, X. *et al.* In-situ observations of early stage oxidation of Ni-Cr and Ni-Cr-Mo alloys. *Corrosion* **74**, 939–946 (2018).
68. Lutton Cwalina, K., Demarest, C. R., Gerard, A. Y. & Scully, J. R. Revisiting the effects of molybdenum and tungsten alloying on corrosion behavior of nickel-chromium alloys in aqueous corrosion. *Curr. Opin. Solid State Mater. Sci.* (2019).
69. Yang, W., Ni, R. C., Hua, H. Z. & Pourbaix, A. The behavior of chromium and molybdenum in the propagation process of localized corrosion of steels. *Corros. Sci.* **24**, 691–707 (1984).
70. Maurice, V. *et al.* Effects of molybdenum on the composition and nanoscale morphology of passivated austenitic stainless steel surfaces. *Faraday Discuss* **180**, 151–170 (2015).
71. Olefjord, I. & Wegrelius, L. Surface analysis of passive state. *Corros. Sci.* **31**, 89–98 (1990).
72. Wegrelius, L. Passivation of Stainless Steels in Hydrochloric Acid. *J. Electrochem. Soc.* **146**, 1397 (1999).
73. Zhang, X. & Shoesmith, D. W. Influence of temperature on passive film properties on Ni-Cr-Mo Alloy C-2000. *Corros. Sci.* **76**, 424–431 (2013).
74. Machet, A. *et al.* XPS and STM study of the growth and structure of passive films in high temperature water on a nickel-base alloy. *Electrochim. Acta* **49**, 3957–3964 (2004).
75. Lee, H. G., Lee, Y. M., Shin, H. S., Jung, C. H. & Hong, G. W. Epitaxial deposition of NiO film on a cube-textured Ni substrate by metal-organic chemical vapor deposition. *Met. Mater.* **6**, 565–570 (2000).
76. Systems, O. OLI Studio. (2017).
77. Tsui, L. & Zangari, G. Maximizing the photoelectrochemical performance of TiO₂ nanotubes for solar energy conversion. *Department of Materials Science and Engineering* (University of Virginia, 2015).

3.10 Tables

Table 3.1. Spectral fitting parameters used to fit XPS data and obtain film composition analysis based on previous literature⁴⁰ where only three most prominent peaks were used

Compound	Peak B.E. (eV)	FWHM ^a	%	Compound	Peak B.E. (eV)	FWHM ^a	%
Ni	852.6 ^b	0.95	81.2	Cr	574.2 ^c	0.90	100
	856.3	2.70	6.3	Cr(OH) ₃	577.3	2.60	100
	858.7	2.70	12.5	Cr ₂ O ₃	575.7	0.94	40.0
Ni(OH) ₂	854.9	1.16	8.1		576.7	0.94	38.9
	855.7	2.29	49.3		577.5	0.94	21.1
	861.5	4.65	42.6	Mo	227.9	0.78	60
NiO	853.7	1.02	15.4		231.0	0.78	40
	855.4	3.25	47.8	MoO ₂	229.5	2.70	60
	860.9	3.76	36.8		232.6	2.70	40
				MoO ₃	232.4	1.65	60
					235.5	1.65	40

^a FWHM used were for 20 eV pass energy

^b Asymmetric CasaXPS peak shape = LA(1.1,2.2,10)

^c Asymmetric CasaXPS peak shape = LA(1.3,4,5)

3.11 Figures

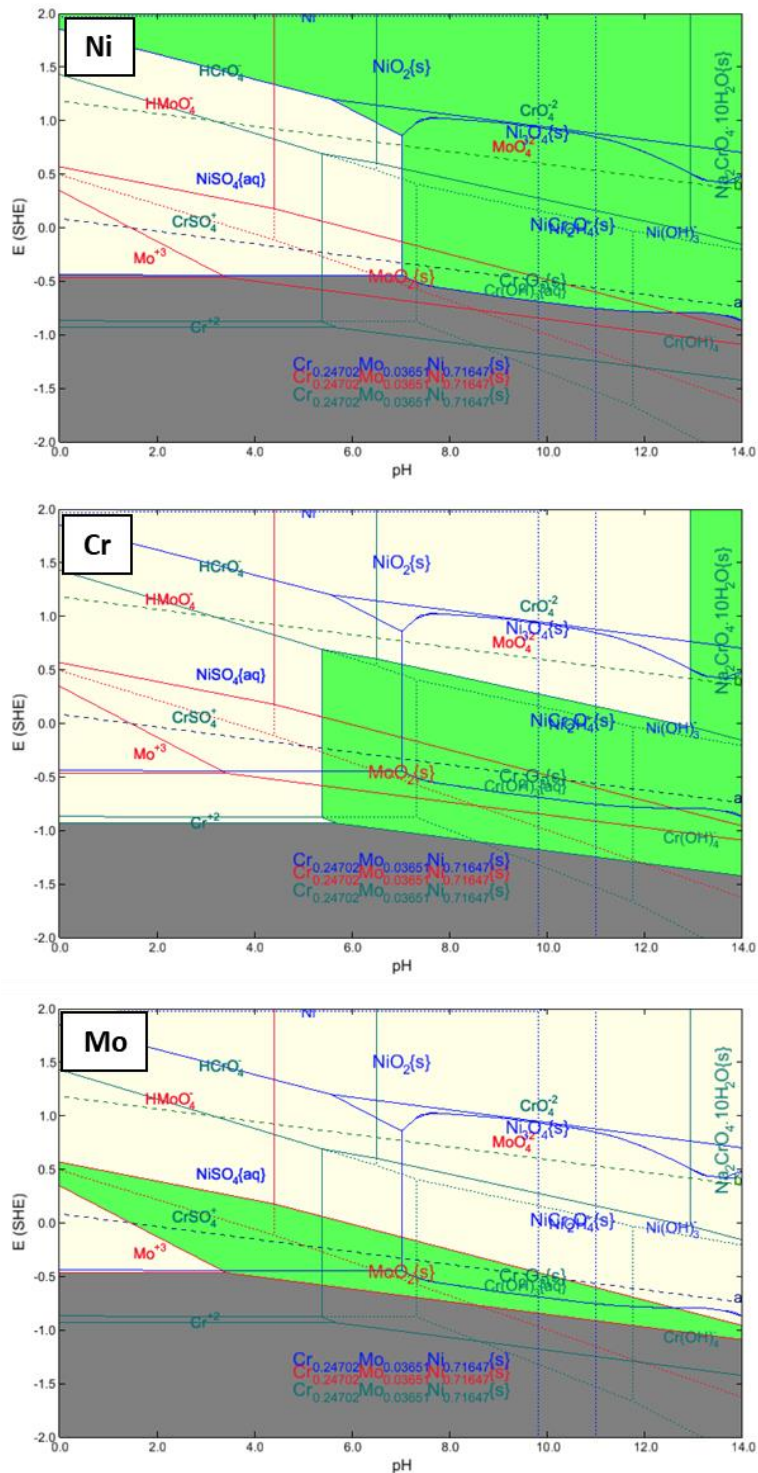


Figure 3.1. E-pH diagrams computed using OLI⁷⁶ for a generic Ni-Cr-Mo alloy exposed to 0.1 M Na_2SO_4 . The gray regions suggest regions of base metal immunity, whereas green and yellow indicate passivity and corrosion, respectively, for specific Ni, Cr, and Mo films.

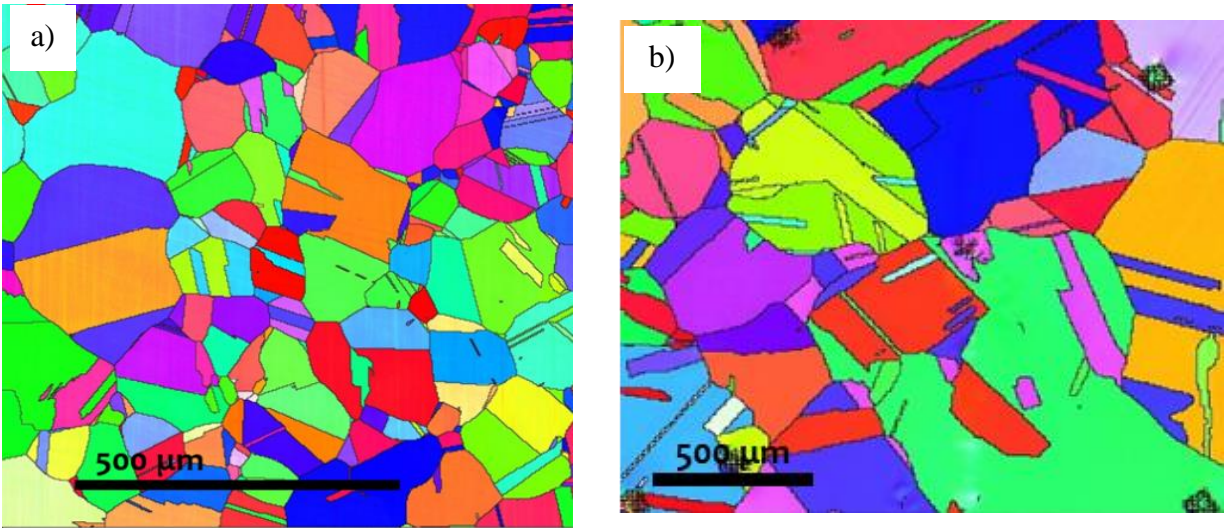


Figure 3.2. EBSD diffraction patterns for the microstructures of the recrystallized a) Ni-22 Cr and b) Ni-22 Cr-6 Mo (wt%) alloys used in this dissertation

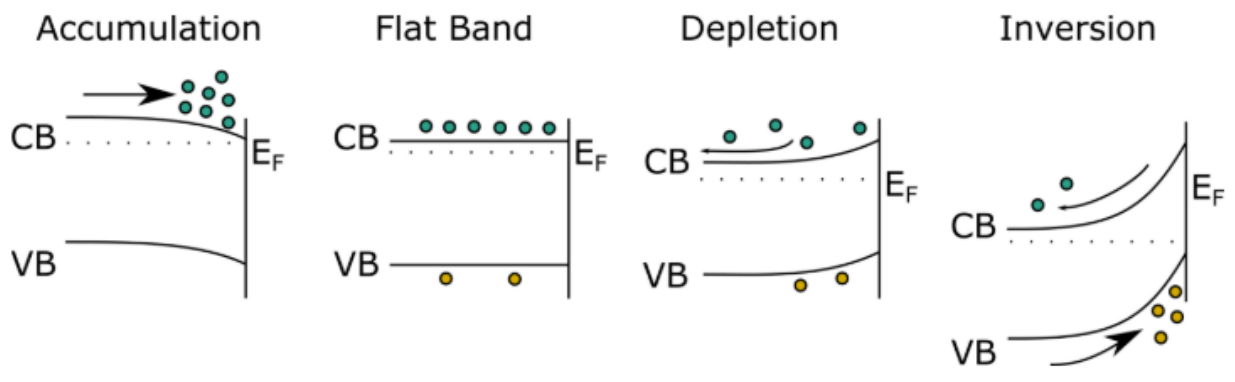


Figure 3.3. Schematic of the transition from cathodic bias (charge accumulation) to n-type (charge depletion) and p-type (inversion) behavior with increasing anodic bias during a Mott-Schottky potential sweep⁷⁷. Holes and electrons are indicated by green and yellow circles, respectively.

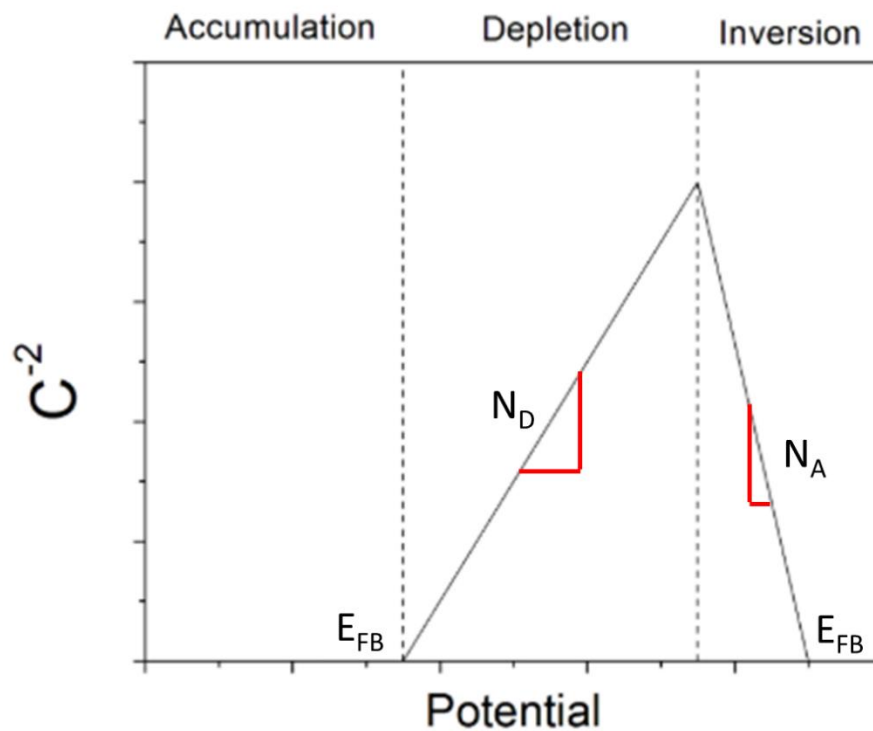


Figure 3.4. Schematic of the expected Mott-Schottky behavior in the accumulation, depletion, and inversion conditions⁷⁷

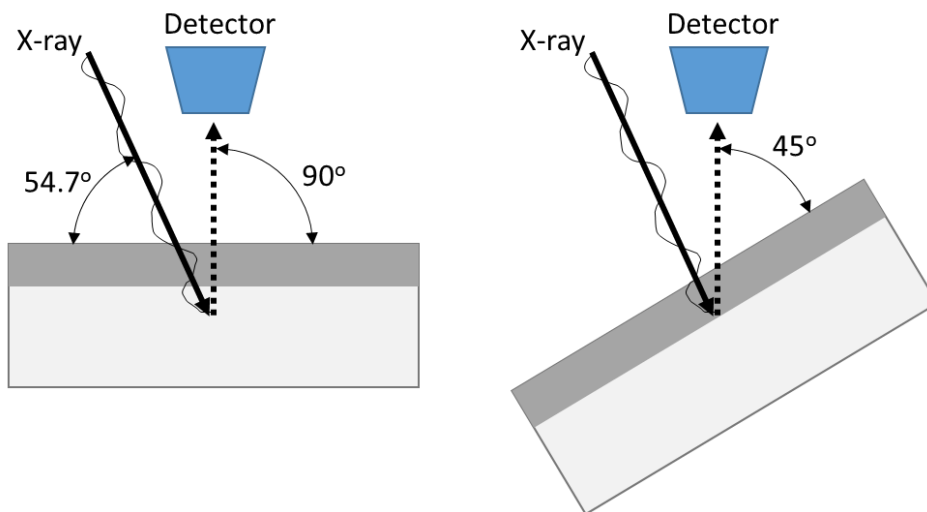


Figure 3.5. Schematic of the angle-resolved XPS set-up and effect of sample tilting on the probe depth.

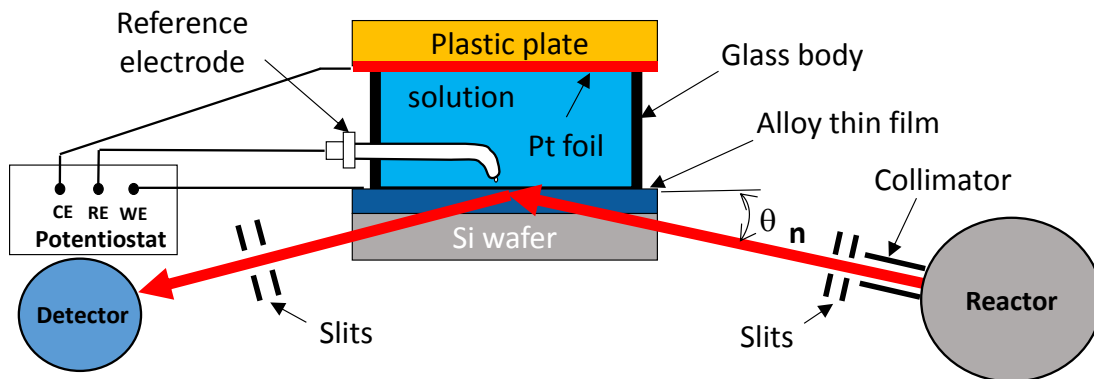


Figure 3.6. Schematic of the *in situ* neutron reflectometry (NR) experiment at the D3 beamline in the NRL reactor

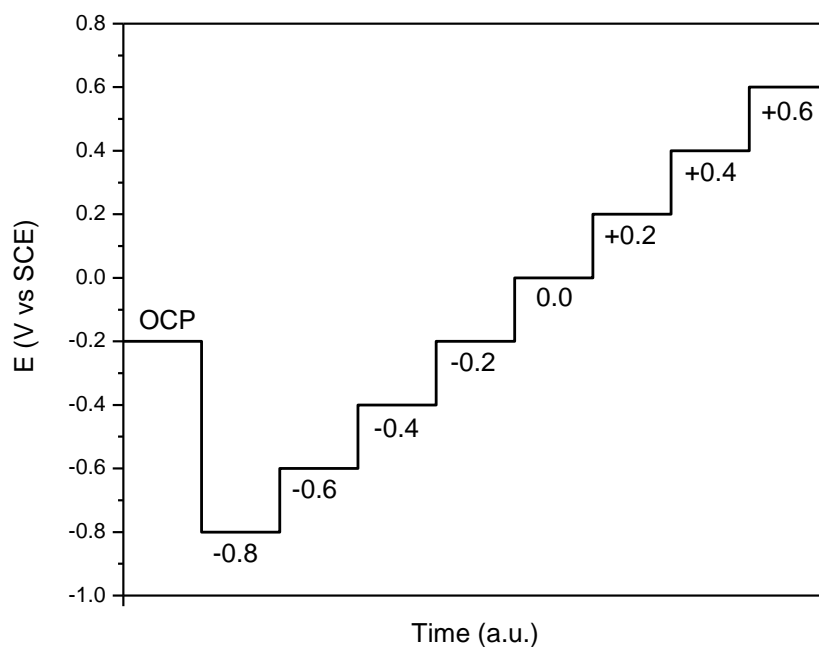


Figure 3.7. Schematic of the potential steps used during *in situ* neutron reflectometry experiments

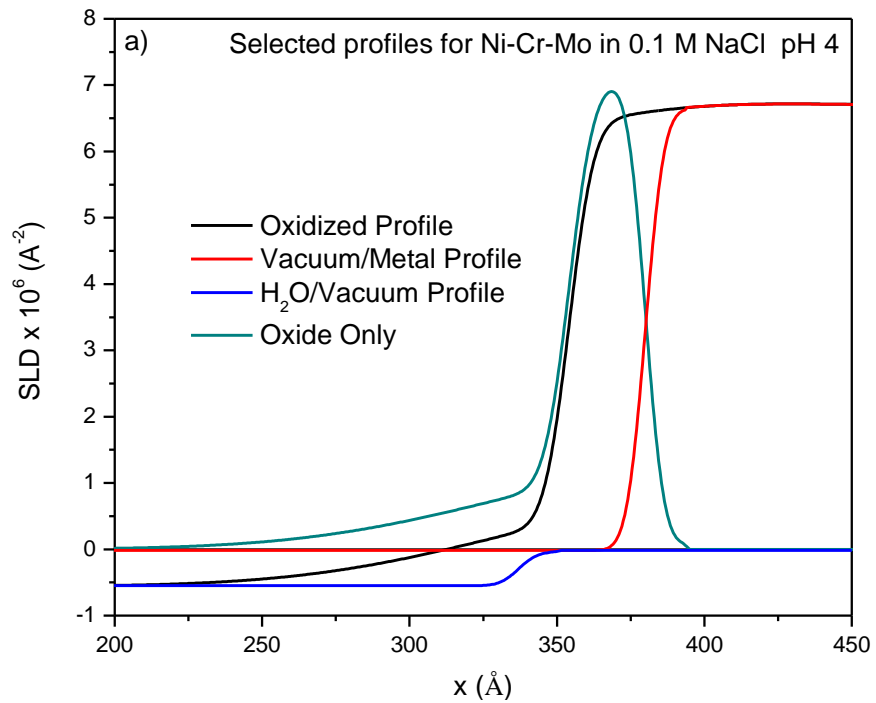


Figure 3.8. Sample profile subtraction for passivated Ni-22 Cr-6 Mo, wt%, where SLD profiles for the unoxidized metal and the H₂O were subtracted from the experimental data in order to isolate the profile for the passive film. The same analysis method applied for all alloys and environments.

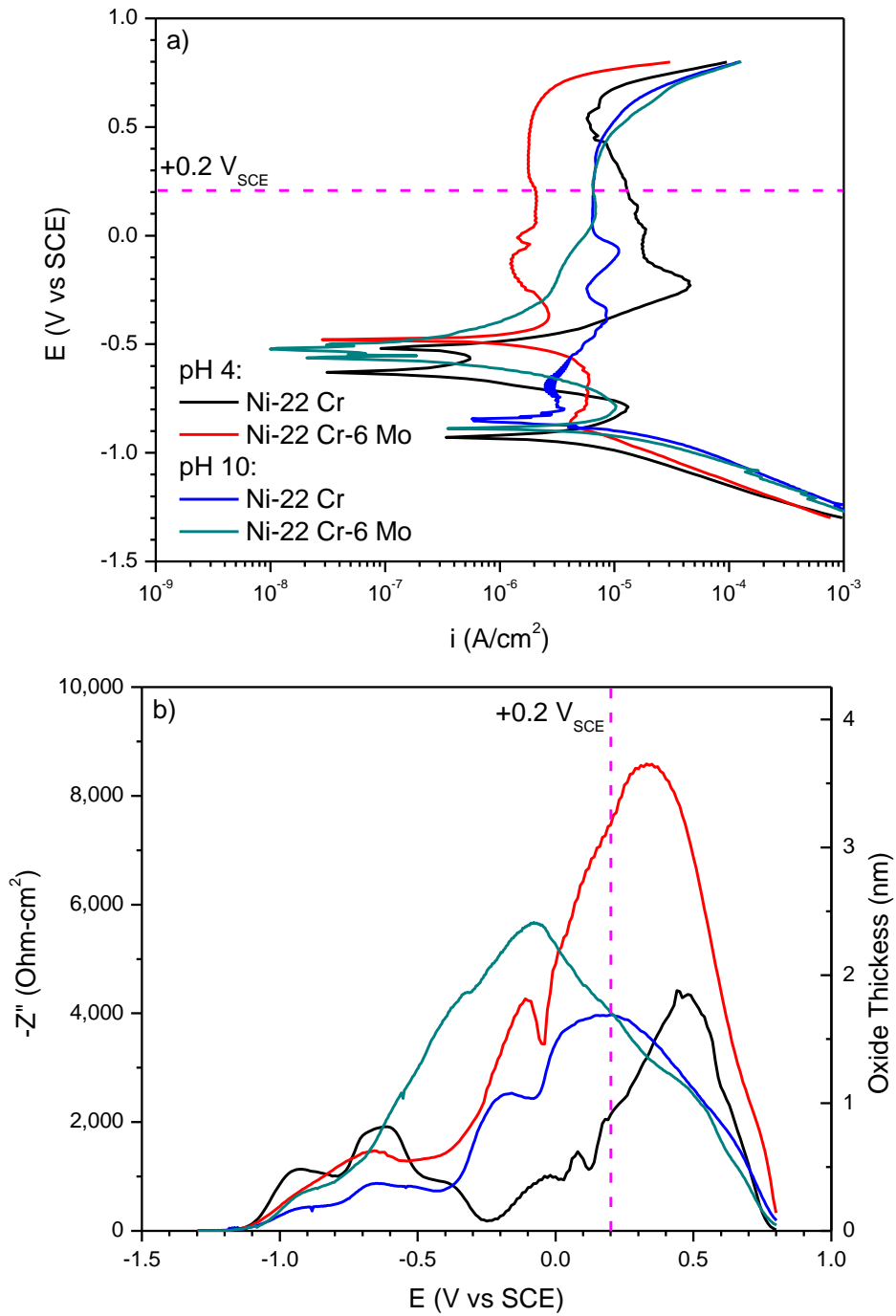


Figure 3.9. a) DC current and b) AC impedance variations during upward potentiodynamic polarization of Ni-22 Cr and Ni-22 Cr-6 Mo, wt%, in deaerated 0.1 M Na₂SO₄ at pH 4 and 10 with the potential used in this study (+0.2 V_{SCE}) indicated

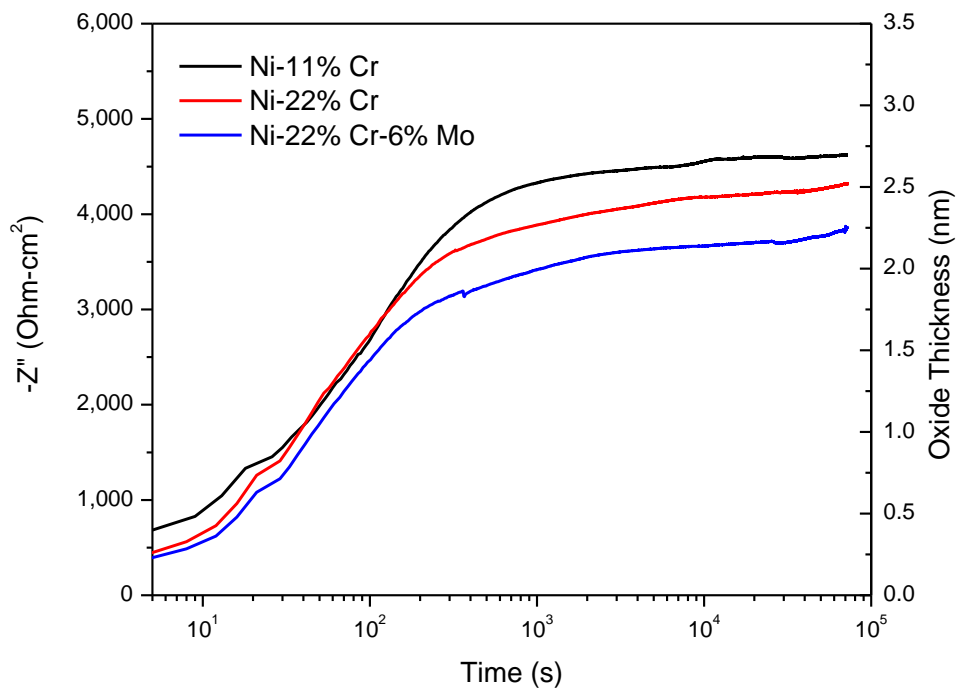


Figure 3.10. Measured increase in $-Z''$ at 1 Hz during passivation of various Ni-alloys at $+0.2 V_{SCE}$ in deaerated $0.1 M Na_2SO_4$ pH 4 for 72 ks with a subsequent full EIS spectrum obtained and fitted in order to compare l_{ox} for each method at the end of passivation time

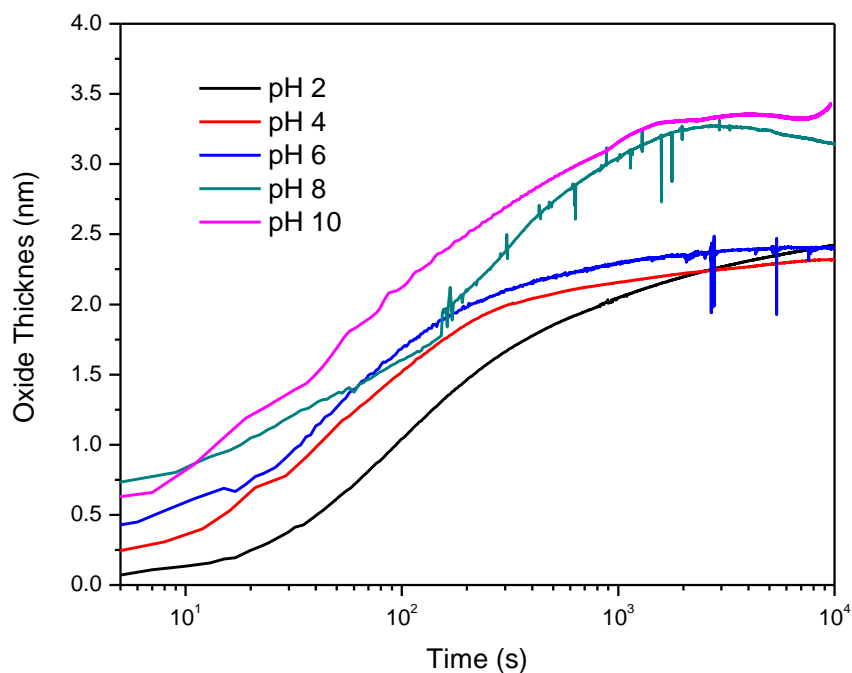


Figure 3.11. Influence of electrolyte pH on the measured film thickness, η , computed using Equation 2.6 for Ni-22 Cr, wt%, in $0.1 M Na_2SO_4$

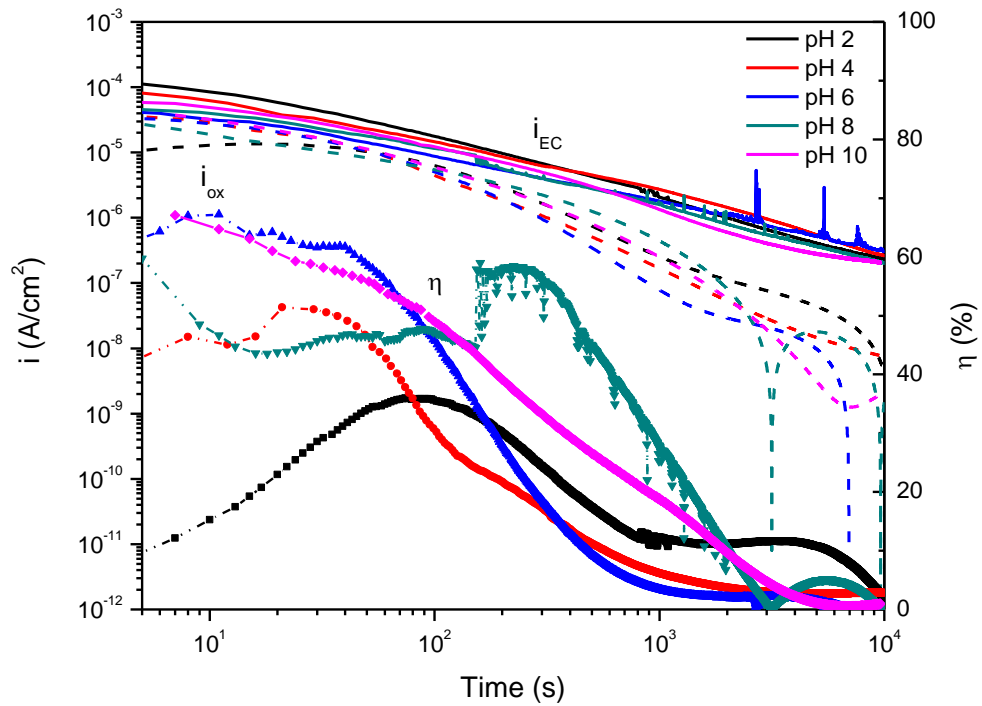


Figure 3.12. Influence of electrolyte pH on the measured i_{tot} and i_{ox} computed using the pSF-EIS results in Figure 3.11 and Equation 2.11, and the current efficiency, η , computed using Equation 2.12 for Ni-22 Cr, wt%, in 0.1 M Na₂SO₄

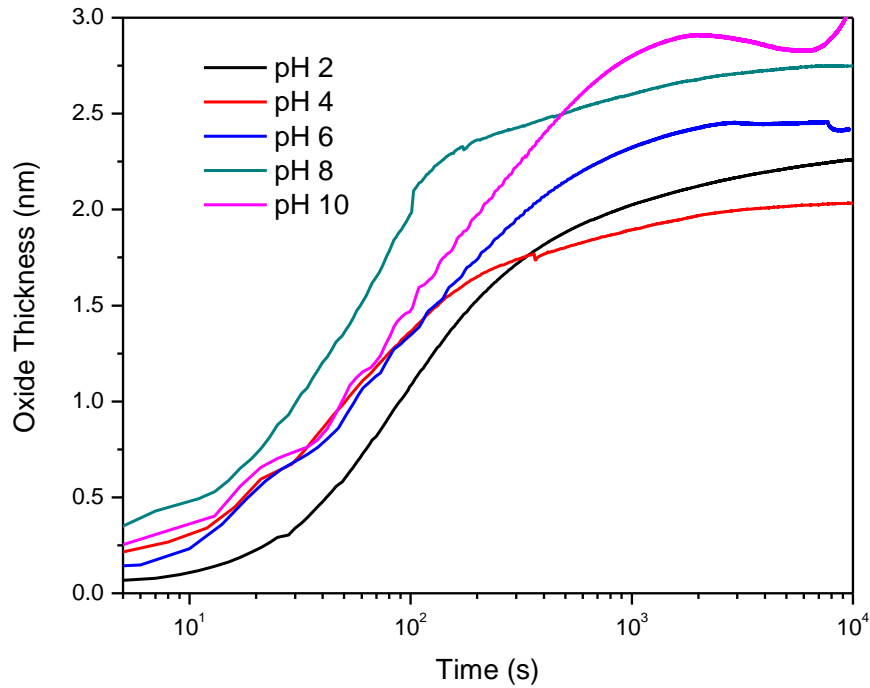


Figure 3.13. Influence of electrolyte pH on the measured film thickness, l_{ox} , computed using Equation 2.6 for Ni-22 Cr-6 Mo, wt%, in 0.1 M Na_2SO_4

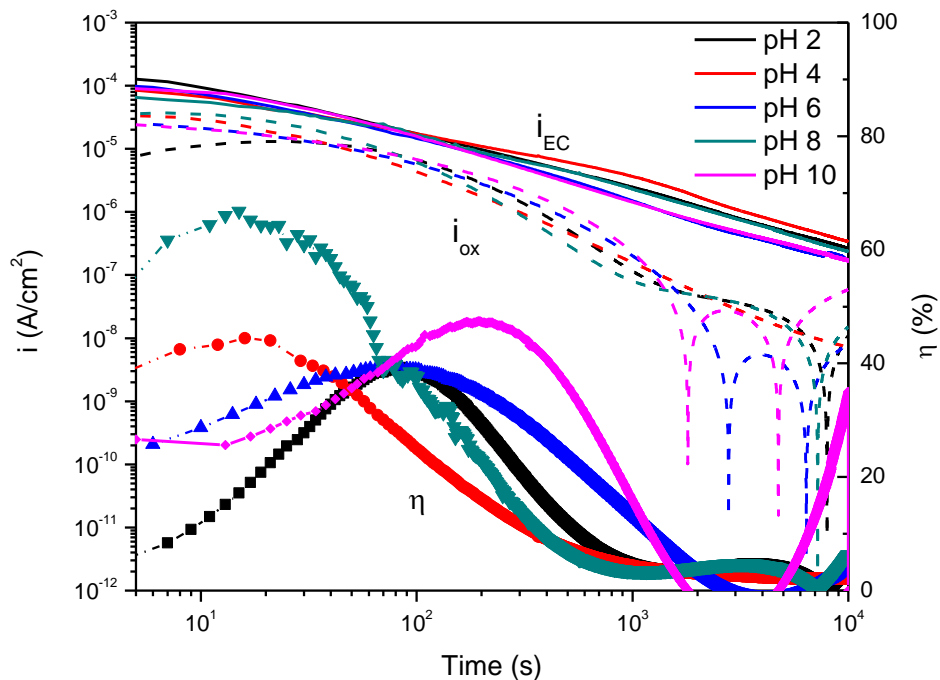


Figure 3.14. Influence of electrolyte pH on the measured i_{tot} and i_{ox} computed using the pSF-EIS results in Figure 3.13 and Equation 2.11, and the current efficiency, η , computed using Equation 2.12 for Ni-22 Cr-6% Mo, wt%, in 0.1 M Na_2SO_4

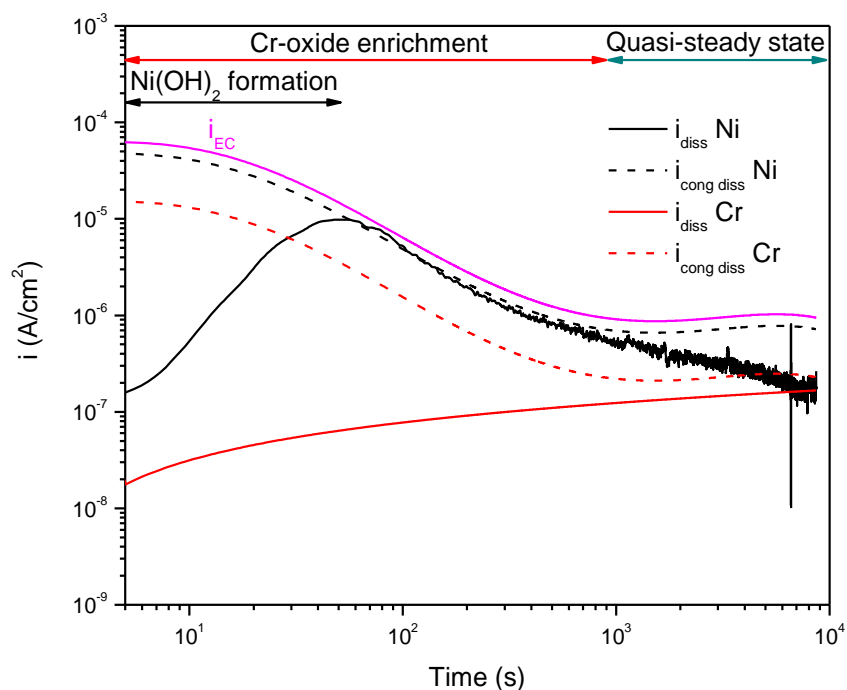


Figure 3.15. Calculated ICP-MS current densities for cation emission versus total element specific current densities for congruent dissolution from Ni-22% Cr, wt%, held at +0.2 V_{SCE} in 0.1 M Na_2SO_4 pH 5.5

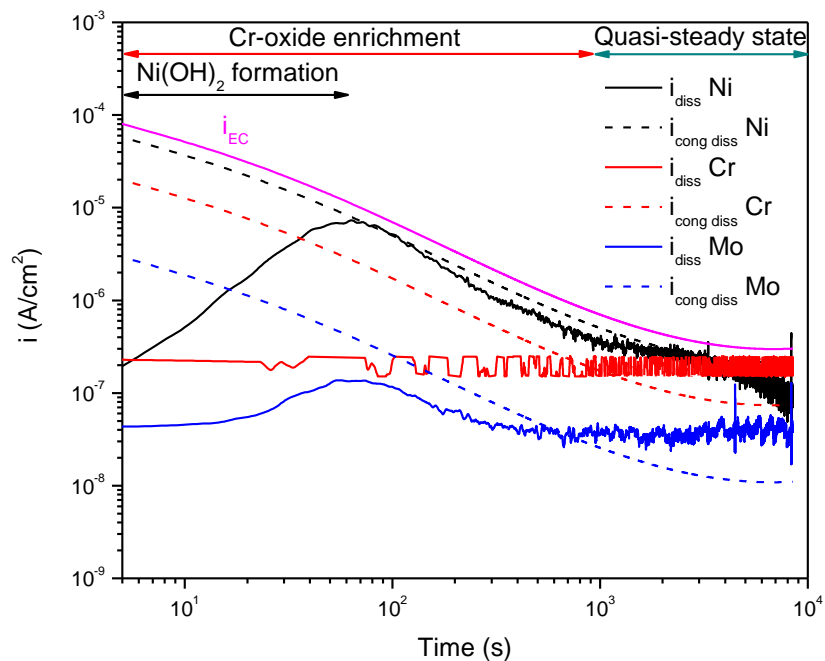


Figure 3.16. Calculated ICP-MS current densities for cation emission versus total element specific current densities for congruent dissolution from Ni-22% Cr-6% Mo, wt%, held at +0.2 V_{SCE} in 0.1 M Na_2SO_4 pH 5.5

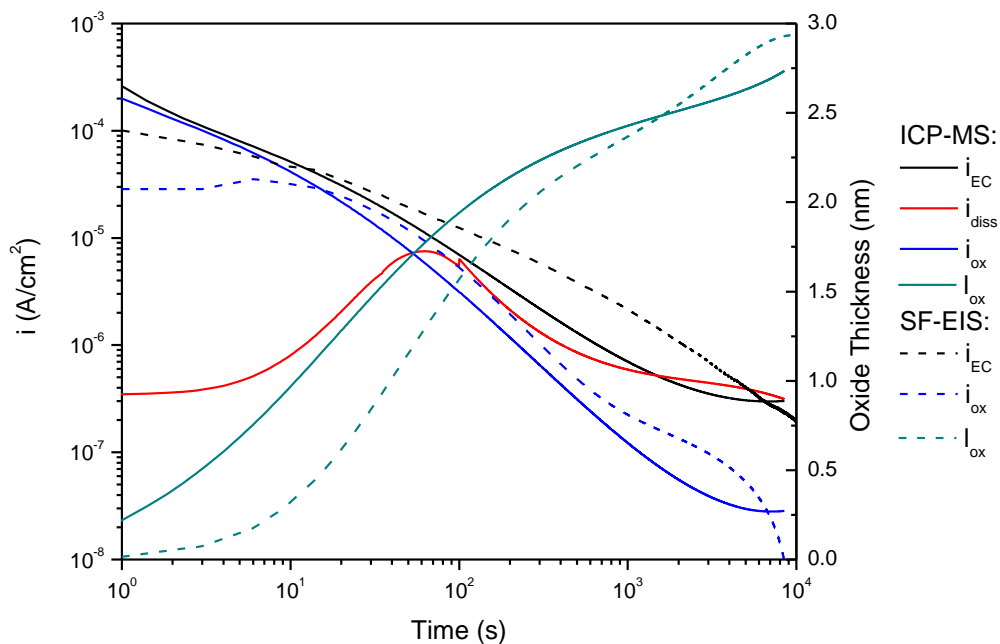


Figure 3.17. Measured ICP-MS and SF-EIS total repassivation i_{EC} , total dissolution current density, i_{diss} , and oxide current density, i_{ox} for passivation at $+0.2 \text{ V}_{SCE}$ for Ni-22% Cr-6% Mo, wt%, in 0.1 M Na_2SO_4 pH 5.5

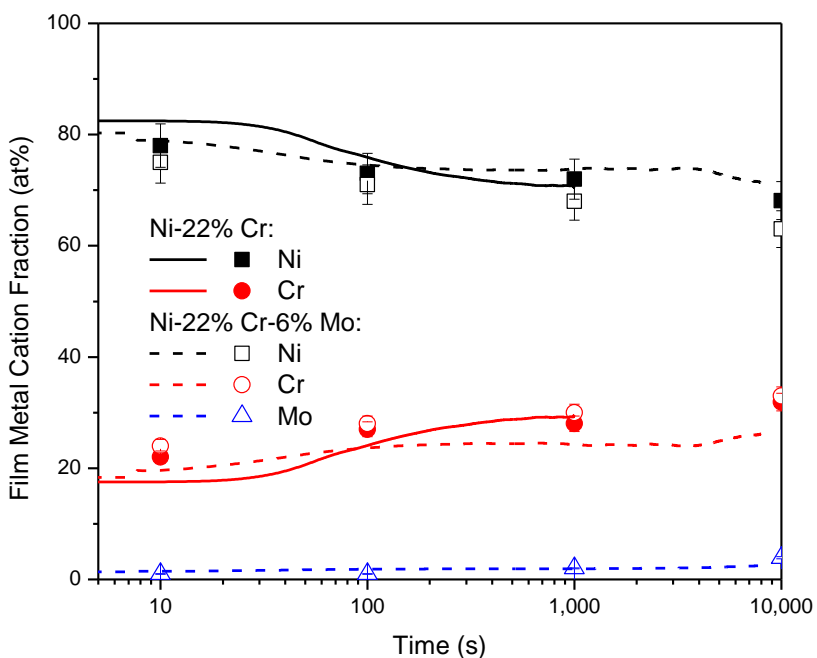


Figure 3.18. Relative accumulation of metal cations in the passive films during growth until localized corrosion initiation at $+0.2 \text{ V}_{SCE}$ according to ICP-MS (lines) and XPS (symbols) measurements on Ni-22 Cr and Ni-22 Cr-6 Mo, wt%, in 0.1 M Na_2SO_4 (pH 5.5) (ICP-MS) and 0.1 M Na_2SO_4 pH 4 (XPS)

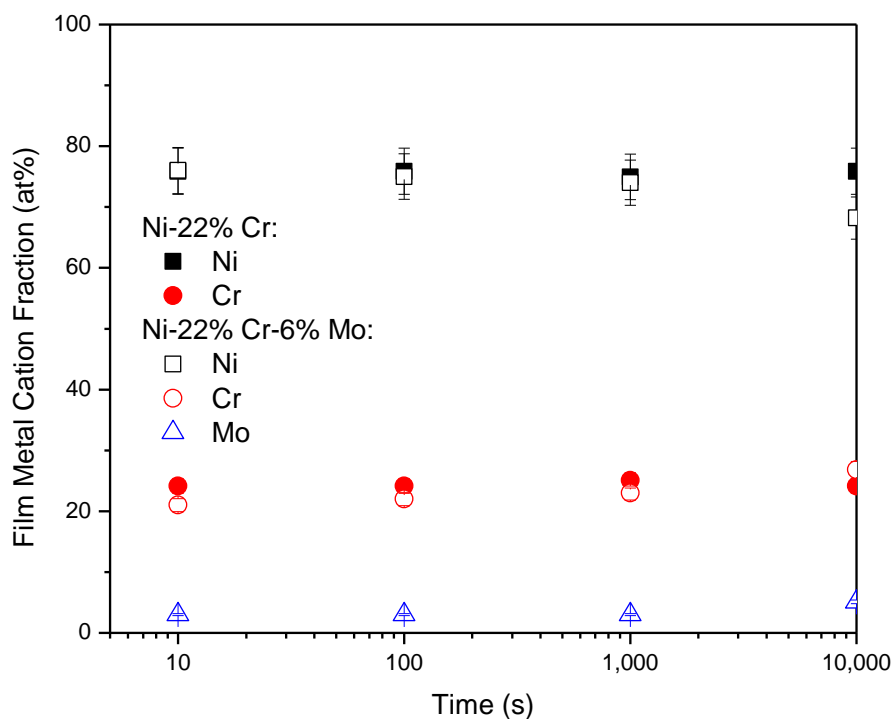


Figure 3.19. Relative accumulation of metal cations in the passive films during growth until localized corrosion initiation at +0.2 V_{SCE} according to XPS measurements on Ni-22 Cr and Ni-22 Cr-6 Mo, wt%, in 0.1 M Na₂SO₄ pH 10

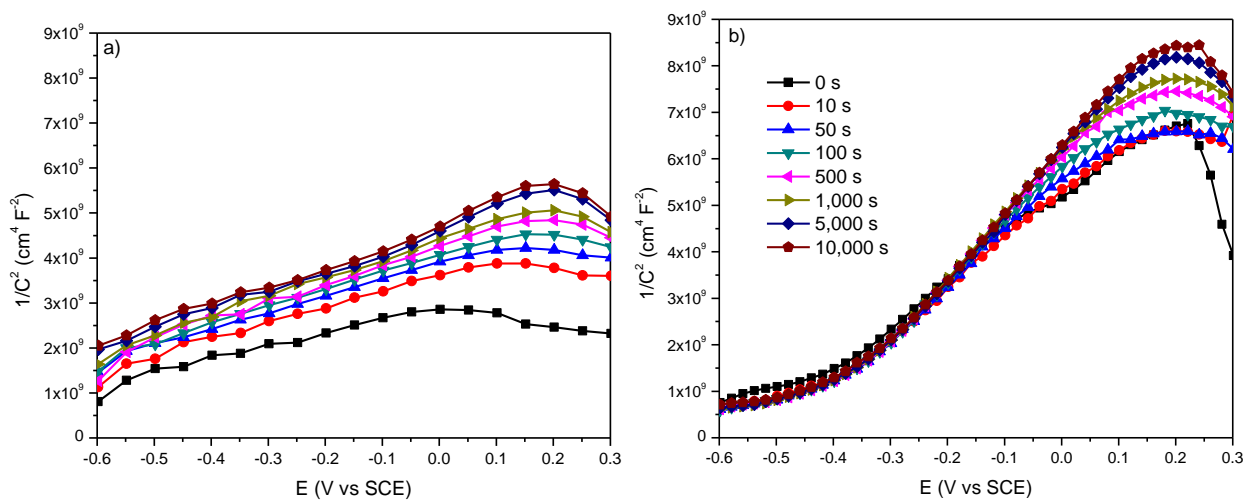


Figure 3.20. Evolution of Mott-Schottky spectra with passivation time for a) Ni-22 Cr and b) Ni-22 Cr-6 Mo, wt%, passivated at +0.2 V_{SCE} for times up to 10,000 s in 0.1 M Na₂SO₄ pH 4 where the potential sweeps were performed at 1,000 Hz

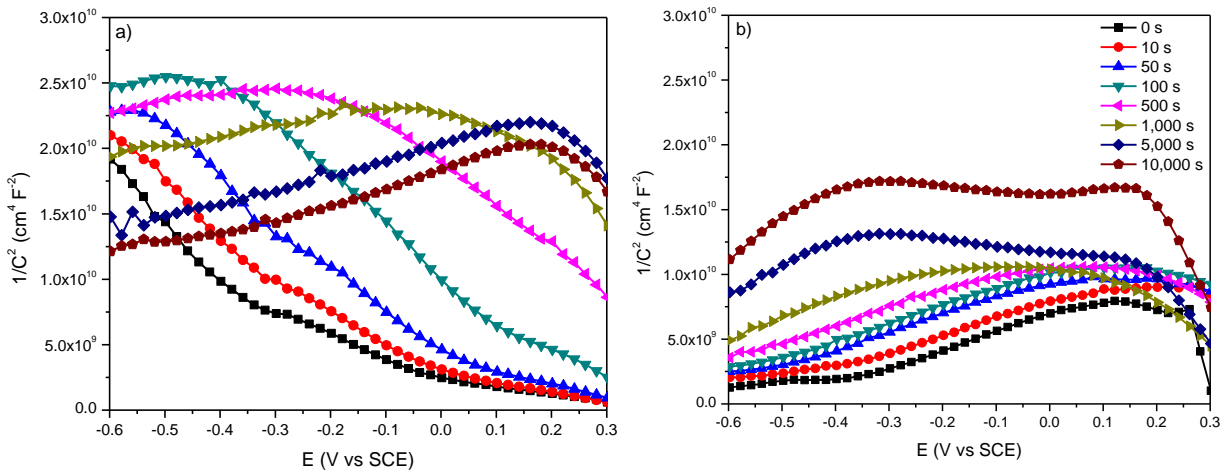


Figure 3.21. Evolution of Mott-Schottky spectra with passivation time for a) Ni-22 Cr and b) Ni-22 Cr-6 Mo, wt%, passivated at +0.2 V_{SCE} for times up to 10,000 s in 0.1 M Na₂SO₄ pH 10 where the potential sweeps were performed at 1,000 Hz

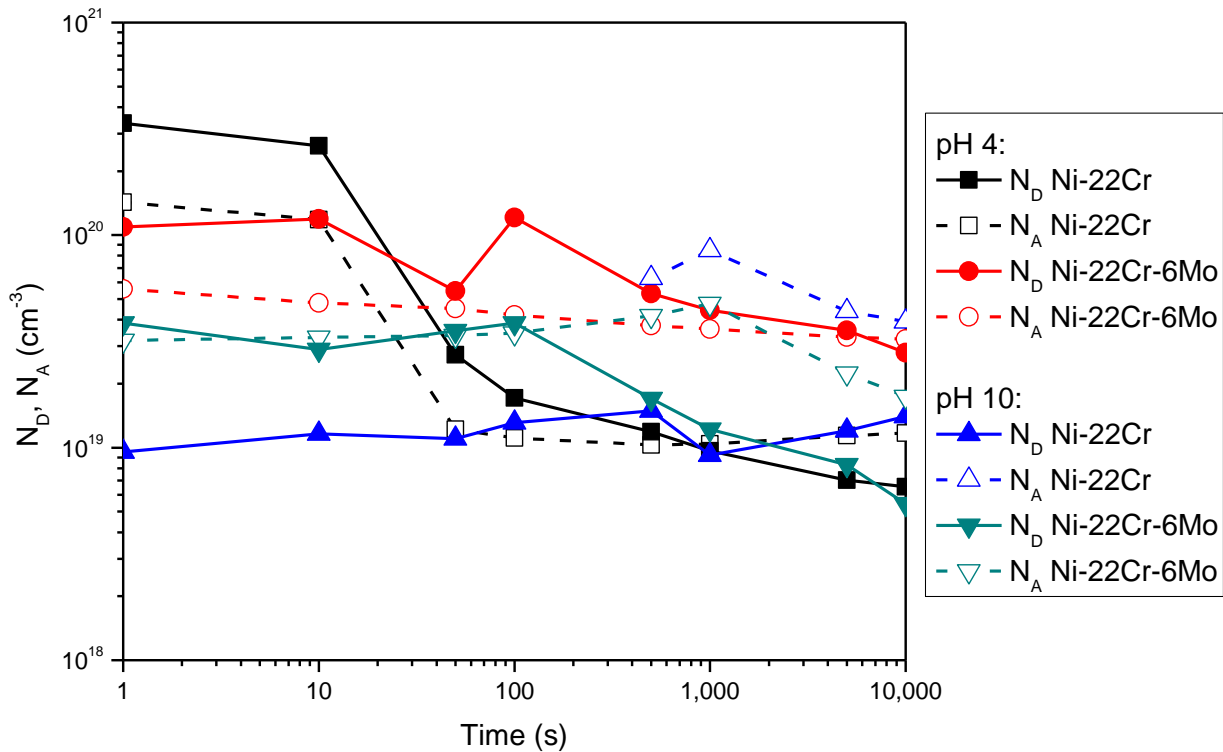


Figure 3.22. Concentration of semiconductor n-type (N_D) and p-type (N_A) point defects during passivation, computed using Equation 3.3 and the data shown in Figure 3.20 and Figure 3.21 for Ni-22 Cr and Ni-22 Cr-6 Mo, wt%, passivated at +0.2 V_{SCE} for times up to 10,000 s in 0.1 M Na₂SO₄ pH 4 and pH 10

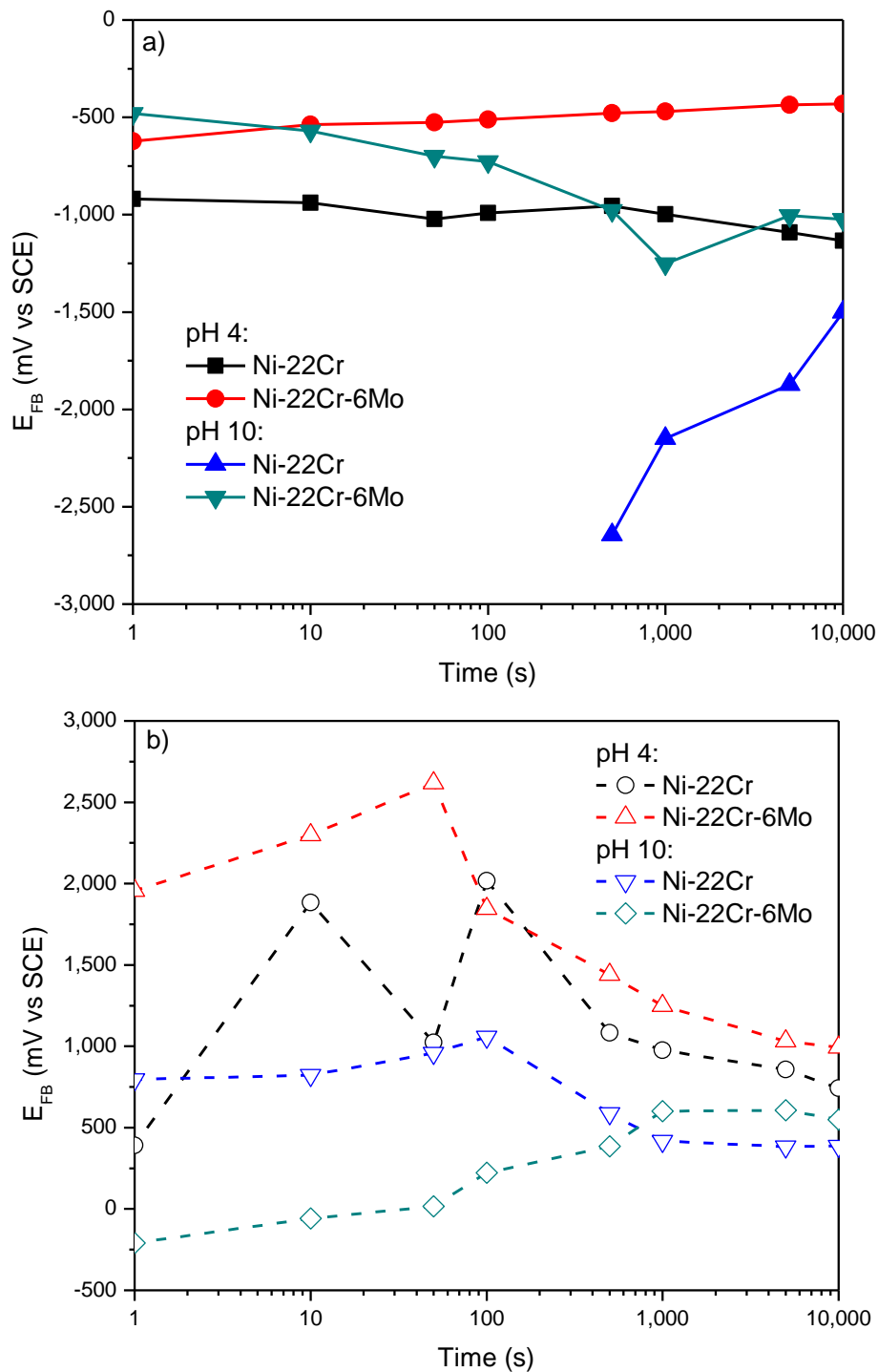


Figure 3.23. Measured semiconductor flat band potentials for a) n-type and b) p-type behavior, computed using Equation 3.3 as indicated in Figure 3.4 for Ni-22 Cr and Ni-22 Cr-6 Mo, wt%, passivated at +0.2 V_{SCE} for times up to 10,000 s in 0.1 M Na₂SO₄ pH 4 and pH 10 (Figure 3.20 and Figure 3.21)

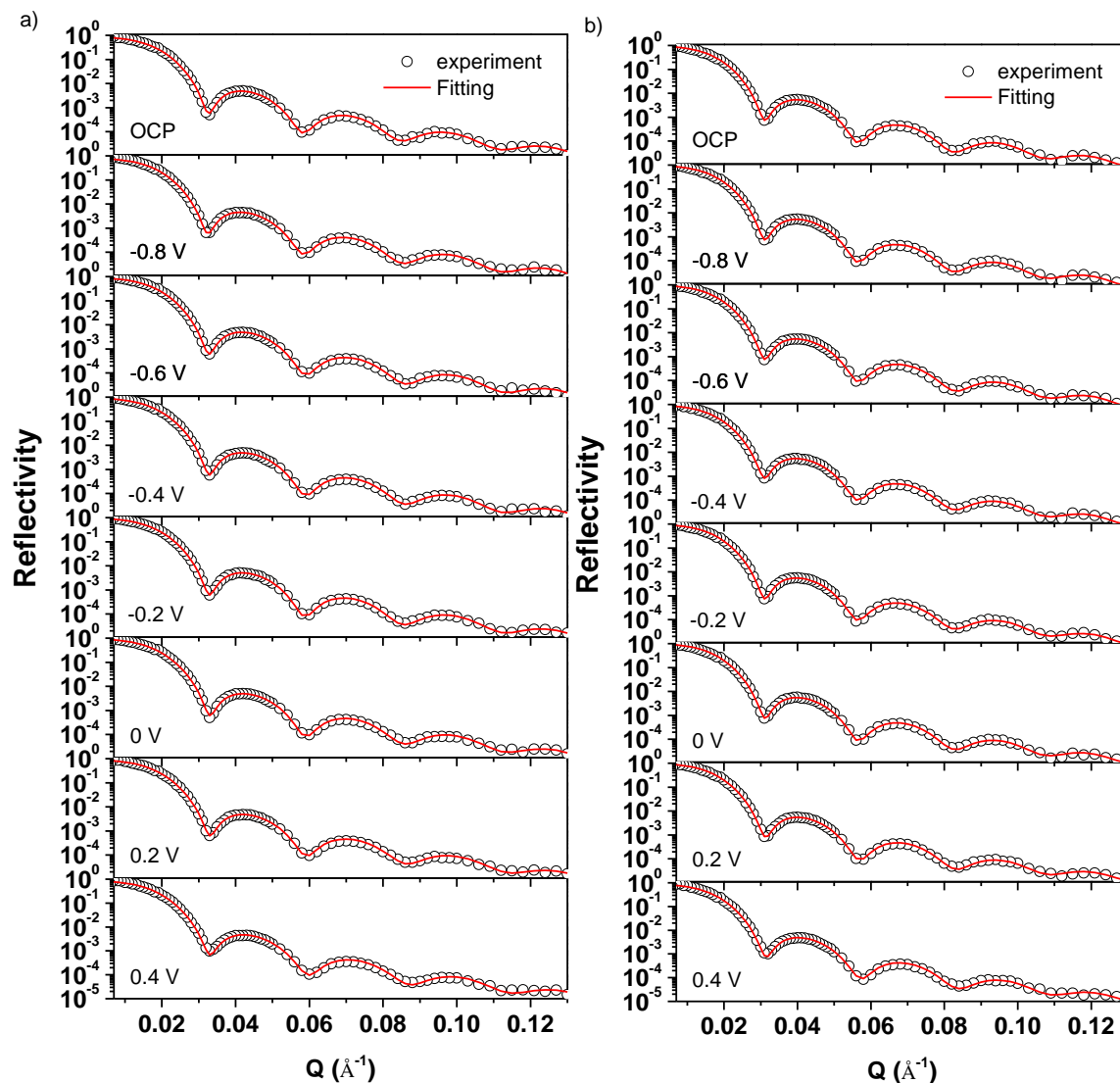


Figure 3.24. Measured reflectivity curves for a) Ni-20 Cr and b) Ni-20 Cr-10 Mo, wt%, oxidized in 0.1 M Na_2SO_4 pH 4 at various potential steps (Figure 3.7) from OCP, to $-0.8 \text{ V}_{\text{SCE}}$, and up to $+0.2 \text{ V}_{\text{SCE}}$ in 200 mV steps every 6 hours where the NR measurements started 1 hr after the applied potential was switched to the set value and each measurement took approximately 90 min to complete

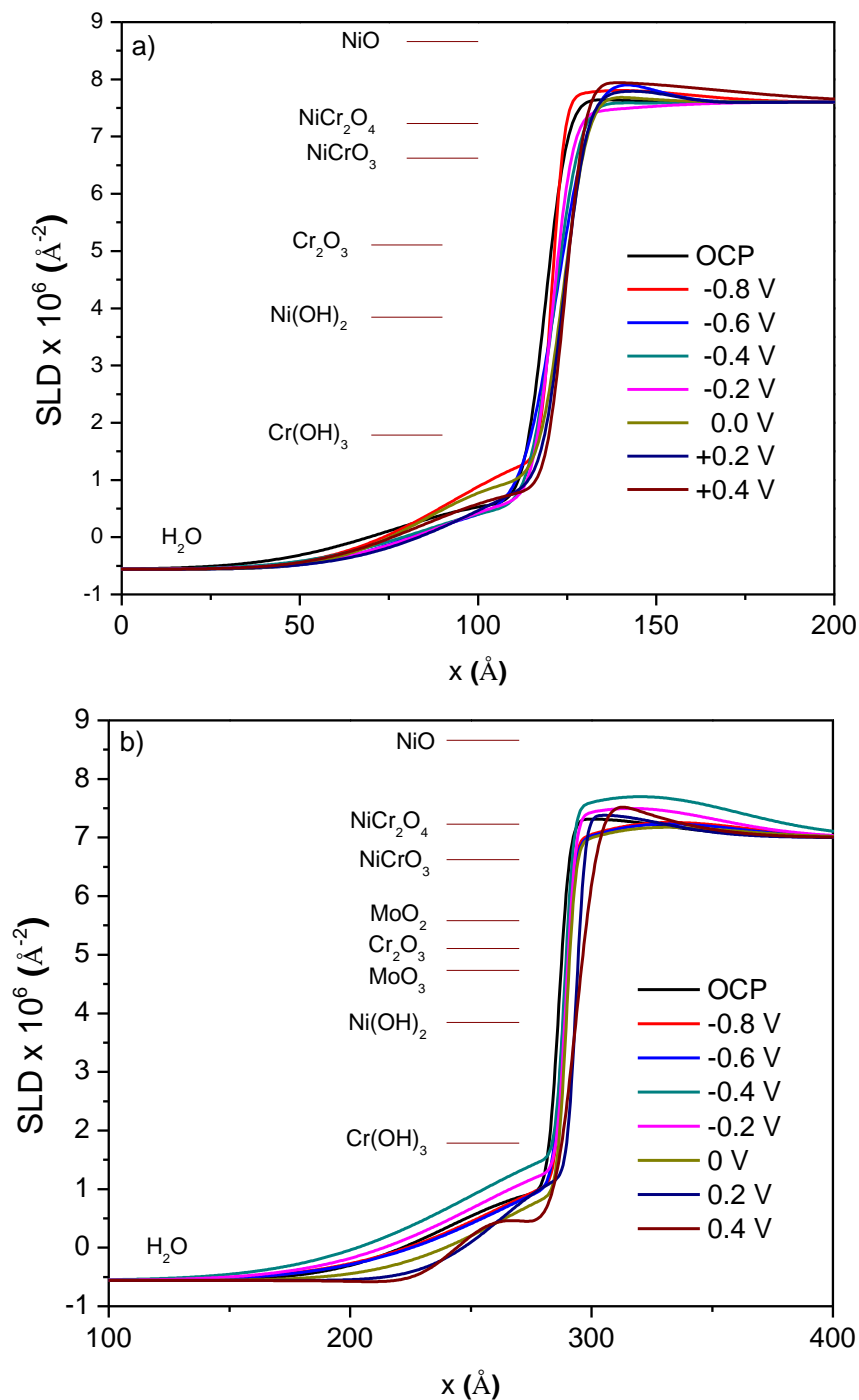


Figure 3.25. Full SLD profiles for a) Ni-20 Cr and b) Ni-20 Cr-10 Mo, wt%, oxidized in 0.1 M Na₂SO₄ pH 4 at various potential steps from OCP, to -0.8 V_{SCE}, and up to +0.2 V_{SCE} in 200 mV steps every 6 hours where the NR measurements started 1 hr after the applied potential was switched to the set value and each measurement took approximately 90 min to complete. SLD values for the expected species are given for different film compounds and the spectra, at low depths, corresponds to the electrolyte layer and at high depths, the alloy layer.

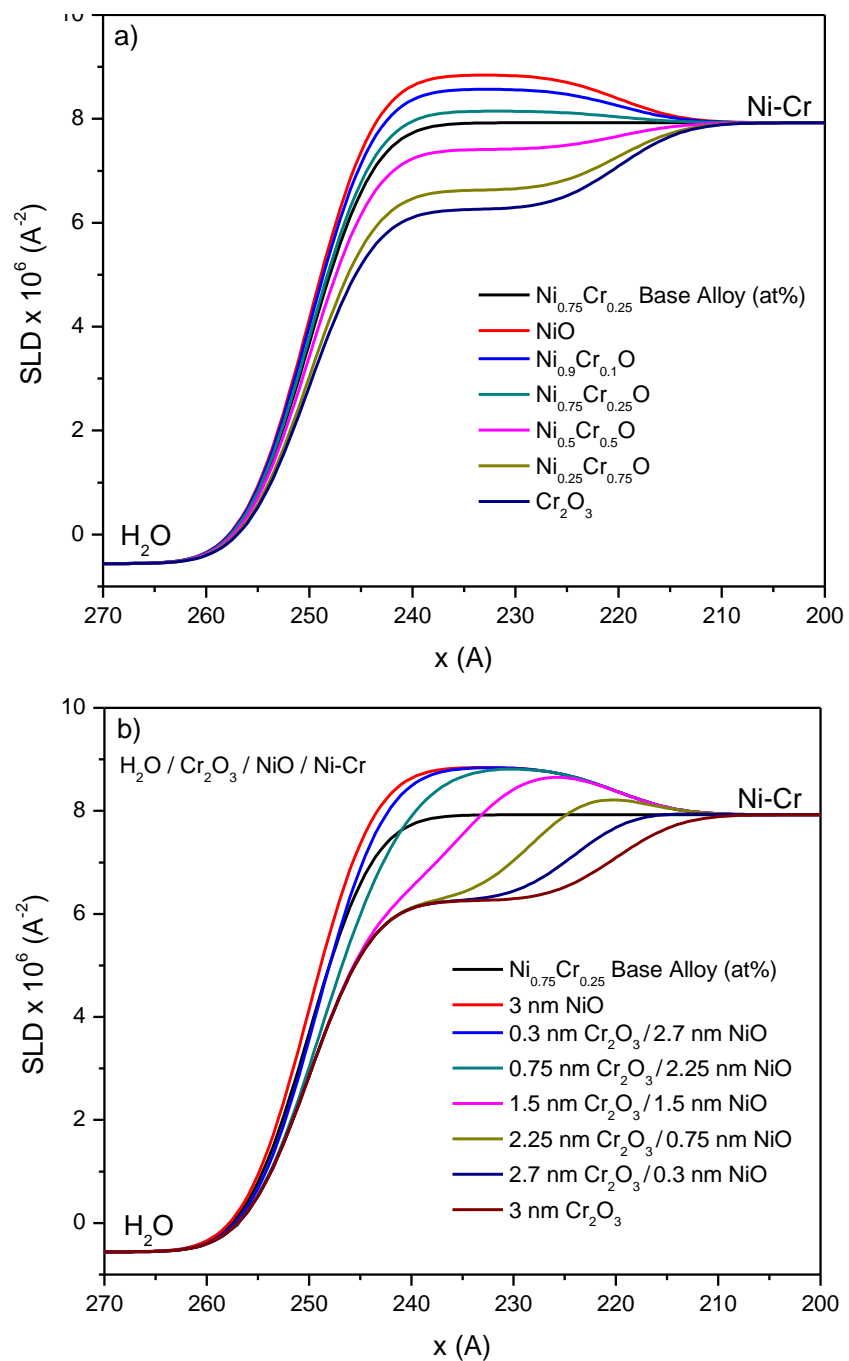


Figure 3.26. Simulated SLD profiles for a) a non-stoichiometric oxide, $\text{Ni}_{1-x}\text{Cr}_x\text{O}$, containing varying % Cr^{3+} and b) a bilayer oxide comprised of Cr_2O_3 and NiO with varying thicknesses of each conformal layer. An interfacial roughness of 5 \AA was used to replicate the experimental parameter.

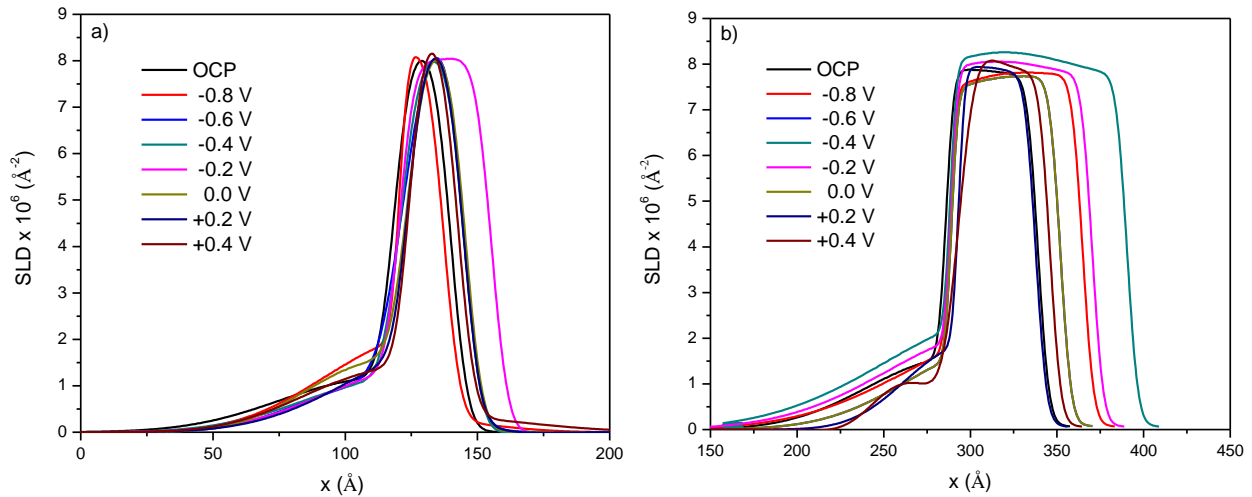


Figure 3.27. Analysis of the NR profiles given in Figure 3.25 where a sample profile for the base metal exposed to water on a SiO₂ substrate was simulated and subtracted from the overall reflectometry curve in order to obtain that of just the passive film for a) Ni-20 Cr and b) Ni-20 Cr-10 Mo, wt%, in 0.1 M Na₂SO₄ pH 4 where the peak SLD correlates to the Cr³⁺ cation fraction and the approximate l_{ox} is indicated by the peak width

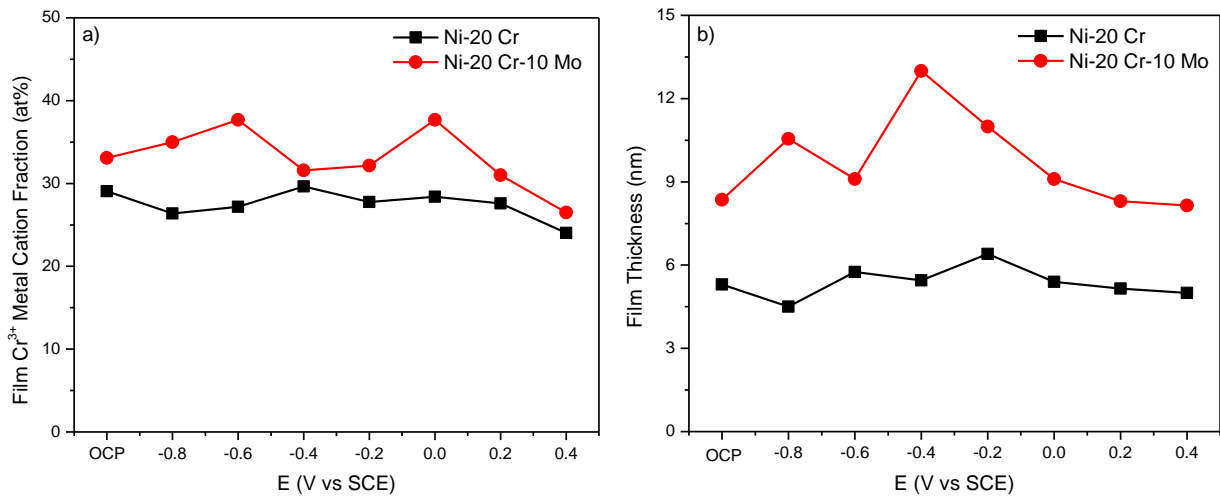


Figure 3.28. a) Metal cation fraction and b) passive film thickness computed from the peak SLD in Figure 3.27 for Ni-20 Cr and Ni-20 Cr-10 Mo, wt%, in 0.1 M Na₂SO₄ pH 4 oxidized at varying potentials

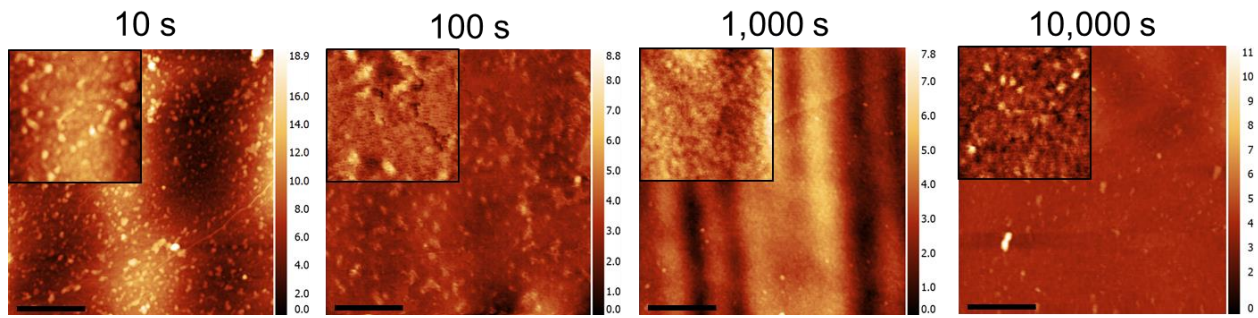


Figure 3.29. Topography images taken with AFM after 10, 100, 1,000, and 10,000 s of passivation of Ni-22 Cr, wt%, in 0.1 M Na_2SO_4 pH 4 with 500 nm^2 image insets. The insets are representative of the area used to measure oxide height (Figure 3.30) and RMS surface roughness. All scale bars are 500 nm and the color bars in units of nm.

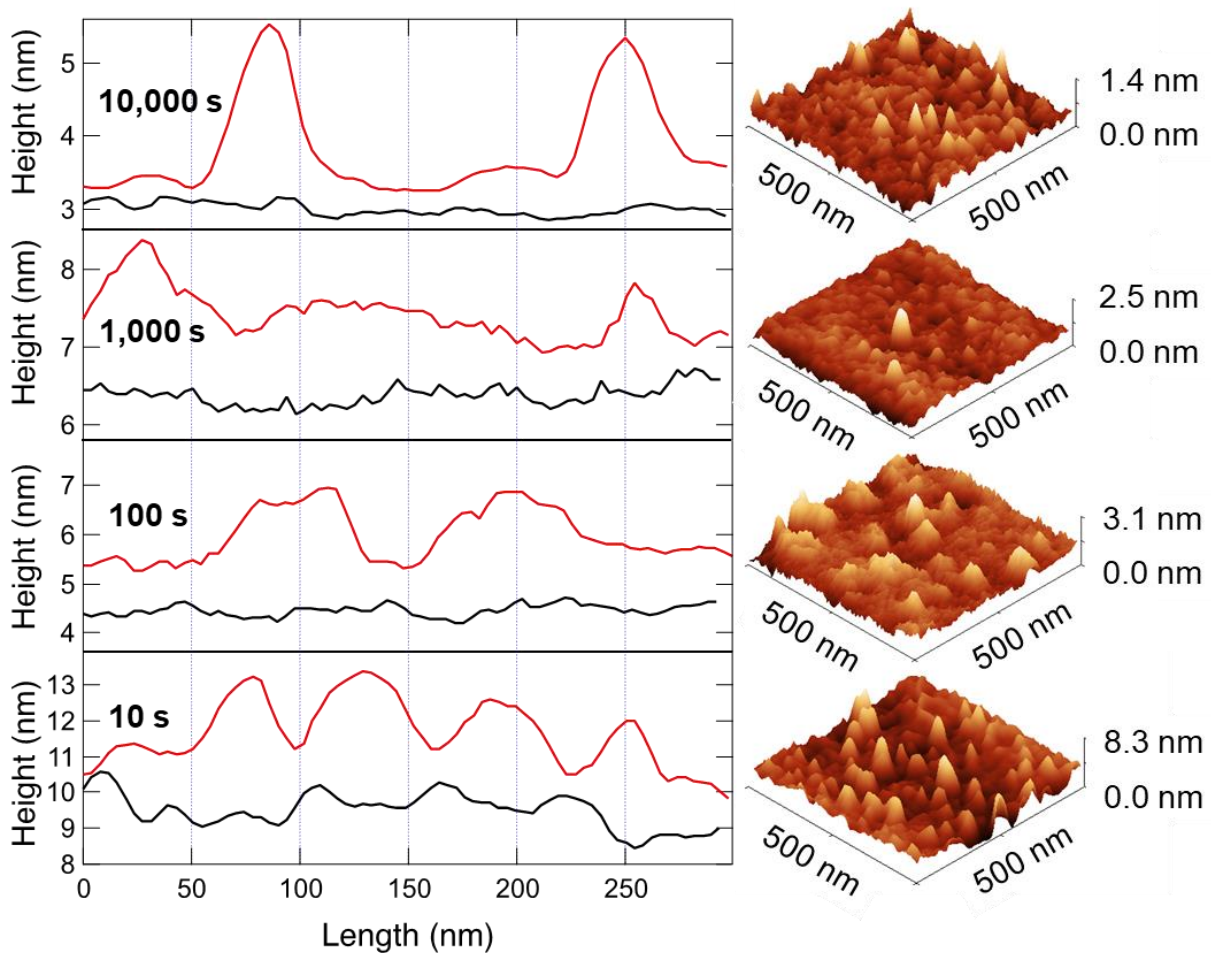


Figure 3.30. Line scans of the surface topography after exposure to 0.1 M Na_2SO_4 pH 4 where the red lines represent the bright protrusion of the electrochemically grown oxide, while the black lines represent the roughness of a fresh surface that has only been air-oxidized for the same amount of time.

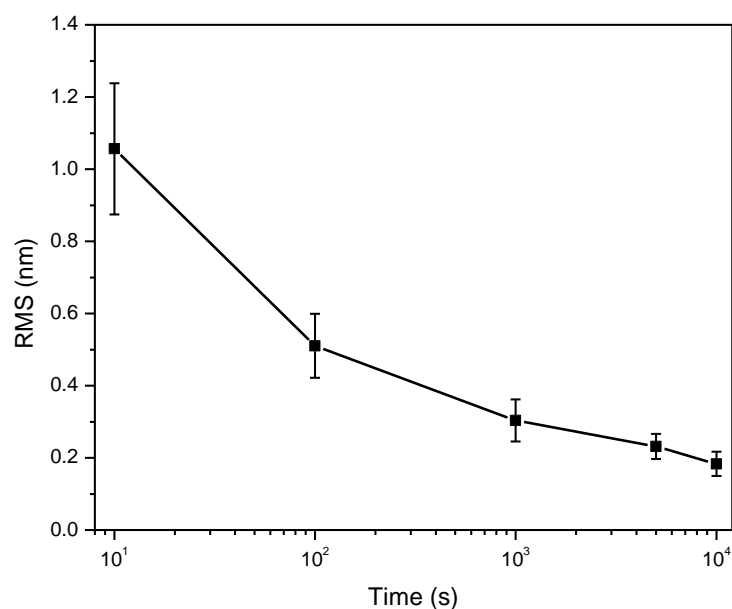


Figure 3.31. Average root mean square (RMS) surface roughness computed for Ni-22 Cr, wt%, passivated at +0.2 V_{SCE} for various times in deaerated 0.1 M Na₂SO₄ pH 4. The RMS was calculated at various areas across the electrochemically oxidized surface to obtain the average RMS value and error bars.

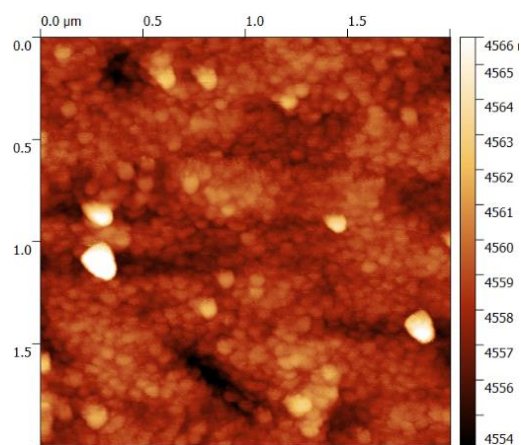


Figure 3.32. Topography image taken with AFM after 10,000 s of passivation of Ni-22 Cr-6 Mo, wt%, in 0.1 M Na₂SO₄ pH 4 (RMS = 2.64 nm). The color bars in units of nm.

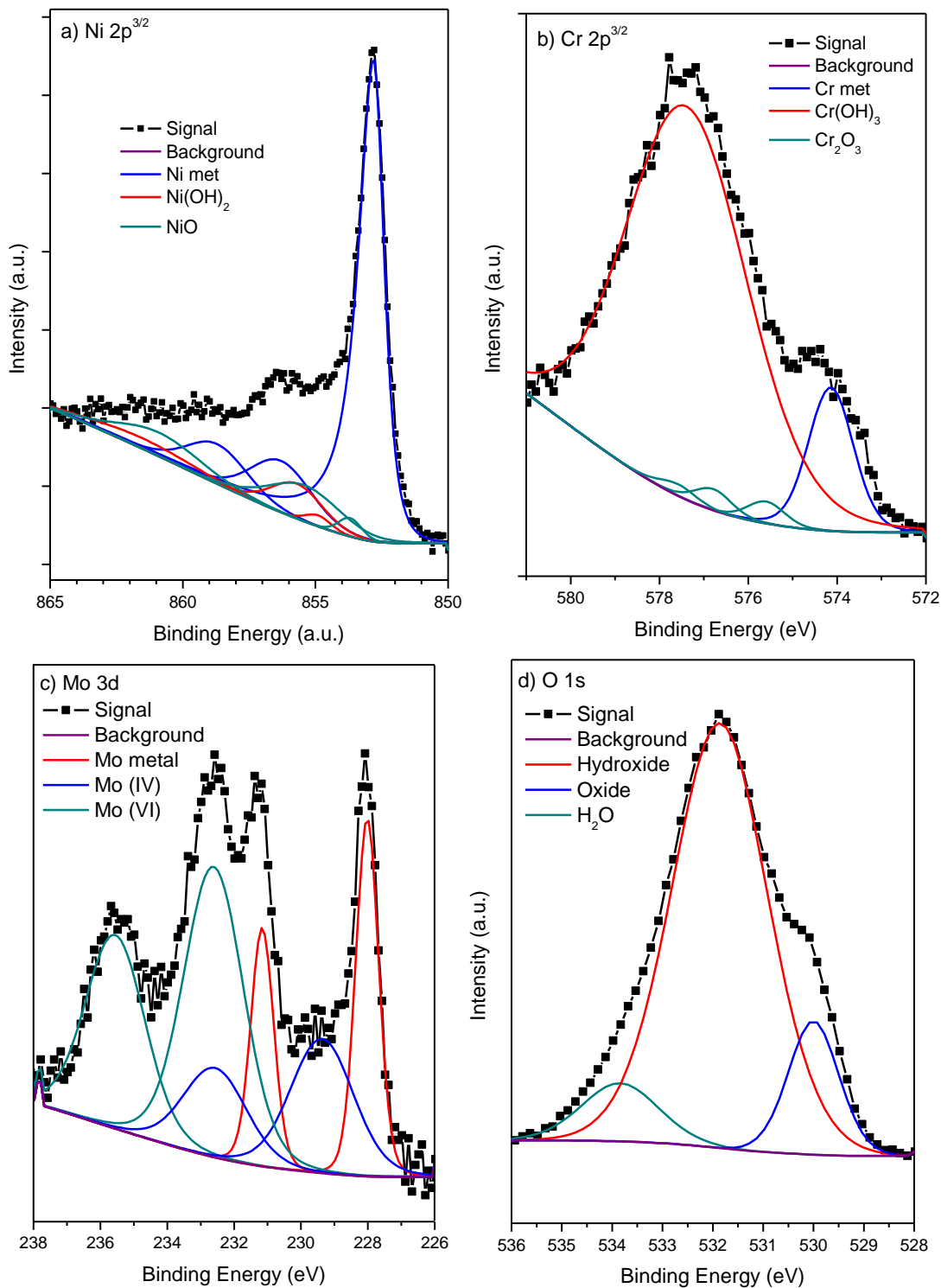


Figure 3.33. Focused, deconvoluted XPS spectra for a) Ni 2p^{3/2}, b) Cr 3p^{3/2}, c) Mo 3d, and d) O 1s bands collected on Ni-22 Cr-6 Mo, wt%, passivated at +0.2 V_{SCE} for 10,000 s in 0.1 M Na₂SO₄ pH 4 where the solid black and magenta lines indicate the Shirley background and overall fit to the spectra, respectively

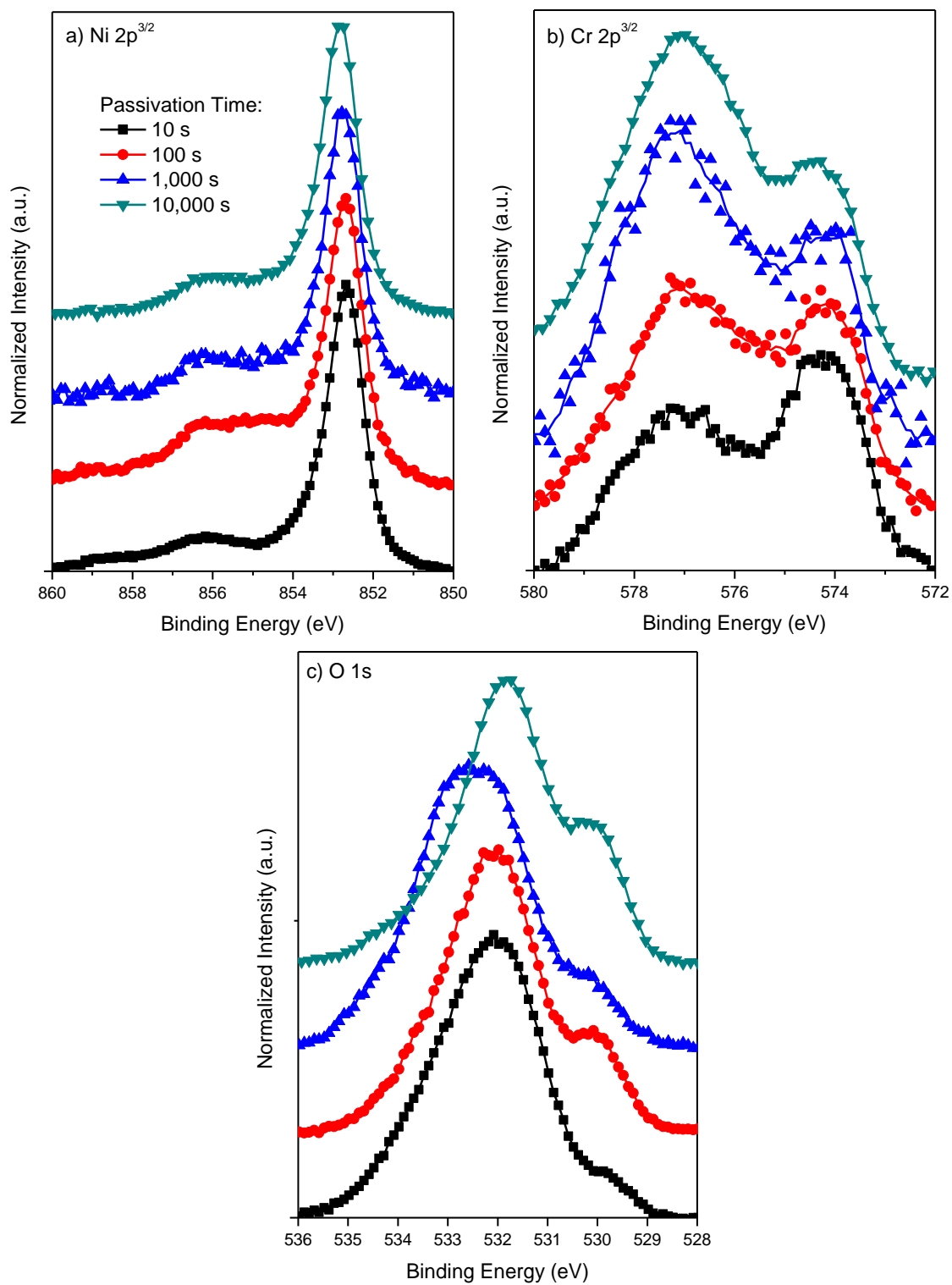


Figure 3.34. a) Ni 2p^{3/2}, b) Cr 2p^{3/2}, and c) O 1s peaks normalized to the metal peaks for Ni-22 Cr, wt%, passivated at +0.2 V_{SCE} for various times up to 10 ks in 0.1 M Na₂SO₄ pH 4

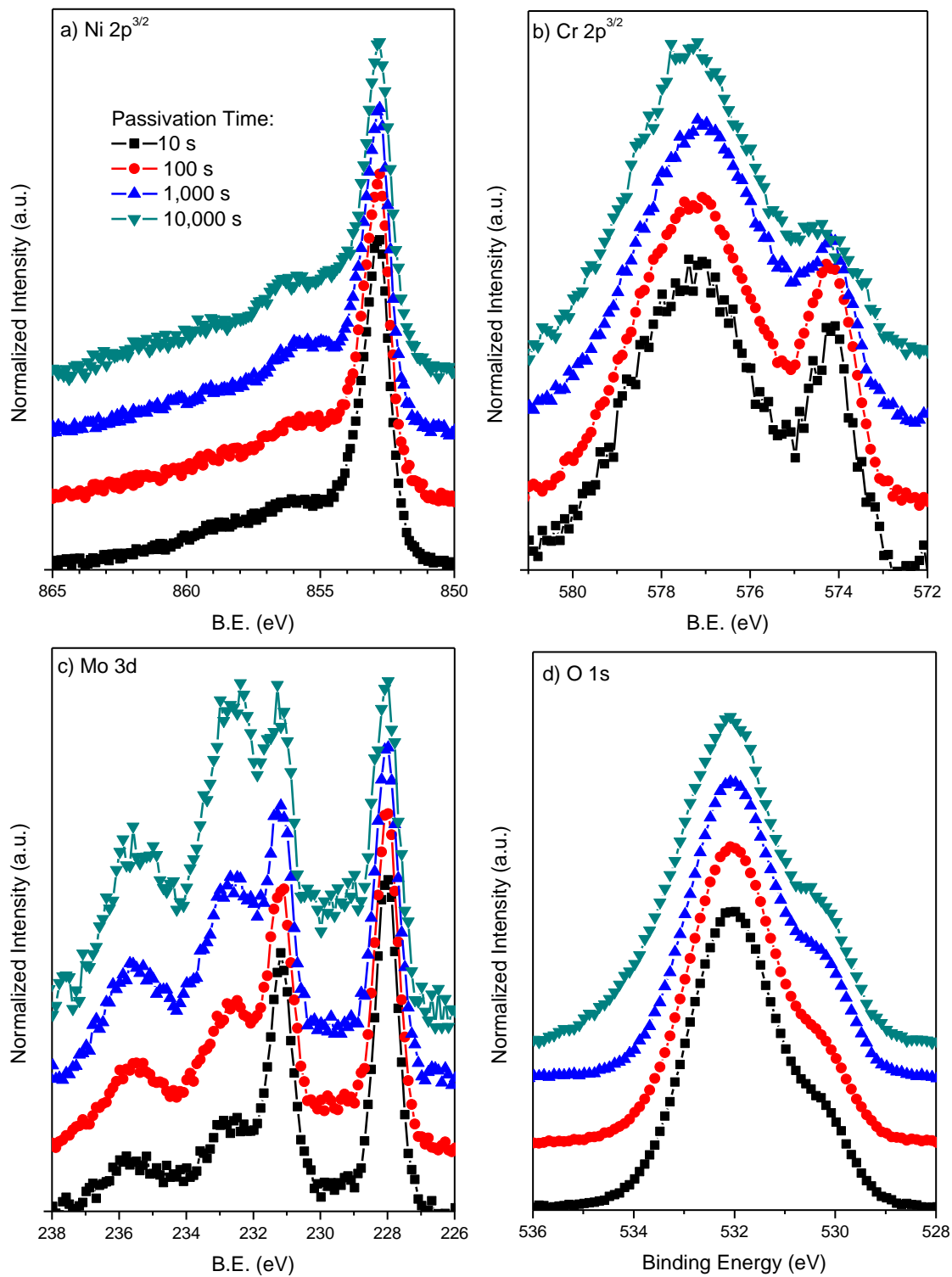


Figure 3.35. a) Ni 2p^{3/2}, b) Cr 2p^{3/2}, c) Mo 3d, and d) O 1s peaks normalized to the metal peaks for Ni-22 Cr-6 Mo, wt%, passivated at +0.2 V_{SCE} for various times up to 10 ks in 0.1 M Na₂SO₄ pH 4

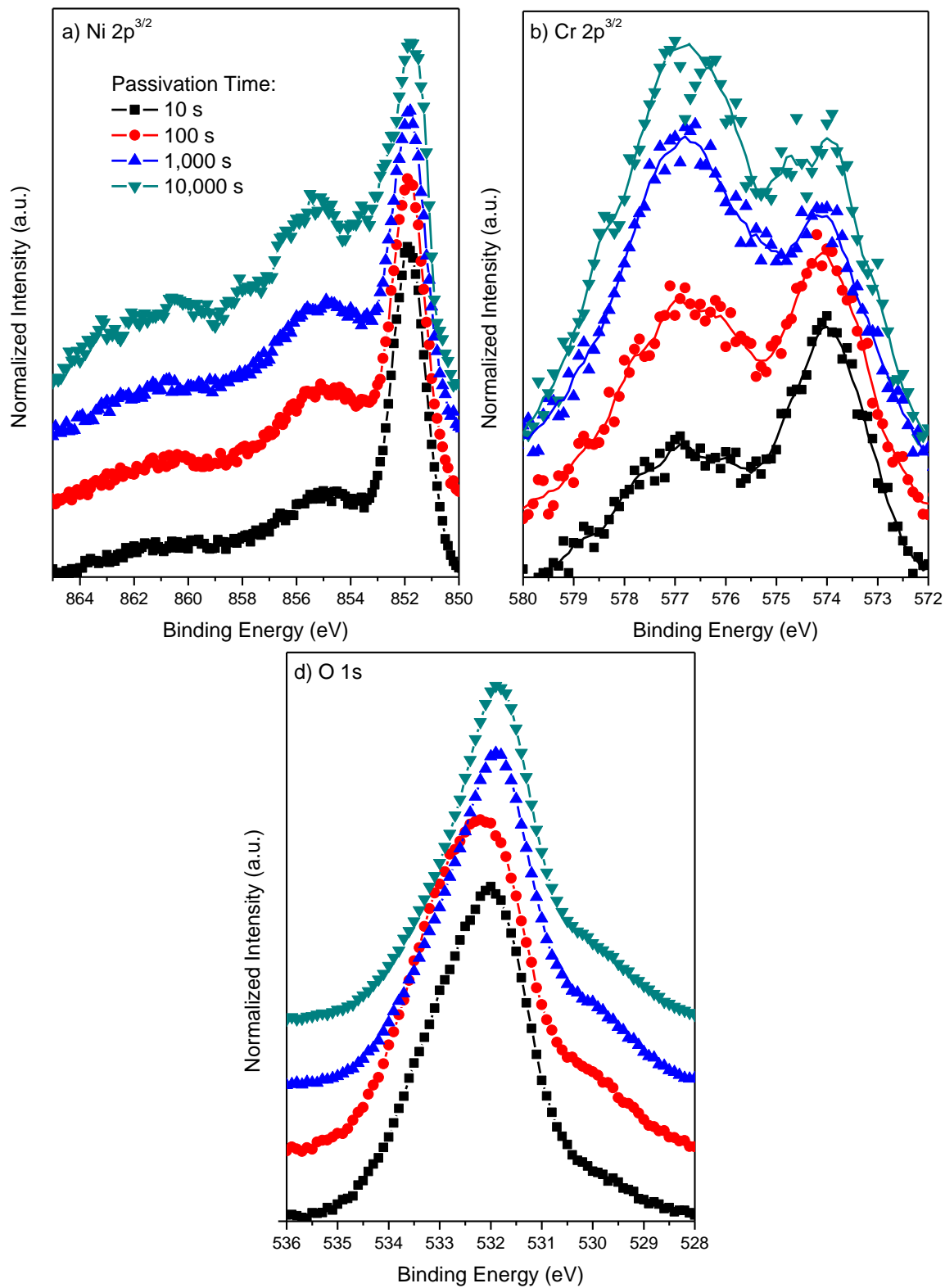


Figure 3.36. a) Ni 2p^{3/2}, b) Cr 2p^{3/2}, and c) O 1s peaks normalized to the metal peaks for Ni-22Cr, wt%, passivated at +0.2 V_{SCE} for various times up to 10 ks in 0.1 M Na₂SO₄ pH 10

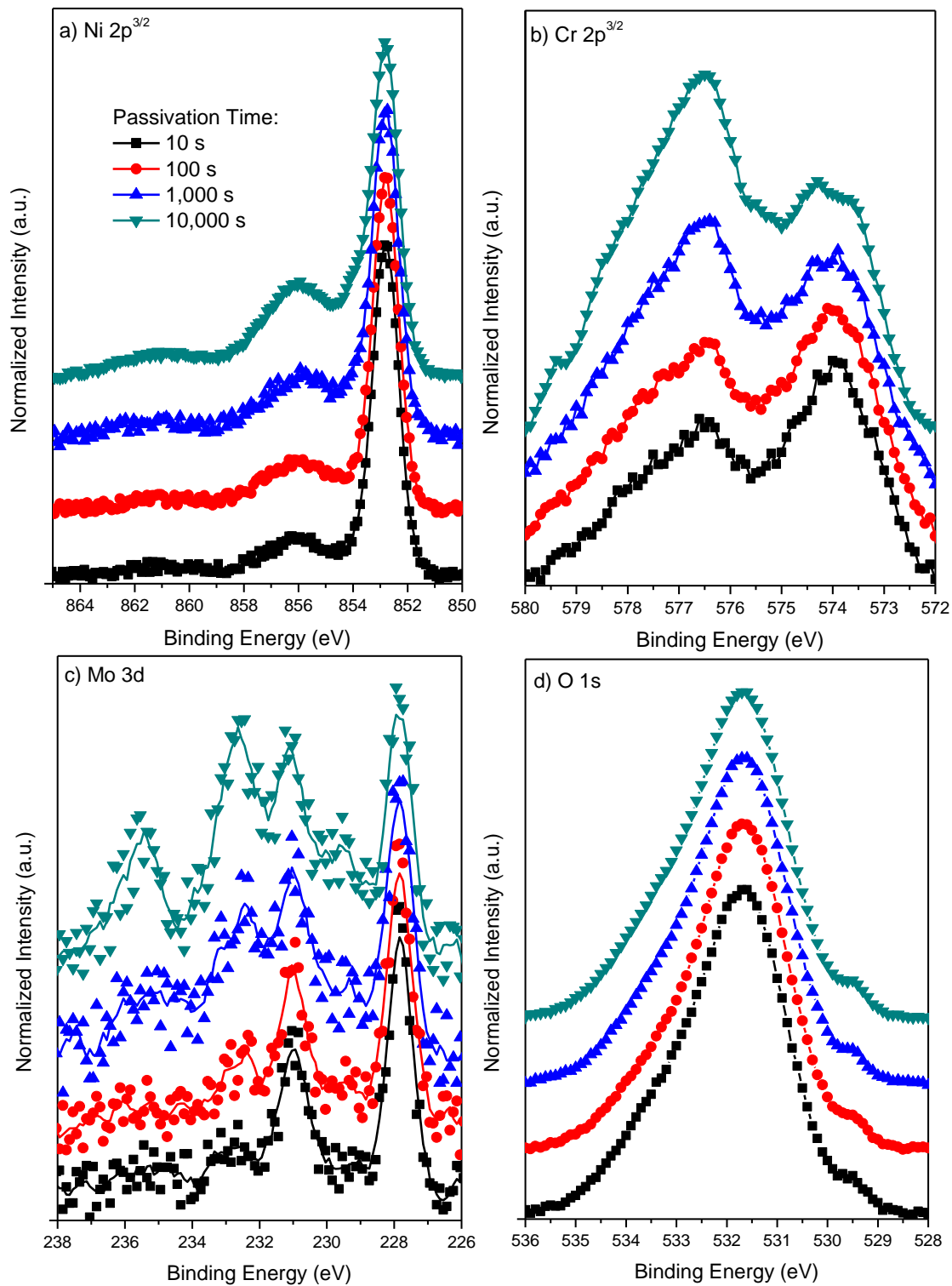


Figure 3.37. a) Ni 2p^{3/2}, b) Cr 2p^{3/2}, c) Mo 3d, and d) O 1s peaks normalized to the metal peaks for Ni-22 Cr-6 Mo, wt%, passivated at +0.2 V_{SCE} for various times up to 10 ks in 0.1 M Na₂SO₄ pH 10

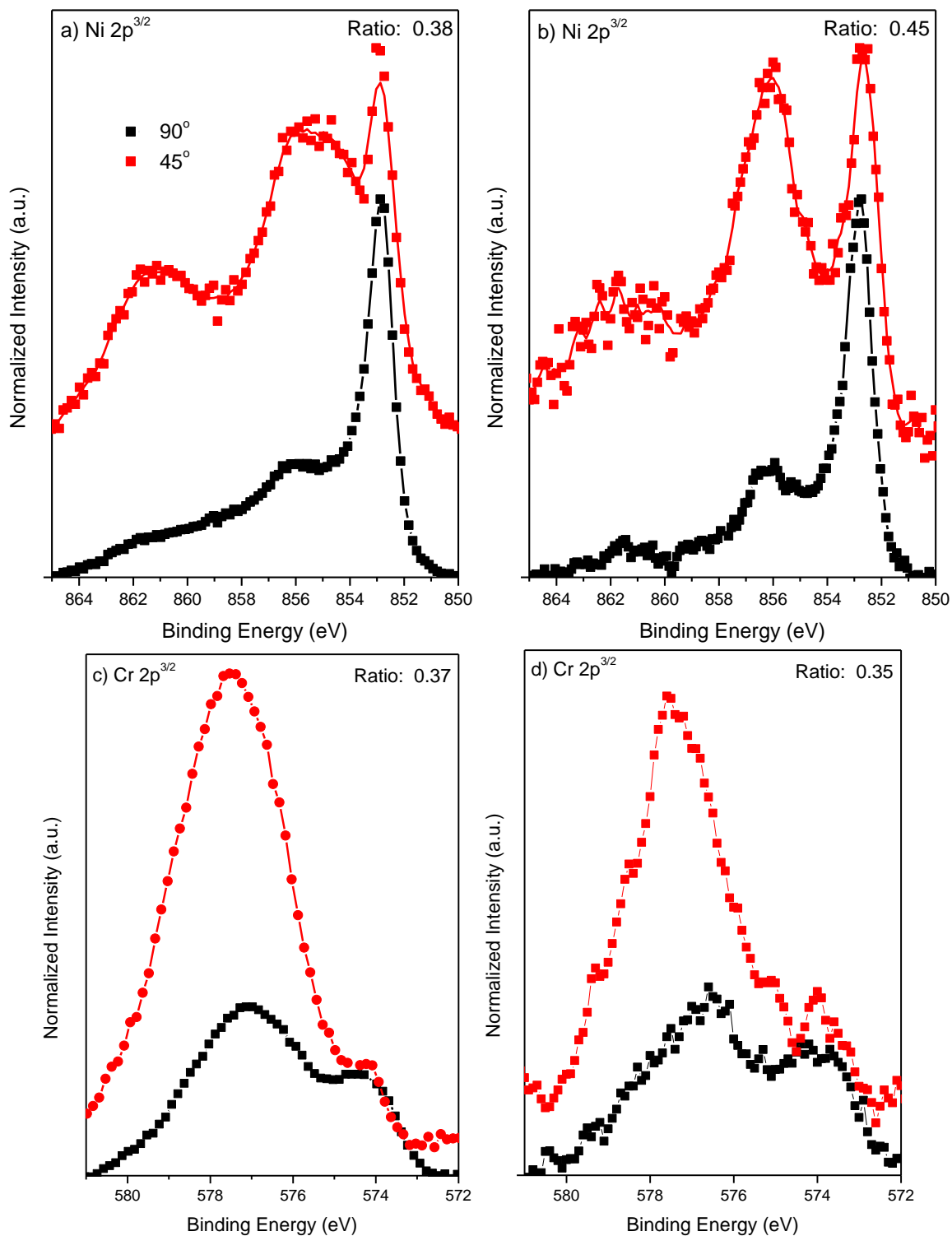


Figure 3.38. a,b) Ni 2p^{3/2} and c,d) Cr 2p^{3/2} angle-resolved XPS spectra which were normalized to the metal peaks for Ni-22 Cr, wt%, passivated at +0.2 V_{SCE} for various times up to 10 ks in 0.1 M Na₂SO₄ a,c) pH 4 and b,d) pH 10. The ratio of the oxide areas for each angle measurement is included for reference.

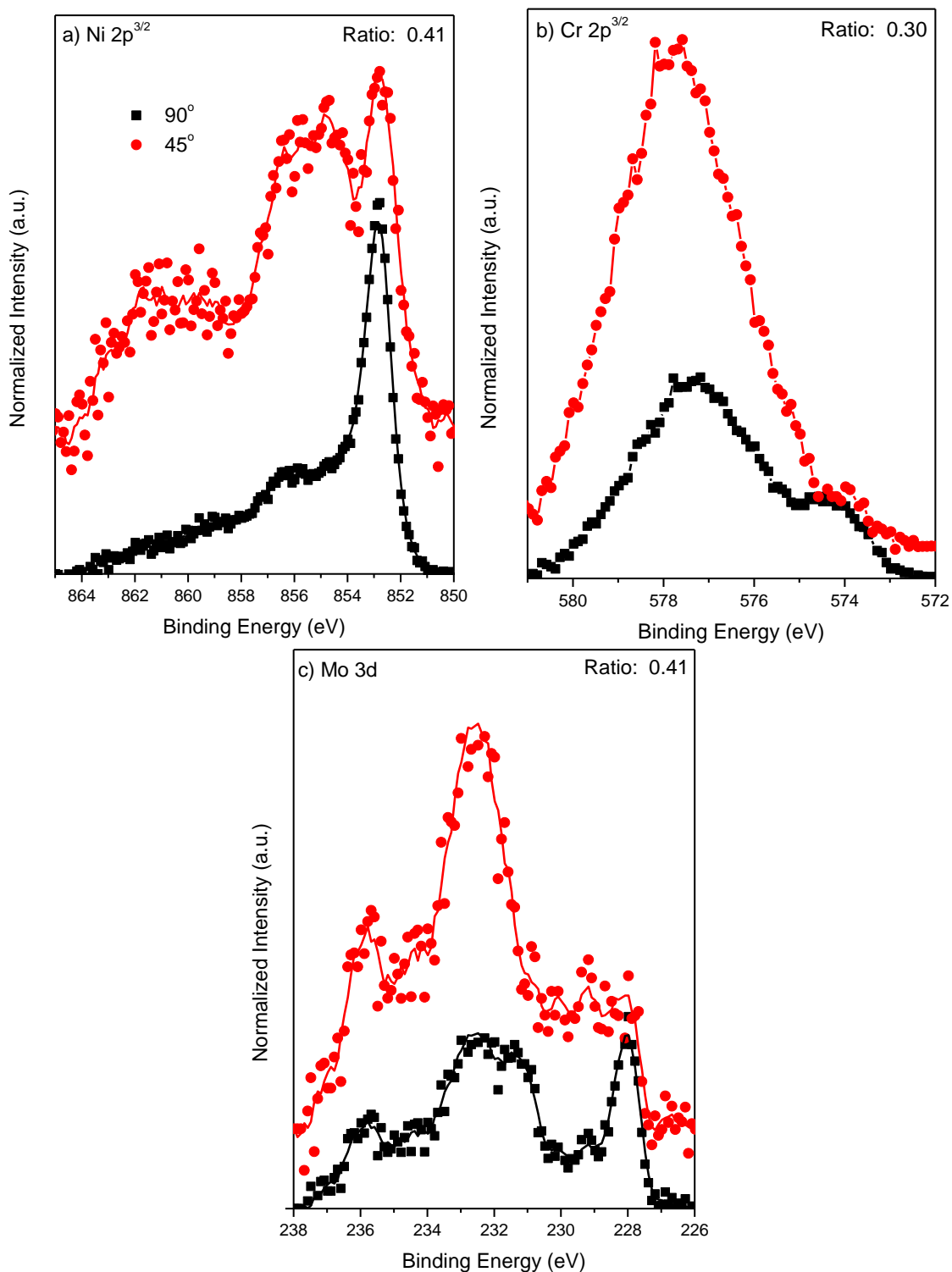


Figure 3.39. a) Ni 2p^{3/2}, b) Cr 2p^{3/2}, and c) Mo 3d angle-resolved XPS spectra which were normalized to the metal peaks for Ni-22 Cr-6 Mo, wt%, passivated at +0.2 V_{SCE} for various times up to 10 ks in 0.1 M Na₂SO₄ pH 4. The ratio of the oxide areas for each angle measurement is included for reference.

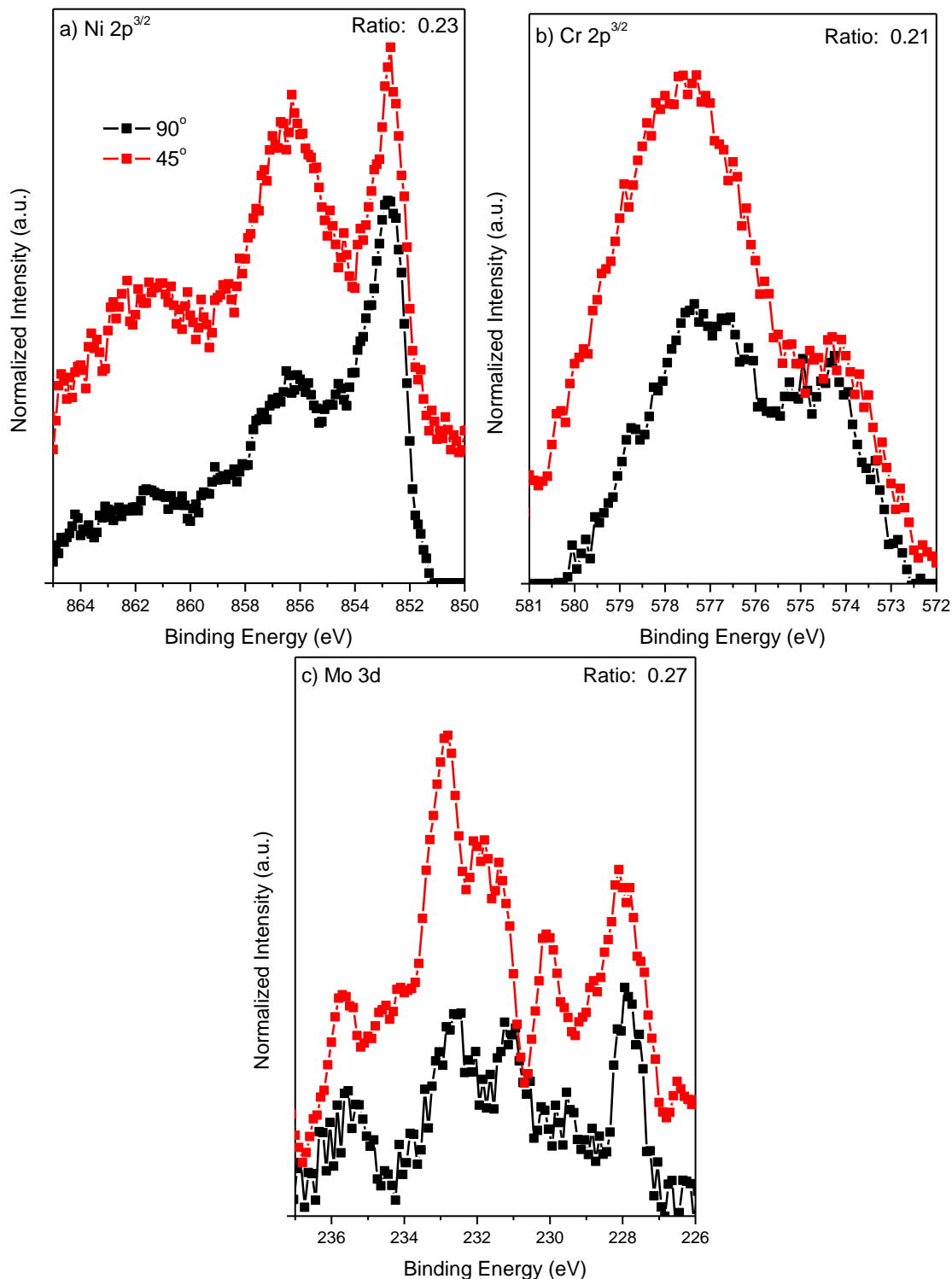


Figure 3.40. a) Ni 2p^{3/2}, b) Cr 2p^{3/2}, and c) Mo 3d angle-resolved XPS spectra which were normalized to the metal peaks for Ni-22 Cr-6 Mo, wt%, passivated at +0.2 V_{SCE} for various times up to 10 ks in 0.1 M Na₂SO₄ pH 10. The ratio of the oxide areas for each angle measurement is included for reference.

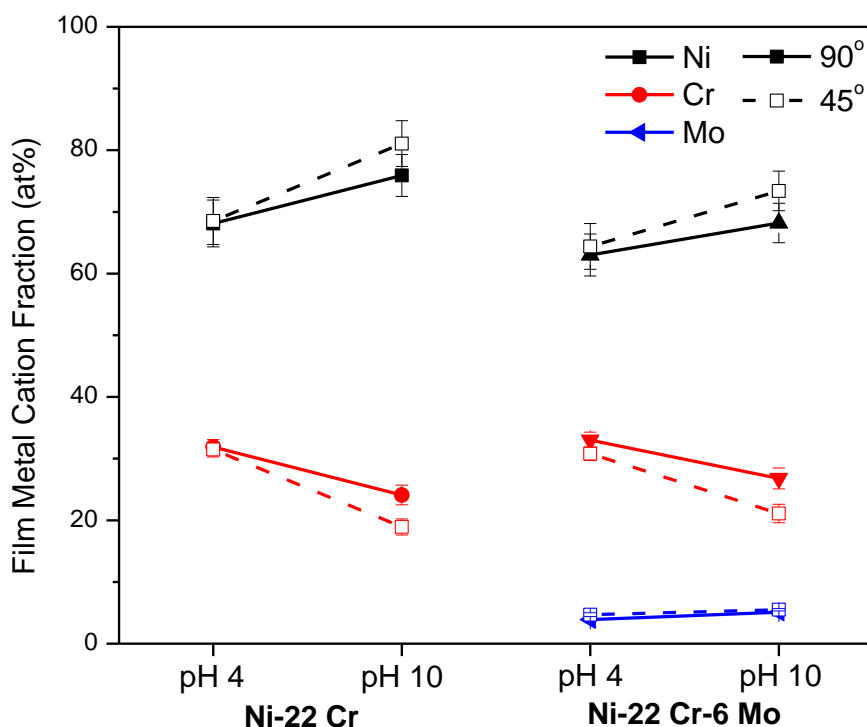


Figure 3.41. Film cation fraction according to angle-resolved XPS measurements at 90° and 45° on Ni-22 Cr and Ni-22 Cr-6 Mo, wt%, surfaces following 10 ks of potentiostatic passivation at +0.2 V_{SCE} in 0.1 M Na_2SO_4 at pH 4 and 10

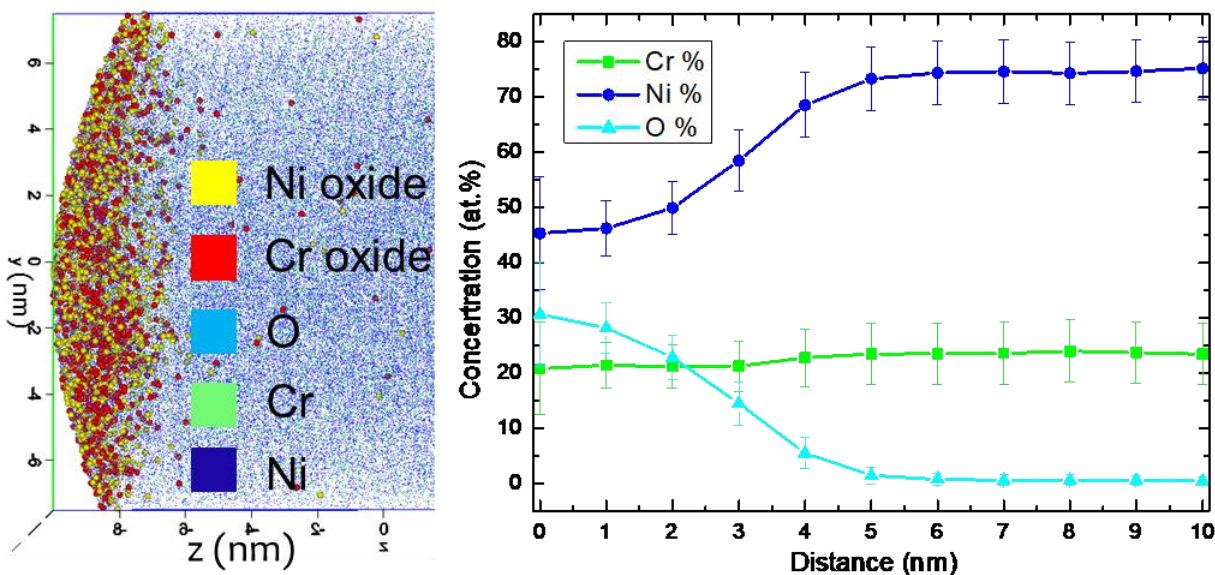


Figure 3.42. APT result for Ni-22 Cr, wt%, with a 12 at% O isosurface corrected for detection efficiencies where the included 1D composition profile through the center of the tip shows the relative Cr-enrichment following a 10 ks exposure to 0.1 M Na_2SO_4 pH 4 + 1 mM $K_2S_2O_8$ ($E_{OCP} = +0.2 V_{SCE}$)

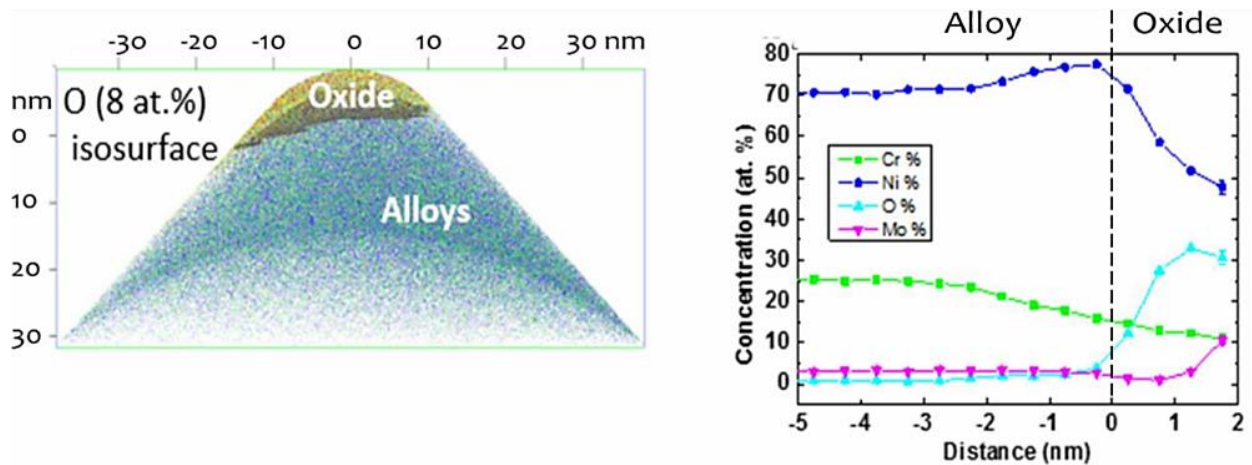


Figure 3.43. APT result for Ni-22 Cr-6 Mo, wt%, with a 12 at% O isosurface corrected for detection efficiencies where the provided 1D composition profile through the center of the tip to show the enrichment of each species following a 10 ks exposure to 0.1 M Na_2SO_4 pH 4 + 1 mM $\text{K}_2\text{S}_2\text{O}_8$ ($E_{\text{OCP}} = +0.2 \text{ V}_{\text{SCE}}$)

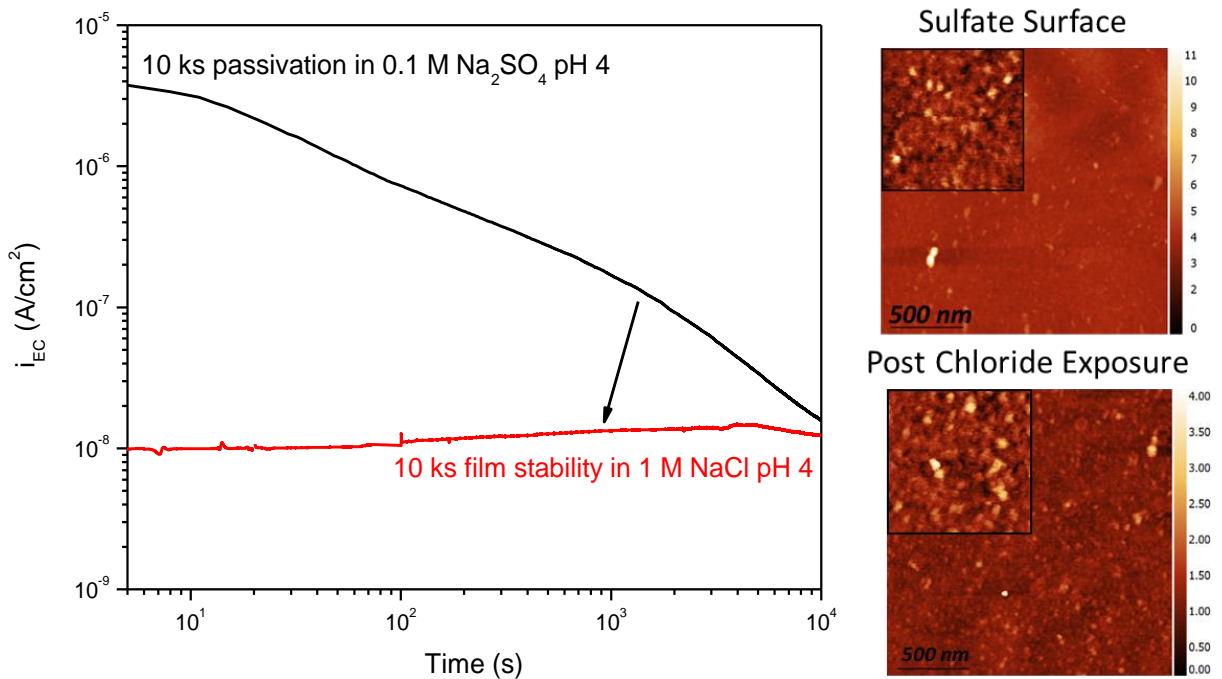


Figure 3.44. Influence of 10 ks surface pretreatment in deaerated 0.1 M Na_2SO_4 pH 4 on the chemical stability and surface roughness of an electrochemically grown passive film that was sequentially exposed to deaerated 1.0 M NaCl pH 4 for 10 ks

4. Potential-Controlled Passivation and Surface Characterization of Ni, Ni-Cr, and Ni-Cr-Mo – Part II. Chloride Environments

A manuscript based on this chapter has been published:

K. Lutton Cwalina, H. M. Ha, N. Ott, P. Reinke, N. Birbilis, and J. R. Scully. (2019). In operando analysis of passive film growth on Ni-Cr and Ni-Cr-Mo alloys in chloride solutions. *Journal of the Electrochemical Society*, 166(11), C3241-C3253.

4.1 Abstract

The instantaneous kinetics of passivation by oxide formation and passive film dissolution were investigated for Ni-22 Cr and Ni-22 Cr-6 Mo, wt%. Experiments were conducted in specific acidic and alkaline chloride specific environments using simultaneous electrochemistry, on-line inductively coupled plasma-mass spectrometry (ICP-MS), and single frequency-electrochemical impedance spectroscopy (SF-EIS) along with *in situ* neutron reflectometry (NR), Mott-Schottky (MS), and *ex situ* X-ray photoelectron spectroscopy (XPS), atomic force microscopy (AFM), and 3D atom probe tomography (3DAPT) following electrochemical testing. The specific roles of pH and Mo during passivation kinetics are highlighted, providing an insight into the fate of the elements which comprise the alloys, and their effects on passivation behavior. It was observed that early oxidation of both Ni and Cr-species occurred in the presence of acidic electrolyte. Preferential dissolution of Ni²⁺ at later times enabled gradual Cr³⁺ enrichment within the surface film. However, greater relative stability of NiO and Ni(OH)₂ was observed in the alkaline condition. Upon alloying with Mo, Cr³⁺ became increasingly enriched in the surface film during anodic polarization. Oxides were interpreted to consist of non-stoichiometric solid solutions formed via solute capture.

4.2 Collaborations

Several collaborations have occurred to perform the broad range of experimental techniques presented in this chapter. In order of appearance, these include: ICP-MS experiments were performed by Dr. Noemie Ott at Monash University, NR experiments and initial analysis were done by Dr. Hung Ha at the Canadian Nuclear Laboratories, AFM measurements and RMS analysis by William Blades at the University of Virginia, and APT sample preparation, measurements, and imaging were performed by Dr. Xiao-Xiang Yu at Northwestern University.

4.3 Introduction

4.3.1 Influence of Chloride Chemisorption

The consequences of specifically chloride anions on varying the properties of passive films and their eventual breakdown have been the subject of numerous studies due to the significance of seawater environments for the engineering applications of Ni-based alloys¹⁻³. Notably, chemisorption of chloride at the surface of passive films can initiate pitting or crevice corrosion^{4,5}. This effect becomes even more significant at elevated temperatures and chloride concentrations⁶⁻⁹. In general, breakdown is inhibited by solid solution alloying minor elements such as Mo and W, but as mentioned previously the exact mechanism by which they inhibit chloride-assisted dissolution and/or localized corrosion is not understood^{10,11}.

The initiation, propagation, and repassivation of corrosion pits is driven by the initial chemisorption of deleterious chloride anions to the surface of an oxide or exposed base metal^{4,12-18}. On a defect-free NiO (111) surface, it was found that the chloride anions substitute hydroxyl groups via an exothermic reaction and this absorption not only encourages more surface coverage, but also induces local thinning of the passive film as chloride-containing compounds (i.e. Ni(OH)Cl or NiCl₂) were observed to detach from step edges¹⁷. Greater chloride-attack and chemisorption occurs at greater [Cl⁻] and pH, resulting in further reductions of the surface energy of the oxide, as shown in Figure 4.1. These factors facilitate film dissolution and breakdown, as will be discussed in more detail below.

The reduction in surface energy following halide chemisorption can be inhibited upon the minor alloying of certain beneficial elements¹⁹. Figure 4.2 demonstrates the favorable formation of oxides versus metal salt species. Notably, Mo has a substantially lower energy required to form MoCl_x compared to MoO_x. This will result in the facilitation of oxide chemisorption rather than chloride and, thus, oxidation is encouraged. As a result of the predicted formation energies in Figure 4.2, the ability for a given minor element to facilitate passivation or block chemical dissolution in chloride environments can be inferred (Figure 4.3). Mo should then, theoretically, have a great effect on inhibiting chloride-assisted dissolution along with the previously discussed facilitation of Cr-oxidation.

4.3.2 Film Surface Roughness and Local Dissolution

Recently, the influence of oxide roughness and irregular morphologies on passive film electrochemical stability has become more understood through the application of the Point Defect Model (PDM) and the supplementation of the Gibbs-Thomson effect and Vetter dissolution^{20–23}. For oxides of a given roughness and perturbation amplitude and wavelength, k , can be modeled. The latter parameter is shown schematically in Figure 4.4. Unstable morphologies occur at high values of k and these are ideally removed in favor of lower energy surfaces.

The inclusion of the Gibbs-Thomson effect results in preferential dissolution at these unstable morphologies possessing a high k and oxidation at low k perturbations (Figure 4.5)²⁰. The amplitude of the oxide layer increases significantly with time due to this increased dissolution at high k , but the distribution in k decreases with the more stable modes being favored. This phenomenon results in an unchanging overall roughness during electrochemical passivation, despite the decreasing local k ²⁴. Such incongruent oxidation and dissolution results in local thinning of the film that can initiate breakdown, as has been previously suggested²⁵.

As was previously mentioned, any initial chemisorption of chloride results in a reduction of the oxide surface energy⁴. This finding has significant ramifications for the competition between oxidation and dissolution across film perturbations. As is shown in Figure 4.6, increasing chloride chemisorption results in an even lower oxide surface energy, γ . This produces an increase in the range of stable k values and morphologies that were unstable at unmodified oxide surfaces. An even rougher oxide surface will be produced as a result of the perturbations that can be formed and will be capable of growing. This is evident by the overall increase in the dissolution rate, σ , and range of k wavelengths where $\sigma > 0$. Such inhomogeneous surfaces are inherently more susceptible to localized breakdown as a result of this local roughening in the presence of chloride^{21,22}.

4.3.3 Preferential Dissolution and Passive Film Composition

There is an abundance of literature on the passive behavior for commercial Ni-based super alloy films in aqueous NaCl environments^{15,26–31}. In general, it was found that C-22, in particular, behaves extraordinarily well and exhibits passive behavior across a broad range of potentials, pH's, and temperatures due to its high Mo and W concentrations³¹. In addition, its oxide defects are less

mobile and numerous than Ni-Cr alloys due to the influence of minor alloying additions on electronic properties²⁷. It was also observed using potentiodynamic curves that the breakdown potential of Ni-alloys is nearly independent of the Mo concentration, whereas that for repassivation is directly dependent³⁰. As for the overall film chemical composition in chloride versus sulfate environments, it is often reported in literature that a significant fraction of the films is attributed to Cr₂O₃ and/or Cr(OH)₃^{26,32}. This is remarkably different from the strong predominance of NiO and/or Ni(OH)₂ observed for Ni-based alloys passivated in Na₂SO₄ environments³³. This suggests the complexity of alloy passivation in chloride-containing environments, in particular Ni-Cr alloys where Cr-enrichment is made possible by chloride-assisted dissolution of Ni²⁺.

Additions of other minor alloying elements, such as Mo, can further impact growth by interacting with the other metals and/or the aqueous solution to promote variations in the film electronic or chemical properties. Their influence has been addressed with regards to the inhibition of localized corrosion events, but rarely during the passivation of alloys and before breakdown initiates. The effect of Mo on film growth is particularly complicated, as previously mentioned, and is theorized to have crucial importance on only film stability during passivation in chloride by modifying the kinetics of various point defect reactions^{32,34}. New evidence suggests this may not entirely be the case.¹⁰

4.4 Objective

In this chapter, ICP-MS and SF-EIS calculations were applied to the elemental contributions and growth rates with independent XPS, 3DAPT, NR, and MS-EIS measurements of film composition, thickness, electronic properties, and their evolution during potentiostatic film growth of Ni-alloys with different Cr and Mo concentrations. The results were analyzed such that the influence of pH (4 vs 10), the fate of the elements, and the individual role of Mo during passivation in chloride environments are ascertained.

4.5 Experimental Methods

The analytical framework established in Chapter 2 will again be applied for analysis of passivation in acidic and alkaline chloride environments. In connection, *in situ* and *ex situ* experiments will be conducted to measure the chemical and electronic properties of the passive films during and after growth occurs.

4.5.1 Materials

The samples used for this study were polycrystalline, solid solution Ni-alloys that model common Cr and Mo concentrations found in commercial Ni-super alloys with the following compositions: Ni-22 Cr and Ni-22 Cr-6 Mo, wt%. The E-pH diagrams for a generic Ni-Cr-Mo alloy in a dilute NaCl environment is given in Figure 4.7. Prior to each experiment, the samples were wet-polished up to 1200 grit using SiC paper, ultrasonically cleaned in alcohol, and rinsed with deionized water (resistivity of 18.2 M Ω -cm) before being placed into the flat cell window. In the case of highly surface-sensitive techniques such as AFM or EBSD, subsequent polishing using polycrystalline diamond suspensions on felt microcloth pads down to 1 and a final ion polishing step for 15 min. The EBSD images for the microstructures of these alloys were previously provided (Figure 3.1).

The various solutions used for testing were 0.1 M NaCl acidified to pH 4 using 1 M HCl and 0.1 M NaCl pH 10 using 1 M NaOH for pH adjustment. All prepared solutions used reagent grade chemicals dissolved in deionized water dispensed from a Milli-Q and were deaerated using ultra-high purity N₂ gas during electrochemical experimentation.

4.5.2 Fundamental Electrochemical Characterization

To initially test the electrochemical passivation behavior of the Ni-Cr and Ni-Cr-Mo alloys in the chloride environments, cyclic polarization scans were performed. This was done by initially mechanically grinding the samples to 1200 grit using successively finer SiC papers. Then, the materials were rapidly placed into the window of a vertical three-electrode electrochemical cell (Figure 2.8) which was then filled with the appropriate solution. Upon insertion of a saturated calomel (SCE) electrode, the solution was then deaerated with N₂ gas through a glass bubbler. Potential and current control was accomplished using a Reference 600 Gamry potentiostat.

An initial cathodic reduction step at -1.3 V_{SCE} for 10 min was used before all electrochemical experiments in order to minimize the existence of air-formed oxides on the alloy surface. Then, the sample was potentiodynamically polarized from -1.3 V_{SCE} up to 0.8 V_{SCE} and back to -1.3 V_{SCE} in 1 mV steps/s. While this speed is higher than what is typical for passivity studies performed to ASTM standards³⁵ (0.1667 mV/s), a faster sweep was necessary to prevent the agglomeration of H₂ gas bubbles evolved at the metal electrode surface when the potential was

sufficiently cathodic. Unlike during the reduction step, their removal was not possible using the pipette attachment as the electrolyte stirring greatly impacted the current measurements. By comparing the current response to the cyclic applied potential for the alloys in different pH environments, the relative improvements via the effects of minor alloying additions and solution chemistry can be inferred. However, these findings are not absolute and as such, the following characterization techniques have been additionally applied.

4.5.3 SF-EIS

The details of the sample preparation and experimental set-up for the SF-EIS experiments are the same as that discussed above. Following the reduction step, the Gamry SF-EIS script was applied at +0.2 V_{SCE} with 1 Hz frequency and a 20 mV AC amplitude. This enabled the measurement of the impedance components Z' and Z'' of the oxide film during passivation (Chapter 2). The measurement time was chosen to be 10,000 s as a pseudo-state in i_{ox} was achieved at this point. In order to apply Equation 2.6 to the SF-EIS results, a full frequency EIS spectrum was acquired from 100 kHz to 1 mHz to obtain Q via a circuit model fit²⁷ (Figure 2.15) and correlate Q to an oxide thickness, l_{ox} . From these results, i_{ox} could also be calculated (Equation 2.11) for each alloy and electrolyte condition.

4.5.4 ICP-MS

In operando ICP-MS experiments were carried out using an experimental setup that have been detailed previously, along with the relevant limits of detection: $2.70 \pm 0.30 \mu\text{g/L}$ for Cr⁵⁰, $0.27 \pm 0.12 \mu\text{g/L}$ for Ni⁵⁸ and $0.074 \pm 0.013 \mu\text{g/L}$ for Mo⁹⁸³³. In terms of the dissolution current density limit of detections, this corresponds to approximately $7.0 \times 10^{-7} \text{ A/cm}^2$ for Cr³⁺, $4.1 \times 10^{-8} \text{ A/cm}^2$ for Ni²⁺, and $2.1 \times 10^{-8} \text{ A/cm}^2$ for Mo⁶⁺ (Equation 2.8). Only concentration data above the detection limits were considered. The electrochemical control was conducted using a Bio-Logic SP-150 potentiostat. An initial cathodic reduction step to minimize the contribution of an air-formed oxide was conducted by holding the working electrode at -1.3 V_{SCE} for 10 minutes^{27,36}. Following this, a potentiostatic step to +0.2 V_{SCE}, was implemented to grow the oxide within the passive region for times up to 10,000 seconds. At this potential, the stable oxidation states are Ni²⁺, Cr³⁺, and Mo⁶⁺³⁷. The element-specific current density contributions for cation species, Mⁿ⁺, released into solution and not retained in the oxide as determined by the ICP measurements, i_{ICP}^M ,

were computed and summed to obtain i_{ICP} , the total current density for dissolution and cation ejection reactions (Equations 2.7 to 2.9). The total ICP current was then subtracted from the total electrochemically measured DC current density, i_{EC} , associated with the total metal oxidation and dissolution in order to compute the total oxide formation current density, i_{ox} (Equation 2.10).

In order to evaluate the contribution of a specific element, M, towards passivation rather than direct cation ejection or film dissolution, the expected, element-specific dissolution current density based on congruent alloy dissolution where E_{app} is well above the Nernst E_r and E_{pp} for each element was computed and the oxidation contribution was similarly obtained using i_{ICP}^M (Equation 2.13 and 2.14). The film's cation composition, C_M , can then be calculated from ICP-MS using Equation 2.16. It is recognized that this computed composition does not account for potential layering. A general schematic of the relative oxidation and dissolution for individual alloying elements is given in Figure 2.8.

4.5.5 Mott-Schottky Analysis

The measurement of electronic property variation was measured during film growth through application of *in situ* MS-EIS. This was accomplished by changing the voltage of the semiconductor artificially through application of a potentiostat. The details of the sample preparation and experimental set-up for the Mott-Schottky sweep experiments are the same as that discussed for SF-EIS. Following the reduction step, and various amounts of passivation, fast MS impedance sweeps were performed at 1,000 Hz from +300 mV_{SCE} down to -600 mV_{SCE} with 20 mV steps, resulting in sufficiently rapid data acquisition. This was accomplished *in situ* following any amount of experimental passivation, at times from 0 to 10,000 s. As mentioned previously, this scan rate was selected in order to measure the impedance variations as a function of potential without the possibility of the space charge layer adjusting. The results were analyzed as discussed in Section 3.5.5.

4.5.6 X-ray Photoelectron Spectroscopy

The variation of film composition and thicknesses was additionally characterized using XPS spectra obtained periodically throughout potentiostatic passive film growth. This technique is well-established in literature for analysis of the identity, concentration, and thicknesses of individual compounds present in films³⁸, especially in the case of Ni-based alloys^{26,27,32}. All XPS

spectra were obtained using a monochromatic Al- $\kappa\alpha$ photon source ($E = 1,486.7$ eV) with surface characterization following various durations of oxide growth. The angle between the sample and detector was fixed at 90 and 45°, whereas that between detector and the X-ray source was fixed at 54.7°. Spectra were calibrated to the 4f^{7/2} binding energy of a metallic Au reference (B.E. = 84 eV) measured at the same time. Survey spectra were recorded on all samples using a pass energy of 200 eV, followed by high resolution spectra of the Ni 2p, Cr 3p, Mo 3d, and O 1s regions using a pass energy of 20 eV.

Commercial CasaXPS software was used to perform Shirley background corrections and spectra fitting³⁹⁻⁴¹. The concentrations of Ni²⁺, Cr³⁺, and Mo⁶⁺ cations in the passive films were computed by fitting the spectra to their observed metallic and oxide/hydroxide peaks, as established in previous literature^{26,32,41-44} and correcting these integrated peak areas to atomic sensitivity factors for Ni, Cr, and Mo (4.044, 2.427, and 3.321 for this detector and source configuration, respectively)⁴¹ (Table 3.1).

4.5.7 Neutron Reflectometry

NR results can be similarly analyzed to produce information regarding the molecular identity and layering of passive films. This is made possible using an *in situ* NR experimental setup at the D3 beamline at the National Research Universal (NRU) reactor (Chalk River, Ontario, Canada) (Figure 3.4). This setup allowed NR measurements performed concurrently with electrochemical experiments. For the purpose of these experiments, thin films were prepared by an electron-beam evaporation system (Angstrom, Ontario, Canada) to produce approximate 25 nm thick Ni-Cr and Ni-Cr-Mo alloys on 100 mm diameter x 6 mm thick polished Si(111) wafers. XPS analysis following thin film preparation yielded bulk compositions of Ni-20 Cr and Ni-20 Cr-10 Mo (wt%).

The thin film samples prepared for NR were stored in a vacuum desiccator and, prior to experiments, were cleaned with methanol and dried in air. Figure 3 shows a schematic of the *in situ* NR experimental setup at the D3 beamline at the National Research Universal (NRU) reactor (Chalk River, Ontario, Canada). This setup allowed NR measurements to be performed concurrently with electrochemical experiments. A conventional three-electrode electrochemical cell with a Pt thin foil counter electrode and a KCl saturated Ag/AgCl reference electrode ($V_{\text{Ag/AgCl}}$

= +47 mV_{SCE}) was used. A Solartron 1287A potentiostat and a Solartron 1255 frequency analyzer were used in electrochemical experiments. A cathodic potential of -1.2 V_{SCE} was applied for 5 min to reduce the air-formed oxide, followed by steps from -0.8 V_{SCE} up to +0.2 V_{SCE} in 0.2 V_{SCE} steps every 6 hr. The thin film samples, Pt foil, and reference electrode were connected to the corresponding terminal of the potentiostat for potential control and electrochemical measurements and the neutron beam travelled to the metal/electrolyte interface through the Si wafer. The NR measurements started 1 hr after the applied potential was switched to the set value and each measurement took approximately 90 min to complete.

D3 uses a collimated neutron beam with a wavelength of 2.37 Å. The neutron beam travelled through the Si wafer before it reached the metal/electrolyte interface at a small grazing angle. The intensity of the specular reflected beam was recorded at different grazing angles, θ , and the reflectivity curves were plotted as a function of the scattering vector, Q , which is related to the incident beam angle and the neutron wavelength (Equation 3.9). The thickness, roughness, and SLD profile of the layers in the thin film sample were obtained by fitting the reflectivity curves to a thin film model using a least square fit algorithm which includes a recursion algorithm developed by Parratt⁴⁵⁻⁴⁸.

4.5.8 Atomic Force Microscopy

Following electrochemical passivation, the samples were removed from the cell, rinsed with deionized water, and sonicated in ethanol to remove any residual salt from the surface that would obstruct imaging. The surface morphology of each sample was captured using an AFM with NT-MDT Solver Pro. The AFM tip, ETALON HA/NC with a radius of curvature less than 10 nm, was kept in tapping mode during imaging. The surface roughness of the samples was ascertained from deviations in the root mean square (RMS) of local surface areas. The RMS data in this study was found using Gwyddion⁴⁹, an open source software package used for Surface Probe Microscopy analysis. To obtain consistent and physically meaningful RMS values, each image was planarized by mean plane subtraction. The variations caused by the contact between the tip and sample along the horizontal scanning directions were also corrected by leveling the horizontal line directions with linear or quadratic polynomials depending on the magnitude of the deviations.

4.5.9 Three-Dimensional Atom Probe Tomography (3DAPT)

More in depth sample preparation steps were required in order to produce tips appropriate for 3DAPT analysis⁵⁰. A standard electropolishing step was used to pre-thin alloy bars (0.5mm×0.5mm×2cm) in an electrolyte of 10 vol% perchloric acid in acetic acid using 12-20 V_{DC}. Afterwards, 2 vol% perchloric acid in a butoxyethanol electrolyte and 12-15 V_{DC} were used to accomplish the final sample thinning. A CAMECA Local Electrode Atom Probe 4000XSi with an ultrafast detector capability was used for APT experiments. Picosecond pulses of a UV laser were utilized to evaporate individual atoms at a repetition rate of 250 kHz with a pulse energy of 20 pJ and an average detection rate of 0.005 ions/pulse. The specimen tip temperature was maintained at 25 K. Data analysis was performed on the 3D reconstructions of the specimen utilizing IVAS V3.6.1 software.

It is established that the oxide compositions measured using APT depend on the laser energy/pulse, with more accurate results achieved at lower energies. To calibrate the data, a tip of pure Ni was prepared, oxidized, and used as a calibrant. This sample indicates that the detection efficiency of O atoms was 0.67. All data herein has been corrected for this inefficiency.

4.6 Results

4.6.1 Fundamental Electrochemistry of Ni-Alloys in Aqueous Chloride Environments

The E-log i passivation behavior of Ni-22 Cr and Ni-22 Cr-6 Mo, wt%, in the acidic and alkaline solutions of concern for most of this study was established initially (Figure 4.8a). The impedance was then measured at 1 Hz to assess the imaginary component of the film impedance and its corresponding capacitance across the same range of applied potentials during a potentiodynamic sweep from -1.3 V_{SCE} to +0.8 V_{SCE} at 1 mV/s (Figure 4.8b). The polarization behavior in Figure 4.8a shows a difference between the pH 4 and 10 environments with a lower passive current density in the latter environment. At +0.2 V_{SCE}, there is a clear difference in the passive film impedance of Ni-Cr and Ni-Cr-Mo in both solutions and as such, this potential was selected for the potentiostatic experiments that will be discussed in detail herein. Specifically, this potential is also near the potential at which crevice corrosion occurs in seawater^{51,52}. Figure 4.8a shows that +0.2 V_{SCE} is within the passive window of Ni-Cr-Mo in both solutions, and just at the potential above which the passive film degrades for Ni-Cr. In Figure 4.8b, the magnitude of Z''

risers at potentials above $-1.2 V_{SCE}$ and peaks at approximately $0 V_{SCE}$, beginning to drop discernably above $+0.1 V_{SCE}$. Both the E-log i and impedance behavior is improved above $+0.2 V_{SCE}$ upon the addition of Mo. Transpassivity is also shifted to potentials above $+0.4 V_{SCE}$ due to Mo stabilizing the passive film^{53,54}. $-Z''$ was near a maximum at $+0.2 V_{SCE}$ for Ni-Cr-Mo in both solutions, whereas the impedance was already declining with potential for Ni-Cr due to film thinning and dissolution (Figure 4.8b).

4.6.2 *In Operando* Characterization

4.6.2.1 0.1 M NaCl pH 4

The element-specific dissolution current densities, i_{ICP}^M , as determined by ICP-MS for Ni-Cr and Ni-Cr-Mo are indicated by the total electrochemical current density, i_{EC} , and those expected for each element assuming congruent dissolution of the bulk alloy ($i_{cong\ diss}^M = (at\% M)i_{EC}$)⁵. The difference between i_{ICP}^M and $i_{cong\ diss}^M$ for each element, M, indicates the specific contribution towards direct film growth formed by oxidation reactions rather than cation ejection or subsequent chemical dissolution of oxides initially formed.

In Figure 4.9a, i_{EC} , i_{ICP}^{Ni} , and i_{ICP}^{Cr} are smooth and decreasing during the first 300 s. i_{ox}^{Ni} and i_{ox}^{Cr} are similarly decreasing and remain in proportion to the alloy composition. Overall, the Cr-rich passive film is still thickening ($i_{cong\ diss}^{Cr} > i_{ICP}^{Cr}$) until ~ 400 s when i_{EC} , i_{ICP}^{Ni} , and i_{ICP}^{Cr} all increase as crevice corrosion initiates for the Ni-Cr alloy. Noticeably, from 100 to 400 s, i_{ICP}^{Cr} is below the aforementioned detection limit for Cr^{3+} and as such, Cr is solely contributing to passivation, whereas there is some detected Ni^{2+} dissolution during the first 400 s. After approximately 1 ks, i_{ICP}^{Ni} and i_{ICP}^{Cr} approach their respective currents for congruent dissolution during crevice corrosion attack which dominates the ICP-MS measurements from this time onward. There is some detected Cr^{3+} dissolution on Ni-Cr (Figure 4.9a) at early times as i_{ICP}^{Cr} was above its corresponding detection limit (7.0×10^{-7} A/cm² for Cr^{3+}).

The overall film formation rates for Ni-Cr (Equations 2.7-2.11 and Figure 4.9a) were compared to calculations completed using the SF-EIS *in operando* technique (Equation 2.11 and

⁵ Congruent dissolution is a starting point and a reasonable assumption when there are large thermodynamic driving forces for dissolution of each alloying element, i.e. $i_{diss} \gg i_{ox}$.

Figure 4.9b). For both techniques, i_{EC} , i_{ox} , and i_{ICP} initially decreased while l_{ox} increased at a decreasing rate overall before localized corrosion initiated. At this point, $i_{ox} \rightarrow 0$ as both i_{EC} and i_{ICP} increased. After crevice corrosion occurs, Equation 2.5 is invalidated because localized attack contributes an additional impedance to the system, resulting in any measured Z'' changes to be caused by both film and corrosion variations. Equations 2.10 and 2.14 are similarly nullified following localized corrosion, as an additional current density proportional to the crevice corrosion rate does not contribute to oxide formation. As such, the l_{ox} obtained using both SF-EIS and ICP-MS following crevice corrosion initiation were excluded from Figure 4.9b.

There is a noticeable distinction between the behaviors of the alloys in 0.1 M NaCl at pH 4: Ni-Cr exhibited crevice corrosion after approximately 300 s (Figure 4.9a) while Ni-Cr-Mo remained passive at all times (Figure 4.10a). All three alloying elements in Ni-Cr-Mo contributed to film formation, as evidenced by $i_{cong\ diss}^M > i_{ICP}^M$ until a steady-state thickness was approached at approximately 5 ks, indicated by the quasi-steady state level of i_{EC} . In particular, i_{ICP}^{Cr} and i_{ICP}^{Mo} were below the relevant detection limits from 400 to 10,000 s and less than $i_{cong\ diss}^M$, indicating that these elements joined the film, whereas selective dissolution of Ni^{2+} occurred during film growth to compensate for the enrichment of the other metal cations. Because $i_{ICP}^{Ni} < i_{cong\ diss}^{Ni}$ up until 3 ks, there was still some net oxidation of Ni cations into the passive film despite the simultaneous observation of dissolved species in the electrolyte stream.

Figure 4.10b shows a similar comparison between the ICP-MS and SF-EIS film growth calculations in the case of Ni-Cr-Mo. Unlike the results shown in Figure 4.9b, Ni-Cr-Mo remained passive with no crevice corrosion initiation throughout the experiment time as i_{EC} , i_{ICP} , and i_{ox} all decrease as l_{ox} increases and thus the two sets of film growth agree well with each other over the entire 10 ks. Overall, Ni-Cr appeared to possess a greater film growth rate until crevice corrosion initiated and a noticeably higher i_{EC} (Figure 4.9). The strong passivity of Ni-Cr-Mo (Figure 4.10) clearly demonstrates one of the many proposed roles of Mo minor alloying additions¹⁰ related to increasing the electrochemical stability of the passive film. Both alloys reached similar maximum film thicknesses: approximately 2.1 nm for Ni-Cr before crevice corrosion initiated and 2.3 nm for Ni-Cr-Mo at the end of the passivation time. For Ni-Cr-Mo, l_{ox} levels off after 2-3 ks when i_{ICP} approaches i_{EC} , suggesting any oxidation, i_{ox} , helps to maintain the passive film (Figure 4.10).

The application of Equations 2.15 and 2.16 to the data shown in Figure 4.9a and Figure 4.10a enabled computation of the film cation fraction during the passivation step (Figure 4.11). Both alloys become increasingly Cr-rich with time as Ni is preferentially dissolved in the chloride-containing solution. The results indicate that the passive film on Ni-Cr-Mo is slightly more enriched with Cr cations compared to Ni-Cr, supporting an additionally suggested role of Mo as a promoter of preferential Cr-oxidation¹⁰. Mo appears to be present only at small concentrations, reaching a maximum of 2.7% of all cations in the passive film by the end of the experiment. This small amount of Mo⁶⁺ is unlikely to result in distinct, stoichiometric MoO_x phases unless they are present as small islands but this is not supported by the constant entrance of Mo cations in the oxide (Figure 4.10a).

4.6.2.2 0.1 M NaCl pH 10

Potentiostatic passivation of Ni-Cr and Ni-Cr-Mo at +0.2 V_{SCE} was also investigated in 0.1 M NaCl adjusted to pH 10 and monitored using SF-EIS and ICP-MS to investigate the varying thermodynamic and kinetic favorability of oxide species in acidic and alkaline environments, as previously suggested by Pourbaix E-pH diagrams (Figure 4.7)³⁷. Figure 4.9a illustrates the dissolution current densities for specific alloying elements in Ni-Cr with a comparison to the total current density for electrochemical reactions during passivation. Ni and Cr oxidation are strongly favored in the case of both alloys at all times ($i_{cong\ diss}^{Ni} > i_{ICP}^{Ni}$ and $i_{cong\ diss}^{Cr} > i_{ICP}^{Cr}$ at all times).

Ni-Cr (Figure 4.12a) appears to undergo increased dissolution as i_{ICP}^{Ni} and i_{ICP}^{Cr} both begin to increase after 300 s. Since i_{ox}^{Ni} and i_{ox}^{Cr} remain positive and there are “sharp” upward spikes of Ni and Cr dissolution where i_{ICP}^{Ni} and i_{ICP}^{Cr} afterwards return to an approximately steady value, it can be concluded that the film is experiencing periodic localized corrosion, rather than the stable crevice corrosion evidenced by the increasing i_{ICP} seen for pH 4 (Figure 4.9). It is worth noting that these peaks only appear sharp due to the logarithmic scale, but they exhibit a residence time distribution characteristic for flow cell-based measurements when plotted with a linear time axis⁵⁵. The spikes are not evident in i_{EC} due to the low data acquisition rates. Instead, i_{EC} is smoother than i_{ICP} but exhibits abrupt spikes due to some stage of the breakdown events being sampled. This results in an increasing i_{EC} with small, local increases corresponding to local breakdown. As was observed in the pH 4 environments, good agreement was obtained between the ICP-MS and

SF-EIS techniques (Figure 4.12b). There is one distinction, however, because the periodic and relatively infrequent occurrence of localized corrosion events did not significantly impact the impedance measurements, and as such SF-EIS was a valid approach during the entire 10 ks. Some fluctuations in Z'' were measured, evident in i_{ox}^{SF} (Figure 4.12b).

Figure 4.13a shows that Ni-Cr-Mo has similar favorable Ni and Cr oxidation at all times. The calculated i_{ox}^{Ni} appears to dominate film growth ($i_{cong\ diss}^{Ni} \gg i_{ICP}^{Ni}$) and the ICP-MS signal remains above the detection limit. As such, there is still some discernible dissolution, albeit less than was observed for Ni-Cr in either environment or Ni-Cr-Mo in pH 4, despite the more significant amounts of oxidation. This agrees with the predicted electrochemical stability of NiO and Ni(OH)₂ at +0.2 V_{SCE} in pH 10 environments^{37,56,57}. There is no localized corrosion observed in the ICP-MS data owing to the effect of Mo in Ni-Cr. Ni-Cr-Mo (Figure 4.13a) attains a nearly quasi-steady state overall thickness after 10 ks at pH 10 and does not exhibit localized breakdown. The very slight increase in i_{EC} after long times is, instead, caused by preferential dissolution of Mo from the passive film, as is evident in Figure 4.13a in which $i_{ICP}^{Mo} > i_{cong\ diss}^{Mo}$ after 1 ks. Mo-oxides are not predicted to be thermodynamically favorable in the alkaline environment; instead, soluble MoO₄²⁻ will form³⁷.

Figure 4.13b compares the current densities and overall film growth computed using ICP-MS (Equation 2.11) and SF-EIS (Equation 2.6) for Ni-Cr-Mo. The methods predict similar trends, as discussed for the previous cases. The measured i_{ICP} is much higher for all times for Ni-Cr than for Ni-Cr-Mo due to the influence of Mo on facilitating potential step passivation and resisting localized breakdown. The efficiency of film growth on Ni-Cr-Mo appears very high for all time ($i_{ox}^{ICP} \approx i_{EC}$ in Equation 2.10). A major distinction between the alkaline data in Figure 4.12b and Figure 4.13b and acidic in Figure 4.9b and Figure 4.10b is the increased film growth in the latter; both alloys reached final thicknesses between 5-7 nm in 0.1 M NaCl pH 10, higher than the 2 nm thickness in pH 4. The average electrochemical current efficiencies (Equation 2.12) were computed for each alloy and environment and are given in Table 4.1. There is a significant difference between each alloy and environment. Ni-Cr had a much higher computed oxidation efficiency throughout the 10 ks potential step in the alkaline environment than in the acidic one. Notably, this alkaline efficiency was slightly greater than that of Ni-Cr-Mo in the pH 4

environment due to the increased stability of Ni- and Cr-films. Ni-Cr-Mo had the highest average efficiency in the pH 10 environment despite the significant selective dissolution of Mo at later times.

Additional analysis of the film composition was accomplished using Equation 2.16 for the alkaline data as was previously discussed for the acidic environment (Figure 4.11) and is given in Figure 4.14. The data indicates that there is very minimal variability in film composition at all times at pH 10, with the exception of some slight Ni-depletion after 3 ks. As with the pH 4 environment, Ni-Cr-Mo appears to be slightly more enriched in Cr than Ni-Cr due to Mo functioning as a Cr oxidation promoter^{32,58-63}. Mo remains to be captured at small cation fractions in the film for all times, reaching its maximum overall fraction at the start of experimentation (1.35 at%) and slowly decreasing with time as Mo becomes selectively dissolved.

4.6.3 *In Situ* Characterization

4.6.3.1 Mott-Schottky Analysis

During passivation in the 0.1 M NaCl environments, Mott-Schottky analysis of fast impedance sweeps was applied at times during passivation to characterize the electronic properties of the film and their evolution with time. Noticeably in Figure 4.15, the films predominantly behave as n-type semiconductors within the passive potential region. However, at the passivation potential, +0.2 V_{SCE}, the films exhibit p-type behavior. Additionally, the presence of substitutional defects, notably Cr³⁺ on a Ni²⁺ site or Mo^{4,6+} on a Cr³⁺ site, will result in greater p-type electronic behavior. This effect of Mo is evident in Figure 4.15b where a broader range of p-type behavior was measured. Overall, a clear decrease in the capacitance (and therefore an increase in the oxide thickness) was observed during the passivation time along with a slight shift of the n-to-p-type transition to higher potentials. The impedance sweeps in the alkaline environment (Figure 4.16) exhibited the opposite behavior with primarily p-type semiconductance being observed. Additionally, less capacitive (i.e. more resistive) behavior was observed for Ni-Cr-Mo, suggesting a more corrosion-resistant passive film was formed.

Mott-Schottky analysis of these impedance spectra enabled computation of the n- and p-type point defect concentrations (Figure 4.17) along with the respective flat band potential (Figure 4.17). The concentrations do not appear to vary significantly, with a few exceptions. In the acidic

environment, the concentration of donor defects, indicated by N_D , appears to initially decrease as the film forms. But after approximately 500 s, it increases. This is likely caused by the formation of metal cation vacancies within the passive film as a result of chloride absorption at the film/solution interface. This effect is much less on Ni-Cr-Mo, which only slightly increases after 5,000 s. For both alloys there is an initial increase and then decrease in the concentration of p-type defects, indicated by N_A . This is likely caused by an initial increase in the concentration of substitutional point defects as the film rapidly grows and at longer times, this results in the annihilation of holes⁶⁴. In the alkaline environment, only p-type behavior was exhibited by Ni-22Cr (Figure 4.17a) due to the high concentration of positive dopants (Figure 4.17). These defects slightly increased with time before decreasing, likely caused by the same phenomena explained previously for the alkaline environment. As for Ni-Cr-Mo, for all times the concentration of point defects decreased as the films did not undergo breakdown and any formed early became electrostatically neutralized with increasing passivation time. Overall, the total concentrations of point defects tend to be less for Ni-Cr-Mo than for Ni-Cr in both the acidic and alkaline environments.

The measured passive film flat band potentials tended to increase with passivation time independent of alloy or environment pH (Figure 4.18). For both the potential according to n- and p-type behavior, E_{FB} was higher in the acidic environment and for the Ni-Cr-Mo alloy. This agrees with previous theories that E_{FB} correlates with the pitting potential, E_{pit} , for a passive film. Adding Mo as a minor alloying element has been well-demonstrated to increase E_{pit} ^{52,58,65-68}. The effect of pH is less certain, however. Upon consideration of the previous ICP-MS results (Figure 4.11 versus Figure 4.14), the increase in E_{FB} could be attributed to increased enrichment of Cr^{3+} within the passive film in acidic environments. Oxides containing a large amount of Cr_2O_3 and/or $Cr(OH)_3$ are commonly reported for Ni-based alloys which exhibit phenomenal corrosion resistance^{26,32,69}.

4.6.3.2 Neutron Reflectometry

The reflectivity curves for the two alloys in 0.1 M NaCl pH 4 and pH 10 are given in Figure 4.19 and Figure 4.20, respectively. These data sets were fit using an algorithm developed by Parratt⁴⁵⁻⁴⁸ to produce neutron SLD profiles versus depth (Figure 4.21 and Figure 4.22). At low depths, the SLD corresponded to the electrolyte layer, followed by a steep, almost linear increase

upon reaching the oxide layer. Finally, the SLD of the base metal alloys was reached at still greater depths. Annotated on Figure 4.21 and Figure 4.22 as horizontal lines are the theoretical SLD of several stoichiometric oxides. Based on the figures, the profiles suggest films rich in Ni-oxide species. There is no clear layering within the passive film as a plateau within the pseudo-linear region would be evident, and instead there is a continuous increase between the theoretical value for $\text{Cr}(\text{OH})_3$ and either the SLD peak (for Ni-Cr) or the base metal (for Ni-Cr-Mo).

Simulated SLD profiles were produced using GenX software for a non-equilibrium film with varying Cr^{3+} content or a bilayer oxide composed of varying thickness NiO and Cr_2O_3 layers (Figure 3.20). Upon comparing Figure 4.21 and Figure 4.22 to Figure 3.20 it is evident that the SLD profiles agree with non-stoichiometric, solid solution oxides, as shown in Figure 3.20a. It could be argued that the layered NiO and Cr_2O_3 appear to agree when there is a small l_{ox} for the latter species, but it is apparent in the ICP-MS results (Figure 4.11 and Figure 4.14) that this would not accurately apply to the observed film composition.

Upon subtraction of the metal and electrolyte SLD (Figure 3.6), the oxide peaks do not demonstrate any layers (Figure 4.23). These results additionally allow for the estimation of l_{ox} and the Cr^{3+} cation fraction using the width and height of the profile, respectively (Table 3). Films with an SLD closer to the value of NiO ($8.7 \times 10^{-6} \text{ \AA}^{-2}$) will have a lower % Cr^{3+} compared to those near the value of Cr_2O_3 ($5.1 \times 10^{-6} \text{ \AA}^{-2}$), and the non-stoichiometric rocksalt film has an SLD in between the two. There is some Ni-enrichment apparent at the metal/electrolyte interface, as previous work has reported^{32,70,71}, but for Ni-Cr-Mo the outer SLD decreases with applied potential as Ni^{2+} undergoes selective dissolution in favor of Cr-enrichment (Figure 4.23b). Since the fraction of Mo cations in the film is insignificant compared to Ni^{2+} and Cr^{3+} (Figure 4.11), any substitutional $\text{Mo}^{4,6+}$ defects within the oxide would not result in the observed, substantial decrease in the SLD for passivated Ni-Cr-Mo. There is also a rough, outer interface of the passive films that is very highly hydrated. The thickness of this region is estimated to be approximately 1 nm, which is on the order of the experimental passive film surface roughness²⁴.

Analysis of the Cr^{3+} metal cation fraction and the passive film thickness using the profile width and peak SLD values in Figure 4.23 and Figure 4.24 is provided in Figure 4.25 and Figure 4.26 for the acidic and alkaline environments, respectively. As suggested previously, Ni-Cr-Mo exhibited significantly greater Cr-enrichment across all potentials than Ni-Cr (Figure 4.25 and

Figure 4.26). Following rapid film dissolution of Ni-Cr at +0.2 V_{SCE} in the alkaline environment (Figure 4.24a), selective Ni-dissolution resulted in a slightly higher Cr cation fraction than the Ni-Cr-Mo alloy (Figure 4.26a). The film thickness was also consistently thinner on Ni-Cr-Mo at every potential, suggesting that despite the increase in dissolution, a greater driving force facilitated the formation of a thick film on Ni-Cr⁷². This difference was less noticeable in the alkaline environment, presumably because Ni- and Cr-oxide species are both thermodynamically stable³⁷. This resulted in a decreased driving force for passivation on Ni-Cr. In comparison to the films formed during passivation in Na₂SO₄, there is significantly greater Cr-enrichment for Ni-Cr-Mo in NaCl (Figure 3.22 versus Figure 4.25 and Figure 4.26). The films also appear thinner due to the effect of chloride-assisted dissolution.

4.6.4 *Ex situ* Characterization

4.6.4.1 Atomic Force Microscopy

At various times throughout the passivation processes, AFM imaging provided additional details concerning the influence of solution chemistry on the development of the surface topography. Once the oxide was electrochemically grown, the alloy surfaces were measured immediately after exposure to reduce the effect of ambient conditions on the surfaces. Several area sizes were measured using AFM (e.g. 5x5 and 2x2 μm²), with smaller areas (e.g. 100x100 to 500x500 nm²) used to provide representative topography measurements between polishing marks. Figure 4.27 shows a representative set of the AFM images captured after different passivation times for Ni-Cr in 0.1 M NaCl pH 4. The inset images give an accurate representation of the areas used to perform the RMS surface roughness measurements. The nucleation and growth of the film during the passivation process can also be represented using line scans across the inset images as given in Figure 4.28. The topographies of the air-oxidized surface are given separately from the electrochemically oxidized ones in Figure 4.28. The significant difference in each of these topographies measured using line scans demonstrates that the images and the relevant changes in surface morphology in Figure 4.27 are caused by electrochemically passivation and not any underlying roughness of the metal following polishing.

The coverage of the oxide particles increases with exposure time to the environment (Figure 4.27). However, the initially rough morphology caused by distinct islands of particles

which nucleated remains significant even after film growth occurs. This is a stark contrast to the film topography previously shown for passivation in a sulfate environment, where a smooth, conformal film was achieved after 1,000 s (Figure 3.22). Instead the local dissolution of the passive film as a result of chloride adsorption results in a perpetually rough, undulating surface even after the apparent coalescence of oxide nuclei. Between 10 and 100 s, Figure 4.28 shows a broadening in the oxides at the metal surface. This continues at longer times despite the chloride-induced chemical etching of the oxide surface.

The RMS values for Ni-Cr following passivation in the aqueous environment are given in Figure 4.29. The variability across the surface, indicated by the error bars in Figure 4.29, remains significant during the entire exposure time. This large deviation is caused by the markedly different RMS values obtained from a variety of spots on Ni-Cr. This difference can be understood by the known preferential grain dependent etching chloride displays when reacting with Ni-Cr alloys⁷³. Interestingly, the RMS value for the chloride is initially lower at 10 seconds than its sulfate counterpart (Figure 3.24). It is possible that the chloride-induced dissolution of the surface oxides results in less pronounced oxide heights, yielding a numerically lower RMS value. However, this effect changes after 100 s and the chloride begins to exhibit a rougher surface (Figure 4.29).

Ni-Cr-Mo, however, has a noticeably different surface topography after the same passivation conditions (Figure 4.30). Numerous perturbations exist at the surface, causing the measured RMS to be greater for Ni-Cr-Mo (1.36 nm) than the highest average measured value for Ni-Cr which occurred after passivation for 100 s (0.75 nm). This surface roughness can be attributed to the effect of Mo and provides evidence of it likely being enriched at the surface. Previously, Mo has been observed to re-passivate at the film surface in low pH environments in the form of polymeric species containing Mo⁶⁺^{53,74}. Dissolution of the passive film in the acidic, chloride environment can result in the redeposition of Mo cations on the surface, producing the rough morphology evident in Figure 4.30. For Ni-Cr, however, this re-passivation does not occur and instead, chloride-attack can result in the formation of metastable nanopits at the oxide surface (Figure 4.30b). These small features range from about 50 to 300 nm in diameter and occur on the otherwise smooth passive film on susceptible grain orientations⁷³ and contribute towards the high variability in the RMS. Even with the occurrence of film breakdown in Figure 4.30b, however, the measured RMS is considerably less than that of Ni-Cr-Mo (Figure 4.30a).

4.6.4.2 X-ray Photoelectron Spectroscopy

An example of the XPS spectra deconvolution for Ni-Cr-Mo passivated for 10 ks in 0.1 M NaCl pH 4 is shown in Figure 4.31. The fitted peaks indicate each observed metallic, hydroxide, and oxide species. Based on the spectra peaks, the consistent hydroxide and oxide species included were Ni(OH)₂, NiO, Cr(OH)₃, Cr₂O₃, MoO₂, and MoO₃ with the utilized spectral fitting parameters given in Table 3.1. It should be noted that previous literature has additionally identified spinel compounds (e.g. NiCr₂O₄)⁷⁵⁻⁷⁹, but they were found during peak fitting to constitute an insignificant fraction (~1%) of the total integrated area and as such was excluded from analysis. The integrated peak areas for the aforementioned passive film species are directly compared to each other, and the ICP-MS measurements of film metal cation composition for both alloys passivated at +0.2 V_{SCE} in 0.1 M NaCl adjusted to pH 4 and 10 were given in Figure 4.11 and Figure 4.14, respectively.

In the acidic environment, Ni-Cr-Mo exhibited greater enrichment of Cr-species, resulting in a higher cation fraction of Cr³⁺ according to the peak areas and Equation 3.6 (Figure 4.33 and Figure 4.35). This result agrees with the previous observation that Ni-rich films form first, followed by the slower growth of Cr-rich ones (Figure 4.9-Figure 4.10 and Figure 4.32-Figure 4.35)^{50,79}. Additionally, the result supports the previous theory¹⁰ that Mo alloying promotes the oxidation of Cr. Upon comparing passivation in an acidic environment (Figure 4.11) to that in an alkaline one (Figure 4.14), there is an apparent difference between the films. Notably, the fraction of Ni²⁺ as measured using XPS peak fitting and ICP-MS analysis remained steady for Ni-Cr, whereas there was minor enrichment of Cr³⁺ within the film on Ni-Cr-Mo throughout the passivation time. For all times, there was additionally a slightly greater fraction of Cr³⁺ within the film on Ni-Cr-Mo than on Ni-Cr after 10 ks (Figure 4.11 and Figure 4.14). Finally, the calculated enrichment of Mo^{4,6+} cations was lower for pH 10 (Figure 4.14) than that observed at pH 4 (Figure 4.11), due to its likely selective dissolution in the alkaline environment as MoO₄²⁻.

In the alkaline environment, some NiO peaks were discernable at 10 s, but afterwards the measured spectra was essentially representative of only Ni metal and Ni(OH)₂ (Figure 4.34 and Figure 4.35). The same applied for Cr, where Cr₂O₃ and Cr(OH)₃ formed quickly and the former became quickly hydrated. There was clear oxide species present at all times in the acidic environment because of the influence of its favorable thermodynamics over the hydroxides,

whereas both were stable at pH 10 and the oxides remain hydrated as $\text{Ni}(\text{OH})_2$ and $\text{Cr}(\text{OH})_3$. Less $\text{Mo}^{4,6+}$ was found within the passive film and, as explained previously, this can be attributed to its poor thermodynamic stability in high pH environments. The low oxide concentration and corresponding depletion of Mo at the surface of the base alloy caused a poor Mo 3d signal, requiring more cumulative scans to produce Figure 4.35.

The spectra obtained after 10 ks were also characterized at a 45° take-off angle to indicate any preferential segregation of cations to the metal/film or film/electrolyte interface, along with the presence of bilayer versus solid solution oxides (Figure 4.36-Figure 4.38)⁸⁰⁻⁸². Comparisons of the oxide areas at 90° and 45° for each individual metal can suggest relative variations in the chemical distribution of the passive film. The results for Ni-Cr suggest that after 10 ks of passivation at $+0.2 \text{ V}_{\text{SCE}}$, there is slight surface enrichment of Cr^{3+} in the pH 4 environment, presumably caused by preferential Ni^{2+} dissolution (Figure 4.36ac). However, substantial surface enrichment of Ni^{2+} was observed in the alkaline environment. There is still some Cr^{3+} present, however, suggesting that the film composition remains mixed. In Figure 4.36b,d, the metal peaks are not present due to the thickness of the film and the low probing depth of x-rays at a photoelectron take-off angle of 45° (approximately 3.5 nm). Because this depth is less than the film thickness (approximately 6.5 nm), it can be rationalized that a clear $\text{Ni}(\text{OH})_2/\text{Cr}(\text{OH})_3$ layered structure is not present as the inner $\text{Cr}(\text{OH})_3$ would not be present at low take-off angles. Ni-Cr-Mo, however, has different distributions of cations evident in the angle-resolved spectra as a result of Mo and its promotion of Cr-oxidation (Figure 4.37 and Figure 4.38). In the acidic environment, there is enrichment of Ni^{2+} and Mo^{6+} evident at the oxide surface whereas in the alkaline one, there is only some depletion of Mo^{6+} as a result of its reduced thermodynamic stability, as previously discussed. These results indicate only, however, relative changes and do not provide true composition profiles. As such, limited tomography experiments were performed and the results are presented in the following section.

4.6.4.3 3D Atom Probe Tomography

The atomic resolution of APT enables a more detailed representation of the physical and chemical structure of nanometer-thick passive films on Ni-Cr (Figure 4.40) and Ni-Cr-Mo (Figure 4.41 and Figure 4.42). Similar to the passive film on Ni-Cr formed in Na_2SO_4 (Figure 3.28), there

is no apparent layering of any Ni or Cr-oxides within the film layer formed on Ni-Cr following passivation in the chloride environment. The ratio of Ni- and Cr-oxides remains around 2.5:1, respectively, until increasing at the metal/film interface as the fraction of O decreases significantly in unoxidized area of the tip. There is additionally no enrichment within the film despite the assertions in previous literature of this phenomena^{32,70,71}. Instead the oxide appears similar to a solid solution of NiO/Ni(OH)₂ and Cr₂O₃/Cr(OH)₃ based on the chemical compounds states detected by XPS (Figure 4.32). This observation is indicative of a solute-captured passive oxide forming, which will be explained in more detail in Chapter 6.

While the previous APT results implied very similar passive films for Ni-Cr and Ni-Cr-Mo in sulfate environments (Figure 3.28 and 3.29), drastically different cation profiles were measured for Ni-Cr-Mo following passivation in NaCl (Figure 4.41 and Figure 4.42). An outer, Ni-rich region in the passive film is present and substantially enriched in Mo^{4,6+}, as was previously indicated in the sulfate environment. Beneath this, however, is a Cr-rich region where the ratio of Ni²⁺ to Cr³⁺ goes closer towards 1:1. The APT results indicate accumulation of Mo^{4,6+} at the metal/film interface and, therefore, some depletion at the metal surface. Based on the compositions of the apparently chemical layers, there is still no distinct NiO/Ni(OH)₂ and/or Cr₂O₃/Cr(OH)₃, however. Ni²⁺ remains enriched throughout the passive film with some solute Cr³⁺ and Mo^{4,6+} present at certain thicknesses. This occurrence is due in part to the effect of chloride-assisted film dissolution, but also the promotion of Cr-enrichment in the presence of Mo alloying additions.

Unique to the APT results in chloride are the occurrence of oxide fingers penetrating into the metallic tip (Figure 4.40 and Figure 4.41). This phenomena has been rationalized to occur due to metastable nanopitting and repassivation within the corroded area⁸³. These regions were roughly 30 nm deep and 10 nm wide. While there was no metallurgical channels for local breakdown present (e.g. a grain boundary or secondary phase), some morphological instability²⁰ likely produced by the sample preparation process was likely attacked preferentially by the chloride anions in solution and produced the nanopit before the surface was repaired via repassivation. The oxide fingers into Ni-Cr-Mo are substantially shorter than those on Ni-Cr: 10 nm versus 30 nm. This is due to the effect of Mo alloying additions on increasing repassivation following film breakdown in the presence of chloride.

Chloride-attack at the film/electrolyte interface resulted in some Cl signal in the APT results (Figure 4.40 and Figure 4.42). For Ni-Cr, the chloride concentration was high (~5 at. %) at the oxide surface and decreases rapidly to zero moving into the oxide (about 1 nm in depth), which clearly indicates that there is chemical absorption on the surface rather than any incorporation of chlorine ion into the oxide layers. This would be unlikely, because the chlorine ionic radius is large and its penetration would be difficult, or rather impossible, according to prior DFT calculations^{4,83}. The adsorption of Cl⁻ was apparently less on the surface of Ni-Cr-Mo, perhaps due to local repassivation at any absorption sites. There was a clear effect of the halide anions on the passive film compositions, however. Both Ni-Cr and Ni-Cr-Mo exhibited greater, overall enrichment of Cr³⁺ in the acidic NaCl environment compared to their counterparts in sulfate (Figures 3.28 and 3.29).

Overall the APT findings confirm several of the previous assertions made using *in operando*, *in situ*, and even the *ex situ* XPS results. The passive films are enriched in Ni²⁺ relative to Cr³⁺ and, for Ni-Cr-Mo, Mo^{4,6+}. While there is some enrichment of Mo^{4,6+} at the film/electrolyte interface, it is likely insufficient to form a distinct phase and rather the cations are operating as substitutional defects in the Ni-rich oxide. Ni-Cr-Mo had greater, relative enrichment of Cr³⁺ than Ni-Cr and the presence of Mo at various locations in the film had strong implications for the local breakdown of passive films. The influence of dissolution resulted in some cation segregation within the passive film, but no layering of oxide species was evident as the films remained richest in Ni²⁺, with areas of relative Cr³⁺ and Mo^{4,6+} enrichment present because of preferential Ni²⁺ ejection.

4.7 Discussion

4.7.1 Influence of Chloride and pH

The thermodynamic favorability of Cr-rich oxides and spinels relative to NiO and Ni(OH)₂ is well known. For instance, $\Delta G_{f NiO}^o = -212 \frac{kJ}{mol}$, $\Delta G_{f Ni(OH)_2}^o = -447 \frac{kJ}{mol}$, $\Delta G_{f Cr_2O_3}^o = -1,058 \frac{kJ}{mol}$, $\Delta G_{f Cr(OH)_3}^o = -834 \frac{kJ}{mol}$, and $\Delta G_{f NiCr_2O_4}^o = -1,257 \frac{kJ}{mol}$ ⁸⁴. Based on both conventional Pourbaix diagrams^{37,85} (Figure 4.7) and chemical stability diagrams⁸⁶, the expected stoichiometric oxides at +0.2 V_{SCE} are Cr₂O₃ and Cr(OH)₃ in acidic and alkaline environments, while NiO and Ni(OH)₂ are stable at a pH greater than 5^{56,57}.

The results in Figure 4.11 appear to differ from these predictions. The film was measured to predominantly contain Ni^{2+} as a result of slow dissolution kinetics. At early oxidation times, the rapidly moving oxidation front results in passive film cation fractions approximate to the bulk metal composition as a result of non-equilibrium solute capture (NSC), i.e. 22 wt. % Cr^{3+} becomes frozen into the NiO lattice as non-stoichiometric $\text{Cr}_{1-x}\text{Ni}_x\text{O}_{1.5-x/2}$ ⁵⁰. However, gradual enrichment of Cr^{3+} results in the behavior shown in Figure 4.11 and Figure 4.14. Additionally, the SLD profiles in Figure 4.21 and Figure 4.22 suggest the existence of solute-captured films as no distinct layers are observed.⁶ The results indicate a very different picture of aqueous electrochemical passivation than has been previously reported^{3,26,28,31–33,87–90}. Ni and Cr are equally oxidized at the early stages of passivation in acidic and alkaline chloride solutions according to the ICP-MS (Figure 4.9-Figure 4.14) and XPS (Figure 4.11 and Figure 4.14) results.

Upon passivating the alloys in the alkaline environment, Ni^{2+} cations in the film remain passive at all times and no preferential ejection occurs, enabling Cr^{3+} enrichment (Figure 4.14). Instead, film thickening continues with notably slower preferential enrichment of the more thermodynamically stable, Cr-rich species. Similar stability of Ni^{2+} -rich oxides in an alkaline environment was observed in previous literature⁸⁹. The concentrations of Mo^{4+} and Mo^{6+} metal cations, as governed initially by NSC, both increased in the film with passivation time, with the latter having greater peak areas and thus a greater film concentration (Figure 4.31), albeit both were low compared to Ni^{2+} and Cr^{3+} . It is possible that $\text{Mo}^{4,6+}$ substitutes for Cr^{3+} in the films, as will be discussed later.

The interplay between kinetics and thermodynamics apparently results in the nucleation and growth of NiO/Ni(OH)₂ along with Cr₂O₃/Cr(OH)₃^{89,90}. When surface energy is factored into oxide stability, the Ni/NiO epitaxy may favor NiO and any hydrated, overlying Ni(OH)₂^{33,91–93}. Later during passivation, enrichment is driven by kinetic factors^{93,94}. Preferential dissolution of Ni^{2+} in chloride environments enables further enrichment of Cr^{3+} in the film. Following 8+ hrs of passivation in harsh chloride electrolytes, this enrichment has been previously shown to result in Cr-rich species dominating the passive film for other commercial Ni alloys of similar alloying

⁶ The existence of NiO and Cr₂O₃ nuclei next to each other could produce similar SLD versus depth curves, but this nanoscale heterogeneous surface has not yet been observed experimentally and would be prone to localized corrosion at the Cr-depleted surface areas.

compositions^{26,28,29,32,95}. Notably, Ni-20 Cr, wt%, passivated in 1 M NaOH and 0.5 M H₂SO₄ exhibited a film richer in Cr³⁺ for the latter environment and became increasingly enriched with time⁸⁹. At these longer times, significant enrichment of solute Cr³⁺ cations can result in the formation of non-stoichiometric corundum with a chemical composition of Cr_{2-x}Ni_xO_{3-y}. This classically Cr³⁺-rich film can still contain significant amounts of Ni²⁺ cations until longer times at which point annealing would produce stoichiometric films not representative of NSC⁵⁰. The oxides evidently first form according to the principles of NSC but then kinetics dominates until a steady-state has been reached and thermodynamics controls the film structure and composition³³.

4.7.2 Chemical Identity of Passive Films

The passive films on Ni-Cr and Ni-Cr-Mo were predominantly rich in Ni²⁺ during the 10 ks passivation time, with Cr-enrichment occurring continuously and especially for the Mo-containing alloy. The NR and 3DAPT results suggest that the film on Ni-Cr is more representative of solute capture than Ni-Cr-Mo, with inner enrichment of Cr³⁺ occurring after a steady-state film thickness has been reached. In the alkaline environment, the chemical stability of Ni species resulted in substantial Ni-enrichment at the oxide surface which is not dissolved during exposure to the environment. This was not observed for Ni-Cr-Mo in the same environment as both Ni and Cr are oxidized during the entire passivation time due to the effect of Mo. This element exists as primarily Mo⁶⁺ in the film at longer exposure times, albeit at low concentrations. At pH 4, it and Ni²⁺ are enriched at the oxide surface but Mo cations are depleted in the outer region of the film at pH 10.

In previous work, the existence of Mo-oxides within passive films was proposed with no detailed explanation of the quantity or location¹¹. Moreover, the cation molecular identity was attributed to stoichiometric MoO₂ and MoO₃^{37,96-98}. The presence of Mo alloying additions also resulted in the increased enrichment of Cr³⁺ within the passive film^{32,99}. This phenomenon is evident in Figure 4.11 and Figure 4.14, where the fraction of Cr³⁺ tends to be higher, especially after long passivation times. Fundamental density-functional theory (DFT) models have recently demonstrated that Mo promotes the adsorption of O on Ni-Cr surfaces⁹⁹. In particular, the theorized synergistic oxidation of Cr in the presence of Mo was shown to result from the favorable adsorption energy compared to surface sites containing Ni. In this (Figure 4.11, Figure 4.14, Figure

4.25, and Figure 4.26) and previous passivation studies^{32,52,58,100}, similar behavior has been observed where Ni-Cr-Mo alloys exhibited greater fractions of Cr^{3+} species in their films. Other recent DFT studies have demonstrated the increased favorability of corundum upon alloying with Mo, where the driving force for nucleation decreases by 0.64 eV per Mo atom in the oxide formula unit cell⁷⁹. The impact of Mo on encouraging Cr passivation is only one of the several proposed theories regarding film growth and stability¹⁰.

4.7.3 Electronic Properties of Passive Films

The passive films on Ni-Cr and Ni-Cr-Mo during passivation in an acidic and alkaline environment exhibited different electronic behavior. At pH 4, the passive films were controlled by n-type behavior whereas p-type was observed at pH 10. This was a result of the dominant point defects for each alloy and environment combination. At +0.2 V_{SCE} , however, acceptor defects were observed to dominate. This suggests that for the operando passivation results shown, oxygen vacancies dictate the relevant oxidation kinetics¹⁰¹. The flux of the latter was the point defect within a passive film has been previously theorized to be the rate determining step for passivation¹⁰¹⁻¹⁰³. Greater range of p-type defect behavior was measured for Ni-Cr-Mo due the substitutional doping of Mo as a positively-charged defect. The effect of chloride resulted in an increase in n-type defects (i.e. N_D) as metal cation vacancies are generated by chloride adsorption (Figure 4.17). This effect was much greater for Ni-Cr compared to Ni-Cr-Mo in the acidic environment. In comparison, N_A increases early due to the initial defective nature of the passive films, but at longer times electron holes can be annihilated and produce the observed decrease⁶⁴.

The observed influence of Mo on oxidation processes has also been attributed to the element acting as a dopant with very high concentrations (at% rather than ppm) and modifying the electronic properties of the ternary alloy. The addition of small concentrations of Mo^{6+} in the passive film will result in the formation of substitutional defects (i.e. $\text{Mo}_{\text{Ni}}^{4\cdot}$, and $\text{Mo}_{\text{Cr}}^{\cdot\cdot}$) following rapid oxidation and solute capture^{50,64,79}. The SVIM suggests this phenomena will result in improvements in the film's electrochemical stability following the annihilation of p-type metal cation vacancy defects (e.g. $V_{\text{Ni}}^{\prime\prime}$ and $V_{\text{Cr}}^{\prime\prime\prime}$), which are theorized to be major contributors to the initiation of localized corrosion^{64,104}. This is posited to occur by the interaction between the positively-charged substituted Mo site and negatively-charged metal cation vacancies, forming

less mobile, neutral defects. The diffusion of these defects is not accelerated by the electric field and, as such, won't contribute towards film growth and/or breakdown reactions^{34,104,105}. The effect of Mo is also demonstrated through increases in E_{FB} for Ni-Cr-Mo in comparison to Ni-Cr. The continued enrichment of Cr^{3+} in the film also increases E_{FB} and the related increase in the pitting resistance of a passive film^{52,58,65–68}.

4.8 Conclusions

The passivation and dissolution of Ni-22 Cr and Ni-22-6 Mo (wt%), were investigated during *in operando* potentiostatic conditions using electrochemical ICP-MS and SF-EIS in both an acidic and alkaline NaCl environment, coupled with *in situ* NR and *ex-situ* XPS conducted during and following film growth. The combination of the techniques utilized enabled determination of i_{ox} distinctly from i_{EC} with high temporal resolution. Contrary to some previous work which suggested rapid NiO formation in a chloride-free environment, it was determined that both Ni and Cr-rich films form early during the passivation process, indicating the combined influence of thermodynamic and kinetic factors. Surface films produced during anodic polarization at +0.2 V_{SCE} were consistent with non-stoichiometric solid solution rocksalt and corundum oxide structures, likely containing solute captured Ni^{2+} , Cr^{3+} , and $Mo^{4,6+}$ cations. No layering was observed during oxide formation, with the films instead being Ni-rich at the film/electrolyte and Cr-rich at the metal/film interfaces. Oxides were first formed, with compositions governed by non-equilibrium solute capture. At long times, kinetic factors enabled enrichment whereas thermodynamics determined the longer-term passive film behavior. The electrochemical stability of Cr^{3+} cations also increased with alloying of Mo in the base metal, noted by the respective dissolution currents being measured below the detection limit for the Ni-Cr-Mo alloy in each environment. Surface films produced during anodic polarization in the alkaline environment were found to be enriched in Ni^{2+} cations because of the increased stability of NiO and Ni(OH)₂.

4.9 References

1. Rebak, R. B. *Corrosion and Environmental Degradation. Corrosion and Environmental Degradation Vol. II* (2000).
2. Rebak, R. B. Corrosion of Non-Ferrous Alloys. I. Nickel-, Cobalt-, Copper-, Zirconium- and Titanium-Based Alloys. in *Materials Science and Technology* 71–111 (Wiley-VCH Verlag GmbH & Co. KGaA, 2013). doi:10.1002/9783527603978
3. Rebak, R. B. & Payer, J. H. Passive corrosion behavior of alloy 22. in *11th International*

- High Level Radioactive Waste Management Conference* 1–7 (2006).
4. Marks, L. Competitive Chloride Chemisorption Disrupts Hydrogen Bonding Networks: DFT, Crystallography, Thermodynamics and Morphological Consequences. *Corrosion* **74**, 295–311 (2017).
 5. Natishan, P. M. *et al.* Chloride Interactions with the Passive Films on Stainless Steel. *J. Electrochem. Soc.* **158**, C7 (2011).
 6. Hornus, E. C., Giordano, C. M., Rodriguez, M. A., Carranza, R. M. & Rebak, R. B. Effect of Temperature on the Crevice Corrosion of Nickel Alloys Containing Chromium and Molybdenum. *J. Electrochem. Soc.* **162**, C105–C113 (2014).
 7. Zhang, X. & Shoesmith, D. W. Influence of temperature on passive film properties on Ni-Cr-Mo Alloy C-2000. *Corros. Sci.* **76**, 424–431 (2013).
 8. Evans, K. J. *et al.* Long term corrosion potential and corrosion rate of creviced Alloy 22 in chloride plus nitrate brines. in *NACE - International Corrosion Conference Series* 1–25 (2006).
 9. Rebak, R. B. Factors affecting the crevice corrosion susceptibility of alloy 22. in *Corrosion* 1–17 (2005).
 10. Lutton Cwalina, K., Demarest, C. R., Gerard, A. Y. & Scully, J. R. Revisiting the effects of molybdenum and tungsten alloying on corrosion behavior of nickel-chromium alloys in aqueous corrosion. *Curr. Opin. Solid State Mater. Sci.* (2019).
 11. Scully, J. R. Corrosion chemistry closing comments: opportunities in corrosion science facilitated by operando experimental characterization combined with multi-scale computational modelling. *Faraday Discuss. Faraday Discuss* **180**, 577–593 (2015).
 12. Bouzoubaa, A., Diawara, B., Maurice, V., Minot, C. & Marcus, P. Ab initio study of the interaction of chlorides with defect-free hydroxylated NiO surfaces. *Corros. Sci.* **51**, 941–948 (2009).
 13. Landolt, D., Mischler, S., Vogel, A. & Mathieu, H. J. Chloride Ion Effects on Passive Films on FeCr and FeCrMo Studied by AES, XPS and SIMS. *Corros. Sci.* **31**, 431–440 (1990).
 14. Natishan, P. M. & O’Grady, W. E. Chloride Ion Interactions with Oxide-Covered Aluminum Leading to Pitting Corrosion: A Review. *J. Electrochem. Soc.* **161**, C421–C432 (2014).
 15. Seyeux, A., Maurice, V., Klein, L. H. & Marcus, P. In Situ STM Study of the Effect of Chloride on Passive Film on Nickel in Alkaline Solution. *J. Electrochem. Soc.* **153**, B453–B463 (2006).
 16. Rodríguez, M. A., Carranza, R. M. & Rebak, R. B. Passivation and Depassivation of Alloy 22 in Acidic Chloride Solutions. *J. Electrochem. Soc.* **157**, C1–C8 (2010).
 17. Bouzoubaa, A., Diawara, B., Maurice, V., Minot, C. & Marcus, P. Ab initio modelling of localized corrosion: Study of the role of surface steps in the interaction of chlorides with passivated nickel surfaces. *Corros. Sci.* **51**, 2174–2182 (2009).
 18. Heine, M. A., Keir, D. S. & Pryor, M. J. The Specific Effects of Chloride and Sulfate Ions on Oxide Covered Aluminum. *J. Electrochem. Soc.* **112**, 24–32 (1965).
 19. Taylor, C. D., Lu, P., Saal, J., Frankel, G. S. & Scully, J. R. Integrated computational materials engineering of corrosion resistant alloys. *npj Mater. Degrad.* **2**, 1–10 (2018).
 20. Ramanathan, R. & Voorhees, P. W. Morphological Stability of Steady-State Passive Oxide Films. *Electrochim. Acta* (2019).
 21. Okada, T. Considerations of the Stability of Pit Repassivation during Pitting Corrosion of

- Passive Metals. *J. Electrochem. Soc.* **131**, 1026–1032 (1984).
22. Okada, T. A Theory of Perturbation-Initiated Pitting. *J. Electrochem. Soc.* **132**, 537–544 (1985).
 23. Vetter, K. J. & Gorn, F. Kinetics of layer formation and corrosion processes of passive iron in acid solutions. *Electrochim. Acta* **18**, 321–326 (1973).
 24. Lutton Cwalina, K., Blades, W. H., Reinke, P. & Scully, J. R. Oxide Morphologies during Electrochemical Passivation in Sulfate and Chloride Environments PLACEHOLDER. (2019).
 25. Marcus, P., Maurice, V. & Strehblow, H. H. Localized corrosion (pitting): A model of passivity breakdown including the role of the oxide layer nanostructure. *Corros. Sci.* **50**, 2698–2704 (2008).
 26. Lloyd, A. C., Noël, J. J., McIntyre, N. S. & Shoesmith, D. W. The open-circuit ennoblement of alloy C-22 and other Ni-Cr-Mo alloys. *JOM* **57**, 31–35 (2005).
 27. Jakupi, P., Zagidulin, D., Noël, J. J. & Shoesmith, D. W. The impedance properties of the oxide film on the Ni-Cr-Mo Alloy-22 in neutral concentrated sodium chloride solution. *Electrochim. Acta* **56**, 6251–6259 (2011).
 28. Zhang, X., Zagidulin, D. & Shoesmith, D. W. Characterization of film properties on the NiCrMo Alloy C-2000. *Electrochim. Acta* **89**, 814–822 (2013).
 29. Ebrahimi, N., Biesinger, M. C., Shoesmith, D. W. & Noël, J. J. The influence of chromium and molybdenum on the repassivation of nickel-chromium-molybdenum alloys in saline solutions. *Surf. Interface Anal.* **49**, 1359–1363 (2017).
 30. Hayes, J. R., Gray, J. J., Szmodis, A. W. & Orme, C. A. Influence of chromium and molybdenum on the corrosion of nickel-based alloys. *Corrosion* **62**, 491–500 (2006).
 31. Gray, J. J., Hayes, J. R., Gdowski, G. E., Viani, B. E. & Orme, C. A. Influence of Solution pH, Anion Concentration, and Temperature on the Corrosion Properties of Alloy 22. *J. Electrochem. Soc.* **153**, B61–B67 (2006).
 32. Lloyd, A. C., Noël, J. J., McIntyre, S. & Shoesmith, D. W. Cr, Mo and W alloying additions in Ni and their effect on passivity. *Electrochim. Acta* **49**, 3015–3027 (2004).
 33. Lutton, K., Gusieva, K., Ott, N., Birbilis, N. & Scully, J. R. Understanding multi-element alloy passivation in acidic solutions using operando methods. *Electrochem. commun.* **80**, 44–47 (2017).
 34. Macdonald, D. D. The Point Defect Model for the Passive State. *J. Electrochem. Soc.* **139**, 3434–3449 (1992).
 35. Standard test method for conducting cyclic potentiodynamic polarization measurements to determine the corrosion susceptibility of small implant devices. *ASTM F2129-06* (2001).
 36. Sato, N. Anodic breakdown of passive films on metals. *J. Electrochem. Soc.* **129**, 255–260 (1982).
 37. Pourbaix, M. *Atlas of electrochemical equilibria in aqueous solutions*. (National Association of Corrosion Engineers, 1974).
 38. Strohmeier, B. R. An ESCA method for determining the oxide thickness on aluminum alloys. *Surf. Interface Anal.* **15**, 51–56 (1990).
 39. Biesinger, M. C. *et al.* Resolving surface chemical states in XPS analysis of first row transition metals, oxides and hydroxides: Cr, Mn, Fe, Co and Ni. *Appl. Surf. Sci.* **257**, 2717–2730 (2011).
 40. Werfel, F. & Minni, E. Photoemission study of the electronic structure of Mo and Mo

- oxides. *J. Phys. C Solid State Phys.* **16**, 6091–6100 (1983).
41. Moulder, J. F., Stickle, W. F., Sobol, P. E. & Bomben, K. D. Handbook of X-ray Photoelectron Spectroscopy. 261 (1992).
 42. Biesinger, M. C., Payne, B. P., Lau, L. W. M., Gerson, A. & Smart, R. S. C. X-ray photoelectron spectroscopic chemical state Quantification of mixed nickel metal, oxide and hydroxide systems. *Surf. Interface Anal.* **41**, 324–332 (2009).
 43. Biesinger, M. C. *et al.* Quantitative chemical state XPS analysis of first row transition metals, oxides and hydroxides. *J. Phys. Conf. Ser.* **100**, 012025 (2008).
 44. Baltrusaitis, J. *et al.* Generalized molybdenum oxide surface chemical state XPS determination via informed amorphous sample model. *Appl. Surf. Sci.* **326**, 151–161 (2015).
 45. Fritzsche, H. *et al.* Neutron Reflectometry. in *Neutron Scattering and Other Nuclear Techniques for Hydrogen in Materials* 115–158 (Springer, Cham, 2016). doi:10.1007/978-3-319-22792-4_5
 46. Penfold, J. & Thomas, R. K. The application of the specular reflection of neutrons to the study of surfaces and interfaces. *J. Phys. Condens. Matter* **2**, 1369–1412 (1990).
 47. Parratt, L. G. Surface studies of solids by total reflection of x-rays. *Phys. Rev.* **95**, 359–369 (1954).
 48. Björck, M. & Andersson, G. GenX: An extensible X-ray reflectivity refinement program utilizing differential evolution. *J. Appl. Crystallogr.* **40**, 1174–1178 (2007).
 49. Nečas, D. & Klapetek, P. Gwyddion: An open-source software for SPM data analysis. *Cent. Eur. J. Phys.* **10**, 181–188 (2012).
 50. Yu, X. X. *et al.* Nonequilibrium Solute Capture in Passivating Oxide Films. *Phys. Rev. Lett.* **121**, 145701 (2018).
 51. Rebak, R. B. & Crook, P. Influence of the Environment on the General Corrosion Rate of Alloy 22. in *American Society of Mechanical Engineers Pressure Vessels and Piping Division Conference* 1–8 (2004). doi:10.1115/PVP2004-2793
 52. Lillard, R. S., Jurinski, M. P. & Scully, J. R. Crevice Corrosion of Alloy-625 in Chlorinated ASTM Artificial Ocean Water. *Corrosion* **50**, 251–265 (1994).
 53. Henderson, J. D., Li, X., Shoesmith, D. W., Noël, J. J. & Ogle, K. Molybdenum surface enrichment and release during transpassive dissolution of Ni-based alloys. *Corros. Sci.* **147**, 32–40 (2019).
 54. Kobe, B. *et al.* Application of quantitative X-ray photoelectron spectroscopy (XPS) imaging: investigation of Ni-Cr-Mo alloys exposed to crevice corrosion solution. *Surf. Interface Anal.* **49**, 1345–1350 (2017).
 55. Shkirskiy, V., Maciel, P., Deconinck, J. & Ogle, K. On The Time Resolution of the Atomic Emission Spectroelectrochemistry Method. *J. Electrochem. Soc.* **163**, C37–C44 (2016).
 56. Huang, L.-F., Hutchison, M. J., Santucci, R. J., Scully, J. R. & Rondinelli, J. M. Improved Electrochemical Phase Diagrams from Theory and Experiment: The Ni-Water System and Its Complex Compounds. *J. Phys. Chem. C* **121**, 9782–9789 (2017).
 57. Huang, L.-F. & Rondinelli, J. Electrochemical Stabilities of Ni-Based Compounds from Bulk to Nanoscale Dimensions. *Bull. Am. Phys. Soc.* (2018).
 58. Sugimoto, K. & Sawada, Y. Role of Alloyed Molybdenum in Austenitic Stainless Steels in the Inhibition of Pitting in Neutral Halide Solutions. *Corrosion* **32**, 347–352 (1976).
 59. Sugimoto, K. & Sawada, Y. The role of molybdenum additions to austenitic stainless steels in the inhibition of pitting in acid chloride solutions. *Corros. Sci.* **17**, 425–445 (1977).

60. Lizlovs, E. A. & Bond, A. P. Anodic Polarization Behavior of 25% Chromium Ferritic Stainless Steels. *J. Electrochem. Soc.* **118**, 22–28 (1971).
61. Olefjord, I. The passive state of stainless steels. *Mater. Sci. Eng.* **42**, 161–171 (1980).
62. Marshall, P. I. & Burstein, G. T. Effects of alloyed molybdenum on the kinetics of repassivation on austenitic stainless steels. *Corros. Sci.* **24**, 463–478 (1984).
63. Tomio, A. *et al.* Role of alloyed molybdenum on corrosion resistance of austenitic Ni–Cr–Mo–Fe alloys in H₂S–Cl⁻ environments. *Corros. Sci.* **98**, 391–398 (2015).
64. Hutchison, M. J. & Scully, J. R. Solute Capture and Doping of Al in Cu₂O: Corrosion, Tarnish Resistance, and Cation Release of High-Purity Cu–Al Alloys in Artificial Perspiration. *J. Electrochem. Soc.* **165**, C689–C702 (2018).
65. Newman, R. C. The dissolution and passivation kinetics of stainless alloys containing molybdenum—II. Dissolution kinetics in artificial pits. *Corros. Sci.* **25**, 341–350 (1985).
66. Zadorozne, N. S., Giordano, C. M., Rodríguez, M. A., Carranza, R. M. & Rebak, R. B. Crevice corrosion kinetics of nickel alloys bearing chromium and molybdenum. *Electrochim. Acta* **76**, 94–101 (2012).
67. Tobler, W. J. & Virtanen, S. Effect of Mo species on metastable pitting of Fe₁₈Cr alloys—A current transient analysis. *Corros. Sci.* **48**, 1585–1607 (2006).
68. Emran, K. M. & Al-Refai, H. Pitting resistivity of Ni-based bulk metallic glasses in chloride solution. *RSC Adv.* **7**, 37349–37358 (2017).
69. Mishra, A. K. & Shoesmith, D. W. Effect of Alloying Elements on Crevice Corrosion Inhibition of Nickel-Chromium-Molybdenum-Tungsten Alloys Under Aggressive Conditions: An Electrochemical Study. *Corrosion* **70**, 721–730 (2014).
70. Zhang, X. & Shoesmith, D. W. Influence of temperature on passive film properties on Ni–Cr–Mo Alloy C-2000. *Corros. Sci.* **76**, 424–431 (2013).
71. Zhang, X., Qin, Z., Zagidulin, D., Noël, J. J. & Shoesmith, D. W. Effect of Oxide Film Properties on the Kinetics of O₂ Reduction on Alloy C-22. *J. Electrochem. Soc.* **164**, 911–917 (2017).
72. Lutton Cwalina, K. *et al.* In Operando Analysis of Passive Film Growth on Ni–Cr and Ni–Cr–Mo Alloys in Chloride Solutions. *J. Electrochem. Soc.* **166**, C3241–C3253 (2019).
73. Gusieva, K. *et al.* Repassivation Behavior of Individual Grain Facets on Dilute Ni–Cr and Ni–Cr–Mo Alloys in Acidified Chloride Solution. *J. Phys. Chem. C* **122**, 19499–19513 (2018).
74. Jakupi, P., Wang, F., Noël, J. J. & Shoesmith, D. W. Corrosion product analysis on crevice corroded Alloy-22 specimens. *Corros. Sci.* **53**, 1670–1679 (2011).
75. Luo, L. *et al.* In situ atomic scale visualization of surface kinetics driven dynamics of oxide growth on a Ni–Cr surface. *Chem. Commun.* **52**, 3300–3303 (2016).
76. Luo, L. *et al.* In-situ transmission electron microscopy study of surface oxidation for Ni–10Cr and Ni–20Cr alloys. *Scr. Mater.* **114**, 129–132 (2016).
77. Baran, G. R. Oxide Compounds on Ni–Cr Alloys. *J. Dent. Res.* **63**, 1332–1334 (1984).
78. Unutulmazsoy, Y., Merkle, R., Mannhart, J. & Maier, J. Chemical diffusion coefficient of Ni in undoped and Cr-doped NiO. *Solid State Ionics* **309**, 110–117 (2017).
79. Yu, X. *et al.* In-situ observations of early stage oxidation of Ni–Cr and Ni–Cr–Mo alloys. *Corrosion* **74**, 939–946 (2018).
80. Jeng, S.-P., Holloway, P. H. & Batich, C. D. Surface passivation of Ni/Cr alloy at room temperature. *Surf. Sci.* **227**, 278–290 (1990).

81. Marcus, P. & Grimal, J. M. The anodic dissolution and passivation of NiCrFe alloys studied by ESCA. *Corros. Sci.* **33**, 805–814 (1992).
82. Wegrelius, L. Passivation of Stainless Steels in Hydrochloric Acid. *J. Electrochem. Soc.* **146**, 1397 (1999).
83. Yu, X., Gulec, A., Lutton Cwalina, K., Scully, J. & Marks, L. New Insights on the Role of Chloride During the Onset of Local Corrosion: TEM, APT, Surface Energy, and Morphological Instability. *CORROSION* (2019). doi:10.5006/2991
84. Speight, J. G. & Lange, N. A. *Lange's handbook of chemistry*. (McGraw-Hill Education, 2017).
85. Lu, P. *et al.* Computational materials design of a corrosion resistant high entropy alloy for harsh environments. *Scr. Mater.* **153**, 19–22 (2018).
86. Santucci, R. J., McMahon, M. E. & Scully, J. R. Utilization of chemical stability diagrams for improved understanding of electrochemical systems: evolution of solution chemistry towards equilibrium. *npj Mater. Degrad.* **2**, 1 (2018).
87. Rodríguez, M. A. & Carranza, R. M. Properties of the Passive Film on Alloy 22 in Chloride Solutions Obtained by Electrochemical Impedance. *J. Electrochem. Soc.* **158**, C221 (2011).
88. Kehler, B. A., Ilevbare, G. O. & Scully, J. R. Comparison of the crevice corrosion resistance of alloys 625 and C22. *Passiv. Localized Corros. an Int. Symp. Honor Profr. Norio Sato* **99**, 644–654 (1999).
89. Jabs, T., Borthen, P. & Strehblow, H. H. X-Ray Photoelectron Spectroscopic Examinations of Electrochemically Formed Passive Layers on Ni-Cr Alloys. *J. Electrochem. Soc.* **144**, 1231–1243 (1997).
90. Takei, A. & Nii, K. The Growth Process of Oxide Layers in the Initial Stage of Oxidation of 80Ni-20Cr Alloy. *Trans. Japan Inst. Met.* **17**, 211–219 (1976).
91. Lee, H. G., Lee, Y. M., Shin, H. S., Jung, C. H. & Hong, G. W. Epitaxial deposition of NiO film on a cube-textured Ni substrate by metal-organic chemical vapor deposition. *Met. Mater.* **6**, 565–570 (2000).
92. Kitakatsu, N., Maurice, V., Hinnen, C. & Marcus, P. Surface hydroxylation and local structure of NiO thin films formed on Ni(111). *Surf. Sci.* **407**, 36–58 (1998).
93. Huang, L.-F., Ha, H. M., Lutton Cwalina, K., Scully, J. R. & Rondinelli, J. M. Electrochemical Stabilities of Ni-Compound Nanofilms Revealed by A Comparative Theory-Experiment Approach. *Submitt. to J. Phys. Chem. C* (2019).
94. Kirchheim, R., Heine, B., Hofmann, S. & Hofsäss, H. Compositional changes of passive films due to different transport rates and preferential dissolution. *Corros. Sci.* **31**, 573–578 (1990).
95. Lloyd, A. C., Shoesmith, D. W., McIntyre, N. S. & Noël, J. J. Effects of Temperature and Potential on the Passive Corrosion Properties of Alloys C22 and C276. *J. Electrochem. Soc.* **150**, B120–B130 (2003).
96. Okonkwo, I. A. *et al.* Oxidation states of molybdenum in oxide films formed in sulphuric acid and sodium hydroxide. *Thin Solid Films* **520**, 6318–6327 (2012).
97. Yang, W., Ni, R. C., Hua, H. Z. & Pourbaix, A. The behavior of chromium and molybdenum in the propagation process of localized corrosion of steels. *Corros. Sci.* **24**, 691–707 (1984).
98. Spevack, P. a. & McIntyre, N. S. A Raman and XPS investigation of supported molybdenum oxide thin films. 1. Calcination and reduction studies. *J. Phys. Chem.* **97**, 11020–11030 (1993).

99. Samin, A. J. & Taylor, C. D. First-principles investigation of surface properties and adsorption of oxygen on Ni-22Cr and the role of molybdenum. *Corros. Sci.* **134**, 103–111 (2018).
100. Clayton, C. R. & Lu, Y. C. A Bipolar Model of the Passivity of Stainless Steel: The Role of Mo Addition. *J. Electrochem. Soc.* **133**, 2465–2473 (1986).
101. Seyeux, A., Maurice, V. & Marcus, P. Oxide Film Growth Kinetics on Metals and Alloys: I. Physical Model. *J. Electrochem. Soc.* **160**, C189–C196 (2013).
102. Chao, C. Y., Lin, L. F. & Macdonald, D. D. A point defect model for anodic passive films I. Film growth kinetics. *J. Electrochem. Soc.* **128**, 1187–1194 (1981).
103. Bojinov, M. *et al.* Electrochemical study of the passive behavior of Ni-Cr alloys in a borate solution - a mixed-conduction model approach. *J. Electroanal. Chem.* **504**, 29–44 (2001).
104. Urquidi, M. & Macdonald, D. D. Solute-vacancy interaction model and the effect of minor alloying elements on the initiation of pitting corrosion. *J. Electrochem. Soc.* **132**, 555–558 (1985).
105. Urquidi-Macdonald, M. & Macdonald, D. D. Theoretical Analysis of the Effects of Alloying Elements on Distribution Functions of Passivity Breakdown. *J. Electrochem. Soc.* **136**, 961–967 (1989).
106. Marcus, P. On some fundamental factors in the effect of alloying elements on passivation of alloys. *Corros. Sci.* **36**, 2155–2158 (1994).
107. Mao, H., Chen, H.-L. & Chen, Q. TCHEA1: A Thermodynamic Database Not Limited for “High Entropy” Alloys. *J. Phase Equilibria Diffus.* 1–16 (2017). doi:10.1007/s11669-017-0570-7
108. Systems, O. OLI Studio. (2017).

4.10 Tables

Table 4.1. Averaged oxidation efficiency (%) (Equation 2.12) computed for the results shown in Figure 4.9 - Figure 4.13) for Ni-22 Cr and Ni-22 Cr-6 Mo, wt%, passivated at +0.2 V_{SCE} in 0.1 M NaCl for 10,000 s with the pH adjusted to either 4 or 10

Electrolyte	Ni-22 Cr	Ni-22 Cr-6 Mo
pH 4	4.0	31.5
pH 10	43.2	90.2

4.11 Figures

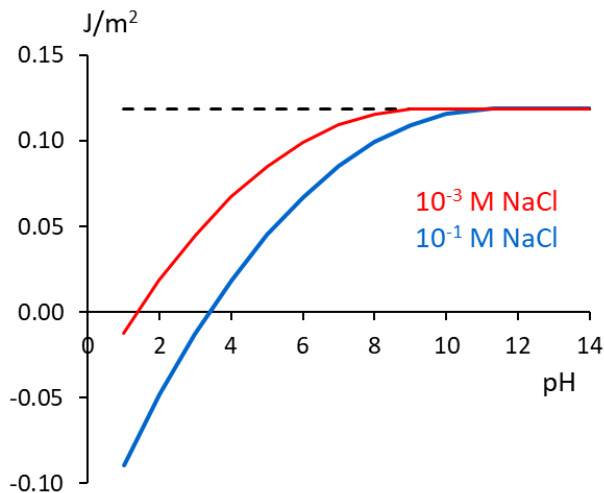


Figure 4.1. Surface energy of NiO (111) following chemisorption of chloride anions in 0.1 and 0.001 M NaCl at varying pH's predicted using DFT⁴. The reference energy for the oxide in a chloride-free environment is given by the dashed line.

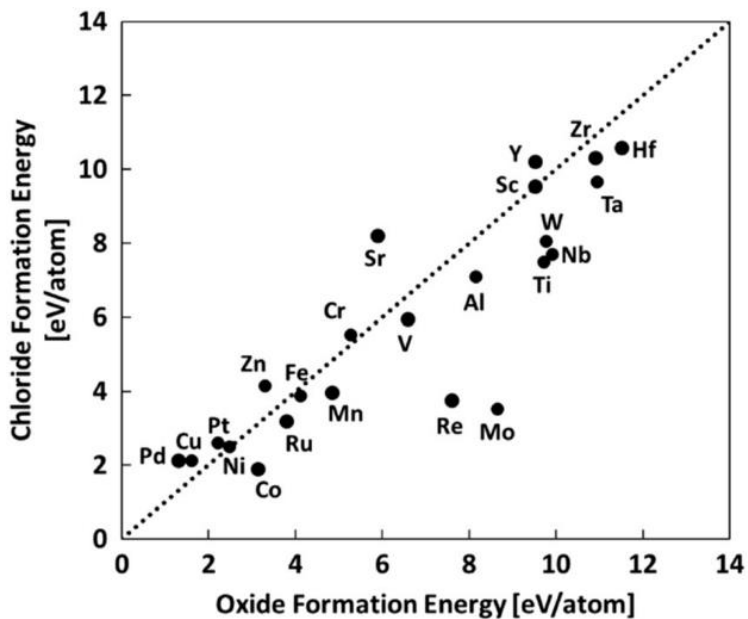


Figure 4.2. Comparison between metal-rich oxide and chloride DFT-predicted formation energies for different metals¹⁹

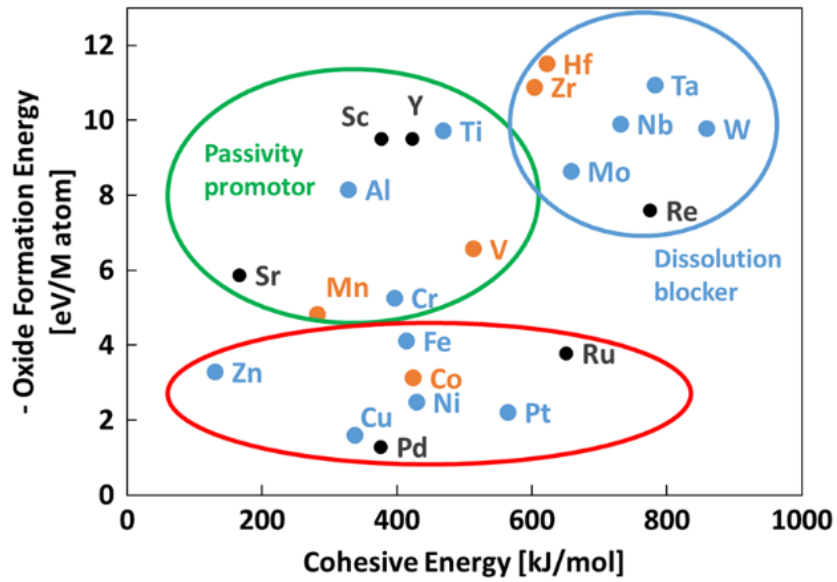


Figure 4.3. Cohesive energy as a proxy descriptor for metal dissolution resistance, plotted against the oxide formation as a proxy for ease of passivation, based on various thermodynamic modeling approaches^{19,106,107}

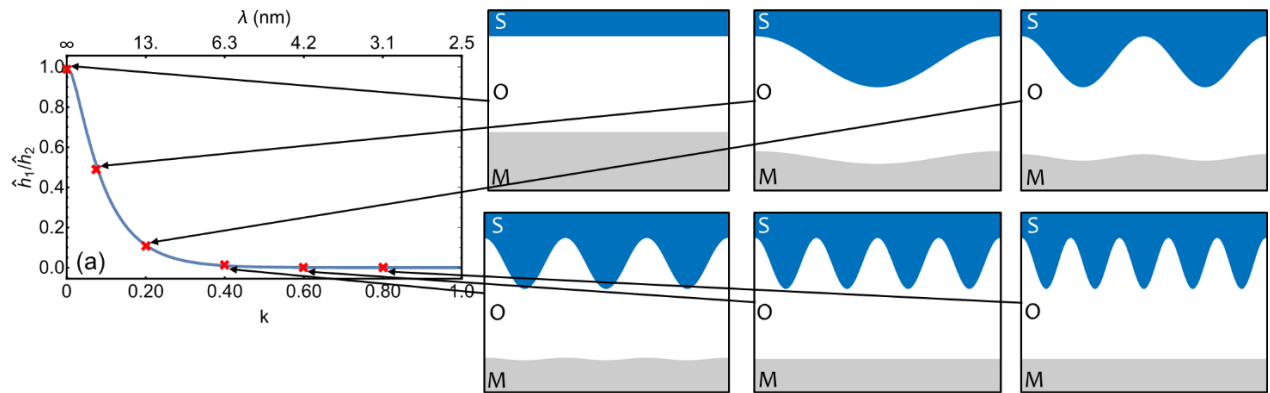


Figure 4.4. Relationship between the wave vector wavelength of a surface perturbation, k , and the apparent surface roughness²⁰ where notably, small fluctuations at the metal/film interface significantly influence the observed oxide morphology

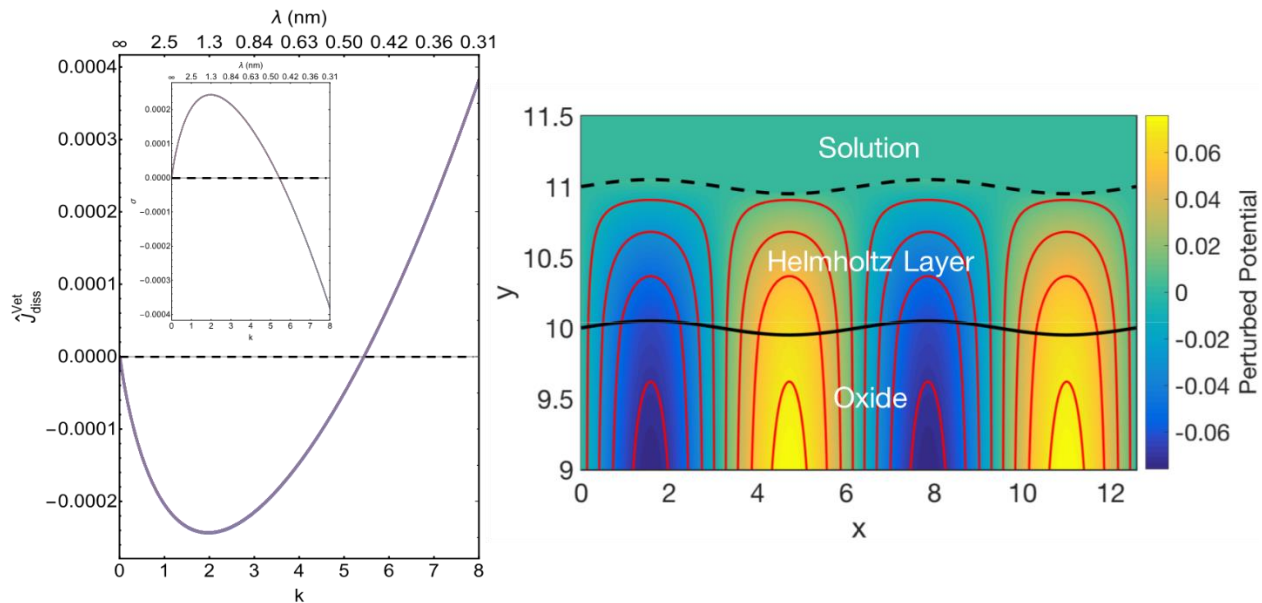


Figure 4.5. Local dissolution current, j_{diss} , and oxidation rate, σ , modeled for morphological instabilities of varying wavelengths corresponding to k . The resulting model of the perturbed potential across the peaks and troughs of the film/electrolyte interface is given, where the red lines are equipotentials, meant to give an indication of the direction of the perturbed electric field, and at the troughs of the interface, the potential drop through the Helmholtz layer is increased.

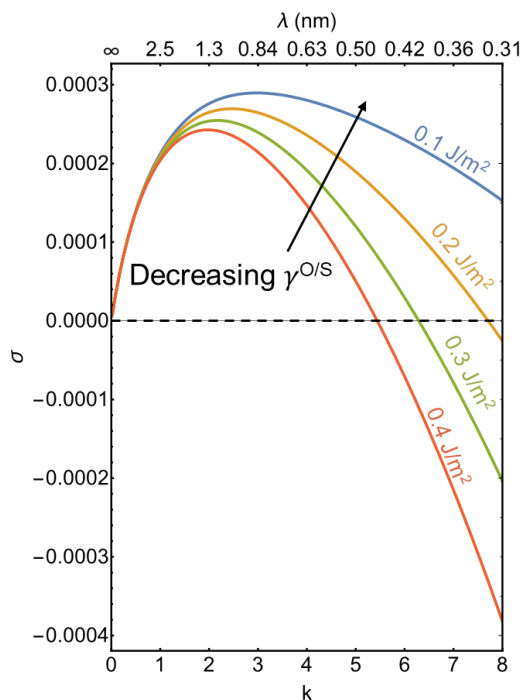


Figure 4.6. Effect of increased chloride absorption on the surface energy and resulting oxidation and dissolution rates²⁰

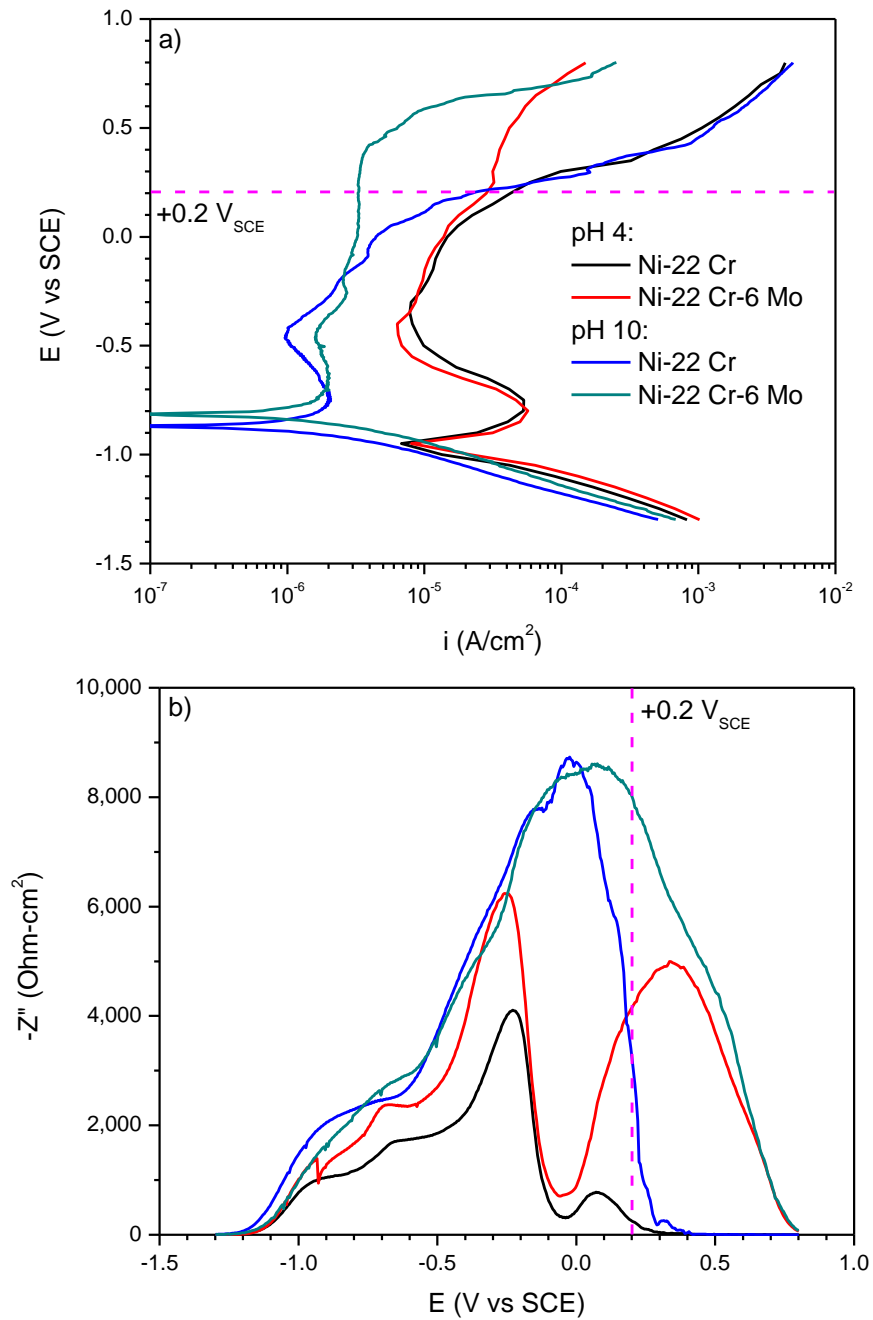


Figure 4.8. a) DC current and b) AC impedance variations during upward potentiodynamic polarization of Ni-22 Cr and Ni-22 Cr-6 Mo, wt%, in deaerated 0.1 M NaCl at pH 4 and 10 with the potential used in this study ($+0.2 V_{SCE}$) indicated

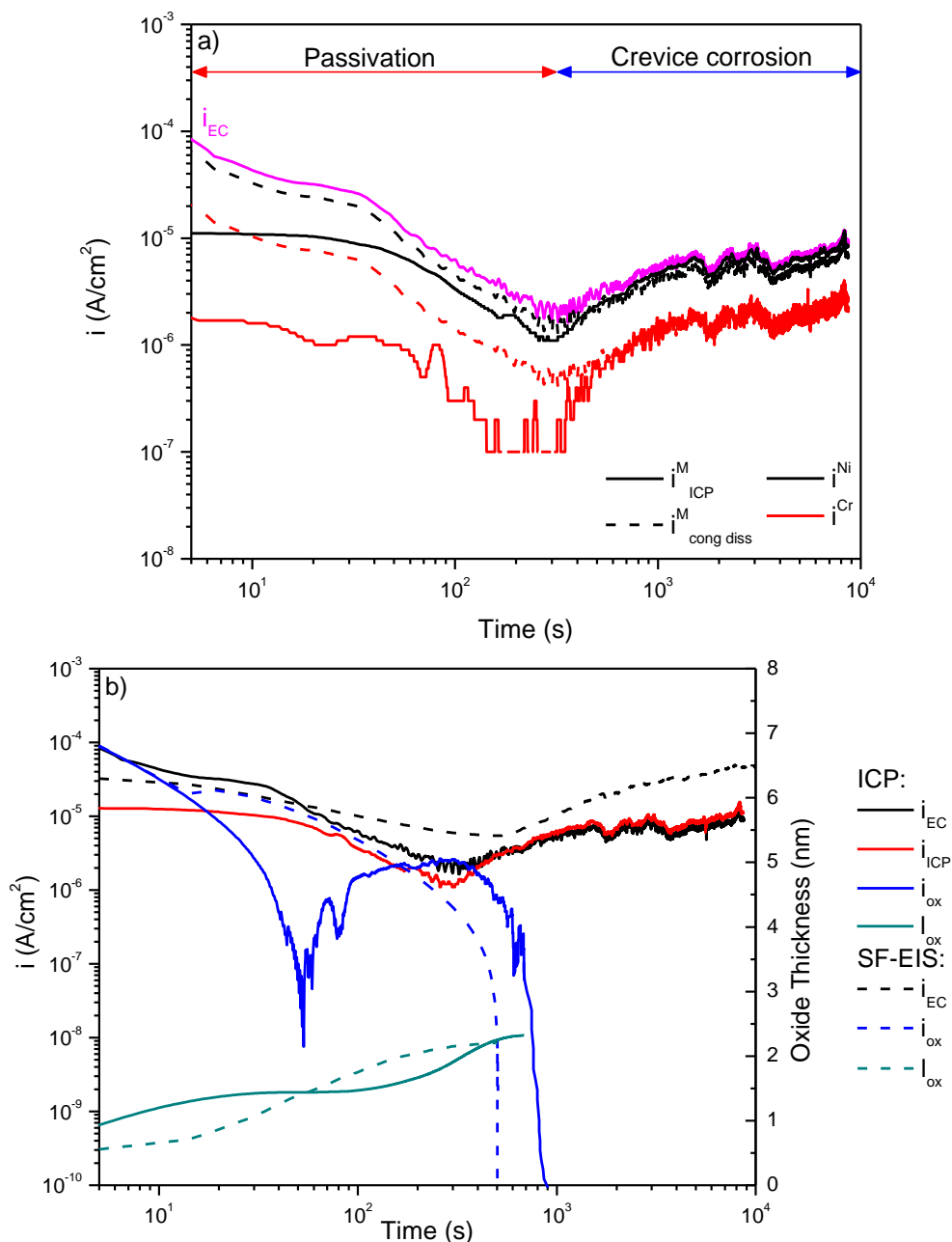


Figure 4.9. a) Calculated ICP-MS current densities for cation emission or dissolution versus the total element-specific current densities assuming congruent dissolution and b) ICP-MS and SF-EIS overall (i_{EC}), total dissolution (i_{ICP}), and oxidation (i_{ox}) current densities along with calculated film growth (l_{ox}) during passivation of Ni-22 Cr, wt%, at +0.2 V_{SCE} in 0.1 M NaCl pH 4. Instantaneous DC currents had their time convoluted in order to put them on the same scale as ICP-MS measurements.

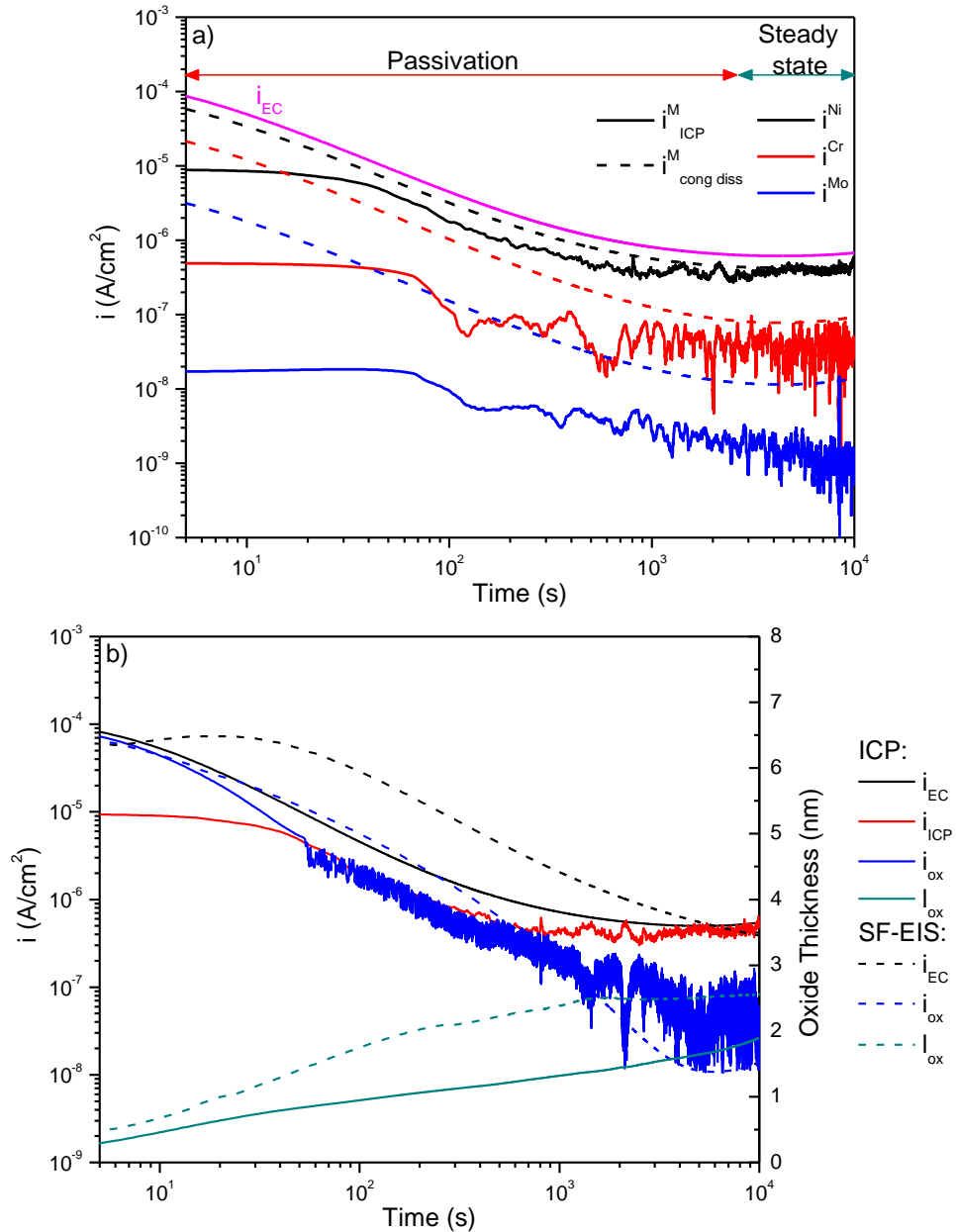


Figure 4.10. a) Calculated ICP-MS current densities for cation emission or dissolution versus the total element-specific current densities assuming congruent dissolution and b) ICP-MS and SF-EIS overall (i_{EC}), total dissolution (i_{ICP}), and oxidation (i_{ox}) current densities along with calculated film growth (l_{ox}) during passivation of Ni-22 Cr-6 Mo, wt%, at +0.2 V_{SCE} in 0.1 M NaCl pH 4. Instantaneous DC currents had their time convoluted in order to put them on the same scale as ICP-MS measurements.

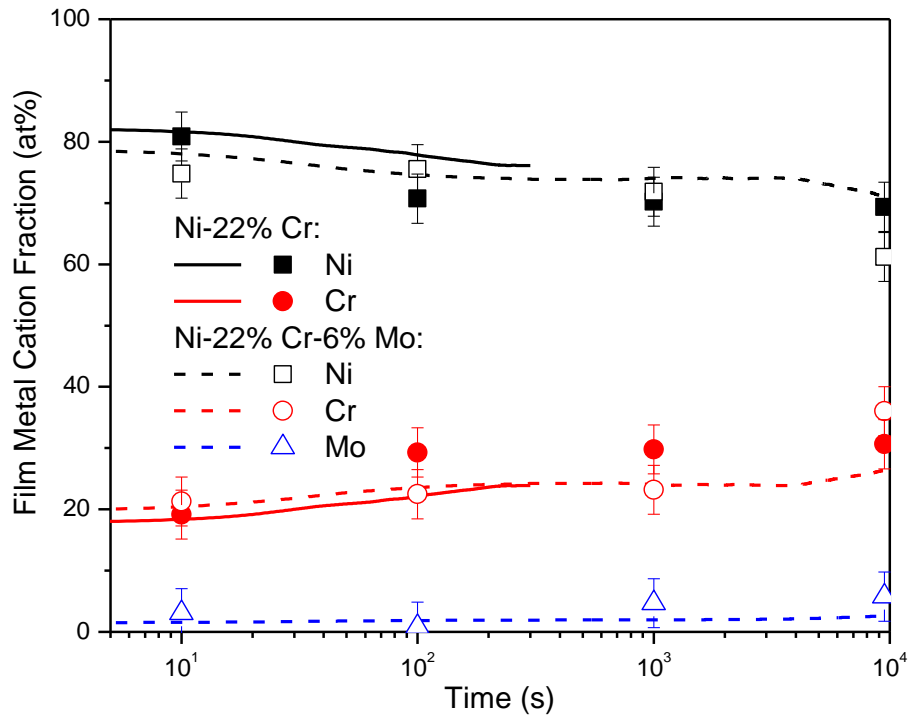


Figure 4.11. Relative accumulation of metal cations in the passive films during growth until localized corrosion initiation at +0.2 V_{SCE} according to ICP-MS (lines) and XPS (symbols, results obtained from Figure 4.32 and Figure 4.33) measurements on Ni-22 Cr and Ni-22 Cr-6 Mo, wt%, in 0.1 M NaCl pH 4

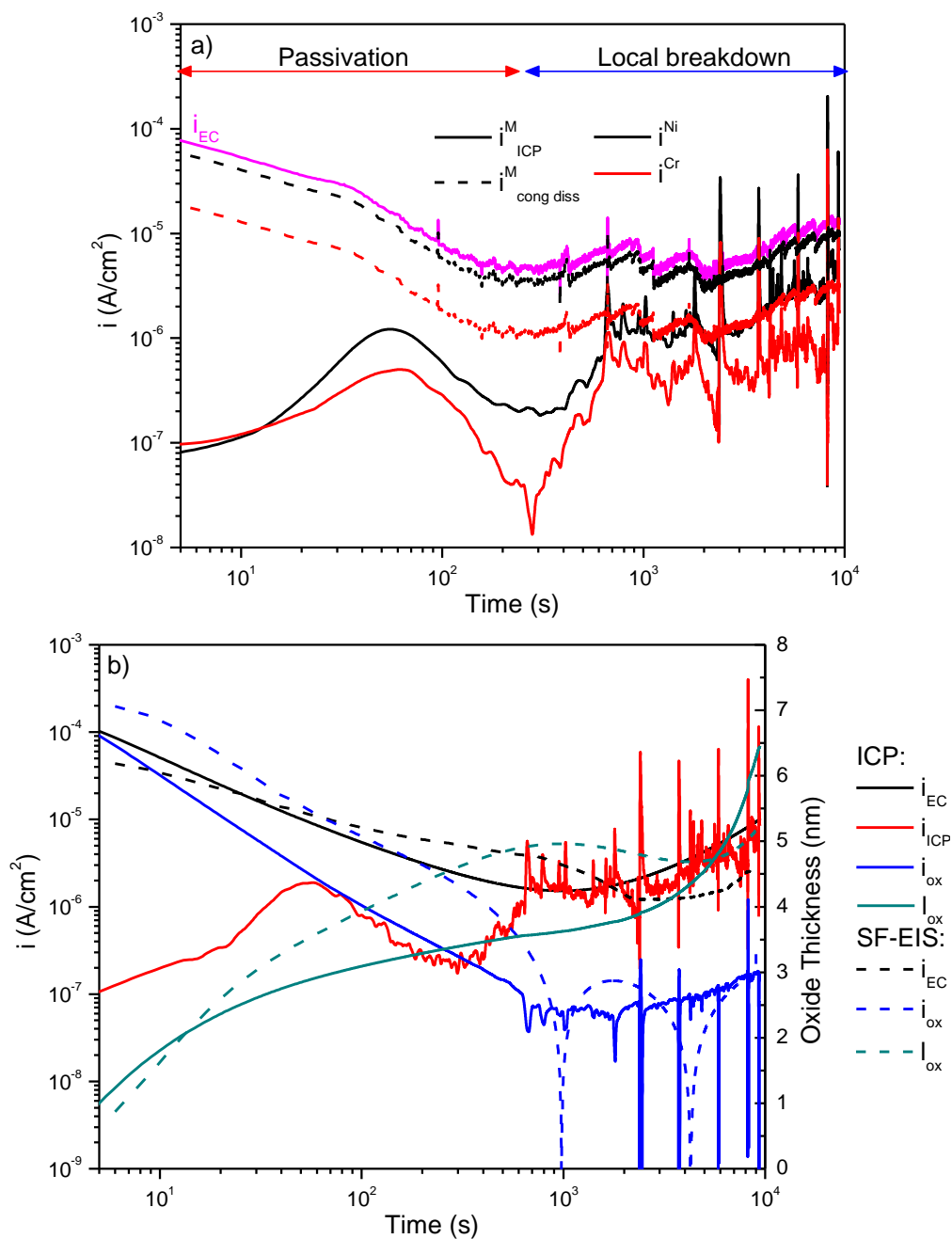


Figure 4.12. a) Calculated ICP-MS current densities for cation emission or dissolution versus the total element-specific current densities assuming congruent dissolution and b) ICP-MS and SF-EIS overall (i_{EC}), total dissolution (i_{ICP}), and oxidation (i_{ox}) current densities along with calculated film growth (l_{ox}) during passivation of Ni-22 Cr, wt% at +0.2 V_{SCE} in 0.1 M NaCl pH 10. Instantaneous DC currents had their time convoluted in order to put them on the same scale as ICP-MS measurements.

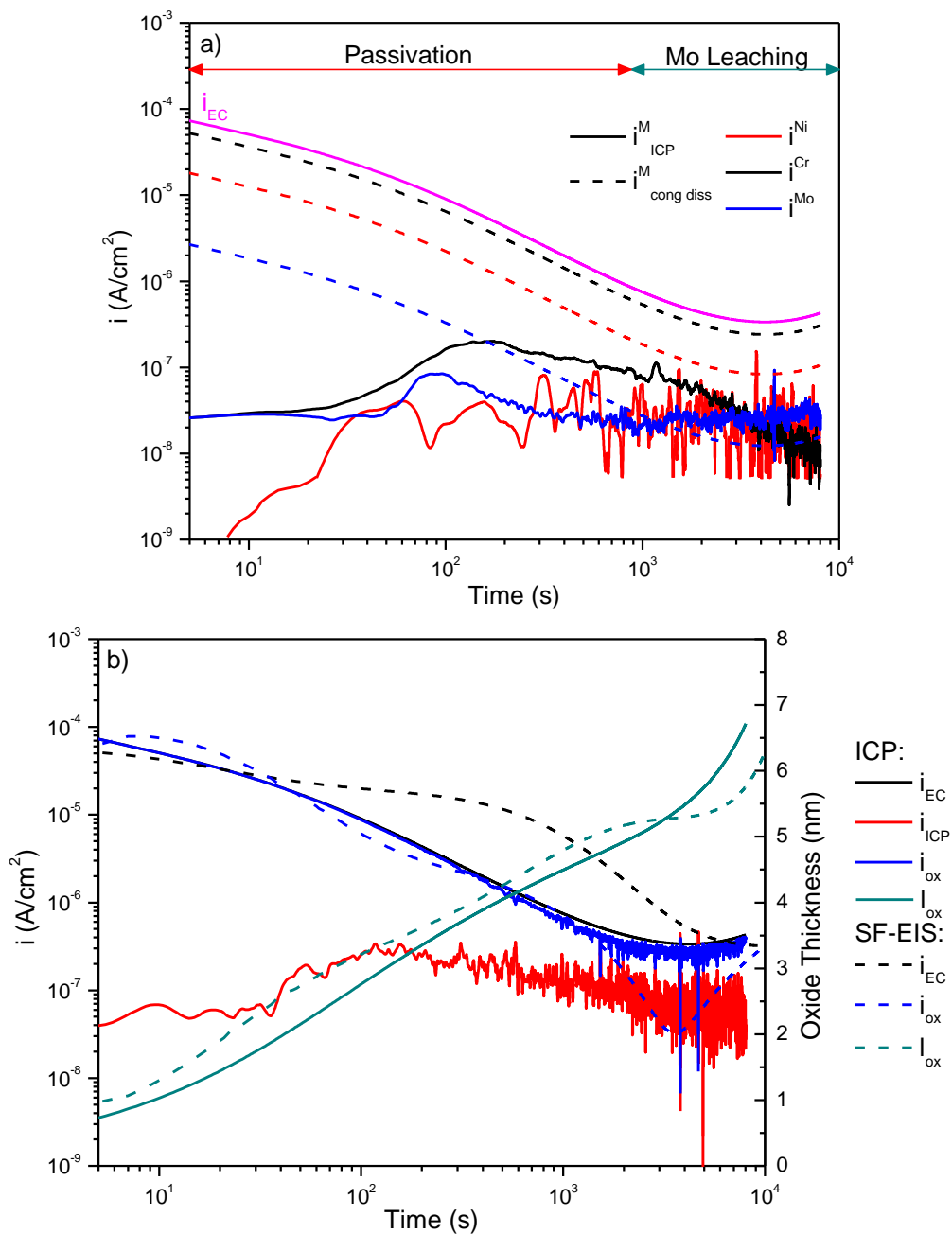


Figure 4.13. a) Calculated ICP-MS current densities for cation emission or dissolution versus the total element-specific current densities assuming congruent dissolution and b) ICP-MS and SF-EIS overall (i_{EC}), total dissolution (i_{ICP}), and oxidation (i_{ox}) current densities along with calculated film growth (l_{ox}) during passivation of Ni-22 Cr-6 Mo, wt% at +0.2 V_{SCE} in 0.1 M NaCl pH 10. Instantaneous DC currents had their time convoluted in order to put them on the same scale as ICP-MS measurements.

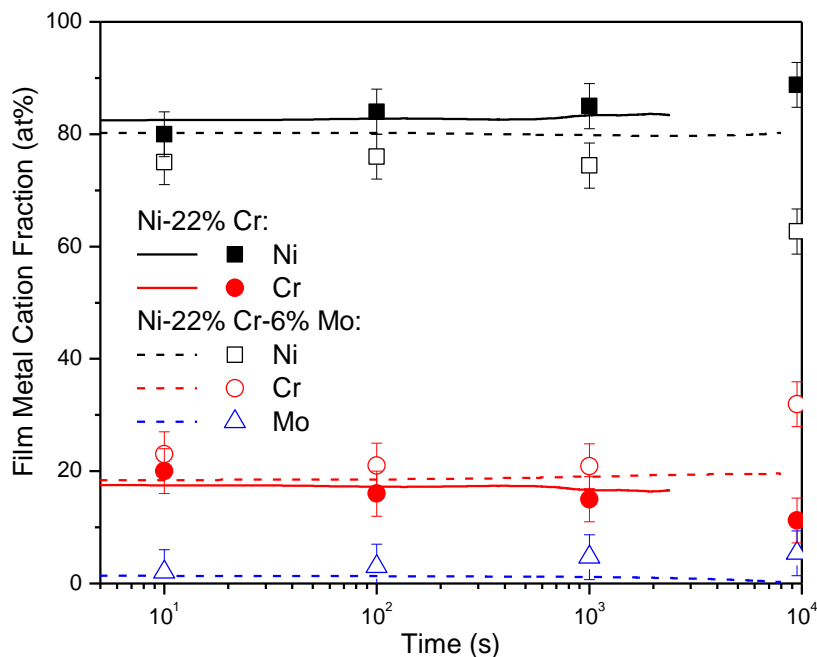


Figure 4.14. Relative accumulation of metal cations in the passive films during growth until localized corrosion initiation at +0.2 V_{SCE} according to ICP-MS (lines) and XPS (symbols) measurements on Ni-22 Cr and Ni-22 Cr-6 Mo, wt%, in 0.1 M NaCl pH 10

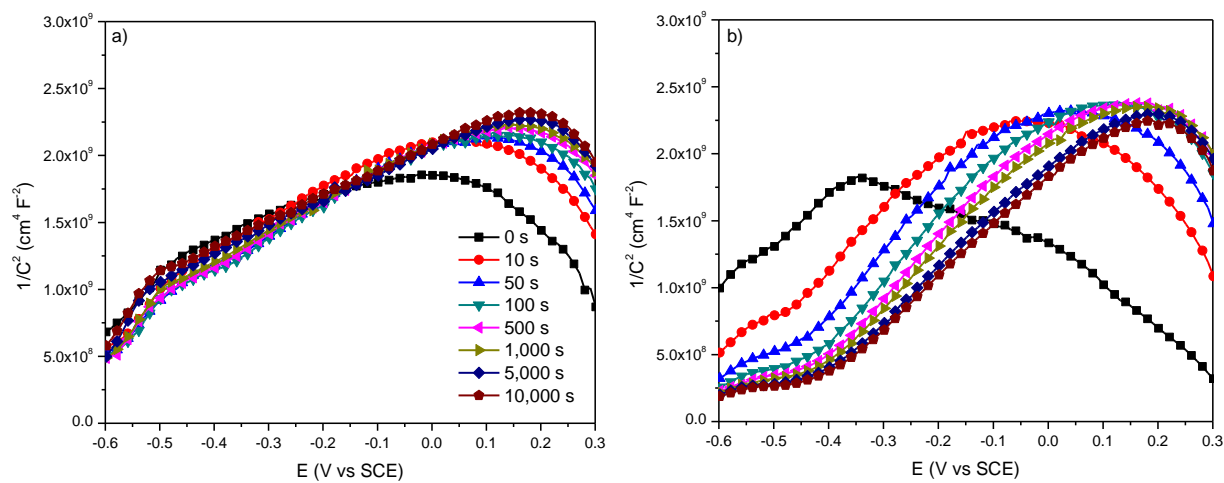


Figure 4.15. Evolution of Mott-Schottky spectra with passivation time for a) Ni-22 Cr and b) Ni-22 Cr-6 Mo, wt%, passivated at +0.2 V_{SCE} in 0.1 M NaCl pH 4 where the potential sweeps were performed at 1,000 Hz

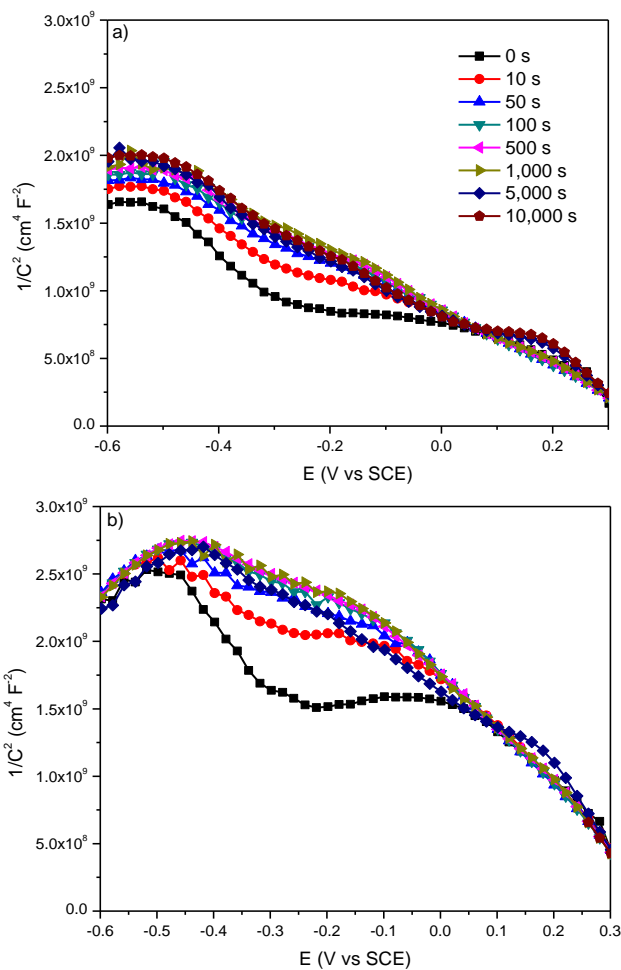


Figure 4.16. Evolution of Mott-Schottky spectra with passivation time for a) Ni-22 Cr and b) Ni-22 Cr-6 Mo, wt%, passivated at +0.2 V_{SCE} in 0.1 M NaCl pH 10 where the potential sweeps were performed at 1,000 Hz

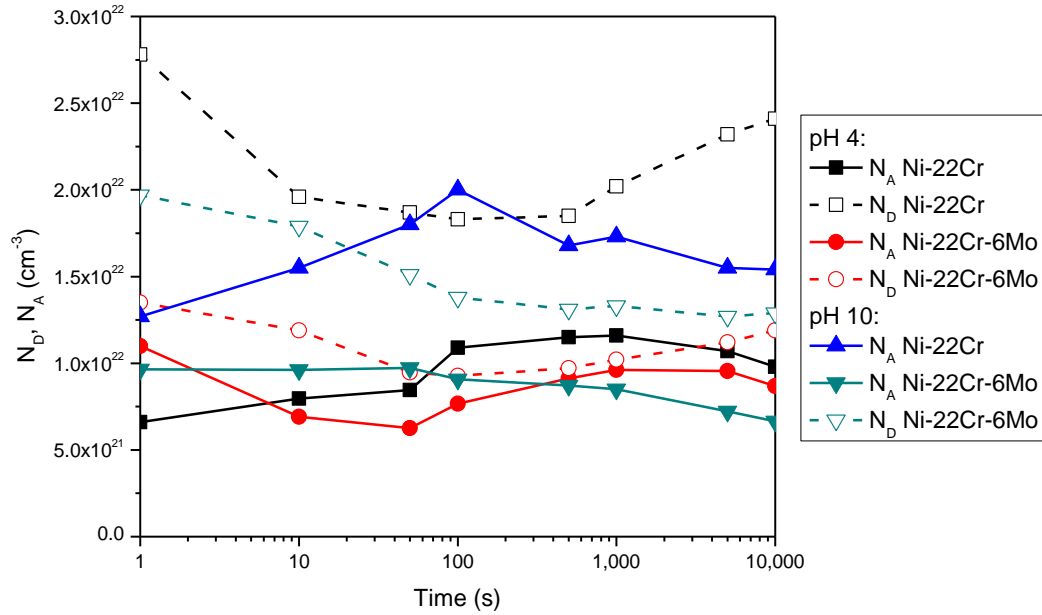


Figure 4.17. Concentration of n-type (N_D) and p-type (N_A) point defects during passivation, computed using Equation 3.3 and the data shown in Figure 4.15 and Figure 4.16 for Ni-22 Cr and Ni-22 Cr-6 Mo, wt%, passivated at $+0.2 V_{SCE}$ for times up to 10,000 s in 0.1 M NaCl pH 4 and pH 10

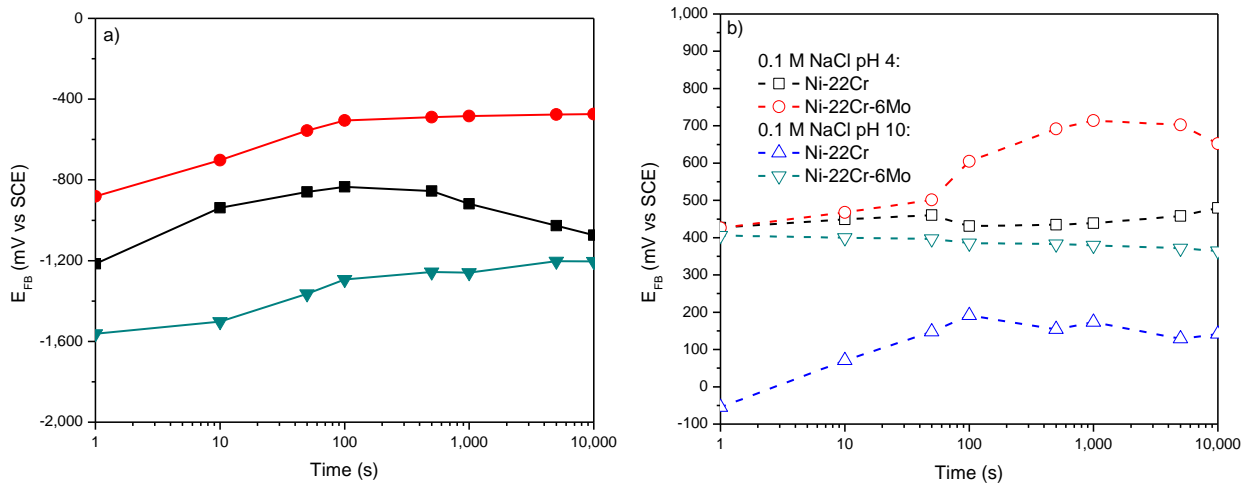


Figure 4.18. Measured semiconductor flat band potentials, E_{FB} , for a) n-type and b) p-type behavior, computed using Equation 3.3 as indicated in Figure 3.3 for Ni-22 Cr and Ni-22 Cr-6 Mo, wt%, passivated at $+0.2 V_{SCE}$ for times up to 10,000 s in 0.1 M NaCl pH 4 and pH 10 (Figure 4.15 and Figure 4.16)

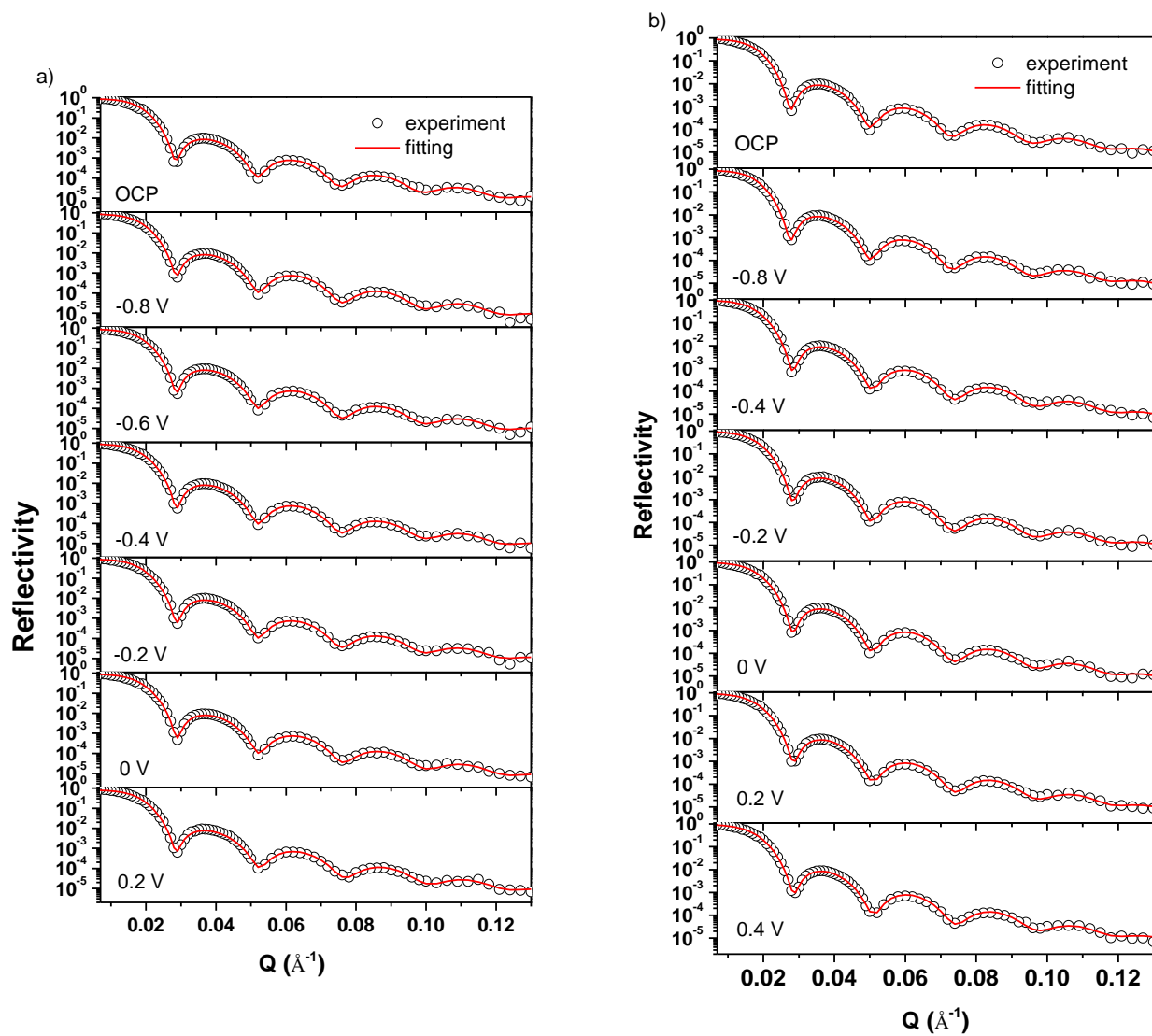


Figure 4.19. Measured reflectivity curves for Ni-20 Cr and Ni-20 Cr-10 Mo, wt%, oxidized in 0.1 M NaCl pH 4 at various potential steps (Figure 3.5) from OCP, to $-0.8 V_{SCE}$, and up to $+0.2 V_{SCE}$ in 200 mV steps every 6 hours where the NR measurements started 1 hr after the applied potential was switched to the set value and each measurement took approximately 90 min to complete

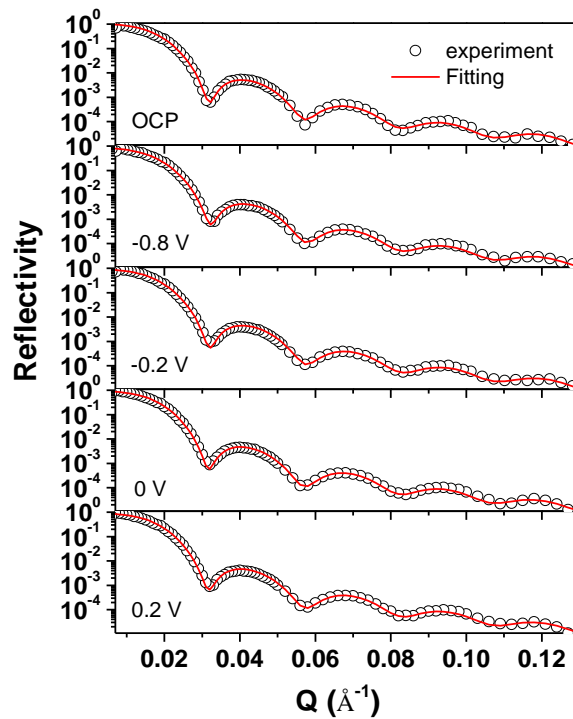
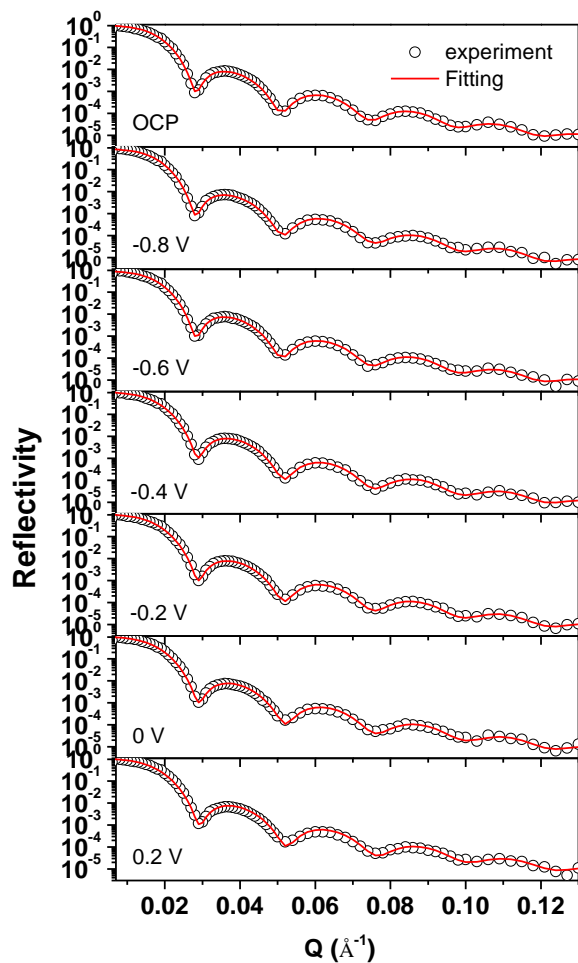


Figure 4.20. Measured reflectivity curves for Ni-20 Cr and Ni-20 Cr-10 Mo, wt%, oxidized in 0.1 M NaCl pH 10 at various potential steps (Figure 3.5) from OCP, to $-0.8 V_{SCE}$, and up to $+0.2 V_{SCE}$ in 200 mV steps every 6 hours where the NR measurements started 1 hr after the applied potential was switched to the set value and each measurement took approximately 90 min to complete

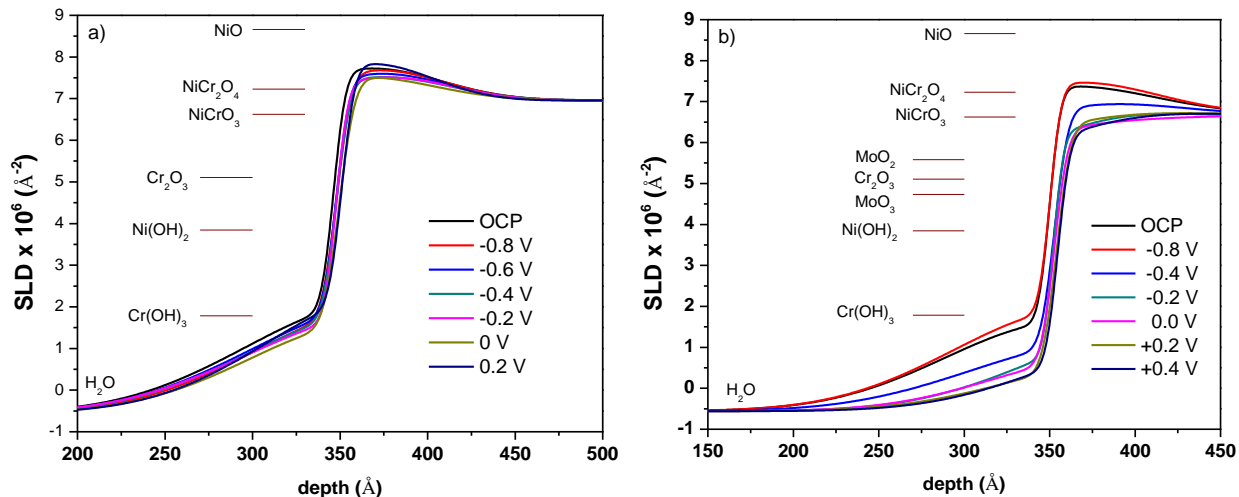


Figure 4.21. Full SLD profiles for a) Ni-20% Cr and b) Ni-20% Cr-10% Mo, wt%, oxidized in 0.1 M NaCl pH 4 at various potential steps from OCP, to $-0.8 V_{\text{SCE}}$, and up to $+0.2 V_{\text{SCE}}$ in 200 mV steps every 6 hours where the NR measurements started 1 hr after the applied potential was switched to the set value and each measurement took approximately 90 min to complete. SLD values for the expected species are given for different film compounds and the spectra, at low depths, corresponds to the electrolyte layer and at high depths, the alloy layer.

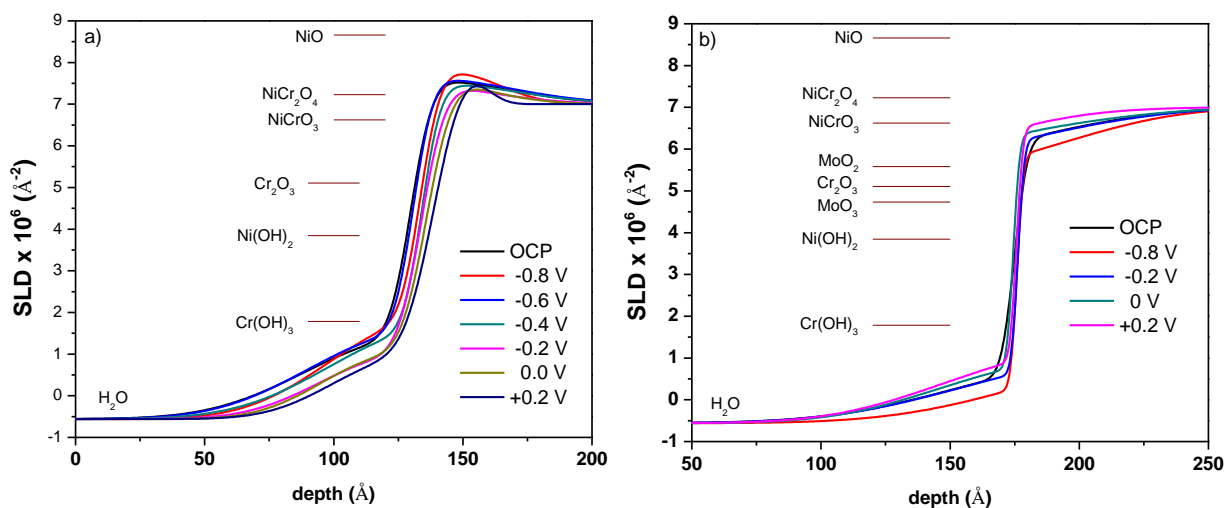


Figure 4.22. Full SLD profiles for a) Ni-20% Cr and b) Ni-20% Cr-10% Mo, wt%, oxidized in 0.1 M NaCl pH 10 at various potential steps from OCP, to $-0.8 V_{\text{SCE}}$, and up to $+0.2 V_{\text{SCE}}$ in 200 mV steps every 6 hours where the NR measurements started 1 hr after the applied potential was switched to the set value and each measurement took approximately 90 min to complete. SLD values for the expected species are given for different film compounds and the spectra, at low depths, corresponds to the electrolyte layer and at high depths, the alloy layer.

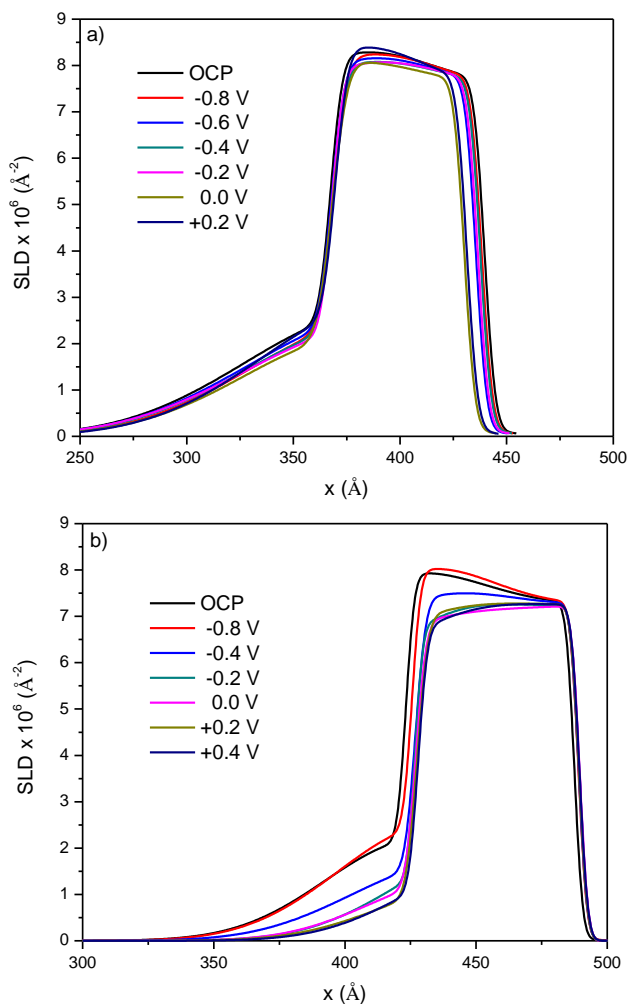


Figure 4.23. Analysis of the NR profiles given in Figure 4.21 where a sample profile for the base metal exposed to water on a SiO_2 substrate was simulated and subtracted from the overall reflectometry curve in order to obtain that of just the passive film for a) Ni-20 Cr and b) Ni-20 Cr-10 Mo, wt%, in 0.1 M NaCl pH 4 where the peak SLD correlates to the Ni^{2+} cation fraction and the approximate l_{ox} is indicated by the peak width

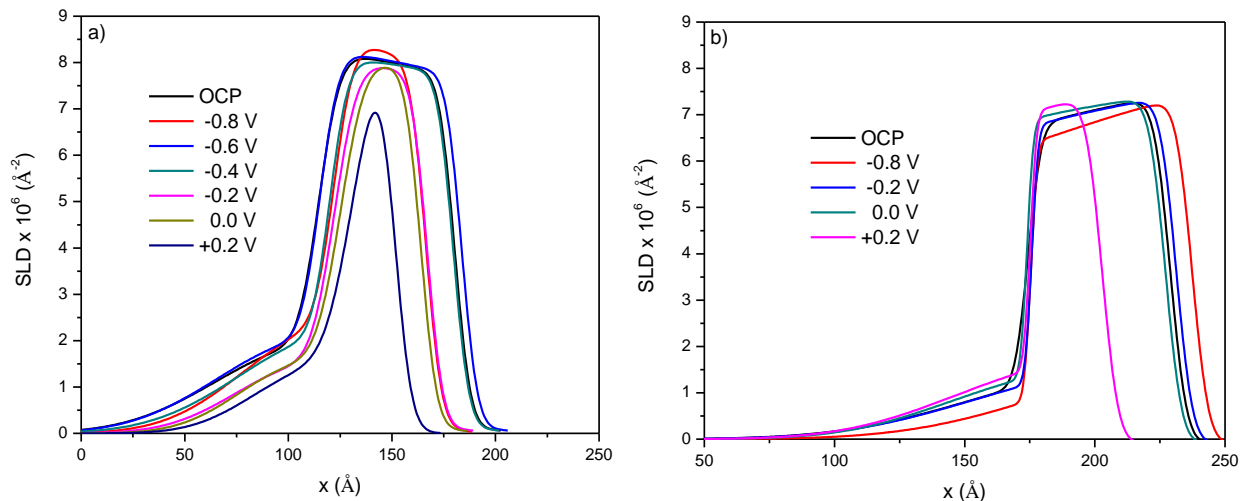


Figure 4.24. Analysis of the NR profiles given in Figure 4.22 where a sample profile for the base metal exposed to water on a SiO₂ substrate was simulated and subtracted from the overall reflectometry curve in order to obtain that of just the passive film for a) Ni-20 Cr and b) Ni-20 Cr-10 Mo, wt%, in 0.1 M NaCl pH 4 where the peak SLD correlates to the Ni²⁺ cation fraction and the approximate l_{ox} is indicated by the peak width

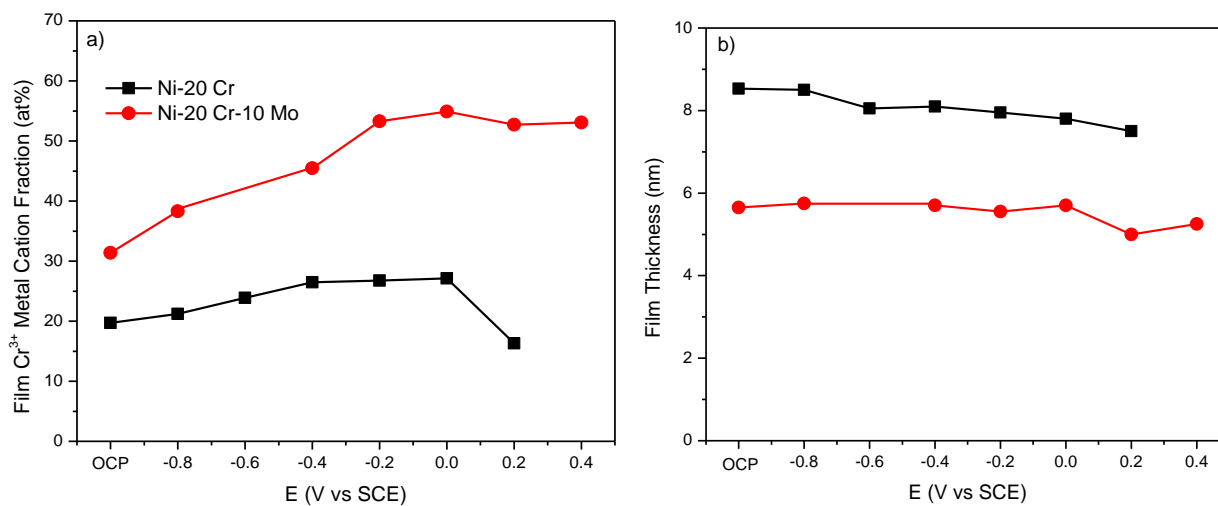


Figure 4.25. a) Metal cation fraction and b) passive film thickness computed from the peak SLD in Figure 4.23 for Ni-20 Cr and Ni-20 Cr-10 Mo, wt%, in 0.1 M NaCl pH 4 oxidized at varying potentials

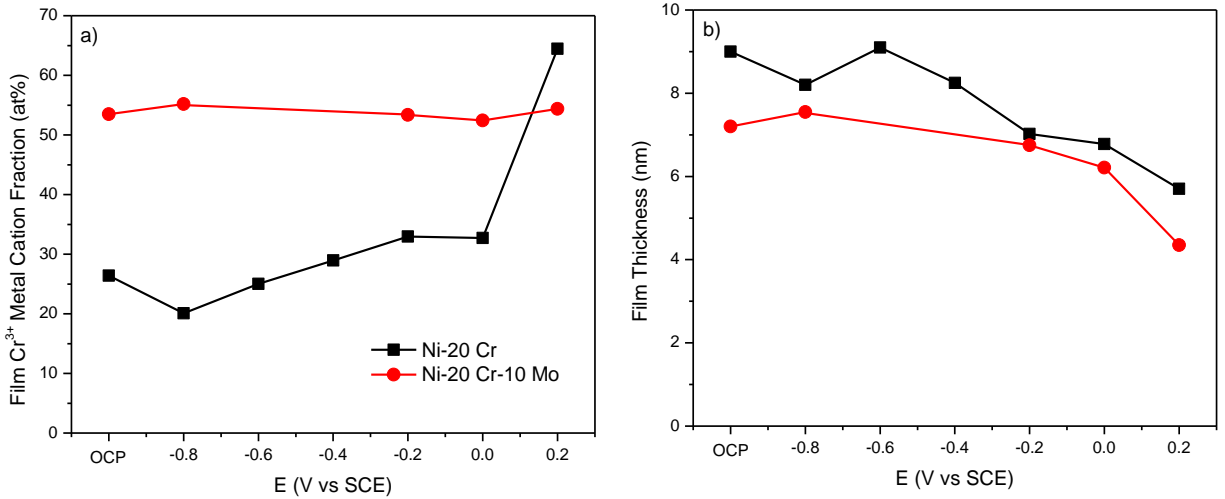


Figure 4.26. a) Metal cation fraction and b) passive film thickness computed from the peak SLD in Figure 4.24 for Ni-20 Cr and Ni-20 Cr-10 Mo, wt%, in 0.1 M NaCl pH 10 oxidized at varying potentials

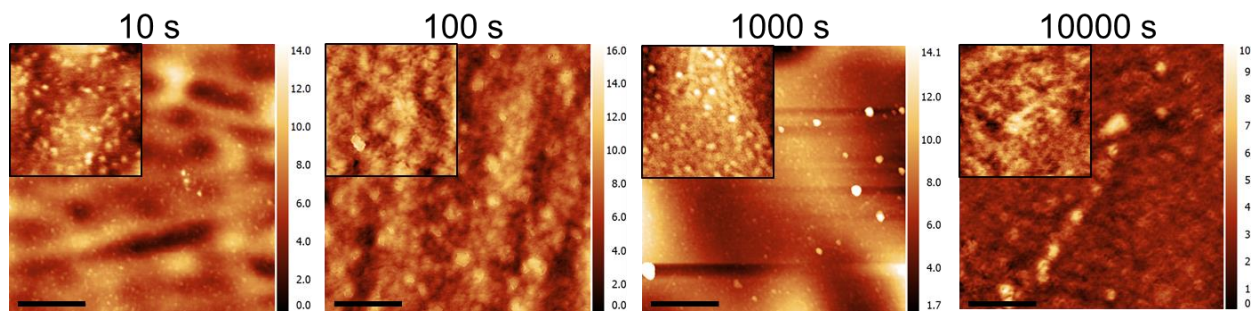


Figure 4.27. Topography images taken with AFM after 10, 100, 1,000, and 10,000 s of passivation of Ni-22 Cr, wt%, in 0.1 M NaCl pH 4 with 500 nm² image insets. The insets are representative of the area used to measure oxide height (Figure 4.28) and RMS surface roughness (Figure 4.29). All scale bars are 500 nm and the color bars in units of nm.

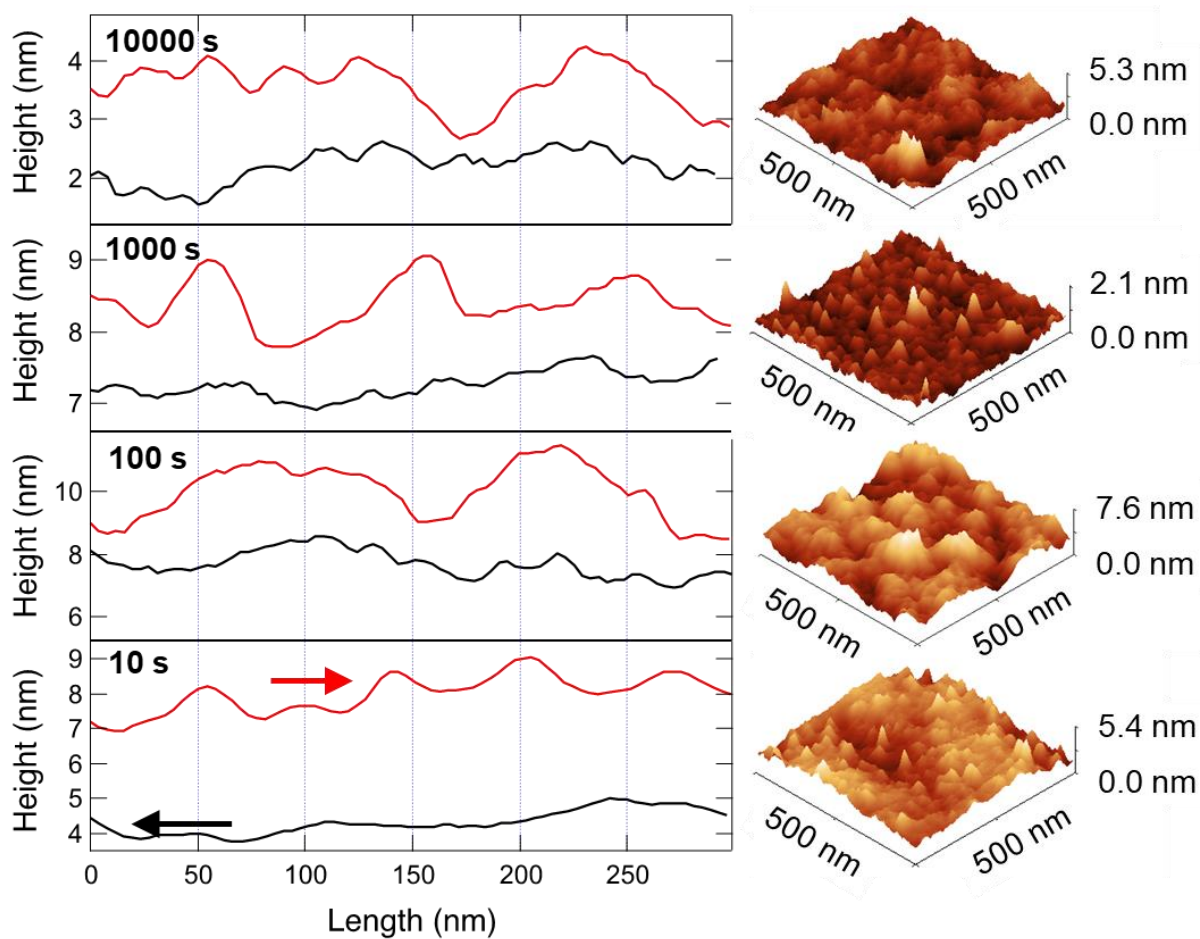


Figure 4.28. Line scans of the surface topography after exposure to 0.1 M NaCl pH 4 where the red lines represent the bright protrusion of the electrochemically grown oxide, while the black lines represent the roughness of a fresh surface that has only been air-oxidized for the same amount of time

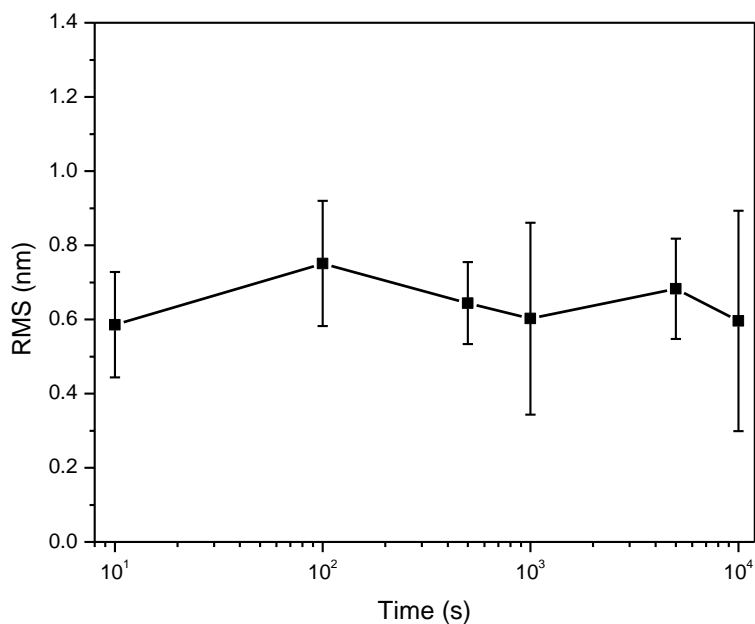


Figure 4.29. Average root mean square (RMS) surface roughness computed for Ni-22 Cr, wt%, passivated at +0.2 V_{SCE} for various times in deaerated 0.1 M NaCl pH 4. The RMS was calculated at various areas across the electrochemically oxidized surface to obtain the average RMS value and error bars.

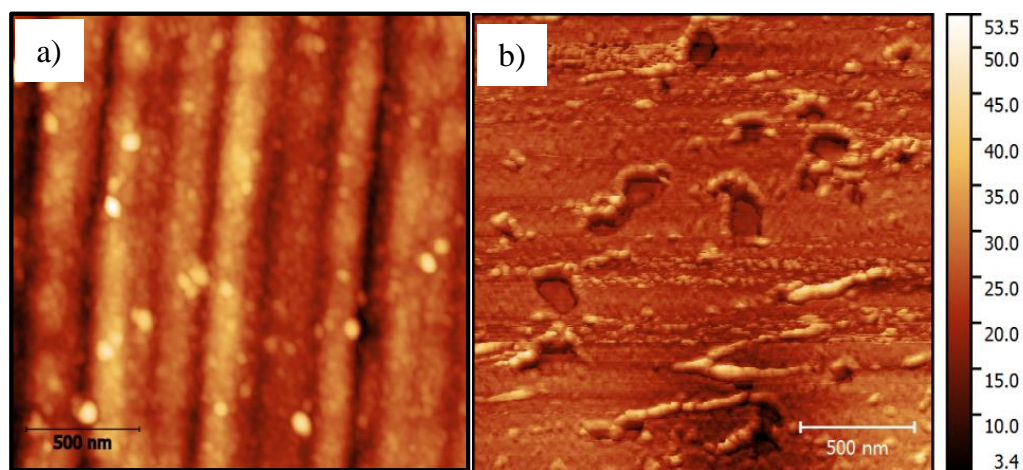


Figure 4.30. Comparison of surface topography images taken with AFM after exposure of a) Ni-22 Cr-6 Mo (RMS = 1.36 nm) and b) Ni-22 Cr (RMS = 1.14 nm), wt%, to 0.1 M NaCl pH 4 for 1,000 s. The color bar is given in units of nm.

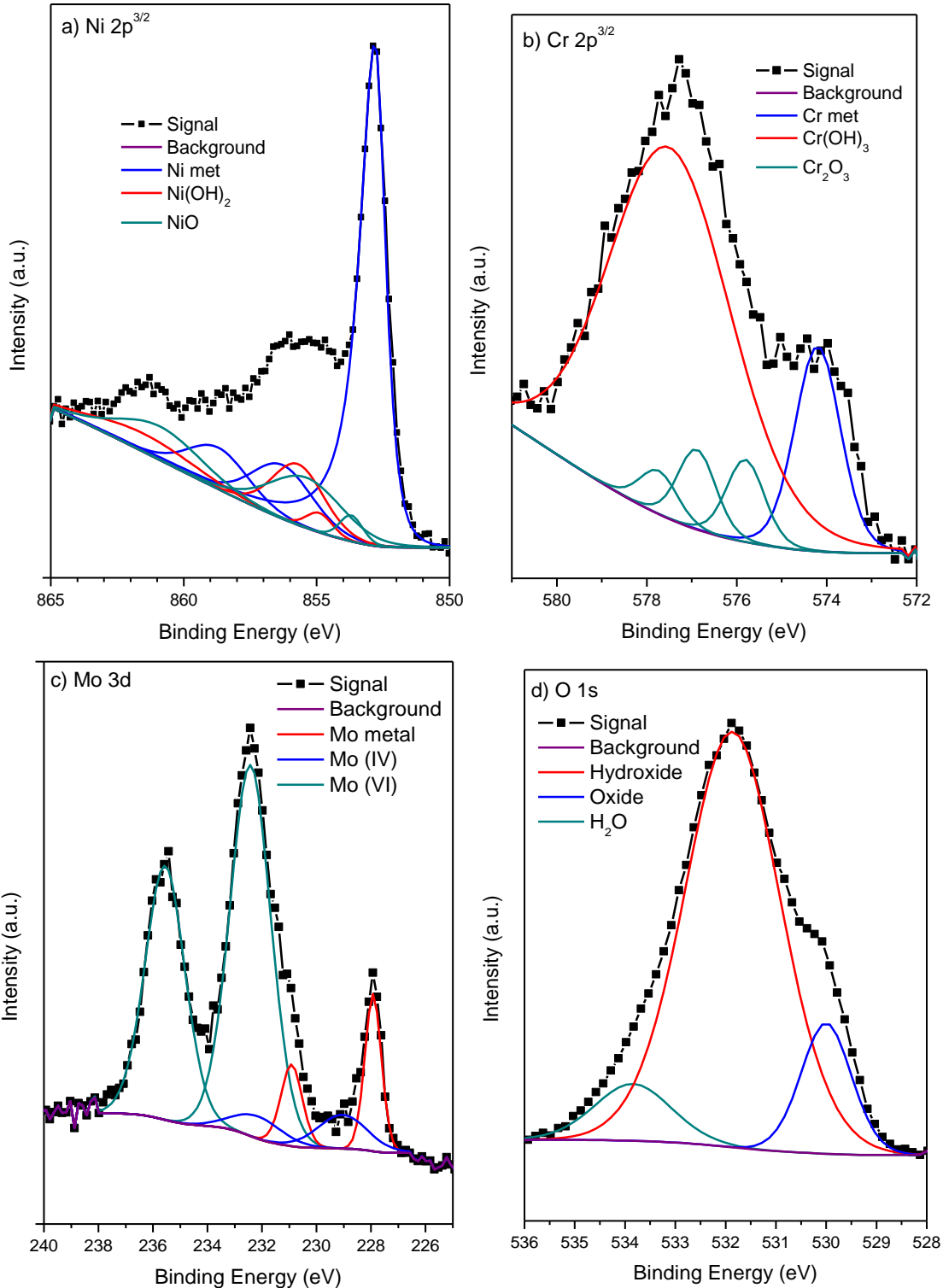


Figure 4.31. Focused, deconvoluted XPS spectra for a) Ni 2p^{3/2}, b) Cr 3p^{3/2}, c) Mo 3d, and d) O 1s bands collected on Ni-22 Cr-6 Mo, wt%, passivated at +0.2 V_{SCE} for 10,000 s in 0.1 M NaCl

pH 4 where the solid black and magenta lines indicate the Shirley background and overall fit to the spectra, respectively

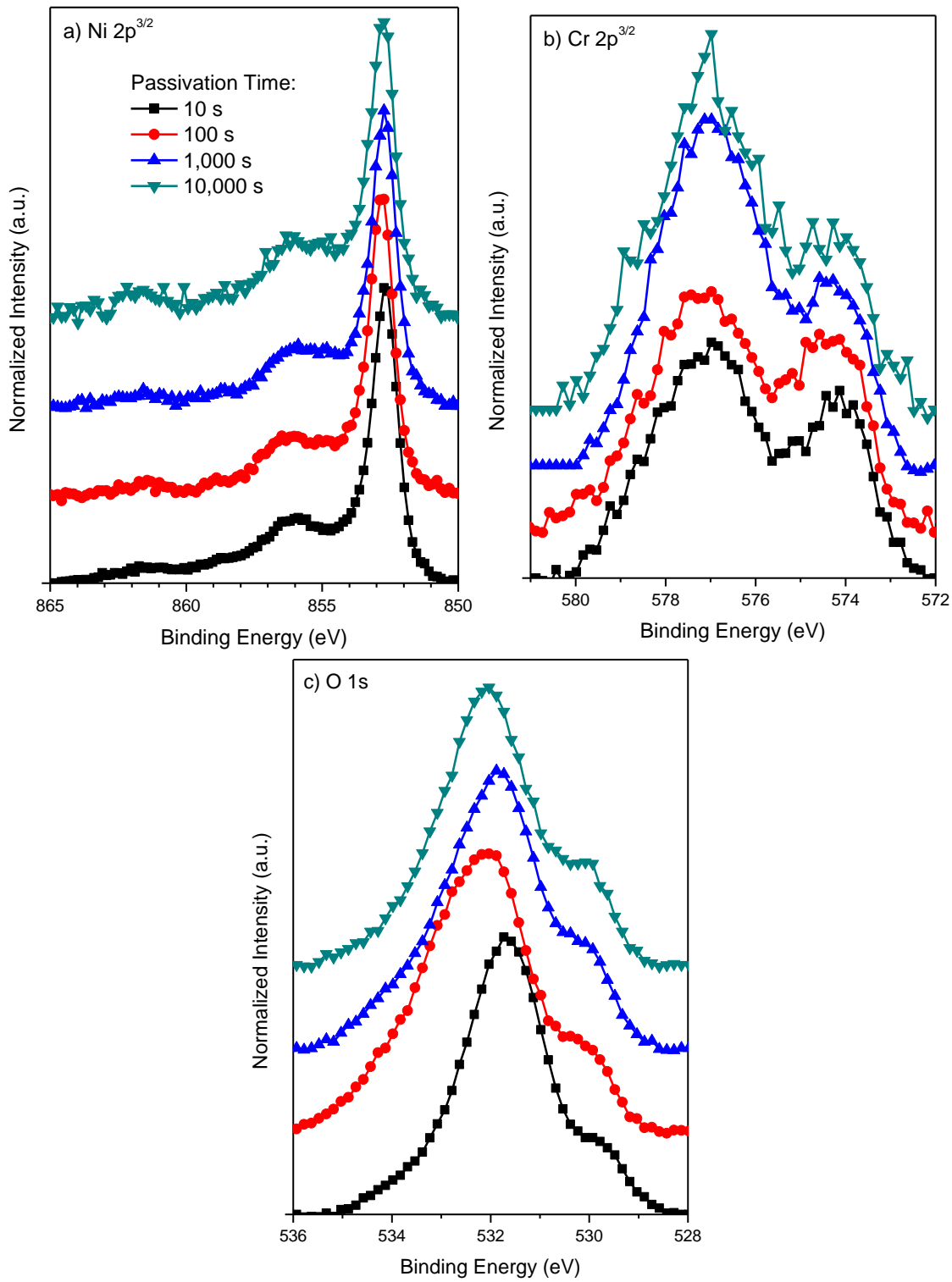


Figure 4.32. XPS spectra using an Al- $\kappa\alpha$ source ($h\nu = 1,486.68$ eV) for a) Ni $2p^{3/2}$, b) Cr $2p^{3/2}$, and c) O $1s$ obtained at 12 kV with a 20 eV pass energy for Ni-22 wt% Cr, Shirley background-subtracted, normalized to the corresponding metallic peaks, and offset for clarity following passivation at $+0.2$ V_{SCE} for up to 10 ks in deaerated 0.1 M NaCl pH 4

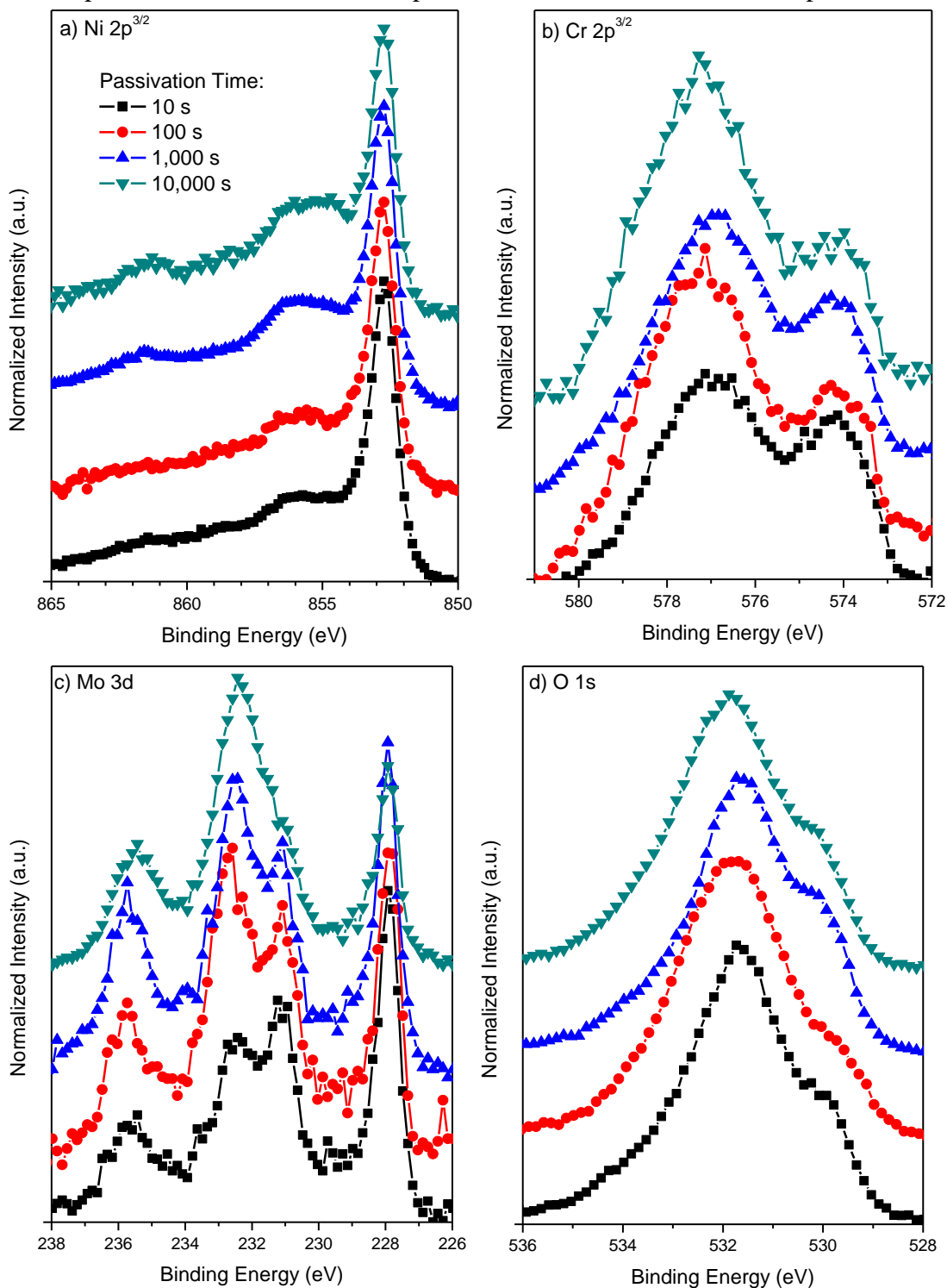


Figure 4.33. XPS spectra using an Al- α source ($h\nu = 1,486.68$ eV) for a) Ni $2p^{3/2}$, b) Cr $2p^{3/2}$, c) Mo $3d$, and d) O $1s$ obtained at 12 kV with a 20 eV pass energy for Ni-22 Cr-6 Mo, wt%, Shirley background-subtracted, normalized to the corresponding metallic peaks, and offset for clarity following passivation at +0.2 V_{SCE} for up to 10 ks in deaerated 0.1 M NaCl pH 4

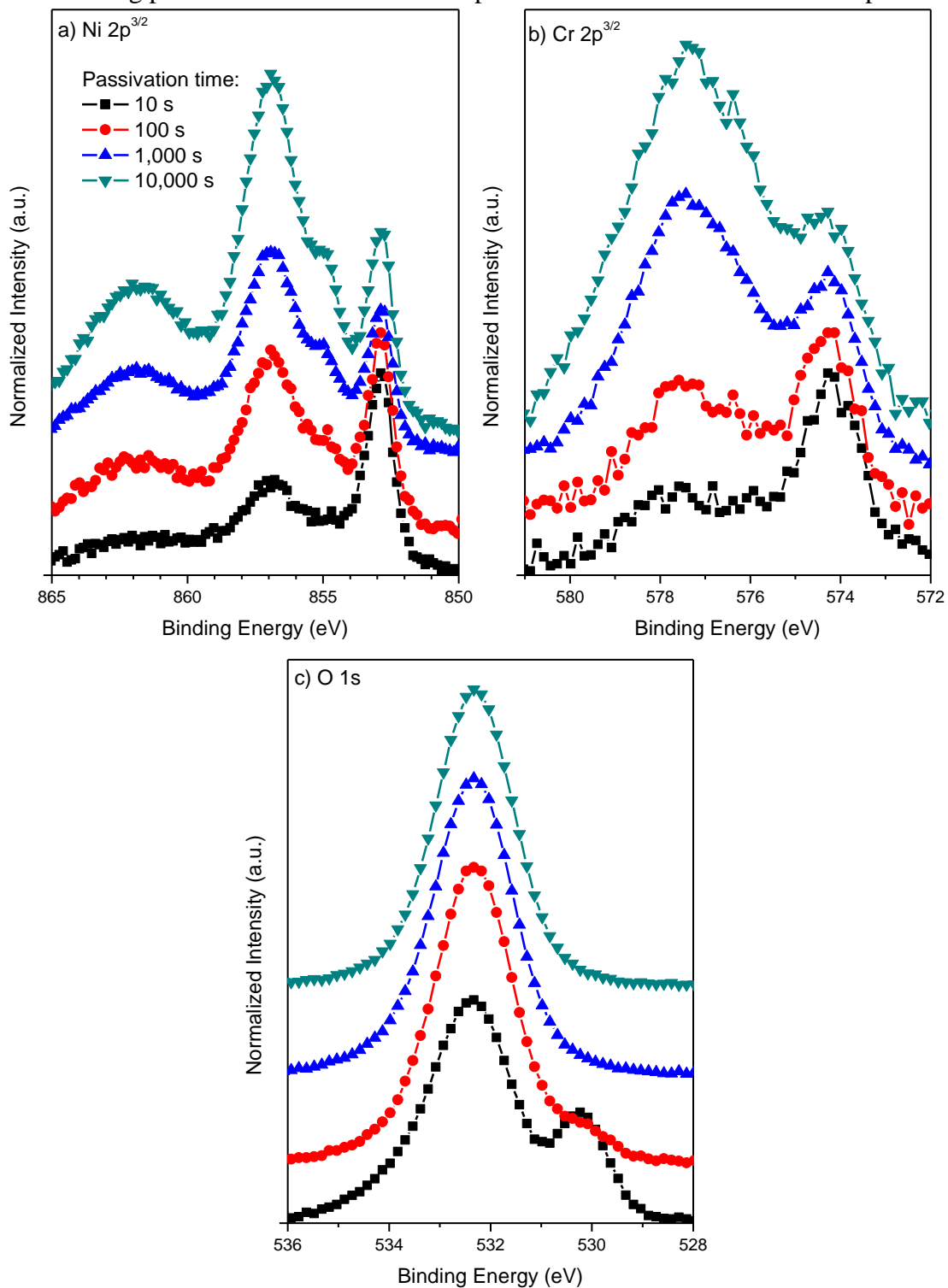


Figure 4.34. XPS spectra using an Al- $\kappa\alpha$ source ($h\nu = 1,486.68$ eV) for a) Ni $2p^{3/2}$, b) Cr $2p^{3/2}$, and c) O $1s$ obtained at 15 kV with a 50 eV pass energy for Ni-22 wt% Cr, Shirley background-subtracted, normalized to the corresponding metallic peaks, and offset for clarity following passivation at +0.2 V_{SCE} for up to 10 ks in deaerated 0.1 M NaCl pH 10

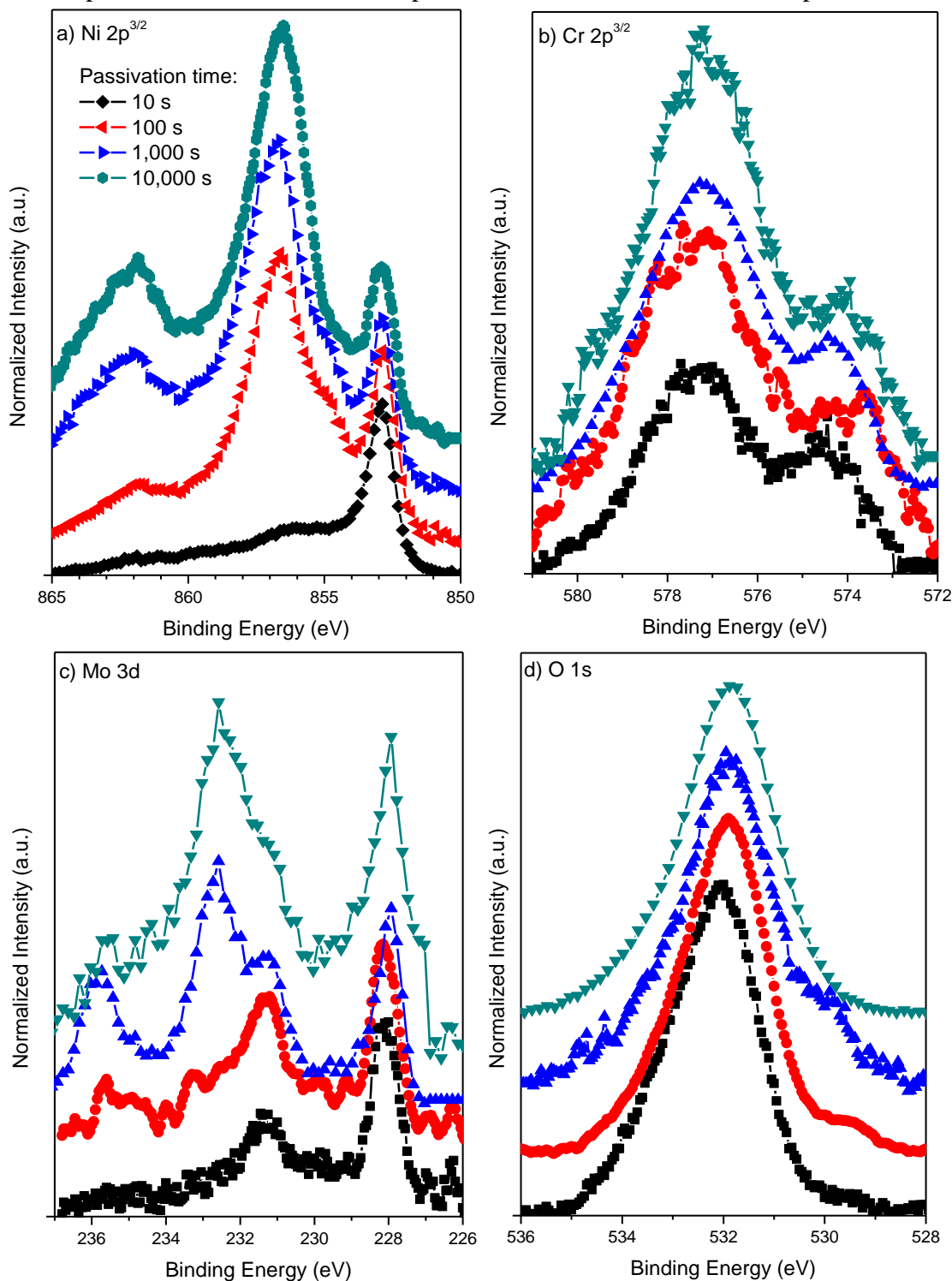


Figure 4.35. XPS spectra using an Al- $\kappa\alpha$ source ($h\nu = 1,486.68$ eV) for a) Ni $2p^{3/2}$, b) Cr $2p^{3/2}$, c) Mo $3d$, and d) O $1s$ obtained at 15 kV with a 50 eV pass energy for Ni-22 Cr-6 Mo, wt%, Shirley background-subtracted, normalized to the corresponding metallic peaks, and offset for clarity following passivation at +0.2 V_{SCE} for up to 10 ks in deaerated 0.1 M NaCl pH 10

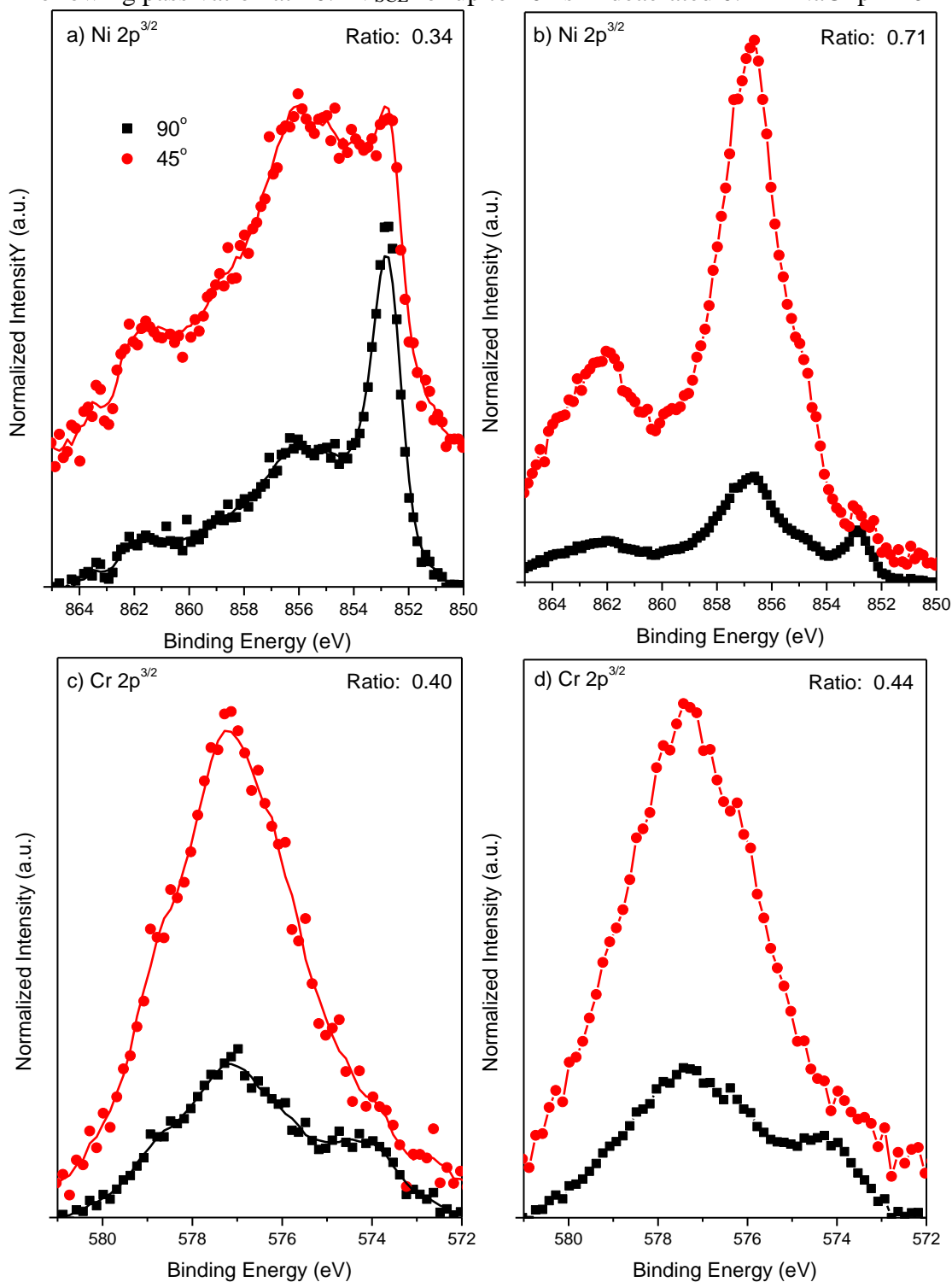


Figure 4.36. a,b) Ni 2p^{3/2} and c,d) Cr 2p^{3/2} angle-resolved XPS spectras which were normalized to the metal peaks for Ni-22 Cr, wt%, passivated at +0.2 V_{SCE} for 10 ks in 0.1 M NaCl a,c) pH 4 and b,d) pH 10. The ratio of the oxide areas for each angle measurement is included for reference.

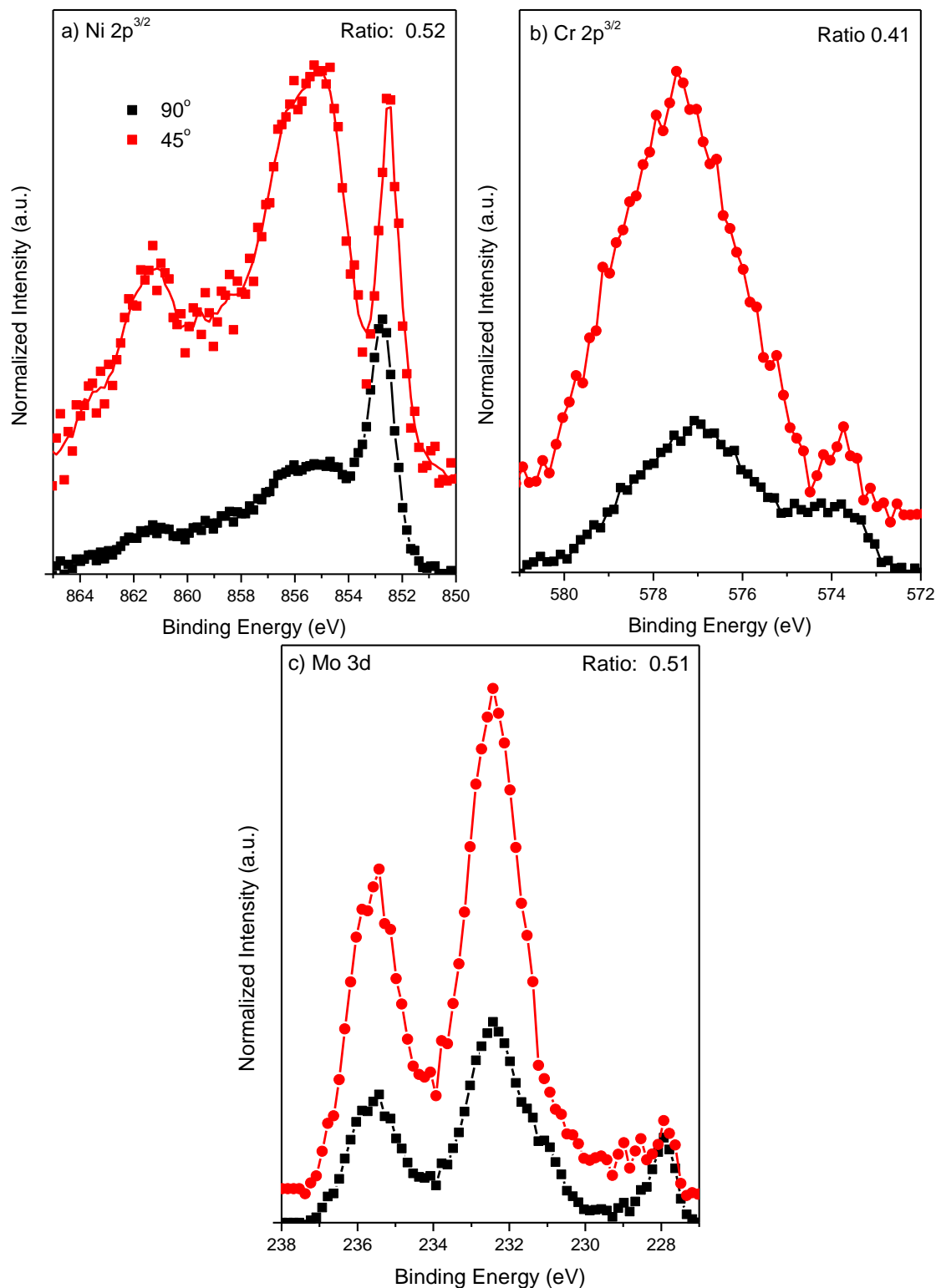


Figure 4.37. a) Ni 2p^{3/2}, b) Cr 2p^{3/2}, and c) Mo 3d angle-resolved XPS spectra which were normalized to the metal peaks for Ni-22 Cr-6 Mo, wt%, passivated at +0.2 V_{SCE} for 10 ks in 0.1 M NaCl pH 4. The ratio of the oxide areas for each angle measurement is included for reference.

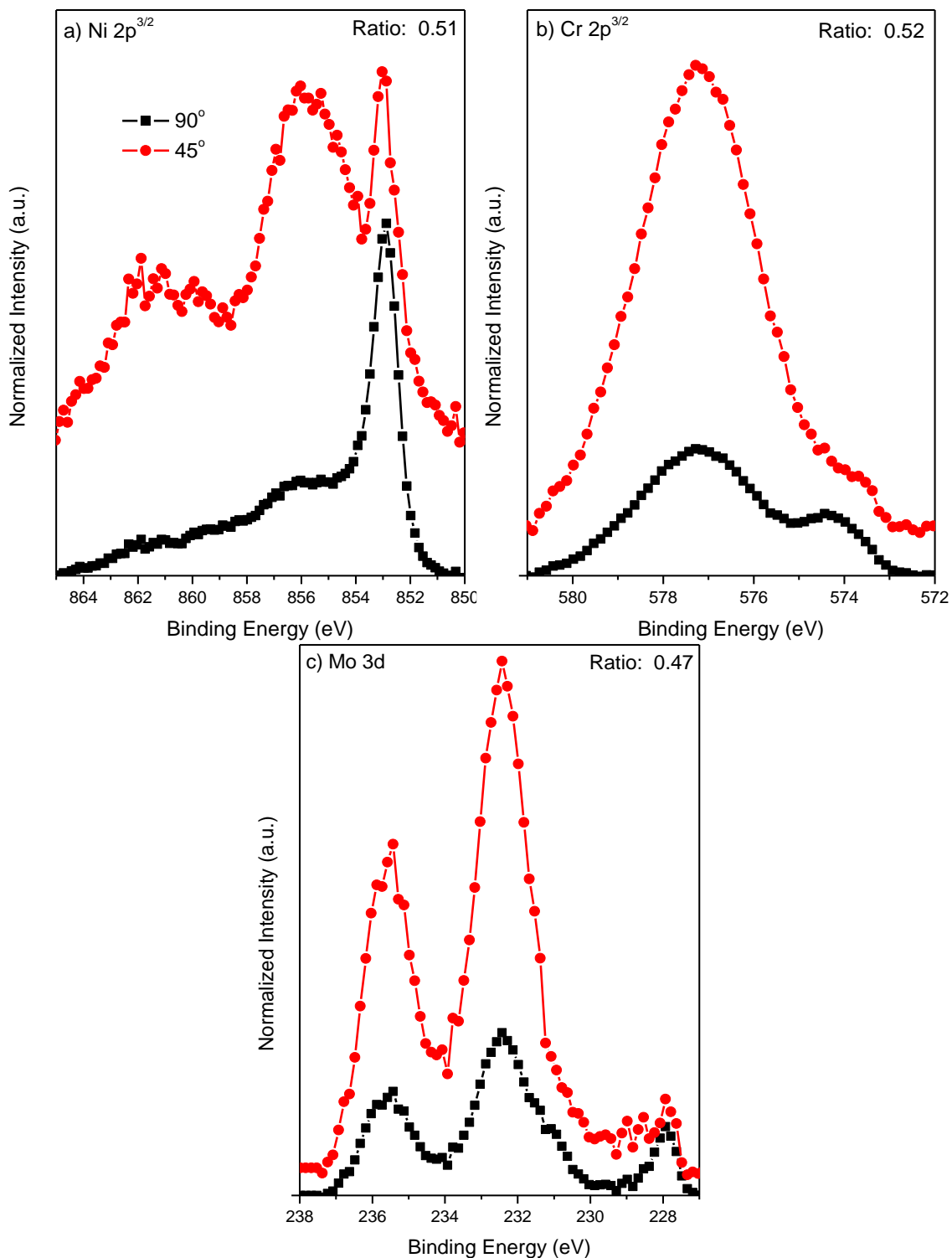


Figure 4.38. a) Ni 2p^{3/2}, b) Cr 2p^{3/2}, and c) Mo 3d angle-resolved XPS spectra which were normalized to the metal peaks for Ni-22 Cr-6 Mo, wt%, passivated at +0.2 V_{SCE} for 10 ks in 0.1 M NaCl pH 10. The ratio of the oxide areas for each angle measurement is included for reference.

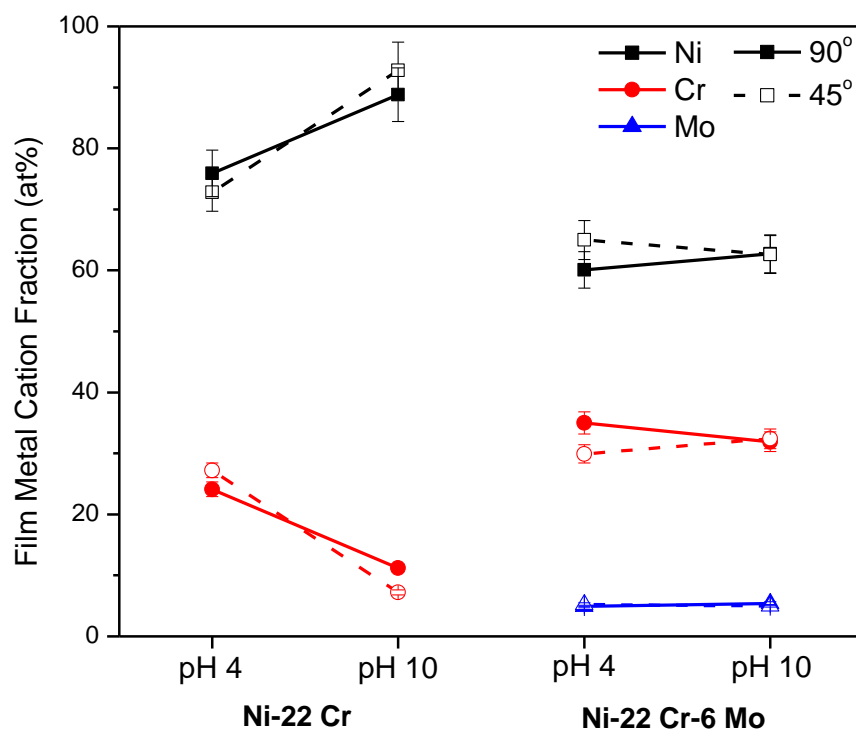


Figure 4.39. Film cation fraction according to angle-resolved XPS measurements at 90° and 45° on Ni-22 Cr and Ni-22 Cr-6 Mo, wt%, surfaces following 10 ks of potentiostatic passivation at +0.2 V_{SCE} in 0.1 M NaCl at pH 4 and 10

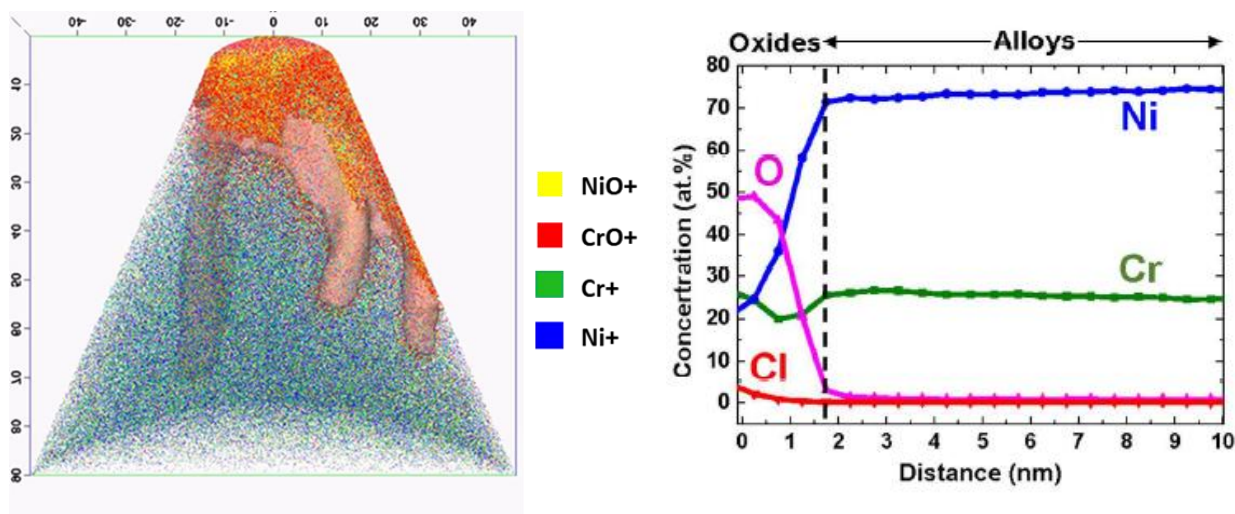


Figure 4.40. APT result for Ni-22 Cr, wt%, with a 10 at% O isosurface corrected for detection efficiencies where the included 1D composition profile through the center of the tip shows the relative Cr-enrichment following a 10 ks exposure to 0.1 M NaCl pH 4 + 1 mM H_2O_2 ($E_{OCP} = +0.2 V_{SCE}$)

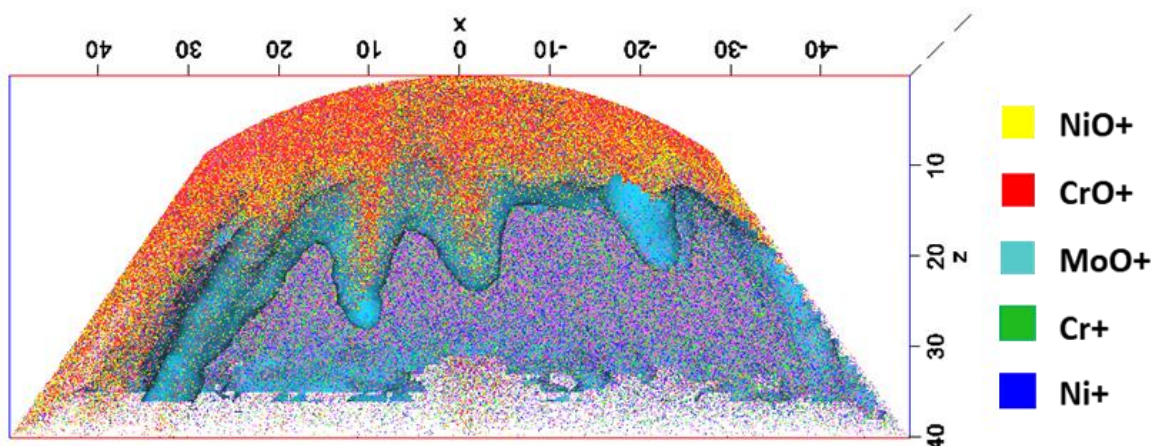


Figure 4.41. Overall APT result for a Ni-22 Cr-6 Mo, wt%, tip oxidized for 10 ks in 0.1 M NaCl pH 4 + 1mM H₂O₂ ($E_{OCP} = +0.2 V_{SCE}$) with a 5 at% O isosurface

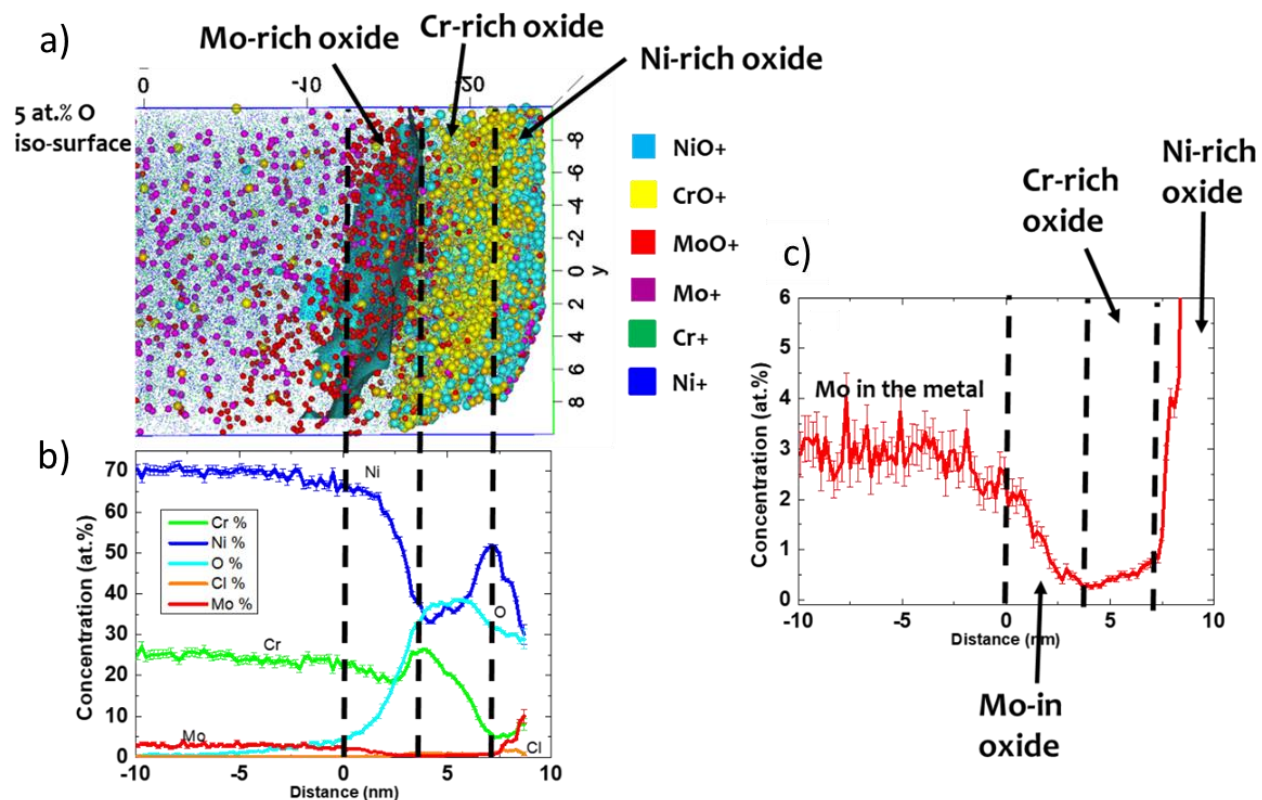


Figure 4.42. a) Detailed chemical data for the oxide on Ni-22 Cr-6 Mo, wt%, for the APT results in Figure 4.41 including a b) 2D compositional line scan and c) a focus on the slight enrichment of Mo throughout the oxide thickness

5. Understanding the Benefit(s) of Mo in a Ni-Cr Alloy: Linking Passivity to Localized Film Initiation and Breakdown in Acidic Environments

5.1 Abstract

The passivation and localized breakdown of several solid solution Ni-22 Cr-x Mo alloys, where $x = 3, 6, 9,$ and $12,$ wt%, was investigated during potentiostatic passivation at $+0.2 V_{SCE}$. Experiments were conducted in acidified $1.0 M NaCl$ using *in operando* single frequency-electrochemical impedance spectroscopy (SF-EIS), *in situ* Mott-Schottky (MS) analysis, and *ex situ* angle-resolved X-ray photoelectron spectroscopy (XPS) following electrochemical testing. The specific roles of Mo minor alloying additions on promoting the enrichment of Cr^{3+} -rich films across several time scales, along with inhibiting localized breakdown are presented. The results provide an increased understanding of the influence Mo cations, when acting as substitutional dopants within a passive film, can have during several stages of passivity: oxide nucleation, growth, breakdown, and repassivation. Specifically, it was found that $9 wt\%$ Mo yielded the optimal corrosion resistance and that ineffective doping can occur for higher Mo base alloy concentrations. This results in poor repassivation due to a decline in the surface enrichment of available, solute-captured $Mo^{4,6+}$ cations.

5.2 Introduction

The benefit of small amounts of Mo in combination with Cr in both nickel-based and ferrous-based alloys have been known for a quite some time and the existence of a Cr–Mo synergy is suggested based on empirical evidence, e.g. Figure 5.1. Neither Ni-Mo nor Ni-Cr alloys achieve the beneficial combined impact of Cr and Mo in combination in acidic chloride solutions demonstrated in Figure 5.1. A part of the community posits that it is well established that Mo is operative during the repassivation stage while chromium is effective mainly towards passivation¹. This view largely neglects the role of Mo in the passive film even though evidence of Mo benefits towards passivation are seen in Fe-Ni-Cr-Mo and Ni-Cr-Mo alloys². To this end, many works in the field often concern only repassivation and/or pit stabilization. However, another part of the research community has argued for many years that Mo operates with benefit towards passivation and providing resistance towards trigger events and leading to local corrosion breakdown of the passivating layer³⁻⁵. This subject was recently debated at a Faraday Discussion of the Royal

Society of Chemistry^{6,7}. Recently, it was also emphasized that highly resistant alloys in relatively benign environments suffer from pitting⁸ due to the controlling passive film and its breakdown, while in harsh environments and for alloys containing many defects including detrimental phases, oxide breakdown is a forgone conclusion and pit stabilization at readily formed initiation sites is the critical factor responsible for attack.

The role of Mo in the pit stabilization and repassivation stages is well supported by experimental findings. However, increasing evidence supports the notion that aliovalent Mo cation oxidation states present in the Cr-rich oxide play an important role towards passivation and resisting passivation breakdown. This finding was originally proposed by Macdonald in the Solute-Vacancy Interaction Model⁹ but high fidelity data is lacking. This finding has recently been seen in a new light due to the high likelihood that Mo is solute trapped or captured in rapidly growing oxides films dominated by Ni(II) and Cr(III) oxides¹⁰. Hence, solid solution oxides containing Mo solute as substitutional impurities at solvent cation sites in super-saturated concentration are likely.

The occurrence of metastable and/or stable pitting along with crevice corrosion can be prevented by alloying with Mo and W due to their facilitation of film repassivation following any initial film thinning before fast dissolution occurs¹¹⁻¹³. The exact mechanism by which this occurs is not fully understood, but there are multiple theories that will be discussed below. In general, however, the induction time for pitting or crevice corrosion will increase with alloying content. Figure 5.2 demonstrates this, where the Ni-11 Cr-x Mo, wt%, alloys creviced after only approximately 100 s, whereas the Ni-22 Cr-x Mo, wt%, remained passive for thousands of seconds. The W-containing alloy, however, remained passive for the entire measurement time.

5.2.1 Phase-Separated Oxides, E-pH, and Speciation Diagrams

The electrochemical stability of a passive film in aqueous environments is often directly tied to its thermodynamic stability. By inspecting the standard Gibbs formation energy, ΔG_f^o , for individual, stoichiometric oxide or hydroxide species that can be possibly formed, the dominant compound can be ascertained. The computed ΔG_f^o values can then be converted into chemical potentials, μ , and, for a given electrochemical reaction, the Nernst equilibrium potential, E_o ¹⁴. For example, when pure Ni metal passivates, it typically forms NiO ($\Delta G_f^o \approx -215 \frac{kJ}{mol}$), and/or Ni(OH)₂ in a state of hydration, following any of the various cathodic reactions possible in aqueous

environments¹⁴⁻¹⁶. Often for the case of multi-element alloys, there may exist a stable species for each metal component that contribute towards film growth. In many cases, the most thermodynamically-stable oxide will form, but there are other situations in which the most kinetically, energetically, or otherwise favorable oxide will instead be favored^{10,15}. For Ni-Cr-based alloys, the most stable species is often Cr-rich (e.g. $\Delta G_{f\text{Cr}_2\text{O}_3}^o = -1,058 \frac{\text{kJ}}{\text{mol}}$ and $\Delta G_{f\text{NiCr}_2\text{O}_4}^o = -1,257 \frac{\text{kJ}}{\text{mol}}$)¹⁷. These formation energies support the thermodynamic notion that the dominant oxides are corundum and Ni spinels.

The thermodynamic stability of pure metals at varying electrochemical potentials and pH's are portrayed in Pourbaix E-pH diagrams such as Figure 5.3 which demonstrates the individual stability regions for Ni, Cr, and Mo species in 1.0 M NaCl¹⁴, represented only as individual elements in passive spinels or stoichiometric, single element oxides. At sufficiently low potentials, the metallic element is stable for all pH with regions of passivation and corrosion, typically evident at high and low pH's, respectively, observed at greater potentials. For some elements (e.g. Al and Fe), amphoteric dissolution can occur in both highly acidic and alkaline environments¹⁴. These diagrams exist for thermodynamic equilibrium conditions and do not take kinetics into consideration. Through overlaying the chemical equilibrium Pourbaix diagrams for each element present in an alloy, its general stability can be inferred. In practical applications, however, actual observed passivity extends past what is predicted by Pourbaix diagrams such as those in Figure 5.3 alone due to the existence of kinetically stable films balanced between metastable film formation and their dissolution. As such, Cr-rich films are often observed to remain passive at pH 3 and below^{1,18-21} using E-log i polarization curves.

5.2.2 Observed Passive Films and Fate of Minor Alloying Elements

While in general the empirical corrosion properties of Ni-alloys, especially common commercial ones like C-22, are well-established^{19,20,22-24}, a full understanding of the exact atomic mechanism by which specific alloying elements act has not yet been achieved²⁵. The results are mainly empirical with some insight mechanistically through work on waste repository engineered container work and confined to commercial alloys^{1,23,26-29}. Similar to stainless steels, additions of Cr will decrease the corrosion rate of Ni-Cr alloys in reducing acid, neutral, and chloride solutions¹¹. The corrosion rate drops significantly, however, when a critical concentration is

reached (>12 wt% Cr for Fe, >8-11 wt% Cr for Ni) and a uniform, Cr-rich, passive film layer (often assumed to be Cr_2O_3 or $\text{Cr}(\text{OH})_3$) forms across the oxide surface^{1,30-32}. Likewise, alloying of Mo and W encourage a similar decrease in the measured uniform passive corrosion rate in both Fe-Cr and Ni-Cr-based alloys³³. There is also an influence on the preferential oxidation of Cr over Ni, as shown in Figure 5.4, where the fraction of Ni-rich oxides formed decreased as [Mo+W] increased between C-22, C-2000, and Alloy 625, all of which have an approximately constant bulk Cr composition²⁷. While the single role of Cr on enabling passive film stability is thoroughly understood, there remains controversy with respect to the additional complexation of minor alloying elements and their function regarding the growth mechanism, distribution, and structure of passive films formed in electrochemical environments²⁵. This disparity is valid specifically with regards to the role of Mo atoms on promoting passivation and repassivation reactions through an unknown, synergistic interaction with the major alloying addition, Cr^{1,3,9,34,35}. Because of the uncertainty, the effects of other dopants as alloying elements cannot be predicted and these alloy choices evolve by trial and error versus scientific understandings.

The bulk of literature concerning the constant-potential passivation of Ni-based superalloys, such as C-22, is accomplished in moderately concentrated NaCl solutions and reports layered, phase-separated oxides based on XPS or ToF-SIMS measurements where a Cr_2O_3 or $\text{Cr}(\text{OH})_3$ -rich film is present at the inner interface and an outer NiO or $\text{Ni}(\text{OH})_2$ film^{24,36,37}, with reported segregation of Mo^{+6} and/or Mo^{+5} cations to the oxide/electrolyte interface as separate MoO_x phase. More recent work utilizing 3DAPT has observed similar distribution of elements throughout the film. However, non-stoichiometric oxide compounds were instead detected¹⁰. As for the mechanism of film growth, *in situ* transmission electron microscopy (TEM) was applied to the early stages of Ni-Cr alloys at 700 °C^{38,39}. In these studies, the initial stage oxidation of dilute Ni-10 at% Cr was revealed to proceed by an adatom mechanism involving surface diffusion of the Ni and O atoms and the nucleation of sub-surface Cr_2O_3 ³⁸. There is some nucleation of NiCr_2O_4 islands, but it was observed that secondary NiO “whisker” phases grew out of the oxide plane and resulted in uneven layering of the different oxides. For the case of Ni-20 at% Cr, the subsurface Cr_2O_3 nuclei are able to coalesce and large NiCr_2O_4 islands emerged from the NiO layer³⁹.

Recently⁴⁰, it was also found that Ni-Cr-Mo alloys similarly exhibit an epitaxial rock-salt oxide early during oxidation, but there were no Kirkendall voids found during *in situ* TEM

experiments, suggesting the influence of Mo^{+6} dopants on inhibiting vacancy coalescence into voids and also increasing the nucleation rate of corundum. Shortly after, metastable corundum-structured and solute captured $\text{Ni}_{2-x}\text{Cr}_x\text{O}_3$ was formed, given in Figure 5.5.a. For comparison, the rocksalt-structured oxide formed on Ni-Cr containing Kirkendall voids is shown in Figure 5.5.b. These results are, however, only indicative of film growth in dry oxidation conditions. There will be a significant influence of environment and subsequent aqueous dissolution during nucleation and growth in electrochemical environments and thus the mechanism will likely adjust¹⁵. It has been shown that water-vapor enhances passivity via the dissociation of protons as they can occupy interstitial lattice positions in the oxide and consequently lower the vacancy formation energy and decrease the diffusion barrier of both cations and anions, therefore facilitating oxidation kinetics⁴¹.

The quantitative effects of alloying Fe with Cr, Ni, and Mo on passivation kinetics have been studied in literature and it was found that both the passivation rate and protectiveness of the film increased with concentration of minor elements. A synergistic affect has been previously observed for both Ni-based and stainless steel alloys, where Mo increases the localized corrosion resistance of Cr-rich passive films by improving passivity and increasing the induction time for pit formation, pitting potential, and decreasing the passive current density^{9,27,35,42,43}. However, this only occurs when Cr and Mo are both present. Kinetic analysis of oxidation through the application of the Cabrera-Mott model has similarly shown that Mo facilitates repassivation and decrease the SCC susceptibility of Fe-Cr stainless steels³³. Similarly, the influences of these alloying additions on high temperature oxidation were found to be similar, where Cr cation transport controls scale growth⁴⁴ and Mo impacts growth by increasing the passivation rate and preventing the formation of Kirkendall voids at the metal/scale interface presumably through electrostatically interacting with metal cation vacancies and reducing their mobility⁴⁵.

The influence of minor alloying elements on the chemical identity of passive films grown slowly on Ni-Cr-based alloys by high temperature oxidation^{38,39,44,46} or using electrochemical potentiostatic or open circuit potentials^{1,26,27,37} has been well-addressed. It has been found that, in general, Cr and Mo preferentially segregate to the metal/film and film/electrolyte interfaces, respectively⁴⁷. Ni-enrichment in passive films on various Ni-Cr-Mo alloys similarly occurs at the inner interface, resulting in the common observation of a distinct “layered” structure of distinct phase-separated oxides with a thin MoO_x outer layer, followed by thick CrO_x and then NiO_x closest

to the metal¹. This analysis might be flawed as it is based on solely binding energies similar to Mo^{4,5,6+}, Cr³⁺ and Ni²⁺ as seen in MoO_x, CrO_x, and NiO_x layers, often suggested by ToF-SIMS^{1,48}, but chemical characterization findings do not indicate structural information which proves that these distinct phase-separated oxides exist. If Mo exists as a dopant in some parent oxide, the next question is its function and relevance towards electrochemical passivation.

Recent modeling work has demonstrated the beneficial impact of Mo alloying on O²⁻ absorption on Ni (111) and Ni-Cr (111) surfaces⁴⁹. While the first-principles model showed that absorption was thermodynamically favorable adjacent to Cr and Mo atoms (Figure 5.6). However, a significant influence of Mo is seen when O is bonded to Ni and/or Mo atoms as it stabilized the reaction by donating more charge than Ni or Cr. While this model is simplistic for a perfect Ni-Cr surface, the observation that Mo facilitates O₂ absorption for various configurations of the atoms can be broadly applied to understand the general and enhanced passivity of Ni-Cr-Mo alloys.

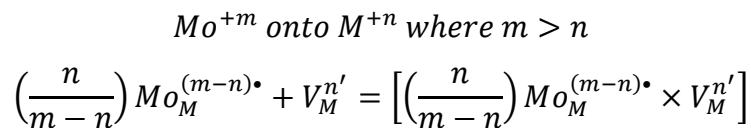
5.2.1 Mechanism for Localized Breakdown

Chloride environments are well-known to complicate passivation reactions through chemical dissolution across the film layer^{13,20,50-57}. As previously mentioned, surface instabilities may be produced which trigger an abrupt breakdown event. Sub-surface penetration can be achieved but is unlikely for non-defective terraces in the passive film. The presence of defects in the film would only mediate halide anion absorption and subsurface penetration. This is evident for preferential depassivation at grain boundaries, for example¹³. Absorption becomes further complicated upon the introduction of multi-element alloys. The PDM indicates that the dissolution of individual minor alloying elements during passive film growth can result in a modification of the oxide chemistry^{4,58}. In particular, the selective dissolution of a specific element can result in the enrichment of others. This phenomenon has been studied previously for Al-based alloys in 3% NaCl solution using AESEC⁵⁹. Competitive formation and chloride-assisted dissolution of both Al(OH)₃ and SiO₂ were observed, whereas Mg appeared to form insoluble MgSiO₃ surface precipitates. This influence of solution chemistry results in greatly different film properties when compared to those grown in sulfate environments. In addition, chloride anion attack at the film/solution interface results in the formation of metal cation vacancies which can aggregate and form Kirkendall voids at the metal/film interface, shown schematically in Figure 5.7¹³. These

clusters may cause instabilities and induce mechanical stresses in the film which, upon reaching a critical size, can burst and form a corrosion pit. As mentioned previously, the addition of minor alloying elements such as Mo is theorized to somehow inhibit the mobility of metal cation vacancies and, therefore, help prevent the formation of Kirkendall voids⁵⁸. In environments containing aggressive anions, such as Cl⁻, most passive films become unstable and degrade at discrete sites, resulting in film breakdown and localized corrosion⁶⁰.

5.2.2 Defect Chemistry with Minor Alloying Elements

In passive films on Ni-based alloys, Ni typically exists as a +2 charged metal cation (Ni²⁺), Cr as Cr³⁺, and Mo as Mo^{4,5,6+ 1}. The influence of specifically Mo on the atomic-scale physical, chemical, and electronic processes relevant for passive film growth has been proposed^{3,6,9,34,36,45,61} but several controversial models exist. It has been observed in previous literature that solute can be captured into a crystal structure during growth (i.e. Cr³⁺ present on a Ni²⁺ site in NiO), resulting in chemical doping of the passive film, often only considered within typical solubility limits but now shown to extend well beyond equilibrium stability^{9,10,44,62,63}. For the situation where Mo⁺⁶ is substituted onto a Ni²⁺ or Cr³⁺ lattice site, the net positive electrostatic charge results in the annihilation of electron holes and the attraction of negatively charged defects, such as metal cation vacancies formed at the film/solution interface by halide anion adsorption^{4,9,64,65}. The resulting complex is neutrally charged and will not contribute towards growth of the cation vacancy condensates which the Point Defect Model (PDM) proposes is a precursor for pit formation⁴. This process is shown schematically in Figure 5.8. The generic reaction for this substitutional effect is given as⁹:



This suggested influence of alloying additions such as Mo among other high cation valency elements on point defect transport across passive films corresponds well with previous work concerning the inhibition of the earliest stages of crevice corrosion on commercial Ni-based superalloys where the effect was largely brought about using low concentrations of Mo in the bulk⁶⁶⁻⁶⁹. The effect of Mo on vacancy mobility has been additionally observed in the case of high temperature oxidation, where the alloying of small (<1%) concentrations reduced the formation of

Kirkendall voids at the metal/oxide interface⁴⁵. An example of this significant impact on void formation is shown in Figure 5.9.

5.2.3 Stabilization and Repassivation of Local Corrosion Sites

Local corrosion stabilization of Ni-Cr-Mo alloys involve a necessary but not sufficient combination of the modified Pickering IR model of activation for a passive material which possesses or develops and active-passive transition and the critical chemistry change model of Galvele and advanced in the case of crevice corrosion in seawater by the dissolution-hydrolysis-acidification chloride ion migration model⁷⁰⁻⁷². This is also consistent with models which propose $E_{ocp} > E_{crit}$ because the IR drop from the mouth of the crevice to the crevice corrosion site places the potential in the nose of the active passive transition especially when local sporadic breakdown occurs⁶⁹. In the case of Ni-Cr-Mo alloys, the critical chemistry change model accounts for the development of the active region in an acidified crevice at high Cl^- . The combination of factors leads to the development of a nose in the anodic current-potential behavior at an occluded site such as a geometric crevice at a critical depth beneath. The nose accounts for the formation of crevice corrosion sites at a depth beneath the crevice mouth that become stabilized when a critical concentration for depassivation is attained⁷³. In order to stabilize the crevice site against repassivation, the crevice growth rate equals or exceeds the dilution rate from the crevice. A salt film may aid this process by buffering this dilution process to maintain the chemistry^{8,74}. Mo enriches at crevice surfaces and decrease the magnitudes of anodic dissolution. Raman spectroscopy indicates polymeric Mo^{x+} species^{28,75}. As more Mo was alloyed the depth of attack is not as deep as Ni-Cr-Mo alloys with less Mo and the attack tends to spreads out suggesting initiation is not improved as much as propagation is hindered⁶⁹. Further evidence of this is seen in an alloy with only 15 wt% Cr but also 22 wt% Mo (HYBRID BC 1) where the passive current density was poor but the repassivation potential was high compared to alloys with less Mo and more Cr⁷⁶.

In light of this, the various roles of Mo on these various processes or stage of local corrosion may be reviewed. First, Mo forms thermodynamically stable oxides at acidic pH levels compared to Cr and Ni. Moreover, the free energy of formation $MoCl_3$ does not suggest its formation compared to Mo oxides⁷⁷. Anderko described the solution chemistry of Mo in acidified chloride

solutions and found stable MoO_2 and MoO_3 at low pH stabilized by higher dissolved Mo and not reduce by decreasing pH and increasing chloride content⁷⁸⁻⁸⁰. Hence, Mo can help Ni-Cr-Mo alloys resists formation of the critical chemistry and thus development of the active E-I nose. Mo on the surface of the alloy effects active dissolution and lowers the crevice passivation potential. Steigerwald, Lizlovs, and Bond first showed the effect Mo on the active passive transition in Fe-Ni-Cr alloys⁸¹. Newman showed that active dissolution in artificial pits lowered the kinetics of Fe-Cr-Mo alloy dissolution⁷⁸. Bocher showed the same effect in Ni-Cr-Mo alloys in strong HCl solution⁶⁶. Mo has beneficial and detrimental effects in the solution phase at local corrosion sites. Mo dissolution may also form MoO_4^{2-} species which has been observed to lower pit or crevice dissolution rates by inhibiting the anodic reaction³⁵. Jakupi furthered the work of these investigators by showing that Mo and W enriched on surfaces and tungstate and molybdate polymeric species are observed in crevices by Raman spectroscopy⁷⁵. Hence it is clear that Mo affects the local corrosion site stabilization and growth stage as well as passivation and breakdown stages of local corrosion. The question arises as to the effect of Mo during passivation. A summary of the possible benefits is given here:

1. Facilitating O^{2-} adsorption^{49,77}
2. Decreased favorability for Cl^- adsorption^{77,82}
3. Encouraging film enrichment of Cr^{3+} ^{1,27,37}
4. Chemical and/or electronic doping of the oxide with Mo^{4,5,6+ 9}
5. Favorable binding energy of Mo cations to metal cation vacancies^{40,45}

5.3 Objective

The influence of Mo alloying on morphological, chemical, electronic, and corrosion properties was characterized with respect to defect density, flat band potential, pitting potentials, metastable pit initiation, and the composition and thickness of passive films. The measured chemical and electronic property variations were correlated to the passive film metastability assessed during potentiostatic holds. The location of Mo was characterized in passive film structure, such as preferential segregation to a particular interface or being located only within a Cr-rich region, for example. By achieving this understanding and through varying the

concentration of Mo in the alloys, the exact mechanisms by which Mo enables passivation and repassivation following metastable breakdown initiation can inform alloy design.

5.4 Approach

The effect of Mo was investigated by applying the analytical framework established in Chapter 2 for analysis of potentiostatic passivation of Ni-22 wt% Cr alloyed with varying Mo content (3, 6, 9, 12 wt% Mo) concentrated 1 M NaCl acidified to pH 4. Additional measurements quantified the chemical, physical, and electronic properties of the passive films during and after growth occurs, including the initiation of metastable film breakdown through analysis of metastability events during the potentiostatic condition along with intermittent MS-EIS and *ex situ* angle-resolved XPS.

5.5 Experimental Methods

The analytical framework established in Chapter 2 was again applied for analysis of passivation for Ni-Cr-Mo alloys with a constant [Cr] and varying [Mo]. To most effectively observe variations in passive behavior and induce some metastable film breakdown, an acidified and more concentrated NaCl environment was used. In connection, *in situ* and *ex situ* experiments were conducted to measure the chemical and electronic properties of the passive films during and after growth occurred.

5.5.1 Materials

The samples used for this study were polycrystalline, solid solution Ni-alloys based off the compositions used previously in this thesis with increasing concentrations of Mo. The achieved compositions are given as Ni-22 wt% Cr-x wt% Mo where $x = 3, 6, 9,$ and 12 based on EDS measurements. The materials were arc-melted, cast, rolled, solutionized, recrystallized, and sectioned. Prior to each experiment, the samples were wet-polished up to 1200 grit using SiC paper, ultrasonically cleaned in alcohol, and rinsed with deionized water (resistivity of 18.2 M Ω -cm) before being placed into the flat cell window. The EBSD images for these alloys following polishing down to 1 μm are given in Figure 5.10.

The solution used for testing were 1.0 M NaCl acidified to pH 4 using 1 M HCl, prepared using reagent grade chemicals dissolved in deionized water dispensed from a Milli-Q. During

electrochemical testing, the electrolyte was deaerated using ultra-high purity N₂ gas during electrochemical experimentation.

5.5.2 Fundamental Electrochemical Characterization

To initially test the electrochemical passivation behavior of the Ni-Cr and Ni-Cr-Mo alloys in the chloride environments, cyclic polarization scans were performed. This was done by initially mechanically grinding the samples to 1200 grit using successively finer SiC papers. Then, the materials were rapidly placed into the window of a vertical three-electrode electrochemical cell (Figure 2.8) which was then filled with the appropriate solution. Upon insertion of a saturated calomel (SCE) electrode, the solution was then deaerated with N₂ gas through a glass bubbler. Potential and current control was accomplished using a Reference 600 Gamry potentiostat.

An initial cathodic reduction step at $-1.3 V_{SCE}$ for 10 min was used before all electrochemical experiments in order to minimize the existence of air-formed oxides on the alloy surface. Then, the sample was potentiodynamically polarized from $-1.3 V_{SCE}$ up to $0.8 V_{SCE}$ and back to $-1.3 V_{SCE}$ in 1 mV steps/s. While this speed is higher than what is typical for passivity studies performed to ASTM standards⁸³ (0.1667 mV/s), a faster sweep was necessary to prevent the agglomeration of H₂ gas bubbles evolved at the metal electrode surface when the potential was sufficiently cathodic. Unlike during the reduction step, their removal was not possible using the pipette attachment as the electrolyte stirring greatly impacted the current measurements. By comparing the current response to the cyclic applied potential for the alloys in different pH environments, the relative improvements via the effects of minor alloying additions and solution chemistry can be inferred. However, these findings are not absolute and as such, the following characterization techniques have been additionally applied.

5.5.3 SF-EIS

The details of the sample preparation and experimental set-up for the SF-EIS experiments are the same as that discussed above. Following the reduction step, the Gamry SF-EIS script was applied at $+0.2 V_{SCE}$ with 1 Hz frequency and a 20 mV AC amplitude. This enabled the measurement of the impedance components Z' and Z'' of the oxide film during passivation (Chapter 2). The measurement time was chosen to be 10,000 s as a pseudo-state in i_{ox} was achieved at this point. In order to apply Equation 2.6 to the SF-EIS results, a full frequency EIS spectrum

was acquired from 100 kHz to 1 mHz to obtain α via a circuit model fit²⁸ (Figure 2.15) and correlate $Z''(t)$ to an oxide thickness, $l_{ox}(t)$. From these results, $i_{ox}(t)$ could also be calculated (Equation 2.11) for each alloy and electrolyte condition.

5.5.4 Mott-Schottky Technique

The measurement of electronic property variation were measured during film growth through application of *in situ* MS-EIS. This was accomplished by changing the voltage of the semiconductor artificially through application of a potentiostat. The details of the sample preparation and experimental set-up for the Mott-Schottky sweep experiments are the same as that discussed for SF-EIS. Following the reduction step, and various amounts of passivation, fast MS impedance sweeps were performed at 1,000 Hz from +300 mV_{SCE} down to -600 mV_{SCE} with 20 mV steps, resulting in sufficiently rapid data acquisition. This was accomplished *in situ* following any amount of experimental passivation, at times from 0 to 10,000 s. As mentioned previously, this scan rate was selected in order to measure the impedance variations as a function of potential without the possibility of the space charge layer adjusting. The results were analyzed as discussed in Section 3.5.5.

5.5.5 Angle-Resolved X-ray Photoelectron Spectroscopy

The variation of film composition and thicknesses were additionally characterized using XPS spectra obtained periodically throughout potentiostatic passive film growth. This technique is well-established in literature for analysis of the identity, concentration, and thicknesses of individual compounds present in films⁸⁴, especially in the case of Ni-based alloys^{1,27,28}. All XPS spectra were obtained using a monochromatic Al- $\kappa\alpha$ photon source ($E = 1,486.7$ eV) with surface characterization following various durations of oxide growth. The angle between the sample and detector was adjusted to 30 and 90°, whereas that between detector and the X-ray source was fixed at 54.7°. Spectra were calibrated to the 4f^{7/2} binding energy of a metallic Au reference (B.E. = 84 eV) measured at the same time. Survey spectra were recorded on all samples using a pass energy of 200 eV, followed by high resolution spectra of the Ni 2p, Cr 3p, Mo 3d, and O 1s regions using a pass energy of 20 eV.

Commercial CasaXPS software was used to perform Shirley background corrections and spectra fitting⁸⁵⁻⁸⁷. The concentrations of Ni²⁺, Cr³⁺, and Mo⁶⁺ cations in the passive films were

computed by fitting the spectra to their observed metallic and oxide/hydroxide peaks, as established in previous literature^{1,27,87-90} and correcting these integrated peak areas to atomic sensitivity factors for Ni, Cr, and Mo (4.044, 2.427, and 3.321 for this detector and source configuration, respectively)⁸⁷ (Table 3.1).

5.5.6 Metastable Pit Event Analysis

The methods previously established for characterizing metastable pit breakdown events will be applied^{69,91-93}. This is shown schematically in Figure 5.11 for a single event. For the Ni-22 Cr-x Mo, wt%, alloys in this task, potentiostatic holds for 10 ks were used at +0.2 V_{SCE}, which is below E_{pit} , yet above E_{rp} , as determined using cyclic potentiodynamic polarization. Each experiment and the relevant metastable breakdown analysis were performed three times, with one data set representative of the whole included herein and the average cumulative number and charge of the breakdown events is provided. Additionally, the presented results in Chapter 4 suggest that the use of 1 M NaCl acidified to pH 4 using 1 M HCl should facilitate film breakdown.

A threshold current increase of 50 nA/cm² was selected based on a previous study which focused on C-22⁶⁹. Through application of analytical tools^{69,91} to compute the cumulative number and peak charge of metastable events during the passivation of each Ni-22 Cr-x Mo, wt%, alloy, the effect of Mo and its theorized function as a point defect which resists film breakdown can be better understood. To ensure the rapid metastable events were sufficiently captured, a low data acquisition rate was used: 20 Hz. The relationship between this rate and the current peaks are demonstrated in Figure 5.12. Based on the peak current, $i_{peak} - i_{baseline}$, and the time elapsed, t_{start} to t_{finish} (Figure 5.11), the anodic charge and corresponding hemispherical pit volume, V_{pit} , and radius, r_{pit} , can be computed through application of Faraday's law:

$$q_{pit} = \int_{t_{start}}^{t_{finish}} i_{peak} - i_{baseline} dt \quad \text{Equation 5.1}$$

$$V_{pit} = \frac{2}{3} \pi r_{pit}^3 = \frac{qM}{z\rho F} \quad \text{Equation 5.2}$$

where the other constants were previously provided for application of SF-EIS and ICP-MS. Based on the sensitivity of the experiment, metastable pits with radii greater than approximately 100 nm can be captured.

5.6 Results

5.6.1 Fundamental Electrochemistry of Ni-Cr-Mo Alloys in Aqueous Chloride Environments

The E-log i passivation behavior of the Ni-Cr-Mo alloys was established in Figure 5.13a. Impedance measurements at 1 Hz enabled assessment of the imaginary component of the passive film impedance and its corresponding capacitance across the same range of applied potentials during potentiodynamic sweeps from $-1.3 V_{SCE}$ to $+0.8 V_{SCE}$ at 1 mV/s (Figure 5.13b). The polarization behavior in Figure 5.13a shows subtle differences between the passivity and transpassivity of each alloy. For these alloys, $+0.2 V_{SCE}$ remains a potential where every alloy is passive and as such it was continued to be used for future experiments. Figure 5.13a shows that $+0.2 V_{SCE}$ is just below the potential above which the passive film degrades for Ni-Cr-3 Mo and slightly below that for Ni-Cr-6 Mo in the acidified 1 M NaCl environment. Additionally, the passive current density decreases with [Mo]. The magnitude of Z'' rises at potentials above $-1.2 V_{SCE}$ and peaks around $+0.2 V_{SCE}$ for every alloy with the exception of Ni-Cr-12 Mo which rapidly passivates before reaching its peak around $-0.1 V_{SCE}$ (Figure 5.13b). Around $+0.2$, however, there is a pseudo-steady state film thickness. The potential at which transpassive dissolution begins appears to increase with [Mo] except for Ni-Cr-9 Mo and Ni-Cr-12 Mo, whose films dissolve at the limit for Cr-rich oxides ($E \approx +0.55 V_{SCE}$). These alloys also exhibited a wide range of passivity from $+0.2$ to $+0.5 V_{SCE}$ before this fast dissolution initiated. Additionally, the peak film thickness was observed for Ni-Cr-12 Mo, whereas that on Ni-Cr-3 Mo was the thinnest.

5.6.2 *In Operando* Characterization

Potentiostatic passivation of Ni-Cr-x Mo at $+0.2 V_{SCE}$ was also investigated in 1.0 M NaCl adjusted to pH 4 and monitored using SF-EIS to investigate the varying thermodynamic and kinetic favorability of oxide species in this particularly corrosion-inducing environment. The measured increases in l_{ox} using the former technique at 1 Hz and $+0.2 V_{SCE}$ are given in Figure 5.14a. It is immediately evident that, similar to the potentiodynamic results in Figure 5.13b, $l_{ox}(t)$ increases with [Mo]. The alloys all exhibited a similar l_{ox} initially, with 12 Mo being slightly thinner. After this, the thickening rate, i_{ox} , appeared to increase with [Mo] to produce the film thickness differences (Figure 5.14b). Because the overall electrochemical rate, given by i_{EC} , was similar for

the alloys, this increase in i_{ox} resulted in greater, average passivation current efficiencies, η , for the alloys richer in Mo, as given in Table 5.1.

5.6.3 Mott-Schottky Analysis

During passivation in the 1.0 M NaCl environments, Mott-Schottky analysis of fast impedance sweeps was applied at times during passivation to characterize the electronic properties of the film and their evolution with time. Noticeably in Figure 5.15, the films predominantly behave as n-type semiconductors within the passive potential region. However, upon increasing the concentration of Mo in the alloys, p-type behavior was dominant at early times and with time, the transition potential shifted to higher values. Ni-Cr-3Mo notably exhibited a similar evolution in C^{-2} with passivation time as the previously shown results for Ni-Cr in 0.1 M NaCl pH 4 (Figure 4.17). As explained previously for Ni-Cr-Mo passivated in 0.1 M NaCl, greater amounts of substitutional defects such as $Mo^{4,6+}$ on a Ni^{2+} or Cr^{3+} site will result in greater p-type behavior. As a result, the dominant point defects for low [Mo] alloys and at lower potentials are likely metal cation vacancies. These are theorized to be detrimental by contributing towards pitting and other forms of film breakdown^{4,57}. At +0.2 V_{SCE}, however, no clear n-type behavior was observed. All alloys exhibited either strong-p-type behavior or a mix between that and n-type (Figure 5.15). Because of this, it is likely oxygen vacancies which control the oxidation process and the relevant kinetics. The flux of the latter was the point defect within a passive film has been previously theorized to be the rate determining step for passivation^{65,94,95}.

Mott-Schottky analysis of these impedance spectra (Figure 5.15) enabled computation of the n- and p-type point defect concentrations (Figure 5.16) along with the respective flat band potential (Figure 5.16). The concentrations do not appear to vary significantly, with a few exceptions. The concentration of mobile n-type point defects clearly decreased during the passivation time with the concentration of Mo in the bulk alloy. The concentration of p-type defects did not strongly vary other than some measured increases for Ni-Cr-9 Mo and Ni-Cr-12 Mo, wt%, after approximately 100 s. This suggests that the capture of Mo as a substitutional, p-type defect occurs early and only enriches for the very high [Mo] alloys. It also acts to minimize the effect of detrimental n-type cation vacancies. Whether this reduction in the amount of these point defects results in better resistance to pitting will be investigated later in this chapter.

The measured passive film flat band potentials tended to increase with passivation time independent of alloy or environment pH (Figure 5.17). Interestingly, the p-type E_{FB} appeared to decrease with [Mo] (Figure 5.17a). The opposite was observed previously in 0.1 M NaCl, where Ni-Cr had a consistently lower p-type E_{FB} than Ni-Cr-Mo (Figure 4.20). This parameter has previously been thought to correlate towards film resistance to localized corrosion and breakdown, shown schematically in Figure 5.18. The alloys all exhibited increasing n-type E_{FB} values with time (Figure 5.17b). However, these increased with the alloying concentration of Mo. These are not typically operative at the potential of interest, +0.2 V_{SCE}, but it is worth noting that for the highest [Mo], the initial E_{FB} was approximately the same as that after 10 ks. The other high-Mo alloys approached this value with the initial values being higher as [Mo] increases. This parameter appears to vary more closely with the film resistance to pitting due to the decreased effect of n-type doping for each alloy. At early times, the greater [Mo] alloys have an exceptional E_{FB} due to the favorable enrichment of Cr₂O₃ within the film. The leveling off of E_{FB} after 50 s suggests that 6 wt% Mo is the critical concentration to achieving the synergistic effect, but it occurs earlier for 9 and 12 wt% Mo.

5.6.4 Angle-Resolved X-Ray Photoelectron Spectroscopy

During the SF-EIS passivation shown in Figure 5.14, focused XPS spectra were obtained at various times: 10, 100, 1,000, and 10,000 s. The Ni 2p^{3/2}, Cr 2p^{3/2}, Mo 3d and O 1s results for the various Ni-Cr-Mo alloys studied in this chapter are given in Figure 5.24 - Figure 5.27. For the most dilute alloy, Ni-22 Cr-3 Mo, wt%, there is a substantial amount of Ni oxidation apparent during the exposure, especially at longer times. The same applies to Cr³⁺ enrichment and after 10ks, it appears that the base alloy surface became effectively depleted of metallic Cr as a result (Figure 5.24b). Mo also almost becomes depleted during the passivation time as it enriches in the film as almost entirely Mo⁶⁺ rather than Mo⁴⁺. The O 1s spectra suggest an early formation of oxides, due to the initially low binding energy at which the peak intensity occurs, but between 1 and 10 ks, noticeable hydration of the film occurs and hydroxides (i.e. Ni(OH)₂ and Cr(OH)₃) dominate the film's molecular identity rather than oxides (i.e. NiO and Cr₂O₃).

The evolution of the passive films on the 6 Mo alloy is similar (Figure 5.25). Upon comparing the Ni 2p^{3/2} metallic and oxide peaks to the spectra for 3 Mo, it is evident that less Ni²⁺ oxidation occurs over 10 ks in favor of Cr³⁺ joining the oxide film. Regarding the Mo 3d spectrum,

there is again predominantly Mo^{6+} cations present, but unlike 3 Mo, some existence of Mo^{4+} is evident. Finally, similar hydration of the film occurred later in the exposure time. Further increases in the Mo concentration within the bulk alloy to 9 and 12 wt% Mo, given in Figure 5.26 and Figure 5.27, continue the same trend. As the fraction of Mo increases, the area for the Ni^{2+} oxide peaks decreases as that for Cr^{3+} films increases. The presence of predominantly Mo^{6+} with some additional Mo^{4+} also occurs, with the areas increased as [Mo] did within the bulk alloy. Moreover, a distinction between the dilute and more concentrated Ni-Cr-x Mo alloys is evident from the O 1s spectra for 9 and 12 wt% Mo. The binding energies at which the peak intensities occur suggests that the films are predominantly hydrous rather than anhydrous oxides. This would arise as a result of less overall film dissolution, also indicated by the oxidation efficiencies in Table 5.1. The continuous replenishment of the film would result in only oxides existing, whereas the more stable films on the 9 and 12 wt% Mo alloys persist and have time to react with the electrolyte to become hydrated.

The compositions for these alloys were computed by fitting the XPS spectra to literature peaks^{85,87}, as explained in detail in the previous chapters. The results are given in Figure 5.23. As suggested by the general appearance of the spectra, the enrichment of Cr^{3+} increases with [Mo] in the bulk alloy. For the alloys more concentrated with Mo, there is no enrichment of $\text{Mo}^{4,6+}$ observed within the film and the final cation fractions appear to be more similar to the fraction within the metal. On the linear time scale, the enrichment of Cr^{3+} and $\text{Mo}^{4,6+}$ continues almost linearly, compensated by the depletion of Ni^{2+} from within the film. Interestingly, the initial fraction of Cr^{3+} cations also increases as [Mo] increases within the bulk. This suggests the oft-held theory that Mo promotes the nucleation of Cr_2O_3 ^{1,2,49,96}.

The films passivated for the entirety of the 10 ks experiment were also characterized using a grazing incident angle (45°) for the X-ray beam. These results are given in Figure 5.24 - Figure 5.27, with the film composition computed by fitting these peak areas obtained at 90° and 45° given in Figure 5.28. In general, there was not substantial layering evident in the spectra. For the most dilute alloy, 3 wt% Mo, there was some slight outer enrichment of Ni^{2+} . This likely arises as a consequence of the lowest fraction of Cr^{3+} within the film and the large amount of dissolution occurring during the $+0.2 \text{ V}_{\text{SCE}}$ potential step (Table 5.1). Regardless, 3 Mo and the other alloys all appeared to demonstrate films which were solid solution oxides, rather than precipitated phases

or layers. It is likely that initially, the oxide matrix is akin to a NiO rocksalt with some solute captured Cr^{3+} where the concentration of the latter occurs during the extended exposure^{10,97,98}. Whether this film changes structure to corundum is uncertain, as XPS spectra only suggest local chemistries, rather than the crystallographic structure of an oxide.

5.6.5 Metastable Pitting Event Analysis

To test the resistance of these films to localized breakdown, metastable pitting experiments were performed for each alloy thrice in order to generate some statistics. This is shown for 3 Mo in Figure 5.29. The replicability of this data is demonstrated. For reference, the occurrence of crevice corrosion along with some metastable events is included in Figure 5.29. Experiments which behaved in this way were excluded from further analysis. In comparison, the three current decays for the most concentrated alloy, 12 Mo, are given in Figure 5.30. The characteristic metastable breakdown of the potentiostatically-formed passive films on the Ni-Cr-x Mo alloys in 1.0 M NaCl acidified to pH 4 is given in Figure 5.31. The effect of increasing concentrations of Mo are immediately evident. The overall current appeared to decrease with increases in [Mo]. The 3 Mo alloy underwent a substantial number of metastable pitting events at early times and only a few later on. This suggests that the available cathodic current for pitting was consumed early. The high Mo alloys – 9 and 12 wt% - similarly had most breakdown occurring early, albeit with lower current spikes because of the effect of Mo on repassivation.

Detailed analysis of the size and frequency of the metastable pitting activity shown in Figure 5.31 is provided in Figure 5.33. As can be directly inferred from the original figure, Ni-Cr-3 Mo exhibited significant and numerous pitting events during potentiostatic passivation (Figure 5.33a). This was especially true at early times before the breakdown rate decreased. Ni-Cr-6 Mo behaved similarly with fast, early pitting that leveled off (Figure 5.33ab). Regarding the higher [Mo] alloys, 9 Mo had slow, small pitting behavior at early times which leveled off. The sizes of metastable pits forming were much larger for 12 Mo (Figure 5.33c), albeit less frequent at longer times (Figure 5.33ac). 12 Mo also underwent faster and more significant pitting at early times than 9 Mo. The charge for pits formed for 6 Mo at longer times was, however, substantial and resulted in small increases in the cumulative value (Figure 5.33c) whereas 3 Mo reached a steady state somewhat early on. Overall, the pitting damage increased as $9 \text{ Mo} < 12 \text{ Mo} < 6 \text{ Mo} < 3 \text{ Mo}$. This suggests that there is an optimal Mo alloying concentration where it can best achieve synergy with

the Cr-rich film but there is not too much chemical doping of the film. In this case, excess $\text{Mo}^{4,6+}$ concentrations could result in the precipitation of Mo-oxides (i.e. MoO_2 and/or MoO_3) from the Ni and/or Cr-rich films and therefore Mo cations expend less protection towards resisting localized breakdown.

5.7 Discussion

5.7.1 Chemical Identity of Passive Films

There are substantial consequences that varying the concentration of Mo, the minor alloying element within the presented Ni-22 Cr, wt%, alloy, can have on the corrosion behavior of the material. Of these, the most fundamental effect is the chemical composition of the electrochemically-produced passive film. Other variations in properties and behavior originate from these sometimes seemingly inconsequential differences. In the results presented, the amount of Mo within the metallic matrix was varied from 3 to 12 wt%. While the $\text{Mo}^{4,6+}$ cation fraction did noticeably increase as a result, the most substantial effect was the strong enrichment of Cr^{3+} within the film. This occurred as a consequence of the greater presence of Mo within the base alloy.

Noticeably, the alloy content also substantially influenced the film after only 10 s of passivation. Figure 4.14 previously demonstrated early Ni^{2+} oxidation with concurrent, albeit slowed, Cr^{3+} enrichment occurring at longer times for the 6 Mo alloy passivated in 0.1 M NaCl acidified to pH 4. However, the same alloy passivated in 1.0 M NaCl has slightly more favorable Cr-oxidation initially, followed by a steady increase in the fraction of Cr^{3+} cations. This suggests an influence of the environment, similar to what was previously observed for transitioning from passivating in aqueous sulfate to the dilute Cr. The heightened influence of chloride resulted in more substantial early and continuing preferential Ni^{2+} dissolution in Figure 5.23. Because Cr_2O_3 and $\text{Cr}(\text{OH})_3$ films are inherently more protective than NiO and $\text{Ni}(\text{OH})_2$ ^{1,30,31,99}, the increased fraction of Cr^{3+} cations, enabled by greater alloying of Mo, would suggest increased performance of the alloys. However, such significant Cr^{3+} -enrichment resulted in some apparent depletion of Cr from the surface of the base alloy upon comparison of the XPS peak intensities for metallic Ni and Cr in the respective $2p^{3/2}$ spectra.

There was also no observed segregation of cations within the films due to the constant chloride-assisted dissolution occurring and instead, the films appear to remain predominantly solute captured during the 10 ks experiment time^{10,97}. This is crucial for the alloys which are more concentrated with Mo, as the precipitation of a local MoOx precipitate would lend less protection against localized corrosion. However, if this occurred homogeneously within the film, AR-XPS would not detect this and a more structure-sensitive technique such as TEM would be necessary,

Along with the chemical identity, the molecular arrangement of the cations also varied. The O 1s spectra obtained for the 3 Mo (Figure 5.19) and 6 Mo (Figure 5.20) alloys suggested that the passive films remained crystalline oxides until hydration occurred at later times. Most likely, this is caused by the significant dissolution of the film in the 1.0 M NaCl environment. The constant replenishment of the oxide effectively inhibited any hydration until a conformal, protective layer was achieved after 1 ks. This greater amount of dissolution is reflected in the decreases in $l_{ox}(t)$, $i_{ox}(t)$, and $\eta(t)$ (Figure 5.14 and Table 5.1). The more inherently protective and Cr³⁺-rich films on the 9 Mo (Figure 5.21) and 12 Mo (Figure 5.22) alloys became hydrated early due to the lower dissolution and oxidation efficiency also shown in Figure 5.14 and Table 5.1.

5.7.2 Electronic Behavior of Passive Films

The existence of these solute captured and relatively homogeneous passive films has strong implications for the electronic behavior and related localized breakdown of the passive films as both processes are governed by the presence of point defects. The substantial chemical doping of the film, whether it be Cr_{Ni}^* , Mo_{Ni}^{4+} , or Mo_{Cr}^{3+} , results in a highly complex balance of ionic defects. For instance, increasing the concentration of Mo within the bulk alloy resulted in greater p-type behavior due to the increased enrichment of the three solute-captured species previously indicated (Figure 5.15). Mott-Schottky analysis of the impedance sweeps revealed the concentrations of n and p-type point defects tends to decrease with time as annealing occurs and with [Mo] as greater doping results in subsequent balancing of dislike charges. However, upon increasing the Mo alloying content beyond 6 wt%, there was some slight, and late increases in both N_D and N_A measured. The larger change was observed for N_A as greater concentrations of Mo dopants became enriched in the film (Figure 5.23) and to compensate, the concentration of n-type defects also

increased. However, for these two alloys there was also an unexpected overall increase in both N_D and N_A when going from 9 to 12 wt% Mo. The increased concentration of the defects for the latter alloy could come as a result of excessive Mo doping, perhaps to the point of the film behaving as a degenerate semiconductor¹⁰⁰⁻¹⁰². There is also some likelihood of local precipitation of homogeneous MoOx phases, as suggested previously, and therefore a decreased capability for inhibiting the motion of point defects and subsequent localized corrosion^{103,104}.

The n-type flat-band potential functions in a semiconductor to fix the position of the conduction band^{105,106}. The limit demonstrated in Figure 5.17 suggests that this is approximately a constant value, unlike the steadily increasing p-type E_{FB} . Therefore, the greater p-type doping of the passive film with higher [Mo] results in effective acceptor states within the bandgap for the oxide and, therefore, a smaller bandgap (Figure 5.18). Previously, an increase in the pitting potential with decreasing p-type E_{FB} was observed for Ni-based alloys as the concentration of Cr in the bulk increased¹⁰⁶. This behavior is the same as shown for Ni-Cr-x Mo, as local film breakdown (Figure 5.13) and the p-type E_{FB} have been demonstrated to decrease with [Mo]. As a consequence of the changes to the bandgap upon alloying, it should be apparent that absolute differences in E_{FB} do not necessarily correlate to film stability. Rather, for a single alloy an increasing E_{FB} indicates relative improvements in the resistance to localized breakdown.

The metastable pitting behavior demonstrated appears to be closely tied to the Mott-Schottky results as localized breakdown is thought to derive from the flux of metal cation vacancies^{2,4,94}. Notably, the best overall corrosion performance was achieved by the 9 Mo alloy rather than 12 Mo. This is presumably caused by the excessive doping of the film on the latter and local precipitation of MoOx throughout the passive film at long times. Additional characterization, of both the electronic and crystallographic structure of these passive films is necessary in order to conclusively establish the atomistic cause for the slight decline in performance for 12 Mo compared to 9, but overall it still underwent less significant breakdown than the 3 and 6 Mo alloys.

5.7.3 Influence of Mo

In Figure 5.23 there was a consistent increase in the fraction of Cr^{3+} cations as [Mo] in the bulk alloy also increased. The overall electrochemical behavior also improved, resulting in increases of l_{ox} , E_{trans} , and a decrease in i_{pass} (Figure 5.13 and Figure 5.14). During the metastable pitting experiments, there was an observed decrease in the average i_{EC} as [Mo]

increased (Figure 5.31). This overall improvement in passivity likely comes as a result of Mo encouraging Cr³⁺ enrichment^{1,2}. Recently, it has been demonstrated that when Mo and Cr are adjacent to each other on the metal surface, Mo stabilizes the adsorption of oxygen and makes Cr-oxidation more thermodynamically favorable⁴⁹. Therefore, the probability of Mo being the nearest neighbor to a Cr atom increases as the bulk alloying content increases.

Mott-Schottky analysis of the impedance sweeps revealed that varying [Mo] similarly had a substantial effect on the electronic behavior. Increasing the Mo^{4,6+} cation fraction within the passive layer clearly demonstrated a decrease in the effective concentrations of detrimental defects (Figure 5.16). The observed doping of the film as a consequence of solute capture^{10,98} produced localized donor states within the electronic band structure of the semiconducting oxides, effectively lowering the gap¹⁰³. The consequence of this is easier passivation and neutralization of oppositely charged point defects, e.g. $V_{Cr}''' \times Mo_{Cr}^{3\bullet}$ ^{98,107}. The promotion of Cr₂O₃ formation ($E_g \approx 3 \text{ eV}$), rather than NiO ($E_g = 3.6 - 4 \text{ eV}$), also helps to lower the overall gap of the oxide, as established using photocurrent spectroscopy¹⁰⁸.

As discussed previously, excessive doping of Mo^{4,6+} cations within the film resulted in a corresponding increase in the concentration of detrimental n-type metal cation vacancies. Localized corrosion for the 12 Mo alloy was observed as worse than that on 9 Mo due to the ease of repassivation for the latter. Film dissolution via events like pitting often results in the precipitation of Mo-rich oxides as a means for reestablishing a local passive layer^{2,109,110}. In the case of the 12 Mo alloy. It is speculated that this is not as possible despite the higher overall fraction of Mo^{4,6+} cations observed within the film as the local accumulation and precipitation of local Mo-oxides inhibits their ability to enrich at the surface and repassivate a metastable pit once dissolution occurs. This is demonstrated schematically in Figure 5.36. The 9 Mo alloy does not have the same difficulty, and this results in the lower corrosion damage after 10 ks compared to 12 Mo despite a higher number of events occurring. Photocurrent emission spectroscopy has demonstrated that the presence of deep-level donor states, as could occur for the excessive doping within the film on the 12 Mo alloy, the film resistance decreases and, therefore, localized corrosion becomes more likely¹⁰³.

An optimal concentration of 9 wt% Mo appears to exist for the presented Ni-Cr-Mo alloys. The Mott-Schottky measurements of E_{FB} also suggest that 3 Mo is insufficient for achieving the

optimal synergy between Cr and Mo. The existence of solute captured passive films produced by continuous chloride adsorption, film dissolution, and subsequent replenishment resulted in a homogeneous distribution of cations within the film. However, in the less corrosive media studied previously (i.e. 0.1 M Na₂SO₄ and 0.1 M NaCl) or with extended passivation times the occurrence of Mo^{4,6+} cation segregation and phase precipitation would afford less benefit with regards to localized corrosion. This was observed to be the case of 12 Mo, where the film was observed to be more corrosion resistant overall due to its greater Cr³⁺ cation content, but the lessened surface enrichment of Mo^{4,6+} resulted in slower repassivation and, therefore, greater localized corrosion damage.

5.8 Conclusions

The passivation and localized breakdown of several Ni-22 Cr-x Mo alloys, where x = 3, 6, 9, and 12, wt%, was investigated during in operando potentiostatic passivation at +0.2 V_{SCE} using SF-EIS in an acidified 1.0 M NaCl environment. In situ impedance sweeps were obtained during film growth to enable Mott-Schottky analysis of the electronic behavior of the passive oxides. Similarly, angle-resolved XPS spectra unveiled the chemical identity of the passive films. The results upheld the literature theory that increasing the alloying concentration of Mo in a Ni-Cr matrix increases the fraction of Cr³⁺ cations within the passive films produced during anodic polarization. The influence of Mo on lessening the thermodynamic and kinetic barriers for the early nucleation and enrichment of Cr₂O₃ rather than NiO was also evident. Results were consistent with Mo doping, but no proof was obtained. Varying the bulk concentration of Mo resulted in significant electronic benefits and drawbacks following Mo^{4,6+} solute within the Ni²⁺ and Cr³⁺-rich passive film. Notably, excessive doping of the surface film on the 12 w% Mo alloy resulted in poorer localized corrosion behavior than the 9 wt% Mo, despite its increased Cr³⁺ content. This suggests that the latter alloy affords more optimal corrosion behavior overall in the acidic 1.0 M NaCl environment.

5.9 References

1. Lloyd, A. C., Noël, J. J., McIntyre, S. & Shoesmith, D. W. Cr, Mo and W alloying additions in Ni and their effect on passivity. *Electrochim. Acta* **49**, 3015–3027 (2004).
2. Lutton Cwalina, K., Demarest, C. R., Gerard, A. Y. & Scully, J. R. Revisiting the effects of molybdenum and tungsten alloying on corrosion behavior of nickel-chromium alloys in aqueous corrosion. *Curr. Opin. Solid State Mater. Sci.* (2019).

3. Clayton, C. R. & Lu, Y. C. A Bipolar Model of the Passivity of Stainless Steel: The Role of Mo Addition. *J. Electrochem. Soc.* **133**, 2465–2473 (1986).
4. Lin, L. F., Chao, C. Y. & Macdonald, D. D. A point defect model for anodic passive films II. Chemical breakdown and pit initiation. *J. Electrochem. Soc.* **128**, 1194–1198 (1981).
5. Macdonald, D. D. Some personal adventures in passivity—A review of the point defect model for film growth. *Russ. J. Electrochem.* **48**, 235–258 (2012).
6. Maurice, V. *et al.* Effects of molybdenum on the composition and nanoscale morphology of passivated austenitic stainless steel surfaces. *Faraday Discuss* **180**, 151–170 (2015).
7. Frankel, G. *et al.* Localised corrosion: general discussion. *Faraday Discuss.* **180**, 381–414 (2015).
8. Frankel, G. S., Li, T. & Scully, J. R. Localized Corrosion: Passive Film Breakdown vs Pit Growth Stability. *J. Electrochem. Soc.* **164**, C180–C181 (2017).
9. Urquidi, M. & Macdonald, D. D. Solute-vacancy interaction model and the effect of minor alloying elements on the initiation of pitting corrosion. *J. Electrochem. Soc.* **132**, 555–558 (1985).
10. Yu, X. X. *et al.* Nonequilibrium Solute Capture in Passivating Oxide Films. *Phys. Rev. Lett.* **121**, 145701 (2018).
11. McCafferty, E. *Introduction to corrosion science.* Springer (Springer, 2010). doi:10.1007/978-1-4419-0455-3
12. Jones, D. A. *Principles and prevention of corrosion.* (Prentice Hall, 1996).
13. Marcus, P., Maurice, V. & Strehblow, H. H. Localized corrosion (pitting): A model of passivity breakdown including the role of the oxide layer nanostructure. *Corros. Sci.* **50**, 2698–2704 (2008).
14. Pourbaix, M. *Atlas of electrochemical equilibria in aqueous solutions.* (National Association of Corrosion Engineers, 1974).
15. Lutton, K., Gusieva, K., Ott, N., Birbilis, N. & Scully, J. R. Understanding multi-element alloy passivation in acidic solutions using operando methods. *Electrochem. commun.* **80**, 44–47 (2017).
16. Huang, L.-F., Hutchison, M. J., Santucci, R. J., Scully, J. R. & Rondinelli, J. M. Improved Electrochemical Phase Diagrams from Theory and Experiment: The Ni-Water System and Its Complex Compounds. *J. Phys. Chem. C* **121**, 9782–9789 (2017).
17. Speight, J. G. & Lange, N. A. *Lange's handbook of chemistry.* (McGraw-Hill Education, 2017).
18. Rodríguez, M. A., Carranza, R. M. & Rebak, R. B. Passivation and Depassivation of Alloy 22 in Acidic Chloride Solutions. *J. Electrochem. Soc.* **157**, C1–C8 (2010).
19. Rebak, R. B. & Payer, J. H. Passive corrosion behavior of alloy 22. in *11th International High Level Radioactive Waste Management Conference* 1–7 (2006).
20. Gray, J. J., Hayes, J. R., Gdowski, G. E., Viani, B. E. & Orme, C. A. Influence of Solution pH, Anion Concentration, and Temperature on the Corrosion Properties of Alloy 22. *J. Electrochem. Soc.* **153**, B61–B67 (2006).
21. Lu, P. *et al.* Computational materials design of a corrosion resistant high entropy alloy for harsh environments. *Scr. Mater.* **153**, 19–22 (2018).
22. Rebak, R. B. & Crook, P. Influence of the Environment on the General Corrosion Rate of Alloy 22. in *American Society of Mechanical Engineers Pressure Vessels and Piping Division Conference* 1–8 (2004). doi:10.1115/PVP2004-2793

23. Jakupi, P., Noël, J. J. & Shoesmith, D. W. The evolution of crevice corrosion damage on the Ni-Cr-Mo-W alloy-22 determined by confocal laser scanning microscopy. *Corros. Sci.* **54**, 260–269 (2012).
24. Zagidulin, D., Zhang, X., Zhou, J., Noël, J. J. & Shoesmith, D. W. Characterization of surface composition on Alloy 22 in neutral chloride solutions. *Surf. Interface Anal.* **45**, 1014–1019 (2013).
25. Scully, J. R. Corrosion chemistry closing comments: opportunities in corrosion science facilitated by operando experimental characterization combined with multi-scale computational modelling. *Faraday Discuss. Faraday Discuss* **180**, 577–593 (2015).
26. Lloyd, A. C., Shoesmith, D. W., McIntyre, N. S. & Noël, J. J. Effects of Temperature and Potential on the Passive Corrosion Properties of Alloys C22 and C276. *J. Electrochem. Soc.* **150**, B120–B130 (2003).
27. Lloyd, A. C., Noël, J. J., McIntyre, N. S. & Shoesmith, D. W. The open-circuit ennoblement of alloy C-22 and other Ni-Cr-Mo alloys. *JOM* **57**, 31–35 (2005).
28. Jakupi, P., Zagidulin, D., Noël, J. J. & Shoesmith, D. W. The impedance properties of the oxide film on the Ni-Cr-Mo Alloy-22 in neutral concentrated sodium chloride solution. *Electrochim. Acta* **56**, 6251–6259 (2011).
29. Mishra, A. K., Ramamurthy, S., Biesinger, M. & Shoesmith, D. W. The activation/depassivation of nickel-chromium-molybdenum alloys in bicarbonate solution: Part I. *Electrochim. Acta* **100**, 118–124 (2013).
30. McCafferty, E. Relationship Between Graph Theory and Percolation Approaches in the Passivity of Fe–Cr Binary Alloys. *J. Electrochem. Soc.* **155**, C501–C505 (2008).
31. McCafferty, E. Graph theory and the passivity of binary alloys. *Corros. Sci.* **42**, 1993–2011 (2000).
32. McCafferty, E. Oxide networks, graph theory, and the passivity of binary alloys. *Corros. Sci.* **44**, 1393–1409 (2002).
33. Cho, E.-A., Kim, C.-K., Kim, J.-S. & Kwon, H.-S. Quantitative analysis of repassivation kinetics of ferritic stainless steels based on the high field ion conduction model. *Electrochim. Acta* **45**, 1933–1942 (2000).
34. Sugimoto, K. & Sawada, Y. Role of Alloyed Molybdenum in Austenitic Stainless Steels in the Inhibition of Pitting in Neutral Halide Solutions. *Corrosion* **32**, 347–352 (1976).
35. Lillard, R. S., Jurinski, M. P. & Scully, J. R. Crevice Corrosion of Alloy-625 in Chlorinated ASTM Artificial Ocean Water. *Corrosion* **50**, 251–265 (1994).
36. Hayes, J. R., Gray, J. J., Szmodis, A. W. & Orme, C. A. Influence of chromium and molybdenum on the corrosion of nickel-based alloys. *Corrosion* **62**, 491–500 (2006).
37. Zhang, X., Zagidulin, D. & Shoesmith, D. W. Characterization of film properties on the NiCrMo Alloy C-2000. *Electrochim. Acta* **89**, 814–822 (2013).
38. Luo, L. *et al.* In-situ transmission electron microscopy study of surface oxidation for Ni-10Cr and Ni-20Cr alloys. *Scr. Mater.* **114**, 129–132 (2016).
39. Luo, L. *et al.* In situ atomic scale visualization of surface kinetics driven dynamics of oxide growth on a Ni–Cr surface. *Chem. Commun.* **52**, 3300–3303 (2016).
40. Yu, X. *et al.* In-situ observations of early stage oxidation of Ni-Cr and Ni-Cr-Mo alloys. *Corrosion* **74**, 939–946 (2018).
41. Luo, L. *et al.* Atomic origins of water-vapour-promoted alloy oxidation. *Nat. Mater.* **17**, 514–518 (2018).

42. Ebrahimi, N. The Influence of Alloying Elements on The Crevice Corrosion Behaviour of Ni-Cr-Mo Alloys. (The University of Western Ontario, 2015).
43. Marshall, P. I. & Burstein, G. T. Effects of alloyed molybdenum on the kinetics of repassivation on austenitic stainless steels. *Corros. Sci.* **24**, 463–478 (1984).
44. Takei, A. & Nii, K. The Growth Process of Oxide Layers in the Initial Stage of Oxidation of 80Ni-20Cr Alloy. *Trans. Japan Inst. Met.* **17**, 211–219 (1976).
45. Yun, D. W., Seo, H. S., Jun, J. H., Lee, J. M. & Kim, K. Y. Molybdenum effect on oxidation resistance and electric conduction of ferritic stainless steel for SOFC interconnect. *Int. J. Hydrogen Energy* **37**, 10328–10336 (2012).
46. Luo, H., Gao, S., Dong, C. & Li, X. Characterization of electrochemical and passive behaviour of Alloy 59 in acid solution. *Electrochim. Acta* **135**, 412–419 (2014).
47. Marcus, P. On some fundamental factors in the effect of alloying elements on passivation of alloys. *Corros. Sci.* **36**, 2155–2158 (1994).
48. Zhang, X. & Shoesmith, D. W. Influence of temperature on passive film properties on Ni-Cr-Mo Alloy C-2000. *Corros. Sci.* **76**, 424–431 (2013).
49. Samin, A. J. & Taylor, C. D. First-principles investigation of surface properties and adsorption of oxygen on Ni-22Cr and the role of molybdenum. *Corros. Sci.* **134**, 103–111 (2018).
50. Marks, L. Competitive Chloride Chemisorption Disrupts Hydrogen Bonding Networks: DFT, Crystallography, Thermodynamics and Morphological Consequences. *Corrosion* **74**, 295–311 (2017).
51. MacDougall, B. Effect of Chloride Ion on the Localized Breakdown of Nickel Oxide Films. *J. Electrochem. Soc.* **126**, 919–925 (1979).
52. Natishan, P. M. Perspectives on Chloride Interactions with Passive Oxides and Oxide Film Breakdown. *Corrosion* (2017).
53. Kunze, J., Maurice, V., Klein, L. H., Strehblow, H. H. & Marcus, P. In situ STM study of the effect of chlorides on the initial stages of anodic oxidation of Cu(111) in alkaline solutions. *Electrochim. Acta* **48**, 1157–1167 (2003).
54. Bouzoubaa, A., Diawara, B., Maurice, V., Minot, C. & Marcus, P. Ab initio modelling of localized corrosion: Study of the role of surface steps in the interaction of chlorides with passivated nickel surfaces. *Corros. Sci.* **51**, 2174–2182 (2009).
55. Kolotyrkin, J. M. Effects of Anions on the Dissolution Kinetics of Metals. *J. Electrochem. Soc.* **108**, 209–216 (1961).
56. Sosa, S., Rodriguez, M. A. & Carranza, R. M. Determining the Effect of the Main Alloying Elements on Localized Corrosion in Nickel Alloys using Artificial Neural Networks. *Procedia Mater. Sci.* **8**, 21–28 (2015).
57. Ter-Ovanessian, B., Mary, N. & Normand, B. Passivity Breakdown of Ni-Cr Alloys: From Anions Interactions to Stable Pits Growth. *J. Electrochem. Soc.* **163**, C410–C419 (2016).
58. Macdonald, D. D. The Point Defect Model for the Passive State. *J. Electrochem. Soc.* **139**, 3434–3449 (1992).
59. Serdechnova, M., Volovitch, P., Brisset, F. & Ogle, K. On the cathodic dissolution of Al and Al alloys. *Electrochim. Acta* **124**, 9–16 (2014).
60. Natishan, P. M. & O’Grady, W. E. Chloride Ion Interactions with Oxide-Covered Aluminum Leading to Pitting Corrosion: A Review. *J. Electrochem. Soc.* **161**, C421–C432 (2014).

61. Bojinov, M. *et al.* Influence of molybdenum on the conduction mechanism in passive films on iron-chromium alloys in sulphuric acid solution. *Electrochim. Acta* **46**, 1339–1358 (2001).
62. Douglass. The oxidation mechanism of dilute Ni-Cr alloys. *Corros. Sci.* **8**, 665–678 (1968).
63. Liang, D., Shao, W. & Zangari, G. Selection of phase formation in electroplated Ag-Cu alloys. *J. Electrochem. Soc.* **163**, 40–48 (2016).
64. Unutulmazsoy, Y., Merkle, R., Mannhart, J. & Maier, J. Chemical diffusion coefficient of Ni in undoped and Cr-doped NiO. *Solid State Ionics* **309**, 110–117 (2017).
65. Chao, C. Y., Lin, L. F. & Macdonald, D. D. A point defect model for anodic passive films I. Film growth kinetics. *J. Electrochem. Soc.* **128**, 1187–1194 (1981).
66. Bocher, F., Huang, R. & Scully, J. R. Prediction of critical crevice potentials for Ni-Cr-Mo alloys in simulated crevice solutions as a function of molybdenum content. *Corrosion* **66**, 1–15 (2010).
67. Kehler, B. A., Ilevbare, G. O. & Scully, J. R. Comparison of the crevice corrosion resistance of alloys 625 and C22. *Passiv. Localized Corros. an Int. Symp. Honor Profr. Norio Sato* **99**, 644–654 (1999).
68. Kehler, B. a, Ilevbare, G. O. & Scully, J. R. Crevice Corrosion Stabilization and Repassivation Behavior of Alloys 625 and 22. *Corrosion* **57**, 1042–1065 (2001).
69. Kehler, B. A. & Scully, J. R. Role of metastable pitting in crevices on crevice corrosion stabilization in Alloys 625 and 22. *Corrosion* **61**, 665–684 (2005).
70. Pickering, H. W. Important Early Developments and Current Understanding of the IR Mechanism of Localized Corrosion. *J. Electrochem. Soc.* **150**, K1 (2003).
71. Shaw, B. A., Moran, P. J. & Gartland, P. O. The role of ohmic potential drop in the initiation of crevice corrosion on alloy 625 in seawater. *Corros. Sci.* **32**, 707–719 (1991).
72. Galvele, J. R. Transport Processes and the Mechanism of Pitting of Metals. *J. Electrochem. Soc.* **123**, 464 (1976).
73. Bocher, F., Presuel-Moreno, F. & Scully, J. R. Investigation of Crevice Corrosion of AISI 316 Stainless Steel Compared to Ni–Cr–Mo Alloys Using Coupled Multielectrode Arrays. *J. Electrochem. Soc.* **155**, C256 (2008).
74. Li, T., Scully, J. R. & Frankel, G. S. Localized Corrosion: Passive Film Breakdown vs Pit Growth Stability: Part II. A Model for Critical Pitting Temperature. *J. Electrochem. Soc.* **165**, C484–C491 (2018).
75. Jakupi, P., Wang, F., Noël, J. J. & Shoesmith, D. W. Corrosion product analysis on crevice corroded Alloy-22 specimens. *Corros. Sci.* **53**, 1670–1679 (2011).
76. Mishra, A. K. & Frankel, G. S. Crevice Corrosion Repassivation of Alloy 22 in Aggressive Environments. *CORROSION* **64**, 836–844 (2008).
77. Taylor, C. D., Lu, P., Saal, J., Frankel, G. S. & Scully, J. R. Integrated computational materials engineering of corrosion resistant alloys. *npj Mater. Degrad.* **2**, 1–10 (2018).
78. Newman, R. C. The dissolution and passivation kinetics of stainless alloys containing molybdenum—II. Dissolution kinetics in artificial pits. *Corros. Sci.* **25**, 341–350 (1985).
79. Newman, R. C. The dissolution and passivation kinetics of stainless alloys containing molybdenum—1. Coulometric studies of Fe-Cr and Fe-Cr-Mo alloys. *Corros. Sci.* **25**, 331–339 (1985).
80. Wang, P., Wilson, L. L., Wesolowski, D. J., Rosenqvist, J. & Anderko, A. Solution chemistry of Mo(III) and Mo(IV): Thermodynamic foundation for modeling localized

- corrosion. *Corros. Sci.* **52**, 1625–1634 (2010).
81. Steigerwald, R. F., Bond, A. P., Dundas, H. J. & Lizlovs, E. A. The New Fe-Cr-Mo Ferritic Stainless Steels. *Corrosion* **33**, 279–295 (1977).
 82. Tobler, W. J. & Virtanen, S. Effect of Mo species on metastable pitting of Fe18Cr alloys-A current transient analysis. *Corros. Sci.* **48**, 1585–1607 (2006).
 83. Standard test method for conducting cyclic potentiodynamic polarization measurements to determine the corrosion susceptibility of small implant devices. *ASTM F2129-06* (2001).
 84. Strohmeier, B. R. An ESCA method for determining the oxide thickness on aluminum alloys. *Surf. Interface Anal.* **15**, 51–56 (1990).
 85. Biesinger, M. C. *et al.* Resolving surface chemical states in XPS analysis of first row transition metals, oxides and hydroxides: Cr, Mn, Fe, Co and Ni. *Appl. Surf. Sci.* **257**, 2717–2730 (2011).
 86. Werfel, F. & Minni, E. Photoemission study of the electronic structure of Mo and Mo oxides. *J. Phys. C Solid State Phys.* **16**, 6091–6100 (1983).
 87. Moulder, J. F., Stickle, W. F., Sobol, P. E. & Bomben, K. D. Handbook of X-ray Photoelectron Spectroscopy. 261 (1992).
 88. Biesinger, M. C., Payne, B. P., Lau, L. W. M., Gerson, A. & Smart, R. S. C. X-ray photoelectron spectroscopic chemical state Quantification of mixed nickel metal, oxide and hydroxide systems. *Surf. Interface Anal.* **41**, 324–332 (2009).
 89. Biesinger, M. C. *et al.* Quantitative chemical state XPS analysis of first row transition metals, oxides and hydroxides. *J. Phys. Conf. Ser.* **100**, 012025 (2008).
 90. Baltrusaitis, J. *et al.* Generalized molybdenum oxide surface chemical state XPS determination via informed amorphous sample model. *Appl. Surf. Sci.* **326**, 151–161 (2015).
 91. Lunt, T. T. Interactions Among Localized Corrosion Sites Investigated Through Experiments and Models. (University of Virginia, 2001). doi:10.16953/deusbed.74839
 92. Wu, B., Scully, J. R., Hudson, J. L. & Mikhailov, A. S. Cooperative Stochastic Behavior in Localized Corrosion I. Model. *J. Electrochem. Soc.* **144**, 1614–1620 (1997).
 93. Lunt, T. T., Pride, S. T., Scully, J. R., Hudson, J. L. & Mikhailov, A. S. Cooperative Stochastic Behavior in Localized Corrosion II. Experiments. *J. Electrochem. Soc.* **144**, 1620–1629 (1997).
 94. Seyeux, A., Maurice, V. & Marcus, P. Oxide Film Growth Kinetics on Metals and Alloys: I. Physical Model. *J. Electrochem. Soc.* **160**, C189–C196 (2013).
 95. Bojinov, M. *et al.* Electrochemical study of the passive behavior of Ni-Cr alloys in a borate solution - a mixed-conduction model approach. *J. Electroanal. Chem.* **504**, 29–44 (2001).
 96. Samin, A. J. & Taylor, C. D. A Combined Density Functional Theory and Monte Carlo Investigation of the Competitive Adsorption of Atomic Oxygen and Chlorine to the Ni (111) Surface. **165**, 302–309 (2018).
 97. Yu, X., Gulec, A., Lutton Cwalina, K., Scully, J. & Marks, L. New Insights on the Role of Chloride During the Onset of Local Corrosion: TEM, APT, Surface Energy, and Morphological Instability. *CORROSION* (2019). doi:10.5006/2991
 98. Hutchison, M. J. & Scully, J. R. Solute Capture and Doping of Al in Cu₂O: Corrosion, Tarnish Resistance, and Cation Release of High-Purity Cu-Al Alloys in Artificial Perspiration. *J. Electrochem. Soc.* **165**, C689–C702 (2018).
 99. McCafferty, E. Oxide networks, graph theory, and the passivity of Ni-Cr-Mo ternary alloys. *Corros. Sci.* **50**, 3622–3628 (2008).

100. Bonham, D. B. A Mathematical Model for the Influence of Deep-Level Electronic States on Photoelectrochemical Impedance Spectroscopy I. Theoretical Development. *J. Electrochem. Soc.* **139**, 118–126 (1992).
101. Bonham, D. B. & Orazem, M. E. A Mathematical Model for the Influence of Deep- Level Electronic States on Photoelectrochemical Impedance Spectroscopy II . Assessment of Characterization Methods Based on Mott-Schottky Theory. *J. Electrochem. Soc.* **139**, 127–131 (1992).
102. Macdonald, J. R. Theory of space-charge polarization and electrode-discharge effects. *J. Chem. Phys.* **58**, 4982–5001 (1973).
103. Schmuki, P. & Böhni, H. Metastable Pitting and Semiconductive Properties of Passive Films. *J. Electrochem. Soc.* **139**, 1908–1913 (1992).
104. Sunseri, C., Piazza, S. & Di Quarto, F. Photocurrent spectroscopic investigations of passive films on chromium. *J. Electrochem. Soc.* **137**, 2411–2417 (1990).
105. Policastro, S. A., Anderson, R. M., Roeper, D. F. & Horton, D. J. Analysis of the effect of formation potential on the electrochemical response of doped titanium oxides. *Electrochim. Acta* **224**, 419–428 (2017).
106. Ter-Ovanesian, B., Alemany-Dumont, C. & Normand, B. Electronic and transport properties of passive films grown on different Ni-Cr binary alloys in relation to the pitting susceptibility. *Electrochim. Acta* **133**, 373–381 (2014).
107. Tsui, L. & Zangari, G. Maximizing the photoelectrochemical performance of TiO₂ nanotubes for solar energy conversion. *Department of Materials Science and Engineering* (University of Virginia, 2015).
108. Quarto, F. Di, Zaffora, A., Franco, F. Di & Santamaria, M. Critical Review—Photocurrent Spectroscopy in Corrosion and Passivity Studies: A Critical Assessment of the Use of Band Gap Value to Estimate the Oxide Film Composition. *J. Electrochem. Soc.* **164**, C671–C681 (2017).
109. Henderson, J. D., Li, X., Shoesmith, D. W., Noël, J. J. & Ogle, K. Molybdenum surface enrichment and release during transpassive dissolution of Ni-based alloys. *Corros. Sci.* **147**, 32–40 (2019).
110. Kobe, B. *et al.* Application of quantitative X-ray photoelectron spectroscopy (XPS) imaging: investigation of Ni-Cr-Mo alloys exposed to crevice corrosion solution. *Surf. Interface Anal.* **49**, 1345–1350 (2017).
111. Systems, O. OLI Studio. (2017).

5.10 Tables

Table 5.1. Averaged oxidation efficiency (%) (Equation 2.12) computed for the results shown in Figure 5.14 for for Ni-22 Cr-x Mo where x = 3, 6, 9, 12, wt%, passivated at +0.2 V_{SCE} in 1.0 M NaCl pH 4 for 10,000 s

3 Mo	6 Mo	9 Mo	12 Mo
15.6	18.5	26.3	30.5

5.11 Figures

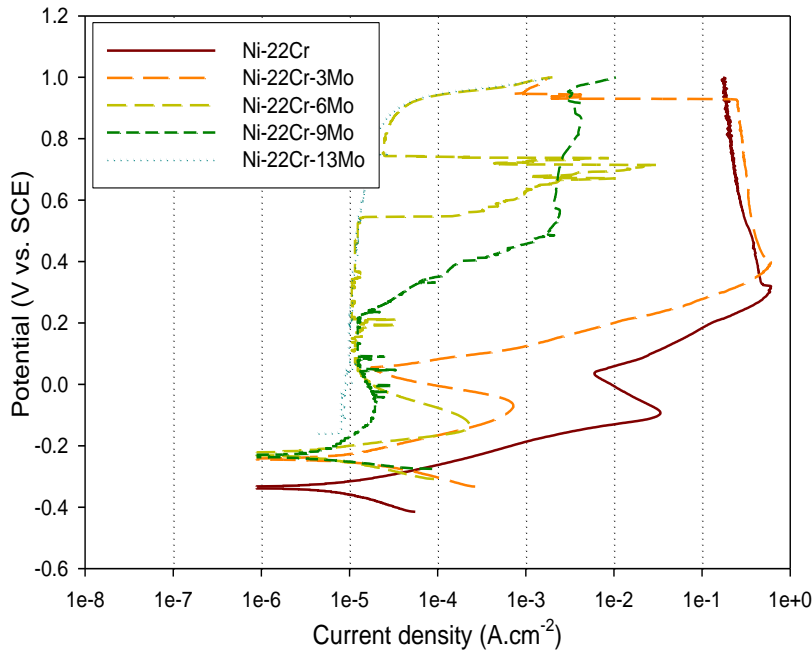


Figure 5.1. Influence of Mo alloying additions on the passivity of Ni-Cr-Mo alloys during upward potentiodynamic polarization in deaerated 1 M HCl⁶⁶

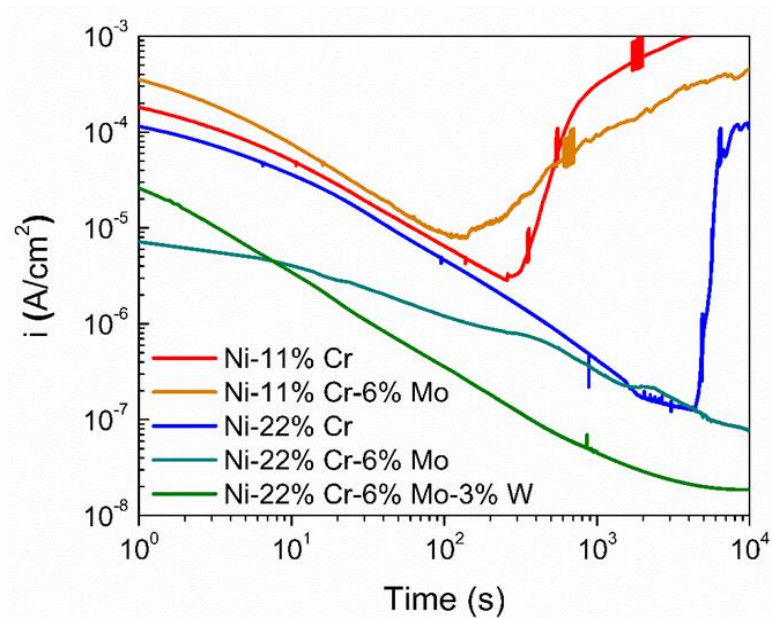


Figure 5.2. Current measured during potentiostatic passivation at +200 mV_{SCE} for various Ni-based alloys (wt%) in 0.1 M NaCl pH 4 where the initial decay indicates film growth, whereas the low concentration alloys exhibited abrupt current increases at longer times, indicative of localized pitting or crevice corrosion

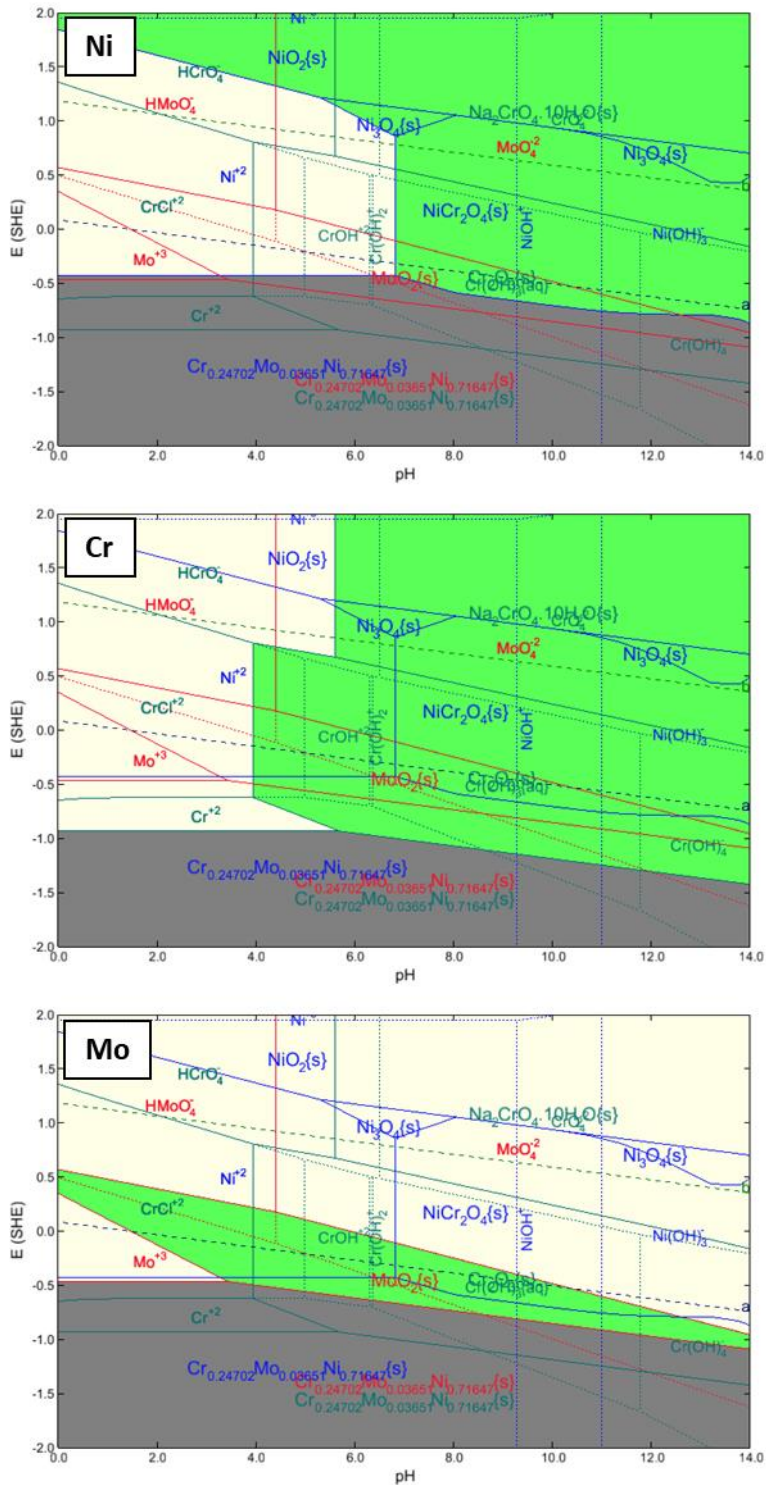


Figure 5.3. Pourbaix diagrams computed using OLI¹¹¹ for a generic Ni-Cr-Mo alloy exposed to 1.0 M NaCl. The gray regions suggest regions of base metal immunity, whereas green and yellow indicate passivity and corrosion, respectively, for specific, stoichiometric Ni, Cr, and Mo oxide films.

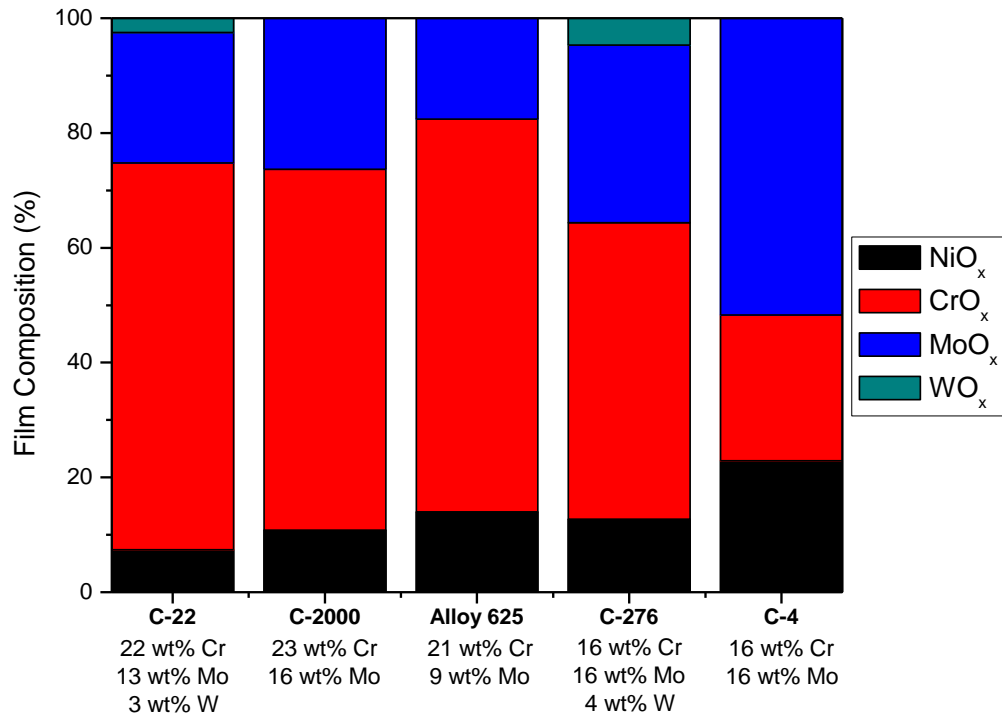


Figure 5.4. Film composition of various commercial Ni-alloys measured using XPS following passivation at +305 mV_{SCE} for 3 d in aqueous 1.0 M NaCl pH 0 solution heated to 75°C²⁷. The analysis considered only stoichiometric, phase-separated oxides and hydroxides.

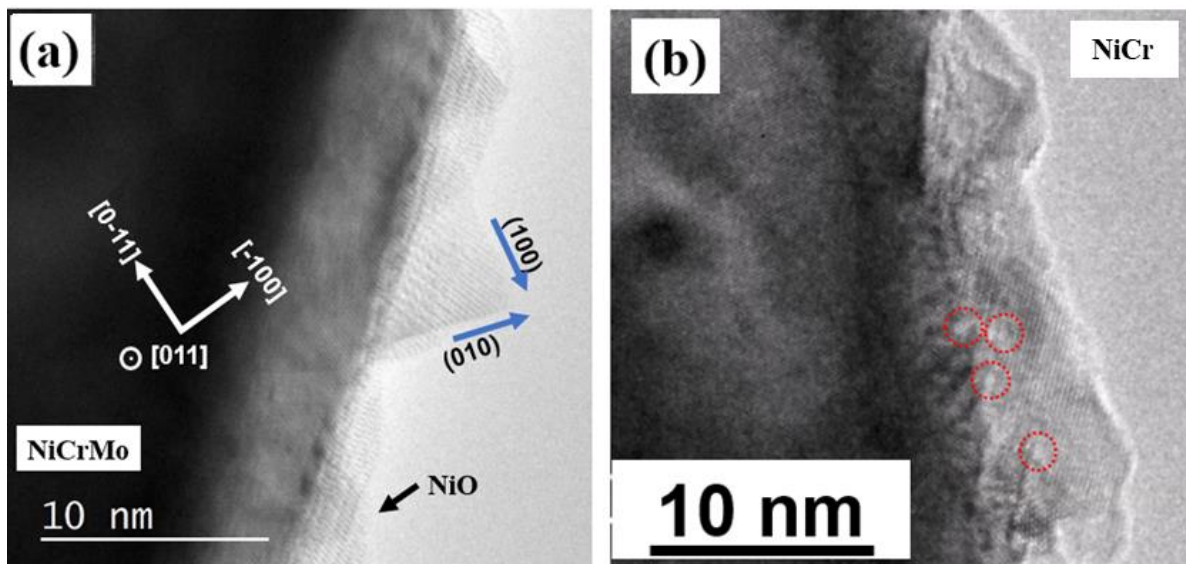


Figure 5.5. a) In situ TEM images of initial layer-by-layer growth of NiO on Ni-Cr-Mo surfaces at 700°C where the NiO island has {100} surfaces and the blue arrows show the layer-by-layer growth direction. For comparison, b) presents in situ TEM images showing Kirkendall voids (dotted circles) formed near the oxide-metal interface of the Ni-Cr alloy⁴⁰

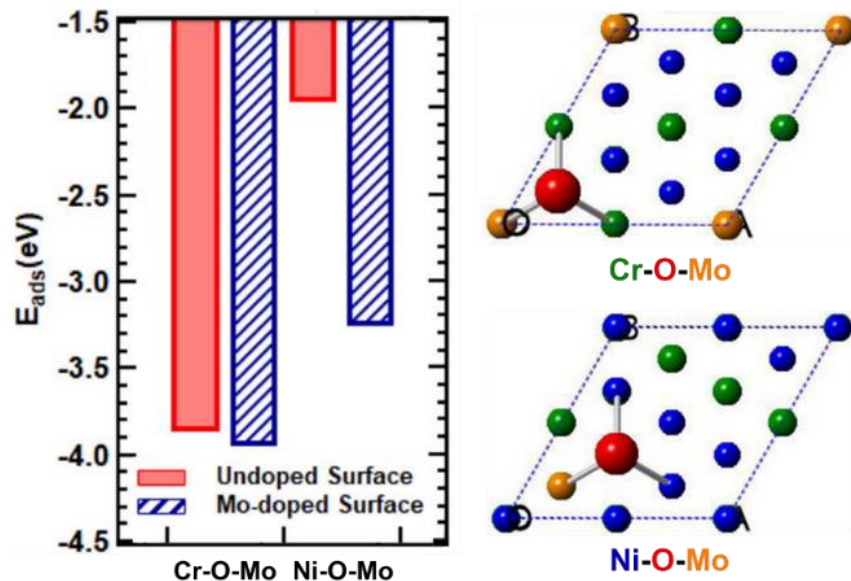


Figure 5.6. Comparison of the FCC-site oxygen absorption energy at 0.25 ML for the cases of the (111) alloy surfaces directly cut from the bulk and Mo-doped alloy surfaces with the relevant doped cases shown on the right⁴⁹

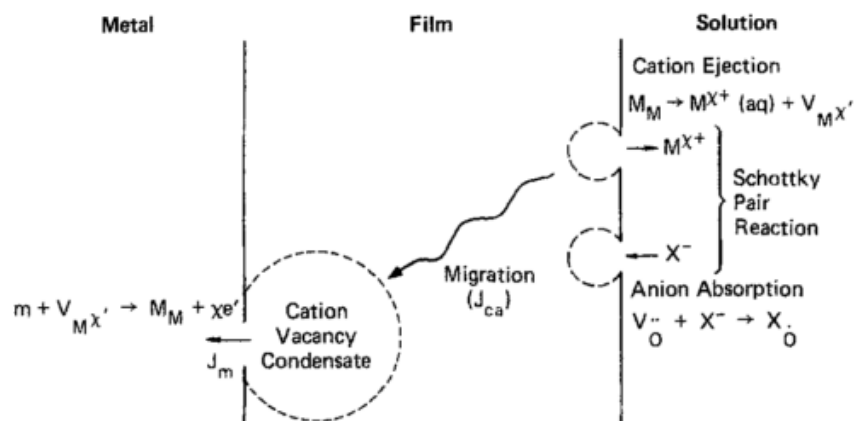


Figure 5.7. Processes leading to the breakdown of passive films according to the Point Defect Model⁴

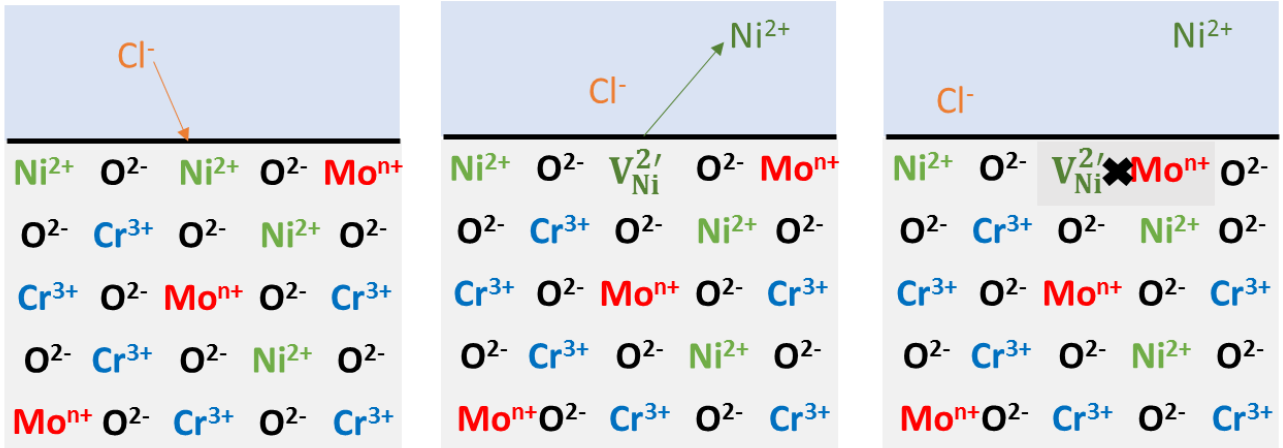


Figure 5.8. Schematic of the production of a metal cation vacancy following chloride adsorption and the subsequent formation of an immobile complex upon interaction with a Mo dopant

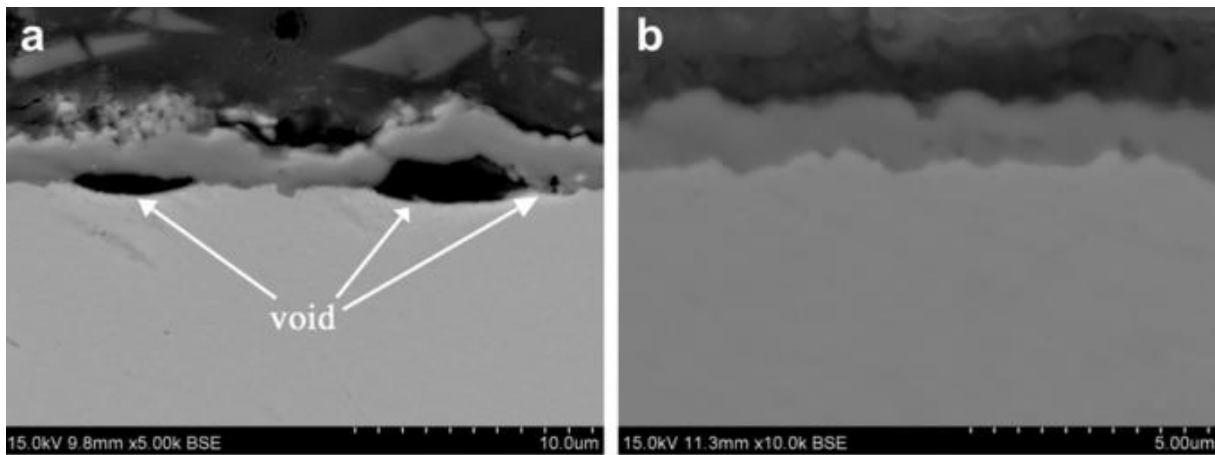


Figure 5.9. Cross-sectional SEM images of the specimens after 500 h oxidation at 800°C in air: (a) Fe-22 Cr-0.5 Mn and (b) Fe-22 Cr-0.5 Mn-0.1 Mo, wt%⁴⁵

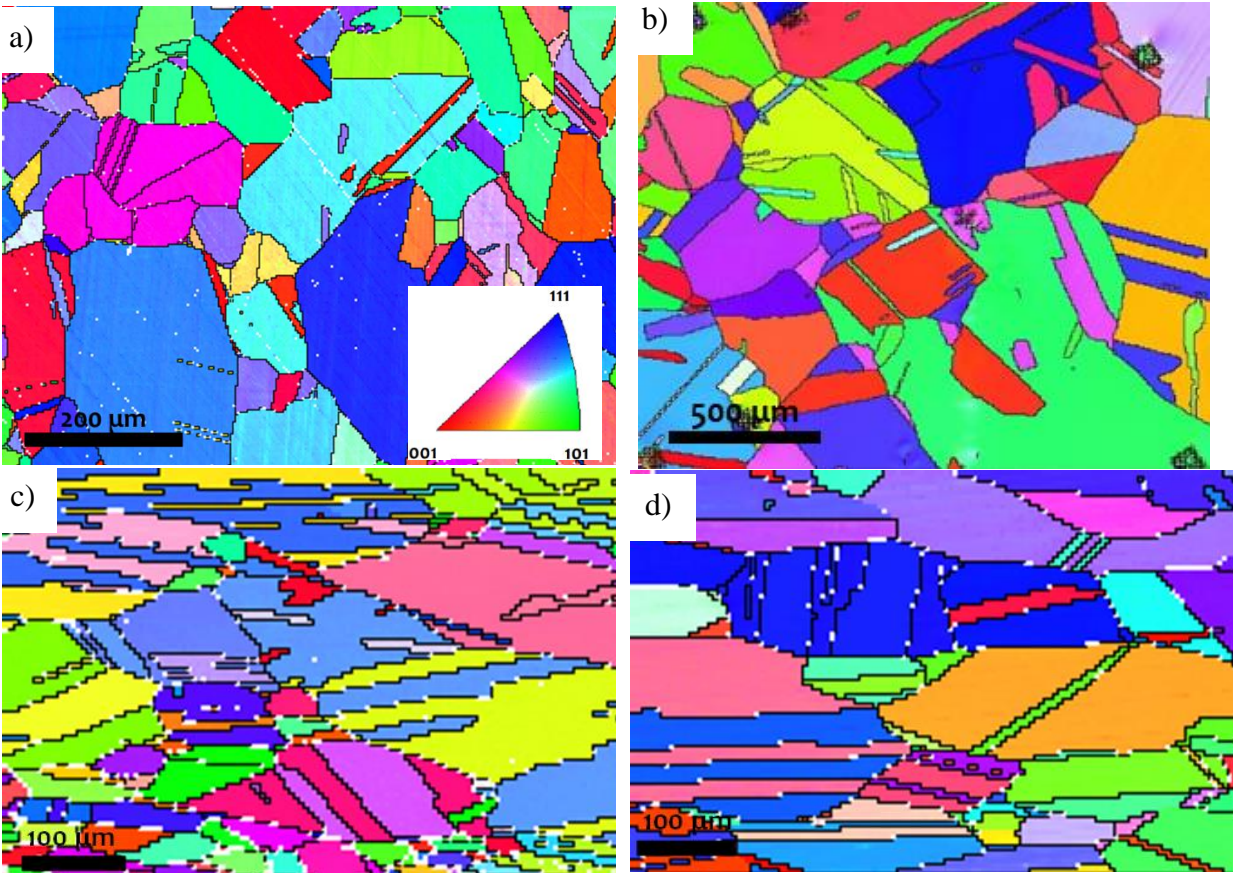


Figure 5.10. EBSD images of the Ni-Cr-xMo alloys used in this chapter: a) Ni-22 Cr-3 Mo, b) Ni-22 Cr-5 Mo, c) Ni-22 Cr-9 Mo, and d) Ni-22 Cr-12 Mo, wt%. The average grain sizes for the alloys were computed to be, respectively, $7,830 \mu\text{m}^2$; $5,063 \mu\text{m}^2$; $4,490 \mu\text{m}^2$; and $6,770 \mu\text{m}^2$. For reference, the stereographic triangle is inset.

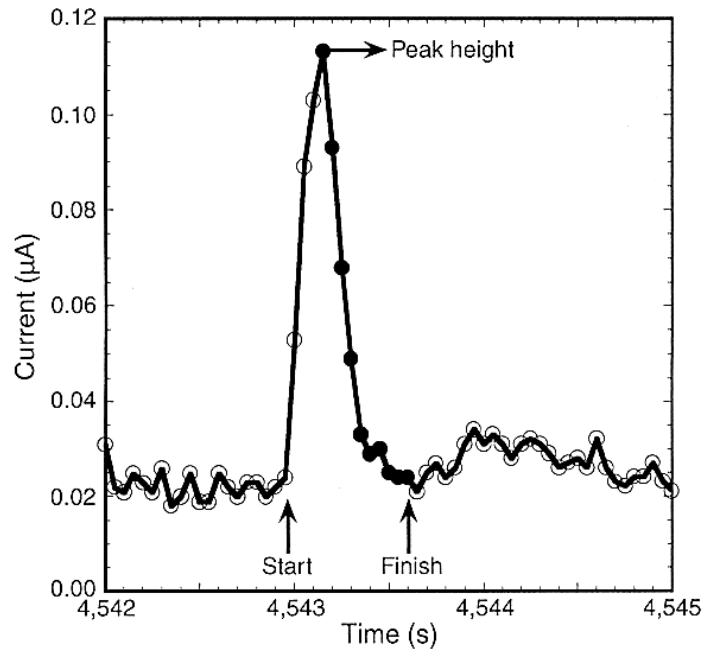


Figure 5.11. Example of a single metastable event showing the entire event above the background passive current, where the lifetime of the pit and its peak current are indicated⁶⁹. The peak integrated charge is determined above the baseline between the start and finish times for the event.

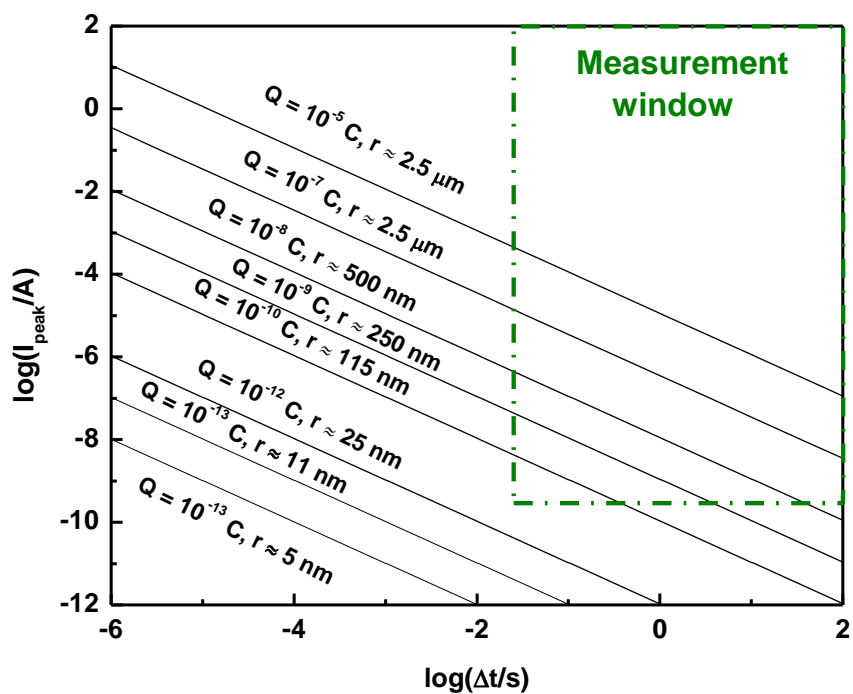
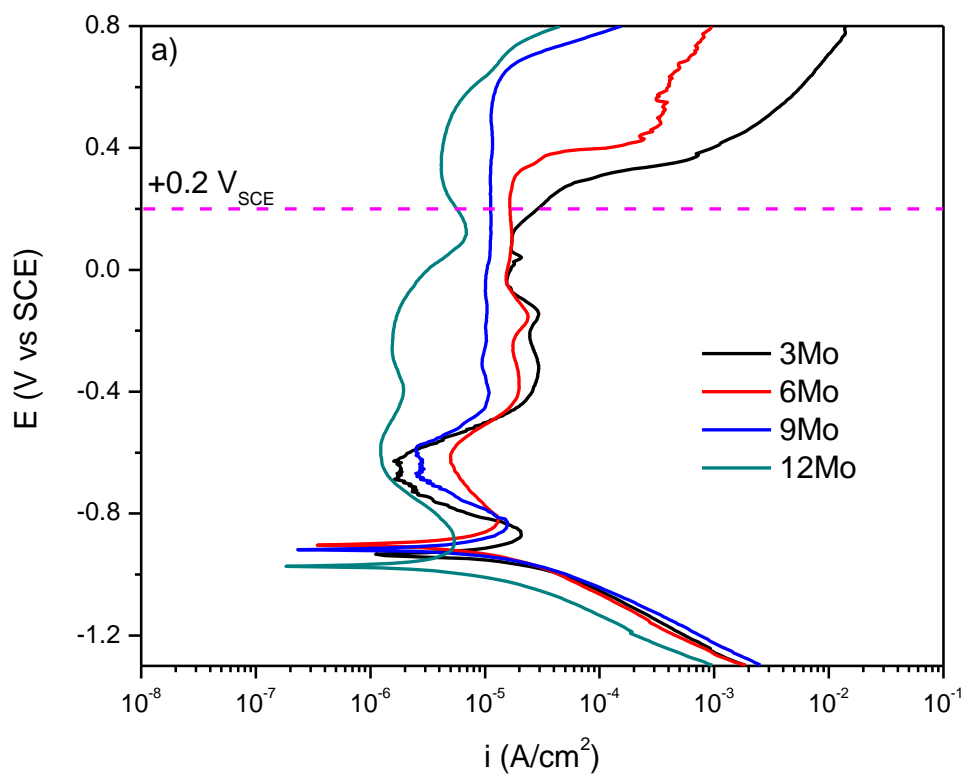


Figure 5.12. Schematic of the metastable pit sizes that are able to be measured using the given data acquisition rate (20 Hz) and potentiostat sensitivity (approximately 1 nA) based on their elapsed time and peak currents



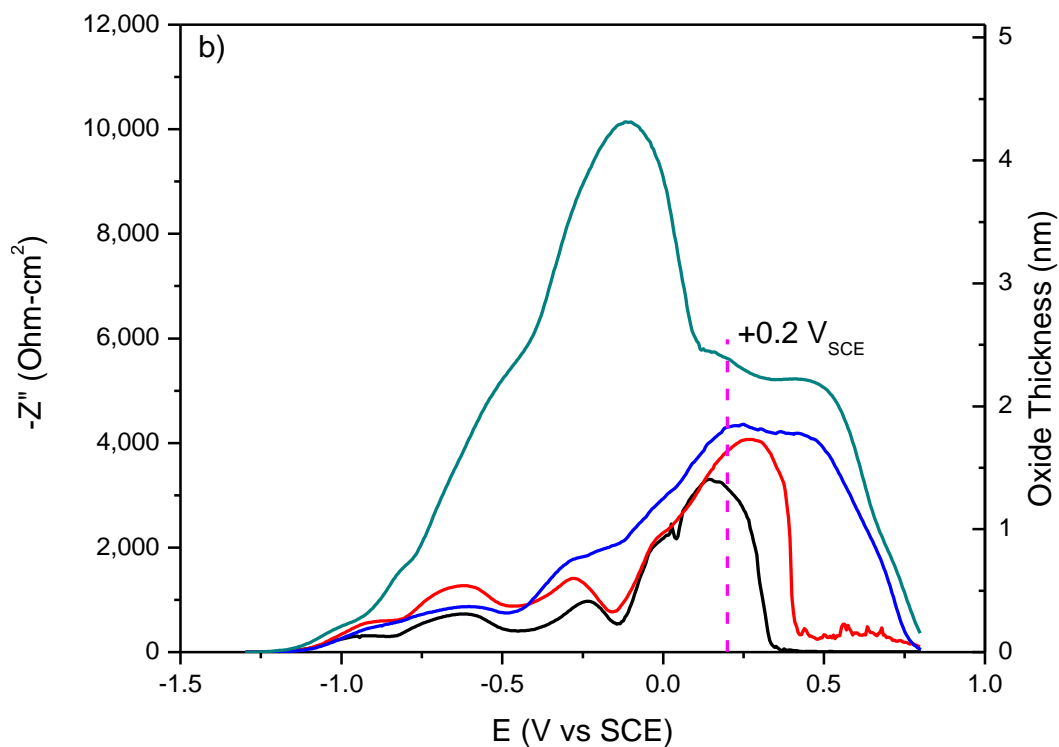
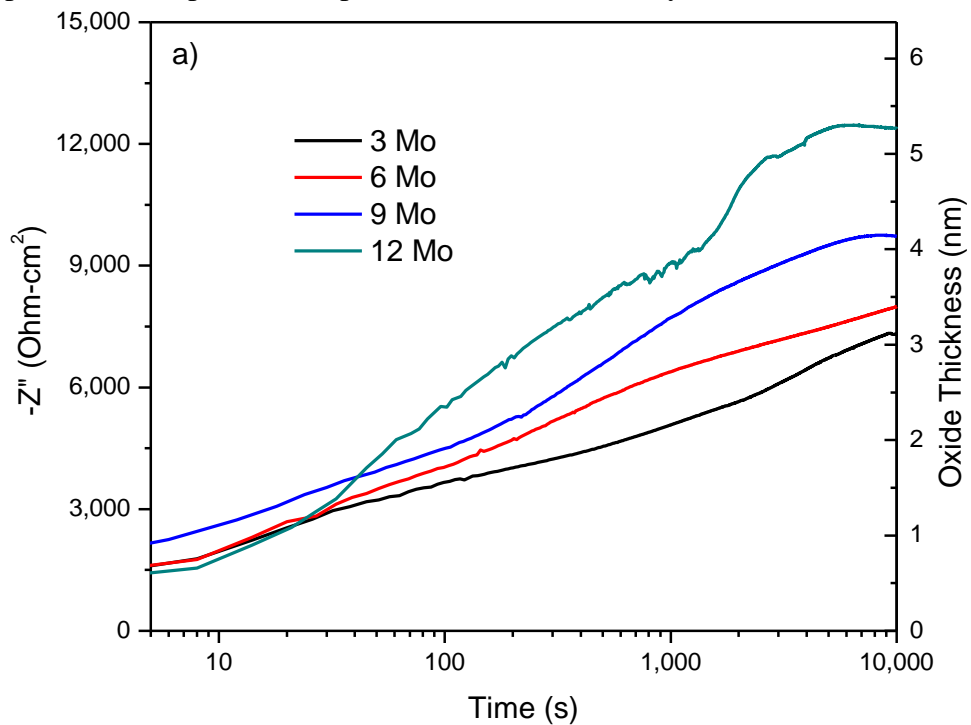


Figure 5.13. a) DC current and b) AC impedance variations during upward potentiodynamic polarization of Ni-22 Cr-x Mo, wt%, where x = 3, 6, 9, and 12 wt% in deaerated 1.0 M NaCl at pH 4 with the passivation potential used in this study (+0.2 V_{SCE}) indicated



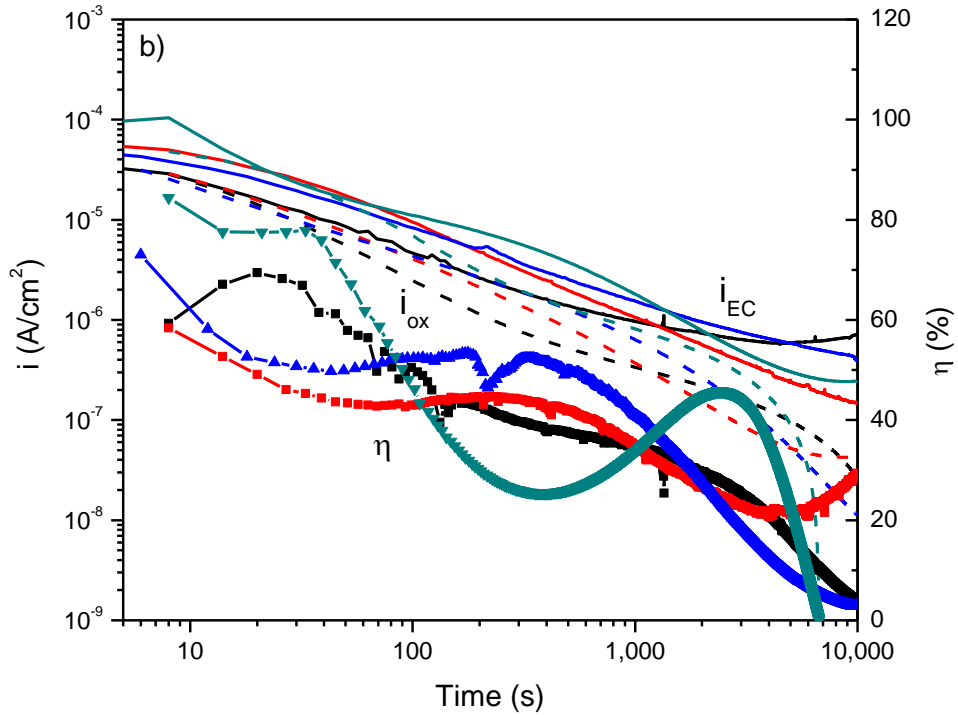
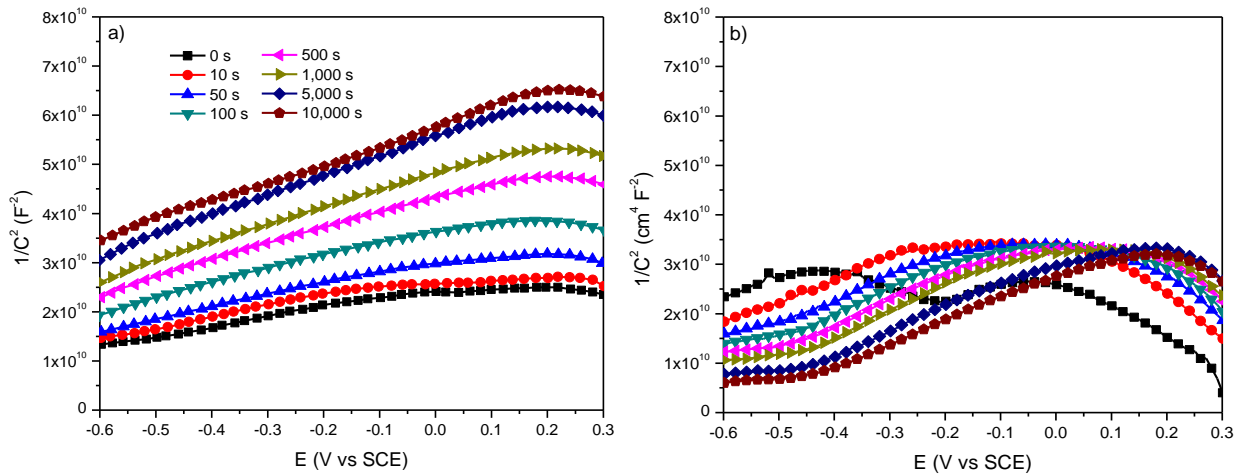


Figure 5.14. a) Increases in $-Z''$ and the corresponding l_{ox} (Equation 2.16) and b) corresponding total electrochemical (i_{EC} , solid line) and oxidation (i_{ox} , dashed line) (Equation 2.11) current densities along with the resulting current efficiencies (η , scatter) (Equation 2.12) for comparison during potentiostatic SF-EIS of Ni-22 Cr-x Mo, wt%, where x = 3, 6, 9, and 12 wt% in deaerated 1.0 M NaCl at pH 4



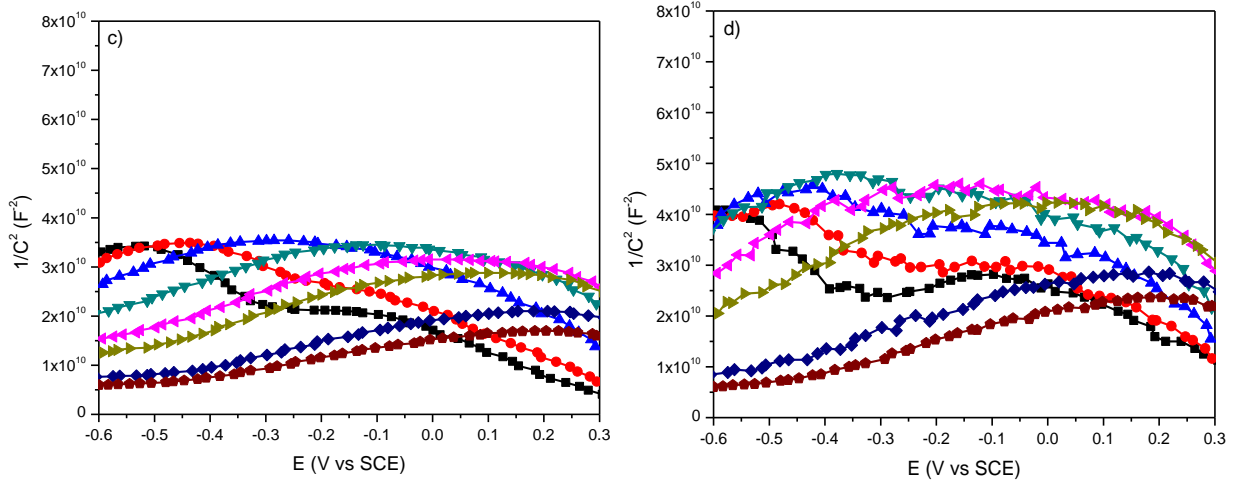


Figure 5.15. Evolution of Mott-Schottky spectra with passivation time for Ni-22 Cr-x Mo, wt%, alloys where x = a) 3 b) 6, c) 9, and d) 12 wt% Mo passivated at +0.2 V_{SCE} in 1.0 M NaCl pH 4 where the potential sweeps were performed at 1,000 Hz

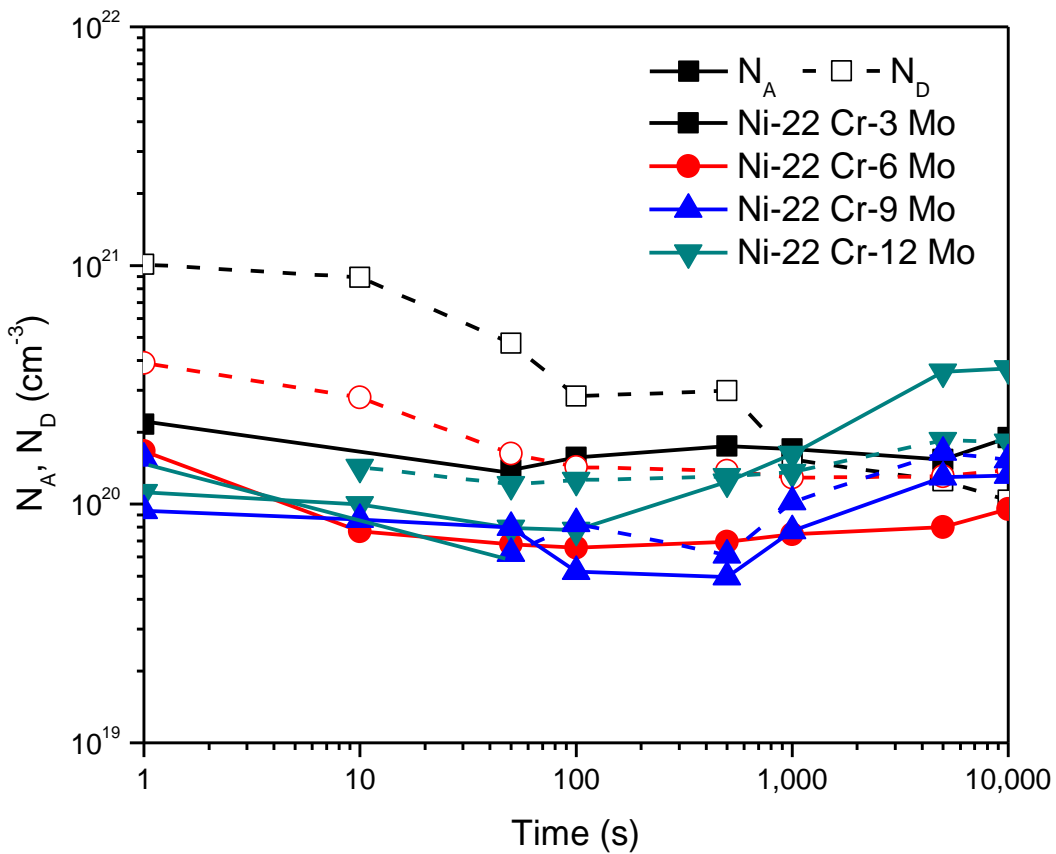


Figure 5.16. Concentration of n-type (N_D) and p-type (N_A) point defects according to Mott-Schottky analysis of Figure 5.15 (Section 3.5.5)

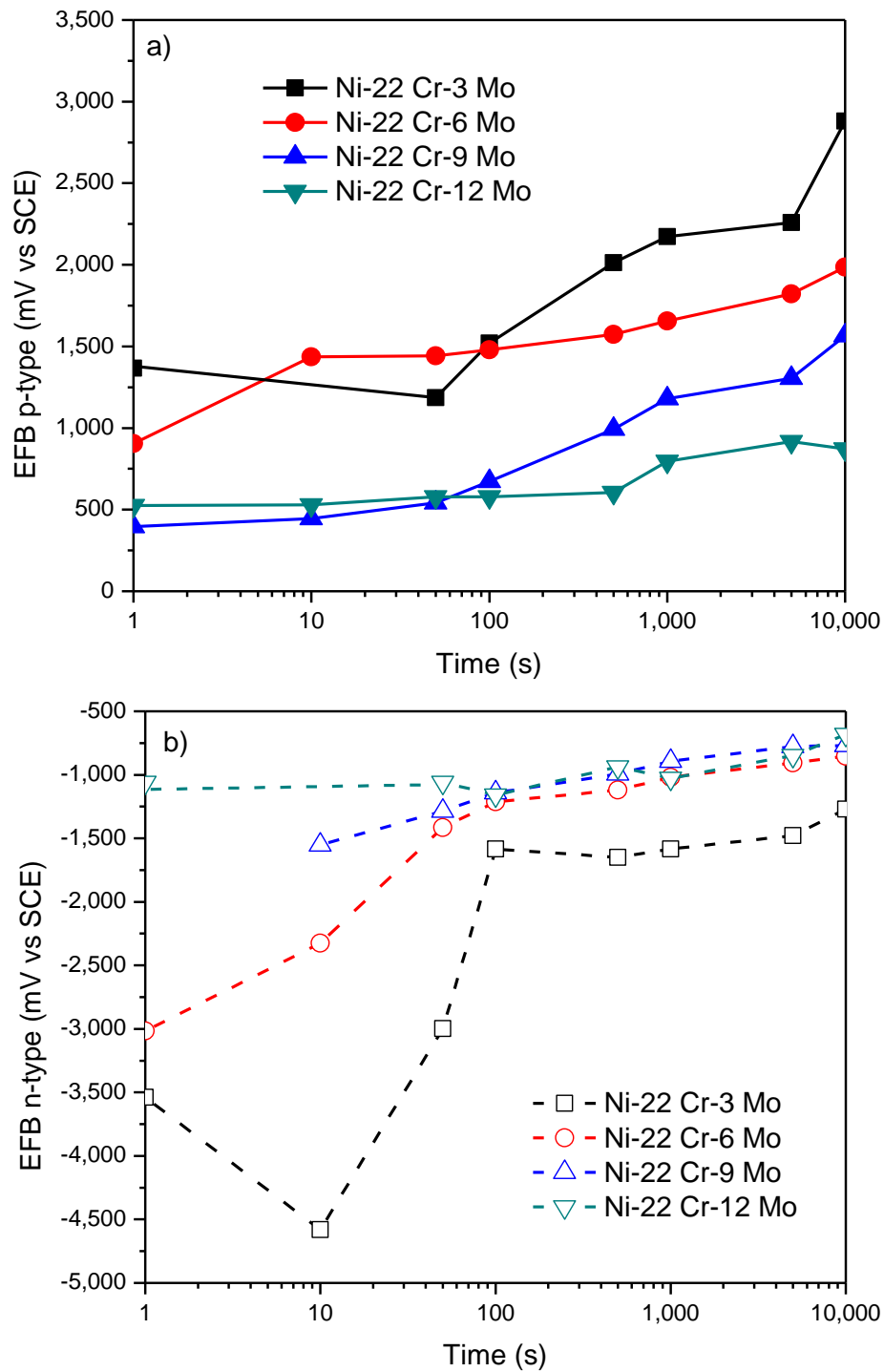


Figure 5.17. a) p-type and b) n-type semiconductor flat band potentials according to Mott-Schottky analysis of Figure 5.15 (Section 3.5.5)

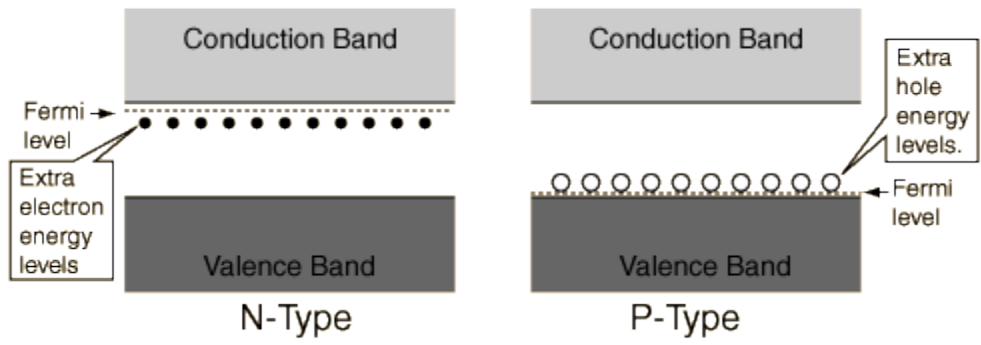


Figure 5.18. Schematic of the effect of n-type and p-type dopants on the band gap structure in a semiconductor

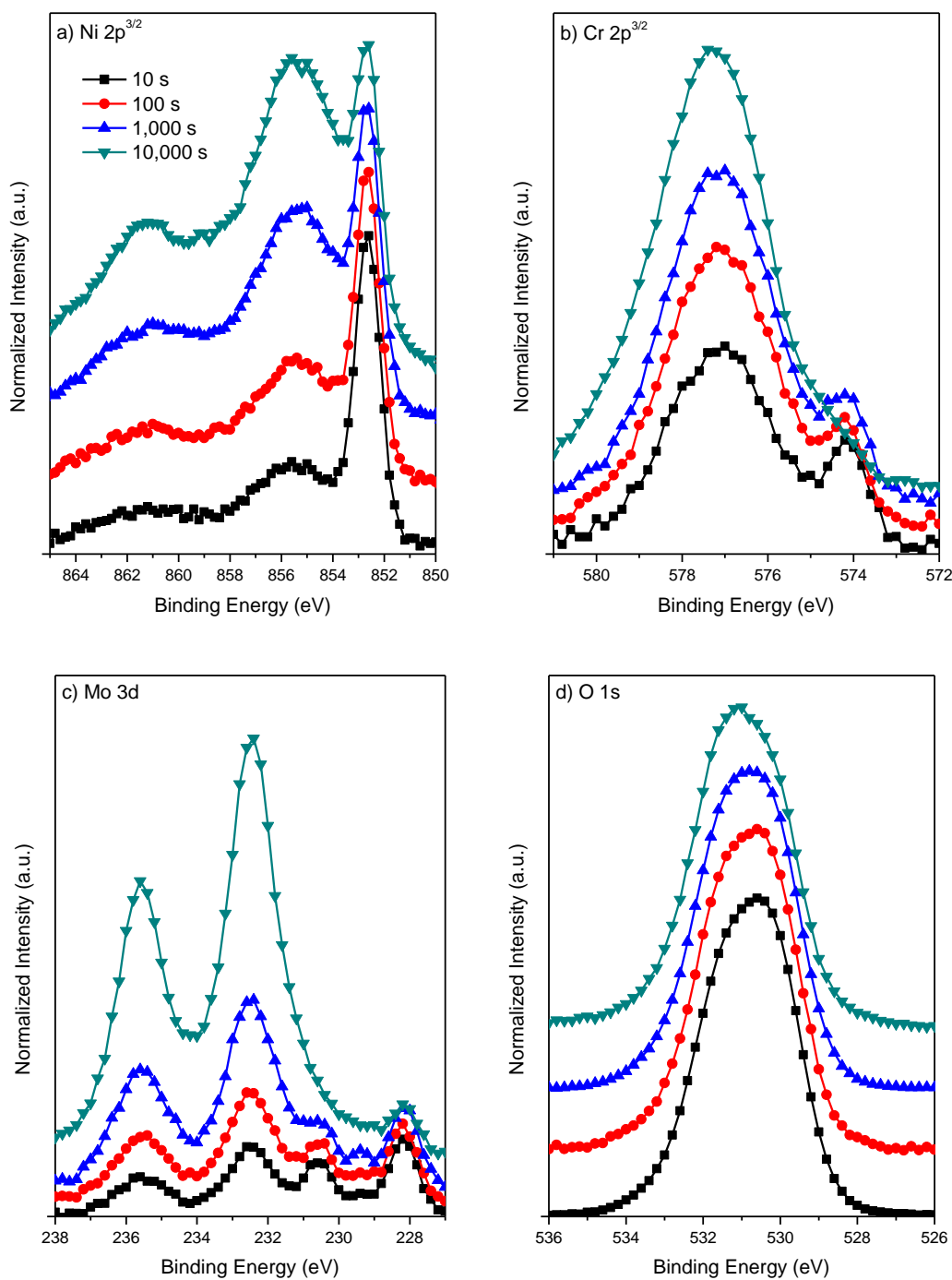


Figure 5.19. XPS spectra obtained at 90° using an Al- $\kappa\alpha$ source ($h\nu = 1,486.68$ eV) for a) Ni 2p^{3/2}, b) Cr 2p^{3/2}, c) Mo 3d, and d) O 1s obtained at 15 kV with a 50 eV pass energy for Ni-22 Cr-3 Mo, wt%, Shirley background-subtracted, normalized to the corresponding metallic peaks, and offset for clarity following passivation at +0.2 V_{SCE} for up to 10 ks in deaerated 1.0 M NaCl pH 4

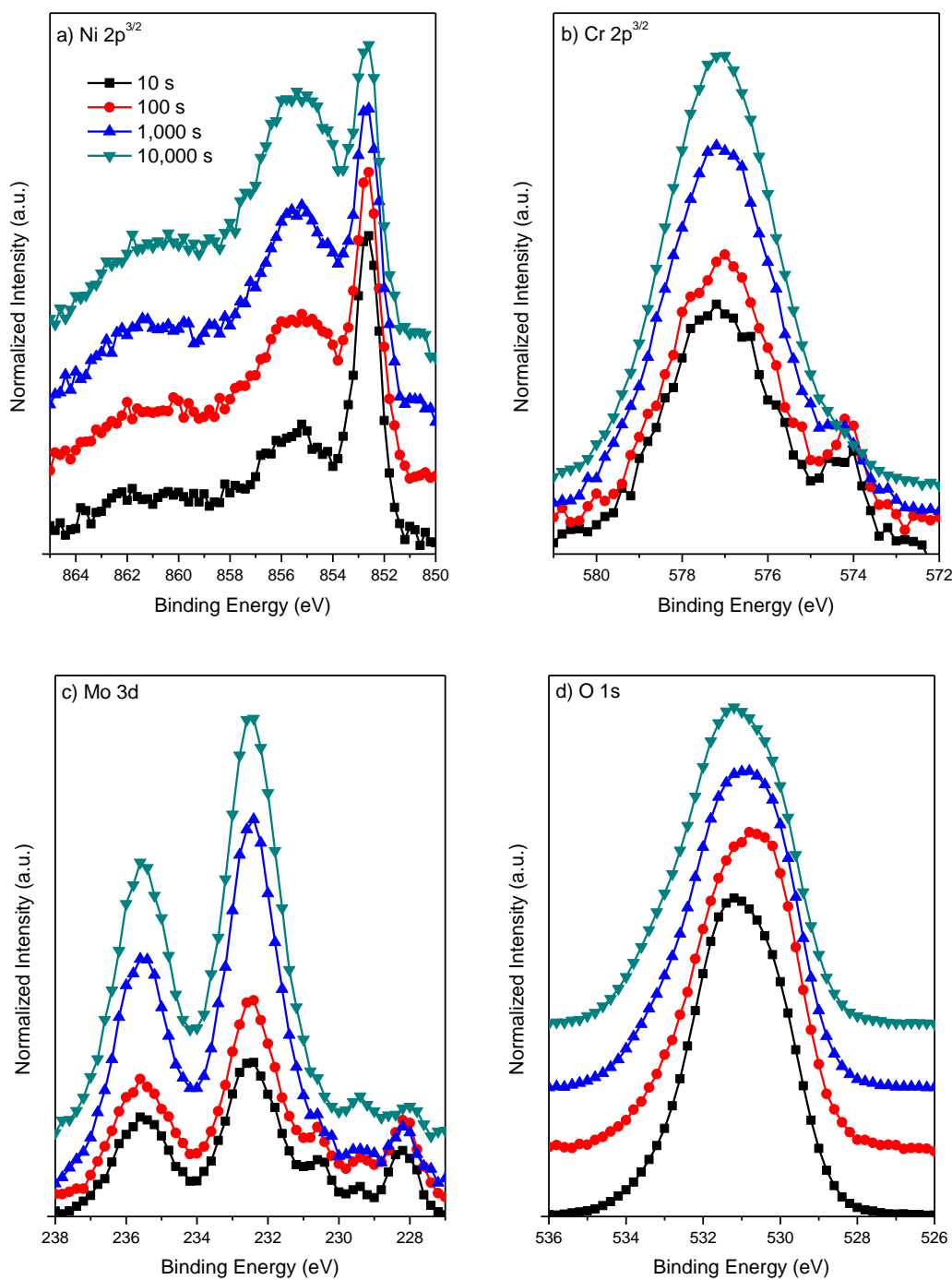


Figure 5.20. XPS spectra obtained at 90° using an Al- $\kappa\alpha$ source ($h\nu = 1,486.68$ eV) for a) Ni 2p^{3/2}, b) Cr 2p^{3/2}, c) Mo 3d, and d) O 1s obtained at 15 kV with a 50 eV pass energy for Ni-22 Cr-6 Mo, wt%, Shirley background-subtracted, normalized to the corresponding metallic peaks, and offset for clarity following passivation at +0.2 V_{SCE} for up to 10 ks in deaerated 1.0 M NaCl pH 4

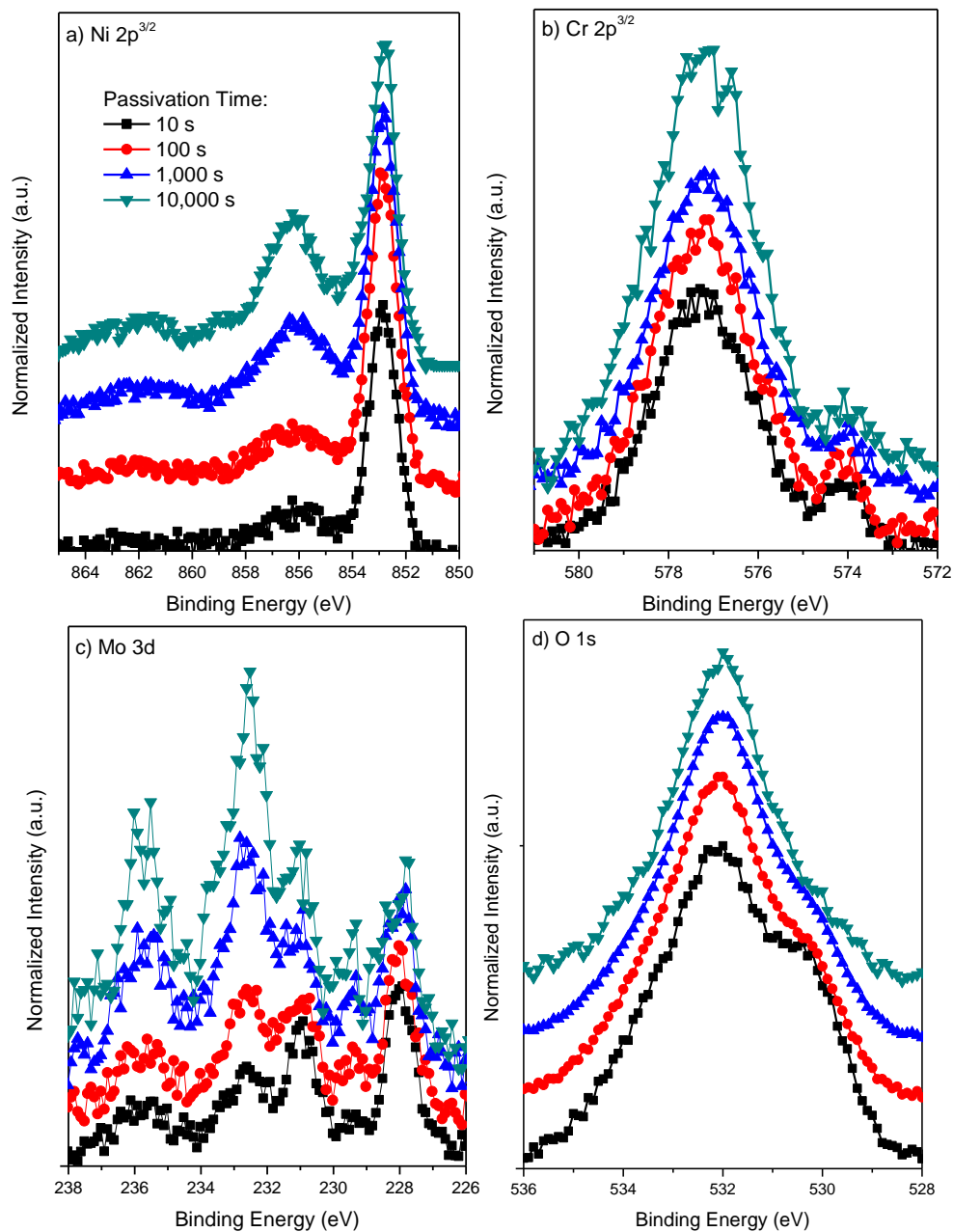


Figure 5.21. XPS spectra obtained at 90° using an Al- $\kappa\alpha$ source ($h\nu = 1,486.68$ eV) for a) Ni 2p^{3/2}, b) Cr 2p^{3/2}, c) Mo 3d, and d) O 1s obtained at 15 kV with a 50 eV pass energy for Ni-22 Cr-9 Mo, wt%, Shirley background-subtracted, normalized to the corresponding metallic peaks, and offset for clarity following passivation at +0.2 V_{SCE} for up to 10 ks in deaerated 1.0 M NaCl pH 4

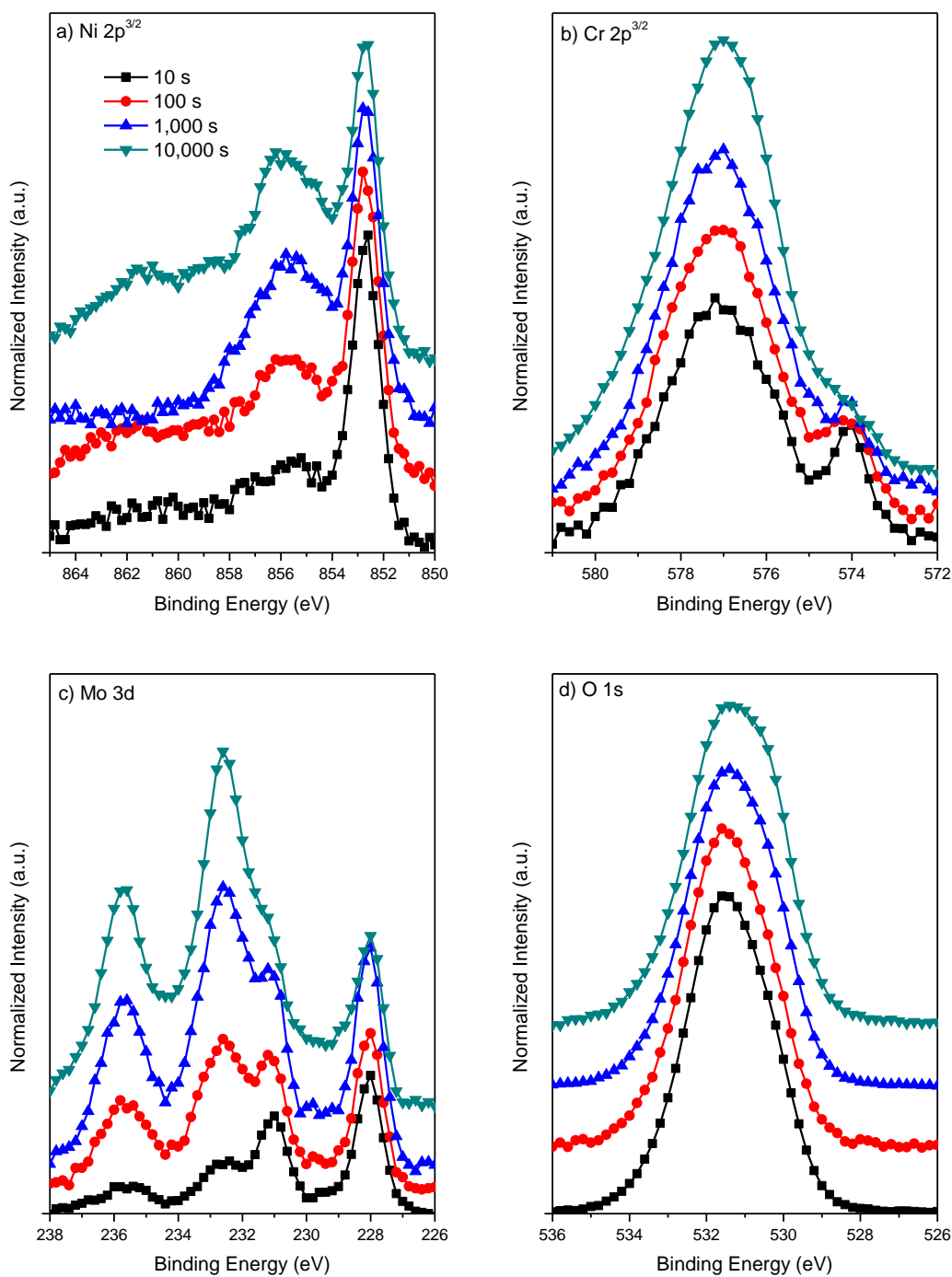


Figure 5.22. XPS spectra obtained at 90° using an Al- $\kappa\alpha$ source ($h\nu = 1,486.68$ eV) for a) Ni 2p^{3/2}, b) Cr 2p^{3/2}, c) Mo 3d, and d) O 1s obtained at 15 kV with a 50 eV pass energy for Ni-22 Cr-12 Mo, wt%, Shirley background-subtracted, normalized to the corresponding metallic peaks, and offset for clarity following passivation at +0.2 V_{SCE} for up to 10 ks in deaerated 1.0 M NaCl pH 4

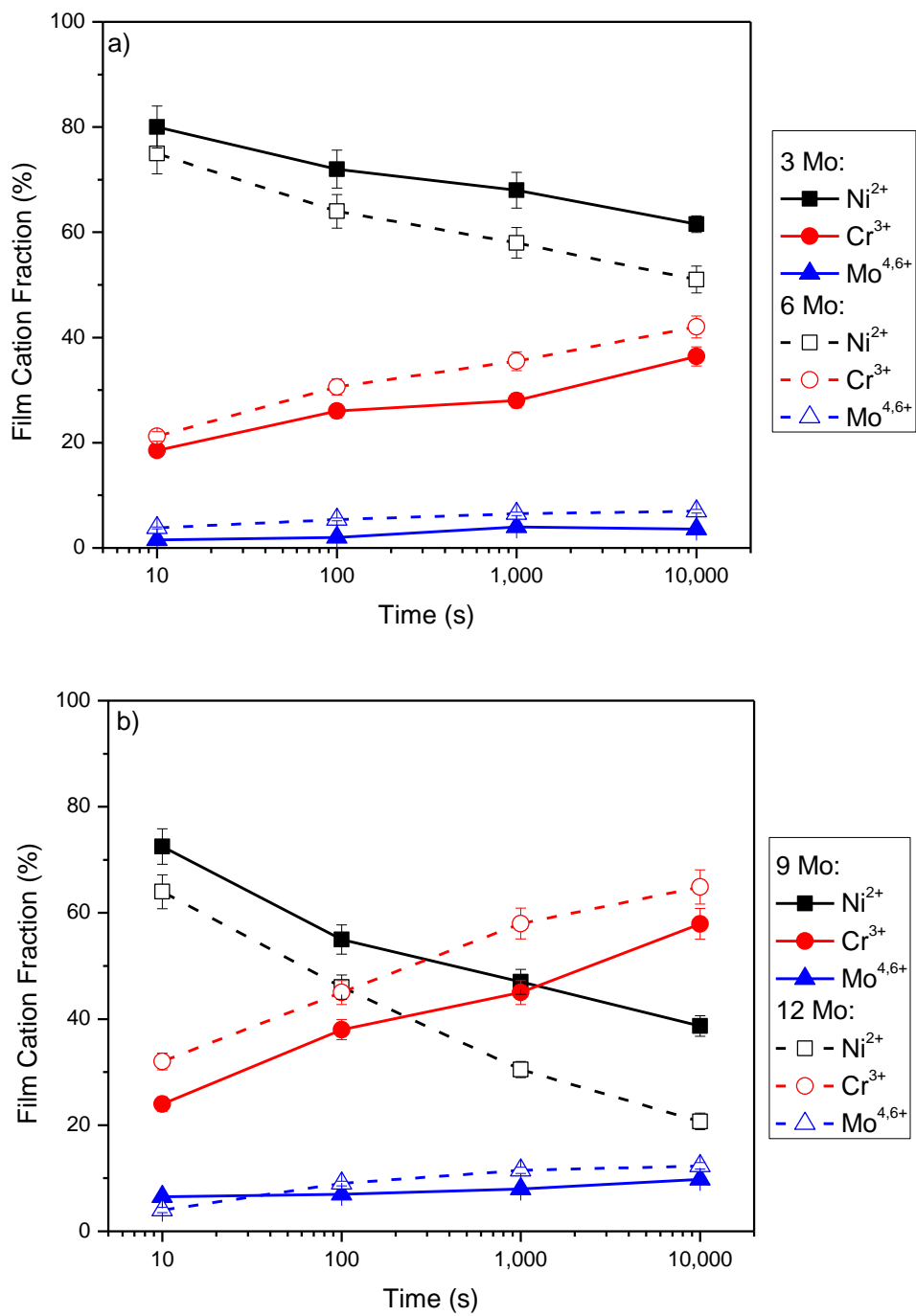


Figure 5.23. Relative accumulation of metal cations in the passive films during growth until localized corrosion initiation at +0.2 V_{SCE} according to XPS measurements on Ni-22 Cr-x Mo where x = a) 3, 6 and b) 9, 12, wt%, in 1.0 M NaCl pH 4

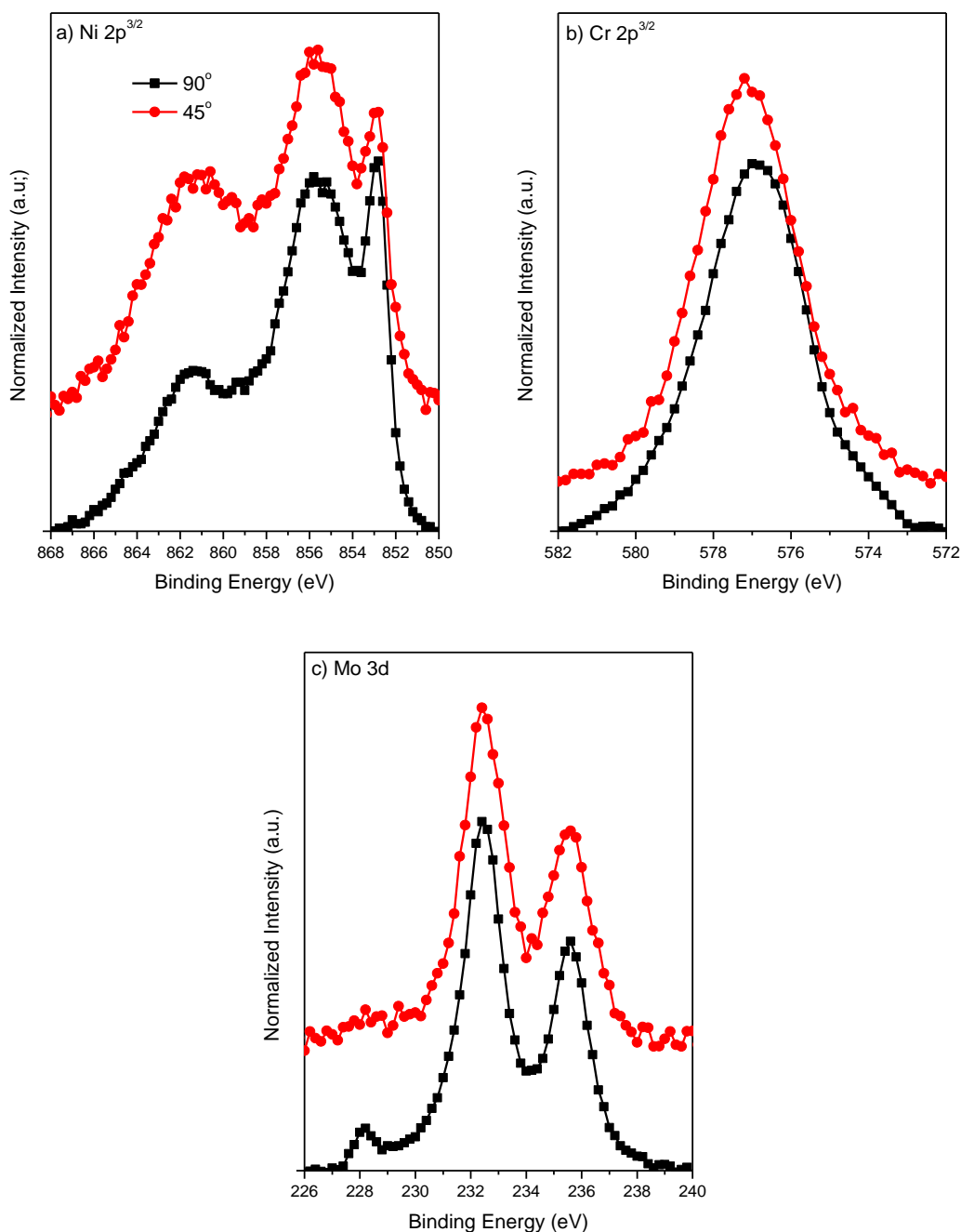


Figure 5.24. a) Ni 2p^{3/2}, b) Cr 2p^{3/2}, and c) Mo 3d angle-resolved XPS spectra obtained at 45° which were normalized to the metal peaks for Ni-22 Cr-3 Mo, wt%, passivated at +0.2 V_{SCE} for 10 ks in 1.0 M NaCl pH 4. The ratio of the oxide areas for each angle measurement is included for reference.

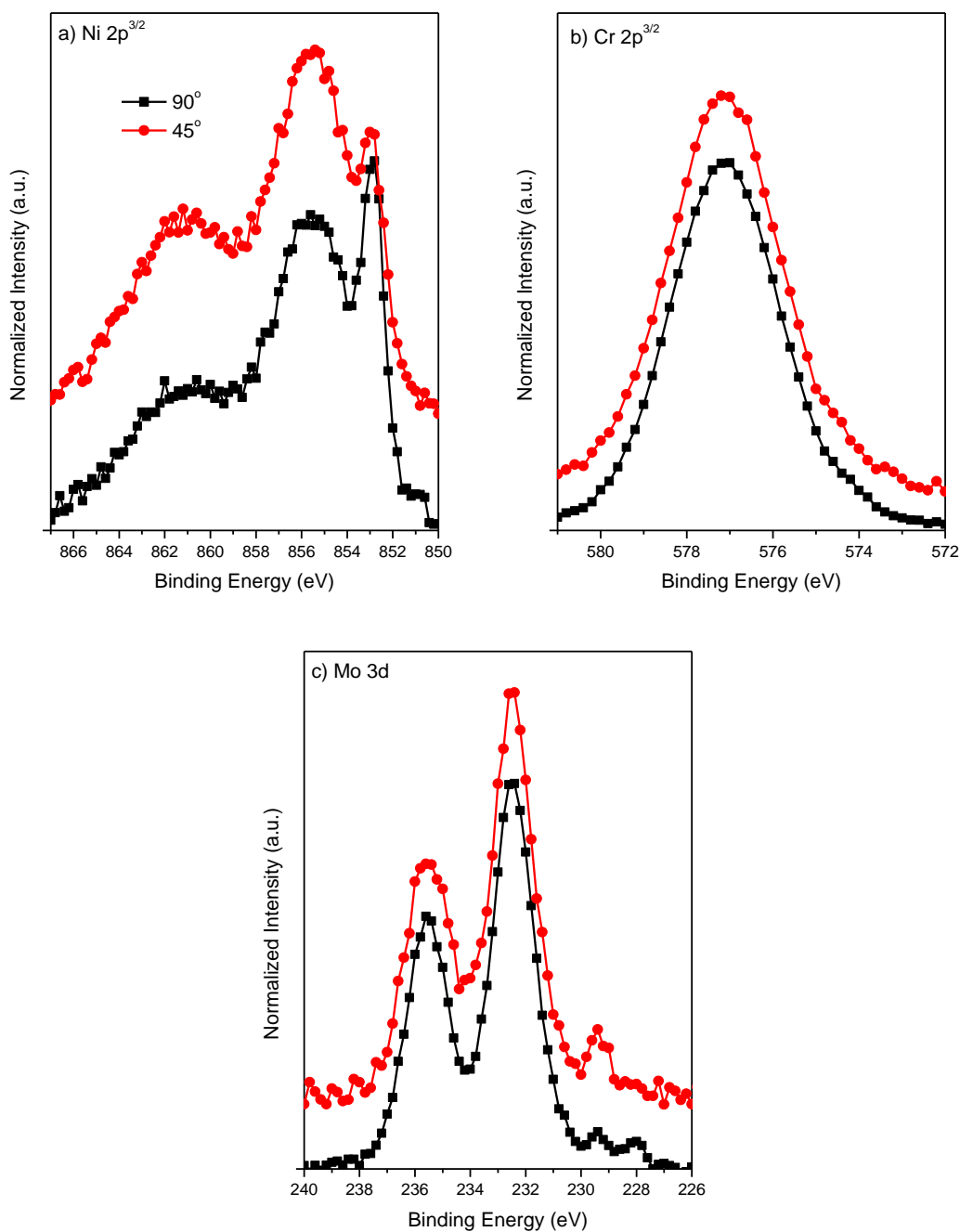


Figure 5.25. a) Ni 2p^{3/2}, b) Cr 2p^{3/2}, and c) Mo 3d angle-resolved XPS spectra obtained at 45° which were normalized to the metal peaks for Ni-22 Cr-6 Mo, wt%, passivated at +0.2 V_{SCE} for 10 ks in 1.0 M NaCl pH 4. The ratio of the oxide areas for each angle measurement is included for reference.

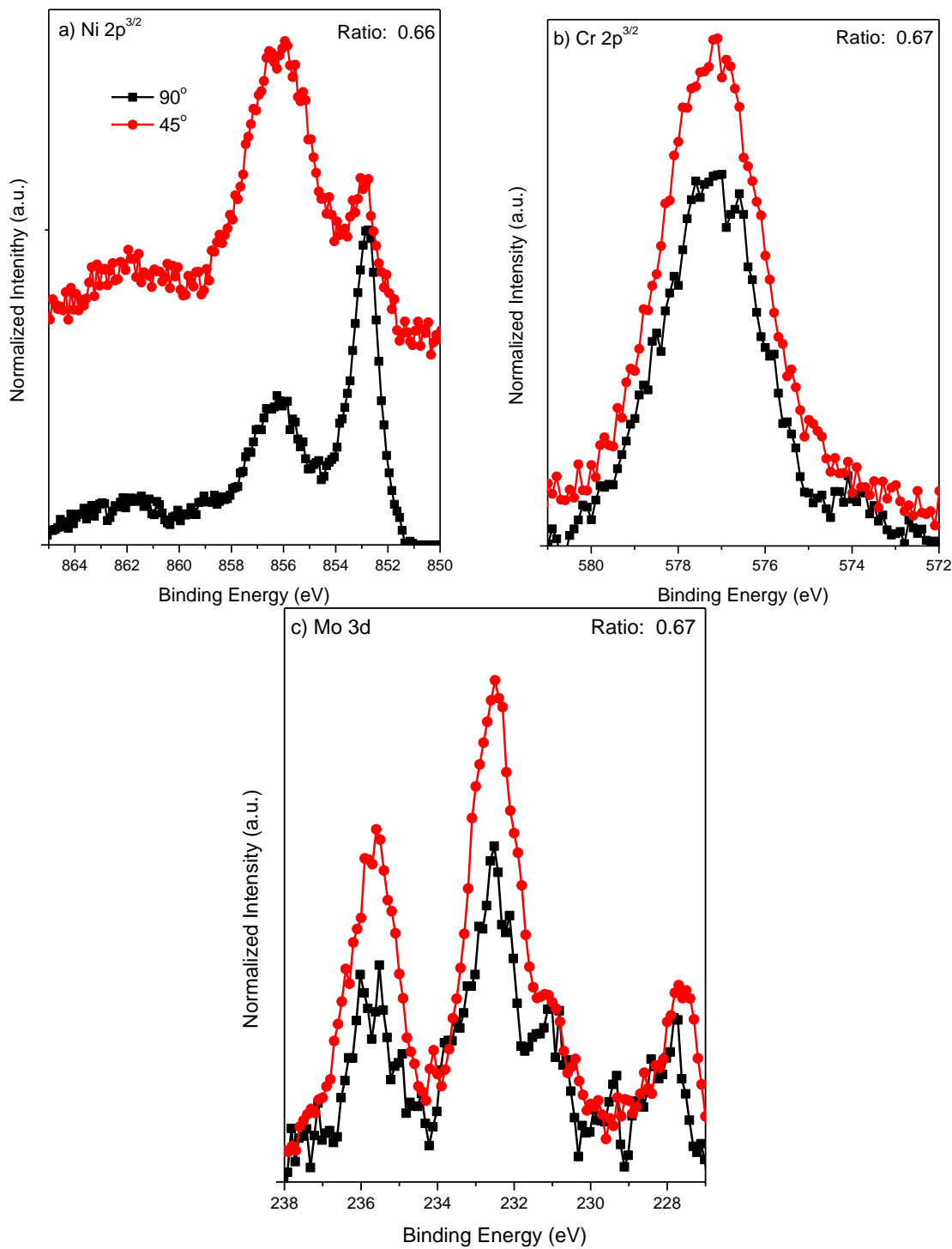


Figure 5.26. a) Ni 2p^{3/2}, b) Cr 2p^{3/2}, and c) Mo 3d angle-resolved XPS spectra obtained at 45° which were normalized to the metal peaks for Ni-22 Cr-9 Mo, wt%, passivated at +0.2 V_{SCE} for 10 ks in 1.0 M NaCl pH 4. The ratio of the oxide areas for each angle measurement is included for reference.

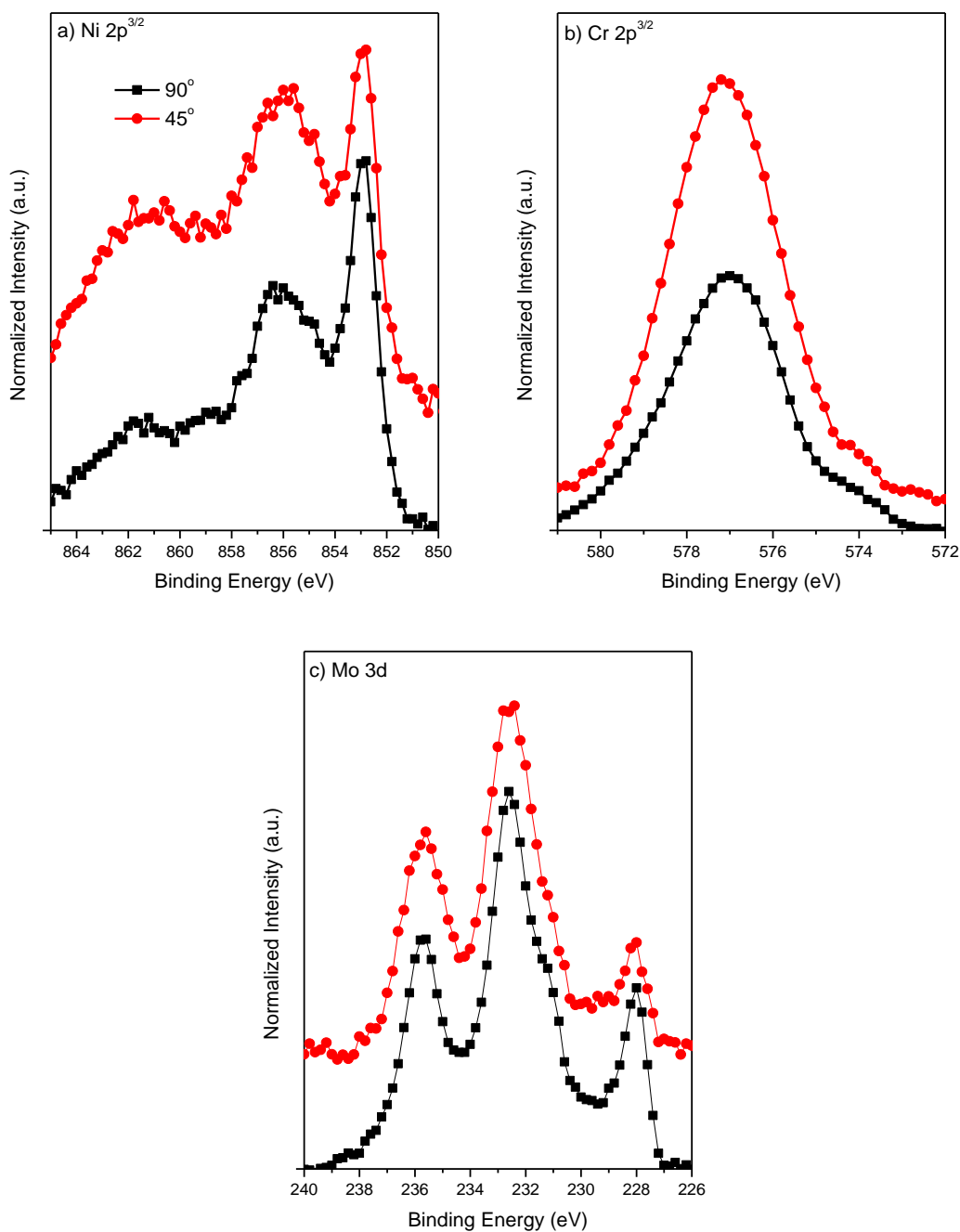


Figure 5.27. a) Ni 2p^{3/2}, b) Cr 2p^{3/2}, and c) Mo 3d angle-resolved XPS spectra obtained at 45° which were normalized to the metal peaks for Ni-22 Cr-12 Mo, wt%, passivated at +0.2 V_{SCE} for 10 ks in 1.0 M NaCl pH 4. The ratio of the oxide areas for each angle measurement is included for reference.

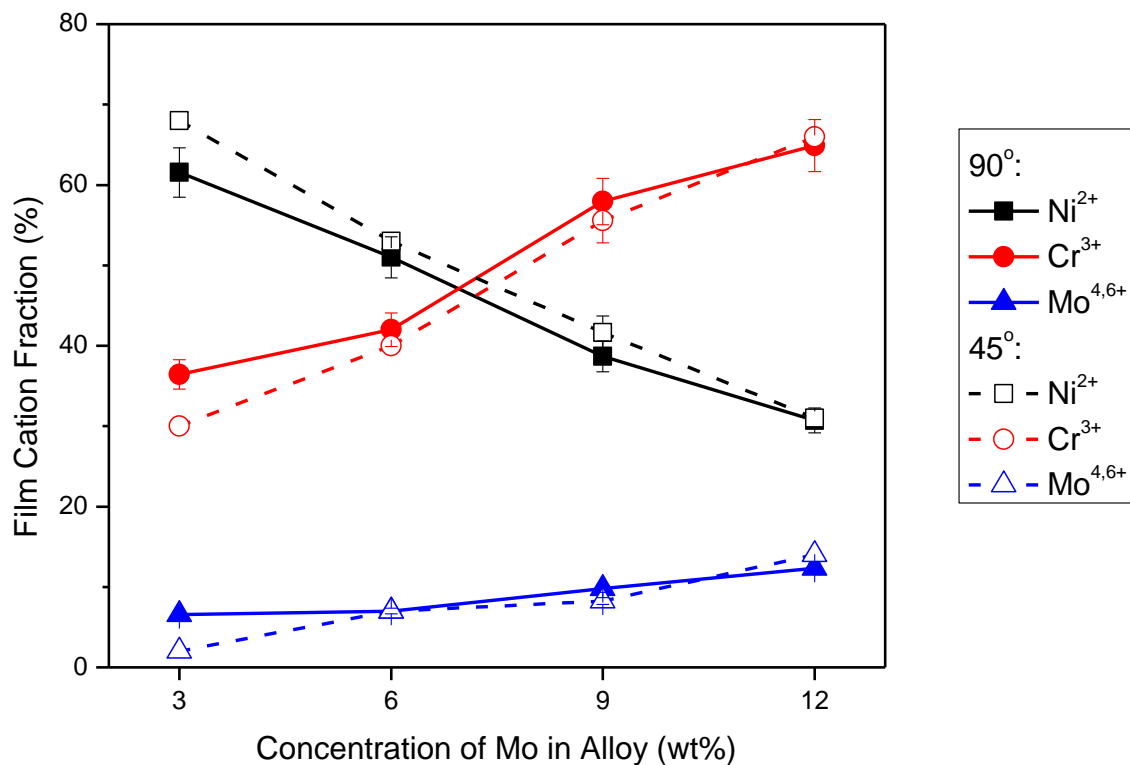


Figure 5.28. Film cation fraction according to angle-resolved XPS measurements at 90° and 45° on Ni-22 Cr-x Mo where x = 3, 6, 9, 12, wt%, surfaces following 10 ks of potentiostatic passivation at +0.2 V_{SCE} in 1.0 M NaCl pH 4

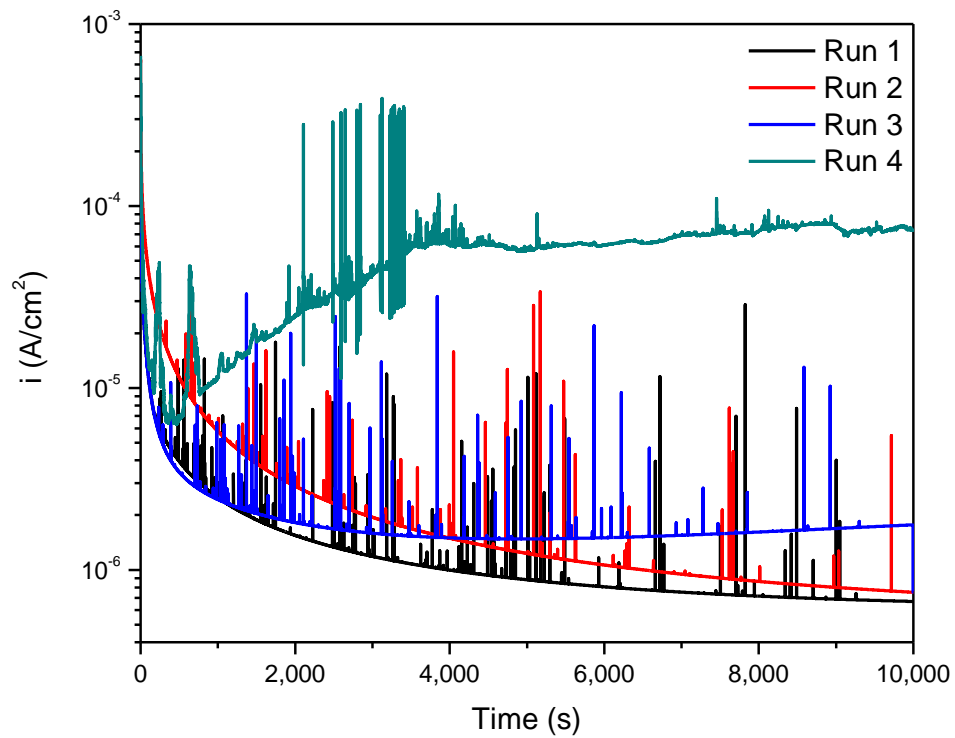


Figure 5.29. Metastable activity for the film on Ni-22 Cr-3 Mo, wt%, during passivation at +0.2 V_{SCE} for 10 ks in deaerated 1.0 M NaCl pH 4. Runs 1-3 remained passive following the observed localized breakdown events, whereas some crevice corrosion occurred during run 4 until repassivation around 4 ks occurred.

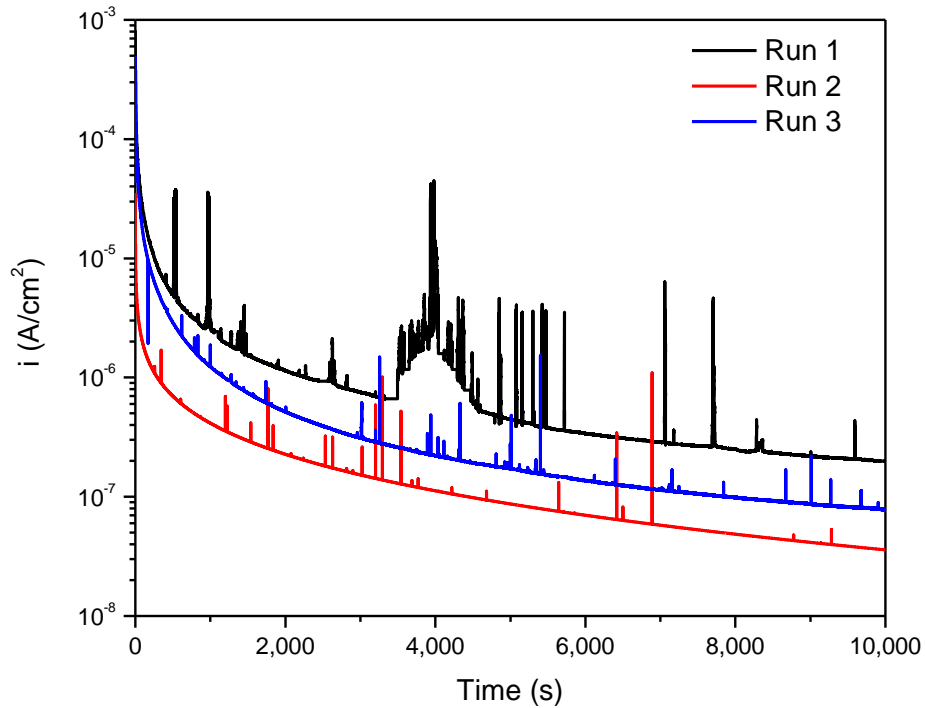


Figure 5.30. Metastable activity for the film on Ni-22 Cr-12 Mo, wt%, during passivation at +0.2 V_{SCE} for 10 ks in deaerated 1.0 M NaCl pH 4

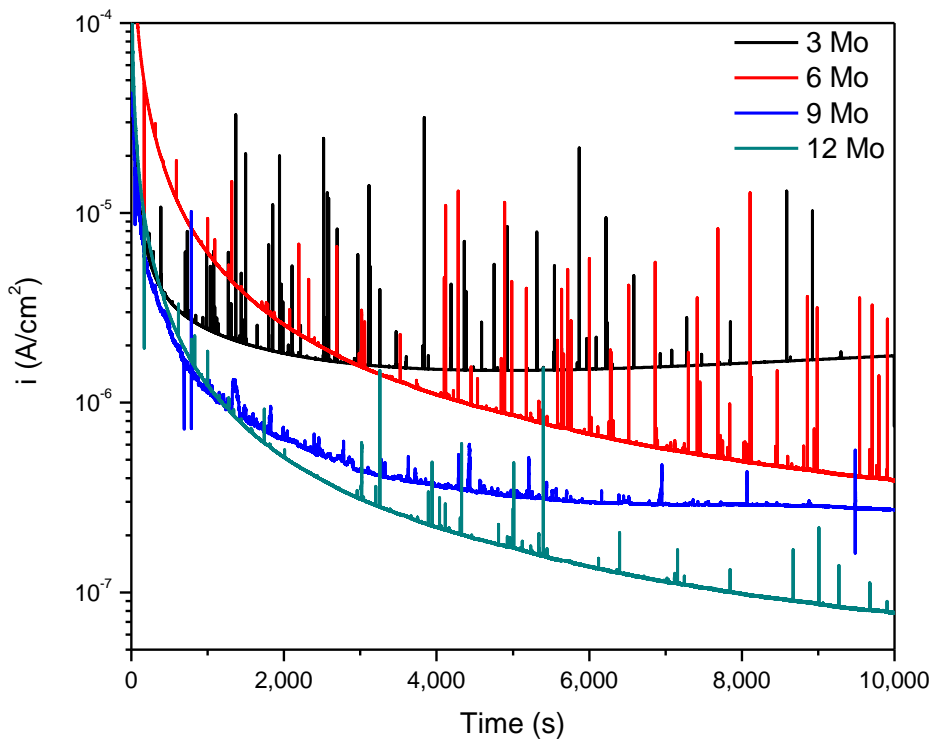


Figure 5.31. Comparison of the passivity of Ni-22 Cr-x Mo where x = 3, 6, 9, 12, wt%, at +0.2 V_{SCE} for 10 ks in deaerated 1.0 M NaCl pH 4

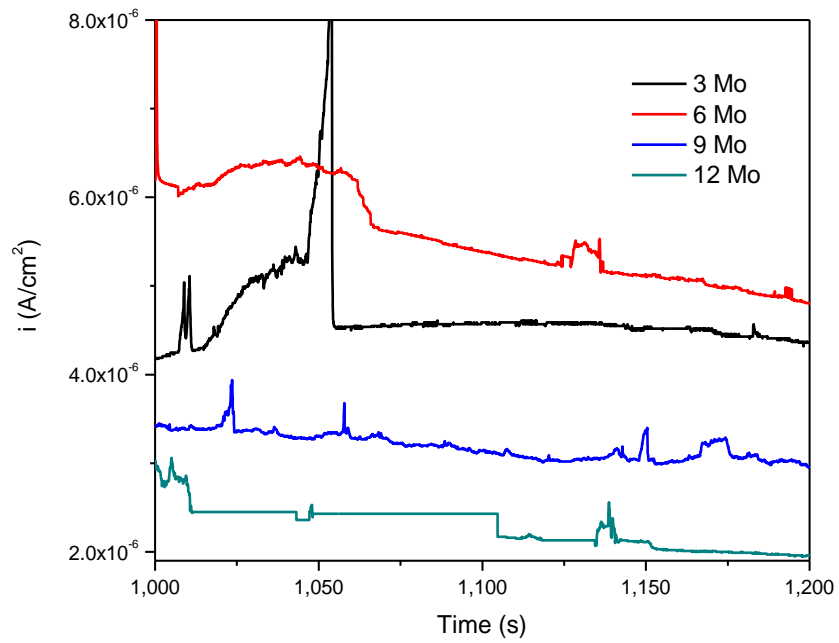


Figure 5.32. Focused Figure 5.31 over 1,000 to 1,200 s following the initial, often rapid film breakdown where characteristic individual metastable pitting events for each alloy can be observed

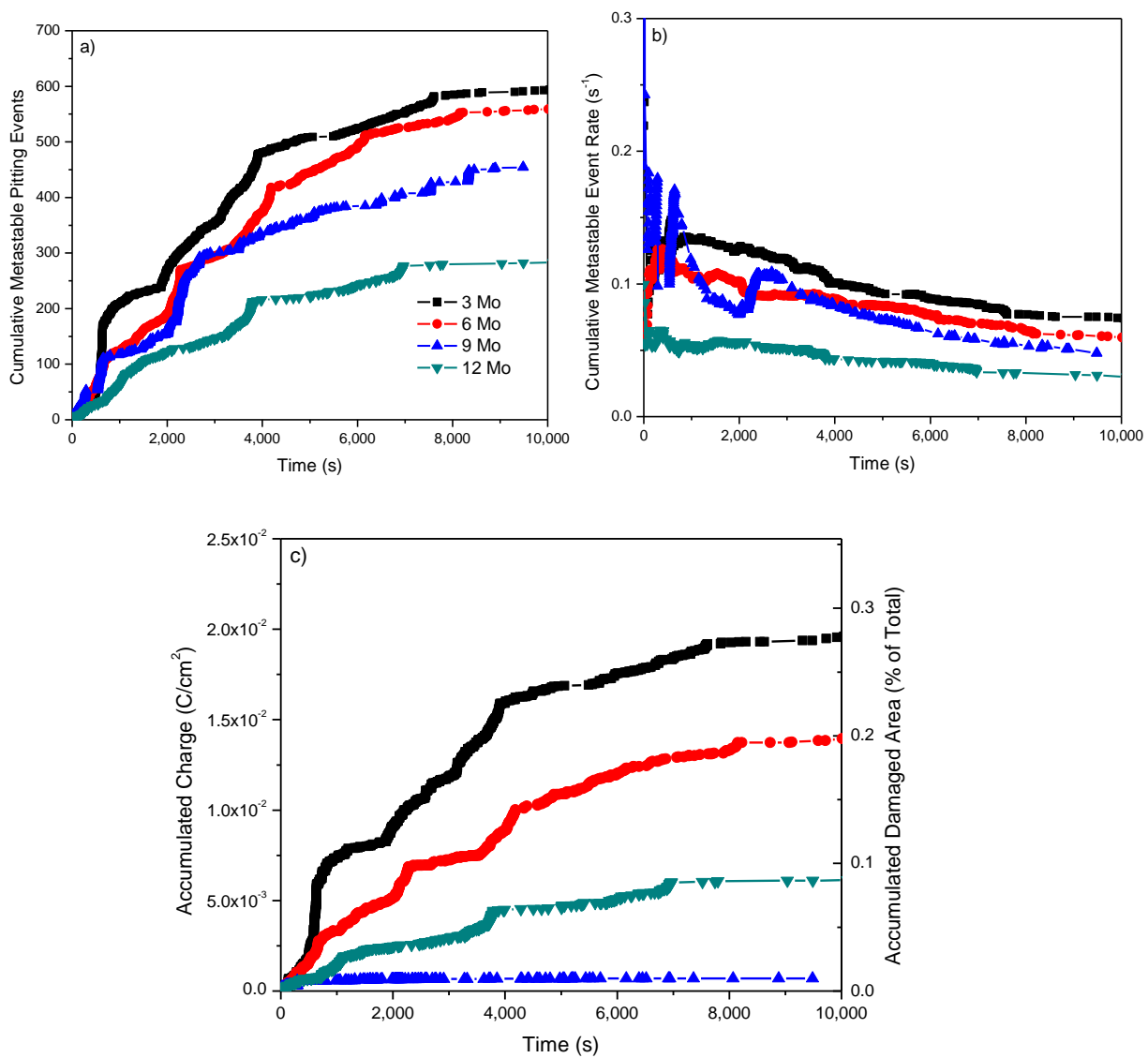


Figure 5.33. Comparison between the cumulative a) number, b) rate, and c) charge of metastable pitting events and the corresponding damaged area fraction relative to the total exposed one (0.1 cm²) following passivation of Ni-22Cr-xMo where x = 3, 6, 9, 12, wt%, at +0.2 V_{SCE} for 10 ks in 1.0 M NaCl pH 4 (Figure 5.31)

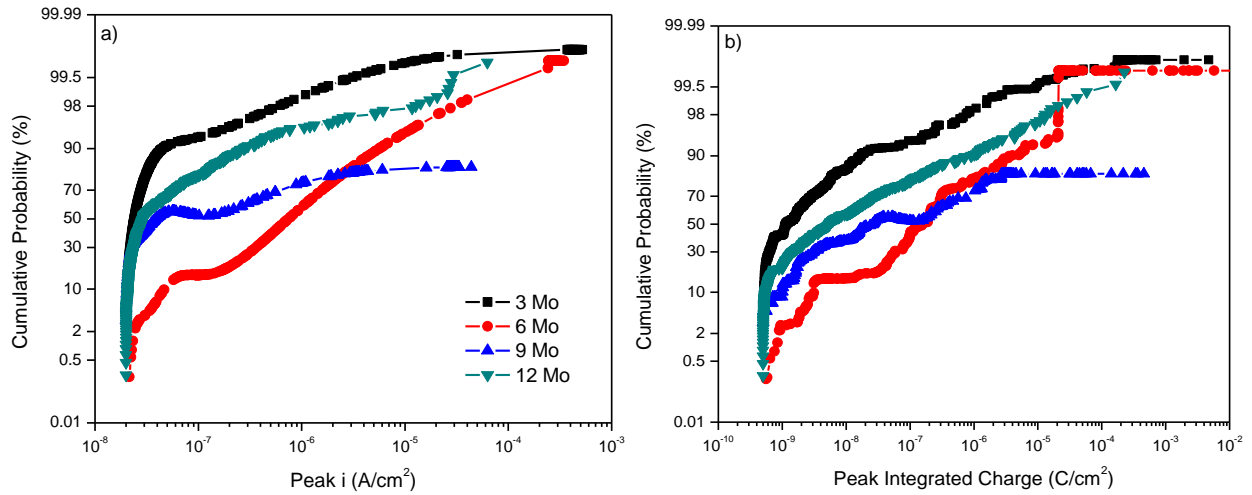


Figure 5.34. Cumulative probability plots of metastable peak a) current heights and b) integrated charge of events following passivation of Ni-22 Cr-x Mo where x = 3, 6, 9, 12, wt%, at +0.2 V_{SCE} for 10 ks in 1.0 M NaCl pH 4 (Figure 5.31 and Figure 5.33)

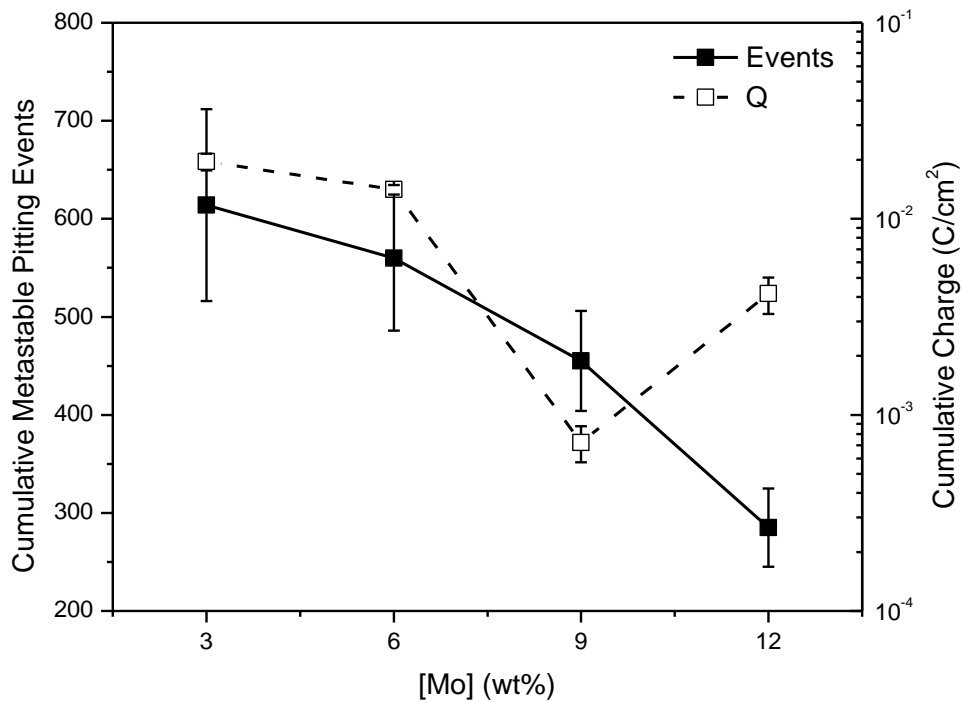


Figure 5.35. Average final cumulative number of metastable pitting events and charge during a +0.2 V_{SCE} hold for 10 ks on Ni-22 Cr-x Mo, wt%, where x = 3, 6, 9, and 12 wt% Mo, in deaerated, 1.0 M NaCl pH 4.

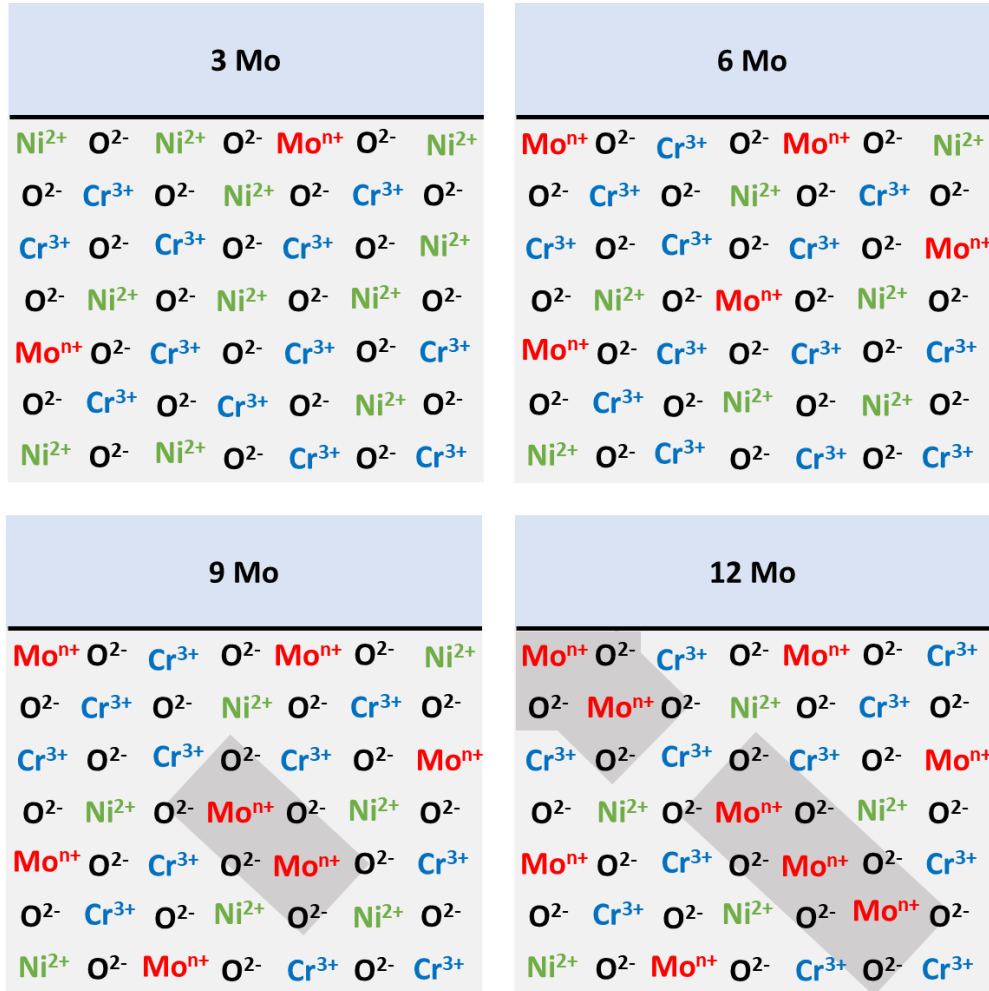


Figure 5.36. Schematic of the passive film composition evolutions with increasing concentrations of Mo within the bulk alloy. Both the fraction of solute captured Cr³⁺ and Moⁿ⁺ increase with [Mo], but some clustering of local Mo-oxides can occur at higher concentrations and produce local precipitates, indicated by the dark regions within the film.

6. Influence of Solute Capture Versus Phase Separation Produced by Fast and Slow Film Growth on Passivity, Electrochemical Stability, and Local Breakdown Events

6.1 Abstract

The implications of varying passivation rates and non-equilibrium solute capture (NSC) on the physical, chemical, and electronic properties of films, along with the electrochemical stability, were investigated for Ni-22 Cr and Ni-22 Cr-6 Mo, wt%. Experiments were conducted in an acidified NaCl environment using predominantly *in operando* Single-Frequency-Electrochemical Impedance Spectroscopy (SF-EIS) applied galvanostatically at varying applied currents. Subsequent *in situ* analysis was performed using Mott-Schottky impedance scans and metastable pit breakdown analysis during a potentiostatic hold, +0.2 V_{SCE}. Following the initial passivation step, the films were also characterized *ex situ* through application of atomic force microscopy (AFM) and X-ray photoelectron spectroscopy (XPS). The effect of solute capture on modifying the composition and distribution of metal cations within the passive films, along with the beneficial effect of Mo capture in Ni-Cr-Mo compared to Cr in Ni-Cr are presented. Specifically, it was found that the higher valency of Mo dopants enabled greater film tolerance to breakdown. Growth at slower rates produced films with segregation of Ni²⁺ and Mo^{4,6+} to the film/electrolyte interface, leaving Cr³⁺ enriched at the metal/film interface.

6.2 Collaborations

In this chapter, AFM measurements and RMS analysis were accomplished by William Blades at the University of Virginia.

6.3 Introduction

6.3.1 Liquid to Solid Transformations and Solute Trapping

The field of phase transformations has thoroughly addressed the influence of solidification rate from the liquid field into the solid over the past century or so (e.g. ¹⁻⁴). In particular, the morphology and composition of the resulting microstructure have been studied. This solidification process is often complicated by the non-periodic atomic structure of the liquid phase and the importance of interfacial energies during a liquid to solid transformation. The earliest treatment of growth kinetics for this process came from the model of continuous, or Wilson-Frenkel growth^{5,6}. The expression for the solidification velocity was developed here as a function of the undercooling,

but it only applied to low undercoolings and thus slow solidification. This case is not necessarily applicable to many systems.

From this work, previous literature developed mathematics to describe the kinetics of increasingly faster growth processes. Initially, this involved aspects such as solute redistribution⁷ and variable growth mechanisms at sites of morphological instabilities as a function of the supercooling, temperature gradient, and the interfacial properties^{8,9} among others. The influence of the generic cooling rate versus the resulting physical structure of the solidified microstructure is given in Figure 6.1 below. It can be seen that for a high undercooling and slow growth, homogeneous, planar fronts will be achieved. However, for fast growth and small undercoolings, complicated dendritic structures can be achieved.

All of the previously mentioned kinetic models have focused on the near-equilibrium limit where the solidification front velocity is predominantly controlled by the transport rate of latent heat away from the surface. This enables local thermodynamic equilibrium to be maintained during the rapid processes. There are certain processes where the solidification rate exceeds that where local equilibrium can be maintained, however. At this point, it has been observed that the chemical potential of the solute for a binary alloy increases despite the total free energy of the system dropping as it must by the laws of thermodynamics¹⁰⁻¹⁶. This enables the retention of solute concentrations far above those predicted by equilibrium solid solubility limits. As such, the kinetic model of solute trapping was developed to describe such rapid solidification processes and the resultant solid compositions^{10,17}. To put it simply, solute trapping occurs when crystallization is occurring faster than diffusion, or:

$$\frac{v_{diff}}{v_{int}} < 1 \quad \text{Equation 6.1}$$

$$v_{diff} = \frac{D}{a} \quad \text{Equation 6.2}$$

where v_{int} gives the overall solidification rate, v_{diff} is the long-rate diffusive speed of solute, D is the solute diffusivity in the liquid phase, and a is interatomic spacing. When Equation 6.1 is satisfied, short-range atomic rearrangement into a crystalline lattice will occur, resulting in non-equilibrium phase compositions. In the original paper, it was shown that ΔG decreased while

μ_{solute} increased following stepwise and continuous growth and the model could be applied to and satisfy previous kinetic models (e.g. Baker and Cahn³).

6.3.2 Solid to Solid Transformations and Non-Equilibrium Solute Capture

In the case of electrochemical passivation, there is no true transformation of the liquid phase to a solid one, as the initial system involves an interface between a metallic solid and a typically aqueous solution with an entirely different composition than the metal. As such, the mathematics of classical solute trapping are not applicable. In addition, the atoms for the literature model add to the moving solidification front and as such the velocity is directly related to this diffusional process¹⁸. However, for the oxidation of passive films, thickening is typically considered to be controlled by the velocity of vacancies and/or interstitials¹⁹⁻²². And finally, there are two separate interfacial velocities that must be considered compared to the single one relevant for solute trapping: the metal/film interface which moves inward during oxidation and the film/solution interface, which also moves inward following solution-assisted film dissolution. As such, the original concept of solute trapping was extended to the electrochemical oxidation case in the model of non-equilibrium solute capture (NSC).

The thermodynamic conditions required NSC are similar to the original ones established by the solute trapping literature. First, the free energy of oxide formation must be negative. This has been shown to be satisfied for the non-equilibrium capture of either Cr^{3+} in rocksalt ($Fm\bar{3}m$) and Ni^{2+} in corundum ($R\bar{3}c$) crystallographic structures (Figure 6.2). The resulting chemical compounds can be written as $\text{Cr}_{1-x}\text{Ni}_x\text{O}_{1.5-x/2}$ and $\text{Cr}_{2-x}\text{Ni}_x\text{O}_{3-y}$, respectively.¹⁸ It is worth noting that Cr^{2+} and Ni^{3+} can similarly become trapped and result in slightly different chemical compounds of the same rocksalt or corundum structure, but these cation states are not commonly observed within the passive films on Ni-alloys. Second, the metal/film interfacial velocity must be too fast for equilibrium diffusion to occur. Due to the additional influence of dissolution at the film/solution interface, the net velocity, v_{eff} , must be considered:

$$v_{eff} = v_{echem} - v_{diss} \quad \text{Equation 6.3}$$

where v_{echem} gives the net measured electrochemical reaction rate which includes that of the total oxidation, v_{eff} , and dissolution, v_{diss} , reactions. Equation 6.1 can thus be written to include this distinction and compute the extent of NSC ($\beta > 1$):

$$\beta = \frac{v_{eff}}{v_{diff}} \quad \text{Equation 6.4}$$

In general, non-equilibrium phase compositions will be formed when $\beta \gg 1$ so long as the total free energy change for the system is negative. This is theorized to occur for any combination of transition metals, including but not limited to Fe, Cr, Ni, Cu, and Co. Other minor solutes are also possible in some cases due to their high solubility, valency, and similar ionic radii, such as Mo, W, and Al¹⁸.

The existence of metastable, kinetically-favored oxides has been previously demonstrated²³, but the long-term stability of these solute-captured compounds cannot be predicted through thermodynamics alone. According to the phase diagram provided in Figure 6.3, there is very minimal solubility of Cr₂O₃ in NiO at low temperatures and no solubility of NiO in Cr₂O₃. Instead, the NiCr₂O₄ spinel is conventionally expected to form as it has the lowest overall ΔG_f ^{24,25}. However, this compound has a unique crystallographic structure ($Fd\bar{3}m$) that is easily discernable from the rocksalt and corundum structures in diffraction patterns.

Recent studies have shown that in the event of NSC, oxide properties can vary significantly as a function of growth rate¹⁸. This effect is especially complexed in electrochemical environments where dissolution and oxidation are fast and the concentration and transport of point defects directly control film growth. As shown in Figure 6.4, a typical diffusion velocity for passive film growth is approximately $10^{-6} \frac{nm}{s}$ based on a field-assisted diffusivity of $10^{-20} \frac{cm^2}{s}$ and an atomic jump distance of $1 nm$ ^{18,26}. The relative velocities for electrochemical processes that occur at varying rates are also displayed in Figure 6.4. For a mildly corrosive environment like seawater²⁷, C-22's passive current density indicates quasi-equilibrium growth of phase-separated compounds is possible whereas in an oxidizing one like HCl, C-22 grows adequately fast for solute capture to occur²⁸. The effective passivation velocity can be estimated by an electrochemical rate using the following expression:

$$v_{eff} = \frac{M_{ox}}{nF\rho_{ox}} i \quad \text{Equation 6.5}$$

The most significant tool for affecting v_D and the susceptibility of a given reaction to induce quasi-equilibrium oxidation rather than NSC is the diffusivity. Because of the Arrhenius-dependence on temperature and, in the presence of an electric field, the field strength, the

diffusivity of point defects can be varied by orders of magnitude. In the case of dry oxidation reactions, this is most readily accomplished by changing the O₂ partial pressure or the temperature of the environment, as shown in Figure 6.5. Only at extremely high temperatures and low pO₂ is $\beta < 1$, shown in Figure 6.5 as the region under the green plane where $\beta = 1$. In the electrochemical case, the diffusivity can be easily varied using different solution temperatures and applied electric fields (Figure 6.6). At longer exposure times, the occurrence of steady state passive films could result in the annealing of NSC films and the formation of more stoichiometric phases, such as Cr₂O₃ from a solute-captured Ni_{1-x}Cr_xO_y rocksalt once the Cr³⁺ enriches to a significant composition following selective dissolution of Ni²⁺, for example.

6.3.3 Implications of Non-Equilibrium Solute Capture for Material Properties

Very few electrochemical studies have been conducted with respect to the influence of growth rate on film structure, chemical identity, stability, and ultimately the effects of corrosion. Slower growth is conventionally thought to form more “annealed” and less-defective passive films and is more likely to form thermodynamically predicted phase-separated oxides such as those predicted by Pourbaix E-pH diagrams (Figure 4.10). Film growth is, however, a rapid process where the oxide interface velocity is so great that long-range and field-assisted diffusion is not faster than the velocity of the corroding interface and thermodynamically-unexpected compounds form. This is not identical to the formation of metastable phases which might involve the same amount of compositional partitioning as formation of the most stable phase.

Previously, electrodeposited Au-Ni films were observed to exist in a non-phase-separated state which exhibited greater cohesive energy than the typical case²⁹. Similarly electroplated Ag-Cu alloys were grown in an ordinary and in a complexing solution and it was observed that different morphologies resulted from each case because of varying surface mobilities³⁰. This is directly related to the effect of diffusivity and migration observed for passive films. Another literature study using electron diffraction and X-ray microanalysis found that the passive film grown on Ni-Cr was a solute-captured NiO rocksalt structure containing nearly twice as much Cr as Ni, but following an annealing heat treatment in vacuum the film phase-separated into thermodynamically stable species: some NiO and predominantly Cr₂O₃ (Figure 6.7)³¹. However, upon annealing the samples in air, additional oxidation was observed and instead, NiCr₂O₄ was

formed with small amounts of NiO and Cr₂O₃ still evident in the diffraction pattern. For both anneals, the overall cation fraction of the films did not change.³¹

Solute capture can result in significant ramifications for not only the chemical and physical structure of passive films, but also electronic properties¹⁸. As previously explained, the effect of substitution of higher valence cations onto lattice sites is similar to the doping of semiconductors, was modeled by the SVIM³² and is theorized, not proven, to lead to the inhibition of pitting. The same observation has been made for Zr-alloys alloyed with Nb^{33,34}. The n-type dopant has a lower oxidation state and will result in the attraction of anion oxygen vacancies in ZrO₂. Nb²⁺ or Nb³⁺ substitutional defects in ZrO₂ additionally balance the build-up of positive charges in the oxide layer, increasing the oxygen vacancy and electron mobilities along with changing the growth kinetics from sub- to near-parabolic³³.

NSC has been demonstrated in more recent work. Both high temperature oxidation and electrochemical passivation of Ni-Cr and Ni-Cr-Mo were demonstrated to produce the solute-captured oxides suggested previously based on chemical and structural analysis using 3D atom probe tomography (3DAPT), electron energy loss spectroscopy (EELS), and transmission electron microscopy (TEM)¹⁸. One example of the analysis accomplished for chemically oxidized Ni-Cr-Mo is provided in Figure 6.8. The results presented were noteworthy in that they demonstrated theoretically and experimentally the existence of these highly non-stoichiometric oxides for the first time. To test the metastability of these films and the possibility to anneal the NSC compounds into distinct NiO, Cr₂O₃, and/or NiCr₂O₄ phases, as mentioned previously (Figure 6.7)³¹, the freshly oxidized samples were left in lab air for approximately a year and re-analyzed. Upon doing so it was evident that corundum was precipitated from the NSC rocksalt, as indicated in Figure 6.9. Overall, the dominant structure is still the rocksalt-structured Cr_{1-x}Ni_xO_{1.5-x/2} despite this long-term aging. This demonstrates the high kinetic barriers to anneal NSC compounds at standard conditions, whereas with elevated diffusivities achieved at high temperatures, the same feat can be accomplished more rapidly (Figure 6.7).

The Cu-Al binary alloy system provides a classic example of two oxides with no thermodynamic solubility within each other. In essence, the presence of any Al³⁺ substitutional defects within a Cu₂O oxide would phase-separate at equilibrium and produce a distinct Al₂O₃ layer or some spinel species (i.e. CuAlO₂ or CuAl₂O₄)³⁵. However, recent work on this alloying

system has demonstrated that despite this non-existent solubility according to equilibrium considerations, Al^{3+} cations were captured into the cuprous oxide layer³⁵. This was established through X-ray measurements of crystalline lattice stretching, coulometric reduction, XPS indication of Al^{3+} within the film, and Mott-Schottky-measured changes in the film defect chemistry. The results demonstrated that cation vacancies were generated and electronic holes annihilated to compensate for the positive charge of Al^{3+} on a Cu^+ site, $\text{Al}_{\text{Cu}}^{\bullet\bullet}$, as shown schematically in Figure 6.10. This resulted in a significant difference in the electrochemical behavior of the passive cuprous films. With more Al^{3+} content, greater solute capture occurred and as a result a great number of p-type defects such as holes became eliminated (Figure 6.11). This has a significant effect on the kinetics of oxidation as it is driven by point defect migration. The oxide thickness was observed to decrease whereas the tarnish resistance improved with increasing Al^{3+} content as a result of NSC. This was highly desirable for the alloy system, as the release of Cu^+ necessary for antimicrobial function was not impacted by the facilitation of the formation of a tarnish-resistant layer³⁵.

6.4 Objective

The film growth at high and low rates can result in increased defect density and “rougher” morphologies along with different chemical species forming based on these kinetic considerations rather than thermodynamic rules (i.e. solute capture). This effect has been minimally studied in literature. In some cases, the capture of solute cations and subsequent increase in the overall defect density can be attractive, as has been the postulated beneficial impact of Mo and W in previous literature³⁶. The overall effect of intentionally solute-captured versus phase-separated films on chemical stability, passivity, and metastable pit initiation is unknown and demands further study. The potential effects of alloying element concentrations on film stability and the impacts of fast and slow growth on pit initiation were investigated through application of *in operando* galvanostatic SF-EIS to mediate film growth along with *in situ* MS-EIS and *ex situ* XPS and AFM. The objective of this study was to connect the effects of NSC versus phase-separated oxides on electrochemical stability and, in particular, localized breakdown.

6.5 Approach

The galvanostatic SF-EIS (gSF-EIS) framework established in Chapter 2 was applied. Oxides will be grown slowly and/or quickly using applied galvanostatic current densities or

alternatively, slowly through natural exposure in solution. After fast or slow growth, MS-EIS potential sweeps measured the electronic character (N_a , N_d , E_{fb}) and a current decay (i.e. potentiostatic hold) at the final gSF-EIS potential in order to probe metastable film activity and electrochemical stability in an environment. Sequential angle-resolved XPS and AFM measurements of the surface were performed to investigate the chemical identity, element distribution, and physical surface structures formed at varying growth rates. These factors were related to pit initiation.

6.6 Experimental Methods

For this chapter, several of the analytical techniques used were applied again. While before, the focus of the experiments was on potential-controlled passivation, here rate-controlled passivation was used to induce either solute capture or quasi-equilibrium formation of stoichiometric phases. This was accomplished through the application of the galvanostatic SF-EIS method previously presented in Chapter 2. The unique experimental details for the results provided herein are given below.

6.6.1 Materials

The samples used for this study were polycrystalline, solid solution Ni-alloys that model common Cr and Mo concentrations found in commercial Ni-superalloys with the following compositions: Ni-22% Cr and Ni-22% Cr-6% Mo, wt%. The materials were arc-melted, cast, rolled, solutionized, recrystallized, and sectioned. Thermodynamic predictions for a generic Ni-Cr-Mo alloy exposed to a dilute NaCl environment were previously given in Figure 4.10. Prior to each experiment, the samples were wet-polished up to 1200 grit using SiC paper, ultrasonically cleaned in alcohol, and rinsed with deionized water (resistivity of 18.2 M Ω -cm) before being placed into the flat cell window. In the case of highly surface-sensitive techniques such as AFM or EBSD, subsequent polishing using polycrystalline diamond suspensions on felt microcloth pads down to 1 or 0.25 μ m and a final ion polishing step for 20 min. The EBSD images for these alloys were previously provided (Figure 3.1).

The various solutions used for testing were 0.1 M NaCl acidified to pH 4 using 1 M HCl. Additionally, 1.0 M NaCl pH 4 was similarly prepared. All prepared solutions used reagent grade

chemicals dissolved in deionized water dispensed from a Milli-Q and were deaerated using ultra-high purity N₂ gas during electrochemical experimentation.

6.6.2 gSF-EIS

Following the reduction step, the Gamry Galvanostatic SF-EIS script was applied at various applied current densities (Table 6.1) with 1 Hz frequency and a 5 nA/cm² AC amplitude. This enabled the measurement of the impedance components Z' and Z'' of the oxide film (Chapter 2) during passivation at the various applied rates. Notably, the lowest possible applied galvanostatic current, i_{DC} , is 0.5 $\mu\text{A}/\text{cm}^2$ due to the early occurrence of film breakdown before a conformal layer is achieved on Ni-Cr, long before even a potential of +200 mV_{SCE}. No slower passivation rates were feasible, despite β being slightly greater than 1 for an i_{DC} of 0.5 $\mu\text{A}/\text{cm}^2$. These values of β were estimated based on 100% charge efficiency. However, during galvanostatic passivation this is not entirely valid and as such, the true β is less than those given in Table 6.1 and will approach 1 for the sufficiently slow applied current densities.

6.6.3 Mott-Schottky Impedance Analysis

Immediately following passivation at varying galvanostatic rates (Table 6.1), the electronic defect properties of the films on Ni-22 Cr and Ni-22 Cr-6 Mo, wt%, were measured using fast impedance sweeps at 1,000 Hz from +300 mV_{SCE} to -600 mV_{SCE} with 20 mV steps, resulting in sufficiently rapid data acquisition. As mentioned previously, this scan rate was selected in order to measure the impedance variations as a function of potential without the possibility of the space charge layer adjusting. The results were analyzed as discussed in Section 3.5.5.

6.6.4 Atomic Force Microscopy Surface Imaging

Following electrochemical passivation, the samples were removed from the cell, rinsed with deionized water, and sonicated in ethanol to remove any residual salt from the surface that would obstruct imaging. The surface morphology of each sample was captured using an AFM with NT-MDT Solver Pro. The AFM tip, ETALON HA/NC with a radius of curvature less than 10 nm, was kept in tapping mode during imaging. The surface roughness of the samples was ascertained from deviations in the root mean square (RMS) of local surface areas. The RMS data in this study was found using Gwyddion³⁷, an open source software package used for Surface Probe Microscopy analysis. To obtain consistent and physically meaningful RMS values, each image

was planarized by mean plane subtraction. The variations caused by the contact between the tip and sample along the horizontal scanning directions were also corrected by leveling the horizontal line directions with linear or quadratic polynomials depending on the magnitude of the deviations.

6.6.5 Angle-Resolved X-ray Photoelectron Spectroscopy

The variation of film composition and thicknesses was additionally characterized using XPS spectra obtained periodically throughout potentiostatic passive film growth. This technique is well-established in literature for analysis of the identity, concentration, and thicknesses of individual compounds present in films³⁸, especially in the case of Ni-based alloys³⁹⁻⁴¹. All XPS spectra were obtained using a monochromatic Al- $K\alpha$ photon source ($E = 1,486.7$ eV) with surface characterization following various durations of oxide growth. The angle between the sample and detector was adjusted to 45 and 90°, whereas that between detector and the X-ray source was fixed at 54.7°. Spectra were calibrated to the 4f^{7/2} binding energy of a metallic Au reference (B.E. = 84 eV) measured at the same time. Survey spectra were recorded on all samples using a pass energy of 200 eV, followed by high resolution spectra of the Ni 2p, Cr 3p, Mo 3d, and O 1s regions using a pass energy of 20 eV.

Commercial CasaXPS software was used to perform Shirley background corrections and spectra fitting⁴²⁻⁴⁴. The concentrations of Ni²⁺, Cr³⁺, and Mo⁶⁺ cations in the passive films were computed by fitting the spectra to their observed metallic and oxide/hydroxide peaks, as established in previous literature^{39,40,44-47} and correcting these integrated peak areas to atomic sensitivity factors for Ni, Cr, and Mo (4.044, 2.427, and 3.321 for this detector and source configuration, respectively)⁴⁴ (Table 3.1).

6.6.6 Metastable Pitting Event Analysis

The methods previously established for characterizing metastable pit breakdown events was applied as previously shown in Figure 5.7.⁴⁸⁻⁵¹ Passive films on Ni-22 Cr and Ni-22 Cr-6 Mo, wt%, were grown at varying galvanostatic rates (Table 6.1). When the potential reached the established metastable potential, +200 mV_{SCE}, the potentiostat was switched to potentiostatic control at the same potential for 10 ks. The same threshold current increase of 50 nA/cm² was selected⁵¹. The implications of NSC for passive film metastability in acidic chloride electrolytes will then be analyzed via application of analytical tools^{48,51}. The methods and data computation were previously presented in Chapter 5.

6.7 Results

6.7.1 Initial Assessment of Fast Versus Slow Passivation and Film Breakdown

The dependence of solute capture on the passivation rate can be experimentally controlled by both an applied electrochemical current and a temperature. The effect of the later was initially studied by exposing Ni-Cr oxidized at varying conditions (Table 6.2) to 0.1 M NaCl acidified to pH 4 (Figure 6.12). The occurrence of metastable breakdown events on the alloys evidently varied with the exposure. The air-oxidized sample, which is predicted to exhibit phase-separation and little to no NSC, had the lowest total current. This indicates a more passive film which dissolved less in the NaCl environment. The intermediate oxidation rate at 100°C had the highest current, however, but the lowest apparent metastable pitting rate. In general, all oxidation rates resulted in significant metastable breakdown at early times which decreased with time. This decline in the event frequency is anticipated based on previous literature⁵¹⁻⁵⁴. For direct comparison of the metastable pitting event statistics, more detailed analysis was performed and is given in Figure 6.13. The total number of observed metastable pitting events, average rate, and charge during exposure at +0.2 V_{SCE} to deaerated 0.1 M NaCl pH 4 clearly increased with β (Table 6.2). For approximately the first 10 s of the potentiostatic hold, all three oxides exhibited similar breakdown, before substantially increasing for the 200 °C case. The scale formed at 100 °C similarly increased, but only slightly whereas the air-oxide pitting rate continuously decreased with time (). At early times, however, greater current spikes and therefore large pits, were formed after 100 °C oxidation. Later breakdown events were insignificant. These air-formed oxides are simplified models of the effects of solute capture because there is no added influence of film dissolution during film growth. Electrochemical passivation will, therefore, be more complicated due to the rapid velocity of the metal/film and film/electrolyte interfaces.

The electrochemical stability of passive films formed at varying rates in aqueous environments were similarly investigated. Figure 6.30 provides a detailed look at the breakdown evident on Ni-22 Cr-6 Mo, wt%, following rapid passivation. The film grown slowly did not exhibit any discernable breakdown. Rather, only electrochemical noise was measured as true pits only exhibit upward increase from the baseline. Notably, the baseline current density was almost an order magnitude higher for the rapid passivation case. This is due to an increase in the dissolution rate of the increasingly solute-captured and likely defective film. This effect of

electrochemical passivation rate and the resulting chemical stability of passive films will be studied in more detail herein.

6.7.2 *In Operando* Galvanostatic Passivation

Measurements of film thickening during galvanostatic passivation were made possible through application of the SF-EIS method (Section 2.5.4). This is notably only possible within the passive region of metal as below E_{pp} , $-Z''$ is dominated by other capacitive features of the electrical circuit such as the Helmholtz double layer. This effect is more noticeable for slower passivation rates (Figure 6.14a) as more time is allowed to build charge in the double layer and increase the impedance at non-passive potentials. For the bare metal surface, the potential is initially around $-1 V_{SCE}$ before increasing as the film nucleates and grows under the anodic applied current (Figure 6.14). Past E_{pp} , the film thickening rate (i.e. nm/s) is theorized to be proportional to the applied current, i_{DC} . This can be quantified by computation of $i_{ox}(t)$, as shown in Figure 6.15a and for every potential, it increases in magnitude with i_{DC} . The potential-dependent oxidation thinning rate appears to be relatively independent of the passivation rate and is approximately 2.5 nm/V from +300 to +400 mV_{SCE} (Figure 6.14b). Dissolution still has a significant influence on the measurable passivation rate. This shown in Figure 6.15b, where η decreases in magnitude with i_{DC} . This observed decrease in efficiency is the result of incomplete oxidation at higher rates and excessive dissolution at exposed metal areas on the surface when the film passivates rapidly.

The effect of alloying additions on the efficiency and rate of passivation under galvanostatic conditions can be similarly investigated through application of SF-EIS (Figure 6.16). As was demonstrated by the findings in previous chapters, adding Mo results in increased efficiencies. As a result, thicker films were observed for Ni-Cr-Mo compared to Ni-Cr at a given i_{DC} . This difference was much less significant for fast passivation at 50 $\mu A/cm^2$ than it was for the slow case at 0.5 $\mu A/cm^2$ (Figure 6.16). The magnitude of i_{ox} and η were, therefore, greater for Ni-Cr-Mo in Figure 6.17 and, for a single alloy, the slow passivation case. This finding is the same as was discussed for Figure 6.15. Notably in Figure 6.17, $i_{ox}(t) \rightarrow 0$ for the slow passivation case due to the two order of magnitude difference in i_{DC} but η was slightly improved for film thickening and thinning. This is the opposite from what was observed in Chapters 3 and 4, where Ni-Cr consistently exhibited the thickest film. The difference can be attributed to the effects of the driving

force: overpotential for potentiostatic and rate for galvanostatic. Presumably Mo facilitates passivation by decreasing the overpotential, but increasing the rate, allowing a thinner film to form more rapidly.

6.7.3 Mott-Schottky Analysis of Passive Film Electronic Properties

Following galvanostatic passivation at varying rates, fast impedance sweeps through the passive region can enable Mott-Schottky analysis of the electronic character of these films as a result of NSC. A comparison between the capacitance curves obtained for Ni-Cr and Ni-Cr-Mo passivated slowly ($0.5 \mu\text{A}/\text{cm}^2$) and rapidly ($50 \mu\text{A}/\text{cm}^2$) is given in Figure 6.18. An increase in C^{-2} and therefore a thicker film^G is again observed for Ni-Cr-Mo as a consequence of faster enrichment of Cr^{3+} . Mott-Schottky analysis of the concentration of n and p-type defects and the observed flat band potentials are given in Table 6.3. Ni-Cr-Mo consistently exhibits lower point defect densities with the difference in n-type ones being significant. Notably, this category includes metal cation vacancies which are detrimental for the localized breakdown of passive films⁵⁵. The Mo-containing alloy also has higher flat band potentials, suggesting a greater film resistance to dissolution and breakdown. The effect of passivation rate and NSC are also evident as across both alloys, slow growth ($0.5 \mu\text{A}/\text{cm}^2$) resulted in decreased densities and increased flat band potentials. The decline in these parameters was remarkably less for Ni-Cr-Mo than Ni-Cr due to the beneficial capture of Mo.

A more detailed look into the effect of varying the passivation rate on the measured impedance curves within the passive region is given for Ni-Cr and Ni-Cr-Mo in Figure 6.19 and Figure 6.21, respectively. For Ni-Cr, the effect of increasing passivation and NSC is evident as the passive film capacitance consistently decreases as i_{DC} increases. Along with decreasing capacitance, increasing p-type behavior was observed. Mott-Schottky analysis of the passive film electronic properties yielded that, instead, the concentration of n-type defects, N_D , was much greater than p-type ones, N_A , and this difference became even more significant at greater passivation rates (Figure 6.20). Both the n-type and p-type E_{FB} decreased at approximately the same rate with i_{DC} as a result of decreased film resistance to localized breakdown.

^G $C^{-1} = (\epsilon\epsilon_0 A)^{-1} l_{ox}$

With increasing i_{DC} on Ni-Cr-Mo, there is an initial decrease in the capacitance from 0.5 to 1 $\mu\text{A}/\text{cm}^2$, followed by an increase as C^{-2} decreases. The transition potential also shifts to the left as i_{DC} increases for Ni-Cr-Mo. Both of these phenomena occur as a result of increasing Mo capture in the film as the passivation rate increases. This effect was observed previously in Section 5.3.7.1 where greater concentrations of $\text{Mo}^{\text{n+}}$ in the film resulted in increased p-type behavior and a decreased semiconductor bandgap. Analysis of the defect densities and flat-band potentials (Figure 6.22) suggests similar behavior where at greater i_{DC} , Mo cations are increasingly captured in the film. The measured E_{FB} values both decrease with increasing passivation rates as a result of NSC. In Figure 6.22, the concentration of donor defects remains approximately constant due to the inhibition of cation vacancy motion with increasing Mo capture, which is suggested by the increase in N_A with increasing passivation rate. N_D , however, remains approximately constant by the same rationale. This is different from what was observed for Ni-Cr, where a large increase in N_D was measured with increasing i_{DC} and N_A hardly changed (Figure 6.20 and Table 6.3).

6.7.4 Surface Topography Following Fast and Slow Passivation

At various times throughout the passivation processes, AFM imaging provided additional details concerning the influence of the electrochemical oxidation rate and NSC on the development of the surface topography. Once the oxide was electrochemically grown, the alloy surfaces were measured immediately after exposure to reduce the effect of ambient conditions on the surfaces. Several area sizes were measured using AFM (e.g. 10x10, 5x5, and 2x2 μm^2). Figure 6.23 and Figure 6.24 provide representative sets of the AFM images captured after fast (50 $\mu\text{A}/\text{cm}^2$) and slow (0.5 $\mu\text{A}/\text{cm}^2$) passivation times for Ni-22 Cr and Ni-22 Cr-6 Mo, wt%, respectively, in 0.1 M NaCl pH 4. The passive film morphology on Ni-Cr is greatly influenced by passivation rate, where rapid passivation resulted in a discontinuous oxide that preferentially nucleated along polishing marks and underwent substantial chemical etching, whereas a smooth, conformal film was formed by the slow passivation (Figure 6.23). This can be characterized by RMS measurements of the AFM topography images which are included in Table 6.4. Notably, these values are greater than those previously provided for Ni-Cr and Ni-Cr-Mo passivated at +0.2 V_{SCE} for 10 ks in the same environment (Figures 4.31 and 4.32), suggesting a difference in the kinetics of passivation versus chloride-assisted dissolution and etching during potentiostatic versus

galvanostatic control. Despite these increased RMS measurements, rougher films were achieved following rapid passivation (Table 6.4).

As occurred previously, somewhat rougher films were observed for Ni-Cr-Mo following slow passivation due to the surface enrichment of Mo⁶⁺-containing species. These films were also continuous and smooth beneath such surface features. Following fast passivation, however, a remarkable decrease in the RMS was measured despite the film being non-conformal as a result of favorable oxidation occurring within scratch marks. Rapid passivation likely resulted in minimal surface segregation of Mo and instead, a continuous mix of Ni²⁺, Cr³⁺, and Mo^{4,6+} cations within the passive film occurred as a result of NSC¹⁸. Chemical etching likely resulted in some Mo repassivation at the film surface, evident in Figure 6.24a as small surface particles. This effect on the roughness was outweighed by the overall decrease in chemical etching during rapid passivation as a result of Mo additions. This resulted in a smoother film surface being achieved for Ni-Cr-Mo compared to Ni-Cr. At longer times, however, continued repassivation of the rapidly-formed film would result in the surface of Ni-Cr-Mo having a higher RMS than certainly slowly passivated Ni-Cr and Ni-Cr-Mo, and possibly also Ni-Cr oxidized quickly. This would only occur if the redeposition of Mo-rich species became more significant than the decreased etching of the surface as a result of chloride adsorption.

6.7.5 Angle Resolved X-ray Photoelectron Spectroscopy

Following galvanostatic passivation at slow, medium, and fast rates ($i_{DC} = 0.5, 5, \text{ and } 50 \mu\text{A}/\text{cm}^2$, respectively) in acidic 0.1 M NaCl, the samples were characterized using XPS obtained at both 90° and 45°, where the latter angle is more sensitive to the composition of the surface. The results are given in Figure 6.25 - Figure 6.28 for Ni-22 Cr and Ni-22 Cr-6 Mo. The effect of i_{DC} and NSC are immediately apparent, especially for Ni-Cr (Figure 6.25 and Figure 6.27). There was significant oxidation of NiO/Ni(OH)₂ following passivation at 50 $\mu\text{A}/\text{cm}^2$, evident by the ratio of the peak area and heights for the film compared to the metal. The amount of Cr³⁺ enrichment, however, decreases for Ni-Cr films as i_{DC} increases. This observed competition between Ni²⁺ and Cr³⁺ oxidation has been previously discussed with regards to the difference in kinetics during film growth^{24,25}. Fitting these spectra, as discussed in several previous chapters and demonstrated by Figure 4.34 suggests that at this rate, the ratio of oxides to hydroxides formed increases as the kinetics of film growth occur much faster than those of oxide hydration in comparison to the more

slowly-grown films. This is also clear in Figure 6.25c, where the peak for the hydroxide around 532 eV increases as i_{DC} decreases but that of the oxide around 531 eV remains constant.

The film composition for Ni-Cr-Mo, however, has a noticeably different dependence on i_{DC} . The previous enrichment of Ni^{2+} within the film on Ni-Cr is not evident in Figure 6.26a. In fact, the greatest apparent oxidation of Ni^{2+} relative to the metal peak occurred following passivation at $0.5 \mu A/cm^2$. This comes as a result of the increased passivation time rather than the effect of solute capture and/or kinetics. The enrichment of Cr^{3+} , however, increases as i_{DC} decreases and at low rates, depletion of metallic Cr at the alloy surface is evident as a result of this substantial oxidation^H. The enrichment of Mo^{4+} remained approximately constant and at the slowest rate, the amount of Mo^{6+} within the film appeared to increase. Overall the behavior of Mo cations did not vary as much as Cr^{3+} and Ni^{2+} did with i_{DC} . Instead, the major impact is that the captured $Mo^{4,6+}$ supports the oxidation of Cr rather than Ni, where the latter was substantially favored within the film on Ni-Cr, as previously discussed.

The overall film compositions for Ni-Cr and Ni-Cr-Mo based on spectra fitting⁴² are given in Figure 6.29. As was suggested by the spectra normalized to the intensities of the metal peaks, Ni-Cr appears to be more enriched in Ni^{2+} than Ni-Cr-Mo, which more strongly favors Cr^{3+} oxidation. The overall composition of the Ni-Cr films only varied slightly following Cr-enrichment during slower passivation. The Ni-Cr-Mo films, however, experienced substantial Ni-depletion and Cr-enrichment during passivation at slower rates and minimal changes in the fraction of Mo, with the depletion of Ni^{2+} facilitating the slight $Mo^{4,6+}$ enrichment that is evident in Figure 6.29.

The results obtained at 45° provide an ever more in-depth look at the effect of passivation rate on the composition and distribution of films on Ni-Cr(-Mo). Notably, following rapid oxidation, the spectra do not appear to vary significantly with the measurement angle. This observation is not valid for the slower film growth conditions. Notably, the fraction of Ni^{2+} appears to increase for the surface as i_{DC} decreases. This applies to the films formed on both Ni-Cr and Ni-Cr-Mo. Included in Figure 6.29 are the compositions of the film surfaces based on these spectra and their fits. The greater divergence in the cation fractions measured at 90° and 45° as i_{DC} decreases suggests segregation within the film. However, the films formed by passivation at 50

^H The surface composition of bulk Ni-22 Cr-6 Mo, wt%, notably decreased from approximately 24 at% to 13 at% following slow passivation at $0.5 \mu A/cm^2$ (Figure 6.25).

$\mu\text{A}/\text{cm}^2$ are exemplary of what is expected for NSC. This confirms the hypothesis that slow passivation encourages diffusion to occur and can produce some phase separation, with Ni^{2+} and Cr^{3+} moving to the film/solution and metal/film interfaces, respectively.

6.7.6 Metastable Pitting Event Analysis

Figure 6.31 shows the effect of NSC on the electrochemical stability of passive films formed on both Ni-22 Cr and Ni-22 Cr-6 Mo. The effect of both the passivation rate and the minor alloying of Mo are immediately evident. For both alloys, slow passivation resulted in few breakdown events with a smaller peak current, suggesting that the pits were smaller and less numerous. Fast growth on Ni-Cr resulted in significant pitting at early times due to detrimental capture of Cr^{3+} in $\text{NiO}/\text{Ni}(\text{OH})_2$. Ni-Cr-Mo, however, remained relatively stable despite the rapid passivation. The slow electrochemical passivation of Ni-Cr-Mo was compared to that in air for a year. Both exhibited very similar corrosion behavior, suggesting that the “slow” procedure applies well to produce non-solute-captured passive films and the true $\beta < 1$, unlike the estimate included in Table 6.1 which does not take into account any passivation inefficiencies.

Detailed analysis of the size and frequency of the metastable pitting activity shown in Figure 6.31 is provided Figure 6.32. As can be directly inferred from the original figure, Ni-Cr exhibited significant and numerous pitting events following the fast passivation step. This was especially true at early times before the breakdown rate decreased. The next highest number of events were exhibited for the slowly passivated Ni-Cr. These events were, however, short and had a low peak current density and as such, it had minimal charge accumulation in Figure 6.32b. Notably, the total event count was greater for slowly passivated Ni-Cr than rapidly passivated Ni-Cr-Mo due to the influence of Mo on stabilizing the passive film, but the damage extent was greater for the latter film. Slow film growth and air oxidation exhibited the best electrochemical stability. As explained earlier, they behaved similarly due to the impacts of dissolution on reducing the actual β of the “slow” step. Both the number and charge for metastable events were low, indicating minimal pitting damage occurred.

This general difference in slow versus fast passivation and the resulting film stability was investigated in more detail for Ni-Cr (Figure 6.33 and Figure 6.35) and Ni-Cr-Mo (Figure 6.37 and Figure 6.39). The results use every galvanostatic film growth rate from Table 6.1 which was previously used for in operando gSF-EIS passivation and Mott-Schottky analysis. Following even

relatively slow passivation at $1 \mu\text{A}/\text{cm}^2$, Ni-Cr exhibits substantial metastable pitting events and both the number and size of these events increases with i_{DC} (Figure 6.33). As suggested previously, the overall dissolution rate, i_{EC} , appears to increase with i_{DC} . Detailed analysis of individual pitting events is given in Figure 6.35 and suggests the same results as the overall look in Figure 6.33. In general, both the computed rate and charge of metastable pitting events appeared to increase with i_{DC} . Moderately fast passivation at $5 \mu\text{A}/\text{cm}^2$ notably exhibited numerous, albeit small, events at early times and therefore had a higher number and rate than $10 \mu\text{A}/\text{cm}^2$, but a smaller charge. At the higher rates, substantial pitting damage was incurred by the passive film and the base Ni-Cr metal. This is presumably caused by the harmful capture of Cr^{3+} solute onto Ni^{2+} in the film during rapid growth, as was previously demonstrated in 3DAPT images obtained after potentiostatic passivation in 0.1 M NaCl pH 4 (Figure 4.37). Unlike what has been theorized for Mo, this substitutional point defect appears to be ineffective at attracting the excess vacancies formed at high passivation rates.

The same analysis was applied to Ni-Cr-Mo following similar passivation (Figure 6.37) and at first glance, minor Mo additions clearly reduce both the number and size of metastable pitting events in comparison to the results on Ni-Cr (Figure 6.33). A similar effect of i_{DC} is apparent in the analysis of the cumulative number, rate, and charge of pitting events (Figure 6.39). There was a consistent increase in these parameters which are characteristic for metastable pitting as i_{DC} increased. The increases, however, were much less than what was observed previously for Ni-Cr in Figure 6.35. A comparison between the two most critical values, the number of events and the cumulative charge, for Ni-Cr and Ni-Cr-Mo after 10 ks is given in Figure 6.41. For uniquely Ni-Cr-Mo, the charge leveled off at high rates ($i_{DC} > 5 \mu\text{A}/\text{cm}^2$) until increasing significantly for the fastest rate, $100 \mu\text{A}/\text{cm}^2$. The charge for Ni-Cr, however, consistently increased with i_{DC} , suggesting that solute captured Mo facilitates repassivation and decreases the formation of large metastable pits. This is critical for fracture behavior, as large, repassivated pits act as stress concentrators and cracks can initiate at the walls of the corrosion site⁵⁶.

6.8 Discussion

6.8.1 Role of Solute Capture on Film Chemical Composition

The effects of passivation rate and solute capture on the chemical composition of passive films are clear in the results mentioned above. Increasing i_{DC} apparently resulted in increasing

concentrations of Ni^{2+} within the film on Ni-Cr (Figure 6.29). Notably, the principles of NSC dictate a certain limit: the bulk alloying concentration of Ni, 78 wt% or approximately 76 at%. The rapidly moving oxidation front, in this case, freezes the metal composition into the oxide. A similar phenomena has been evaluated for solidification, the massive, or rather diffusionless, transformation^{57,58}. Diffusion becomes possible, however, as i_{DC} decreases, resulting in preferential Ni^{2+} -enrichment, Cr^{3+} -enrichment, and the segregation of said cations to the film/electrolyte and metal/film interfaces, respectively.

The film composition becomes more complicated upon the inclusion of Mo into the bulk alloy. The strong oxidation of Ni^{2+} is not as evident in Figure 6.26 and Figure 6.28 due to the synergistic relationship between Mo and Cr and the favorable oxidation thermodynamics and kinetics of the latter^{36,59,60}. Instead, a similar fraction of Cr^{3+} is achieved for passivation of Ni-Cr-Mo at $50 \mu\text{A}/\text{cm}^2$ as is seen for Ni-Cr at $0.5 \mu\text{A}/\text{cm}^2$. Since the aforementioned limit of the bulk alloying content, 22 wt% or approximately 25 at% Cr, is exceeded at all the currents investigated, it can be reasoned that at higher applied i_{DC} values, the same strong Ni-enrichment could be achieved via the favorable kinetics of NiO oxidation^{24,61}. Notably, Mo was captured in the film around its alloying concentration, 6 wt% or approximately 3.5 at%, following rapid passivation (Figure 6.29). It also remained somewhat enriched at the surface. This has been shown in literature to occur via film dissolution and subsequent repassivation of Mo-oxides and other compounds at the film surface. Otherwise, as i_{DC} decreased, $\text{Mo}^{4,6+}$ enriched along with Cr^{3+} as favorable oxidation only occurs when the cations are adjacent.

Greater amounts of oxides (i.e. NiO and Cr_2O_3) were measured by XPS spectra fitting compared to their hydroxide counterparts (i.e. $\text{Ni}(\text{OH})_2$ and $\text{Cr}(\text{OH})_3$) following rapid passivation, especially for the spectra obtained at 90° . This suggests that at high values of i_{DC} , the kinetics for oxide hydration are sufficiently slow and hydroxides are only found at the surface, not throughout as occurs following passivation at $0.5 \mu\text{A}/\text{cm}^2$. Similar chemical, rather than molecular, distributions also occur as a result of solute capture and varying passivation rates. This is demonstrated in Figure 6.29, where a greater Ni^{2+} signal is detected at the grazing measurement angle, 45° , following slower passivation. The capability for diffusive processes to occur allows the cations to segregate and, upon reaching critical local concentrations, can result in the precipitation of a distinct phase of the appropriate oxide and/or hydroxide, eventually forming a true layer at

longer times¹⁸. Similar surface-enrichment and the existence of pseudo-layers following long passivation times and environmental exposures has been demonstrated for various commercial Ni-alloys with more complex bulk compositions^{39,40,62}.

6.8.2 Effect of Cr Versus Mo Capture

The major differences between the demonstrated behavior of Ni-Cr and Ni-Cr-Mo arise from the solute capture of Cr³⁺ in NiO rocksalt versus the capture of both Cr³⁺ and Mo^{4,6+} capture in the rocksalt and, for the latter, potential in local areas of corundum. This distinction is well-demonstrated using Mott-Schottky measurements of the passive films' defect densities and flat-band potentials (Figure 6.20 and Figure 6.22). Increasing i_{DC} appeared to make p-type behavior more favorable, especially at the potential of interest: +0.2 V_{SCE}. This comes as a result of excessive doping of the solute cations into the NiO solvent. However, this phenomenon also results in higher values of N_D and N_A . The concurrent decrease in E_{FB} , a parameter which suggests the film resistance to local breakdown⁶³⁻⁶⁵, confirms that this increasing defective nature of the films will have negative effects on the electrochemical performance of solute-captured oxides.

Ni-Cr-Mo consistently had lower concentrations of both n- and p-type point defects, but especially the latter. This is critical for considering the potential electrochemical of passive films, as donor metal cation vacancies such as V''_{Ni} and V'''_{Cr} have been theorized to form following chloride adsorption at the surface of passive films (Figure 4.7)⁵⁵. Thereafter, they are thought to diffuse to the metal/film interface, coalesce into voids, and eventually burst as pitting events⁶⁶. Greater amounts of Mo^{4,6+} were captured in the films when i_{DC} increased and as a result, there was no continuous variations observed, as occurred for Ni-Cr (Figure 6.20), in the measured defect densities or flat-band potentials up until 50 $\mu\text{A}/\text{cm}^2$. This significant effect suggest the effect of Mo capture is more significant than Cr capture. The major reduction in N_D for Ni-Cr-Mo has been thought to occur due to the interaction of the Mo substitutional dopants with the vacancies produced at the film surface by chloride interactions^{36,55}. Because of the lower valency for Cr dopants (Cr_{Ni}), this same effect is more minimal as there is a lower electrostatic attraction between the positively and negatively charged point defects. At a sufficiently high i_{DC} , the beneficial effect of Mo doping becomes minimal compared to the formation of a physically defective film, as demonstrated by the AFM measurements (Figure 6.23 and Figure 6.24).

6.8.3 Role of Solute Capture on Overall Electrochemical Performance

The aforementioned variations in chemical composition and effects of capturing Cr versus Mo cations results in the demonstrated differences in electrochemical performance. Excessive Cr doping during the passivation of Ni-Cr at increasing rates had no beneficial effect on resisting localized breakdown according to the subsequent Mott-Schottky analysis and metastable pitting results. The induction time, cumulative number, and size of pitting events all increased with i_{DC} (Figure 6.33 and Figure 6.35). It is worth noting that even for a relatively slow passivation rate, $1 \mu\text{A}/\text{cm}^2$, Ni-Cr underwent significant localized breakdown. Ni-Cr-Mo, however, consistently had smaller and less frequent metastable pitting events occur (Figure 6.41) due to the beneficial solute capture of $\text{Mo}^{4,6+}$ cations. As mentioned previously, no noticeable increases in the cumulative number and charge of the current spikes occurred at intermediate applied i_{DC} rates. The effect of Mo is clear, however, upon directly comparing these values measured for Ni-Cr-Mo passivated at $50 \mu\text{A}/\text{cm}^2$ to Ni-Cr at $1 \mu\text{A}/\text{cm}^2$. They are approximately the same, despite the nearly two orders magnitude difference in i_{DC} and, therefore, β (Table 6.1). The significant presence of Mo cations at these intermediate rates enables the resistance to localized breakdown, in spite of increasing defectiveness in the chemical and physical properties of the films.

There are also physical effects of rapid passivation, as shown by the topographies of the film surfaces (Figure 6.23 and Figure 6.24). Because the initial surfaces were not atomically smooth and had some micron-scale roughness following hand-polishing with $1 \mu\text{m}$ silica particles, oxides preferentially nucleated between the polishing marks. Slow passivation enabled a more continuous oxide to be formed and helped provide better overall protection to the base alloy. The rapid case, however, favored kinetics over thermodynamics, as discussed previously in much detail, and resulted in preferential nucleation of the oxides at these higher surfaces and chemical etching within the marks on Ni-Cr. The latter phenomenon results in the increase in the passivation efficiency, η , for the films grown at increasing i_{DC} values (Figure 6.17). The Ni-Cr-Mo surfaces appeared remarkably different. Because of Mo redeposition as Mo-oxide particles following film dissolution^{36,67}, the slowly grown film had a high RMS relative to the other conditions (Table 6.4). Rapid passivation at $50 \mu\text{A}/\text{cm}^2$, however, produced the smoothest passive film following galvanostatic oxidation. Minimal dissolution and redeposition of MoOx -particles has occurred despite the somewhat low η as there had not yet been sufficient time. Instead, the favorable

nucleation and growth of Cr-rich oxides within the scratches occurs and produces the smooth, conformal topography shown in Figure 6.24. This increased connectivity and protection of the film, in tandem with the discussed chemical and electronic considerations, generates a passive film with improved localized breakdown resistance.

6.9 Conclusions

The implications of nonequilibrium solute capture (NSC) and imposed passivation rates were investigated for Ni-22 Cr and Ni-22 Cr-6 Mo (wt%) during *in operando* galvanostatic conditions using SF-EIS in an acidic NaCl environment, coupled with subsequent *in situ* Mott-Schottky impedance scans, metastable pitting analysis, and *ex situ* AFM and AR-XPS characterization. Faster galvanostatic passivation was found to result in films representative of NSC with no cation segregation. However, there was a substantial decline in the electrochemical performance, characterized as an increase in the frequency and size of metastable pitting events, observed for Ni-Cr films. Beneficial solute capture of $\text{Mo}^{4,6+}$ cations, however, facilitated the inhibition of breakdown and the formation of conformal, Cr^{3+} -enriched films which provided for greater protection to the base alloy. Films grown slowly exhibited segregation of Cr^{3+} towards the metal/film interface whereas Ni^{2+} and $\text{Mo}^{4,6+}$ were preferentially located at the film/electrolyte interface. The relatively low defectiveness, characterized topographically and electronically, resulted in less frequent and damaging film breakdown occurring. In addition, greater concentrations of Cr^{3+} were measured. The occurrence of diffusive processes during this substantially longer passivation enabled the local accumulation of like cations and at longer times, aging of the films would likely produce local NiO and Cr_2O_3 phases that eventually coalesce into conformal layers.

6.10 References

1. Flemings, M. C. Thermodynamics of Solidification. in *Solidification Processing* 263–289 (McGraw-Hill, 1974).
2. Flemings, M. C. Plane front solidification of polyphase alloys. in *Solidification Processing* 93–131 (McGraw-Hill, 1974).
3. Baker, J. C. & Cahn, J. W. Thermodynamics of Solidification. in *Solidification* 23–57 (American Society for Metals, 1971).
4. Howe, J. M. *Interfaces in Materials: Atomic structure, thermodynamics and kinetics of solid-vapor, solid-liquid and solid-solid interfaces*. (Wiley-Interscience, 1997).
5. Frenkel, J. Note on a relation between the speed of crystallization and velocity. *Phys. Zeitschrift der Sowjetunion* **1**, 498–510 (1932).

6. Wilson, H. W. XX. On the velocity of solidification and viscosity of super-cooled liquids. *Philos. Mag.* **50**, 238–250 (1900).
7. Tiller, W. A., Jackson, K. A., Rutter, J. W. & Chalmers, B. The redistribution of solute atoms during the solidification of metals. *Acta Metall.* **1**, 428–437 (1953).
8. Mullins, W. W. & Sekerka, R. F. Stability of a planar interface during solidification of a dilute binary alloy. *J. Appl. Phys.* **35**, 444–451 (1964).
9. Peteves, S. D. & Abbaschian, R. Growth kinetics of solid-liquid Ga interfaces. *Metall. Trans. A* **22A**, 1259–1286 (1991).
10. Baker, J. C. & Cahn, J. W. Solute trapping by rapid solidification. *Acta Metall.* **17**, 575–578 (1969).
11. Jackson, K. A., Gilmer, G. H. & Leamy, H. J. Solute Trapping. in *Laser and Electron Beam Processing of Materials* (eds. White, C. W. & Peercy, P. S.) 104–110 (Academic Press, Inc., 1980).
12. Leamy, H. J., Rozgonyi, G. A., Sheng, T. T. & Celler, G. K. Periodic regrowth phenomena produced by laser annealing of ion- implanted silicon. *Appl. Phys. Lett.* **32**, 535–537 (1978).
13. Young, R. T. *et al.* Laser annealing of boron- implanted silicon. *Appl. Phys. Lett.* **32**, 139–141 (1978).
14. Narayan, J., Young, R. T. & White, C. W. A comparative study of laser and thermal annealing of boron- implanted silicon. *J. Appl. Phys.* **49**, 3912–3917 (1978).
15. Biloni, H. & Chalmers, B. Predendritic solidification. *Trans. Metall. Soc. AIME* **233**, 373 (1965).
16. Chernov, A. A. Excess impurity trapping during crystal growth. *Growth Cryst.* **3**, 35–39 (1962).
17. Aziz, M. J. Model for solute redistribution during rapid solidification. *J. Appl. Phys.* **53**, 1158–1168 (1982).
18. Yu, X. X. *et al.* Nonequilibrium Solute Capture in Passivating Oxide Films. *Phys. Rev. Lett.* **121**, 145701 (2018).
19. Cabrera, N. & Mott, N. F. Theory of the oxidation of metals. *Reports Prog. Phys.* **12**, 163–184 (1949).
20. Fehlner, F. P. & Mott, N. F. Low-temperature oxidation. *Oxid. Met.* **2**, 59–99 (1970).
21. Chao, C. Y., Lin, L. F. & Macdonald, D. D. A point defect model for anodic passive films I. Film growth kinetics. *J. Electrochem. Soc.* **128**, 1187–1194 (1981).
22. Seyeux, A., Maurice, V. & Marcus, P. Oxide Film Growth Kinetics on Metals and Alloys: I. Physical Model. *J. Electrochem. Soc.* **160**, C189–C196 (2013).
23. Van Santen, R. A. The Ostwald step rule. *J. Phys. Chem.* **88**, 5768–5769 (1984).
24. Lutton, K., Gusieva, K., Ott, N., Birbilis, N. & Scully, J. R. Understanding multi-element alloy passivation in acidic solutions using operando methods. *Electrochem. commun.* **80**, 44–47 (2017).
25. Lutton Cwalina, K. *et al.* In Operando Analysis of Passive Film Growth on Ni-Cr and Ni-Cr-Mo Alloys in Chloride Solutions. *J. Electrochem. Soc.* **166**, C3241–C3253 (2019).
26. Mrowec, S. & Grzesik, Z. Oxidation of nickel and transport properties of nickel oxide. *J. Phys. Chem. Solids* **65**, 1651–1657 (2004).
27. Inc., T. I. N. C. *The Corrosion Resistance of Nickel-Containing Alloys in Sulfuric Acid and Related Compounds.* (1983).

28. Rebak, R. B. & Crook, P. Influence of the Environment on the General Corrosion Rate of Alloy 22. in *American Society of Mechanical Engineers Pressure Vessels and Piping Division Conference* 1–8 (2004). doi:10.1115/PVP2004-2793
29. Liang, D., Rajput, P., Zegenhagen, J. & Zangari, G. Nanoscale Structuring in Au-Ni Films Grown by Electrochemical Underpotential Co-deposition. *ChemElectroChem* **1**, 787–792 (2014).
30. Liang, D., Shao, W. & Zangari, G. Selection of phase formation in electroplated Ag-Cu alloys. *J. Electrochem. Soc.* **163**, 40–48 (2016).
31. Takei, A. & Nii, K. The Growth Process of Oxide Layers in the Initial Stage of Oxidation of 80Ni-20Cr Alloy. *Trans. Japan Inst. Met.* **17**, 211–219 (1976).
32. Urquidi, M. & Macdonald, D. D. Solute-vacancy interaction model and the effect of minor alloying elements on the initiation of pitting corrosion. *J. Electrochem. Soc.* **132**, 555–558 (1985).
33. Bell, B. D. C., Murphy, S. T., Grimes, R. W. & Wenman, M. R. The effect of Nb on the corrosion and hydrogen pick-up of Zr alloys. *Acta Mater.* **132**, 425–431 (2017).
34. Couet, A., Motta, A. T. & Ambard, A. The coupled current charge compensation model for zirconium alloy fuel cladding oxidation: I. Parabolic oxidation of zirconium alloys. *Corros. Sci.* **100**, 73–84 (2015).
35. Hutchison, M. J. & Scully, J. R. Solute Capture and Doping of Al in Cu₂O: Corrosion, Tarnish Resistance, and Cation Release of High-Purity Cu-Al Alloys in Artificial Perspiration. *J. Electrochem. Soc.* **165**, C689–C702 (2018).
36. Lutton Cwalina, K., Demarest, C. R., Gerard, A. Y. & Scully, J. R. Revisiting the effects of molybdenum and tungsten alloying on corrosion behavior of nickel-chromium alloys in aqueous corrosion. *Curr. Opin. Solid State Mater. Sci.* (2019).
37. Nečas, D. & Klapetek, P. Gwyddion: An open-source software for SPM data analysis. *Cent. Eur. J. Phys.* **10**, 181–188 (2012).
38. Strohmeier, B. R. An ESCA method for determining the oxide thickness on aluminum alloys. *Surf. Interface Anal.* **15**, 51–56 (1990).
39. Lloyd, A. C., Noël, J. J., McIntyre, S. & Shoesmith, D. W. Cr, Mo and W alloying additions in Ni and their effect on passivity. *Electrochim. Acta* **49**, 3015–3027 (2004).
40. Lloyd, A. C., Noël, J. J., McIntyre, N. S. & Shoesmith, D. W. The open-circuit ennoblement of alloy C-22 and other Ni-Cr-Mo alloys. *JOM* **57**, 31–35 (2005).
41. Jakupi, P., Zagidulin, D., Noël, J. J. & Shoesmith, D. W. The impedance properties of the oxide film on the Ni-Cr-Mo Alloy-22 in neutral concentrated sodium chloride solution. *Electrochim. Acta* **56**, 6251–6259 (2011).
42. Biesinger, M. C. *et al.* Resolving surface chemical states in XPS analysis of first row transition metals, oxides and hydroxides: Cr, Mn, Fe, Co and Ni. *Appl. Surf. Sci.* **257**, 2717–2730 (2011).
43. Werfel, F. & Minni, E. Photoemission study of the electronic structure of Mo and Mo oxides. *J. Phys. C Solid State Phys.* **16**, 6091–6100 (1983).
44. Moulder, J. F., Stickle, W. F., Sobol, P. E. & Bomben, K. D. Handbook of X-ray Photoelectron Spectroscopy. 261 (1992).
45. Biesinger, M. C., Payne, B. P., Lau, L. W. M., Gerson, A. & Smart, R. S. C. X-ray photoelectron spectroscopic chemical state Quantification of mixed nickel metal, oxide and hydroxide systems. *Surf. Interface Anal.* **41**, 324–332 (2009).

46. Biesinger, M. C. *et al.* Quantitative chemical state XPS analysis of first row transition metals, oxides and hydroxides. *J. Phys. Conf. Ser.* **100**, 012025 (2008).
47. Baltrusaitis, J. *et al.* Generalized molybdenum oxide surface chemical state XPS determination via informed amorphous sample model. *Appl. Surf. Sci.* **326**, 151–161 (2015).
48. Lunt, T. T. Interactions Among Localized Corrosion Sites Investigated Through Experiments and Models. (University of Virginia, 2001). doi:10.16953/deusbed.74839
49. Wu, B., Scully, J. R., Hudson, J. L. & Mikhailov, A. S. Cooperative Stochastic Behavior in Localized Corrosion I. Model. *J. Electrochem. Soc.* **144**, 1614–1620 (1997).
50. Lunt, T. T., Pride, S. T., Scully, J. R., Hudson, J. L. & Mikhailov, A. S. Cooperative Stochastic Behavior in Localized Corrosion II. Experiments. *J. Electrochem. Soc.* **144**, 1620–1629 (1997).
51. Kehler, B. A. & Scully, J. R. Role of metastable pitting in crevices on crevice corrosion stabilization in Alloys 625 and 22. *Corrosion* **61**, 665–684 (2005).
52. Pistorius, P. C. & Burstein, G. T. Metastable Pitting Corrosion of Stainless Steel and the Transition to Stability. *Philos. Trans. R. Soc. A Math. Phys. Eng. Sci.* **341**, 531–559 (1992).
53. Frankel, G. S., Stockert, L., Hunkeler, F. & Boehni, H. Metastable Pitting of Stainless Steel. *Corrosion* **43**, 429–436 (1987).
54. Ter-Ovanesian, B., Mary, N. & Normand, B. Passivity Breakdown of Ni-Cr Alloys: From Anions Interactions to Stable Pits Growth. *J. Electrochem. Soc.* **163**, C410–C419 (2016).
55. Lin, L. F., Chao, C. Y. & Macdonald, D. D. A point defect model for anodic passive films II. Chemical breakdown and pit initiation. *J. Electrochem. Soc.* **128**, 1194–1198 (1981).
56. Mai, W. & Soghrati, S. A phase field model for simulating the stress corrosion cracking initiated from pits. *Corros. Sci.* **125**, 87–98 (2017).
57. Su, P. & Virkar, A. Y. Massive Transformation in Gd₂O₃-Bi₂O₃ Ceramics. *Journal of the American Ceramic Society* **79**, 371–380 (1996).
58. Virkar, A. V., Su, P. & Fung, K. Z. Massive Transformation in Bismuth Oxide-Based Ceramics. *Metall. Mater. Trans. A* **33A**, 2433–2443 (2002).
59. Samin, A. J. & Taylor, C. D. First-principles investigation of surface properties and adsorption of oxygen on Ni-22Cr and the role of molybdenum. *Corros. Sci.* **134**, 103–111 (2018).
60. Samin, A. J. & Taylor, C. D. A Combined Density Functional Theory and Monte Carlo Investigation of the Competitive Adsorption of Atomic Oxygen and Chlorine to the Ni (111) Surface. **165**, 302–309 (2018).
61. Lee, H. G., Lee, Y. M., Shin, H. S., Jung, C. H. & Hong, G. W. Epitaxial deposition of NiO film on a cube-textured Ni substrate by metal-organic chemical vapor deposition. *Met. Mater.* **6**, 565–570 (2000).
62. Ebrahimi, N., Biesinger, M. C., Shoesmith, D. W. & Noël, J. J. The influence of chromium and molybdenum on the repassivation of nickel-chromium-molybdenum alloys in saline solutions. *Surf. Interface Anal.* **49**, 1359–1363 (2017).
63. Gelderman, K., Lee, L. & Donne, S. W. Flat-Band Potential of a Semiconductor: Using the Mott–Schottky Equation. *J. Chem. Educ.* **84**, 685–688 (2007).
64. Cheng, Y. F. & Luo, J. L. Comparison of the pitting susceptibility and semiconducting properties of the passive films on carbon steel in chromate and bicarbonate solutions. *Appl. Surf. Sci.* **167**, 113–121 (2000).
65. Cheng, Y. F. & Luo, J. L. Electronic structure and pitting susceptibility of passive film on

- carbon steel. *Electrochim. Acta* **44**, 2947–2957 (1999).
66. Macdonald, D. D. Some personal adventures in passivity—A review of the point defect model for film growth. *Russ. J. Electrochem.* **48**, 235–258 (2012).
 67. Henderson, J. D., Li, X., Shoesmith, D. W., Noël, J. J. & Ogle, K. Molybdenum surface enrichment and release during transpassive dissolution of Ni-based alloys. *Corros. Sci.* **147**, 32–40 (2019).
 68. Kou, S. *Welding metallurgy*. (Wiley-Interscience, 2002).
 69. Spencer, P. J. A brief history of CALPHAD. *Calphad Comput. Coupling Phase Diagrams Thermochem.* **32**, 1–8 (2008).
 70. Cruchley, S., Evans, H. E., Taylor, M. P., Hardy, M. C. & Stekovic, S. Chromia layer growth on a Ni-based superalloy: Sub-parabolic kinetics and the role of titanium. *Corros. Sci.* **75**, (2013).

6.11 Tables

Table 6.1. Selected applied current densities and the corresponding passivation rate and β for the typically estimated $v_D = 10^{-6}$ nm/s obtained using Faraday's law and assuming 100% current efficiency

i_{DC} ($\mu\text{A}/\text{cm}^2$)	v_{eff} (nm/s)	β
0.5	2.5×10^{-4}	250
1	5.0×10^{-4}	500
5	2.5×10^{-3}	2,500
10	5.0×10^{-3}	5,000
50	2.5×10^{-2}	25,000
100	5.0×10^{-2}	50,000

Table 6.2. Air oxidation conditions used in Figure 6.12 to achieve films approximately 5 nm in thickness with the estimated oxide growth velocity, v_i , and corresponding β included to demonstrate the propensity for NSC

T, Δt	v_i (nm/s)	$\beta = v_i/v_D$
RT, 2 yr	7.9×10^{-8}	0.08
100 °C, 6 hr	2.2×10^{-4}	220
200 °C, 1 min	8.3×10^{-2}	8.3×10^4

Table 6.3. Comparison of the semiconductor electronic behavior for Ni-22 Cr and Ni-22 Cr-6Mo, wt%, measured following galvanostatic grown at slow ($0.5 \mu\text{A}/\text{cm}^2$) and fast ($50 \mu\text{A}/\text{cm}^2$) applied currents

Alloy	i_{DC} ($\mu\text{A}/\text{cm}^2$)	<i>n-type</i>		<i>p-type</i>	
		$N_D \times 10^{21}$ (cm^{-3})	E_{FB} (mV _{SCE})	$N_A \times 10^{21}$ (cm^{-3})	E_{FB} (mV _{SCE})
Ni-22 Cr	0.5	5.7	-982	6.0	511
	50	69.4	-2780	15.1	312
Ni-22 Cr-6 Mo	0.5	3.9	-670	3.4	581
	50	5.6	-961	3.2	348

Table 6.4. Computed RMS from AFM topography images of passivated Ni-22 Cr and Ni-22 Cr-6 Mo, wt%, surface, as indicated in Figure 6.23 for various passivation rates

Rate	Ni-22 Cr	Ni-22 Cr-6 Mo
Slow	4.7 nm	5.0 nm
Fast	5.9 nm	3.1 nm

6.12 Figures

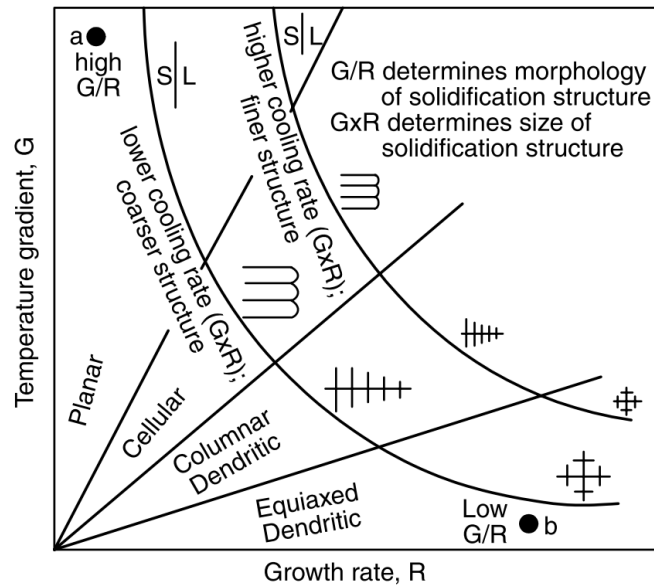


Figure 6.1. Schematic of the influence of the temperature gradient, G , and growth rate, R , on the resulting microstructure following L-S transformation of a metal⁶⁸

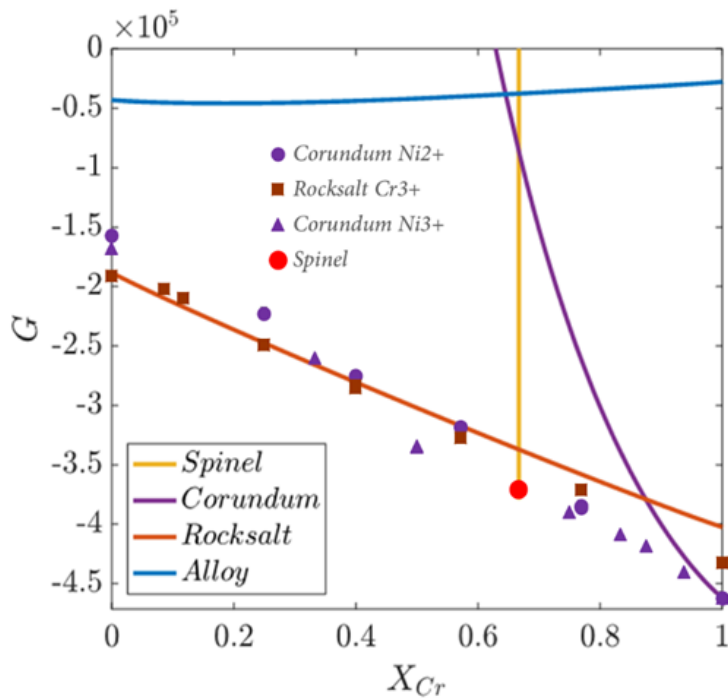


Figure 6.2. Plot of the free energy for the different possible crystallographic phases in J/mol as a function of Cr composition assuming that the valences are always Ni^{2+} and Cr^{3+} with the oxygen content adjusted to achieve valence neutrality as appropriate. Points are from DFT calculations and lines are from a thermodynamic database, both computed using an atmosphere of 700°C and $\log(p\text{O}_2) = -1.56$.¹⁸

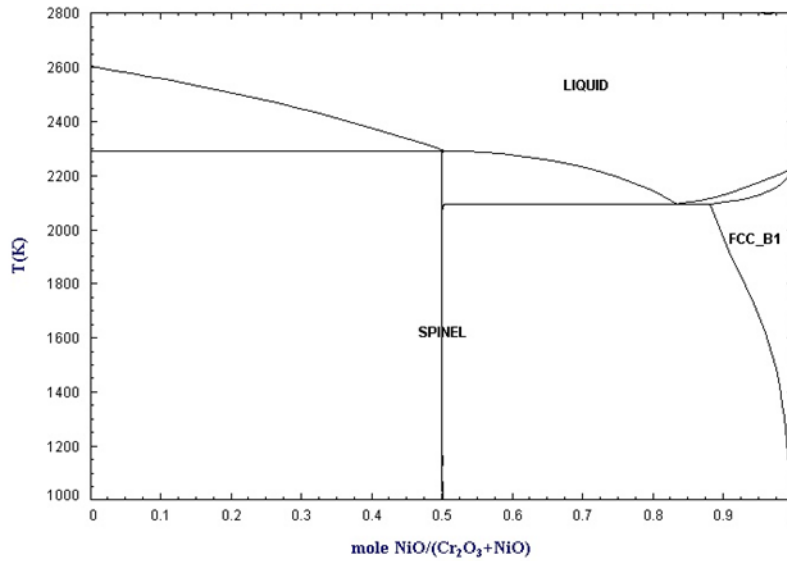


Figure 6.3. Sample phase diagram of Cr₂O₃-NiO computed using fundamental thermodynamics and CALPHAD software⁶⁹

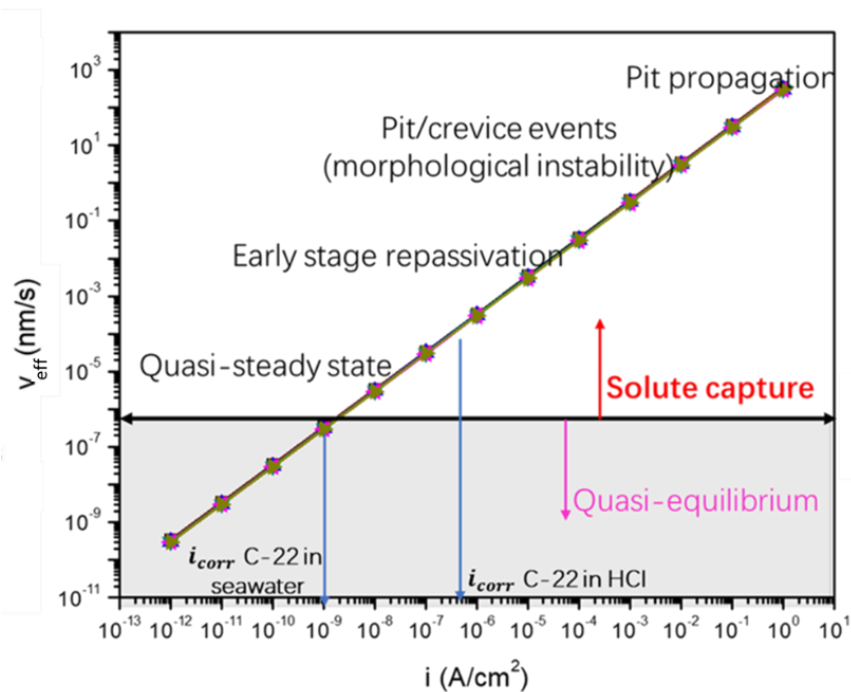


Figure 6.4. Relationship between the measurable electrochemical rate, i , and the effective velocity, v_{eff} , of various electrochemical phenomena of various length scales from thin film dissolution at steady-state, i_{corr} , to the accelerated dissolution found during the propagation of corrosion pits. Based on an estimated v_D of $10^{-6} \frac{nm}{s}$, NSC is predicted to occur for the majority of electrochemical processes due to the rapidly moving oxide interfaces.¹⁸

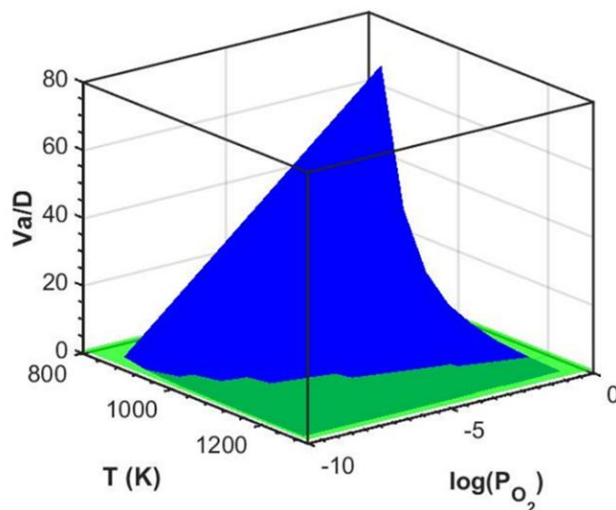


Figure 6.5. Plot of the kinetic conditions for solute capture during oxidation using kinetics based upon literature diffusion constants and reaction rates as a function of exposure temperature and pO_2 in atmospheres where $l_{ox} = 5$ nm and $a = 1$ nm is assumed.

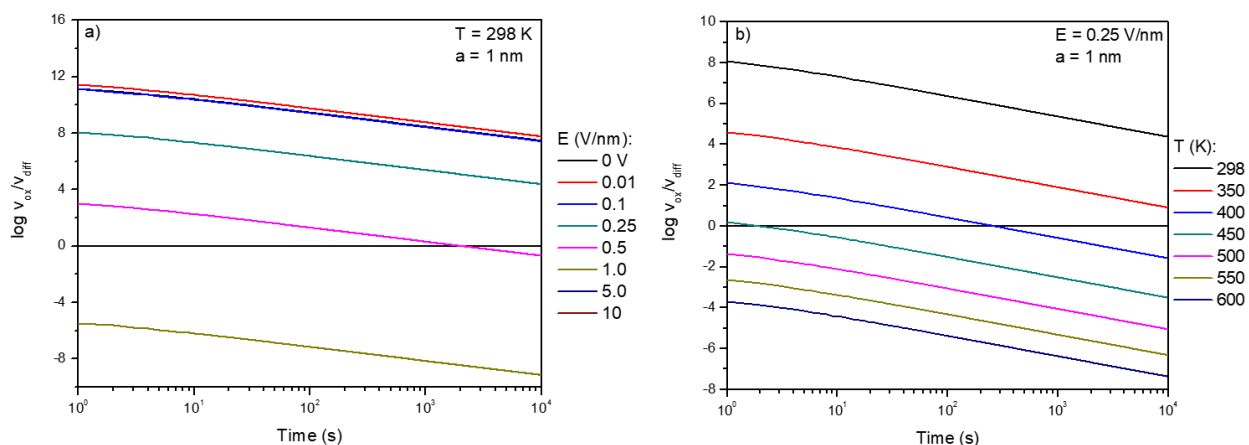


Figure 6.6. Simulation of the oxidation and diffusion velocity ratios for a) various applied electric field strengths at room temperature and b) various solution temperatures at a constant field strength assuming $a = 1$ nm where $\log \frac{v_{eff}}{v_d} > 0$ indicates NSC as $\beta > 1$

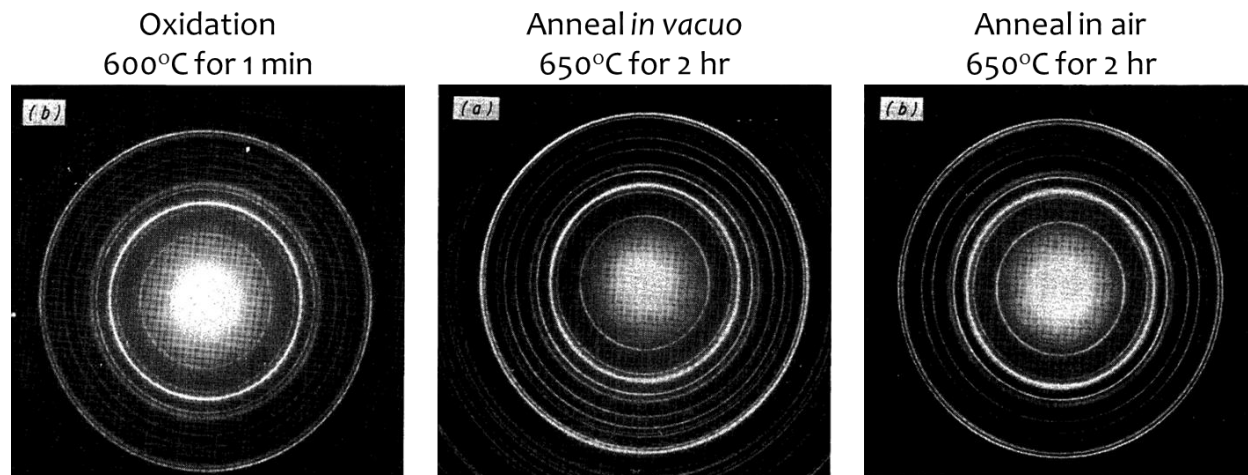


Figure 6.7. TEM diffraction patterns of Ni-20% Cr, wt%, oxidized in dry air for 1 min at 600°C (left) and subsequent annealing steps in either vacuum at 650°C for 2 hr (center) or in air for 650°C for 2 hr³¹

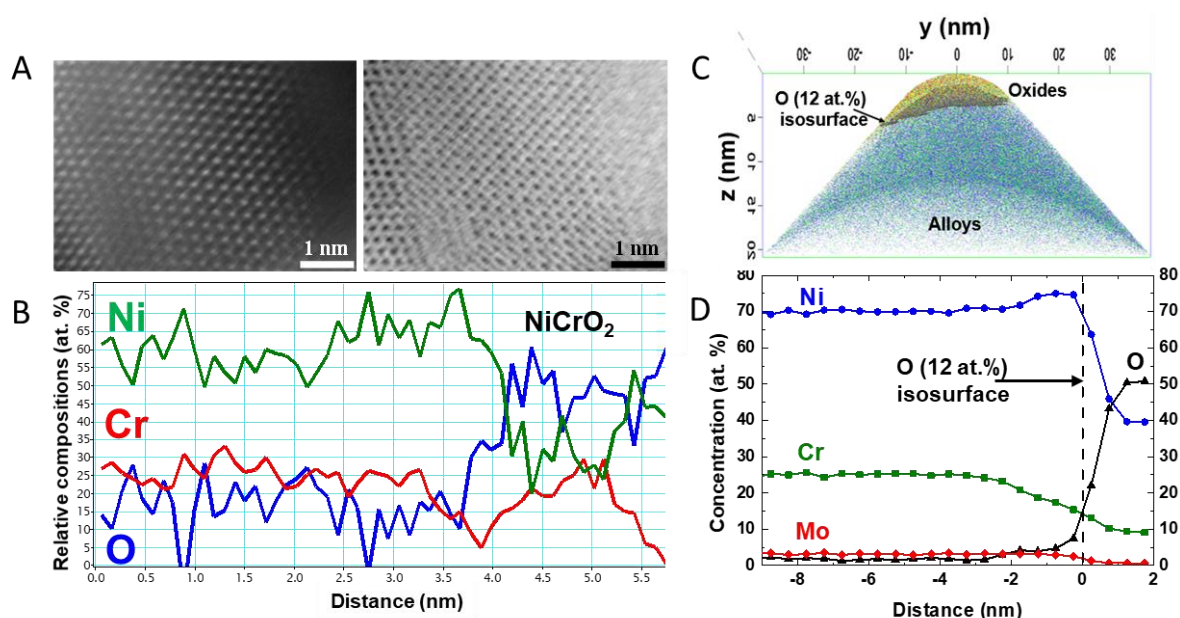


Figure 6.8. Chemical data for the oxide on Ni-22% Cr-6% Mo, wt%, chemically oxidized in 0.1 M Na_2SO_4 pH 4 + $\text{K}_2\text{S}_2\text{O}_8$ ($V_{\text{OCP}} = +0.2 V_{\text{SCE}}$) for 10 ks. A) High-angle annular dark field (left) and bright field (right) images with b) EELS line scan composition profile. C) 3DAPT tomography with a 12 at.% O isosurface and b) a compositional line scan corrected for the oxygen detection efficiency.¹⁸ The 3DAPT results (c,d) were previously shown in Figure 3.30.

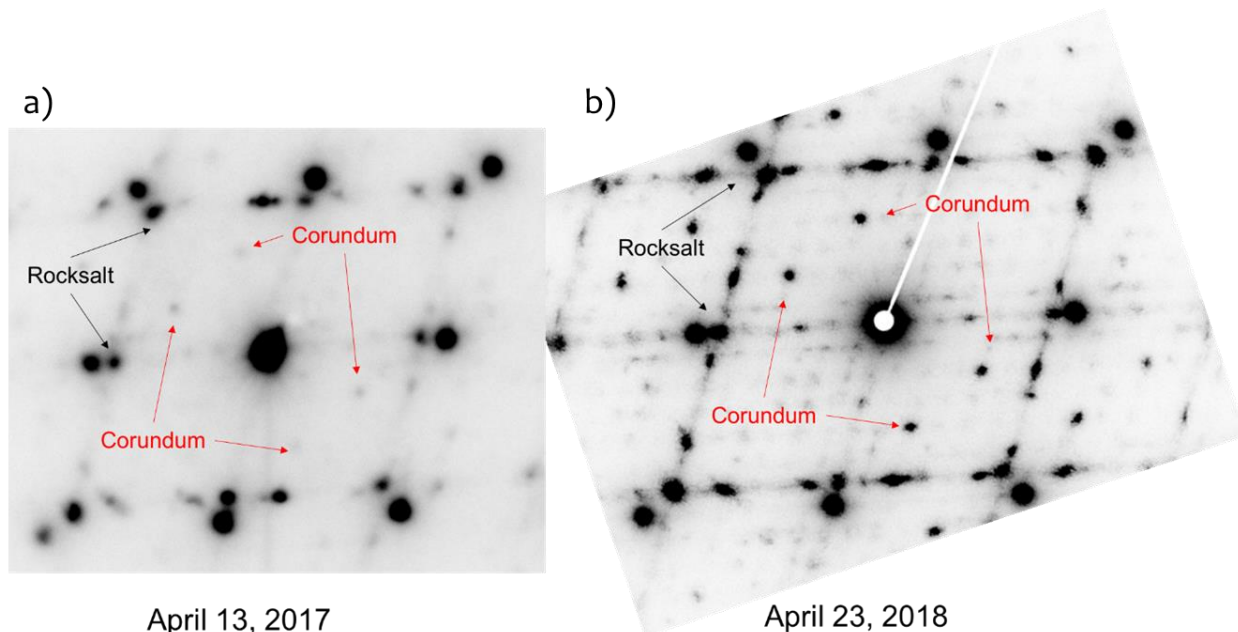


Figure 6.9. TEM diffraction patterns of the metal/oxide interface of Ni-22%Cr-6% Mo, wt%, initially oxidized at 800°C for 24 hr in air with two fresh TEM samples prepared a year apart¹⁸

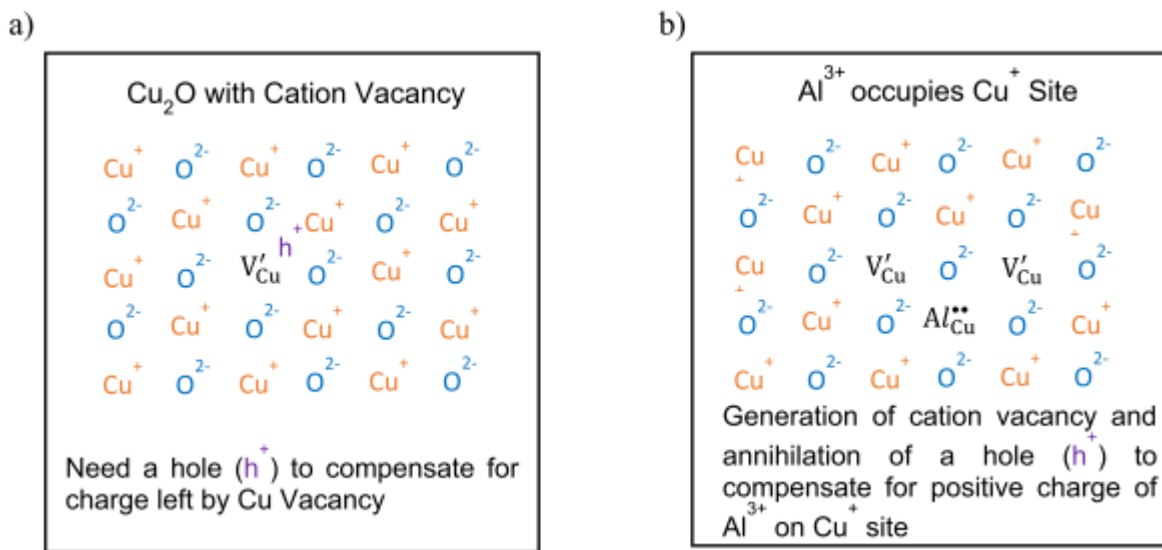


Figure 6.10. Schematic illustration of Al-doping effects on the equilibrium defect chemistry cuprite (Cu₂O) electronic properties for a) intrinsic defects compared to b) Al-doped³⁵

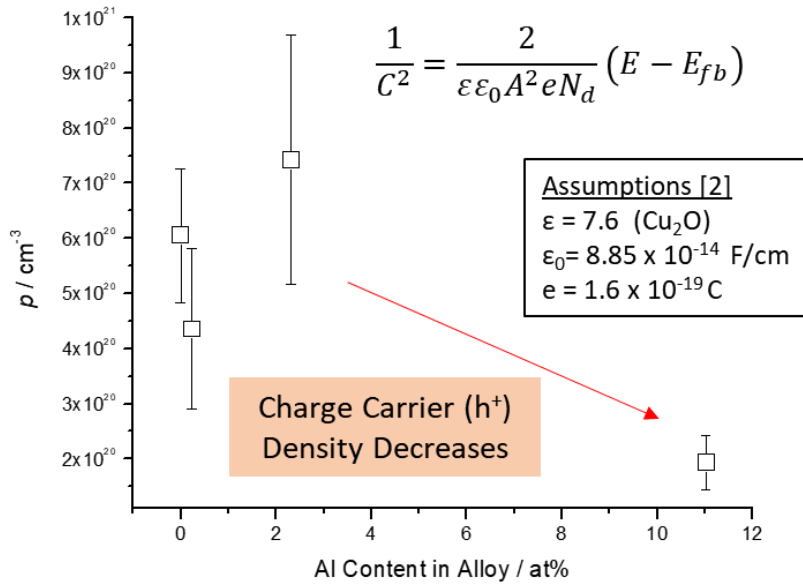


Figure 6.11. Approximate point defect carrier densities computed using Mott-Schottky analysis of the capacitive impedance behavior versus potential for cuprous (Cu_2O) passive films on Cu and Cu-Al alloys formed via NSC at open circuit in artificial perspiration solution³⁵

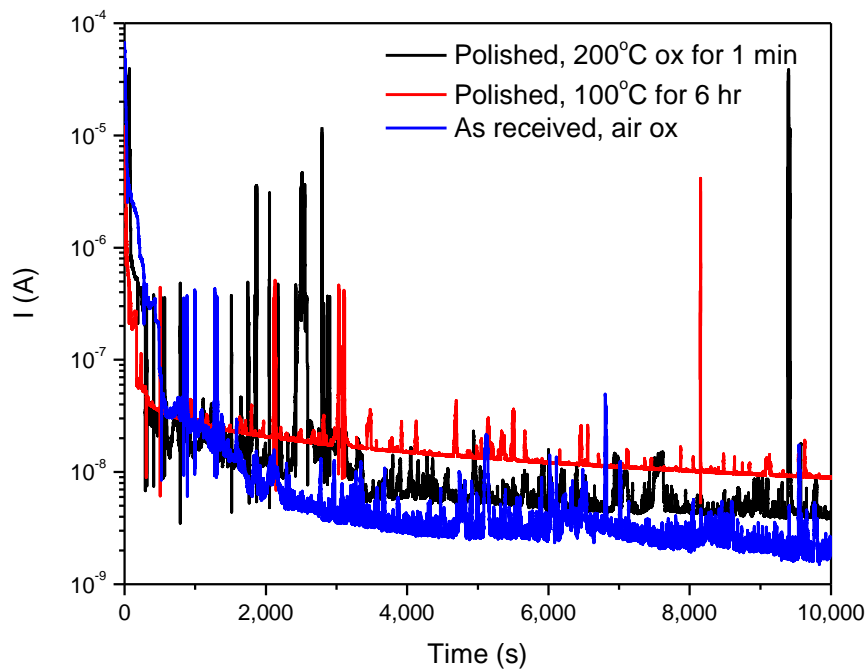


Figure 6.12. Electrochemical breakdown in 0.1 M NaCl pH 4 of oxide scales formed in air on Ni-22 Cr, wt%, following exposure at room temperature air for 2 yr and heating at 100 and 200°C following polishing to 1200 grit using SiC papers. The oxidation times were selected to produce a similar oxide thickness (~ 5 nm)⁷⁰. While the areas were not the exact same, they were similar enough so that the absolute current, I , for each sample can be compared relative to each other.

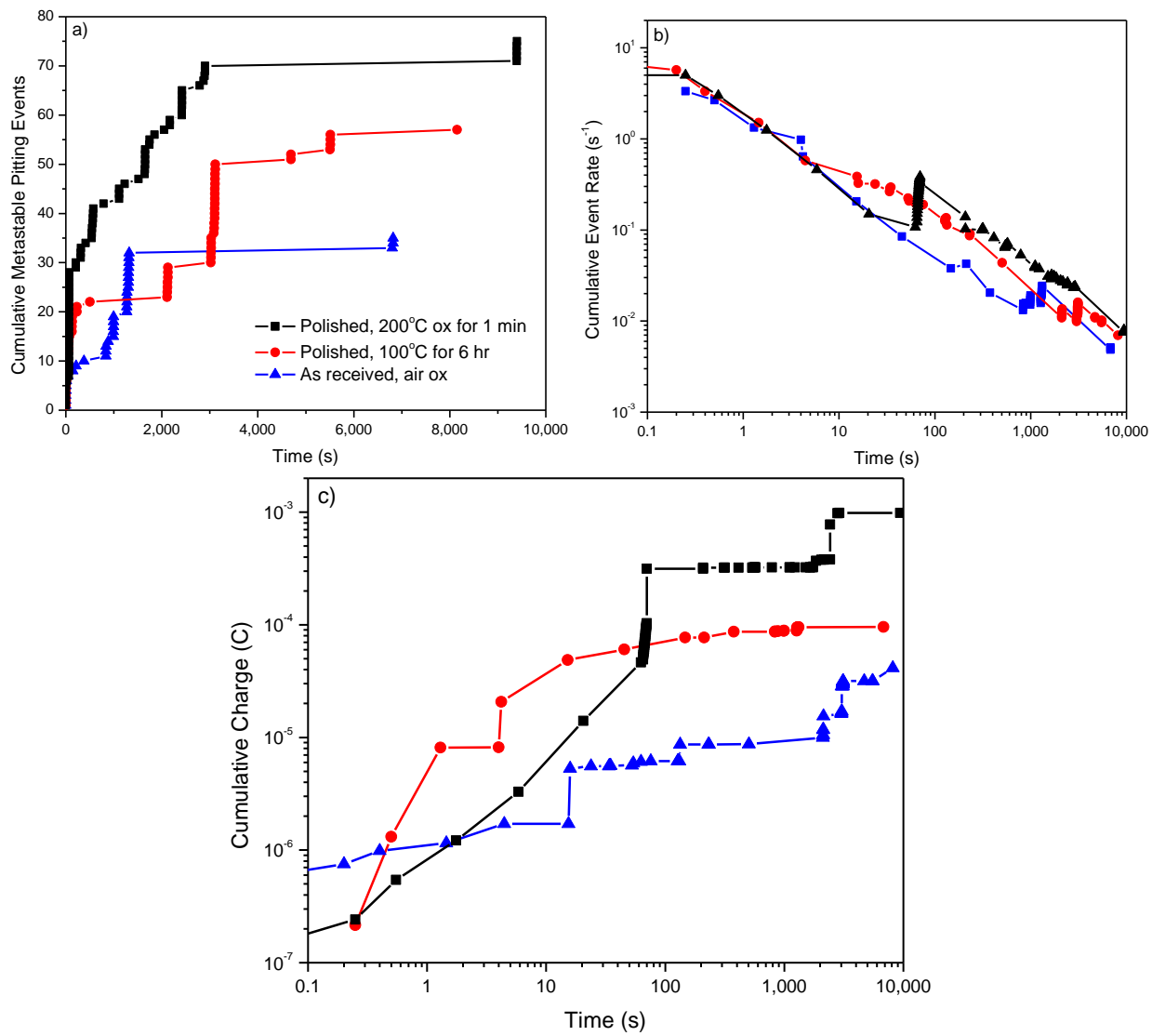


Figure 6.13. Comparison between the cumulative a) number, b) rate, and c) charge of metastable pitting events in deaerated 0.1 M NaCl pH 4 following air, 100 °C (6 hr), and 200 °C (1 min) oxidation of Ni-22 Cr, wt%, (Figure 6.12)

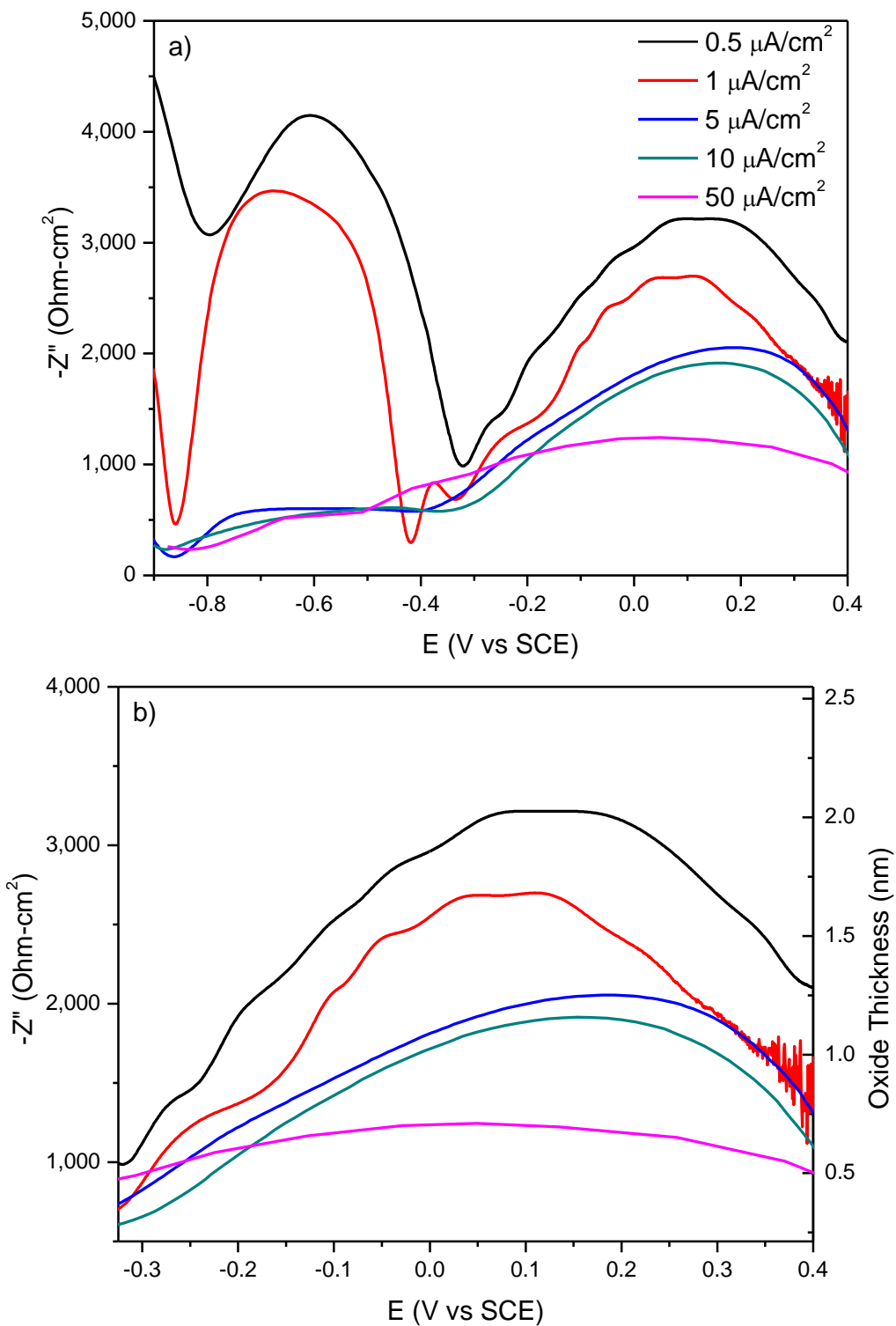


Figure 6.14. SF-EIS measurements of film thickening and thinning during galvanostatic passivation of Ni-22 Cr-6 Mo, wt%, at varying applied rates in 0.1 M NaCl pH 4. The results for the a) entire potential range and b) passive region only are indicated.

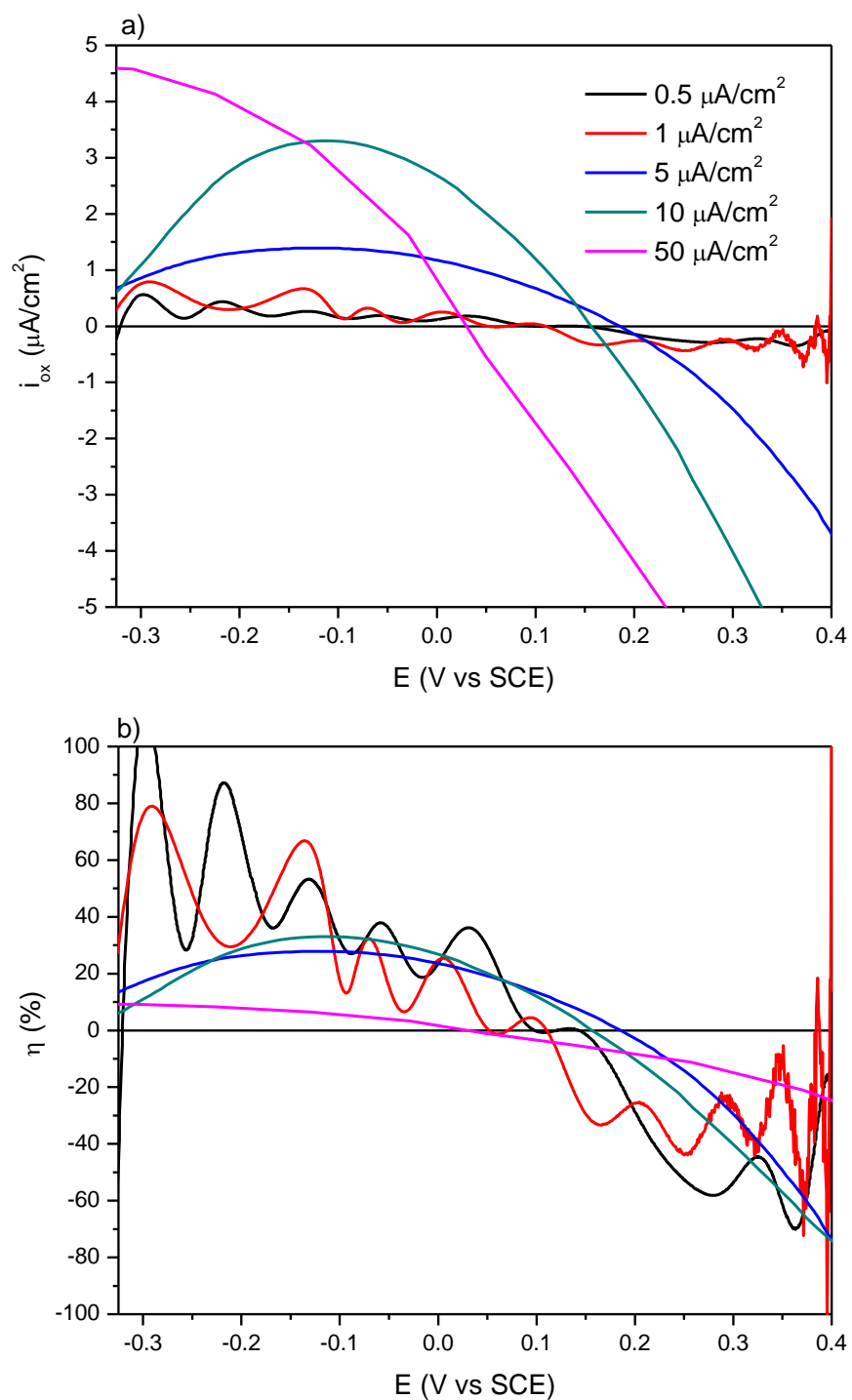


Figure 6.15. Analysis of the a) oxidation current density, i_{ox} , and b) efficiency, η , for galvanostatic passivation within the passive region for Ni-22Cr-6 Mo, wt%, at varying rates in 0.1 M NaCl pH 4

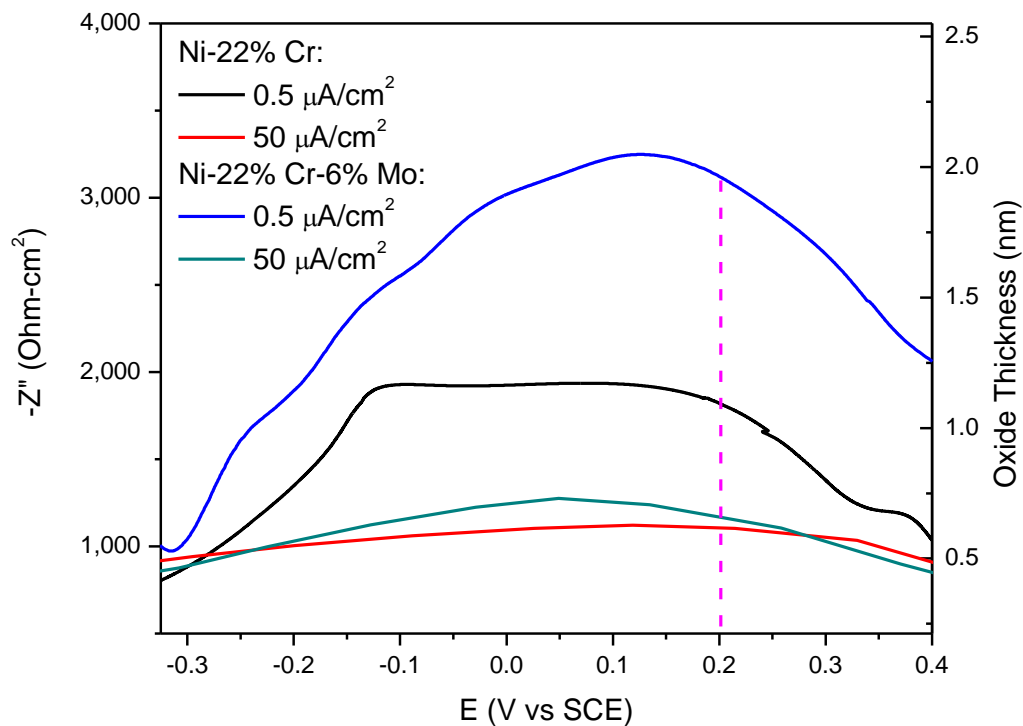


Figure 6.16. Galvanostatic SF-EIS measurements at 1 Hz during the passivation at slow ($0.5 \mu\text{A}/\text{cm}^2$) and fast ($50 \mu\text{A}/\text{cm}^2$) rates of Ni-22 Cr and Ni-22Cr-6 Mo, wt%, in 0.1 M NaCl pH 4, shown for the passive region only

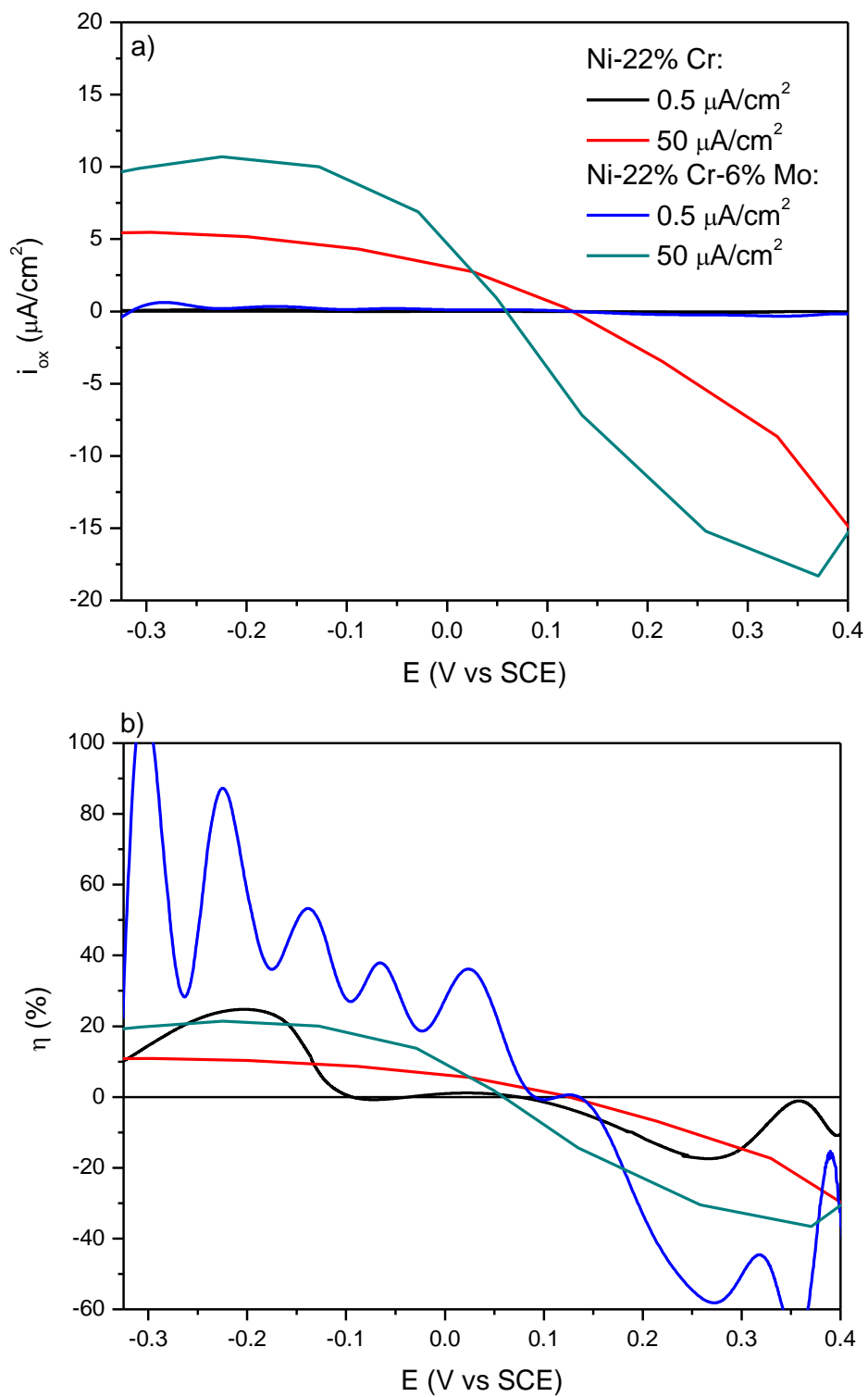


Figure 6.17. Analysis of the a) oxidation current density, i_{ox} , and b) efficiency, η , for galvanostatic passivation at slow ($0.5 \mu\text{A}/\text{cm}^2$) and fast ($50 \mu\text{A}/\text{cm}^2$) rates within the passive region of Ni-22 Cr and Ni-22 Cr-6 Mo, wt%, in 0.1 M NaCl pH 4

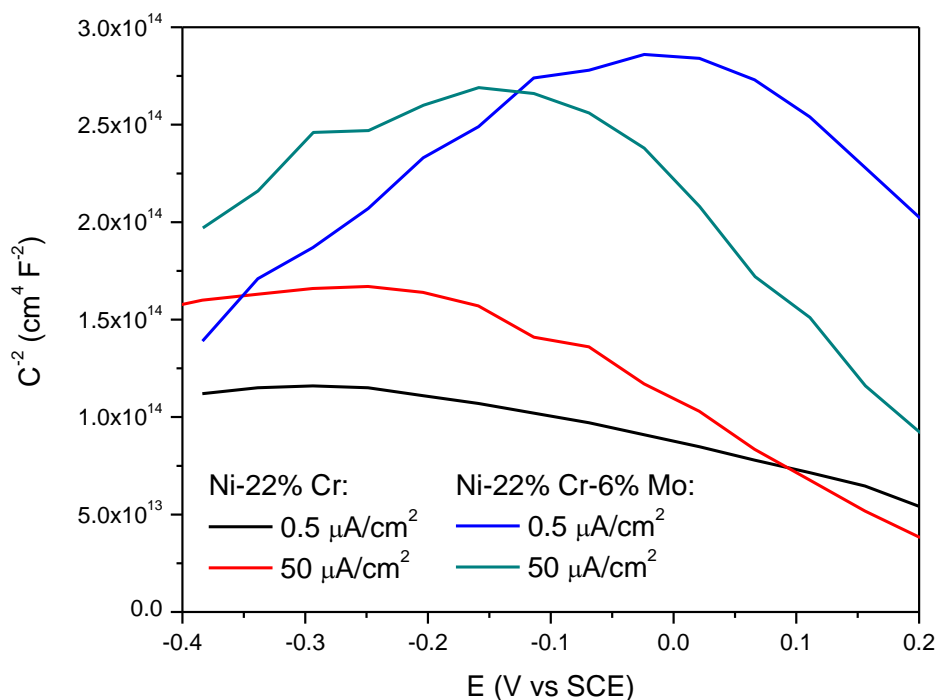


Figure 6.18. Mott-Schottky impedance sweeps at 1,000 Hz of Ni-22 Cr and Ni-22 Cr-6 Mo, wt%, following fast and slow galvanostatic passivation (Figure 6.16) in 0.1 M NaCl pH 4

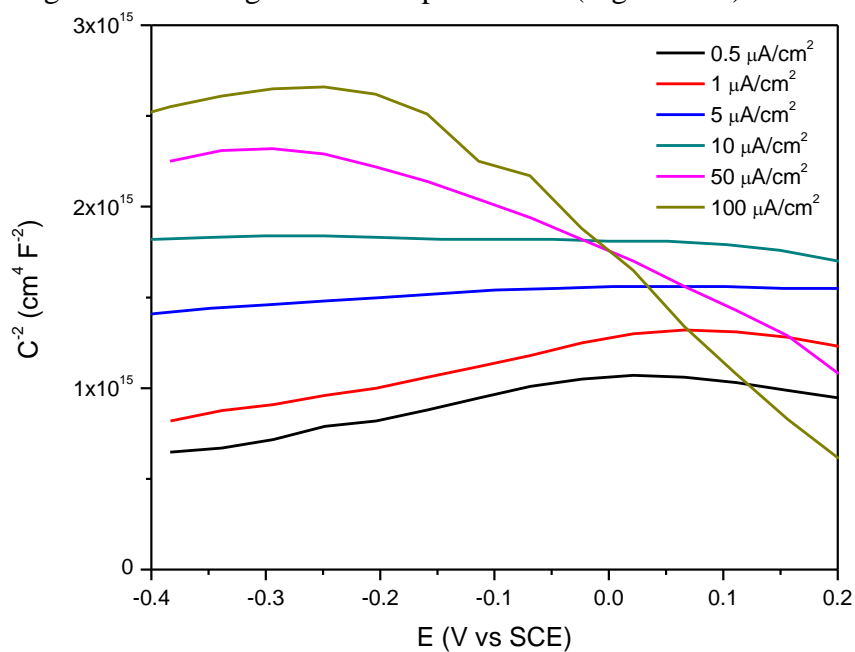


Figure 6.19. Mott-Schottky impedance sweeps at 1,000 Hz of Ni-22 Cr Mo, wt%, following passivation at varying galvanostatic rates (Figure 6.14) up to +0.2 V_{SCE} in 0.1 M NaCl pH 4

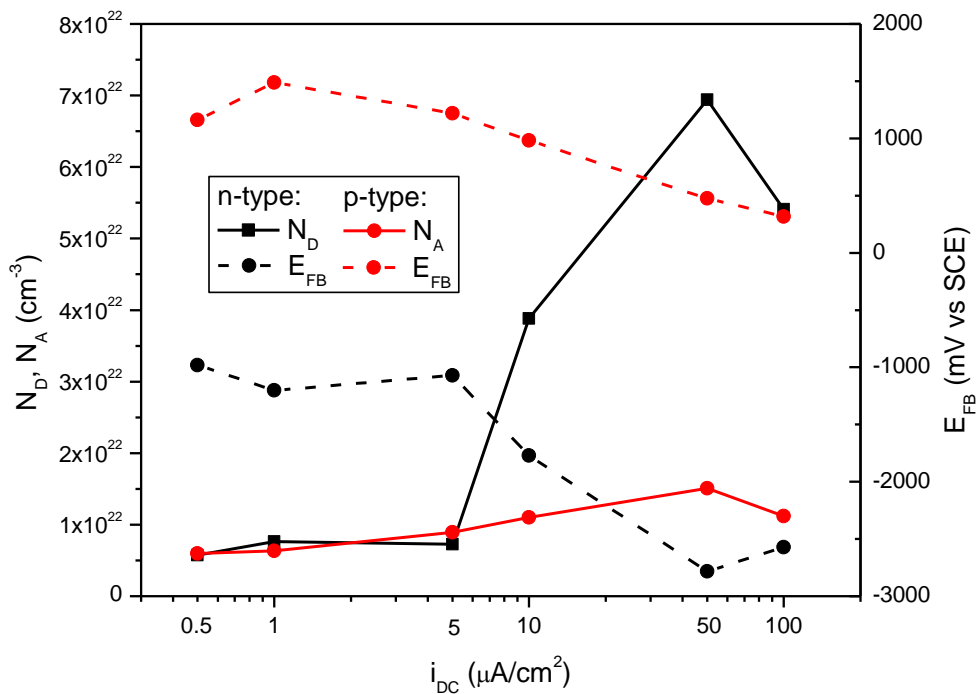


Figure 6.20. Mott-Schottky analysis of the electronic character of passive films on Ni-22 Cr, wt%, formed at varying applied galvanostatic rates in 0.1 M NaCl H 4 (Figure 6.21)

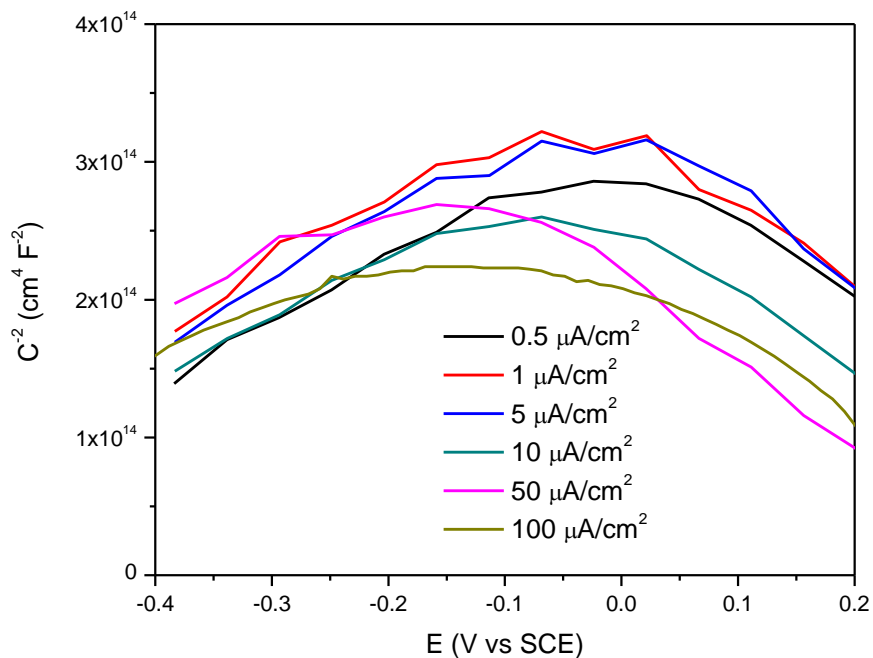


Figure 6.21. Mott-Schottky impedance sweeps at 1,000 Hz of Ni-22 Cr-6 Mo, wt%, following passivation at varying galvanostatic rates (Figure 6.14) up to +0.2 V_{SCE} in 0.1 M NaCl pH 4

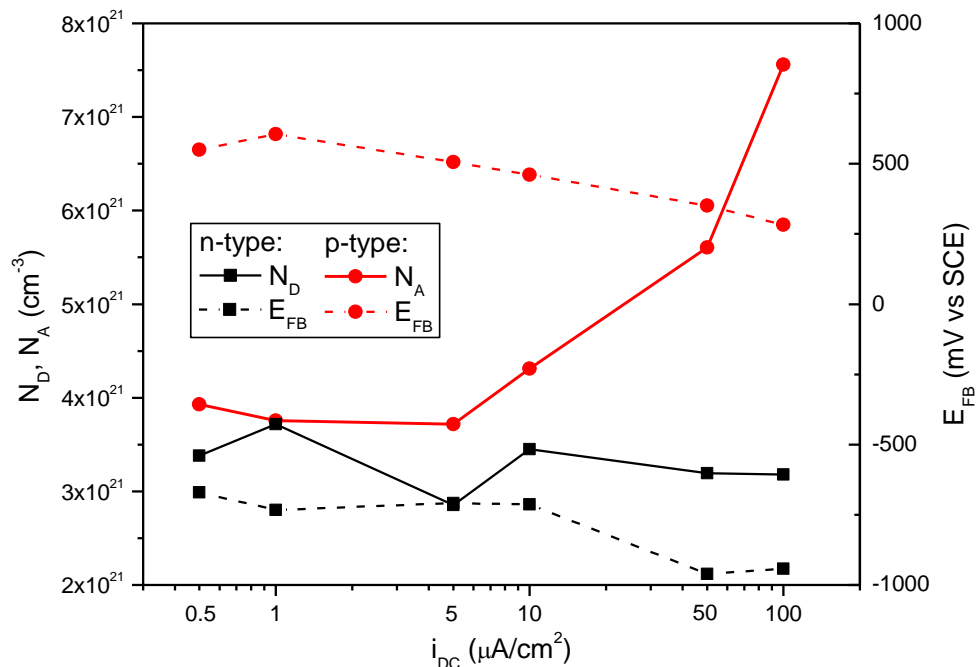


Figure 6.22. Mott-Schottky analysis of the electronic properties of passive films on Ni-22 Cr-6 Mo, wt%, formed at varying applied galvanostatic rates in 0.1 M NaCl H 4 (Figure 6.21)

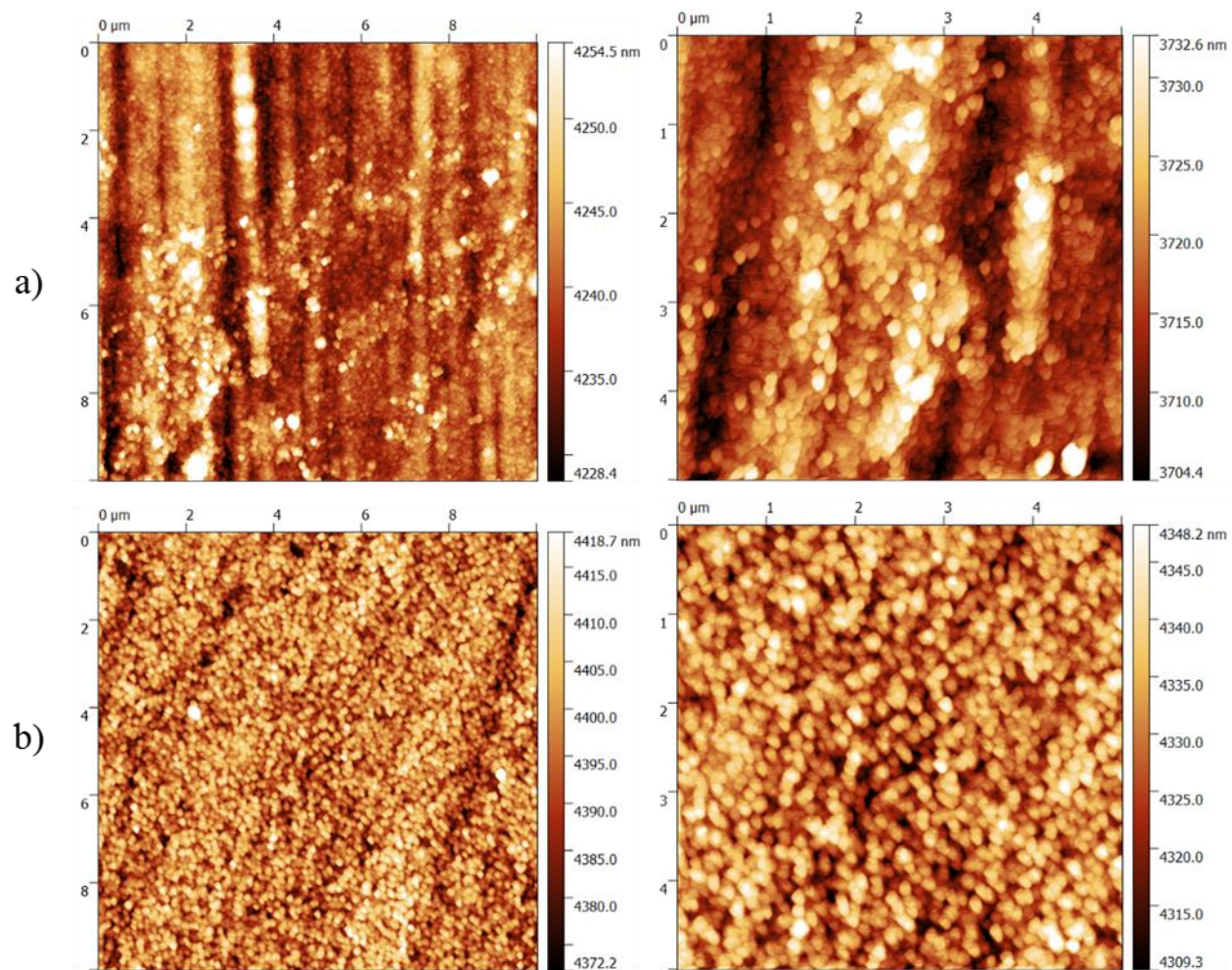


Figure 6.23. Measured AFM topography images for Ni-22 Cr, wt%, immediately following a) fast ($i_{app} = 50 \mu\text{A}/\text{cm}^2$) and b) slow passivation ($i_{app} = 0.5 \mu\text{A}/\text{cm}^2$) in 0.1 M NaCl pH 4

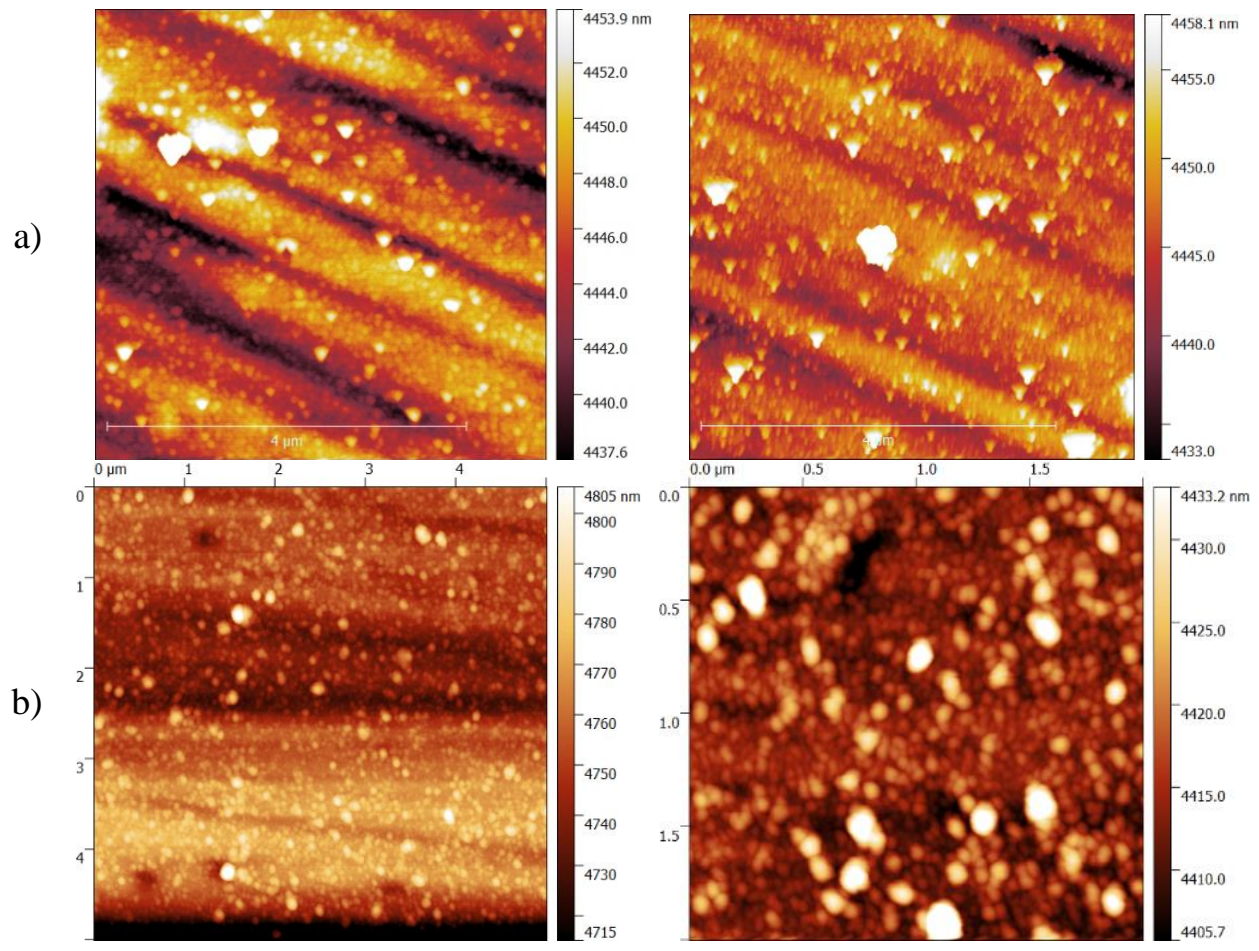


Figure 6.24. Measured AFM topography images for Ni-22 Cr-6 Mo, wt%, immediately following a) fast ($i_{app} = 50 \mu\text{A}/\text{cm}^2$) and b) slow passivation ($i_{app} = 0.5 \mu\text{A}/\text{cm}^2$) in 0.1 M NaCl pH 4

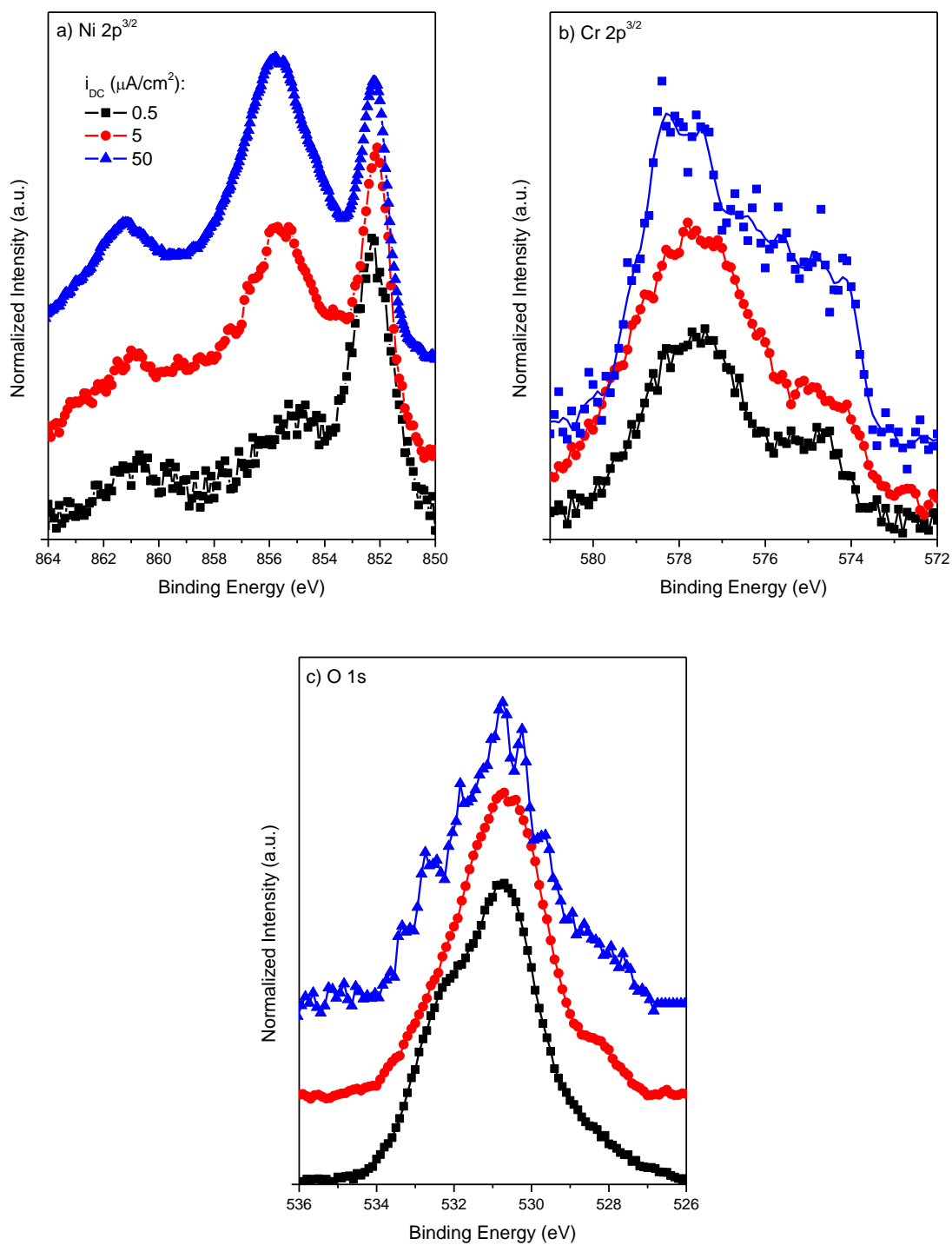


Figure 6.25. a) Ni $2p^{3/2}$, b) Cr $2p^{3/2}$, and c) O $1s$ peaks obtained at 90° and normalized to the metal peaks for Ni-22 Cr, wt%, passivated at 0.5, 5, and $50 \mu\text{A}/\text{cm}^2$ until $+0.2 \text{ V}_{\text{SCE}}$ was reached in 0.1 M NaCl pH 4

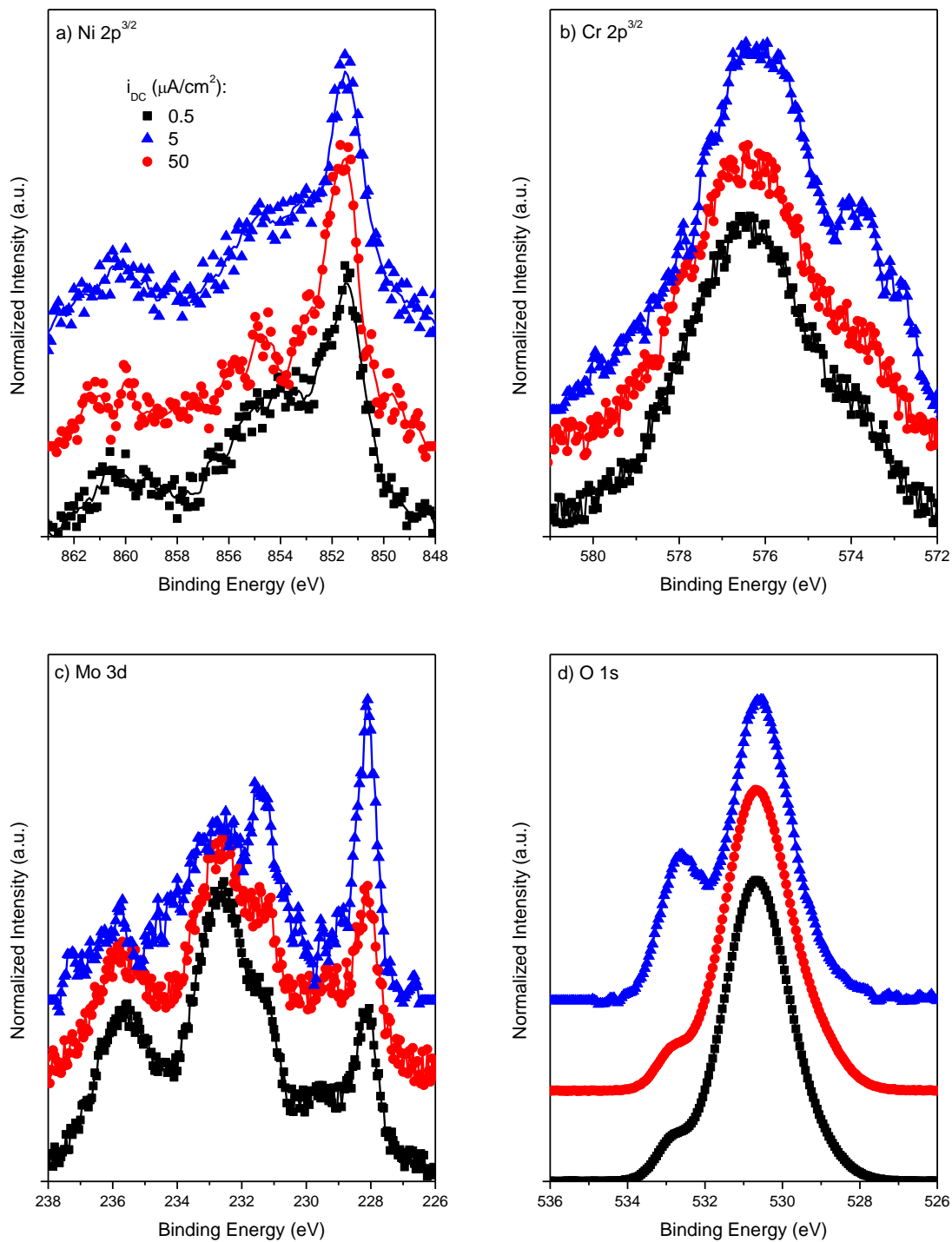


Figure 6.26. a) Ni $2p^{3/2}$, b) Cr $2p^{3/2}$, c) Mo 3d, and d) O 1s peaks obtained at 90° and normalized to the metal peaks for Ni-22 Cr-6 Mo, wt%, passivated at 0.5, 5, and $50 \mu\text{A}/\text{cm}^2$ until $+0.2 \text{ V}_{\text{SCE}}$ was reached in 0.1 M NaCl pH 4

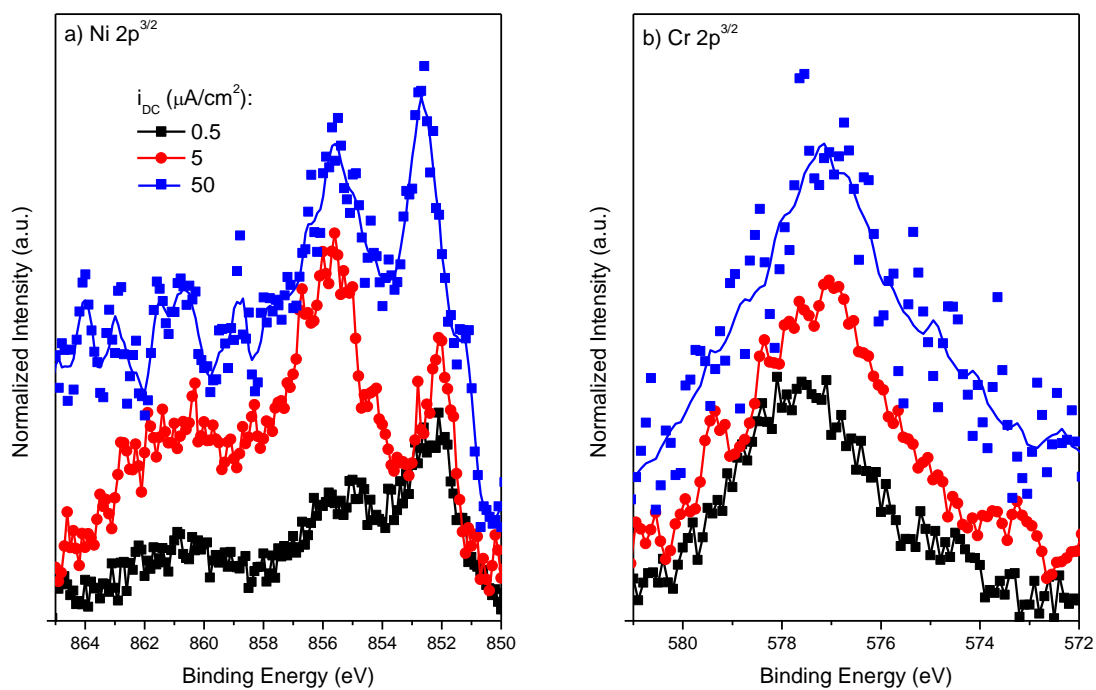


Figure 6.27. a) Ni $2p^{3/2}$ and b) Cr $2p^{3/2}$ peaks normalized to the metal peaks for Ni-22 Cr-6 Mo, wt%, passivated at 0.5, 5, and 50 $\mu\text{A}/\text{cm}^2$ until +0.2 V_{SCE} was reached in 0.1 M NaCl pH 4 measured at 45° . The ratio of the oxide areas for these measurements to those at 90° (Figure 6.25) are included for reference.

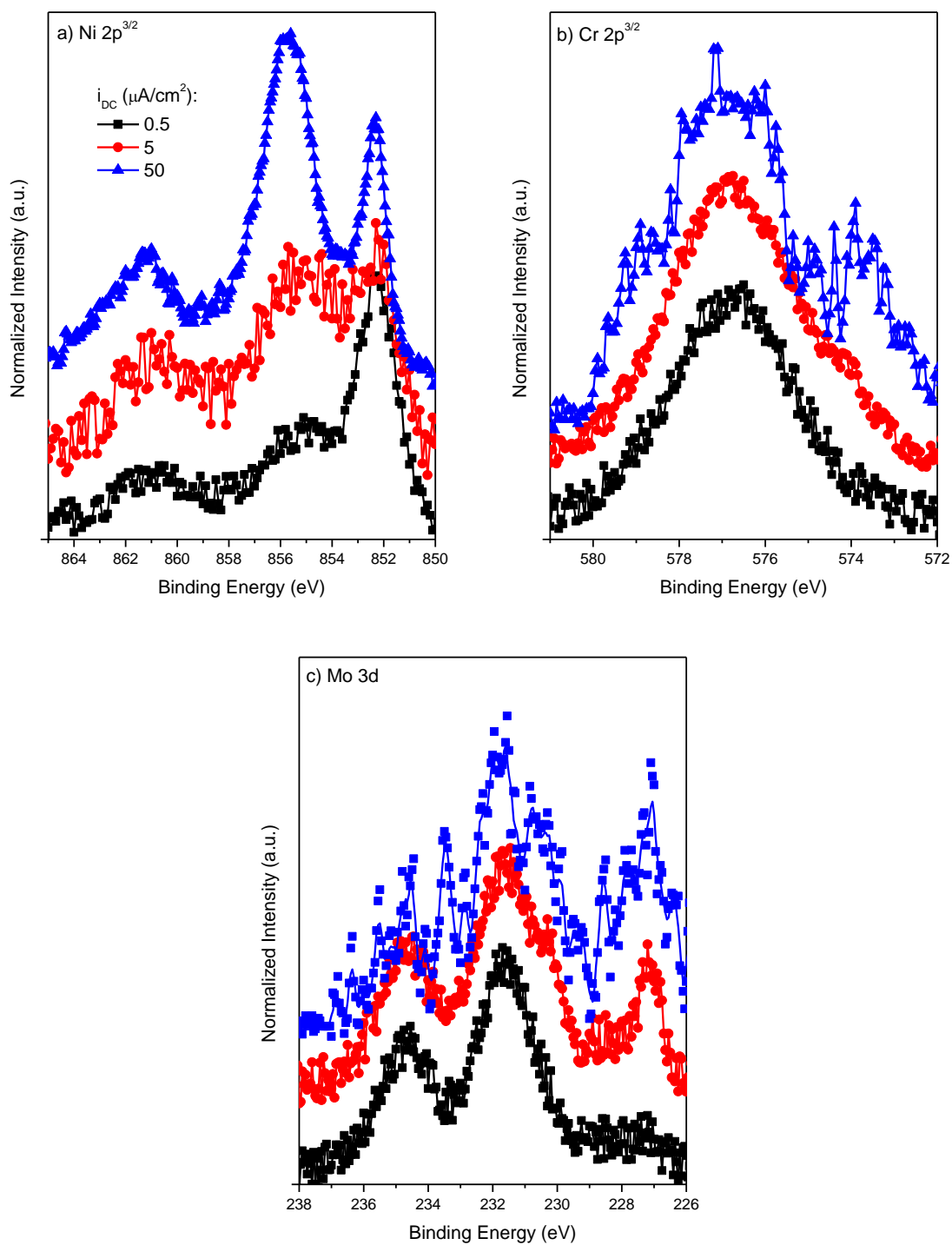


Figure 6.28. a) Ni $2p^{3/2}$, b) Cr $2p^{3/2}$, and c) Mo 3d peaks normalized to the metal peaks for Ni-22 Cr-6 Mo, wt%, passivated at 0.5, 5, and 50 $\mu\text{A}/\text{cm}^2$ until +0.2 V_{SCE} was reached in 0.1 M NaCl pH 4 measured at 45°. The ratio of the oxide areas for these measurements to those at 90° (Figure 6.26) are included for reference.

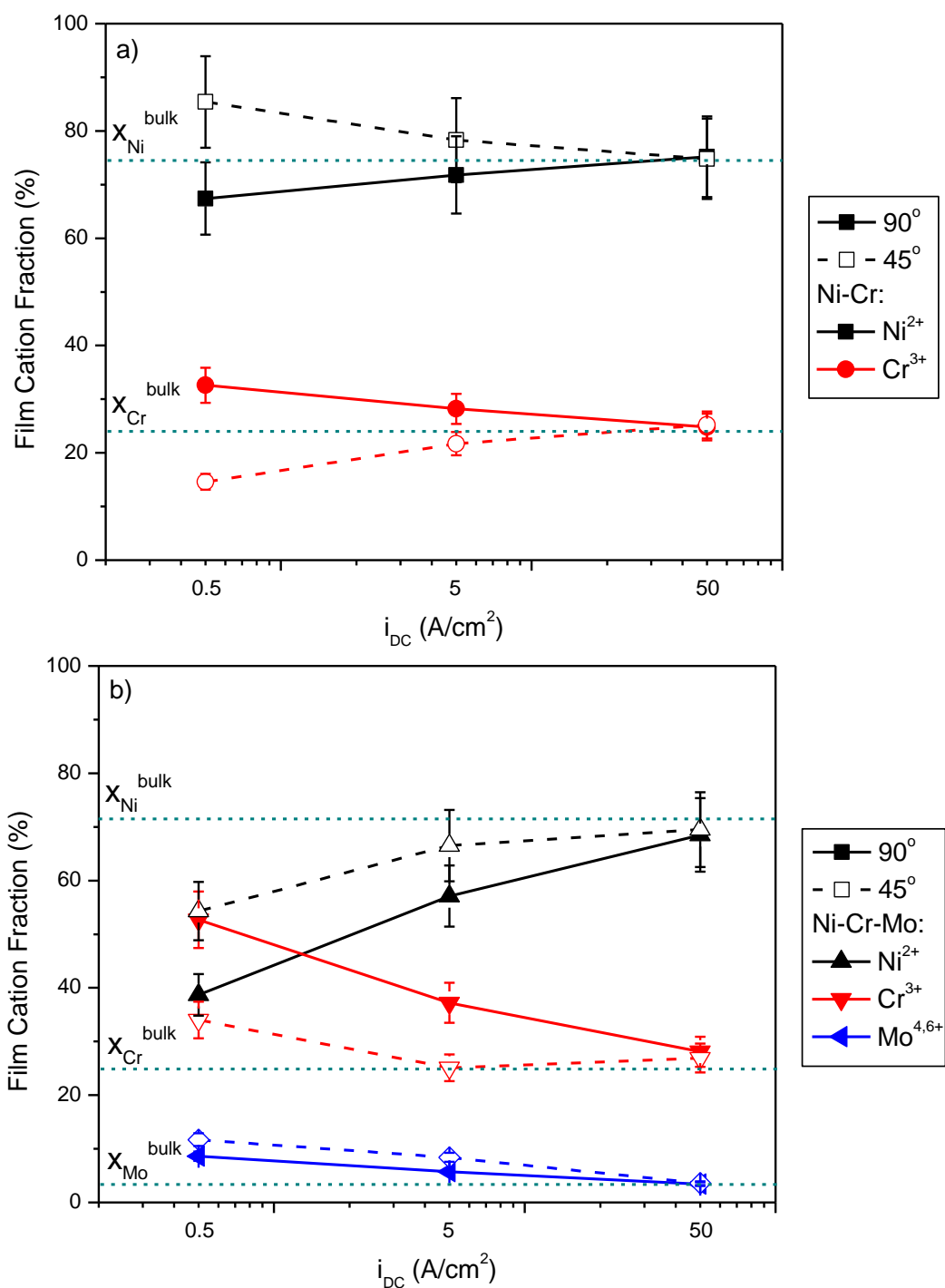


Figure 6.29. Film cation fraction according to angle-resolved XPS measurements at 90° and 45° on a) Ni-22 Cr and b) Ni-22 Cr-6 Mo, wt%, surfaces following galvanostatic passivation at 0.5, 5, and 50 $\mu A/cm^2$ until $+0.2 V_{SCE}$ was reached in 0.1 M NaCl pH 4

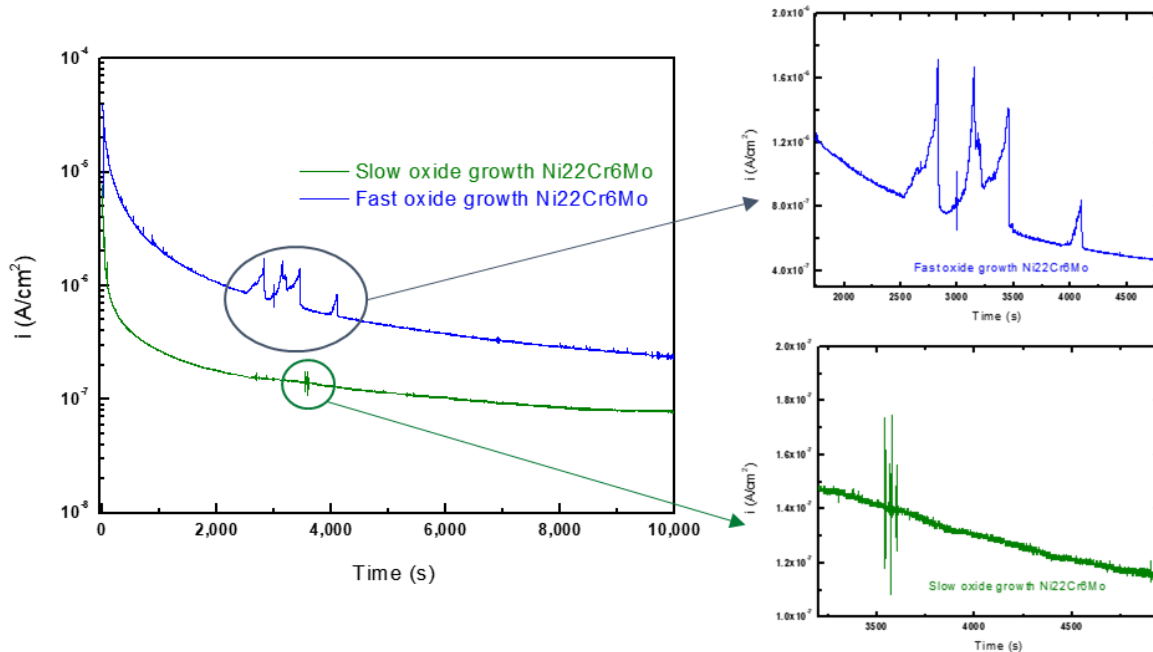


Figure 6.30. Comparison of the passivity of Ni-22 Cr-6 Mo, wt%, ribbons at +0.2 V_{SCE} for 10 ks immediately following slow oxidation at 0.5 $\mu\text{A}/\text{cm}^2$ and fast oxidation at 50 $\mu\text{A}/\text{cm}^2$ in deaerated 0.1 M NaCl pH 4

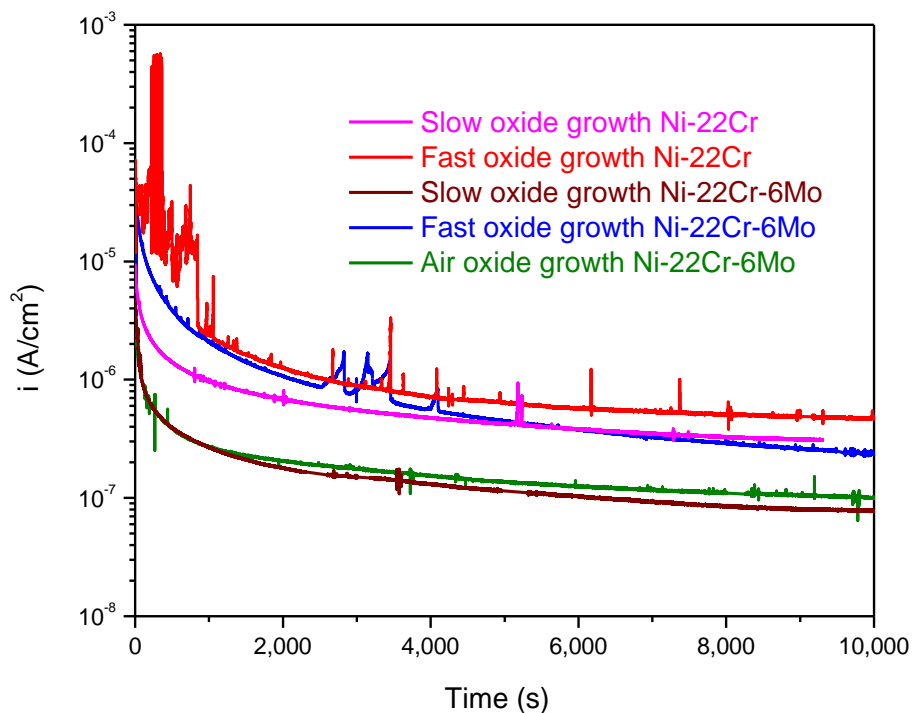


Figure 6.31. Comparison of the passivity of Ni-22Cr and Ni-22 Cr-6 Mo, wt%, ribbons at +0.2 V_{SCE} for 10 ks immediately following air oxidation for 1 yr, slow oxidation at 0.5 $\mu\text{A}/\text{cm}^2$, and fast oxidation at 50 $\mu\text{A}/\text{cm}^2$ in deaerated 0.1 M NaCl pH 4. Included are the results previously given in Figure 6.30.

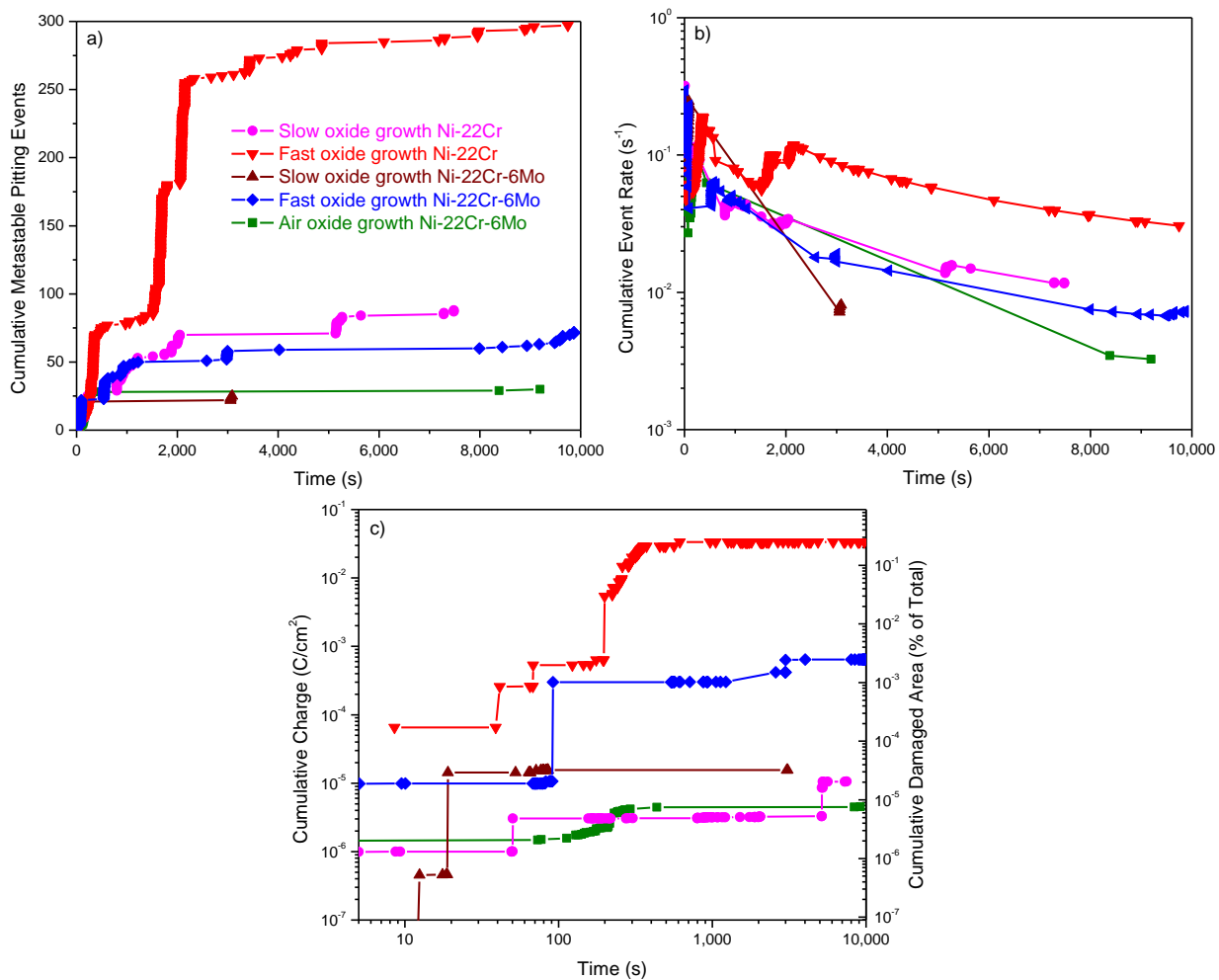


Figure 6.32. Comparison between the cumulative a) number, b) rate, and c) charge of metastable pitting events and the corresponding damaged area fraction relative to the total exposed one (0.1 cm²) following air, slow (0.5 μA/cm²), and fast (50 μA/cm²) passivation of Ni-22 Cr and Ni-22 Cr-6 Mo, wt%, in 0.1 M NaCl pH 4 (Figure 6.31)

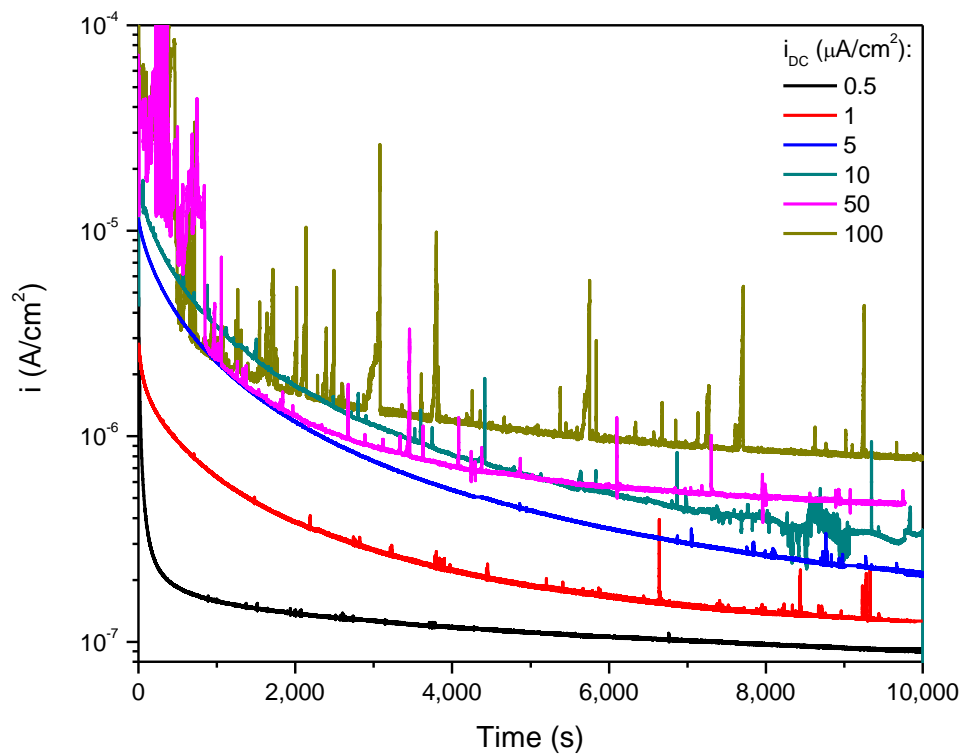


Figure 6.33. Metastable pitting events occurring for the passive films grown galvanostatically at various applied rates, i_{DC} , up to $+0.2 V_{SCE}$ on Ni-22 Cr, wt%, in 0.1 M NaCl pH 4

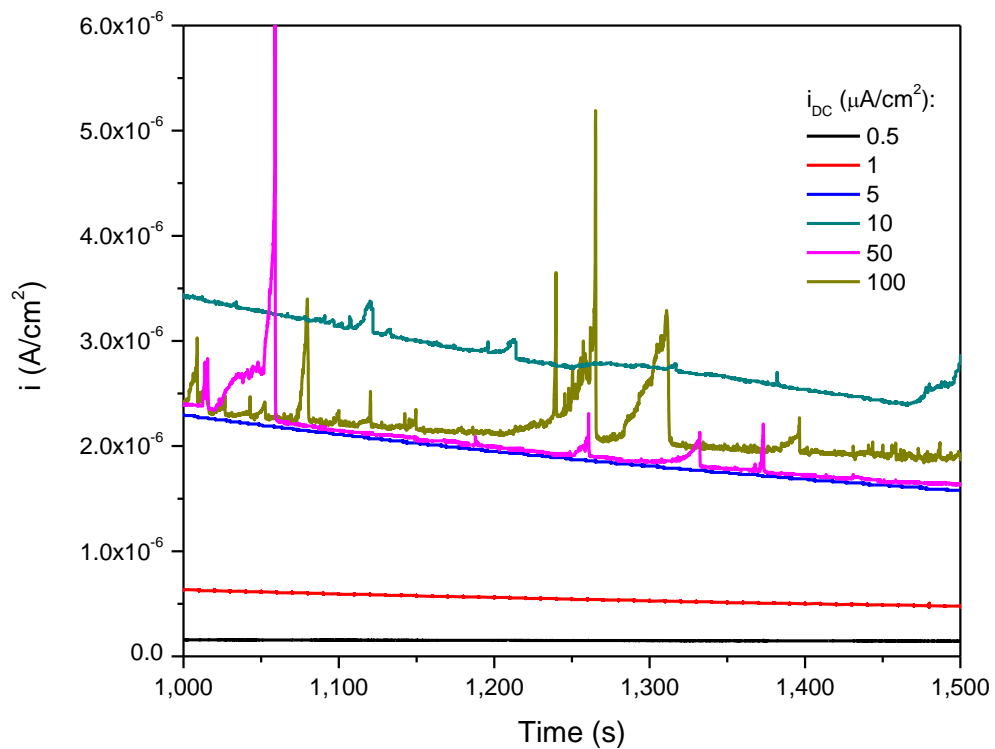


Figure 6.34. Focused metastable breakdown as given in Figure 6.33, for the passive films grown galvanostatically at various applied rates, i_{DC} , up to +0.2 V_{SCE} on Ni-22 Cr, wt%, in 0.1 M NaCl pH 4

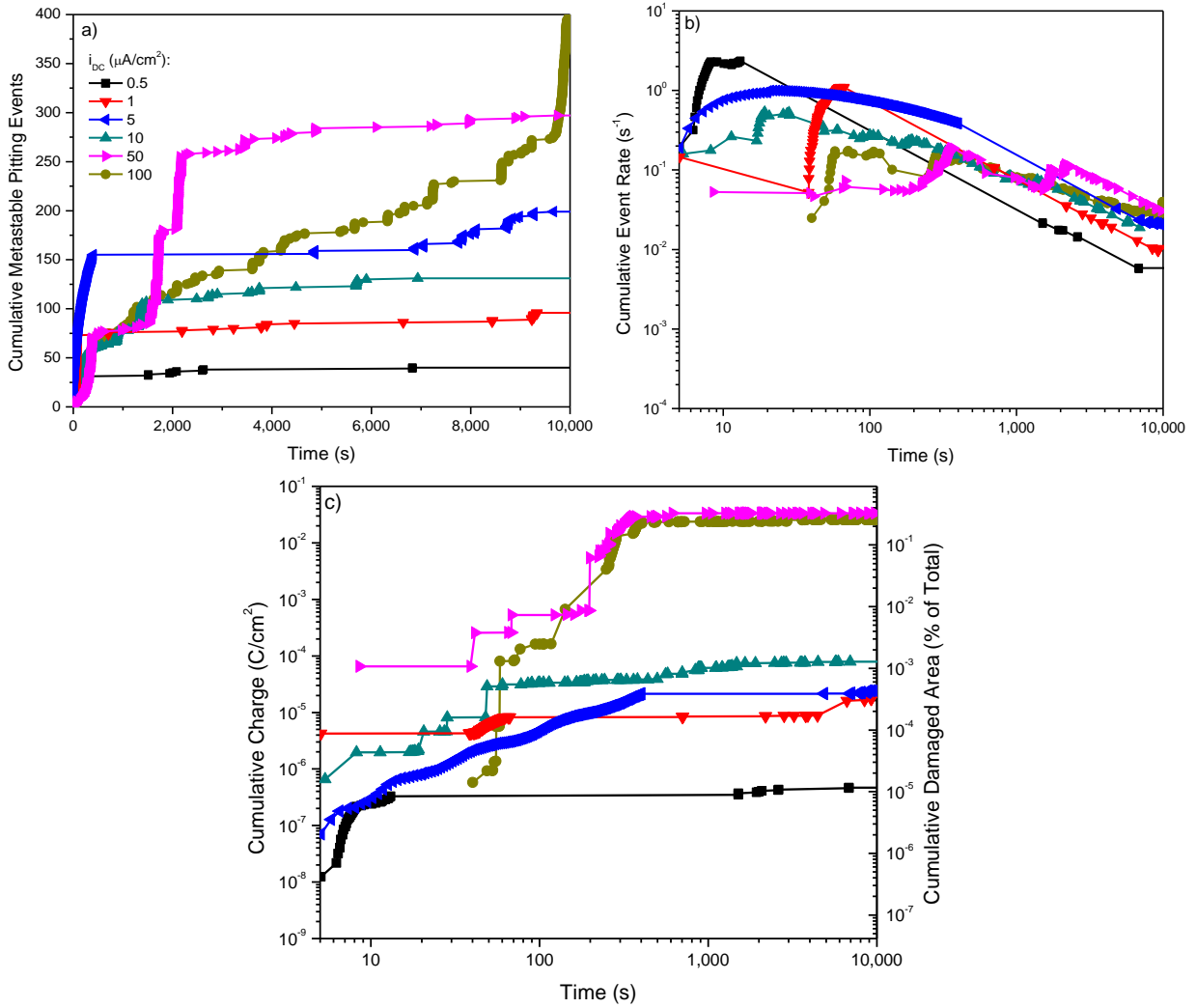


Figure 6.35. Comparison between the cumulative a) number, b) rate, and c) charge of metastable pitting events and the corresponding damaged area fraction relative to the total exposed one (0.1 cm^2) following galvanostatic passivation at varying rates, given by i_{DC} , of Ni-22 Cr, wt%, in 0.1 M NaCl pH 4 (Figure 6.33)

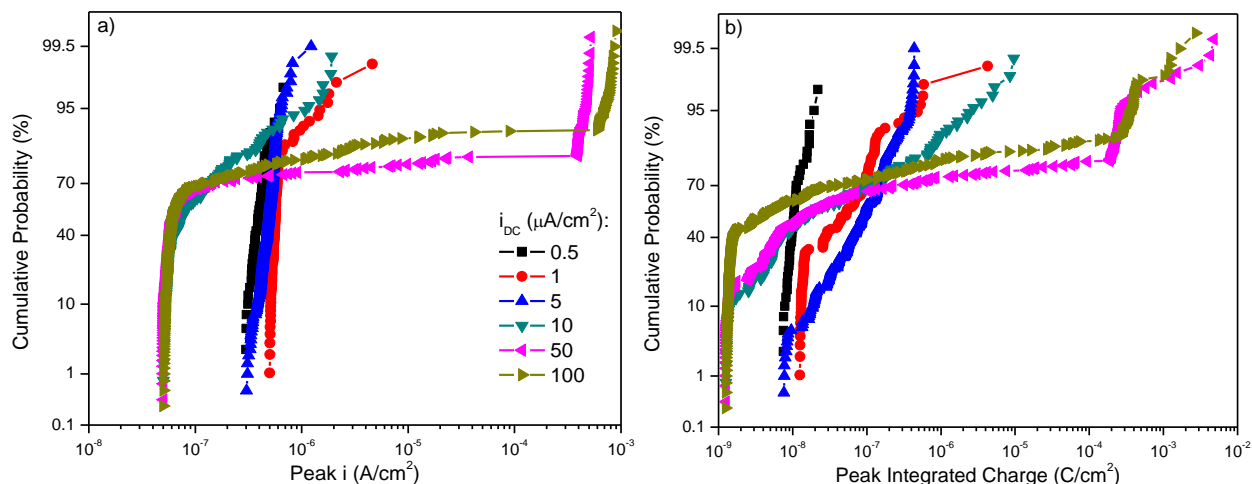


Figure 6.36. Cumulative probability plots of metastable peak a) current heights and b) integrated charge of events following galvanostatic passivation at varying rates, given by i_{DC} , for Ni-22 Cr, wt%, in 0.1 M NaCl pH 4 (Figure 6.33 and Figure 6.35)

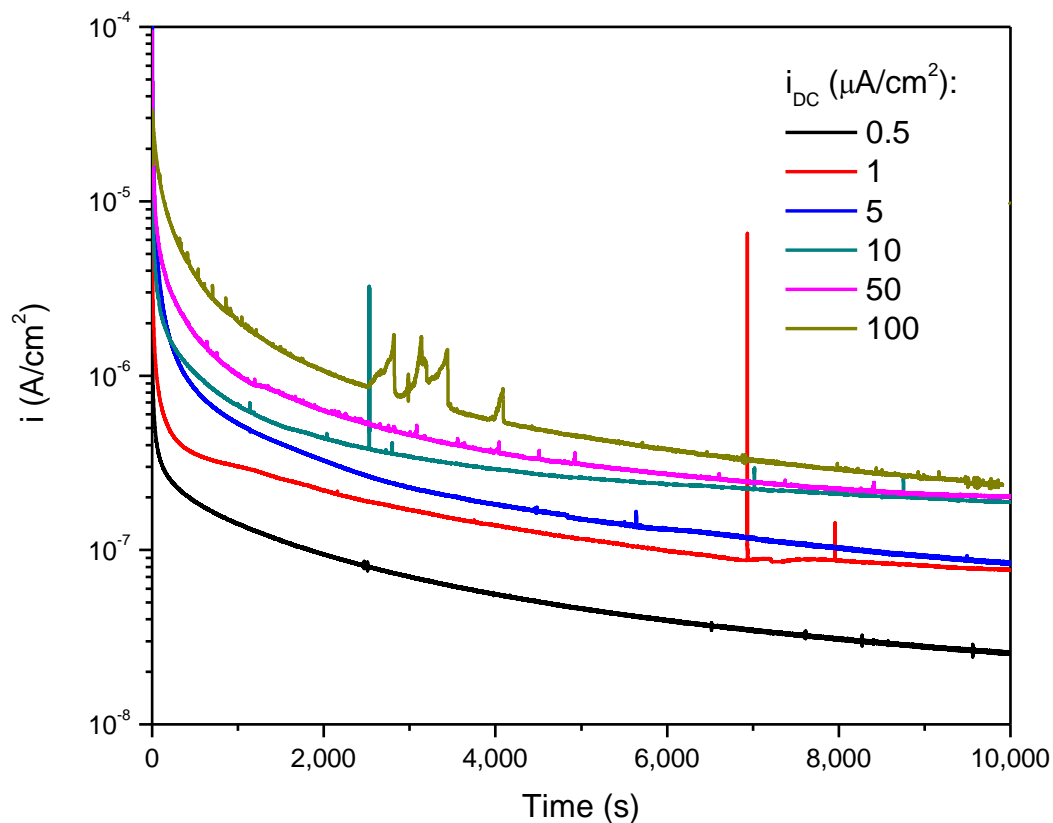


Figure 6.37. Metastable pitting events occurring for the passive films grown galvanostatically at various applied rates, i_{DC} , up to $+0.2 V_{SCE}$ on Ni-22 Cr-6 Mo, wt%, in 0.1 M NaCl pH 4

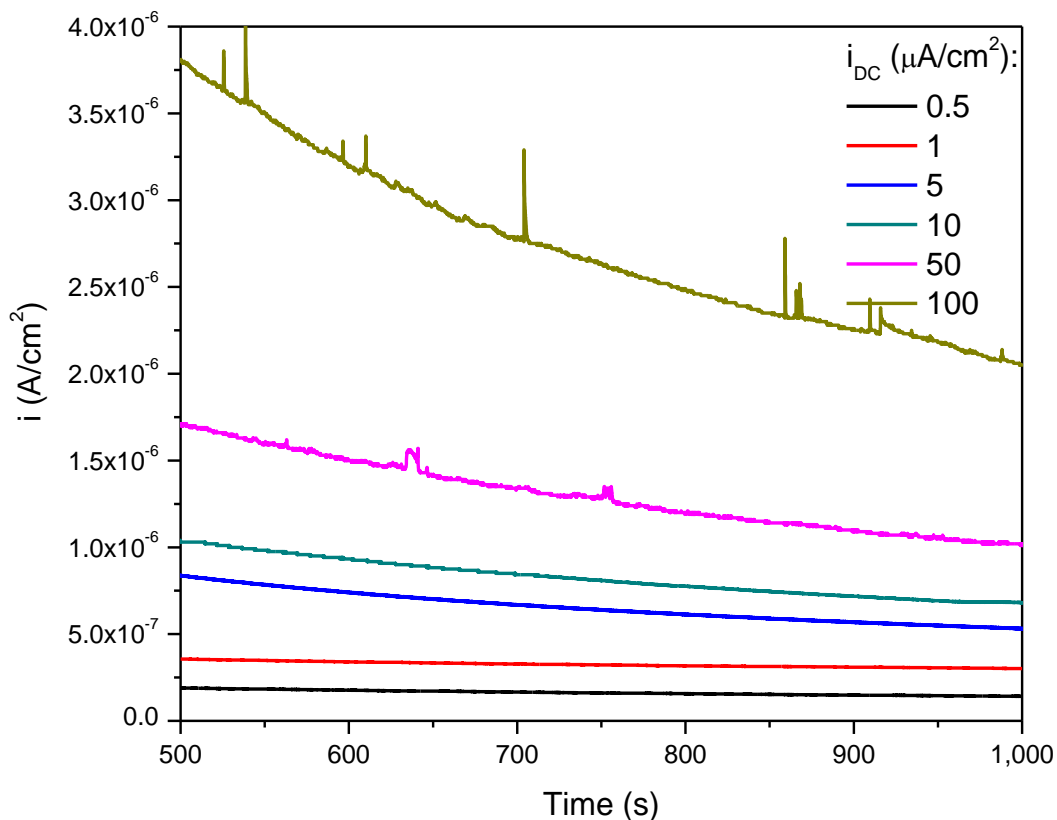
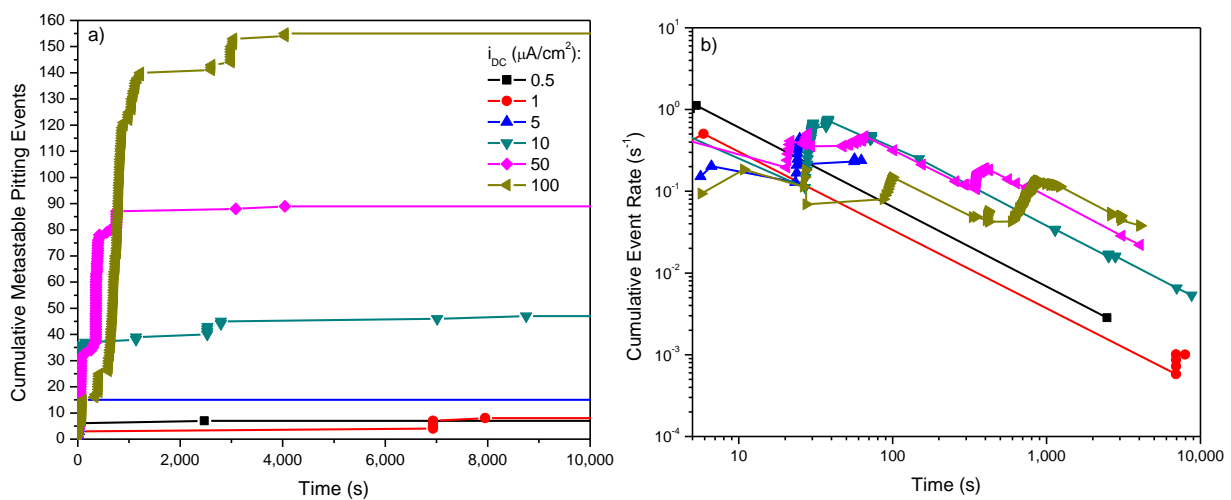


Figure 6.38. Focused metastable breakdown from 0.5 to 1.5 ks, as given in Figure 6.37, for the passive films grown galvanostatically at various applied rates, i_{DC} , up to +0.2 VSCE on Ni-22 Cr-6 Mo, wt%, in 0.1 M NaCl pH 4



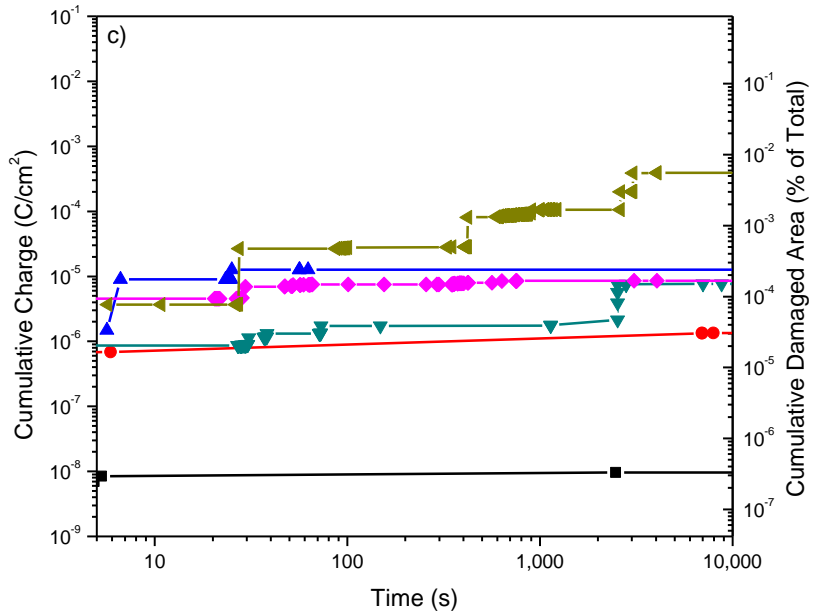


Figure 6.39. Comparison between the cumulative a) number, b) rate, and c) charge of metastable pitting events and the corresponding damaged area fraction relative to the total exposed one (0.1 cm^2) following galvanostatic passivation at varying rates, given by i_{DC} , of Ni-22 Cr-6 Mo, wt%, in 0.1 M NaCl pH 4 (Figure 6.37)

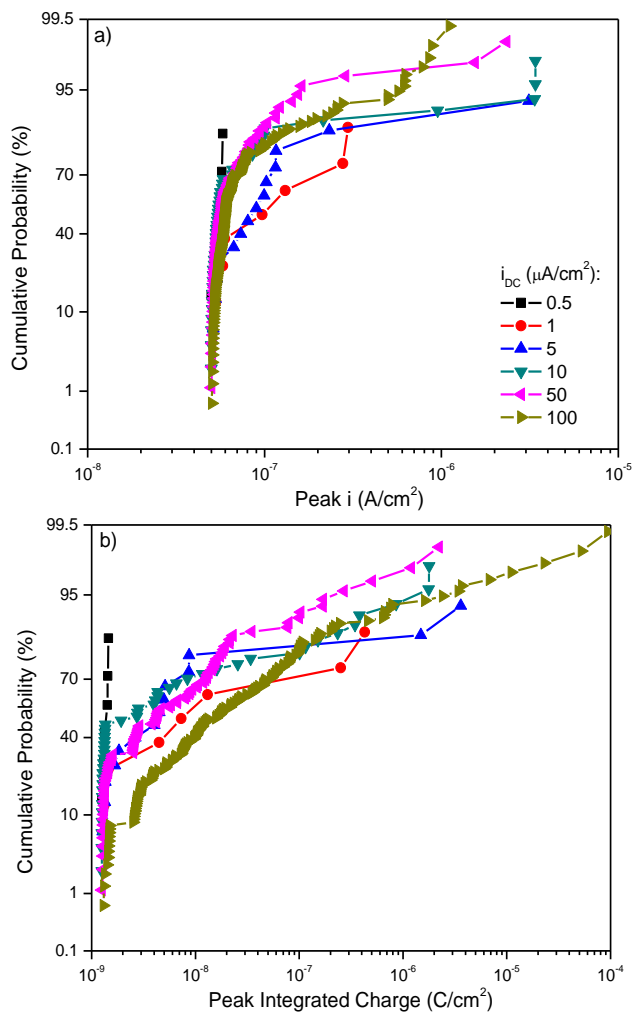


Figure 6.40. Cumulative probability plots of metastable peak a) current heights and b) integrated charge of events following galvanostatic passivation at varying rates, given by i_{DC} , for Ni-22 Cr-6 Mo, wt%, in 0.1 M NaCl pH 4 (Figure 6.37 and Figure 6.39)

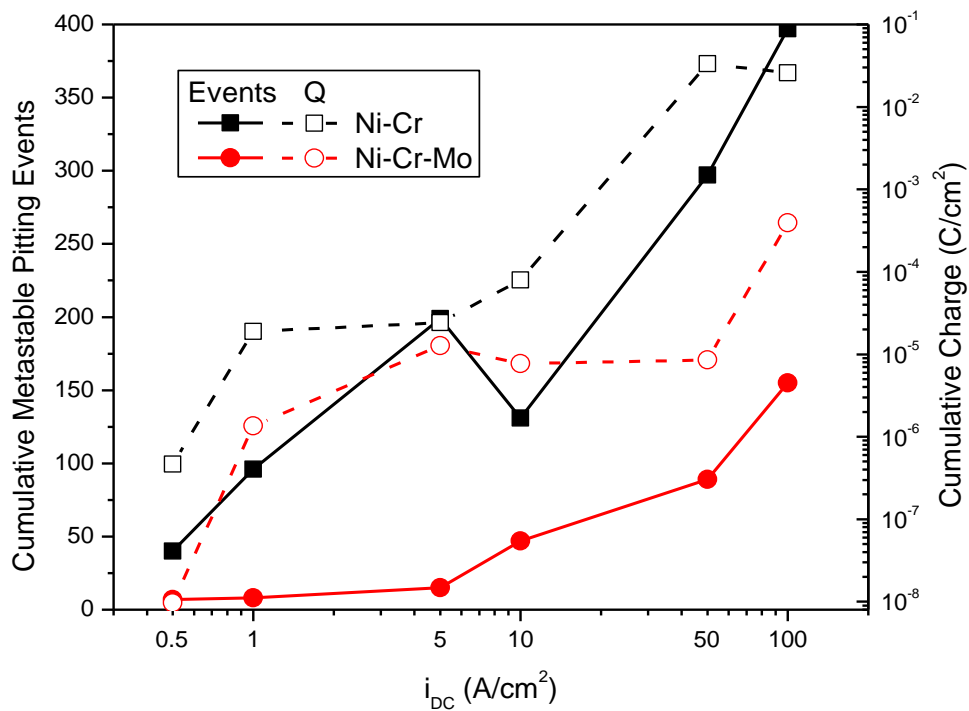


Figure 6.41. Average final cumulative number of metastable pitting events and charge during a +0.2 V_{SCE} hold for 10 ks on Ni-22 Cr and Ni-22 Cr-6 Mo, wt%, following passivation at varying galvanostatic rates, i_{DC} , in 0.1 M NaCl pH 4

7. Thesis Conclusions and Suggested Future Work

7.1 Conclusions

This dissertation further developed an understanding of the meso- and nano-scale properties of passive films and explained the effect and fate of Mo dopants on passive film properties and localized corrosion resistance in both acidic and alkaline sulfate and chloride environments following both fast, solute-captured and slow, phase-separated oxide growth. In addition, a better insight was reached of the influence of growth rate and solute capture on the physical, chemical, and electrochemical properties of passive films. These improvements in the understanding of passivation of Ni-Cr and Ni-Cr-Mo alloys was achieved through combinations of characterization techniques that bridged length and time scales. This notably involved the development of analysis tools for *in operando* passivation analysis, along with more conventional, albeit often not in tandem, application of *in situ* and *ex situ* techniques.

Aqueous oxide growth under potentiostatic conditions was investigated *in operando* using Single Frequency Electrochemical Impedance Spectroscopy (SF-EIS) in a chloride-free environment under both potential- and current-control. The oxidation current density, i_{ox} , was successfully monitored by SF-EIS. The measurement of *in operando* film thickness in real-time has revealed the significant impact of cation ejection during all stages of passivation in acid, especially at longer times, whilst highlighting the contribution of individual alloying elements on the reactions occurring. Processes governing oxide growth must be taken into consideration in order to construct accurate growth laws for thin film passivation. The temporal nature of α has a significant effect on application of SF-EIS as a result of variable film diffusional processes at different time scales. The variations in $\alpha(t)$ during electrochemical passivation are reported. In general, it was found that α increased with time as the passive films nucleated, grew, and converged into a conformal layer. These relatively small changes can result in large experimental errors at early times, as the common convention is to use the α measured after passivation and $l_{ox}(t)$ is exponentially dependent on α . However, it is unclear whether the early values are impacted by the exposed metal surface before the film converges and thickens, resulting in a validation of using the steady-state α . There was also a strong observed influence of solution chemistry and alloying content, where the presence of chlorides espouses diffusion and film growth. The charge transfer inherent to semiconducting films results in $\alpha < 1$ at all times, but each

alloy exposed to each solution has relative increases or decreases in its diffusion behavior. The measured ρ_{δ} similarly varied with alloying content and exposure environment.

The passivation and dissolution of Ni-22 Cr and Ni-22 Cr-6 Mo, wt%, were then investigated *in operando* during potentiostatic conditions using coupled on-line electrochemical ICP-MS and SF-EIS in both an acidic and alkaline Na₂SO₄ environment, coupled with *in situ* NR and *ex-situ* XPS conducted during and following film growth. The combination of the techniques utilized enabled determination of i_{ox} distinctly from i_{EC} with high temporal resolution. It was determined that Ni-rich films form early during the passivation process, indicating the substantial influence of kinetic factors. At longer times, Cr³⁺ enrichment was observed when thermodynamics began to dictate the film composition. Surface films produced during anodic polarization at +0.2 V_{SCE} were consistent with non-stoichiometric solid solution rocksalt and corundum oxide structures, likely containing solute captured Ni²⁺, Cr³⁺, and Mo^{4,6+} cations. No substantial layering was observed during oxide formation, with the films instead being Ni-rich at the film/electrolyte and Cr-rich at the metal/film interfaces. Oxides were first formed, with compositions governed by non-equilibrium solute capture. The electrochemical stability of Cr³⁺ cations also increased with alloying of Mo in the base metal, noted by the respective dissolution currents being measured below the detection limit for the Ni-Cr-Mo alloy in each environment. Surface films produced during anodic polarization in the alkaline environment were found to be enriched in Ni²⁺ cations because of the increased stability of NiO and Ni(OH)₂.

The same methodology was applied towards the passivation of the model alloys in an acidic and alkaline environment. Contrary to the previous results which suggested rapid Cr₂O₃ formation in a chloride-free environment, it was determined that both Ni and Cr-rich films form early during the passivation process, indicating the combined influence of thermodynamic and kinetic factors. Oxides were first formed, with compositions governed by non-equilibrium solute capture. This phenomenon resulted in Moⁿ⁺ doping of the passive film on Ni-Cr-Mo and as a result, improved passivity and increased amounts of Cr³⁺ enrichment were observed for all conditions. This is posited to occur by the interaction between the positively-charged substituted Mo site and negatively-charged metal cation vacancies, forming less mobile, neutral defects. Passivation in an alkaline environment similarly resulted in greater stability of Ni²⁺ within the film, demonstrated through ICP-MS and XPS measurements of the passive film composition. At long times, kinetic

factors enabled enrichment whereas thermodynamics determined the longer-term passive film behavior.

To better the singular effect of Mo on enabling passivity and resisting localized film breakdown, several Ni-22 Cr-x Mo alloys, where $x = 3, 6, 9,$ and $12, \text{ wt}\%$, was investigated during *in operando* potentiostatic passivation at $+0.2 \text{ V}_{\text{SCE}}$ using SF-EIS in an acidified 1.0 M NaCl environment. *In situ* impedance sweeps were obtained during film growth to enable Mott-Schottky analysis of the electronic behavior of the passive oxides. Similarly, angle-resolved XPS spectra unveiled the chemical identity of the passive films. The results upheld the literature theory that increasing the alloying concentration of Mo in a Ni-Cr matrix increases the fraction of Cr^{3+} cations within the passive films produced during anodic polarization. The influence of Mo on lessening the thermodynamic and kinetic barriers for the early nucleation and enrichment of Cr_2O_3 rather than NiO was also evident. Results were consistent with Mo doping, but no proof was obtained. Varying the bulk concentration of Mo resulted in significant electronic benefits and drawbacks following $\text{Mo}^{4,6+}$ solute within the Ni^{2+} and Cr^{3+} -rich passive film. Notably, excessive doping of the surface film on the $12 \text{ w}\%$ Mo alloy resulted in poorer localized corrosion behavior than the $9 \text{ wt}\%$ Mo, despite its increased Cr^{3+} content. This suggests that the latter alloy affords more optimal corrosion behavior overall in the acidic 1.0 M NaCl environment.

Finally, The implications of nonequilibrium solute capture (NSC) and imposed passivation rates were investigated for Ni-22 Cr and Ni-22 Cr-6 Mo ($\text{wt}\%$) during *in operando* galvanostatic conditions using SF-EIS in an acidic NaCl environment, coupled with subsequent *in situ* Mott-Schottky impedance scans, metastable pitting analysis, and *ex situ* AFM and AR-XPS characterization. Faster galvanostatic passivation was found to result in films representative of NSC with no cation segregation. However, there was a substantial decline in the electrochemical performance, characterized as an increase in the frequency and size of metastable pitting events, observed for Ni-Cr films. Beneficial solute capture of $\text{Mo}^{4,6+}$ cations, however, facilitated the inhibition of breakdown and the formation of conformal, Cr^{3+} -enriched films which provided for greater protection to the base alloy. Films grown slowly exhibited segregation of Cr^{3+} towards the metal/film interface whereas Ni^{2+} and $\text{Mo}^{4,6+}$ were preferentially located at the film/electrolyte interface. The relatively low defectiveness, characterized topographically and electronically, resulted in less frequent and damaging film breakdown occurring. In addition, greater

concentrations of Cr^{3+} . The occurrence of diffusive processes during this substantially longer passivation enabled the local accumulation of like cations and at longer times, aging of the films would likely produce local NiO and Cr_2O_3 phases that eventually coalesce into conformal layers.

7.2 Future Work

The fundamental understandings of Mo's role during passivation and repassivation presented in this dissertation can be further enhanced through additional study. Because of the limited time and scope of this research, several experiments were limited. This includes most notably the NR and ICP experiments. The difficulty to deposit specific alloy compositions resulted in the exclusion of NR from Task 4 on Ni-Cr-x Mo alloys. With more precise study, this could be accomplished in the future. Similarly, experimental challenges resulted in ICP-MS not being possible for the Ni-Cr-x Mo alloys. The results would greatly facilitate the presented understanding of Mo facilitating Cr-enrichment such that some pseudo-layers become formed due to chromia precipitation within the oxide layer. The significant enrichment of Mo with greater [Mo] in the bulk alloys would also become evident in the SLD profile, unlike those shown in this thesis. As for the NR measurements, these were cut short at the Canadian Nuclear Laboratory due to the shutdown of the beam line. This resulted in the Ni-Cr and Ni-Cr-Mo materials not being studied in 0.1 M Na_2SO_4 pH 10. In the future, this could be accomplished at another facility, such as Oak Ridge National Labs. Similarly, the effect of passivation rate was not quantified using these techniques. In particular, NR could have demonstrated the existence of distinct layers of NiO/Ni(OH)₂ and $\text{Cr}_2\text{O}_3/\text{Cr(OH)}_3$ within the passive film following sufficiently slow oxidation.

Along with Mott-Schottky, ellipsometry can provide similar *in situ* characterization of the electronic properties of passive films. One critical parameter for SF-EIS was not investigated in this thesis: ϵ . This has been assumed to be 30 for all Ni-based alloys based on modeling performed for C-22. Measurements of this parameter alone would facilitate more accurate application of the SF-EIS method and computation of l_{ox} . Ellipsometry can also provide some thickness measurements and chemical information during electrochemical processes, making it a powerful technique that should be utilized in future work. A newer technique, microwave capacitance microscopy (MCM) could also potentially enable measurements of a passive film's dielectric constant, but also spatially through use of an AFM tip. Future work using this method could demonstrate the accumulation of charge locally before pitting initiates. Measurements for various

alloys grown in different environments would facilitate the electrochemical metastability analysis given previously in this thesis.

Finally, there is new availability of classically *ex situ* techniques which can now characterize materials *in situ* or perhaps even *in operando*. These, when applied to study passive films, are capable of achieving the desired atomic-scale characterization that has been desired by ongoing research efforts. Most notably, improvements of *in situ* TEM and XPS techniques can facilitate study of the evolution of passive films during electrochemical conditions.